ISSN 0288-4534
CODEN:KONAE7

KONA

POWDER AND PARTICLE

No. 9 (1991)

Published by The Party of Powder Technology (JAPAN)

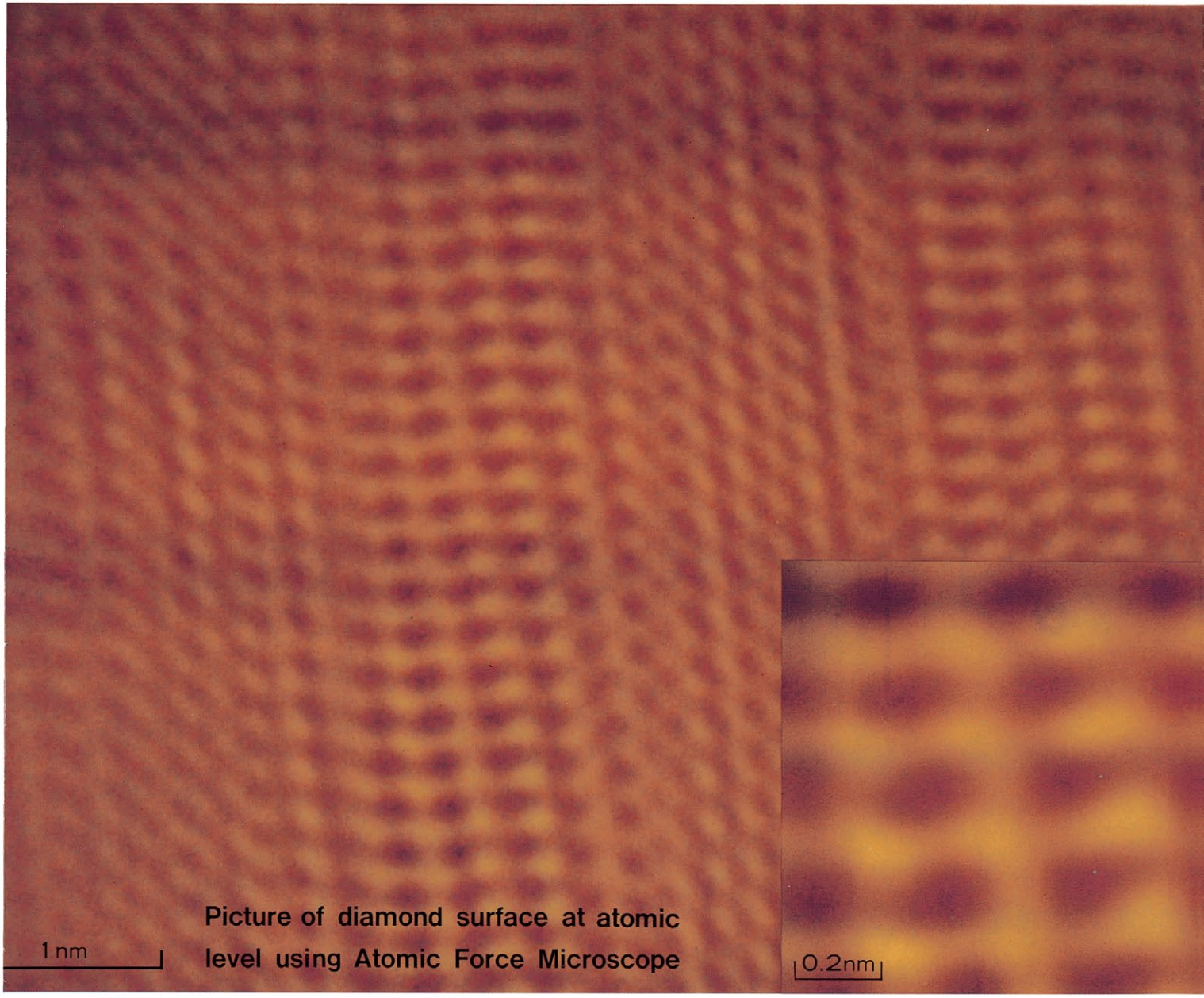

Picture of diamond surface at atomic level using Atomic Force Microscope

KONA

POWDER AND PARTICLE

KONA, being issued annually by the Party of Powder Technology, Japan since 1983, is a refered journal containing articles on powder science and technology which is circulated to interested parties throughout the world.

Explanation of the Cover

"粉"; This Chinese character is pronounced as "KONA" in Japanese and means "Powder". "粉" on the front page was written by the late Mr. Eiichi Hosokawa, founder of Hosokawa Micron Corporation.

Hosokawa Micron Corporation and its R&D Center

Editorial Board

K. Miyanami*	Editor in Chief (Univ. of Osaka Prefecture, JAPAN)
Asian Block	
Y. Kousaka	Block Vice Chairman (Univ. of Osaka Prefecture, JAPAN)
N. Yoshioka	(Okayama Univ. of Science, JAPAN)
G. Jimbo**	(Nagoya Univ., JAPAN)
M. Arakawa	(Former k yoto Institute of Tech., JAPAN)
T. Oshima	(Himeji Institute of Tech., JAPAN)
Y. Morikawa	(Osaka Sangyo Univ. JAPAN)
H. Masuda	(Kyoto Univ. JAPAN)
Y. Tsuji	(Osaka Univ. JAPAN)
H. Emi	(Kanazawa Univ., JAPAN)
Y. Kuwahara	(Government Industrial Research Institute, Nagoya, JAPAN)
T. Yoshida	(Hosokawa Micron Corp., JAPAN)
T. Yokoyama	(Hosokawa Micron Corp., JAPAN)
Secretariat	
T. Suzuki	(Hosokawa Micron Corp., JAPAN)
F. Nakagawa	(Hosokawa Micron Corp., JAPAN)
European Block	
J. Schwedes	Block Chairman (Univ. Braunschweig, GERMANY)
B. Scarlett	Block Vice Chairman (Delft Univ. of Technology, NETHERLAND)
K. Schönert	(Technische Univ. Clausthal, GERMANY)
F. Löffler	(Univ. Karlsruhe, GERMANY)
H. Schubert	(Bergakademie Freiberg, GERMANY)
E. Forssberg	(Univ. Lulea, SWEDEN)
S. R. de Silva	(Postec-Research, Porsgrunn NORWAY)
D. Ocepek	(Univ. Ljubljana, YUGOSLAVIA)
J. F. Davidson	(Univ. of Cambridge, UNITED KINGDAM)
G. Ferrara	(Univ. di Trieste, ITALIA)
Secretariat	
D. Schwechten	(Alpine AG, GERMANY)
Americas Block	
M. McLaren	Block Chairman (State Univ. of Rutgers, U.S.A.)
T. P. Meloy	Block Vice Chairman (West Virginia Univ., U.S.A.)
J. P. Clark	(Massachusetts Institute of Tech., U.S.A.)
R. K. Rajamani	(Univ. of Utah, U.S.A.)
H. Herman	(State Univ. of New York, U.S.A.)
B. H. Kaye	(Laurentian Univ., CANADA)
L. Hixon	(Hosokawa Micron Inter., U.S.A.)
W. Gregg	(Hosokawa Micron Inter., U.S.A.)
Secretariat	
J. Van Cleef	(Hosokawa Micron Inter., U.S.A.)

■Publication Office

The Party of Powder Technology (Japan)
in **Hosokawa Micron Corporation**
No.9, 1-chome, Shoudai Tajika, Hirakata-shi, Osaka 573 Japan

■Notes

- ○Sponsored by Hosokawa Micron Group
- ○ *K. Miyanami is new editor in chief from next issue, No.10(1992).
- ○**G. Jimbo is editor in chief of this issue, No.9(1991).

(Complimentary Copy)

Printed in Japan

KONA

GENERAL INFORMATION

HISTORY OF THE JOURNAL

In 1983 The Party of Powder Technology, Japan (The PPT), a non profit making organization, resolved to publish in Japan, in English, a publication which would provide a worldwide audience with superior Japanese original monographs dealing with powder science and technology. The PPT obtained sponsorship of this project from Hosokawa Micron Corporation (HMC). As a result the annual journal "KONA" was born. KONA was published annually through 1989 (No.7).

It was agreed that it would be appropriate to internalize KONA and to incorporate monographs in English from authors throughout the world. This action began with KONA No.8 (1990).

AIMS AND SCOPE OF THE JOURNAL

KONA Journal is to publish papers in the broad field of powder science and technology which may range from fundamental principle to practical applications. Papers discussing technological experience and critical reviews of existing knowledge in specialised areas will be welcomed.

Paper will be published only when they are judged, by the Editor to be suitable for the progress of powder science and technology, and are approved by each block editorial committee. A paper submitted to the Editorial secretariat journal has not been previously published except translated papers which are selected by block Editorial Committee.

TYPES OF PAPER

- Request papers
  Original research and review papers requested by block KONA Editorial Committee
- Papers of contribution
  Original research and review paper contributed to each KONA Editorial Committee, and refered by the Editors
- Translated papers
  Papers translated into English which are published, selected by the block KONA Editorial Committee, approved by the anthor and copyright holder.

SUBMISSION OF PAPER

Papars should be sent to each block KONA Editorial Secretariat.

- Asian Block Editorial Secretariat
  T.Suzuki or F.Nakagawa
  Hosokawa Micron Corporation Micromeritics Lab.
  No.9, 1-chome, Shoudai Tajika, Hirakata Osaka 573 JAPAN
- European Block Editorial Secretariat
  D.Schwechten
  Alpine AG
  Peter-Dorfler-Strasse 13-25
  Postfach 10 11 09
  D-8900 Augsburg 1
  GERMANY
- Americas Block Editorial Secretariat
  J. Van Cleef
  Hosokawa Micron International Inc.,
  Micron Powder System Div.
  10 Chatham Road Summit, NJ 07901
  U.S.A.

FREQUENCY

KONA journal will be published once each celender year.

SUBSCRIPTION

KONA is distributed free of charge to senior researchers of universities and laboratories as well as to institutions and libraries in this field throughout the world. The publisher is always glad to consider the addition of names of those who wish to obtain this journal regularly to mailing list. Distribution of KONA is made by each Block Secretariat.

INSTRUCTIONS TO AUTHORS

(1)Manuscripts format

- Two copies should be submitted to the Editorial Secretariat, in double-spaced typing on pages of uniform size.
- Authorship is to give author's names, and the mailing address where work was carried out in title page.
  If the present address is diffeent, indicate this in a footnote.
- Abstract of 100-180 words should be indicated at the beginning of the paper.
- Nomenclature should appear at the end of each paper. Symbols and units are listed in alphabetical order with their definitions and dimensions in SI units.
- Literature refernces should be numbered and listed together at the end of the paper, not in the footnotes. Alphabetical order is accepted. Give complete informations as in following examples;
  1) Carslaw, H.C. and J.C.Jaeger: "Conduction of Heat in Solids," 2nd ed., Clarendon Press, Oxford, England (1960).
  2) Howell, P.A.: US Patent, 3,114,603 (1963)
  3) Rushton, J.H., S.Nagata and D.L. Engle: AICHE J., **10**, 298 (1964).
  4) Seborg, D.E.: Ph. D.Dissertation, Princeton Univ., N.J.,U.S.A. (1969).
- Original figures with one copy should be submitted, on separate sheets. Authors' names and figure numbers are marked in corner.
- Figure numbers and captions are listed on a separate sheet.
- Place of figure insertion is to be indicated in the margin of the manuscript.
- Tables should be type on separate sheets.

(2) Reprints

- The author shall receive 50 free reprints. Additional reprints will be furnished when ordered with return of galley proofs.

(3)Publication policy

- All papers submitted for publication become immediately the property of the PPT and remain so unless withdrawn by the author prior to acceptance for publication or unless released by the Editor. Papers are not to be reproduced or published in any form without written permission of the PPT.

Contents

〈**Translated Research paper**〉
- Thermophoresis Velocity of SiO_2 Ultrafine Particles in a Flame — *Korekazu Ueyama, Koichi Miyagawa, Shintaro Furusaki, Hideyo Kawazoe, Akira Iino and Yoshikazu Matsuda* 3
- Particle Size Analysis for Micro-Particles by Capillary Hydrodynamic Chromatography — *Naohiro Shiragami* 13
- The Estimation of Packing Characteristics by Centrifugal Compaction of Ultrafine Particles — *Mitsukuni Mizuno, Atsushi Fukaya and Genji Jimbo* 19
- Dispersion and Continuum Models of Powder Elasticity — *Hirosuke Okamoto* 28
- Relationship between Adhesive Force and Dispersibility of Sub-micron Particles — *Hideo Yamamoto and Shuhei Shinji.* 36
- Computer Simulation on Aggregated Structure of Fine Particles in Slurry — *Takatoshi Kimura, Masafumi Arakawa, Kiyoshi Hirota and Hitoshi Murata* 44
- Dispersion of SiO_2 by Coating with a Thickness of Nano-meters on the Surface of Fine α-alumina Powder — *Mutsuo Sando, Masanobu Awano, Yoshinori Uwamino and Yoshitaka Kuwahara* 54
- Experimental Control of Preparation of Thin Film and Fine Particles by CVD — *Kentaro Oshima, Yoshifumi Torimoto, Keiichi Tsuto and Kikuo Okuyama* 59
- Preparation of Ultrafine Particles by Nanopowder Process-Factors for Milling Rate and Contamination– — *Masamitsu Nishida, Hamae Ando. and Koichi Kugimiya* 72

〈**Review paper**〉
- Preparation of Micro-Controlled Particles Using Aerosol Process Technology — *Kikuo Okuyama, Kentaro Oshima and Keiichi Tsuto.* 79
- Application of Fuzzy Control to Processes Handling Granular Materials and Powders — *Kenzou Wada* 94

〈**Original Research paper**〉
- Dry Powder Size Analysis for Dry Powder Processes — *Janez. Stražišar* 107
- An Electromechanical Valve for Solids — *Mojtaba Ghadiri and Catherine M. Martin* . 113
- Mineral Liberation -Infuence of the curvature of the interfacial surface on the locking Profile at Different Comminution Size — *Ugo Preti* 124
- Air Classification: Computer Models and Experimental Results — *S.R. de Silva D.C. Walsh, S.T. Johansen T. Bergstrom and S. Bernotat* 130
- New Wet Classification Hydrocyclones for Fine Mineral Slurries — *Kari Heiskanen* 139

〈**Review Paper**〉
- Characteristics of Comminution with High Pressure Roller Mills — *Klaus Schönert.* 149
- State Diagrams of Gas/Solid Flows with Partial Phase Separation — *O.Molerus and K.-E. Wirth* 159
- Electrically Charged Air Filters — *R.C. Brown* 174
- Powders for Thermal Spray Technology — *Herbert Herman* 187
- Field-Flow Fractionation:A Versatile Technology for Particle Characterization in the Size Range 10 ^{3}to 10^{2} Micrometers — *J. Calvin Giddings, S. Kim Ratanathanamangs and Myeong Hee Moon* 200
- Describing Filtration Dynamics from the Perspective of Fractal Geometry — *Brain H. Kaye* 218

- Information Articles . . . . . .

See page 18 for description of the cover photograph.

Thermophoresis Velocity of SiO_2 Ultrafine Particles in a Flame †

Korekazu Ueyama
Dept.of Engineering Science, Osaka Unirersity *

Koichi Miyagawa and Shintato Furusaki
*Dept.of Chem.Engineering, Tokyo Univeresity***

Hideyo Kawazoe, Akira Iino and Yoshikazu Matsuda
*Chiba Research Lab.of Furukawa Electric Industry Co****

Abstract

Thermophoresis of ultra - fine SiO_2 particles formed in a flame was experimentally investigated by setting an adhering surface perpendicular to a flame axis. The following results were obtained. 1) Near the adhering surface, the number density of particles is considered to increase up to almost twice that in a flame. This is because the approaching velocity of particles decreased to about half of its original value keeping the cross sectional area of the flowing region constant. 2) The thermophoresis velocity was 1.0~1.4cm/s. 3) A particle diameter corresonding to the thermophoresis velocity is 0.4~0.8μm, which is larger than a particle diameter measured in a flame, that is, 50~60nm. 4) Particles are considered to adhere to each other in the vicinity of the surface. 5) A main mechanism of particle adhesion is thermophoresis, and the effect of inertia can be neglected.

1. Introduction

It is important to understand the adhesion of ultrafine particles produced in a vapor phase reaction to a cooling surface for controlling the field and products of the vapor phase reaction as well as collecting the ultrafine particles. The adhesion of particles to the cooling surface is considered a thermophoresis phenomenon in a sharp temperature gradient fieid. Since the thermophoresis velocity of spherical ultrafine particles have been theoretically and experimentally determined, it can be estimated as a function of the temperature gradient and particle diameter[1]. Ultrafine partticles produced in the vapor phase reaction are, however, not necessarilly spherical and sometimes adhered to each other into secondary particles in complicated shape.

The purpose of this study is to determine the thermophoresis velocity by adhering ultrafine SiO_2 particles produced in a flame to a substrate placed above the flame and compare the *in situ* measurements of ultrafine particles in the flame with those estimated from the thermophoresis velocity.

2. Experimental Apparatus and Method

2.1. Apparatus and gas flow rate

A VAD burner has a quardruplex tube in which $SiCL_4$ as the raw material together with the argon carrier gas (Ar) in the center tube and successively hydrogen (H_2), argon as the sealing gas and oxygen (O_2)in the outer space are passed. The tube O.D.is 17.3mm. The flow

* 1-1, Machikane yama, Toyonaka, osaka 560 Japan
TEL 06-844-1151

** 7-3-1, Hongo, Bunkyo-ku, Tokyo 113 Japan
TEL 03-3812-2111

*** 6, Hachiman Kaigan-dori, Ichihara, Chiba 290

† This report was originally printed in *J. Soc. Powder Technology, Japan,* **26** , 558-564 (1989) in Japanese, before being translated into English with the permission of the editorial Committee of the Soc. Powder Technolory, Japan.

rate of $SiCl_4$,O_2 and H_2 are fixed in accordance with the operating conditions of VAD. The flow rate of those gases are shown in **Table 1.** $SiCl_4$ is hydrolyzed or oxidized in a VAD flame into ultrafine SiO_2 particles which are adhered to a stainless steel substrate 40mm wide and 90mm long placed 4cm above the burner. The configuration ob the substrate and burner is illustrated in **Fig.1.**

Table 1 Gas Flow Rate

	Flow Rate at 273K and 10^5Pa $[m^3/s]$
Carrier Ar	8.3×10^{-7}
H_2	3.3×10^{-5}
Seal Ar	2.5×10^{-5}
O_2	6.7×10^{-5}

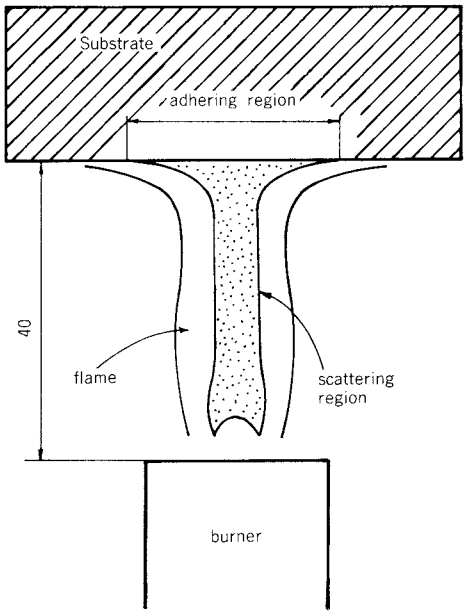

Fig. 1 Expeximental System

2.2 Objects to be measured and measuring methods

2.2.1. Velocity of particle

The velocity destributions of SiO_2 particles in the flame and in the vicinity of the substrate were determined by laser Doppler velocimetry (LDV)[2] using an argon ion laser (wavelength : 514.5nm). Since the linear velocity of the particles in the flow direction was as high as approximately 3m/s, it is necessary to accurately cross two beams split at the beam splitter each other at an angle as small as one degree. Although the crossing of two beams is usually checked with a pinhole, it is very difficult to adjust the optical axis of the beams crossing at such a small angle only

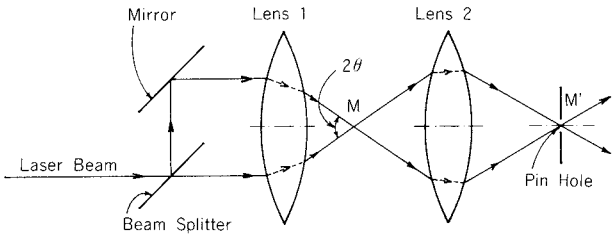

Fig. 2 Laser Beam Adjustment System

with the pinhole. Accordingly, the adjustment system of laser beam illustrated in **Fig.2** was used. The laser beam was adjusted as follows:two laser beams passing through lens 1 crossed each other at the M measuring point:and the two beams passing through lens 2 crossed each other at M':if this crossing angle of the two beams at M' is large, their crossing at M' can be relatively easilly confirmed using a pinhole, whereat the two beams accurately cross each other at the M measuring point. After adjusting the optical axis at the M measuring point, the velocity distributions of the particles in the flame and in the vicinity of the adhering surface were determined moving the burner and adhering surface. The crossing angle of the two beams were fixed at 1.4 and 9.4 degrees for measuring the velocities in the vertical and horizontal directions, respectively.

Scattered light from the measuring point was concentrated through a lens into a pinhole 100μm in diameter to prevent the scattered light entering from the outside. The measurement was repeated 5 to 15 times at a measuring point to eliminate the effect of the

flame flaring during the experiment.The time dependence of the scattered light were converted into the freguency dependence by the fast Fourier transform and the mean spectrum was calculated from the total of the measurements. Fluctuations around the peak signal were smoothed by applying quadratic and cubic polynomial expressions and the peak frequency was determined by differentiating a quadratic polynomial expression. The LDV measuring systems is illustrated in **Fig.3.**

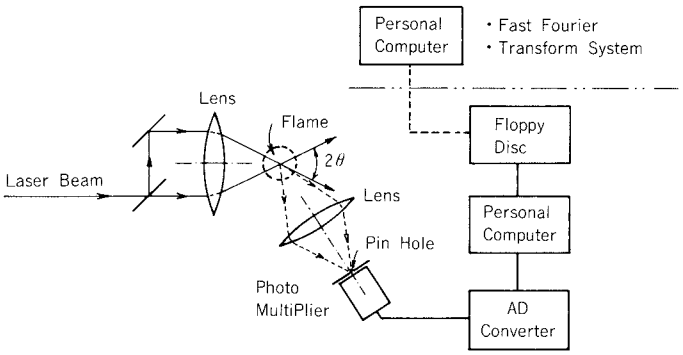

Fig. 3 LDV Measuring System

2.2.2. Temperature of substrate

The temperature of the substrate was measured with a thermocouple, a contact surface themometer and radiation pyrometer. The radiation pyrometer was used only for determining the temperature distribution on the adhering surface because the stainless steel surface was so rapidly covered with SiO_2 that the radiation pyrometer was unsuitable for determining the absolute temperature value.

A hole 1mm in diameter was made in the substrate to insert the thermocouple. The temperature was measured at position 1mm deep from the surface and 25mm away from the flame axis.

Since the surface temperature of the substrate in a flame could not be measured with a contact surface thermometer, it was measured just after taking out the substrate of the flame. Also, the themperature was measured 1 min. after being taken out to estimate the temperature variation caused by the heat radiation.

2.2.3. Temperature distributlon of gas in a flame

The gas temperature in a flame was measured with a B-type thermocouple. Relatively low temperatures in the vicinity of the particle adhering surface ware measured with three sizes, 0.1, 0.3 and 0.5mm in diameter, of the B-type thermocouples, to estimate errors in measurement caused by heat-radiation transfer from the thermocouple and heat-conduction transfer though the lead wire. The temperature distribution in the flame was measured only with a themocouple as thick as 0.5mm in diameter due to high temperature.

2.2.4. Particle-adhering range

The particle-adhering test needs a thermally equilibrium system maintained as accurately as possible. First, the burner was ignited with the argon carrier gas free from $SiCl_4$ to heat the adhering surface, measuring with a themocouple inserted in the substrate until reaching the steady-state temperature to be obtained by heating with a flame containing $SiCl_4$ together with the carrier gas. $SiCl_4$ was then subjected to the flame. After 1-2min., the substrate was taken out of the flame and any adhered particles were removed from the surface. Next, the substrate was places again in the flame for 15sec. Taking it out of the flame, the particle-adhering range was determined.

3. Experimental Results and Discussion

3.1 Particle-velocity distribution

The measurements of particle-velocity distribution by LDV are shown in **Table 2** and **Fig.4** The symbol-in Table 2 indicates the missing value due to too small an intensity of scattered light or too small a particle velocty. The starting point and length of an arrow in Fig.4 indicate the measuring point and velocity, respectively. Vertical and horizontal arrows show the velocity only in the measurable direction and the slanting one is composed of the vertical and horizontal

Tadle 2 Particle Velocity Distribution

h [mm]	r [mm]	u [m/s]		w [m/s]	
		exp.	calc.	exp.	calc.
0.5	0.0	—	0.0	—	0.07
	1.0	0.17	0.13	—	0.07
	2.0	0.24	0.25	—	0.07
	3.0	0.36	0.38	—	0.07
	4.0	0.50	0.50	—	0.07
	5.0	0.74	0.63	—	0.07
	6.0	0.75	0.76	—	0.07
	7.0	—	—	—	—
1.0	0.0	—	0.0	—	0.22
	1.0	0.27	0.18	—	0.22
	2.0	0.46	0.35	—	0.22
	3.0	0.55	0.53	—	0.22
	4.0	0.74	0.70	—	0.22
	5.0	—	—	—	0.22
2.0	0.0	—	0.0	0.56	0.59
	1.0	0.24	0.19	0.53	0.59
	2.0	0.39	0.37	0.53	0.59
	3.0	0.55	0.56	0.35	0.59
	4.0	—	—	—	—
4.0	0.0	—	—	1.27	—
	1.0	—	—	1.19	—
	2.0	—	—	1.14	—
6.0	0.0	—	—	1.73	—
	1.0	—	—	1.66	—
	2.0	—	—	1.66	—
11.0	0.0	—	—	2.28	—
	1.0	—	—	2.30	—
	2.0	—	—	2.28	—
16.0	0.0	—	—	2.51	—
	1.0	—	—	2.49	—
	2.0	—	—	2.57	—
21.0	0.0	—	—	2.66	—
	1.0	—	—	2.64	—
	2.0	—	—	2.70	—
26.0	0.0	—	—	2.57	—
	1.0	—	—	2.60	—
	2.0	—	—	2.66	—

vectors. Particles ascend in the vertical dirction at approximately 2.6m/s from a range of 16 to 26mm away from the adhering surface. The particles are observed only in a cylindrical space 4mm in diameter in which the particle velocity is measurable because of the laminar flame.

The particle velocity decreases to 2.3, 1.7

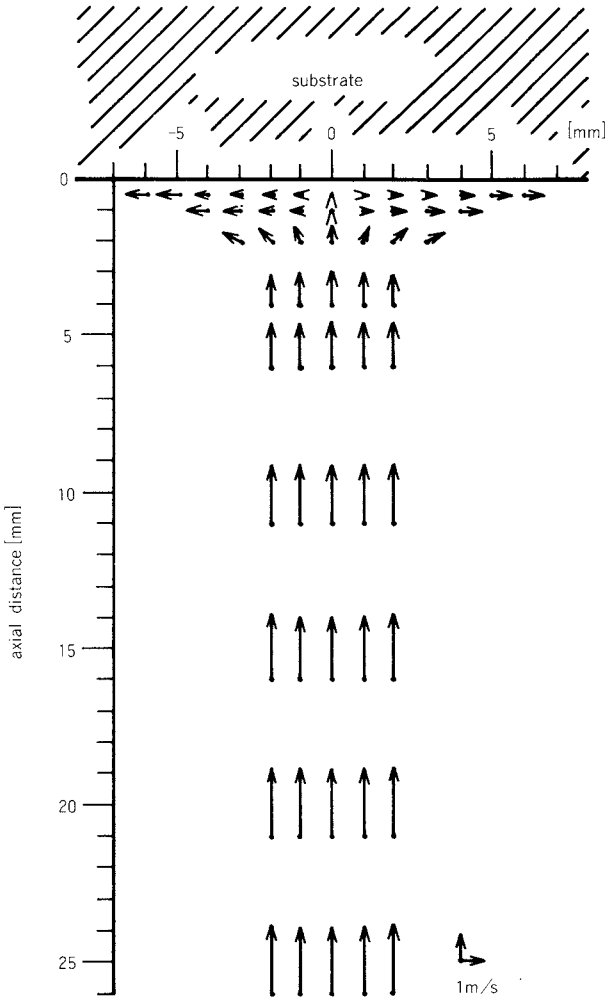

Fig. 4 Particle Velocity Distubution

and 1.3m/s at distances from the surface of 11,6 and 4mm, respectively. Even in these cases, the particles are observed still only in the cylindrical space 4mm in diameter, it is considered that the particle velocity in this space is decreased mainly by gas contraction due to the temperature drop. **Table 4 and 5** reveal the remarkable gas temperature drop in this space as expected.

The particle velocity in the flame axis derection is reduced by half though the diameter of the cylindrical space is unchanged. Assuming that the particles do not adhere to each other, the number of the particle density must be increased 2 fold near the adhering surface.

3.2 Temperature of particle - adhering surface

The temperature of particle-adhering surface measured at point 1mm deep from the surface and 25mm away from the flame axis with the thermocouple gradually increased up to a maximum of 509 to 512K for 10min. After cooling the surface, it was heated up to 463K according to the same procedures as before, and then, $SiCl_4$ was subjected to the flame. At this time, the temperature gradually dropped to 445 to 450K and became constant from 12min. onward. Maybe this is because the $SiCl_2$ particles covering the surface give a lower indication than the actual temperature as well as a decrease in flame temperate through an addition of $SiCl_4$.

Table 4 Gas Temperatnre Distribution near the Surface

h [mm]	r [mm]	T_G [K] 0.1mmϕ	0.3mmϕ	0.5mmϕ
2.0	0.0	1090～1098	1124～1135	1149～1166
	3.0	1161～1172	1136～1160	1161～1172
	6.0	1118～1128	1133～1143	1185～1195
4.0	0.0	1297～1307	1368～1378	1308～1318
6.0	0.0	1421～1430	1490～1498	1361～1370

The surface temperature measured with the contact surface thermometer is shown in **Table 3.** Immedeately after taking out the substrate from the flame at the time when the temperature reached the steady-state after subjected $SiCl_4$ to the flame, the temperatures (Ts_1) at points scattered from the flame axis to the outide on the surface were measured. After left to stand the substrate for 1min., the temperatures (Ts_2) were measured in the same way as before. It took 5 to 10sec for either the Ts_1 or Ts_2 measurement. The temperature decreasing rate at the center was as low as 17K for approximately 1.5min. Since it took approximately 30sec totally for the first temperature measurement, it is considered that the temperature drop during the measurement is no more than several tens degrees K. The temperatures in a circle of radius from 20 to 30 mm were almost constant and the measurements in the circle obtained with the contact surface themometer were similarly almost constant. The temperature measurements obtained with the thermocouple were approximately 60K lower than those obtained with the contact surface thermometer. Maybe this is because the thermocouple is inserted in

Table 3 Surface Temperature

r [mm]	Ts_1 [K]	Ts_2 [K]
0	521	504
10	515	503
20	518	505
30	505	496
40	491	486

Table 5 Gas Temperature Distribution in VAD Flame

r [mm] \ h [mm]	5	10	15	20
0.0	1480～1489	1676～1686	1557～1567	1475～1494
1.0	1569～1579	1665～1675	1503～1513	1431～1450
2.0	1647～1655	1556～1564	1449～1460	1361～1370
3.0	1619～1628	1480～1489	1350～1360	1329～1339
4.0	1509～1517	1291～1300	1178～1188	1161～1172
5.0	1350～1360	1231～1241	1046～1059	976～990
6.0	1149～1160	1033～1045	900～915	900～915
7.0	900～915	813～831	712～733	775～795
8.0	685～695	623～637	689～711	689～710
9.0	513～523	575～583	501～511	546～579
10.0	426～431	403～411	424～432	426～431

the position of 1mm deep and the temperature is decreased by heat-radiation transfer.The thermocouple is, therefore, inadequate for this experiment.

3.3 Gas temperature distribution in flame

3.3.1 Gas temperature distribution near surface

Gas temperature distribution niar the surface determined with the B-type thermocouples, 0.1, 0.3 and 0.5mm in diameter, is shown in Table 4. It is considered that the variation in the temperature measurements according to the diameter of thermocouple is attributed to the difference in the radiation and heat-conduction transfers caused by the difference in the temperature distribution around the measuring points. Selecting the data largely affected by the thermocouple diameter from the measurements, the temperature measured with a thermocouple zero milimeter in diameter is estimated by extrapolating them. **Figure 5 and 6** illustrate the gas temperature diagrams of two points

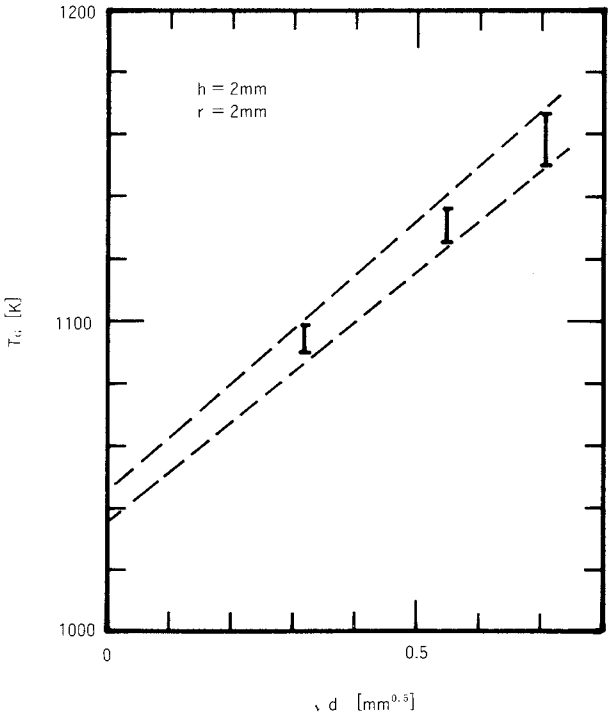

Fig. 5 Gas Temperature by Thermocouple with Various Diameters at h=2mm and r=0mm

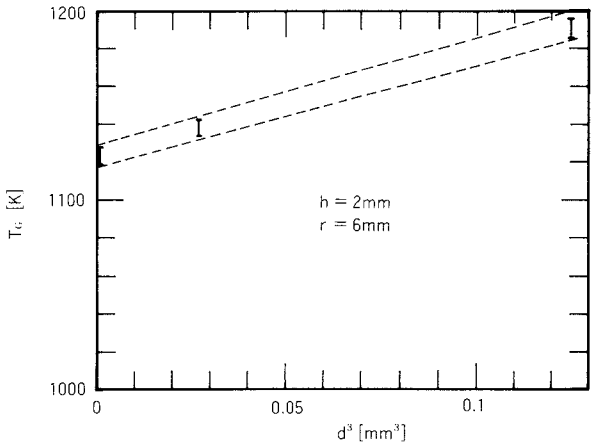

Fig. 6 Gas Temperature by Thermocouples with Varions Diameters at h=2mm and r=6mm

(h:2mm and r:0mm) and (h:2mm and r:6mm), respectively Assuming that the radiation transfer has a great influence on the measurements, the gas temperature must be increased as the diameter of thermocople (d) approaches zero. The trend is, however, adverse as shown in those figures. Maybe this is because the heat - conduction transfer through the lead wire of thermocouple, which is influenced by the temperature distribution around the measuring point, is considerably high. The abscissas in Figs.5 and 6 are graduated in $d^{0.5}$ and d^3, respectively, to obtain straight lines which make extrapolation easy. The temperatures obtained by extrapolating d to zero to eliminate errors in measurement caused by radiation and conduction heat - transfers are 1035 to 1050K at the point (h:2mm and r = 0mm) and 1125 to 1130K at the point (h:2mm and r = 6mm).

3.3.2 Gas temperature distribution in flame

Since thermocouples as thin as 0.1 and 0.3mm in diameter were promptly melted in the high-temperature gas, the thermocouple of 0.5mm in diameter was used for determining the gas temperature distribution in the flame. The result is shown in Table 5. It is considered from the result of 3.3.1 that the data shown in Table 5 give the gas temperature distribution in the flame within several tens to several hundreds degrees K.

3.4 Gas velocity distribution

It is necessary to determine the gas velocity distribution in the vicinity of the particle-adhering surface for evaluating the effect of thermophoresis on the surface. It is difficult, however, to accurately measure the gas velocity at the points nearer than a certain distance.

The particle diameter is so small that the obseved value of a particle is considered equal to the gas velocity vector in its derection. The gas velocity distribution produced by vertically blowing a gas jet against a plane is determined using the theoretical analysis by Froessling [3]. The velocity components parallel and perpendicular to the surface in the vicinity of it expressed as follows:

Velocity component parellel to surface

$$u = ra\phi'(\xi) \quad (1)$$

Velocity component perpendicular to surface

$$w = -2\sqrt{a\upsilon}\phi(\xi) \quad (2)$$

$$\xi = h\sqrt{a/\upsilon} \quad (3)$$

where a = constant, $\phi'(\xi)$ and $\phi(\xi)$ = functions of ξ, υ = kinematic viscosity of fluid.

Introducing the measured values of u and w at the distances h of 0.5, 1.0, and 2.0mm shown in Table 2 into Eqs. (1) to (3) to obtain a and υ, then

$a = 187s^{-1}$ and

$\upsilon = 0.97\times10^{-4}m^2/s$.

The values of u and w calculated from Eqs. (1) to (3) are shown in Table 2. The table reveals that these values agree well with the measurements. Figure 7 shows that gas temperatures at distances (h) of 0 to 2.0mm range from 500 to 1100K. The kinematic viscosity of Ar, O_2 and H_2O for this temporature range are 0.34×10^{-4} to 1.98×10^{-4} 0.38×10^{-4} to 1.41×10^{-4} and 0.39×10^{-4} to $1.98\times10^{-4}m^2/s$, respectively. The υ value obtained from Eqs. (1) to (3) is, therefore, reasanable for determining the gas velocity in the vicinity of the adhering surface.

Consequently, the gas velocity distribution in the vicinity of the adhering surface in this experiment is approximated by the values calculated from a Eqs.(1) to(3) using values of $187s^{-1}$ and υ of 0.97×10^{-4} m^2/s.

3.5 Estimation of thermophoresis velocity by using the width of particle-adhering region

Since the particles are attracted due to the sharp temperature gradient in the vicinity of the adhering surface, the stream line of particle must come to the surface.

After heating the adhering surface in a flame containing $SiCl_4$ until reaching the equilibrium state of temperature, the substrate was rapidly taken out from the flame and particles adhered to the surface were removed. The substrate was heated again in the same manner as before for 15secs, and then, the particle-adhering range was detemined. The particles were distributed in a circle 17mm in radius.

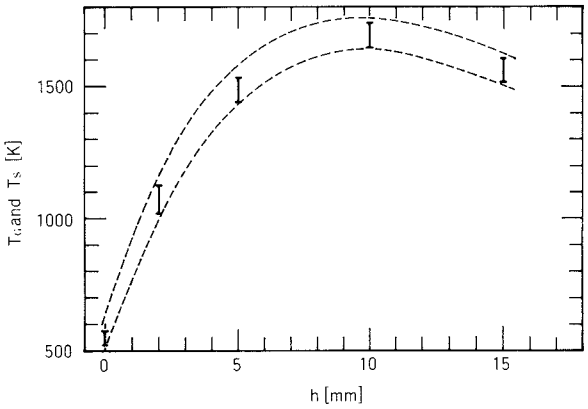

Fig. 7 Temperature Distribution near the Surface

The stream line of particle can be drawn by connecting the velocty vectors composed of the gas velocity and the thermophoresis velocity directing toward the adhering surface. The thermophoresis velocity can be, therefore, determined in such a way that a particle flowing along the circumference of the cylinder of a particle existing range collides

against a point 17mm away from the center on the adhering surface. **Figure 7** reveals that the thermophoresis velocity at a distance 0.5mm or less away from the surface is assumed to be constant because the temperature gradient of gas is almost constant in this range. The streamlines of gas and particles in the vicinity of the adhering surface at thermophoresis velocities, V_T, of 1.0 and 1.4cm/s are illustrated in **Figs. 8** and **9,** respectively. The graduation of ordinate in both figures are enlarged 20 - times those of the abscissa to distinguish the curves from each oter and the adhered particles are sketched schematically. Figures 8 and 9 show that particles colliding against the points 17mm away from the center of the circle are those starting from the points (h:0.5mm and r:6mm) and (h:0.5mm and r:7mm), respectively. The particle velocity at the point (h:0.5mm and r: 6mm) was able to be measured, while that at the point (h:0.5mm and r:7mm) was unable to be measured due to weak particle scattering. The thermophoresis velocity in this experiment is, therefore, estimated to be 1.0 to 1.4cm/s.

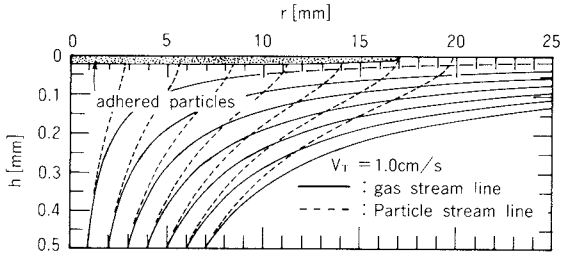

Fig. 8 Stream Lines of Gas and Particles when V_T = 1.0cm/s

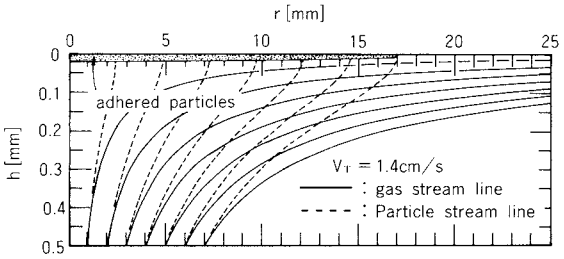

Fig. 9 Stream Lines of Gas and Particles when V_T = 1.4cm/s

3.6 Discussion

The temperature gradient causing the thermophoresis of the particles in the experiment is approximately 2500K/cm as shown in Fig. 7. Knudsen number, Kn, of the particles moving in the field of this temperature gradient at a thermophoresis velocity of 1.0 to 1.4cm/s is 0.75 to 1.4 according to the Hidy and Brook formula for Kn[1]. Kn is the ratio of the mean free pass, l, of a gas molecule to the radius, $d_p/2$, of a particle moving by thermophoresis. The value of l can be obtained by the following formula[6]

$$l = 0.709\upsilon \{\pi M(R.T_G)\}^{0.5} \quad (4)$$

where υ = kinematic viscosity of gas, M = molecular weight of gas, R gas constant, and T_G = gas temperature, Since most of H_2 and O_2 react with each other to H_2O, the gas in the vicinity of the adhering surface is composed of equal volume of Ar, and H_2O. The molecular weight of the gas is, therefore, assumed to be 30 taking an average of the molecular weight of argon, 40, and that of H_2O,18. As the kinematic viscosity of gas, υ, of $0.97\times10^{-4}m^2/s$ obtained in the section 3.4 is used. The gas temperature, T_G is 600K as shown in **Fig.7.** Substituting those values for Eq, (4), then

$$l = 0.3\times10^{-6}m.$$

The diameter of the particles moving by thermophoresis in the vicinity of the adhering surface is, therefore, considered as 0.4 to 0.8 μm.

Meanwhile, the diameter of a SiO_2 particle in a flame was determined under the similar flow conditions in the same apparatus by the dynamic light - scattering method. The result indicated that the diameter of the particle is 50 to 60mm in the longitudinal axis direction of the flame. TEM photographs also show spherical particles with a similar diameter[4].

The particles in the vicinity of the adhering surface have increased chances of colliding each other because the number density of particle increases 2 - fold as descrebed in 3.1

though the gas temperature is decreased. It is considered, therefore, that individual spherical particles 50 to 60nm in diameter existing separately from each other in the flame adhere to each other to larger particles which move by thermophoresis when approaching the adhering surface.

Assuming that the particles collide against the adhering surface by inertia, the larger the particles, the more the particles must adhere to the surface. A paper[4] presents from the experiment, however, that particles do not grow in the flame axis direction in a flame. Our experimental results indicated that the particles grow no more than 1 μm though the particles adhere to each other in the vicinity of the adhering surface. Inertia does not, therefore, act to adhere the particles to the surface as expected[5]. It is most effective to collect by thermophoresis the SiO_2 particles produced in a VAD flame.

Although it is more effective to decrease the surface temperature considering thermophoresis only, particles are not firmly adhered to the surface so that they easily fall off. Since the decrease in the gas temperature also causes gas stagnation in the vicinity of the surface, the particles grow so much by adhering to each other that the effect of thermophoresis is lowered. It is necessary, therefore, to select an appropriate temperature to firmly adhere the particles to the adhering surface and control the growth of particles by preventing the gas from stagnating as well as make thermophoresis effective as much as possible.

4. Conclusions

An experiment was made to investigate the adhering of ultrafine SiO_2 particles produced in a VAD flame to the substrate. The following conclusions were obtained:

1) Assuming that the particles do not adhere to each other by gas stagnation due to the decreased gas temperature in the vicinity of the adhering surface, the number density of the particle must increase 2 - fold.
2) The thermophoresis velocity of particle in the vicinity of he adhering surface is 1.0 to 1.4cm/s. Calculating from the gas temperature gradient, the sphere equivalent diameter of the thermaphoresis particle is approximately 0.4 to 0.8 μm in diameter.
3) Since it was reported that the diameter of a particle in a flame is 50 to 60nm, it is considered that the particles grow in the vicinity of the adhering surface.
4) Particles adhere to the surface mainly by thermophoresis. Inertia of particle is negligible.
5) It is necessary to select an appropriate temperature to firmly adhere the particles to the adhering surface and control the growth of particles by preventing the gas from stagnating as well as make thermophoresis effective as much as possible.

Acknowledgements

The authors would like to acknowledge the special assistance received from the Ministry of Education regarding Grant-in Aid for Developmental Scientific Research (1) 61850163 and Mr. Toru Wakita from the Optical Communication Division, Messrs. Makoto Koguchi and Tsuguo Sato from the Research and Development Division and the staff members of the Chiba Research Laboratory of Furukawa Electric industry Co. in cooperation in this study.

Also, the authors would like to express their gratitude to Mr. Keizo Tanaka of the Master's Course in Chemical Engineering of the Fuculty of Engineering of University of Tokyo for his very kind assistance during the carrying out of this experiment.

Nomenclature

a	:	constant in Eqs. (1)~(3)	[s^{-1}]
d	:	diameter of thermo-couple	[mm]
d_p	:	diameter of a particle moving by thermophoresis	[m]
h	:	distance from an adhering surface	[mm]

$Kn = 2\ell / d_p$: Knudsen number [-]
ℓ : mean free path of a gas molecule [m]
M : molecular weight [g]
γ : radial distance from the center axis of a flame [mm]
T_G : gas temperature [K]
T_S : surface temperature [K]
v_T : thermophoresis velocity of particles [cm · s^{-1}]
z : distance from a top of particles [mm]
ν : kinematic viscosity of fluid [m^2 · s^{-1}]
ξ : parameter difined by Eq. (3) [-]
ϕ : function of ξ in Eq. (2) [-]
ϕ' : function of ξ in Eq. (1) [-]

References

1)Takahashi, K. : "Kiso Aerosol Kogaku"p.33, Yokendo(1982)

2)Nakatani, N. :"Laser Diagnostics and Modeling of Combustion"p. 6, Maruzen (1987)

3)Schlichting, H. :"Boundary Layer Theory"7th ed.,p.99, McGraw-Hill(1979)

4)Ueyama, K., K. Tanaka, H. Kawazoe, A. Iino, Y. Matsuda and S. Furusaki : *J. Soc. of Powder Tech., Japan,* **26,** 151(1989)

5)Takahashi, K. :"Kiso Aerosol Kogaku", p. 29, Yokendo(1982)

6)Takahashi, K. : *ibid.,* p. 11(1982)

Particles Size Analysis for Micro-Particles by Capillary Hydrodynamic Chromatography †

Naohiro Shiragami
Deparment of Bioengineering, Faculty of Bioscience and Biotechnology, Tokyo Institute of Technology *

Abstract

Paricle size analysis for micro-particles by capillary hydrodynamic chromatography was studied experimentally. Retention times of particles depended on their diameter but were independent of their concentration. The linearity of the peak area with particles concentration was found. It is shown that the particles diameter and their concentration can easily and rapidly be analyzed by capillary hydrodinamic chromatography. Resolution of peaks were calculated from chromatograms of binary-particle samples. Particle diameters of a binary-particle sample for complete peak separation were predicted from the resolution of the peaks.

The mechanism of capillary hydrodynamic chromatography was discussed by considering the dependence of the volume flow rate of solvent on the retention time, the resolution of the peak and the peak width.

1. Introduction

Particle size analysis can be classified into a number of categories according to their principles[1]. They include microscopy, screening by sieves, sedimentation techniques, scattering techniques and chromatographic techniques. It is usually difficult for electron microscopy and scattering techniques to measure particles size without change of particles situation. Whereas chromatographic technique, a flow injection method, can be analyzed particles size *in situ.*

Hydrodynamic chromatography[2] (HDC) the first development of chromatographic technique for particle size analysis, is used a column packed with non-porous particles. The principle of HDC is that the length of hydrodynamic pass in a column depends on particles size. HDC can also be applied to separation of micro-particles. However, insufficient recovery of large particles has been pointed out[4].

The capillary hydrodynamic chromatography (C—HDC) is used a long hollow capillary tube as a colum. That is, C—HDC has a major characteristics that there are no packing materials in a column. The problem of insufficient recovery in HDC can be improved in C-HDC and a rapid analysis is possible in C-HDC. Although several experimental[6-8] and theretical[9] studies have been reported, there are still unsolved problems such as the establishment of procedure and the prediction of elution pattern.

The author was reported an influence of column length on particle size analysis in C-HDC[10]. In this paper, the influences of particles diameter, their concentration and volume flow rates on retention times of particles are studied experimentally. The application of. C-HDC to an analysis of particle size distribution is also discussed by experiments using binary-particle samples.

2. Experimental apparatus and procedure

The experimental apparatus is illustrated

* 4259 Nagatsuta-cho, Midori-ku, Yokohama 227 Japan TEL. 045-922-1111 ex.2533

† This report was originally printed in *J.Soc.Powder Technology, Japan* **27** 394-(1990) in Japanease, before being translated into English with the permissian of the editorial Committee of the Soc. Powder Technology Japan.

schematically in **Fig.1.** Pure water is delivered from a storage bottle to the test column by a constant pressure syringe pump(Tosoh Co. Ltd., Tokyo, Japan, CCPE). A solvent, pure water, thoroughly degassed. The test column is a stainless steel capillary tube(Gasukuro Kogyo Inc.)of 92m in length. The capillary

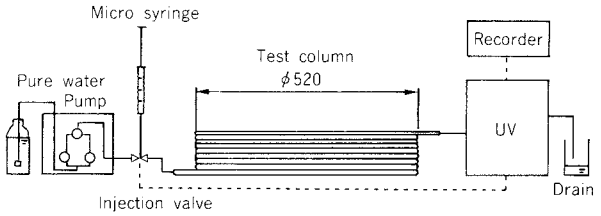

Fig.1 Schematic diagram of experimental apparatus

tube of 260μm I.D. and 1.6mm O.D. was formed into a coil of 52cm in diameter. There were no packing materials in the capillary tube, and no treatment of the inner surface was done. Polystyrene latex particles(Japan Synthetic Rubber Co. Ltd., Tokyo, Japan, STADEX particle standards and DYNOSPHERES particle standards)of 0.05, 0.1, 0.2, 0.5, 1.0, 2.0, 5.0, 10.0, and 20.0μm in mean diameter were used as the test particles. The coefficient of variations are less than 2 percent except 6 percent for the particles of 0.05μm in diameter according to data from the maunfacturer.

Paricle standards were suspended in pure water and introduced to the test column through a loop injection valve(Tosoh Co. Ltd., Tokyo, Japan, Unit A08162, Sample volume 0.1 cm^3). The effluent was detected by a UV spectrophotometer (Tosoh Co, Ltd., Tokyo, Japan, UV-8011), and the signal from the UV spectrophotometer was fed to a standrd chart recorder. The detection was performed by measuring the optical density at 280nm. The retention time was determined by measuring the interval from injection to the top pf the peak in the chromatogram.

The chromatograms were obtained for the particle concentrations of 0.002, 0.006, 0.012, 0.018 and 0.024wt% at the volume flow rates of 0.5, 1.0, 1.5, 2.0, 2.5 and 3.0cm^3/min. The chromatograms were also obtained for twenty-eight binary-particle samples. The binary-particle sample contains two different-sized particles of the same concentration, 0.012wt%.

Since the maximum Reynolds number in the experiments is 245, the flow behavior in the test column is laminar. The relationship between the volume flow rate of solvent and the pressure drop was expressed by the Hagen-Poiseuille's law. That is, no curvature effect of the coiled column was observed in the experiments.

3. Results

The relationship between the retention time and the particles diameter is shown in **Fig.2**.

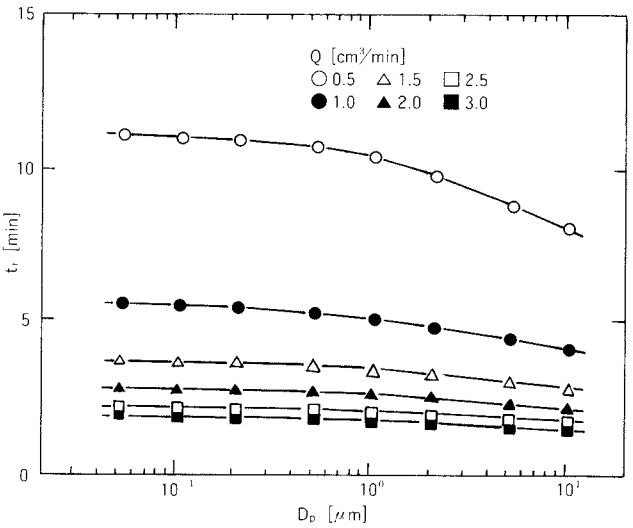

Fig.2 Dependence of particle diameter on retention time

The sample contained particles of the same size and its concentration was 0.012wt%. The retention time for the particles of 20.0μm in diameter was not shown in the figure because it was in contrast to other data. From this result, the measurable maximum particles diameter is predicted to be about 1/20 of the capillary tube diameter. The retention time depended on the particles diameter, and the particles eluted by size with large particles eluting fast. Therefore, the particles diameter can be determined by measuring the retention

time. Since the retention time decreased with increasing the volume flow rate, it is more effective to increase the volume flow rate for rapid detection. However, the volume flow rate was restricted to below 1.0cm^3/min in order to distinguish clearly between the retention times in submicron range. The eluting time for the particles of 0.05μm in diameter was about only 5 min at 1.0cm^3/min.

The influence of the particles concentration

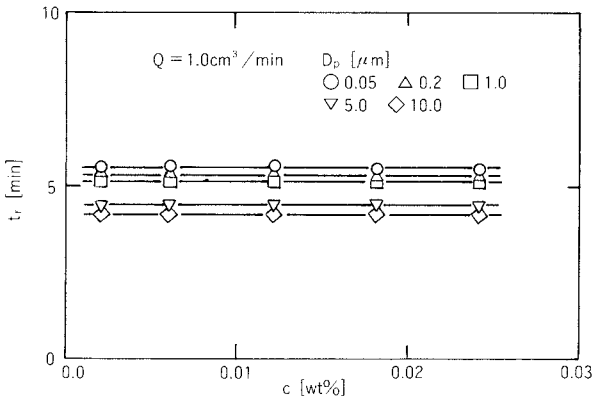

Fig.3 Invariability of retention time with particle concentration

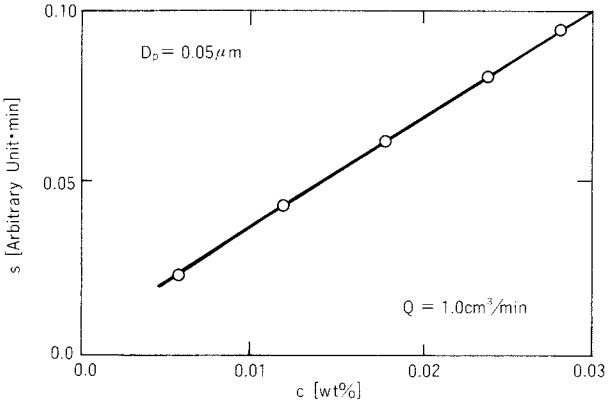

Fig.4 Linearity of peak area with particle concentration

on the retention time at 1.0cm^3/min is shown in **Fig.3**. The retention time was independent of the particles concentration. The same results were obtained at 2.0 and 3.0cm^3/min. Therefore, the invariability of the retention time with particles concentration was found. As shown in **Fig.4**, a straight line through the origin was obtained by plotting the peak area in the chromatogram against the particles concentration. From these results, it is shown that not only particles diameter but also its

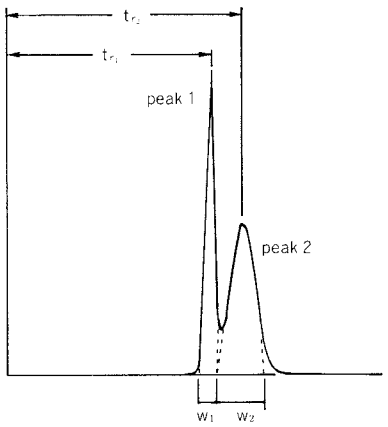

Fig.5 Typical chromatogram of binary particle sample

concentration can easily and rapidly be analyzed by C-HDC.

The typical chromatogram of a binary-particle sample is shown in **Fig.5**. A peak separation was observed in the chromatogram. The retention times, t_{r1} and t_{r2}, and peak widths on the base line,w_1 and w_2, were obtained from the chromatogram, and the resolution of peak was calculted from the following equation.

$$Rs=\frac{2\ (t_{r2}-\ t_{r1})}{w_2+\ w_1} \qquad (1)$$

The Rs value at 1.0cm^3/min and that at 2.0cm^3/min are shown in **Figs.6 and 7,** respectively. The horizontal and vertical axes denote the diameters of large particles and small particles, respectively. The data are expressed by ○ and △ if Rs=0, ◑ and ◭ if 0<Rs<1, and ● and ▲ if Rs≧1. The Rs value increased with increasing the difference of particles diameter. The peak separation becomes better as the Rs value is larger. The curve for Rs=1 can be expected as shown in Figs.6 and 7. The area for Rs≧1 at 2.0cm^3/min is slightly larger than that at 1.0cm^3/min. The Rs value at 3.0cm^3/min was similar to that at 2.0cm^3/min.

4. Discussion

In order to discuss the influence of the volume flow rate on the retention time, the

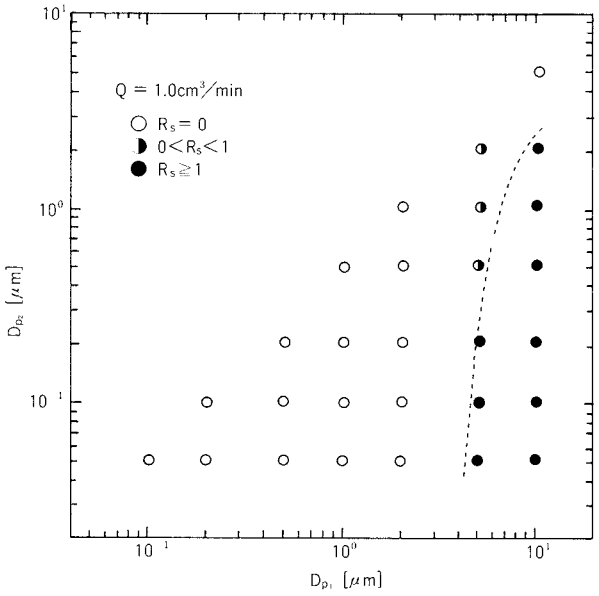

Fig.6 Resolution of peak at 1.0cm³/min

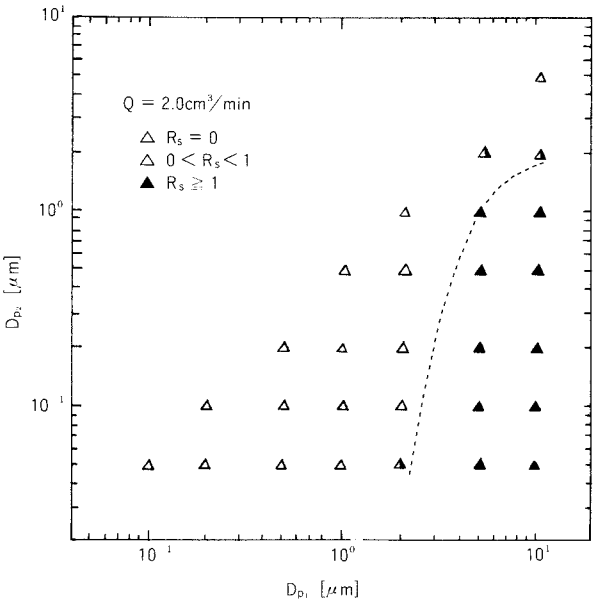

Fig.7 Resolution of peak at 2.0cm³/min

retention time, t_r, is reduced by the mean residence time, T. The dimensionless retention time, t_r/T, was plotted against the volume flow rate, Q, as shown in **Fig.8**. The dimensionless retention time for the particles of 0.05μm in diameter was almost independent of the volume flow rate, whereas that for the particles of 10.0μm in diameter significantly depended on the volume flow rate.

The theoretical dimensionless retention time was calculated from the following equation[9],

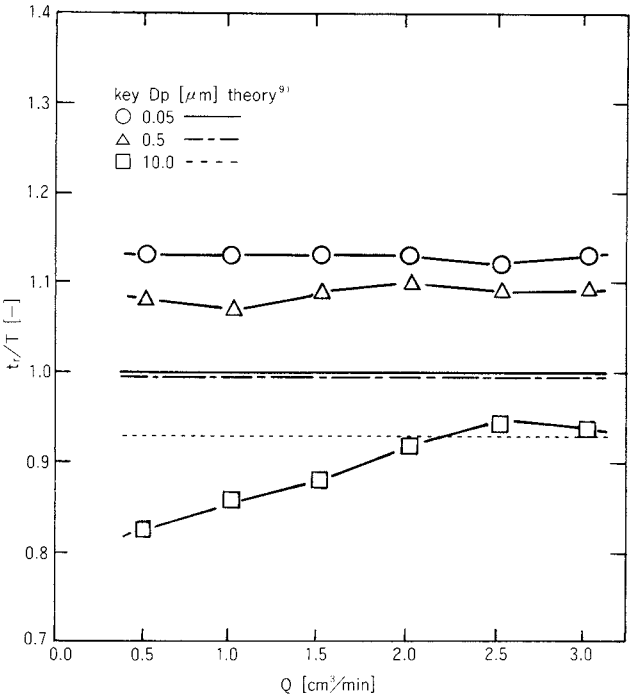

Fig.8 Dependence of flow rate on dimensionless retention time

$$\frac{t_r}{T} = \frac{1}{1+2(D_p/D)-(D_p/D)^2} \qquad (2)$$

where D_p and D denote the particles diameter and the column diameter, respectively. The principle of this theory is that the particles can not flow in the annular region near the capillary tube wall. The thickness of this annulus is given by the half of the particles diameter. The calculated results from Eq.(2) were also illustrated in Fig.8. The dependency of the volume flow rate on the dimensionless retention time for the particles of 10.0μm in diameter cannot explain from this theory. In addition, the calculated dimensionless retention time always has the value below unity. The experimental results for the particles of 0.05 and 0.5μm in diameter conversely have the value above, unity. From these results, the idea of particles unflowable region in the center of the capillary tube will probably be introduced. The mathematical treatment on the basis of this idea can be analyzed by hydrodynamics including the Brownian motion of particles.

The dependence of volume flow rate on the resolution of the peak for a mixture of particles with 0.05 and 10.0μm in diameter is

shown in **Fig.9**. The R_s value depended on the volume flow rate, and an appropriate volume flow rate for maximizing the R_s value was found. The retention times of two peaks coincided precisely with the experimental results in Fig.2. That is, no interaction between large and small particles was observed. The R_s value is related with not only the difference of retention time but also the

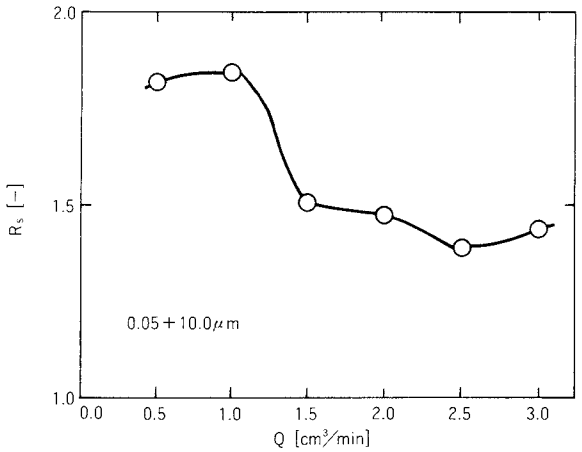

Fig.9 Dependence of flow rate on resolution of peak

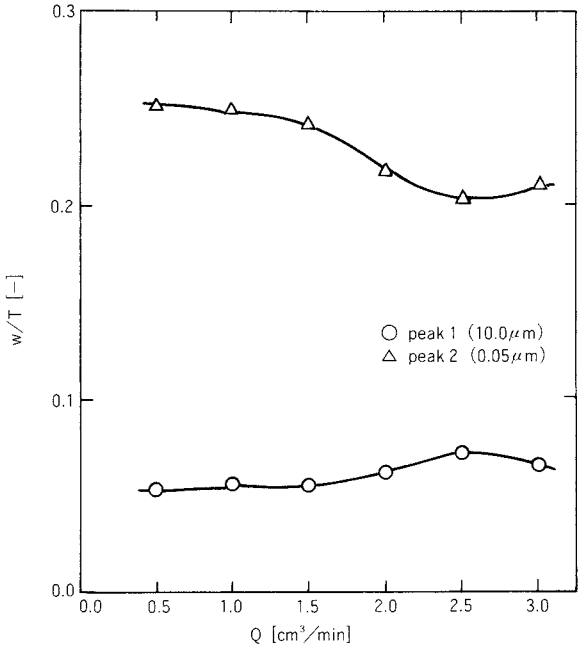

Fig.10 Dependence of flow rate on dimensionless peak width

peak widths on the base line as shown in Eq.(1). The dimensionless peak width, w/T, was plotted against the volume flow rate, Q, as shown in **Fig.10**. Peak 1 and peak 2 correspond to the particles of 10.0 and 0.05μm in diameter, respectively. The dimensionless peak width for the particles of 10.0μm in diameter increased whereas that for the particles of 0.05μm in diameter decreased with increasing the volume flow rate. More data will be required for the application of C-HDC to an analysis of particle size distribution.

5. Conclusion

Particle size analysis for micro-particles by capillary hydrodynamic chromatography was studied experimentally. The influences of the particle diameter, the particle concentration and the volume flow rate on the retention time are discussed, and the following conclusions are obtained.

1) Measurable maximum particle diameter is predicted to be about 1/20 of the capillary tube diameter.

2) The particles diameter and its concentration can easily and rapidly analyzed by C-HDC.

3) The resolution of peak depended on the vopume flow rate.

Acknowledgements

The author thanks Mr.Sigehiro Yamawaki for his assistance in the experimental measurements, and Japan Synthetic Rubber Co., Ltd. for gifting us with polystyrene latex particles. The author are also grateful to professor Hajime Unno,Department of Bioengineering ; and Associate Professor Toshio Kajiuchi, Department of Environmental Chemistry and Engineering, Tokyo Institute of Technology,for helpful suggestions.

Nomenclature

c	:	particle concentration	[wt%]
D	:	column diameter	[μm]
D_P	:	particle diameter	[μm]
Q	:	volume flow rate of solvent	[cm³/min]
R_S	:	resolution of peak	[-]
s	:	peak area	[Arbitrary unit.min]
T	:	mean residence time	[min]
t_r	:	retention time	[min]
w	:	peak width on base line	[min]

References

1) Barth,H.G., S.T.Sun and R.M.Nickol:Anal. Chem., **59**,142R(1987)
2) Small,H.: J.Colloid Interface Sci., **48**, 147(1974)
3) Nagy,D.J., C.A.Silebi and A.J.McHugh: J. Appl. Polymer Sci., **26**, 1567(1981)
4) Silebi,C.A. and A.J.McHugh: ibid.,**23**, 1699(1979)
5) Noel,R.J., K.M.Gooding, F.E.Regnier, D.M.Ball, C.Orr and M.E.Mullins: J. Chromatogr., **166**, 373(1978)
6) Brough,A.W.J., D.E.Hillman and R.W.Perry: ibid., **208**, 175(1981)
7) Tijssen,R., J.P.A.Bleumer and M.E.Van Kreveld: ibid., **260**, 297(1983)
8) Zarrin,F. and N.J.Dovichi: Anal. Chem., **57**, 1826(1985)
9) Tijssen,R., J.Bos and M.E.Van Kreveld: ibid., **58**, 3036(1986)
10) Shiragami,N., T.Kajiuchi and Y.Hoso: Kagaku Kogaku Ronbunshu, **15**, 687(1989)

Explanation of the cover photograph

—Structural Analysis of Diamond Surface at Atomic Level Using Atomic Force Microscope—

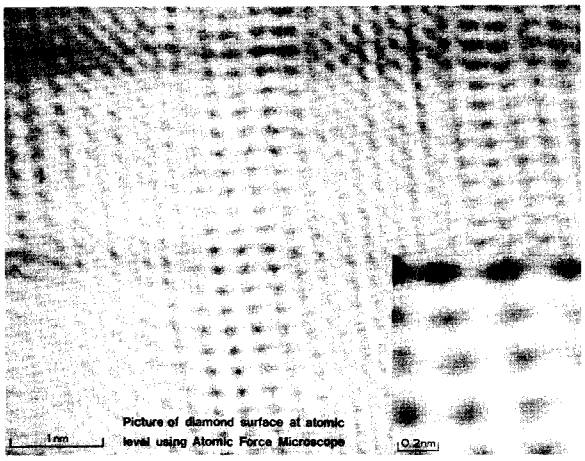

The tunneling microscope is suitable for observing the surface of a conductive material at the atomic level, but cannot be applied to a non-conductive material. The atomic force microscope, which was developed in 1990, can be used for observing the surfaces of both conductive and non-conductive materials. Its actual application so far reported, however, relates to a limited number of samples such as graphite and mica.

The cover photograph shows the surface of the diamond (111) face photographed with the atomic force microscope. Not only the state of a carbon atom on the surface, but also interaction between carbon atms can be seen. The bright zones show the position of the atoms.

By courtesy of Professor Ogino's laboratory, Materials Science and Processing, Faculty of Engineering, Osaka University

The Estimation of Packing Characteristics by Centrifugal Compaction of Ultrafine Particles †

Mitsukuni Mizuno
*Dept. of Mechanical Engineering, Aichi Institute of Technology**

Atsushi Fukaya and Genji Jimbo
*Dept. of Chemical Engineering, Nagoya University***

Abstract

At present, there is no reliable method available for determinating the compaction characteristics of ultrafine particles, the sizes of which ranges from several to one hundred nanometers. In this paper, the authors propose the centrifugal compaction method to evaluate the compaction characteristics of the ultrafine particles by applying the self-compressive stress by centrifugal force in a packed powder bed. With such a system, compressive strains can be determined with good reproducibility as a function of centrifugal force. The relationships between compressive strain and centrifugal force for ten kinds of ultrafine particles, such as Fe, Co, Al, SiO_2, Al_2O_3 and TiO_2 were found to be divided into two categories. One category can be written as a linear relationship between the logarithm of compressive strain and the logarithm of centrifugal force, while the other can be described by a linear relationship between compressive strain and the logarithm of the centrifugal force.

1. Introduction

Ultrafine particles whose sizes range from several nm to one hundred nm have a large number of particles per unit weight, greater specific surface area and stronger adhesive and cohesive forces as compared with conventional powder substances of greater than submicrons in size.[1] Thus, the bed packed with such ultrafine particles has a unique powdery structure with a small bulk density and a very large porosity. In evaluating the packing characteristics of particles, the tapping and compressive compaction methods were employed in the past.[2] In each method, however, drawbacks exist, depending on the magnitude of load when applied. In the former, the arrangement of component particles is apt to become unhomogeneous due to their easy movement during tapping actions and in the latter, the bed porosity of the packed particles is locally distributed specifically on the pressurized surface of the piston and near the wall surface of the cylinder. Considering these, the authors newly developed a centrifugal compaction system[3] which is capable of applying uniform compressive force as a centrifugal force at any height of the bed without causing any local disturbance. This system was found to yield highly reproducible data on the packing characteristics of ultrafine particles.

By this method, furthermore, the hysteresis of packing characteristics could be evaluated for each cycle composed of increasing and decreasing term of applied load to the packed bed of ultrafine particles. In contrast with the acceleration encountered in the conventional

* 1247, Yachikusa, Yakusa-cho, Toyota-shi, 470-03 Japan
TEL 0565-48-8121

** Furoucho, Chikusa-ku, Nagoya, 464 Japan
TEL 052-781-5111

† This report was originally printed in *J.Soc.Powder Technology, Japan,* **26**, 632-637 (1989) in Japanese, before being translated into English with the permission of the editorial committee of the Soc. Powder Technology, Japan.

tapping method, which ranges from several tens to several hundreds G, the pressurizing force corresponding to several hundreds to several thousands G can be obtained by this centrifugal method. When compared with the range of the force attained by the compressive compaction method (exceeding several hundreds KPa), this method is deemed to be a testing method lying in between the tapping and compressive compaction methods. Moreover, this method allows us to observe the compaction process directly from the outside. It enables us observe the dispersed state of the tracer particles when the tracer particles are initially mixed in the form of a layer within the packed bed of ultrafine particles. In addition, the authors observed a group of ultrafine particles of ten kinds by means of an electron microscope and found that secondary particles, which are the agglomerate of the primary particles, could be largely classified into a chainlike structure and a lumplike one. In the present work, the elastic and plastic behavior which is characteristic of the agglomerate of ultrafine particles, was investigated from the compaction processes and discussed in connection with two types of the agglomerates mentioned above. Furthermore, to clarify the internal structure of the packed bed, the authers conducted a series of compaction tests by means of the tapping, compressive and centrifugal methods using tracer particles, and discussed the change in the porosity of the packed bed by comparing with each other.

2. Experimental

2.1 Specimen

The properties of six kinds of ultrafine particles of metals and metal oxides used in this experiment are shown in **Table 1**. Ultrafine particles of metals(hereafter called "UFMP")are prepared by the evaporation process in a gaseous state and ultrafine particles of metal oxides(hereafter called "UFP")are generated by hydrolysis in combustion with oxygen-hydrogen flame. The specimens used are three kinds of silica powders having the same components but different sizes, silica 300 and 380 which have the same particle size but different specific surface areas(BET specific surface areas 300 and 380m^2/g)and Al_2O_3 and TiO_2 powders which have the same particle size but different components. Fe and Co powders of UFMP are available only in the agglomerate state, which sizes approximately range from several mm and several tens mm even when they are kept in a dry and tightly enclosed state. Thus, these agglomerates were unfastened using a sieve with a 110μm mesh opening and the particles which passed through the sieve, were used as the specimens.

2.2 Experimental apparatus and procedures

The schematic flow diagram of the experimental apparatus is shown in **Fig.1**. While the centrifuge works, the cells ②(ϕ26×70mm)become almost horizontal and the top of the cell is situated on the side of the rotating axis and its bottom on the circumference side. Enlarged photos of the boundary surface of the powder bed in the rotating cell of the centrifuge were taken by a VTR camera and the process of the centrifugal compaction was continuously observed. Simultaneously, the image was recorded on a VTR camera. Then,

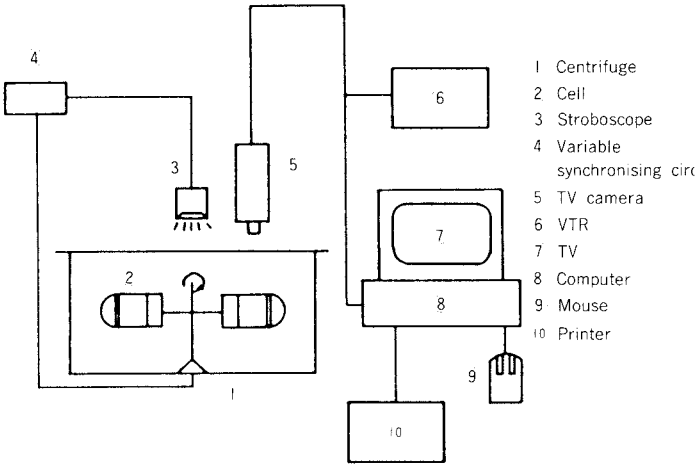

Fig. 1 Schematic flow diagram of experimental apparatus

Table 1 Properties of specimen

Specimen	Metal ultrafine particle				Metal oxide ultrafine particle					
Mean size [nm]	Fe	Co	Cu	Al	SiO_2 130	SiO_2 200	SiO_2 300	SiO_2 380	Al_2O_3	TiO_2
	12	20	50	100	16	12	7	7	21	20
Porosity [%]	99.4	99.2	92.2	91.7	97.6	98.4	97.2	97.7	96.6	97.0
True density [g/cm³]	7.9	8.9	8.94	2.7	2.2	2.2	2.2	2.2	2.9	3.8
Purity	UFMP >99.9%				SiO_2 >99.9%				Al_2O_3 >99.9%	TiO_2 >99.9%

the average positions of the boundary surface were read on the reproduced still iamges using a mouse, and were numerically processed to obtain the average value of the bed height. The compressive strain of the powder bed under a centrifugal compressive force(ε) was calculated from the difference between the initial bed height and the average bed height when the compressive force was applied.

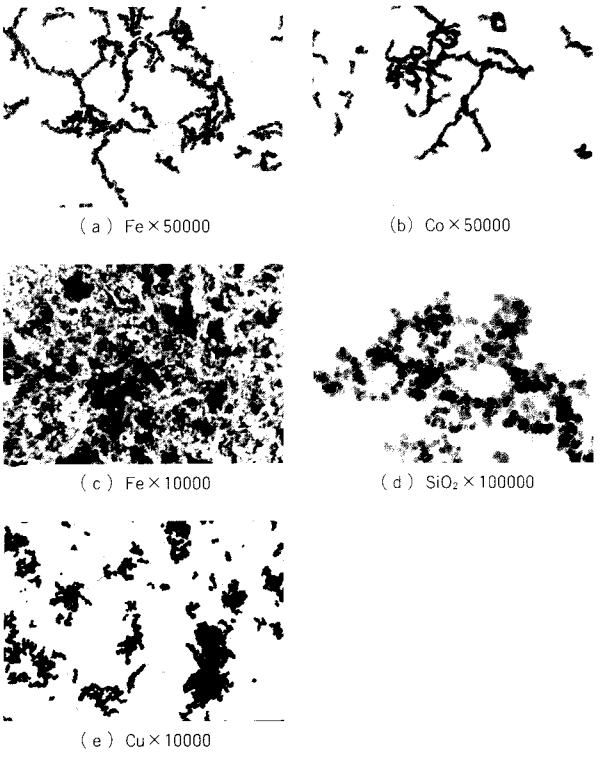

Fig. 2 Transmission electron micro scope photographs of ultraficles of Fe, Co, SiO_2 and Cu

3. Experimental Results and Discussion

3.1 Packing characteristics of ultrafine particles

The results of the observation of the ultrafine particles by means of an electron microscope of scanning-transmission type (STEM H-500, Hitachi)are illustrated in **Fig. 2**(a)through(e).From these images, UFMP of Fe and Co particles which takes the chainlike agglomerate structure as the secondary particles due to the magnetism, and UFP which takes the lumplike structure with several primary particles assembled together, can be cleary distinguished.

3.1.1 Metallic ultrafine particles with chainlike structure

The relationships between the centrifugal force F and compressive strain ε of the powder bed are indicated in the centrifugal compaction of ultrafine Fe and Co particles in **Fig.3**. The relatioaship between these two factors is found to be linear on the logarithmic paper and accordingly, the compressive strain is approximately proportional to the centrifugal force to the power of m, from which the following empirical formula is obtained.

$$\log \varepsilon = m \log F + A \qquad (1)$$

For the packed bed of TiO_2 particles which do not have a chainlike structure but a lumplike one, however, the linear relationship does not hold as depicted by the broken

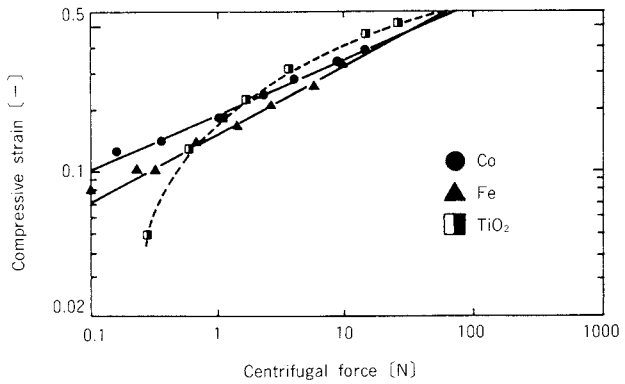

Fig. 3 Relationships between centrifugal force and compressive strain in the centrifugal compaction of ultrafine metal particles of Co and Fe

curve in **Fig.3**.

3.1.2 Metallic ultrafine particles with lumplike structure

The packing characteristics of ultrafine particles of Cu and Al and of oxides SiO_2, TiO_2 and Al_2O_3, are demonstrated in **Fig.4**. From these diagrams, the following equation works well.

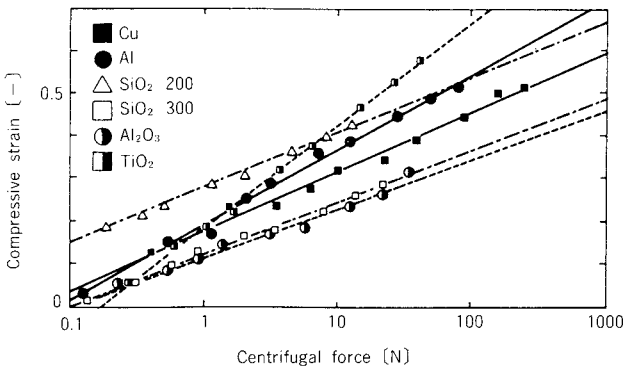

Fig. 4 Relationships between centrifugal force and compressive strain in the centrifugal compaction of ultrafine metal particles of Cu, Al, SiO_2, Al_2O_3 and TiO_2

$$\varepsilon = n \log F + B \qquad (2)$$

The values of the constants in Eqs. (1) and (2) for all of particles covered here were listed in **Table 2**. According to the data on SiO_2 130 and SiO_2 380, the variation of the strain with the centrifugal force deviates toward the higher side as compared with the data on other lumplike particles to which Eq. (2) is applicable, but for the sake of reference the average values determined by the method of least squares are indicated in parentheses. In the past, quite a number of empirical equations were proposed with regard to the compression issue, but none of them dealt with ultrafine particles and there could be found no equations which took an equivalent form to Eq. (1). In a certain way, however, the equation may resemble the empirical rule concerning the deformation during the triaxially isotropic compression of re-kneaded low-plasticity clay[4] as well as the empirical equation proposed by Bal'shin.[5,6]

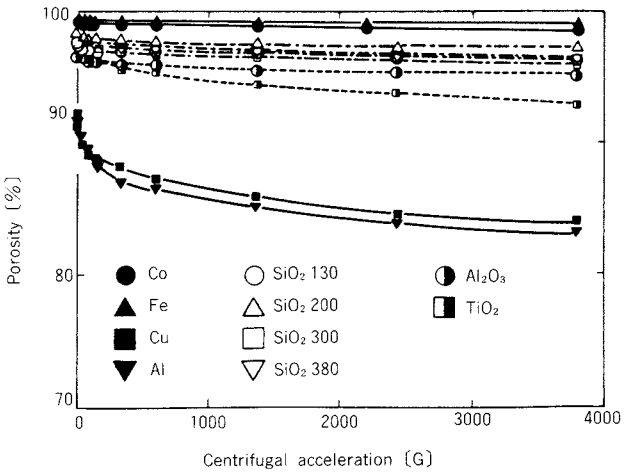

Fig. 5 Relationships between porosity of packed bed and centrifugal acceleration in the packing of ultrafine particles

3.2 Change in porosity of packed ultrafine particles

In **Fig.5**, the relationship between the porosity and the centrifugal acceleration is presented. The porosity of UFP bed tends to increase as the size of the primary particles decreases. In this figure, however, the relationship is reversed. Such a reversion is

Table 2 Values of constants appearing in Eqs.(1) and (2) for ultrafine particles used

Constant	Fe	Co						
m	0.32	0.26						
A	−0.82	−0.72						
Constant	Cu	Al	SiO_2 130	SiO_2 200	SiO_2 300	SiO_2 380	TiO_2	Al_2O_3
n	0.14	0.19	(0.09)	0.13	0.12	(0.14)	0.24	0.11
B	0.18	0.18	(0.21)	0.28	0.12	(0.14)	0.20	0.12

supposed to be caused by the fact that prior to the delivery, the powders would have received a compression treatment at the powder works. It is found in **Fig. 5** and **Table 1** that the porosity is independent of the true density of particle, and in case where the secondary particles exhibit the chainlike structure(Fe and Co particles as shown in **Fig. 2** (a)and(b)), the porosity exceeds 99% and little change in the value of porosity with the centrifugal acceleration is recognized. In case of the lumplike structure, on one hand, the values of porosity for SiO_2 and Al_2O_3 particles slightly change in the beginning, but the change in the porosity becomes very small with a further increase in the acceleration. On the other hand, it is shown in **Fig. 5** that with regard to TiO_2, Cu and Al, the change in the value of porosity with increasing acceleration is remarkable. This difference comes from the difference in the manner of the formation of the secondary particles between the chainlike and lumplike structures, and shows that it is caused by the adhesive and cohesive forces of particles. As mentioned above, in case of Fe and Co particles, the primary particles form secondary particles which take a rosary shape due to magnetism(with chainlike agglomerate structure)as illustrated in **Fig. 2** (a)and(b). **Fig. 2** (c)shows the agglomerate of a meshlike structure which is further agglomerated by these chainlike secondary particles. From **Fig. 2** (d), it is found that the lumplike secondary particles are loose agglomerates of the primary particles. In other words, it may be said that the elements composing the meshlike structure are the chainlike secondary particles, whereas the elements composing the lumplike structure are the primary particles. In such agglomerate structures, the differences in adhesive and cohesive forces among the particles, retard their movement structurally, causing resistance to compaction by the centrifugal force. Thus, it is presumed that the porosity of the powder bed is kept high. Since Fe and Co particles often lumps of a few mm to several tens mm in size locally, even if they are kept in a desiccated container, the particles including such lumps are passed through a sieve of mesh opening 710μm and those which pass through the sieve are used as the specimens. These lumpy particles, subdivided by this sieve, are here called "secondary agglomerated particles". The surface of the secondary agglomerated particles that constitute the meshlike structure exhibits a network structure consisting of interwoven chainlike secondary particles as if a lot of bird nests were connected together (See **Fig. 2** (c)). When these lumps of the agglomerate of the secondary particles classified by the sieve are accumulated and form layers, spaces are formed among the secondary particles. During the process in which these spaces are being filled by the compressive stress, a wide range of compressive strains is realized without any collapse accompanied.

3.3 Elastic and plastic behavior of powder beds

Loading and reloading followed by unloading are repeated to the agglomerate bodies which exhibit two sorts of elasto-plasticity, i.e. chain and lumplike nature. Their elastic and plastic behavior is examined by measuring compressive strains of the

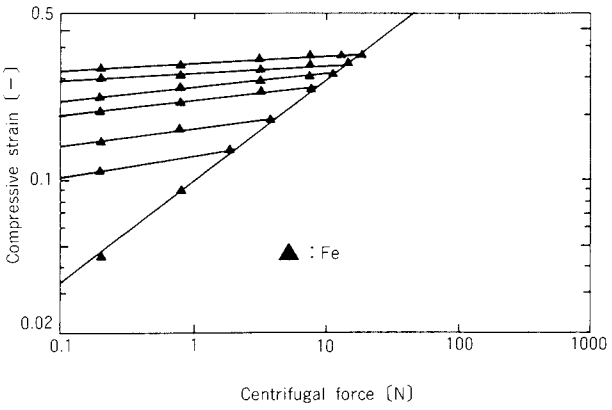

Fig. 6 Variation of centrifugal force vs. compressive strain relation

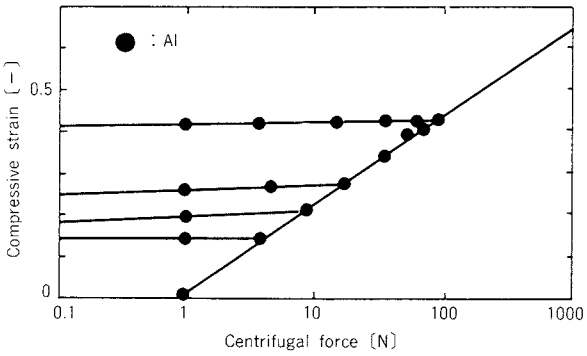

Fig. 7 Variation of centrifugal force vs. compressive strain relation with repeated loading of centrifugal force on Al ultrafine particles

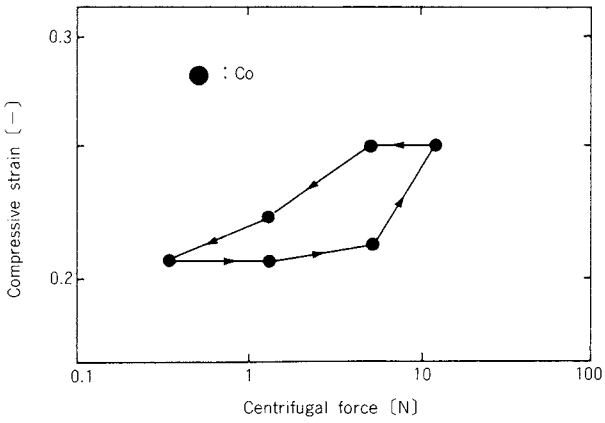

Fig. 8 Hysterisis loop in centrifugal force compressive strain relation of Co ultrafine particles

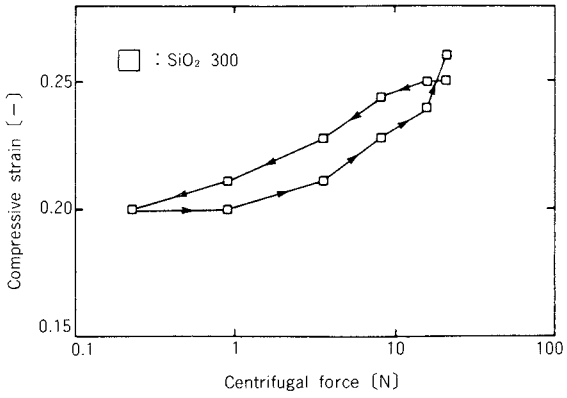

Fig. 9 Hysterisis loop in centrifugal force compressive strain relation of SiO_2 300 ultrafine particles

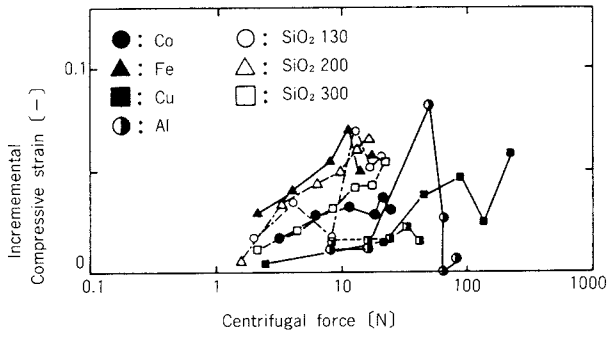

Fig. 10 Relationships between centrifugal force and incremental compressive strain

agglomerate bodies. The results are presented in **Figs. 6** and **7.** It can be seen from these figures that the agglomerate bodies with the chainlike structure are very elastic and do not hardly induce plastic deformation even after repeated cycles of loading and unloading are applied, while those of the lumplike structure induce considerable plastic deformation. Typical examples of the elastic and plastic hysteresis loops for these repetitions of loading and unloading, are indicated in **Figs. 8** and **9.** The operation mode of repeating loading and unloading to the chainlike structure and the similar mode for the lumplike structure are shown in **Figs. 8** and **9,** respectively. In these two operation modes, definite differences are recognized in the loop area and the time lag in the recovery of elasticity. Further, the theory of elasto-plasticity based on Drucker's hypothesis that the yield surface does not conform to the

load surface, is not operative for the lumplike structure, and part of the strain is left every loop of the operation mode. Thus, the relationship between the elastic strain and the centrifugal force for the chainlike and lumplike structures is demonstrated in Fig. 10. From this figure, it can be seen that in the case of Fe and Co particles which are composed of meshlike agglomerates of secondary particles, the increasing rate of the compressive strain, $d\varepsilon/dF$, rises first and reaches a peak value in between 10 N and 100N, then decreases and rises again. On the contrary, in the case of lumplike particles of UFP, $d\varepsilon/dF$ shows a monotonously increasing trend with an increase in F.

3.4 Distinctive features of centrifugal compaction method and comparison with other methods

3.4.1 Relationship between the centrifugal force and the bed height

The difference in the centrifugal forces at the top and bottom of the powder bed due to the difference in the radii of rotation is less than 10%, when the radius of rotation at the bottom of the bed is 12.3cm and the bed height is equal to 2.7cm, and the centrifugal force depends mostly on the amount of particles remaining above the boundary surface of the bed. Therefore, to investigate the characteristics of the particles inside the bed, a tracer method was employed as follows: several portions of specimens with a prescribed equal weight were put into the cylinder while tracer particles of a different color were loaded among the portions, prior to the operation. After applying pressure, the cylindrical cake was cut vertically along a certain diameter and a photo of the section was taken. Then, similar procedures were repeated for the sections prepared by cutting the cake along the diameters at intervals of an equal central angle. The photos taken thus were numerically treated with a digigrammer. As a result, the process in which the saturated compaction layer developes from the bottom to the top of the bed with increasing centrifugal force, was confirmed. For instance, in the case of the cake in which five layers are initially marked with tracer particles and the lower three layers have reached a lower limit of porosity and the same height, the porosity of the top layer is higher by 2.7% and that of the second layer by 1.3% than the lower limit of porosity.

3.4.2 Comparison among the centrifugal compaction, tapping compaction and compressive compaction methods using tracer particles

(1) Compaction conditions and packing states

In the tapping method, the acceleration at the cell impact is apt to be unstable, ranging from several tens to several hundreds G, and in the case of UFP the limit of compaction is nearly reached after several tens tapping actions. In the compressive compaction method, rearrangement of particles and segregation in the particle concentration take place in the vicinity of the piston head and near the top of the cylinder wall, when the compressive stress is applied, causing inhomogeneity in the internal pressure of the bed. In contrast, in the centrifugal method, the compressive force remains the same irrespective of the bed height and the compaction condition is quasi-static, thus a homogeneously packed powder bed which enables one to evaluate the characteristics of the bed, is obtained with good reproducibility. **Figure 11** presents the experimental results using a centrifugal method in which tracers are used in four layers at equal intervals and other two compaction methods, where the change in porosity with the height is shown. In the compression method, a distinctive feature is observed that the concentration of particles at the top and bottom of the bed becomes higher than that in the middle of the bed. In the tapping method, when TiO_2 particles were tested at a falling distance of 1cm, mixing of particles by 150% and 40% at the top of the bed and in the second layer, respectively, was observed. In addition, owing to the friction between the wall surface and the portion of the packed bed, the distribution of tracer particles takes an upward convex shape

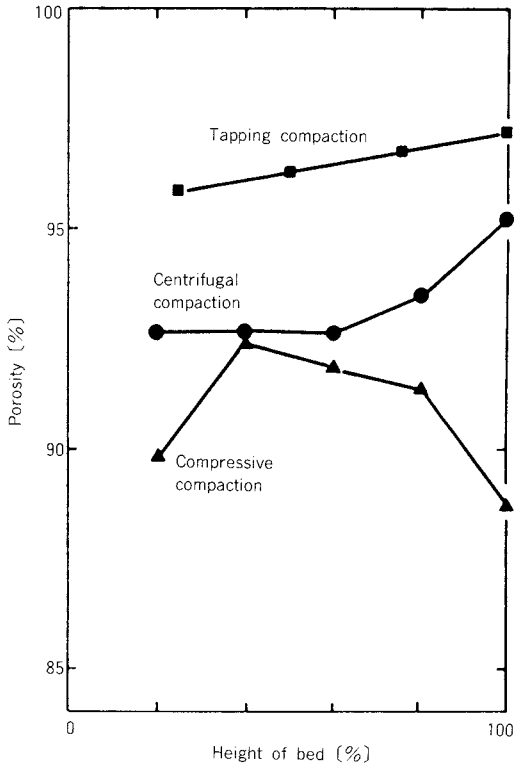

Fig. 11 Variation of bed porosity with bed height in the three types of compaction, viz, centrifugal, compressive and tapping : Height of bed 100% (cell top), 0% (cell bottom)

for the tapping method, whereas in the other two methods it tends to take a downward convex shape.

(2) Influence of the diameter and friction of the tube in each method

In the tapping method applied to TiO_2 particles where the falling distance is 10mm, the influence of the tube diameter is remarkable. When the influence of the wall friction on the bed height was compared for the tube diameters of 20, 30 and 50mm, differences in the values of strain to the initial bed height were estimated to be 20, 25 and 35%, respectively. In the cases for tube diameters of 40 and 50mm, such differences are hardly recognized. In the uiaxial compression test, powders stick around the piston head in a domelike shape and at the tube wall, slipped layers due to the shearing force were observed, starting from the top of the bed close to the piston and running downwards. Their influence diminishes with increasing distance from the piston. When a comparison is made among three methods with respect to the influence of the wall friction exerting when 30 and 50mm pistons are used, the extent of the influence is considerably large for the compressive compaction method, while for the centrifugal and tapping methods, the influence on the bed height for the same tube diameter is 3% or less, which is much smaller than that for the compressive compaction method.

4. Conclusion

A centrifugal compaction system was developed which has distinctive features of being capable of applying a uniform compressive force to any height of the bed and of determining the compressive strain by use of centrifugal force with good reproducibility without disturbing the packed bed. Thereby, the authors found that the relationship between the compressive strain and the centrifugal force for ten kinds of ultrafine particles can largely be divided into two categories. Namely, for Co and Fe particles, the logarithm of the compressive strain is linear to that of the centrifugal force, and for other particles of Cu, Al, SiO_2 TiO_2 and Al_2O_3, the compressive strain is in a good linear relation to the logarithm of the centrifugal force. In the former case, the agglomerate state of particles exhibits elastic and plastic behavior, which is supposed to reflect the meshlike structure composed of chainlike secondary particles. In the latter case, it is presumed that the agglomerate state of particles exhibits a three-dimensional lump-like structure.

Acknowledgment

The authors would like to express gratitude to Fuji Xerrox Co. Ltd. for their cooperation during this study and to Japan Aereosil Co. Ltd. for supplying the ultrafine particles of metal oxides.

Nomenclature

A:constant appearing in Eq.(1)	[−]
B:constant appearing in Eq.(2)	[−]
F:centrifugal forze	[N]
m: constant appearing in Eq.(1)	[−]
n: constant appearing in Eq.(2)	[−]
ε: compressive strain	[−]

References

1)Roller, P.S.: *I & EC.*, , 1206(1930)

2)Rumph, H.: *Chem. Ing. Tech.*, **42,** 538(1970)

3)Otsuka, A., H. Sunada and K. Danjo,: J.Pham. Soc., Japan, **89,** 1013(1969)

4)Namy, D.:Ph. D. Thesis, Cornel Univ.(1970)

5)Bal'shin, M.Yu.: Dokl, Akad. Nauk. SSSR, **67,** 831(1949)

6)Bal'shin, M. Yu.: Dokl. Akad. Nauk. SSSR, **154,** 80(1964)

7)Drucker, D.C.: 1st U.S.National Congress of Applied Mechanics, p.487(1951)

Dispersion and Continuum Models of powder Elasticity †

Hirosuke Okamoto
Engineering Reserch InstituteFaculty of Eng., Univ.of Tokyo *

Abstract

A granular medium is idealized here by a model composed of stress/strain field deviations in a random continuum. Total stress-strain relationships for this model are derived by integrating relationships. Further more, the theory is developed to explain of the dispersion of internal microstress, initial elastic strain, and local yield stress on the macroscopic behavior of a granular medium. Predictions of the theory are reported and agree with the results of the experimental work.

1. Introduction

As is known, granular samples, though produced by a same material, are remarkably showing different deformation behavior and strength characteristics when the preparation procedures are different. Starting from such a condition, which suggests that the initial anisotropy and the physical quantity are showing material property of granule which varies with place, in general. This means that granule must be microscopically treated as a non-homogeneous system consisting of many different structures. One of the characteristics featuring the construction of irregular system formed by this spatial variation is the statis-structure. Here, information on the geometrical configuration of particles around a particle and information on their interface are particle and information on their interface are among the important parameters too. In addition, granule is given the stochastic character derived from an uncertainty coming from the discrete state where a granule is composed of particles. To deal with the mechanical property of granule, therefore, statistical and stochastic techniques are necessary and effective as well.

Regarding such a granule composed of irregular and uncertain elements, the physical quantity can be locally defined if assuming a continuum, where the conventional continuum mechanics can be applied. Moreover, if variations of various quantities are much less than the typical quantities expressing the features of an entire system, or if the optional portions of a system indicate the situation of statistically same variations (distributions), the statistical mechanics will be applicable.

Theories dealing with granule as continuum so far furnished less direct discussions by considering deformation as a principal[1], and treating it according to the stress indication. In understanding the deformation in the light of subsequent observations; the connection and correlation of forces measured externally as even continuum and the microscopic quantities according to the deformation itself were treated in discussions in the multidimensional space generalized, and the relevant equations were examined statistically.

2. Expression As A Random Continuum

In an actual behavior to give force to granule, it is assumed that an even strain is not spread entirely at a moment, but the relative displacement takes place at contacting points

* Yayoi Bunkyo-ku, Tokyo 113 Japan
TEL 03-3812-2111

† This reprt was originally printed in *J. Soc.powder Technolgy, Japan,* **27**,146-152 (1990) in Japanese, before being translated into English with the permission of the editorial committee of the Soc. Powder Technology, Japan.

of finite number, which then appear and where slipping is caused among particles in unstable places; the particles move there in separating or contacting. Portions pulled by the movement and rotate around the particle bulks; the equilibrium and compatibility of the forces are formed entirely.

The writer showed, in the previous report[2], that the noise caused by a flow of particles reflects the contacting state among internal particles, and proved, in an observation then made, that the time interval of a generating sound(collisional sound)caused in a certain time zone took the shape of Poisson distribution. This means thnt contacts among particles appeared nearly at random.

A static test points out that it is to be regarded rational that when the equilibrium state under a combination of some principal stresses is transferred to the equilibrium state by a combination of other succeeding principal stresses through slipping on a contacting point of particle, the distribution of contacting points among particles in an aggregate, spread in all directions at random prior to the initial condition before causing slipping; and this was determined by observing the distribution of contacting point angles[3].

Regarding many granules, it is observed that the relation between the ratio of principal stresses and ratio of principal strain increments is linear[4].

Linear relation means that the present condition can be considered as standard point irrespective of the former history; in combination with the test results mentioned before, the random characteristics in the strain direction immediately before slipping occured on the contacting point of particle is also re-produced in deformation process, namely, the same random characteristics on the optional point as an original one will be assumed.

From the above, a step to consider the mechanical process of granule as a continuum giving a mean value of certain random variable that considered as observed quantity, could also be taken into account. Equation of motion of a granule to be stochastically non-homogeneous continuous medium becomes a non-linear stochastic partial differential equation containing elastic coefficient such as random stochastic variable, where it can be said in general, that it is a difficult problem to obtain its strict analytic solution.

In this paper, for the sake of practical treatment, a large sample is employed and an approximation is used for the interaction effect of stress field of particles, where the most neighboring particles are considered. Variate here is nearly random, where one portion representing sample on an optional point, namely, a part in which sufficently many particles to allow thinking the average number of contact points distributed at random in a contacting condition, can be considered. Now, in order to find how shearing stress τ occured through the contacting point on such part would affect a macroscopic stress, probability density function $p(\tau)$ has been introduced. Macroscopic strain and stress are expressed as in the following equations[5]

$$\langle \varepsilon_{ij} \rangle = \int_0^\infty \varepsilon_{ij}(\tau)\, p(\tau)\, d\tau \tag{1}$$

$$\langle \tau_{ij} \rangle = \int_0^\infty \tau_{ij}\, p(\tau)\, d\tau \tag{2}$$

3. Balance of Internal Stress and Strain

A mechanism to cause internal stress is explained. By nature, a substance does not generate stress, if deformed, without external restriction. Strain caused in such a deformation is called'plastic strain'. Strain not causing internal stress, even if the change of shape(generation of strain)is generated, is a non-elastic strain.

Such a strain, which does not generate stress by itself, can generate internal stress if the strain is produced uneven. On the other hand, however, there is a strain causing an even deformation to material but not generating stress. A few strains, such as those by thermal expansion or change of shape according to the phase transition, are known. The occured strains, when observed only by means of thermal expansion and crystal lattice structure, are of same character as those defined above.

Obviously, the internal stresses generated therein are derived from a given unevenness. In this respect, in considering the change of force giving the relative displacement of particles, a definite difference becomes upparant, where components of internal strain can meet a cause.

To investigate the condition of internal strain generated by such unevenness, the strain deviator defined by subtracting the mean strain from the actual strain, which expresses the adequate stress-strain relation, is taken up. This shows distortion of the system, on which the shearing deformation is completely dependent[6].

Assume that stress deviator σ^D is the same as to the shearing stress causing a relative displacement between two particles, namely,

$$\tau = \sigma^D, \quad \sigma^D = \sigma_{ij} - \frac{1}{3}\sigma_{kk} \tag{3}$$

As illustrated in **Fig. 1,** within an interface between two particles it is observed that a slipping band on periphery and an internal elastic contacting point do exist together[7].

Until an external force becomes and the following condition

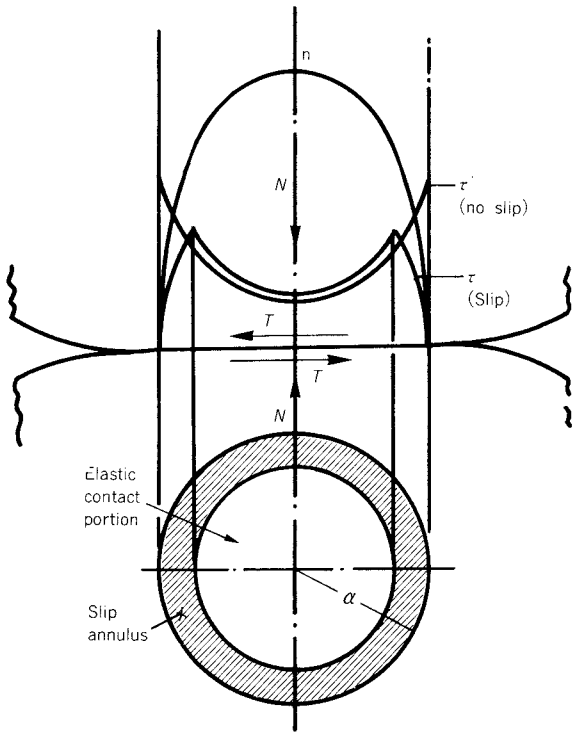

Fig. 1 Distribution of normal(n) and tangential (τ) components of traction on the contact surface of two like sphere subject to a normal force N

$$\tau \geqq \mu \cdot n \tag{4}$$

(μ: friction coefficient, n: vertical force)is satisfied, the slipping annulus on the interface increases gradually, becomes finally a macroscopic slipping and is separated into two units.

When a granule is pressed, on the interface of two contacting particles to be components or in the deformation of infinitesimal granules, an elastic deformation phase and a plastic deformation phase co-exist together, and the deformation process is advanced in parallel. That is, before reaching the yield point observed macroscopically, the deformation is progressed containing local non-elastic deformation. Apparently, the deformation is running with elastic behavior in relation to the entire balance and adaptation, and it reaches the so-called yield condition as one influential force of non-elastic element increases.

Naturally, the stress-strain relation is different on the elastic and plastic phases, being regarded as a gradually changing expression[8]. In this paper, the relation dealt with is up to immediately before the macroscopic yield point. In the following, τ in Eq.(4)will be treated by dividing into an elastic resisting part and a non-elastic resisting part.

Express an elastic component of shearing force τ acting on i-plane in j-direction as τ_{ij}, and a non-elastic strain component by $\varepsilon_{ij}{}^{P}$[9]. That is,

$$\tau_{ij} = \sigma^D - \alpha\varepsilon_{ij}{}^{P} \tag{5}$$

where, α is a quantity expressing the contribution rate to the entire elastic modulus affected by the non-elastic deformation part, which is fixed according to the balance of internal stress and non-elastic deformation, namely, a constant $0 < \alpha \leq 1$.

For complete plasticity, $\alpha = 1$, which is consistent with the expression of conventional mathematical theory of plasticity.

Non-elastic strain here shall be defined as a difference of deflective strain provided that an actual deflective strain and the Hooke's law are realized. Shearing stress-strain relation is obtained by letting a shearing elastic coef-

ficient be G

$$\tau_{ij} = 2G\varepsilon_{ij} = 2G[\varepsilon_{ij}{}^{p} - \beta\varepsilon_{ij}{}^{p}] \tag{6}$$

where, β is a proportional constant.

When an initial elastic microscopic strain ε° is contained, the following equations are utilized by introducing initial strain field ε^{*}

$$\tau_{ij} = \sigma_{ij}{}^{D} - d\varepsilon_{ij}{}^{*} \tag{7}$$

$$\left(\varepsilon_{ij}{}^{*} = \varepsilon_{ij}{}^{p} + \frac{2G}{d}\varepsilon_{ij}{}^{\circ}\right) \tag{8}$$

Condition until a shearing drift of two particles in contact is caused by

$$\varepsilon^{\circ} \lesssim \tau_{p}/2G \tag{9}$$

where, τ_{P} means a yield shearing strain.

The condition decides the correlation among two random parameters and ε°, which also shows that an initial microscopic stress having the strength exceeding the local yield point is not considered as the cause. Actual slipping is caused on the part unstable to infinitesimal variation of stress on contacting points in the critical condition as mentioned in the beginning. To perform actual calculation, therefore, application of equal signs to Eq.(9)regards the effect of microscopic force to be higher from a physical point of view.

4. Distribution of Initial Elastic Microscopic Strain

Express initial elastic microscopic strain $\varepsilon_{ij}{}^{\circ}$ within a range not to destroy the homogeneity and isotropy in an initial macroscopic condition and also express strain field distribution with such strain as in the following variate

$$\varepsilon^{\circ} = \sqrt{\varepsilon_{ij}{}^{\circ}\,\varepsilon_{ij}{}^{\circ}} \tag{10}$$

For a shear giving the relative displacement of particle, a stochastic variate of five strain components is to be considered by deleting the term of volume variation

$$\varepsilon_{1}{}^{\circ} = \sqrt{\frac{3}{2}}\varepsilon_{11}{}^{\circ}, \quad \varepsilon_{2}{}^{\circ} = \sqrt{2}\left(\varepsilon_{22}{}^{\circ} + \frac{1}{2}\varepsilon_{11}{}^{\circ}\right)$$

$$\varepsilon_{3}{}^{\circ} = \sqrt{2}\,\varepsilon_{12}{}^{\circ}, \quad \varepsilon_{4}{}^{\circ} = \sqrt{2}\,\varepsilon_{33}{}^{\circ}, \quad \varepsilon_{5}{}^{\circ} = \sqrt{2}\,\varepsilon_{13}{}^{\circ} \tag{11}$$

From the above, vector length ε_{0} in a five-dimensional strain space is defined as [10]

$$\varepsilon_{0} = \sqrt{\varepsilon_{ij}{}^{\circ 2}\,\varepsilon_{ij}{}^{\circ 2}} = \sqrt{\varepsilon_{1}{}^{\circ 2} + \varepsilon_{2}{}^{\circ 2} + \cdots + \varepsilon_{5}{}^{\circ 2}} \tag{12}$$

Consequently, a so-called yield curved surface is expressed as a five-dimensional hypersurface of the five-dimensional strain vector space. As this $\varepsilon_{ij}{}^{\circ}$ is a random quantity, the mathematical expected value(mean value)of this five-dimensional vector is zero.

Assume, now, the distribution of each ε° follows the normal distribution. It is found by means of the probability theory that a variable fixed according to the square sum of independent variable following an identical normal distribution of a mean value at zero has a chi-square distribution density function of five degrees of freedom in such a case.

Accordingly, probability density of ε_{0} is obtained

$$p(\varepsilon_{0}) = \frac{2}{3}\frac{1}{\sqrt{2\pi}}\cdot\frac{\varepsilon_{0}^{4}}{a^{5}}\exp\left(\frac{-\varepsilon_{0}^{2}}{2a^{2}}\right) \tag{13}$$

where, a^{2} shows a dispersion of $\varepsilon_{k}{}^{\circ}$.

5. Microscopic Strain Distribution and Macroscopic Deformation

By utilizing the results obtained, an entire strain in five-dimensional strain space employed in the previous section, namely,

$$\varepsilon = \varepsilon_{ij}{}^{p} + \varepsilon_{ij}{}^{*} \tag{14}$$

is to be treated, which is

$$\langle\varepsilon_{ij}\rangle = \iiiint \varepsilon_{j}\,p(\varepsilon_{k}{}^{\circ})\,d\varepsilon_{1}{}^{\circ}\,d\varepsilon_{2}{}^{\circ}\cdots d\varepsilon_{5}{}^{\circ} \tag{15}$$

where,

$$p(\varepsilon^{\circ}) = \frac{1}{(2\pi)^{5/2}}\cdot\frac{1}{a^{5}}\exp\left(\frac{-\varepsilon_{0}^{2}}{2a^{2}}\right) \tag{16}$$

Change the above equation to a spherical coordinates system. Jacobian J in this five-dimensional coordinates system is

$$J = \tau^{4}\sin^{3}\theta_{1}\sin^{2}\theta_{2}\sin\theta_{3} \tag{17}$$

and, Eq.(15)becomes

$$\langle\varepsilon_j\rangle=\frac{1}{(2\pi)^{5/2}}\cdot\frac{1}{(2Ga)^5}\int_0^\infty\int_0^\pi\int_0^\pi\int_0^\pi\int_0^{2\pi}\varepsilon_j \times\exp\left(-\frac{\varepsilon_0{}^2}{2a^2}\right)J\,d\tau d\theta_1 d\theta_2 d\theta_3 d\theta_4 \tag{18}$$

This relation is not simple.

In consideration, now, of homogeneous, isotropic and infinitesimal displacement, a case of one dimension is taken up to briefly determine the tendency of the object.

To begin with, a case without initial strain is treated. In this case, $\varepsilon_j{}^{*p}$ becomes a function only of τ as a scalar parameter. The relation with Eq.(18) is

$$\langle\varepsilon_j\rangle=\int_0^\infty\varepsilon_j(\tau)p(\tau)d\tau \tag{19}$$

In

$$\tau_p>\tau \tag{20}$$

it is expected, from the condition Eq.(9), that the probability density of τ has a same shape of ε^{*p}; hence the following equations are formed.

$$p(\tau)=\frac{2}{3}\cdot\frac{1}{\sqrt{2\pi}}\cdot\frac{\tau^4}{b^5}\exp\left(-\frac{\tau^2}{2b^2}\right) \tag{21}$$

$$b^2=(2G)^2\cdot a^2 \tag{22}$$

From Eqs.(7)and(19)

$$\langle\varepsilon_j\rangle=\frac{1}{d}\int_0^\infty(\sigma^p-\tau)p(\tau)d\tau \tag{23}$$

by which the changing rate of ε for the change of σ

$$\frac{d\langle\varepsilon\rangle}{d\sigma}=\frac{1}{d}\int_0^\infty p(\tau)d\tau \tag{24}$$

is obtained.

From Eqs. (23) and (24), an equation of asymptote on the yielding point is formed

$$\langle\sigma\rangle=d\langle\varepsilon\rangle+\langle T\rangle \tag{25}$$

where, $\langle T\rangle$ is a quantity

$$\langle T\rangle=\int_0^\infty\tau p(\tau)d\tau$$

$$=\frac{8}{3\sqrt{2\pi}}\cdot b\cdot\int_0^\infty\exp(-t^2)\cdot t^5\,dt\,(\tau=\sqrt{2}\,bt)$$

$$=\frac{16}{3\sqrt{2\pi}}\cdot b \tag{26}$$

which is a value of slice on the tangential stress axis of stress-strain curve. From the above, if the material is brittle, its yielding stress value can nearly be expressed by the value $\langle T\rangle$ on the yielding point.

Eq.(26) indicates that $\langle T\rangle$ is proportional to the standard deviation value of distribution of τ, and according to Eq.(22), the value is proportional to the standard deviation value of the initial strain distribution. That is, this relation suggests somehow an approach to increase the strength of material.

Now, in order to improve the tenacity of a brittle material(ceramics[11], for instance),a method known to be effective to disperse or deposit the heterogeneous phase as energy dissipative source into material has been proposed. It can be assumed that if there is an uneven part in structure, loading stress is concentrated around the boundary of the part, and a magnitude of the concentrated stress would appear in multiplication of shape, size, arrangement, distribution, difference of modulus of elasticity and thermal expansion to the surroundings.

Moreover, these elements act reversely depending on materials, which may reduce stress.

K_{IC} showing the breaking renacity of material is expressed by the following equation.

$$K_{IC}=(2E\gamma_i)^{1/2} \tag{27}$$

As Young's moduls E is a given material constant, the material is made stronger by increasing the level of fracture energy γ_i. This performance is available by controlling the structure of material. Result of Eq.(26) indicates a strain dispersion effect to the stress concentretion. This indication furnishes that various elements mentioned before produce their own compound effects, work as the energy absorbing mechanisms, and increase the tenacity of material. Applying properly the parameters of normal distribution as-

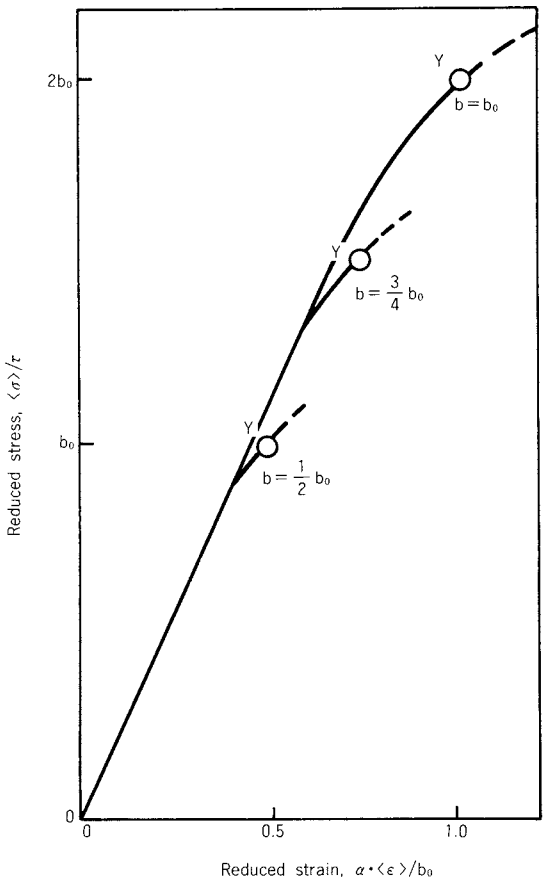

Fig. 2 Stress and strain curves picturing for three different value of the standard deviation b (Y ; effective yield point)

sumed, a sufficient approximation of the Weibull distribution showing the breaking strength characteristics of many materials is given, where actual application can be expected.

In **Fig. 2** graphs and from the above analysis, a tendency of influence of strain distribution to the stress-strain relation becomes obvious.

Then, a case having the initlal elastic microscopic strain is examined. To simplify, distribution density of shearing strength $p(\tau)$ and distribution density of initial elastic microscopic strain $p(\varepsilon_0)$are approximated respectively as in the following.

$$p(\tau) \approx \delta(\tau - \langle\tau\rangle)$$
$$p(\varepsilon_0) \approx \delta(\varepsilon_0 - \langle\varepsilon_0\rangle) \qquad (28)$$

Consequently, from Eq.(18)

$$\langle\varepsilon_k\rangle = \iiiiint \varepsilon_k \delta(\tau - \langle\tau\rangle)\delta(\varepsilon_0 - \langle\varepsilon_0\rangle) \times \sin^3\theta_1 \sin^2\theta_2 \sin\theta_3 \, d\tau d\varepsilon_0 d\theta_1 \cdots d\theta_4 \qquad (29)$$

A case of one dimension is also examined. From Eq.(29)

$$\langle\varepsilon_k\rangle = \frac{3}{4}\int_0^{\pi} \varepsilon_k \sin^3\theta_1 \, d\theta_1 \qquad (30)$$

In this caes, as θ_1 of ε_k, namely, dependence of ε_{11} ◦ can be regarded nearly linear, an equation of asymptote around the yielding point of its stress-strain curve is formed by adding a term regarding the initial strain to Eq.(25), that is

$$2G\langle\varepsilon_0\rangle \qquad (31)$$

which is added linearly, where an increase of the initial strain increases the initial modulus of elasticity within the range of Eq.(9).

Fig. 3 illustrates the shearing test results of quartz sand (average grain daimeter: 0.18 mm)by changing pressure p_i giving thus an initial strain. In a considerable range of shear velocity, it is found that a shearing stress is increased as an initial pressure is increased[12].

It is also found that the grain size affects strength. Grain diameter is relative to the magnitude of surface curvature, and the magnitude of curvature gives an influence to the effect of stress concentration of contacting point.

As the dislocation density is increased, the curvature of particle becomes larger, and consequently it has widely been recognized

$$\tau_p \propto d^{-1/2} \qquad (32)$$

that there is relation between yielding strength τ_p and crystal grain diameter d(Hall-Petch relation[13])on polycrystalline material[14].

Meanwhile, the theory of comminution of granule indiactes that energy used to comminute is reversely proportional to the square root of grain diameter. Stiffness of material is measured by the variation of elastic energy to displacement. Consequently,

$$G \propto d^{-1/2} \qquad (33)$$

According to the relation of the above

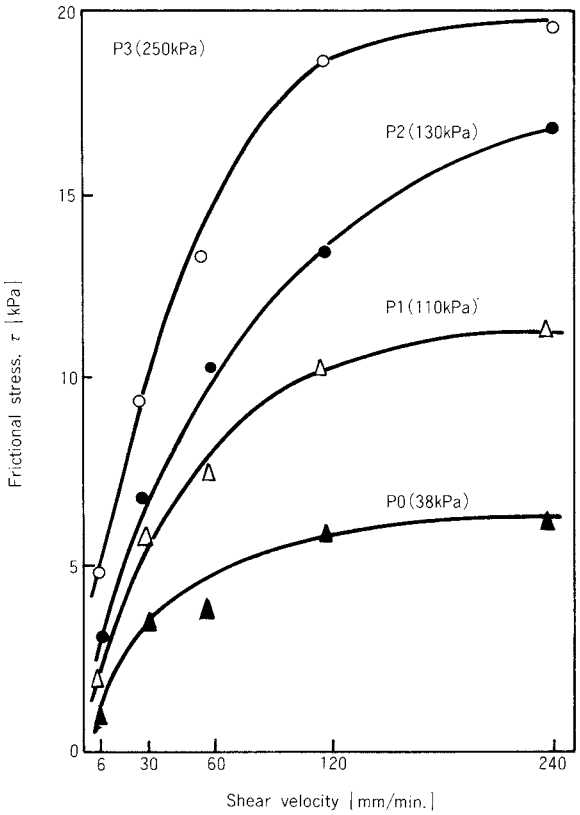

Fig. 3 The relation between initial pressure pi, frictional stress τ and shear velocity

equation to Eqs.(22)and(26)

$$\tau_p = \langle T \rangle \propto 2Ga \propto d^{-1/2} \qquad (34)$$

is obtained, which is approximate to Eq.(32).

Fig. 4 is prepared by re-arranging the test results[15] on the relation of fracture energy of Al_2O_3 and grain size along $d^{-1/2}$ -axis. As plotted, the relation is linear.

Fracture energy and fracture teancity in this case vary with the condition of microcrack inside. Density function p(·)in Eq.(26)is reasonable to be treated as a distribution density of microrack inside grain. Such being the circumstances, the above relation and the conclusion of Eq.(34)indicate that an optimum grain size having the highest strength is existing, which can be estimated.

6. Conclusion

The contacting condition of the grain forming granule was examined; the systme of non-linear elastic action as an expression of interacting mechanism was built in, normal

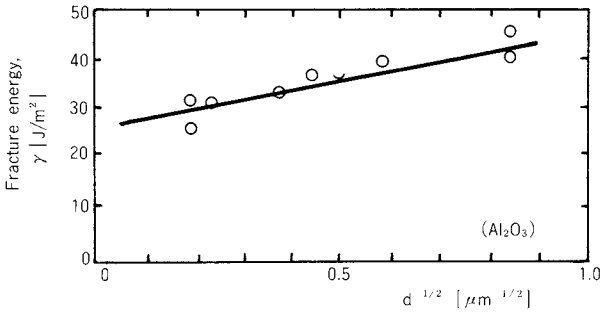

Fig. 4 Dependence of fracture energy on grain size (Data from reference 15)

distribution fulfilling an actual strength characteristics was used as distribution model to decide the combination law of acting elements, and a granule was re-constructed a stochastically non-homogeneous continuous medium, which was compared with an actual example. The main results were

1) influences affecting strength of internal strain distribution were found coincident qualitatively,
2) increase of initial strain coincided with increase of initial elastic modulus experimentally, and
3) relation of elastic limit and grain size were incident analytically. The availability of a technique to treat granule as stochastically inhomogeneous non-individual body non-linear elastic element has been confirmed.

Nomenclature

a^2	:variance of ε°	[−]
b^2	:variance of τ	[−]
d	:diameter of grain	[m]
G	:elastic shear modulus	[Pa]
J	:Jacobian	[−]
n	:normal component of traction	[Pa]
p (τ)	:density of the distribution of τ	[−]
α , β	:scalar coefficient	[−]
ε	:strain	[−]
ε°	:initial elastic microstrain	[−]
ε^p	:non-elastic microstrain	[−]
σ	:stress	[Pa]

τ :random dissipative force of resistance to shear deformation [Pa]

μ :coefficient of friction [−]

$\langle \cdot \rangle$:mathematical expectation of a quantity [−]

References

1) Mogami, T.:"Doshitu Rikigaku", Chap.8, Gihou-Do(1982)

2) Okamoto, H.: *J. Fac. Eng., Univ. Tokyo.*, **36,** 37(1981)

3) Tatsuoka, H.: *Tsuchi to Kiso,* **26-7,** 55(1978)

4) Oda, M. : *Soils and Foundations,* **12-2,** 1(1972)

5) Murzowski, j. "Non-Homogeneity in Elasticity and Plasticity(Ed. by OLSZAK, W)", p.479, Pergamon Press(1959)

6) Kanatani, K.: Tsuchi to Kiso, **28-12,** 5(1980)

7) Deresiewicz, H.: *Adev. Appl. Mech.*, **5,** 233(1958)

8) Hill, R.: "Sosei-Gaku(Trans. by K.Washizu., K. Yamada & A.Kudou)", p. 47, Baifu-Kan(1954)

9) Eshelby, J.D.: *Proc. Roy. Soc.*, **A241,** 376(1957)

10) Flugge, W.: "Tensoru-Kaiseki to Renzokutai- Rikigaku(Trans. by M. Goto)", Chap. **4,** Burain Tosho (1985)

11) Niihara, K., *el al: Seramicus,* **21,** 581～619(1986)

12) Okamoto, H.: *Ann. Rep. of Eng. Res. Inst.,Fac. Eng.,Univ. Tokyo,* **44,** 187(1985)

13) Petch, N.J.: *Phil.Mag.*, **3,** 1089(1958)

14) Barrett, C.R., Nix, W.D. and Tetelman, A.S.: "Zairyou-Kagaku 2"(Trans. by H.Okamura, N.-Igata & M.Doyama)p. 79, Baifuu-Kan(1988)

15) Simpson, L.A.: *J. Am. Ceram. Soc.*, **56,** 7(1973)

Relationship between Adhesive Fore and Dispersibility of Sub-micron Particles †

Hideo Yamamoto
Dept. of Bioengineering,
Faculity of Enginerring.
Soka University *

Shuhei Shinji
Dept. of Industrial chemistry
Wakayama Culloge of Techuology **

Abstract

Adhesive forces of sub-micron particles of limestone were measured by using a split-cell type tensile stregth tester under various vapor pressure conditions of water, etanol and acetone. The adhesive force generated by ethanol vapor or acetone vapor adsorption was smaller than that generated by water vapor adsorption.

Agglomerated particles generated from a miclo-fluidized bed of the limestone sample with various atmospheric gases were dispersed by a high speed gas stream through a small pipe, and the size distribution of the agglomerates was measured. The agglomerates containing adsorbed ethanol were easily dispersed into the single particles by about half the force required for the agglomerates contraining adsorbed water, which qualitatively corresponded to the decrease in the adhesive force of the particles by adsorbing ethanol vapor instead of water vapor.

1. Introduction

With the decrease in particle size, powder materiais tend to increase in adhesion and cohesive aggregation, and consequently, decrease in their dispersibility and fluidity in general. For this reason, fine powder materials, especially submicron powder materials, are very difficult to handle in operations such as dry classification, mixing and pneumatic transportation. In dry classification, for example, it is essentially important to have the feed powder material well dispersed in the from of single primary particles in a gas prior to classification. However, mechanical dispersing means conventionally use such as ejectors and orifices are difficult to provide such a good dispersion as previously mentioned for submicron powder material, for the cohesive force of powder particles increases with a decrease in the particle size and finally becomes very strong in comparison with the dispersing forces such as the inertial impact force and shearing force of air acting on the oarticles from outside. As the one of the most important factors for development of the cohesive force of powder particles, it is known that a liquid bridge forms between particles due to adsorbed substances such as water onto the particles. This component of cohesive force is considered to result from the force generated at the contract area of particles due to the inner negative pressure and surface tension of the bridge forming liquid that appears as a result of, for instance, capillary condensation[1]. If the cohesive force of powder particles would be possible to controll by varying the substance adsorbed onto the particle surface in its molecular type and amount, therefore, the dispersibility of

* 1-236, Tangi-cho, Hachioji-shi, Tokyo. 192. Japan
TEL. 0426-91-2211

** 77. Noshima, Noda-cho. Gobo-shi 644 Japan
TEL. 0738-29-2301

† This report was originally printed in *J. Soc. Powder Technology, Japan,* **27**, 159-164(1990)in Japanese, before being translated into English with the permission of the editorial committee of the Soc. Powder Technology, Japan.

submicron powder materials could be greatly improved. We call such substances to be adsorbed on the surface of particles dispersing aid (DA) in gas plase, and have been studying the effect of alcohol and acetone as DA on the dispersibility of submicron powder materials[2),3)]

In the present wark, submicron powder material is conditioned in various atmospheres of DAs as a sample, the cohesive force of this sample is measured by use of a split-cell type tensile strength tester, and the dispersibility is tested by dispersing aggregated particles of the samples by means of a high-speed gas stream generated in a needle pipe; funthermore, the relationship between them is discussed.

2. Experimentals

2.1 Materials and preparation of test samples

Limestone fine powder material (median diameter : 0.6μm)was used for the submicron powder sample : water, ethanol and acetone were used as DA.

The powder sample was spread on a tray through a 32 mesh sieve, placed in a closed chamber and exposed to DA vapor at a definite relative pressure for more than a week : control of the vapor atmosphere in the camber was done by continuous flowing of nitrogen

relative vapor pressure. In this case, commercial nitrogen gas(H_2O<10ppm)was used to avoid contamination by any other vapor than DA in use. Such conditioning as previously mentioned can be expected to have completely replaced the existing water molecules physically adsorbed on the particle surface of the powder sample by the DA molecules.

2.2 Measurement of cohesive force (tensile fracture test of a compacted powder sample mass)

In this case, a hanging-type tensile strength tester(Cohetester, Hosokawa Micron Co.)as shown schematically in Fig.1 was used. The tester was placed in a glore box (600×1400×

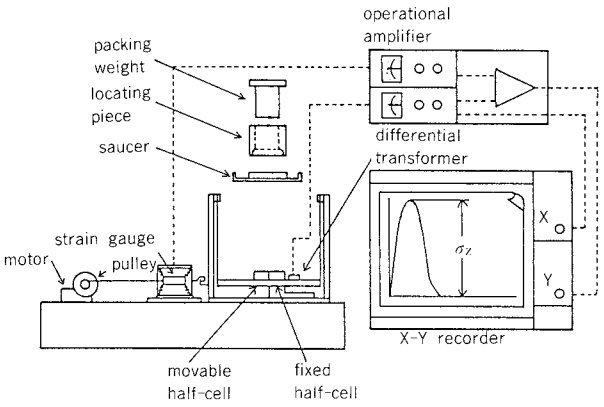

(Split cell type tensile strength tester)

Fig.1 Diagram of split cell type tensile strength tester

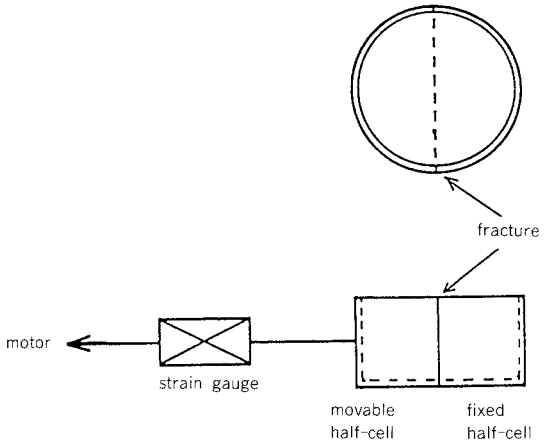

Fig.2 Schematic view of the split cell

700mm), and all of the test procedures, from filling of powder sample to completion of tensile fracture, were carried out under the same atmosphere as that of sample conditioning.

The principle of the cohesive force of measurement is as follows : a cell shown in Fig.2 consisting of two halves is filled with a powder sample for testing, and then, the movable half is pulled horizontally until fracturing of the sample mass occurs so as to measure fracture stress. The cell used was 50mm in inner diameter and 20mm in depth, and was coated with silica sand having a particle size of ca. 1mm on its lower part to prevent the powder sample mass from

slipping. The movable half cell was pulled horisontally at a rate of 2mm/min, during which stress generated was measured with the use of a strain gauge supported by a coil and, at the same time, displacement of the half cell was measured by a differential type transfomer. The movable half cell was hung by means of three band-plates of phosphor bronze with which the half cell was permitted to move horizontally without any frictional resistance. The powder sample was filled in the cell as uniformly as possible by use of a spatula, subjected to compaction with a load of 0.7 to 12kpa for 10min to adjst the porosity of the resulting powder sample mass, brought to a constant volume by sweeping off the excess built up above the level of the upper part of the cell, and then, subjected to the tensile test as mentioned above. Tensile test results showing highly complicated fracture surfaces were excluded from the data.

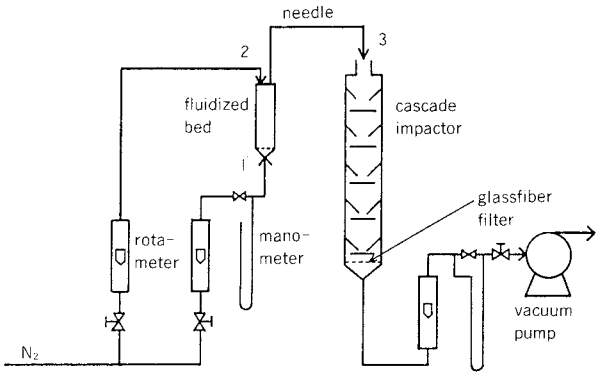

Schematic diagram of the dispersion experiment

Fig.3 Schematic diagram of the dispersion experiment

2.3 Testing of dispersibillity

The apparatus used for dispersibility test is schematically shown in Fig.3. A vibrating fluidized bed ①(inner diameter 20mm, height 200mm, pore diameter of fluidizing plate of porous sintered glass 100μm) was used for dust of aggregated particles genezation. The powder sample conditioned in a DA atmosphere was placed in the apparatus at a still height of 40mm, and then, fluidized by nitrogen gas containing DA and the aggregated particles were generated. With use of the same flow rate(same fluidizing condition), different fluidizing gases should bring a certain powder sample into the same dust generation of aggregated particles(same in size distribution of aggregated particles)[4]. The dust containing the aggregates were transported through a needle pipe together with the stream of the fluidizing gas and dispersed there. The magnitude of the dispersing action of the gas stream can be changed by changing the flow velocity of the gas in the needle pipe by means of changing the diameter of the needle pipe or introducing additional nitrogen gas from ②, according to which the fed powder sample finally flows out of the needle pipe outlet ③ in a dust at various states of dispersion. A slit-type cascade impactor(CI-50, Shimadzu Co.; 8-staged special design) was used to measure the particle size distribution of the dust * foot note. A * This type of cascade impactor can measure the particle size of aggregated particles. The types of needle pipes and the gas streaming conditions in them are listed in Table 1,where Δp is the pressure drop across the needle pipe.

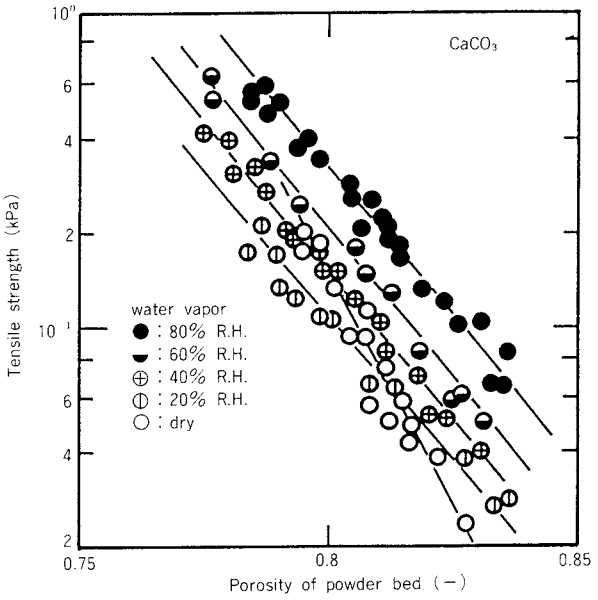

Fig. 4 Tensile strength of the limestone powder exposed to various humidities

*This type of cascade impactor can measure the particle size of aggregated particles.

Table 1 List of dispersing needles

No.	Needle diameter (mm)	Q_f (Nl/min)	$Q\alpha$ (Nl/min)	ΔP (mmHg)
1	1.1	4.0	0	335
2	1.5	4.0	0	160
3	1.8	4.0	1.0	112
4	1.8	4.0	0	86
5	2.5	4.0	1.0	56
6	2.5	4.0	0	28

Needle length : 200mm

Q_f : inlet gas flow rate to fluidized bed

$Q\alpha$: excess gas flow rate from ② in **Fig.3**

ΔP : gas pressure drop across the needle

3. Results and Discussion

3.1 Relation between cohesive force and type of adsorbed molecules

Figure 4 shows the test results of tensile strength at fracture for limestone powder samples conditioned in a water vapor atmosphere at various levels of relative vapor pressure, whrere the axes of the abscissa and ordinate represent the porosity and cohesive force per unit area of the compacted powder samples. It is seen from Fig.4 that the relative humidity at conditioning gave a significant effect to the cohesive force. Furthermore, it was found that the 80% RH caused a considerably higher cohesive force than those less than 80%, which suggests that the higher humidity caused a larger amount of adsorbed water, and thus, at the vicinty of 80% RH, the water vapor was adsorbed to the extent sufficient enough to form a liquid bridge at a contact point between partieles[7]. In addition, the sample conditioned in dry nitrogen gas (hygrometer reading of 3 to 5%) was found to be different in behavior from those conditioned at other levels of humidity. This suggests that, in the case of conditioning in a dry nitrogen gas, the amount of adsorbed water was much less and not enough to develop a monomolecular layer of water, and thus, the cohesive force was brought about from a hydrogen bond of the water molecules, not from liquid bridging.

Figure 5 shows a comparison of the cohesive force for the powder samples conditioned in a vapor of various DAs, where relative vapor pressure was used at a level higher than 80%, and so,it is expected that liquid bridging was able to be developed in all samples. It is clearly seen from Fig.5 that the different DAs gave significantly different cohesive force levels, this indicates that the cohesive force depends greatly on the type of molecules adsorbed on the powder particle surface. Table2 shows the values for various

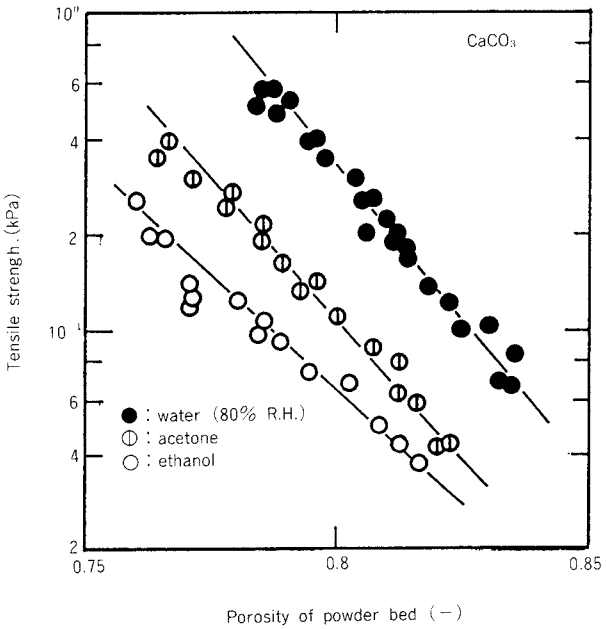

Fig.5 Tensile strength of the limestone powder exposed to various solvents

Table 2 Physical properties of dispersing aids (at 20°C)

	Water (H_2O)	Ethanol (C_2H_5OH)	Acetone (CH_3COCH_3)
M.P. (°C)	0.0	−114.3	−94.2
B.P. (°C)	100.0	78.4	56.2
Vapor pressure (mmHg)	17.5	44.0	179.6
Surface tension (dyne/cm)	72.8	22.6	22.5

properties of DAs at 20℃ : the value of surface tension is much higher for water than for either ethanol or acetone. It is seen from Fig.5 that water vapor provided the powder sample with a highr level of cohesive force than the other two,this fact suggests that the surface tension of the adsorbed substance is greatly involved in the mechanism for developing the cohesive force of powder particles. It is noted, however, that ethanol and acetone which are nearly the same in surface tension gave different cohesive force levels. This is thought to mean that some other factors other than surface tension, amount of vapor condensed (or adsorbed)on the contact area of particles for instance, are also involved in the cohesive force. In the present work, the adsorbed amount of DAs was not measured, and this should be examined in the future.

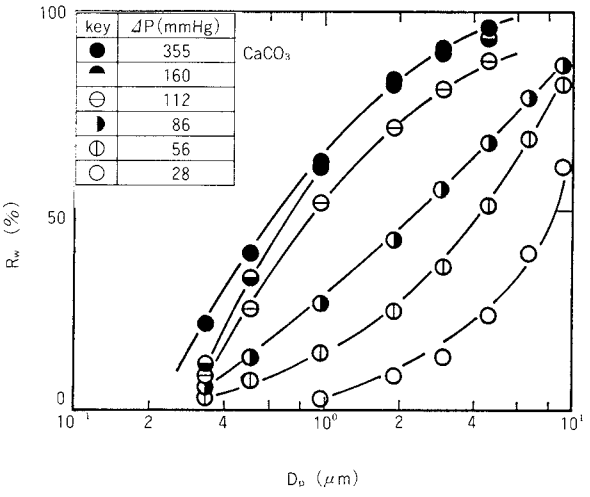

Fig.6 Size disribution of particles dispersed by needled (limestone powder aged under 80% relative humidity)

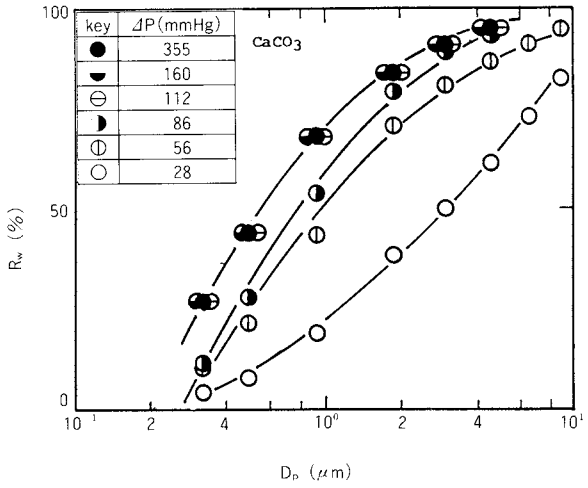

Fig.7 Size distribution of livestone particles dispersed by needles (limestone powder aged under ethanol vapor atmospherie)

3.2 Relation between cohesive force and dispersibility

Figures 6 and 7 show the particle size distributions of the dusts of powder samples dispersed under varions dispersing conditions. The samples were conditioned in water and ethanol vapor, respectively. For each of the powder samples, the gas used for dust generation(or fluidization)was the same in composition as that used during the conditioning. ΔP in Figs.6 and 7 represents the pressure drop of the gas stream across the needle pipe(dispersing pipe), and is used as a parameter indicating the dispersing force ; a higher value for ΔP means a higher dispersing effect of the gas stream. The particle size distribution curve is seen as shiffing to the side of smaller particle size with an increase in ΔP, which means that aggregated particles were dispersed more readily into a smaller

particle form with an increase in ΔP. For the powder sample conditioned in ethanol vapor, the particle size distribution curves showed no difference in the range of ΔP higher than 112mmHg, i.e. no shift to the side of the smaller particle size. This means that the aggregated particles were dispersed almost completely into the form of single primary particles by applying the dispersing force as this level. The sample conditioned in water vapor, on the contrary, was dispersed incompletely even at a level of ΔP higher than 160mmHg.

To compare the results of dispersibility tests more clearly, plotting the median particle diameter was tried as a function of △P, which is shown in Fig.8. The results for the other samples, conditioned in acetone vapor and in dry nitrogen gas, are also shown in Fig.8. It is seen from Fig.8 that the sample conditioned in water vapor was dispersed into the form of single primary particles onry when ΔP as a dispersing force highr than 200mmHg was

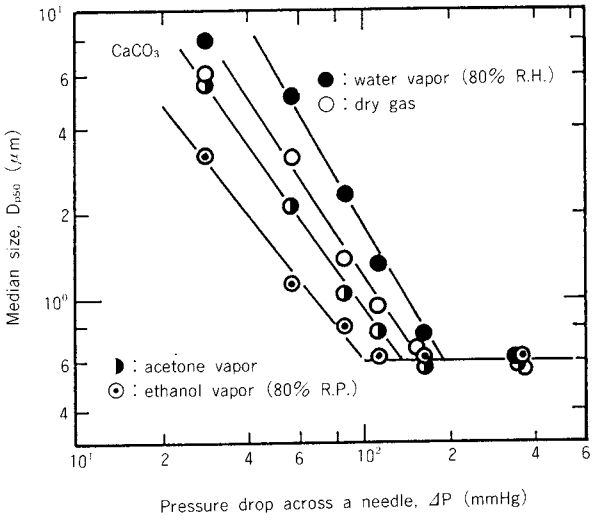

Fig.8 Change in mean size of the limestone Powder total gas pressure drop across a needle

applied, and that, on the contrary, the samples conditioned in ethanol or an acetone vapor were dispersed completely even at the level of dispersing force lower than that required for a dry sample. This means that even a powder material showing strong cohesive force can be greatly improved in gasphase dispersibility by syrface-treatment with the use of a suitable DA.

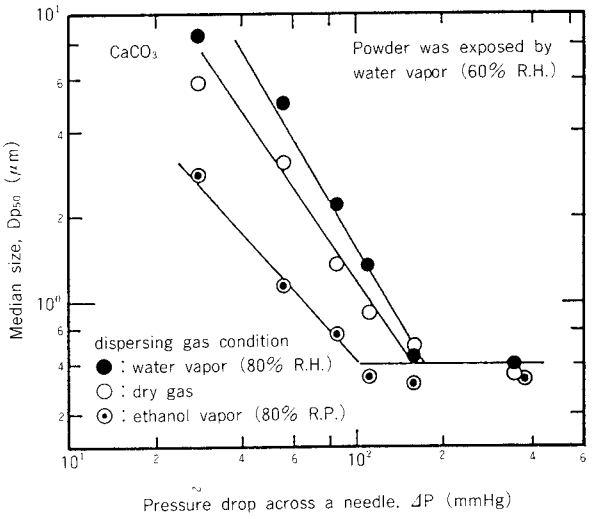

Fig.9 Change in meen size of the limestone powder with total gas pressure drop across a needle

3.3 Dispersing gas and gas phase dispersibility

Figure 9 shows the results of dispersibility tests using various gases containing varions DAs as fluidizing, for the limestone fine powder sample that was conditioned in an atmosphere of 60% RH. From Fig.9, it can be clearly seen that the dispersibility changed with the change in the gas used. It is noted that the gas containing ethanol(relative vapor pressure higher than 90%)brought about nearly the same dispersibility as good as that of the sample(Fig.8)conditioned in ethanol vapor, though the dispersibility test here used the sample which had been conditioned in water vapor at 60% RH for more than a week. As each dispersibility testing required a time not longer than 5 min, it is difficult to expect that the existing adsorbed water molecules were replaced completely by ethanol molecules during such a short time, and so, it is likely that ethanol molecules were adsorbed onto the particle surface to the extent of considerable amount ; so that, the bridge forming liquid have become to be composed of mixture of water and ethanol. Thus, the

surface tension of the liquid bridge would have changed, resulting in a change in the cohesive force of the particles. It should be noted that the value for surface tension of water containing 40% ethanol is ca. one-third that of pure water, showing nearly the same value as that of pure ethanol[8].

Figure 10 shows the cohesive force test results for the limestone fine powder sample

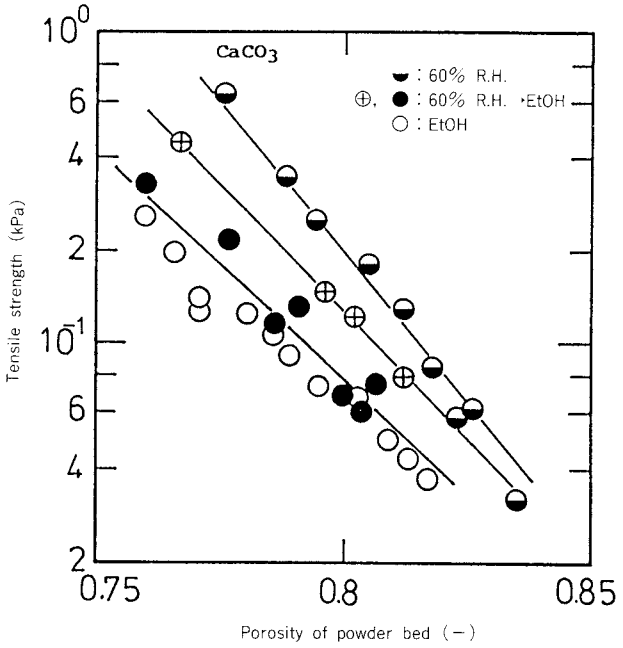

Fig.10 Tensile strength of the limestone Powder after fludized by ethanol atmospheric gas

that was conditioned in water vapor at 60% RH, and then, subjected to fluidization with use of an ethanoic gas stream. Symbol ⊕ in **Fig.10** represents the test results whereby the conditioned sample was subjected to the fluidization under the condition surrounded by atmospheric air, and then, to the cohesive force test in the glove box again containing atmospheric air. As is clear from **Fig.10,** the test results (⊕) of cohesive force came lower than those (◒) of the sample not subjected to the fluidization, but higher than those (○) of the sample conditioned in ethanol vapor for a week. This was thought to have resulted from partial desorption of adsorbed ethanol during the procedures from fransferring of the sample into the glove box after fluidization to testing of cohesive force in the glove box. (As mentioned in section 2.2, testing of cohesive force required ca. 20min). So, all the procedures from fluidization to cohesive force testing were carried out in the glove box containing ethanolic atmosphere, of which the results are shown by (●)in **Fig.10**, this result indicates that the cohesive force was reduced to nearly the same level as that of the sample conditioned in ethanol vapor for a week. This corresponds to the results in **Fig.9** that improvement in dispersibility was obtained by fluidization with use of an ethanolic gas stream. From these, it can be concluded that fluidization with the use of an ethanolic gas stream led the sample conditioned in water vapor to the levels of the sample conditioned in ethanol vapor both in cohesive force and dispersibility.

4. Conclusion

Using limestone fine powder material as the sample after being subjected to conditioning in a vapor atmosphere of various DAs, cohesive force was measured and dispersibility was tested by high speed gas stream in order to investigate the relationship between cohesive force and dispersibility. The results are as follows:

1) Cohesive force varied greatly depending on the molecular type and amount of adsorbed substance on the particle surface.
2) The lower cohesive force was found to give a better dispersibility, so the aggregated powder can be disperced more easily with lower applied dispersing force; therefore even the submicron powder material which is high in cohesive force can be dispersed in gas into the form of single primary particles, if the powder particle surface is treated with a suitable DA.
3) The dispersibility was found to vary by varying the types of vapor contained in the dispersing gas stream: for example, the use of ethanolic gas steam gave the sample conditioned in the water vapor a much improved dispersibility as good as

that of the sample conditioned in ethanolic atmosphere. This fact suggests that a submicron powder material is not necessary to be conditioned as long as for a week, which is worth noting for practical operation.

References

1) "Funtai Kogaku Binran", p.124, Nikkan Kogyo (1986)
2) Yamamoto, H. and O.Matayoshi: Preprints of Spring Meeting of The Soc. of Powder Technol., Japan, p. 79, Osaka (1988)
3) Yamamoto, H: *SEISANKENKYU,* **40,** 350 (1988)
4) Yamamoto, H., A. Suganuma and Y. Mori: *Kogaku Kagaku Ronbunshu,* **1,** 638(1975)
5) Yamamoto, H., A. Suganuma and D.Kunii: *ibid,* **3,** 12(1977)
6) Yamamoto, H. and A. Suganuma: *ibid,* **9,** 183 (1983)
7) Chikazawa, M., W. Nakajima and T.Kanazawa: *J. Soc. Powder Technol., Japan,* **14,** 18 (1977)
8) "Kagaku Kogaku Binran", 5th ed., p.248, Maruzen (1988)

Computer Simulation on Aggregated Structure of Fine Particles in Slurry †

Takatoshi Kimura, Masafumi Arakawa Kiyoshi Hirota and Hitoshi Murata
Faculty of Eng.& Design, Kyoto Institute of Technology *

Abstract

The property of a shaped body by slip casting in ceramic processing greatly depends on the dispersive state in the slurry.

The agglomerate process in a high densed slurry we studied by three dimensional computer simulation. The movement of particles was determined by cohesion probabilty between particles. The aggregative and this process was disussed from the view points of the aggregation rate, the coordination unmber and the aggregative ratio by using cohesion probability.

The experimental results from the measurement of viscosity and SEM observational dried slurries supported this simulation well.

1. Introduction

Slip casting is a method of moulding ceramics which has been practised since old times and uses slurry containing fine particles as raw material dispersed in a medium at a high concentration. As well known, the dispersion aggregation state of the fine particles as raw material in slurry not only exerts large influence over rheological behaviors of the slurry but causes changes in the structure of the moulded or fired products too. Accordingly, it is important to be acquainted with the aggregation state of particles in slurry. However, it is difficult to observe directly the aggregate structure or aggregation process of the particles dispersed at a high concentration in the slurry. Till now, for explanation of aggregate structures, many studies using computer-simulation of the aggregation of particles in slurry have been carried out. In a large part of the studies, the simulation dealt with two-dimensional aggregation and dilute slurry systems. Accordingly, it is impossible to adapt the results of such studies to high densed slurry systems.

In this study, three dimensional computer-simulation of aggregation was carried out to explain the aggregation process of particles. Water-alumina slurry systems which are employed for practical slip casting were used, and the viscosities were measured. The freeze-dried slurries were observed by SEM. Based on the test results, the aggregate structure and the aggregation process in the slurries were examined. A good agreement between the results of the computer simulation and those of the measurement and observation has been obtained.

2. Experimental Procedures

2.1 Simulation of Aggregation

As to the initial state defined for the simulation, 805 model particles, which are uniform in shape and size, were packed into a cube, in which each side is 10 times long as the size of one particle so that the volume concentration of the particles becomes 42

* Goshokaido-cho, Matsugasaki, Sakyo-ku, Kyoto 606 Japan
TEL 075-791-3211

† This report was originally printed in *J. Soc. Powder Technology, Japan,* **27,** 218-224(1990)in Japanese, before being translated into English with the permission of the editorial committee of the Soc. Powder Technology, Japan.

vol.%. The particles were given numbers and optional movement directions. The particles were then, moved to a distance of 3/100 of the particle size along the movement directions. In order to ensure the Brownian movement, the movement directions of the particles were changed with a certain probability. The probability, in which the particles collied and aggregate with each other is defined as cohesion probability. Pseudo-random numbers in the range of 0 to 1, are generated everytime whenever the collision occurs, and they are compared with the cohesion probability. As shown in **Fig. 1,** in the case where the random number is smaller than the cohesion probability, the particles are aggregated. Thereafter, the aggregate is considered as a unit of movement for calculation. On the other hand, in the case where the random number is larger than the cohesion probability, the particles are rebounded and the movement directions are changed. **Fig. 2** illustrates the flow chart of this program. For all the particles, this operation is repeatedly run and the calculation is conducted until the run times reaches 100. Under different aggregation conditions, that is, at different cohesion probabilities of 100%, 50%, 30%, 10% and 5%, the changes in aggregate structure and aggregation process of the particles were examined.

Also, the above-described simulation was carried out at a particle volume concentration of 30 vol.% and 5vol.% respectively.

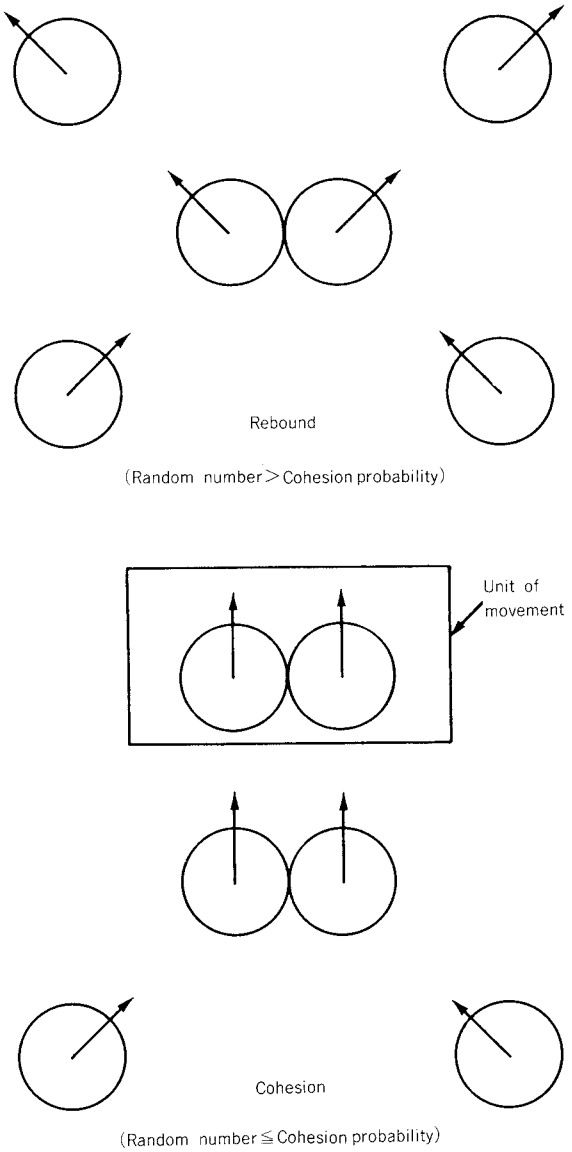

Fig.1 Process of cohesion between two particles

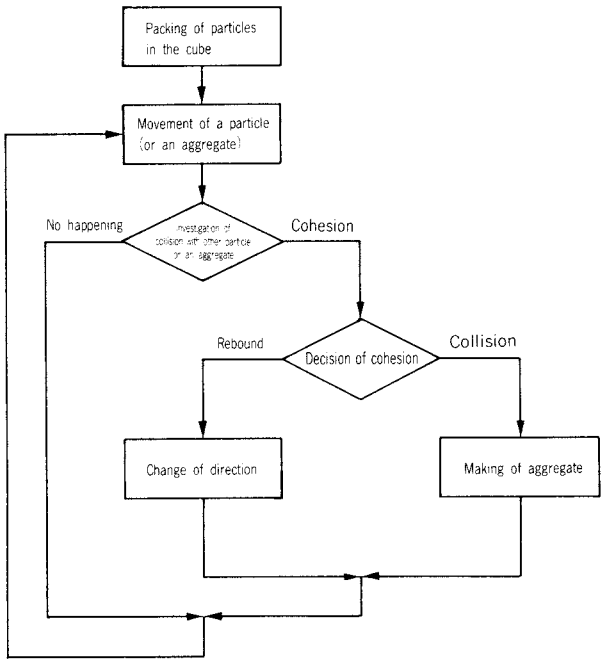

Fig.2 Flow chart of computer simulation

2.2 Preparation of Slurry

As a powdery sample, alumina with easy sintering properties and a low soda content (AL-160SG modified-4 true specific gravity 3.93g/cm^3; BET specific surface area 5.5m^2/g;

manufactured by Showa Denko KK), as previously reported,[2] was used. To the alumina, water and one dispersant(ammonium salt of polyacrylic acid)were added so that the volume ratio of the alumina based on the water became 42 vol.%. To the mixture, alumina balls were added and vibrated for 30 minutes. Thereafter, the mixture was deaerated under vacuum and was used as experimental slurry.

The relationships between the addition amounts of the dispersant and the apparent viscosities of the slurries suggests there are essentially three different regions, namely region(a)where the slurry isn't enough the dispersant; region(b)where the amount of the dispersant is appropriate; and region(c)in which the amount of the dispersant is excessive and with different aggregation states. In this study, three slurry systems(a),(b), and (c)have been considered as representative of the above mentioned regions(a),(b)and(c); the addition amounts of the dispersant are: 0.18g for the system(a), 0.30g for the system(b),and 1.00g for the system(c),based on 100g of the alumina, were prepared. The slurry systems (a),(b)and(c)are defined as a strong aggregation system, a dispersion system, and a weak aggregation system, based on their flow curves, respectively.

2.3 Viscosity Measurement of Slurry

In order to measure the viscosity of the slurries, a rotary viscometer was used. The measurements of the viscosity were recorded on a recorder so that the time-dependent, changes in viscosity of the slurries were examined. The rotation speed of the rotar was set to 3 rpm so that fine changes in the viscosity could be detected. The measurement was conducted immediately after the slurries were deaerated.

2.4 SEM Observation of Freeze-Dried Slurry

In order to get detailed in formation of the real aggregate structures of the slurries, the freeze-dried slurry samples were observed by SEM. To obtain a sample for the observation, each slurry system was placed on a copper mesh, then dipped and freezed quickly in isopentane (−140 °C) cooled with liquid nitrogen so as to avoid the crystal growth of the water. Thereafter, the slurry was dried under vacuum with cooling at −15 °C.

3. Result and Discussion

Fig. 3 illustrates the relationships between the unmber of aggregates and the number of run times at particle volume concentration of 42%, at different cohesion probabilities. In **Fig.3** N_0 is the intial number

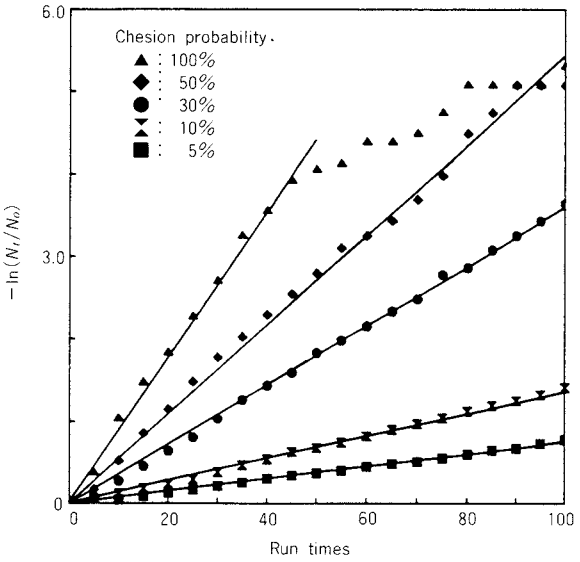

Fig.3 Change in number of aggregates versus run times

of the aggregates (805), and N_t is the total number of aggregates and dispersed particles at the t-th run time. **Table 1** shows the ratios of the gradients (k_t) of the straight lines in **Fig.3** to that of the straight line at cohesion probability of 100%. As shown in **Fig.3**, the decrement retio (k_t) of the particles increases with the cohesion probability, that is, there exists correlationship between the cohesion probability and the aggregation rate. As generally recognized, the aggregation process of a monodispersion system at the initial stage is in accordance with the quadratic process represented by the Smoluchowski's solution. The total number N_t of particles is expressed as follows[4];

$$\frac{dN_t}{dt} = -\frac{4kT}{3\eta}N_t^2 \qquad (1)$$

Table 1 Comparison between cohesion probability and k_1

Cohesion probability	k_1	$k_1/k_{1(100\%)}$ (×100)
100%	0.094	100.0
50	0.057	60.6
30	0.041	43.6
10	0.014	14.8
5	0.008	8.0

In which k is the Boltzman constant, T is the absolute temperature, and η is the viscosity of a medium. The Smoluchowski's solution has been experimentally demonstrated to reveal its adaptability to diluted slurry systems[5]. However, as a result of the simulation, the aggregation of the particles which proceeds according to the linear process has been observed as clearly shown in **Fig. 3.** In such dense slurry systems as simulated in this study, the volume concentrations of particles are large, so that the number of collision times between the particles is very high. That is, the number of collision times of the particles per unit time is very high. Accordingly, it is speculated that the assumed initial stage of the aggregation by the Smoluchowski's solution is completed in a very short time, so that no aggregation process by the quadratic process is presented. Therefore, in this study, the simulation was conducted at different concentrations of the particles in order to elucidate effects of the differences in concentration, that is, in number of collison times of the particles, on the reaction process. **Fig. 4** shows the results. In the simulation, the cohesion probability is set to 100%. In Figs. 4(A), 4(B)and 4(C), the volume concentrations of particles are 42 vol.%, 30 vol.% and 5 vol.% respectively. The changes in number of the aggregates, on the assumption that the aggregation proceeds according to the quadratic and linear processes represented by the formulae(2), (3)are plotted as ordinates in the graphs.

Quadratic process:

$$\frac{dN_t}{dt} = K_2N_t^2$$

$$\frac{1}{N_t} - \frac{1}{N_o} = k_2t \qquad (2)$$

Linear process:

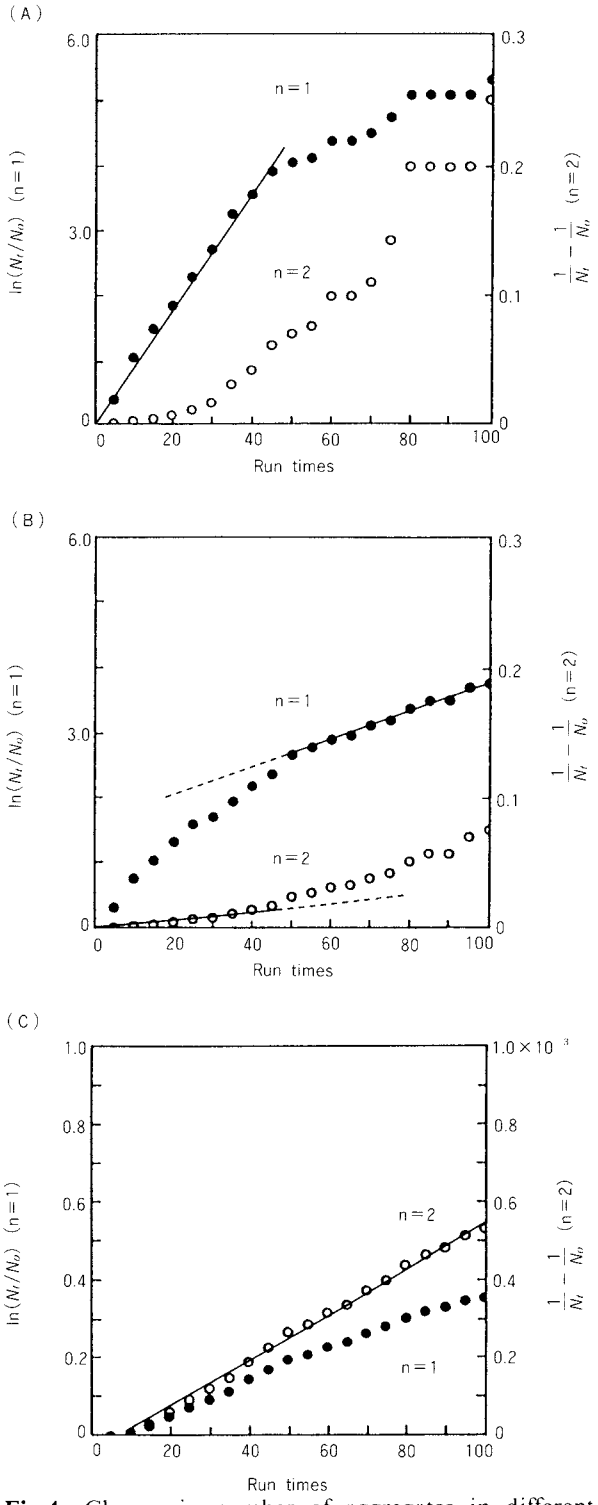

Fig.4 Change in number of aggregates in different concentration

$$\frac{dN_t}{dt} = K_1 N_t$$

$$\ln\left(\frac{N_t}{N_o}\right) = -k_1 t \qquad (3)$$

In which K_1, k_1, K_2 and k_2 represent proportional constants. In **Fig. 4** , n represents the degrees. As shown in **Fig. 4** (A), the aggregation proceeds substantially not according to the quadratic but to the linear process. The aggregation rate decreases remarkably in the latter half of the aggregation process, following the linear process, because the number of aggregates becomes very small. In **Fig. 4** (B), in the initial period, the aggregation proceeds according to the quadratic process, but from the number of run times of about 40 it departs from the quadratic process. Accompanied with the departure, the aggregation proceeds partially according to the linear process. In **Fig. 4** (C), the entire aggregation proceeds according to the quadratic process. In this figure, the straight line has an X intercept, not passing through the origin, because the particles, excluding particles of which the inter-particle distances are small, are packed, so that the particles begin to collide with each other at certain time after the start of the simulation. Based on the foregoing description, when the concentration of particles is low, the aggregation proceeds according to such quadratic process as represented by the Smoluchowskis' solution in the overall simulation range. On the other hand, as the concentration of particles is increased, the aggregation rate is enhanced, so that the aggregation by the quadratic process ceases before the completion of the simulation. Moreover, at a high concentration of 42 vol.%, the aggregation by the quadratic process is completed in a very short time, so that the aggregation can hardly be observed. In the case of relatively high concentrations, the number of collision times of particles is high, resulting in the formation of large aggregates. Probably, this causes the aggregation to depart from the assumption for the Smoluchowski's solution that the particle sizes are not significantly different. This simulation assumes that all the movement distances of the movement units are equal. It is supposed that this is not sufficiently compatible with the assumption of the Smoluchowski's solution. At present, the authors consider effects of the condition that the movement distance changes with the number of particles constituting one movement unit, on the simulation.

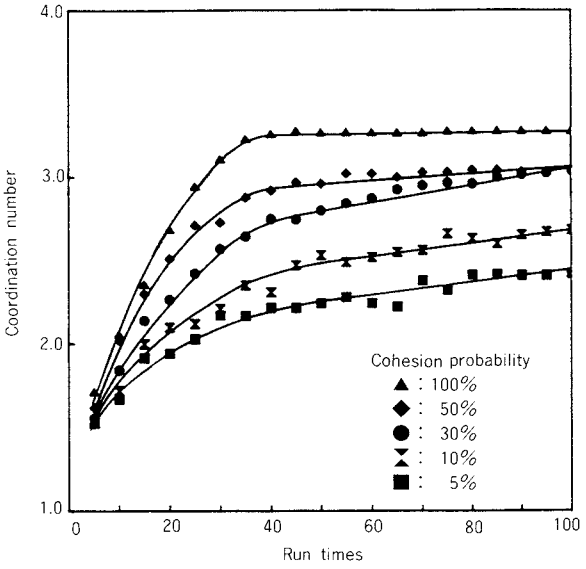

Fig.5 Change in number of coordination versus run times

Fig. 5 shows the relationship between the average coordination number of aggregates and the number of run times at different cohesion probabilities, at a volume concentration of particles of 42 vol.%. The average coordination number is the average number of coordinating particles in the aggregates excluding aggregates with a coordination number of 0, that is, the dispersed particles. At any of the cohesion probabilites, the average coordination number increases with the numbers of run times. Particularly, in the case of the relative high adhesion probabilities, the increase of the average coordination numbers ceases at a certain number of run times and thereafter is kept constant. As to this figure, even at the same number of run times, the aggregation rates are different depending on the cohesion pro-

babilities, so that the numbers of aggregates are different. Accordingly, by **Fig. 5,** no knowledge of effects of the cohesion probabilities on the coordination numbers can be obtained. **Fig.6** shows the relationship between the number of aggregates and the average coordination number of respective aggregates. As understood in **Fig. 6,** when the numbers of aggregates are equal, the average coordination number at the lower cohesion probability is high than that at the higher cohesion probability. This is because that when the cohesion probability is low, the number of collision times of particles increases and the probability of forming aggregates having high coordination number is enhanced. By the model experiment[6] using white alundum by Arakawa, it has been confirmed that when the cohesion becomes low, the coordination number increases. It is suggested that the cohesion probability in this simulation corresponds not only to the aggregation rate but also to the cohesion iteslf.

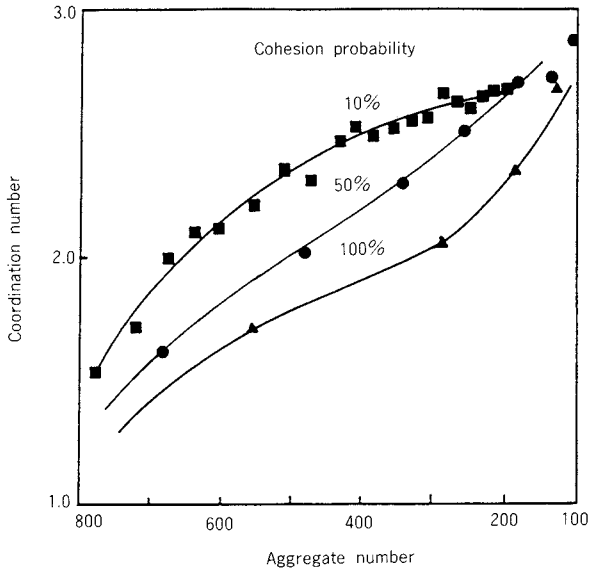

Fig.6 Relation between coordination number and aggregate number

Fig. 7 shows the relationship between the volume ratio of aggregates and the number of run times at particle volume concentration of 42%. For clear understanding of the aggregation process, an aggregate composed of 2 to 5 particles is defined as a small aggregate, and an aggregate composed of at least 6 particles is considered as a large aggregate.

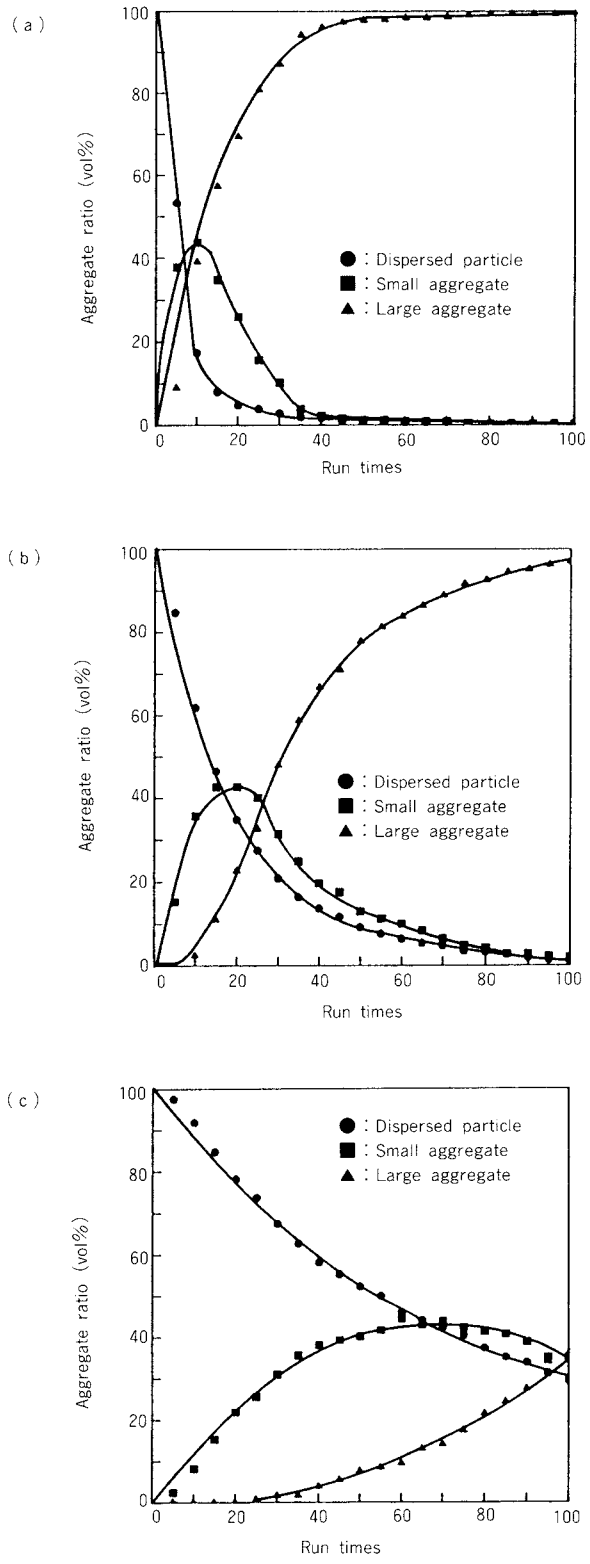

Fig.7 The effect run times on aggregate ratio

The cohesion probabilities are set to 100% for **Fig. 7** (A), 30% for **Fig. 7** (B), and 5% for **Fig. 7** (C). As understood in these figures, the aggregation proceeds like a successive reaction. With the advancement of the run, the collision of the dispersed particles forms small aggregates and increases the volume ratio of the small aggregates irrespective of the cohesion probabilities. However, the small aggregates repeatedly collide against each other to grow into large particles, so that the volume ratio of the small aggregates slowly increases and then decreases. On the other hand, with the reduction in number of small aggregates, the number of large aggregates increases step by step. As to the aggregates obtained in this simulation, these results show that, the dispersed particles grow into small aggregates and then large aggregates.

According to the authors' speculation, when the cohesion probability is high, the aggregation rate is high and large aggregates are instantaneously formed. On the other hand, when the cohesion probability is low, small aggregates are formed with difficulty. Accordingly, the dispersed particles repeatedly collide against each other, so that small aggregates having high coordination numbers are formed as described above. Also, it is difficult for the produced small aggregates to be converted to large ones, and the small aggregates would remain as they are.

Table 2 shows the volume ratios of the aggregates at the number of run times of 100 to be compared with the distributions of the aggregates. As understood in **Table 2,** when the cohesion probability is low, the volume ratios of the dispersed particles and the small aggregates increase. In other words, if the cohesion, that is, the cohesion probability, is low in a dispersion system of particles at a high concentration, small aggregates with large coordination numbers are present together with few large aggregates, at certain time after the start of the simulation. On the other hand, if the cohesion probability is low in the dispersion system, large aggregates with low coordination numbers exist together with few small aggregates.

Table 2 Comparsion between cohesion probability[%] and aggregate ratio [vol. %]

Cohesion probability	Dispersed particle	Small aggregate	Large aggregate
100%	0.25vol%	0.25vol%	99.50vol%
30	1.12	1.99	96.89
5	29.32	35.03	35.65

Fig. 8 shows the schematic models of the aggregation process. When the cohesion probability is high, the dispersed particles quickly move from the step(I)to the step(II), so that small aggregates with low coordination numbers are formed. The small aggregates, by collision against each other, are formed into large aggregates. In contrast, when the cohesion probability is low, the dispersed particles at the step(I) relatively slowly move to the step(II) where, by repeated collision, small aggregates with high coordination numbers are formed. Thereafter, the movement from the step(II) to the step(III) occurs with difficulty, and the small aggregates remain unchanged except one part of the small aggregates that move to the step(III).

3.2 Viscosity Measurement of Slurry

Fig. 9 shows the changes in viscosity of the slurries with time. As the viscosities of the slurries measured 5 minutes after the preparation, the strong aggregation system(a) is highest, followed by the weak aggregation system(c) and then the dispersion system(b). The viscosity of the system(c) increases with time and 40 minutes after the preparation, becomes equal to that of the system(a). Thereafter, the viscosity continues to increase, exceeding that of the system(a). The viscosity of the system(a)remains substantially unchanged with the progress of time. In the case of the system(c)having a weak cohesion, the cohesion probability is low and the aggregation rate is low. Probably, this causes the aggregation to proceed slowly and the viscosity to increase time-dependently. As to one of the causes of the fact that the viscosity of the system(c)becomes higher than the system(a)40 minutes after the preparation, it is

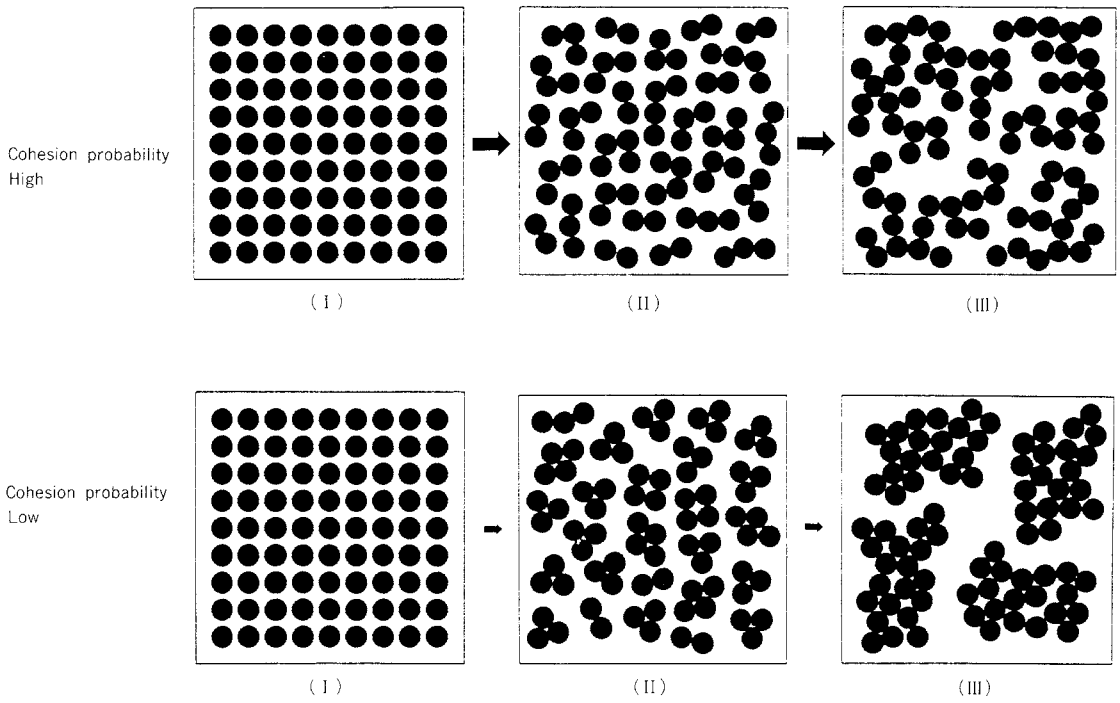

Fig.8 Model of aggregation process

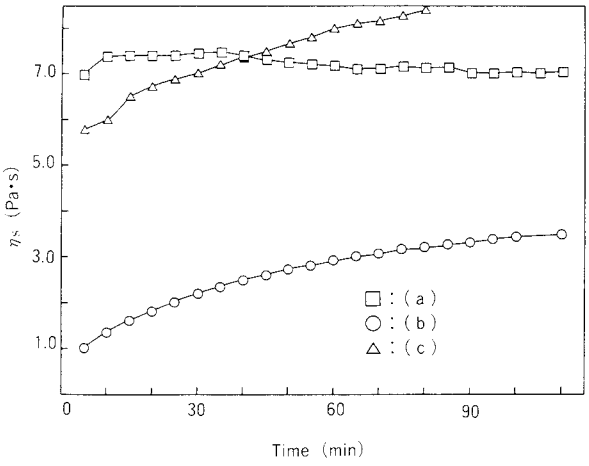

Fig.9 Time dependence of viscosity in slurry

probable that aggregates with higher coordination numbers and closer structures, as compared with the aggregates in the system(a), exist in the system(c)immediately after the preparation. In the case of the system(a) having a strong cohesion, the cohesion probability is high and the aggregation rate is high. Probably, this causes the aggregation to reach its equilibrium five minutes after the preparation, and the viscosity remains unchanged since the equilibrium has been reached.

The above-described experimental results presents a good agreement with those of the simulation.

3.3 Observation of Freeze-Dried Slurries

Fig. 10 shows the SEM photographs of freeze-dried slurries. The letters(A), (B)and (C)designate the SEM photographs of the strong aggregation system(a), the dispersion system(b), and the weak aggregation system (c), respectively. In the photograph(B), a large number of small aggregates with an even particle size are shown. Large aggregates are shown in the photographs(A), (C)and the size of the aggregates in the system(a)is larger if compared with those in the system(c). **Fig. 11** shows the aggregate size distributions of the aggregates obtained in the SEM photographs of the freeze-dried slurries in order to clearly present the above-described differences. The aggregate size distribution for the system (a)is most narrow. That of the system(c)is wider than that of the system(a). In the case of the system(c), the cohesion is low and the aggregation rate is low, so that a large number of small aggregates exist, substant-

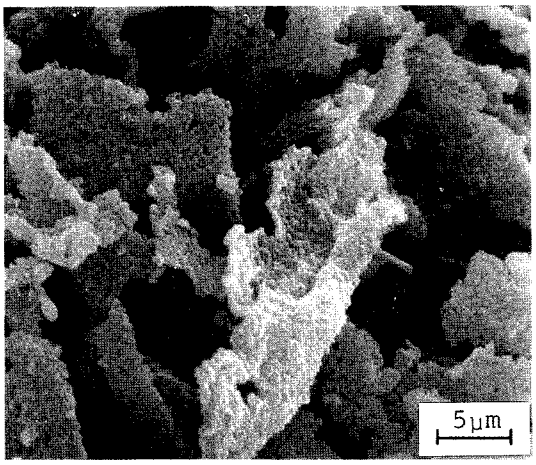

(A)

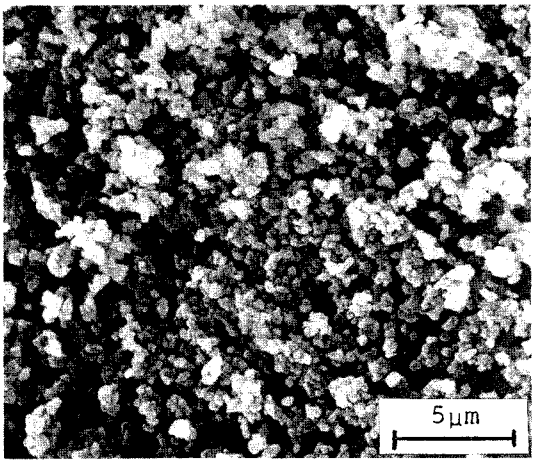

(B)

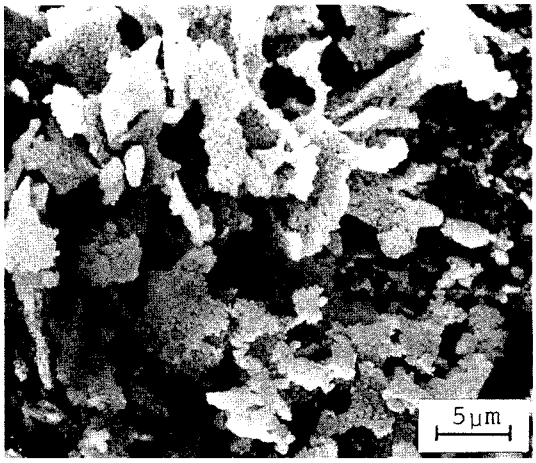

(C)

Fig. 10 SEM photographs of freeze-dried slurries

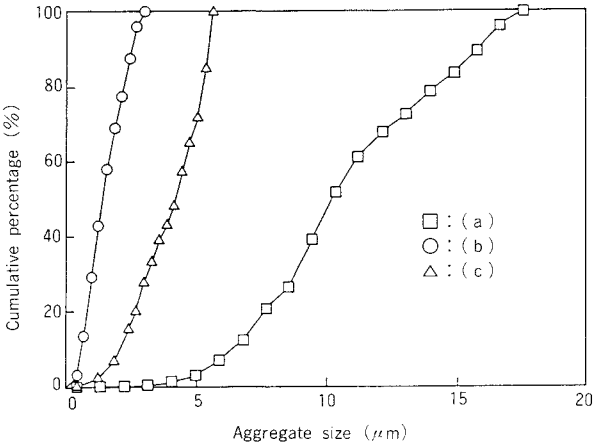

Fig. 11 Aggregate size distribution

ially excluding large aggregates. In contrast, in the case of the system(a), the cohesion is high and the aggregation rate is high, so that most of the dispersed particles are formed into large particles. **Table 3** shows the mean aggregate sizes calculated by using the distribution curves and the densities of the aggregates calculated from the settling speeds. The system(b) has a mean aggregate size almost equal to that of the dispersed particles and a density substantially equal to that of the powder sample. The system(a) has a relatively large mean aggregate size and a smaller density than the system(c). In contrast, the system(c) has a relatively small mean aggregate size and a higher density than the system(a). Based on these experimental results; for the strong aggregation system(a), relatively large aggregates are formed but the structures of the aggregates are sparse with low coordination numbers. In the weak aggregation system(c), small aggregates are formed but their structures are relatively dense and the coordi-nation numbers are high. These results coincide with those of the simulation.

Table 3 Aggregate size and density of sample

System	Mean aggregate size (μm)	Density (g/cm^3)
(a)	10.0	1.04
(b)	1.3	3.57
(c)	3.5	1.23

5. Conclusion

The aggregation process obtained by the simulation is a linear process when the concentration of the particles is high, which departs from the Smoluchowski's solution often used to elucidate aggregation behaviors. As revealed above, this is because an aggregation region in which the aggregation proceeds according to the Smoluchowski's solution is very short, since the high concentration of the particles increases he number of collision. When the concentration is increased to reduce the number of collision times of the particles. The region in which the aggregation proceeds according to the Smoluchowski's solution becomes large. In this study, the movement distance of the movement unit is set to a constant value. Probably, this exerts some influences over the simulation. At present, the authors consider influences by the movement distance in detail. Also, as revealed here, the cohesion probability used in the simulation has a relationship to the cohesion and the coordination number, in addition to the aggregation rate. In the case of the small cohesion probability, the aggregation proceeds with difficulty and a large number of small aggregates with relatively dense structures are present. In contrast, at the high cohesion probability, the aggregation proceeds fast and large aggregates with relarively sparse structures are formed.

The above simulation results were examined by the viscosities of the slurries and the SEM observation of the freeze-dried slurries. In all the cases, good agreement has been obtained. The adaptability of this simulation has been recognized.

Nomenclature

N_o : initial number of particles	[-]
N_t : number of aggregate	[-]
k : Boltzmann constant	[JK_{-1}]
T : temperature	[K]
η : viscosity	[Pa・S]
K_1, K_2, k_1, k_2 : costant	[-]

References

1) Sunada, H., A. Otsuka, Y.Yamada, Y.Kawasima, H.Tetsuya and J.T.Carstensen: *Powder Technol.*, **38,** 311(1984)
2) Arakawa, M., K.Hirota, T.Kimura, H.Kobayashi, Y.Okuda and H.Murata: *J. Soc. Powder Technol., Japan* **26,** 638(1989)
3) Arakawa, M., H.Kobayashi, K.Hirota and K.Inoue: *J. Soc. Powder Technol.,Japan,* **25,** 585(1988)
4) Nippon-funtaikogyo-gijutukyokai: "Gyosyukogaku," p. 55, Nikkankogyo Shinbunsya (1982)
5) Higashitani, K. and Y.Matsuno: *J. Chem. Eng. Japan,* **12,** 460(1979)
6) Arakawa M.: *J. Japan. Soc. Powder and Powder Metallurgy,* **15,**7(1968)

Dispersion of SiO_2 by Coating with a Thickness of Nano-meters on the Surface of Fine α-alumina Powder †

Mutsuo Sando, Masanobu Awano, Yoshinori Uwamino and Yoshitaka Kuwahara
Gorernment Industrial Research Institute, Nagoya. *

Abstract

A α-alumina fine powder was coated by SiO_2 ultra-fine particles with a diameter of nano-meters. SiO_2 by hydrolysis of ethyl silicate with water adsorbed on the powder was precipitated onto the powder in the hydrohobic liquid which contained 90 vol.% ligroin, 10 vol.% ethyl silicate and 0.015 mol/l stearic acid. The thickness of the coated layer was controllable by changing the amount of the adsorbed water up to 10 wt.% of the powder.

1. Introduction

In the production of functional or structural ceramics, powder additives are used for the control of grain boundary etc., whereby they are mixed with the starting powder for mother matrix of ceramics(hereafter, called starting powder)in a mill during the powder preparation process before firing. This method, however, is difficult to provide a homogeneous dispersion of the additives in the starting powder for sintering to the microscopic level, and in particular, when using an additive difficult to diffuse during the sintering process, an inhomogeneous sintered body is often produced, resulting in low quality ceramic products. One of the improving method for this problem may be the coating technique of the ultrafine powder of additives onto the surface of starting powder particles with controlling thickness at nano-meter level. Such a coating technique of am ultrafine powder with a thickness at the nano-mater level is called "nano-coating" hereafter in this paper. In research work regarding nanocoatings, the following methods have been developed: to synthesize colloidal particles of the additive though hydrolysis of metal alkoxide and fix them onto the powder in a mill preparing good use of the particle electrification effect of milling[1] ; to add water adjusted in its pH-value to an alcoholic suspension of alkoxide and powder to have selective hydrolysis of the alkoxide on the surface of the powder particles[2] ; and to hydrolyze emulsified alkoxide in a suspension of the powder[3]. All of these methods, however, require strict control of the reactive conditions to attain the desired compact coating of the power particles with a small amount of the additive with uniform distribution. For this reason, in the present work here for nano-coating, we tried to use a different method from those mentioned above, as follows, though in this method we again used the hydrolysis of metal alkoxide to synthesize the additive in an ultra-fine particle formation: to moisten the fine powder with a water vapor to adsorb a definite amount of water first, disperse the powder in a hydrophobic organic solvent with the use of a fatty cacid, and then, synthesize the ultrafine partiles of the additive by hydrolysis of metal alkoxide in the vicinity of the interface of the adsorbed water layer on the fine powder par-

* 1-1 Hirate-cho, Kita-ku, Nagoya 462, Japan
TEL. 052-911-2111

† This report was originally printed in *J. Soc. Powber Technology, Japan* **27**, 170-173 (1990) in Japanese, before being translated into English with the permission of the editorial committee of the Soc. Powder Technology, Japan.

ticles and the organic solvent and fix them onto these particles.

2. Experimentals

Silicon tetraethoxide (ethyl silicate), which is low in reactivity, was used as the metal alkoxide, mono-dispersible high purity α-alumina powder(Taimicron TM-D, Taimei Chemicals Co ; BET specific surface area 13.6m^2/g)as the base powder, and ligroin as the hydrophobic organic solvent. Stearic acid was used as the dispersing agent of the moistened powder and also as the catalyst of the alkoxide hydrolysis. Control of the thickness of the coat layer was attempted by varying the amount of water being adsorbed by the alumina powder. As such, the amount of the ultrafine particles through hydrolysis was experimentally adjusted by the amount of adsorbed water as mentioned above and experimental runs were performed under the reaction conditions to use ethyl silicate in much excess of the amount of adsorbed water.

2.1. Reaction in liquid phase

The scheme of reaction in the ligroin mixture solution of ethyl silicate and stearic acid is shown in **Figure 1**. In the ideal state. the alumina fine particles each covered by an adsorbed water layer disperse in ligroin under such conditions that the hydrophilic carboxyl group of the stearic acid is adsorbed onto the surface of the adsorbed water layer.Thus, it is assumed that hydrolysis of the ethyl silicate occurs at the vicinity of the interface of the adsorbed water layer and ligroin to form silicon hydroxide which then produces ultrafine silica particles under dehydration-polycondensation with in the adsorbed water layer so that the silica ultra-fine particles are fixed to the surface of the alumina particles.

2.2. Procedures for nano-coating

The porcedures for nano-coating of the alumina fine powder particles are outlined in **Table 1**.

The alumina particles thus treated were observed in their microscopic shape and measured chemical composition and BET specific surface area.

Table 1 Procedure of SiO_2 coating on α-alumina fine powder

1) Weight measurement of alumina powder dried in vacuum at 200°C
2) Adsorption of water in high humidity air at room temperature
3) Measurement of weight increase by water adsorption
4) 50 hours mixing of the powder in hydrophobic liquid (ligroin 90 vol. %. ethyl silicate 10 vol. % and stearic acid)
5) Centrifugation of powder from liquid and washings by ligroin and methanol
6) Drying in vacuum at 200°C

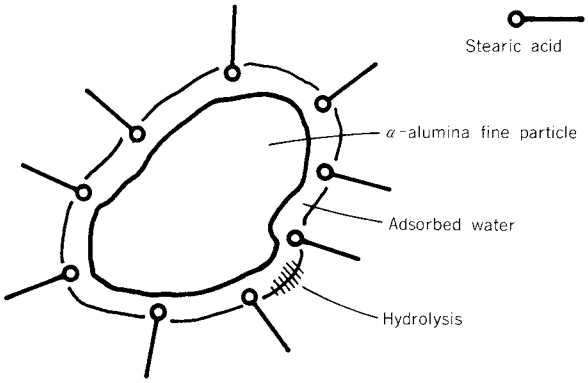

Fig.1 Hydrolysis of ethyl silicate by water adsorbed on α-alumina fine particle in hydrophobic liquid

3. Results and Discussion

Figure 2 shows typical examples of α-alumina particles before and after the treatment with the transmission electron microscopy and EDX analysis. The EDX analysis of the high purity alumina powder showed almost no presence of silicon for the sample before treatment, but did have several percent of silicon for the sample after treatment that had been moistened to adsorb water at a level of 0.1g per gram sample, and then, subjected to a coating treatment. In addition, the latter sample was observed to have an uneven particle surface that could have resulted from ultra-fine particles, several nano-meters in size, being attached to the surface.

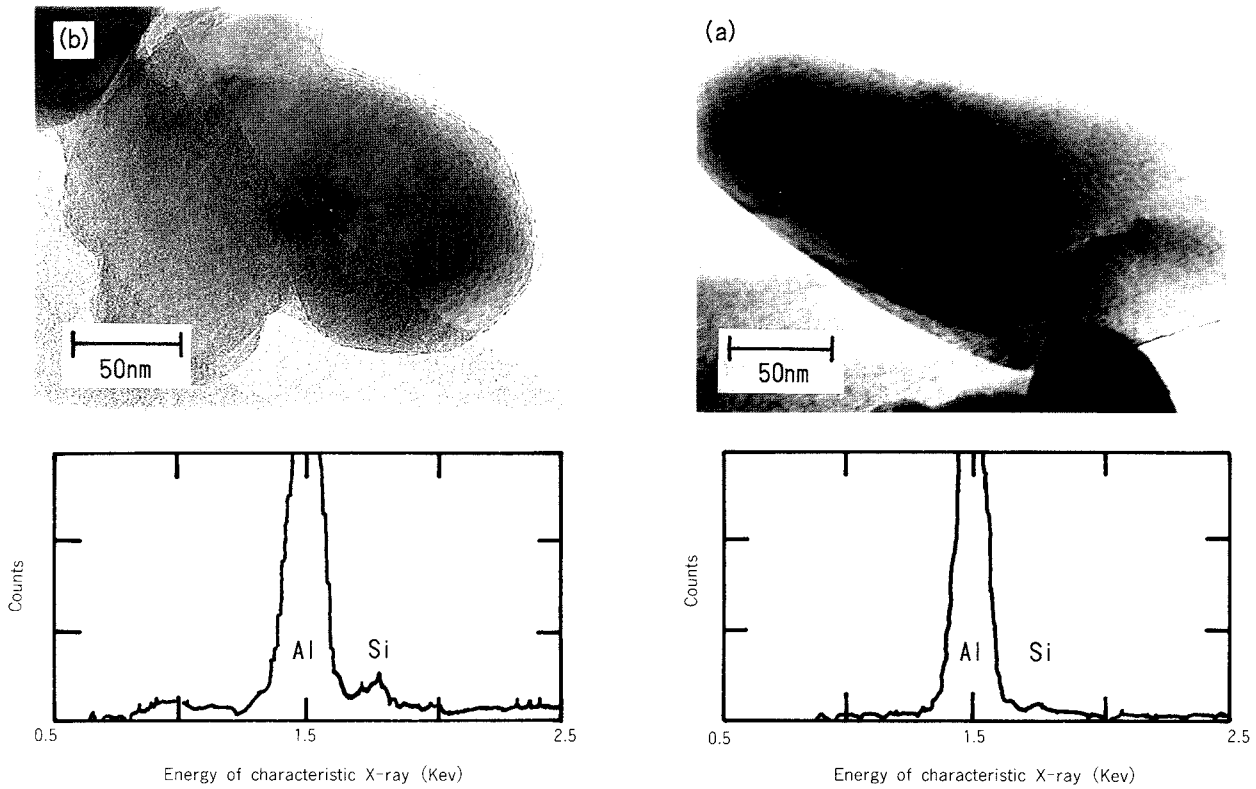

Fig. 2 TEM images and EDX element analysis spectra of α-alumina fine particle (a) and SiO_2 coated fine particle (b)

The sample of alumina powder subjected to the coating treatment consisted mainly of large agglomerates, containing separated single particles and small agglomerates consisting of several particles both in minor proportions. This resulted probably from insufficient dispersion of the moistened alumina fine powder in the hydrophobic organic solvent as well as from insufficient action to prevent particle agglomeration during the hydrolysis process, which suggests the need to use a more suitable surface active agent and an improved means of stirring as well. **Figure 3** shows an example of election microscopic results for the coated powder samples after heat treatment at 600 °C for 1 hr in air. **Figure 3**, which indicates an increase in size of the ultra-fine particles after the heat treatment, shows evidence of the presence of ultra-fine particles even in the intergranular area of the primary alumina particles of the agglomerates, which confirms that our present method can provide a compact coating of individual alumina fine particles with silica

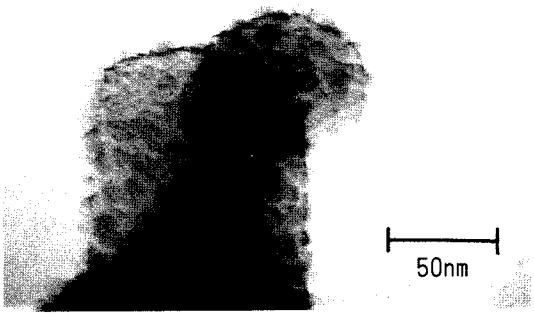

Fig. 3 TEM image of SiO_2 coated α-alumina fine particle after heat treatment of 1 hour at 600°C in air

ultrafine particles.

Results of thermal analysis of a sample of silica coated alumina fine powder are given in **Figure 4**. In **Fig.4**, curves in solid and broken lines correspond to the results in an inert argon gas and in air, respectively. The differential thermal analysis(DTA)showed an endothermic behavior, which was probably

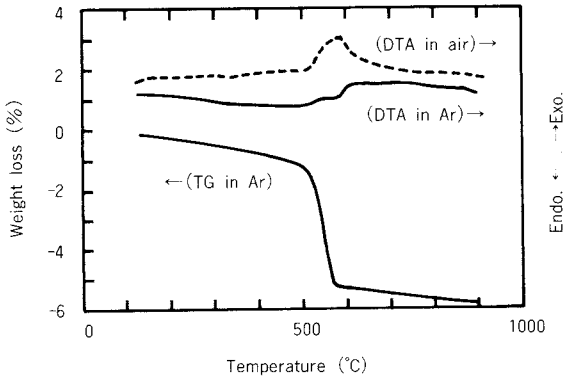

Fig.4 Thermal analysis of SiO_2 coated powder

caused by the dissociation of structural water, until up to ca.600 °C in argon, but an thermogravimetry(TG) in air produced a large weight loss at ca. 550°C, which is concluded to have resulted from the thermal decomposition of organic substances contained in the coat layer, taking into account the DTA results in argon and air. The weight loss in TG was found to be nearly the same in argon and air. The levels of weight loss and exothermic peak seemed to depend approximately on the specific surface area or silica content of the powder.

Stearic acid, which was used as the dispersing agent for moistened alumina fine powder in the hydrophobic organic solvent and served as the catalyst for hydrolysis of ethyl silicate, was tested in the effect of its concentration regarding the results of coating treatment, which is shown in **Figure 5**. Symbols ○ and ● in **Fig.5** represent the values for the BET specific surface area(measures by use of N_2)and silica content, respectively, of the samples of alumina fine powder that were moistened to the level of 7mg adsorbed water per unit BET surface area(ca.0.11g water per 1g powder), and then, subjected to the coating treatment. The symbol◇in Fig.5 represents the value for the specific surface area of the above-mentioned samples after heat treatment in air at 600 °C for 1hr for oxidative decomposition of the organic substances contained in the coat layer. It is seen from Fig.5 that a sudden change in the specific surface area occurred at a certain stearic acid

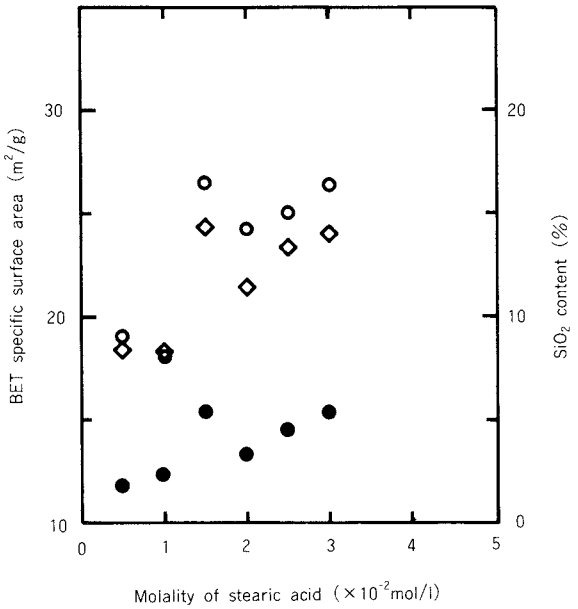

Fig.5 Effect of stearic acid molality in hydrophobic liquid on property of coated powder made from powder adsorbing water about 10wt%

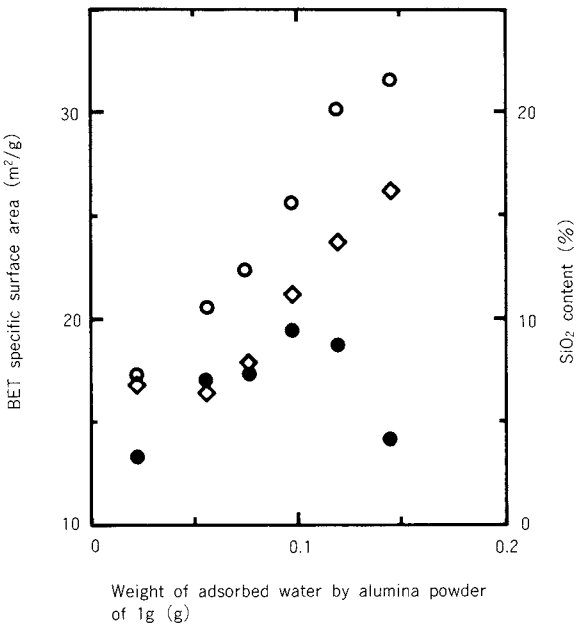

Fig.6 Variation of specific surface area and SiO_2 content due to change of adsorbed water(Hydrophobic liquid contains 0.015 mol/l stearic acid)

concentration between 0.010 and 0.015mol/l, and in fact, below this concentration, there was also observed the presence of both the alumina particles without the desired coat

layer and the agglomerates of silica ultrafine particles in the samples. The silica content showed also a rapid change at this concentration of stearic acid. It should be noted that, for the treated alumina powder samples, reproducibility of the value for the specific surface area was suitable, but that of the absolute value for silica content was insafficient. **Figure 6** shows the effect of the amount of adsorbed water on the specific surface area (○) and silica content (●), whereby the alumina fine powder was moistened to adsorb water at different levels, and then, subjected to the coating treatment under a constant stearic acid concentration at 0.015mol/l. In **Fig.6**, the axis of abscissa represents the amount of adsorbed water per 1g of the alumina powder. The specific surface area is closely increased with the increase of the amount of adsorbed water. On the contrary, the silica content is seen as having increased in the range of adsorbed water less than 0.1g, and then, decreased with an increase in the amount of the adsorbed water, the behavior being quite different from that of the specific surface area. This difference resulted from the presence of some coarse particles of silica which might have been formed due to the localized water such as that which condensed onto the reactor wall surface or located at the intergranular area of the primary alumina particles composing the aggregates. Symbol, ◇, in Fig.6 represents the value for specific surface area of the above-mentioned silica coated alumina powder samples afterheat treatment at 600 °C for 1 hr in air for oxidative decomposition fo organic substances contained in the coat layer. It is seen that the specific area decreased after such a heat treatment, which corresponds to the increase in the size of silica ultra-fine particles afterheat treatment as mentioned above in the paragraph of electron microscopic tests.

4. Conclusion

Nano-coating of alumina fine powder with ultra-fine particles of silica was successfully tried by the following method: to treat alumina fine powder to adsorb water properly, and then, disperse it in a hydrophobic organic solvent added with stearic acid to lead to the reaction of ethyl silicate with the adsorbed water. It was also confirmed that the thickness of the coat layer can be controlled by controlling the amount of adsorbed water. To avoid the formation of coarse particles of silica at the intergranular area of the agglomerated primary alumina fine particles, it is clearly needed to disperse the moistened alumina powder well in the hydrophbic organic solvent into single primary particles.

References

1) Selmi, F.A. and V.R.W. Amarakoon : *J.Am. Ceram. Soc.*, **71**, 934 (1988)
2) Hirano, S., *et. al* : Preprint of 1989 annual meeting of Japan Ceramics Society, Tokyo, May, p.517 (1989)
3) Ohmori, S. and T. Senna : Preprint of 26th Symposium on Powder Science, Kanazawa, Oct., p.13 (1988)

Experimental Control of Preparation of Thin Film and Fine Particles by CVD †

Kentaro Ohshima, Yoshifumi Torimoto and Keiichi Tsuto
Institute for Fundamental Research, Kao Corporation *

Kikuo Okuyama
Dep.of chem.Eng., Hiroshima University **

Ryuichi Ushio and Yasuo Kousaka
Dep. of Chem. Eng., Univ. of Osaka Prefecture, * **

Abstract

The formation of TiO_2 thin film and fine particles by the thermal decomposition of titanium tetraisopropoxide(TTIP)vapor was carried out experimentally using a laminar-flow aerosol reactor(LFAR). TTIP vapor and He gas mixture was introduced into a heated pipe in a laminar flow, and the thin films formed and the particles deposited on the pipe wall were observed using an electron microscope under various supplied concentrations of TTIP vapor, reactor temperatures and operating pressure inside the reactor It has been found that the generation of fine particles is enhanced at higher concentration of TTIP vapor, higher reaction temperature and higher pressure, but the formation of thin films is more enhanced lower pressure. The observed trends agreed qualitatively with the simulation results obtained by numerically solving the aerosol dynamic equation where the particle formation was evaluated by a simplified reaction and coagulation model.

Introduction

Recently, fine materials are being studied in various fields for the purpose of utilizing their specific function and improving their functions to an even higher degree. Among them, a great deal of attention is paid to the technology for material formation through the process where materials are generated in a solid phase including thin film, fine particles, etc. from the gas phase, is i.e., Chemical Vapor Deposition (CVD). A characteristic feature of CVD is that thin film and fine particles that are high in purity are obtainable relatively easily through continuous operation and that thickness and crystalline state for film and size and concentration for particles can be controlled. Particularly, it is qualitatively evident that a change in the pressure condition greatly affects the formation of film and fine particles in a reactor. However, the mechanisms for a gaseous reaction and formation of film and particles have not been fully elucidated, for it is not easy to examine quantitatively the influence of pressure condition upon the formation of film and particles largely due to the experimental difficulties.

Hence, in this study, at first we investigated experimentally how the formation of film and fine particles depend(I) on pressure inside a reactor(from atmospheric pressure to reduced pressure),(II) on temperature of the reactor and (III) on supplied TTIP vapor concentration under various conditions by using an aerosol reactor where thin film and fine

* 1334 Minato Wakayama 640, Japan
TEL.0734 26 8631

** 1 4 1, Kagamiyama, Higashi Hiroshima724, Japan
TEL.0824 22 7111

* ** 4 804 Mozu Umemachi, Sakai 591, Japan
TEL.0722 52 1161

† This report was originally printed in *Kagaku Kougaku Ronbunshu*, **16**, 535-542(1990)in Japanese, before being translated into English with the permission of the editorial committee of the Soc. Chemical Engineers, Japan.

particles are formed through thermal decomposition of vaporized titanium tetraisopropoxide, hereafter abbreviated as TTIP, fed into a heated tube in a laminar flow.

Second, since it is thought that thin film formation may be governed by the diffusion phenomena of a monomer and cluster and that fine particle formation may be governed by their coagulation phenomena, a diffusion equation considering the particle formation based on a simplified reaction and coagulation model[2] was numerically calculated as a simultaneous equation with a heat energy equation in a non-isothermal field. Then, the results were compared with the experimental results.

1. Formation of TiO_2 Thin Film and Fine Particles through Thermal Decomposition of TTIP Vapor

In this experiment, the fromation of a titanium oxide film and the particles[1,3-5] through thermal decomposition of titanium tetraisopropoxide (TTIP) vapor was investigated as a reaction system where thin film and fine particles are generated. According to the following overall thermal decomposition, it is simply considered that TTIP vapor is decomposed into titanium oxide with the simultaneous forming of propylene and water.

$$Ti(OC_3H_7)_4 \rightarrow TiO_2 + 4C_3H_6 + 2H_2O \qquad (1)$$

Here, the rate constant for the overall thermal decomposition is found by determining concentration of the propylene by-product using gas the chromatography. According to the experimental results of Kanai *et al.*[1] and thouse of Okuyama *et al.*[3] assuming that the above reaction is a first-order reaction, K_A is approximated to the following equation.

$$K_A = 3.960 \times 10^5 \exp(-7.046 \times 10^4 / RT) \qquad (2)$$

In addition, in this experiment, the TiO_2 formation through a reaction between TTIP vapor and the water by-product is thought negligible since the concentration of TTIP vapor is less than about 0.4%[1]

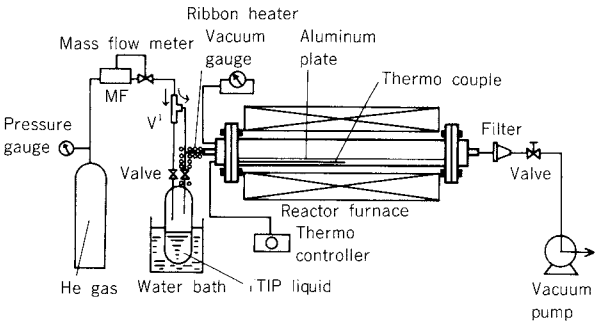

Fig. 1 Schematic diagram of experimental apparatus used in the experiments

1.1. Apparatus and Method for Experiment

A flow diagram of the experimental apparatus is shown in **Figure 1**. Passing He gas with mass flow rate Q determined by mass-flow meter MF which indicates Q converted into the gas, flow rate at 239K under 1.01×10^5Pa, it is introduced into an evaporator containing TTIP liquid to be saturated with TTIP vapor and the resulting gas is red into a reactor heated in a furnace. Quantity of generating TTIP vapor, i.e., concentrarion, can be varied by adjusting the water bath temperature. Temperature of the heating furnace can be controlled with a thermocouple inserted in a reactor tube. Pressure of the reactor tube is regulated by a vacuum pump isntalled after the reactor and is measured with a vacuum gauge. Furthermore, to avoid condensation of the effluent gas from the evaporator before flowing into the reactor, the connecting tubes are warmed to about 323K with heating tapes.

The reactor tube is a stainless steel pipe having a 0.025m I.D. and a 0.7m lenght and both of its ends have O-rings sandwiched between flanges in construction to keep the tube airtight. A thin plate of aluminum, 0.02m in width and 0.7m in length, is mounted in the lower part of the reactor as the basal plate. Then, it is taken out after each experiment for observation of film and deposited particles generated on the basal plate through the

Table 1 CVD experimental condition.

Run	Pressure P [Pa]	Volume flow Q [m^3/s]	TTIP concentration*1) C [%]	Furnace temperature T [K]
a	1.01×10^5	1.67×10^{-5}	0.1	523
b	1.13×10^4			
c	1.13×10^3			
d	1.01×10^5			623
e				723
f	1.13×10^3			623
g	1.01×10^5		0.025	523
h			0.4	
i	1.13×10^3		0.025	
j			0.4	

*1) This value was calculated from the saturated vapor pressure P_{sat} of TTIP vapor*2) shown in the below.

Temperature [K]	312	323	351
P_{sat} [Pa]	25.3	101.3	404.0

*2) P_{sat} Of TTIP is referred to the catalog of articles printed by TRI CHEMICAL LABORATORY INC..

reaction. In addition, a filter unit, using a GB100R filter paper supplied by TOYO ROSHI, is fitted closely after the outlet of the reactor to collect particles.

The experimental procedure is as follows. Experiments were carried out under atmospheric or reduced pressure. In both cases, He gas is passed through a by-pass beforehand by switching with the V_1 valve so that He gas alone flows through the reactor tube. Then, the V_1 valve is opened to the side of TTIP evaporator and the TTIP vapor accompanied by He gas is introduced into the reactor tube to be decomposed thermally in the tube, resulting in the generation of titanium oxide. Experimental conditions, i.e., operating conditions of the reactor are shown in **Table 1**, Particularly under reduced pressure as shown in **Table 1**, the flow rate of He gas is lowered considering its cubic expansion caused depending on a pressure drop so that TTIP vapor concentration at the tube inlet and the gas residence time in the tube are abjusted similarly to those under atmospheric pressure. Accordingly, in these experiments, the flow rate of He gas is regulated with the mass flow meter so that the gas residence time in the tube is abjusted to 20.6sec. independently of the pressure.

1.2 Results and Discussion

As shown in **Table 1,** the experiments were conditioned in the following cases. Pressure inside the reactor is chose from(I)1.01×10^5 Pa(=1 atm),(II) 1.13×10^4Pa and (III)1.13×10^3Pa. The TTIP concentration is chosen from 0.025, 0.1 and 0.4%. The flow rate of the reactant gas is $1.67\times10^{-5}m^3/s$ calculated considering the cubic expansion due to reduced pressure inside the reactor tube as mentioned previously. Set temperature of the reactor tube is chosen from 523,623 and 723K, where the temperature distribution is in a convex form (**see Fig.2**).

Running time in each experiment is 2 hr. A standard operating condition selected for the reactor is a combination of 1.01×10^5 Pa for pressure, 0.1% for TTIP vapor concentration, $1.67\times10^{-5}m^3/s$ for the flow rate of reactant gas and 523K for the setting temperature of the reactor. Then, the formation of thin film and fine particles was investigated experimentally

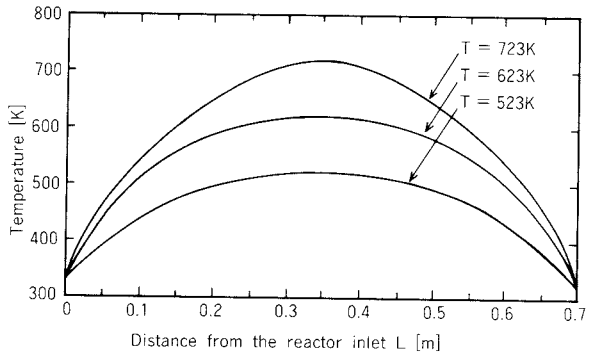

Fig. 2 Temperature distributions of the reactor

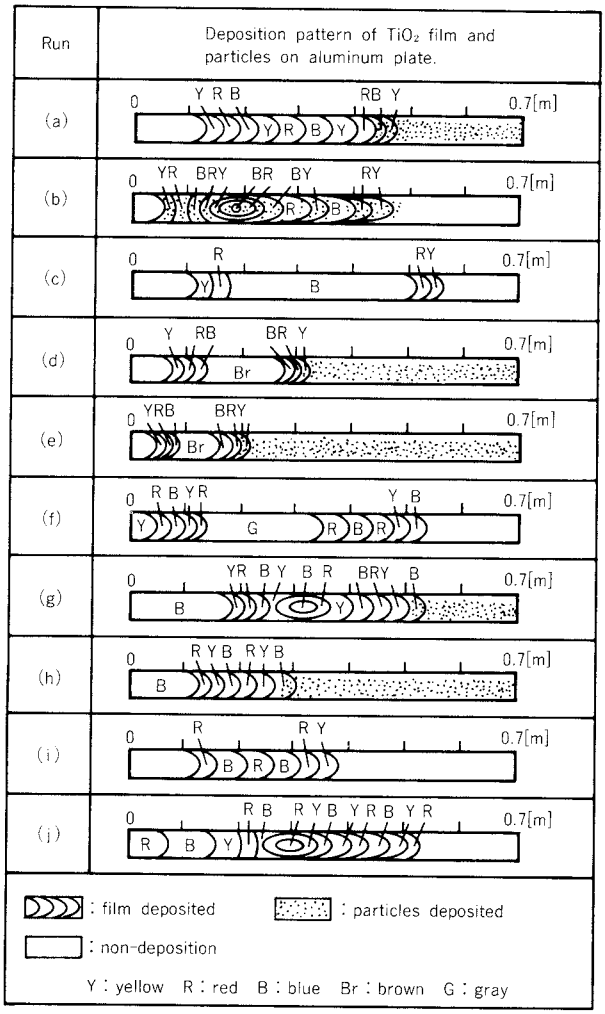

Fig. 3 Schematic representation of CVD experimental results

by varying pressure, temperature and gas concentration to this standard condition. Each experiment was repeated at least more than 2 times under the same condition for reproducibility checking to take sufficient care not be influenced by contamination with instruments. Experimental results concerning thin film and deposited particles on aluminum plates are shown schematically in **Figure 3** (a)-(j).

(I) Effect of Operating Pressure inside the Reactor

In the experiments under atmospheric pressure as shown in **Fig.3**(a), TiO_2 film causing interference fringes(yellow, red and blue)is fromed from a point about 0.13m to 0.5m from the inlet. This coloring of the interference fringes is attributable to diffraction of visible light by a thin layer, i.e., TiO_2 thin film in this experiment, formed on the basal plate. Since this color, with a wavelenght of the interference fringes, is almost in proportion to the film thickness, there appears a distribution of thickness in the film obtained by the experiment. Furthermore, deposition of white fine powder was observed from the point about 0.46m from the inlet to the outlet. **Figure 4** (a),(b) indicate the observation results with a scanning electron microscope (SEM) in respect to the particles, deposited around the tube as outlet, and the film, the red part on the aluminum plate.

This SEM photo reveals that particles are spherical in form and are almost uniform in size. On the other hand, on the surface of the film, the red part, parallel stripes and granular unevennesses are obserbed, as is similar to the parts of interference fringed of different colors. In addition, **Fig.4**(**c**), the SEM photo. of the aluminum plate surface before the experiment, shows also parallel strips on the surface, so that stripes on the film in **Fig.4**(**b**) are considered to reflect the surface of the basal plate. Moreover, the TiO_2 film does not peeled off when it was touched rather strongly by fingers since it adheres strongly to the aluminum oxide coating through a chemical bond. As for the white fine powder of TiO_2, it could be removed easily from the basal plate since it was deposited simply physically onto the surface.

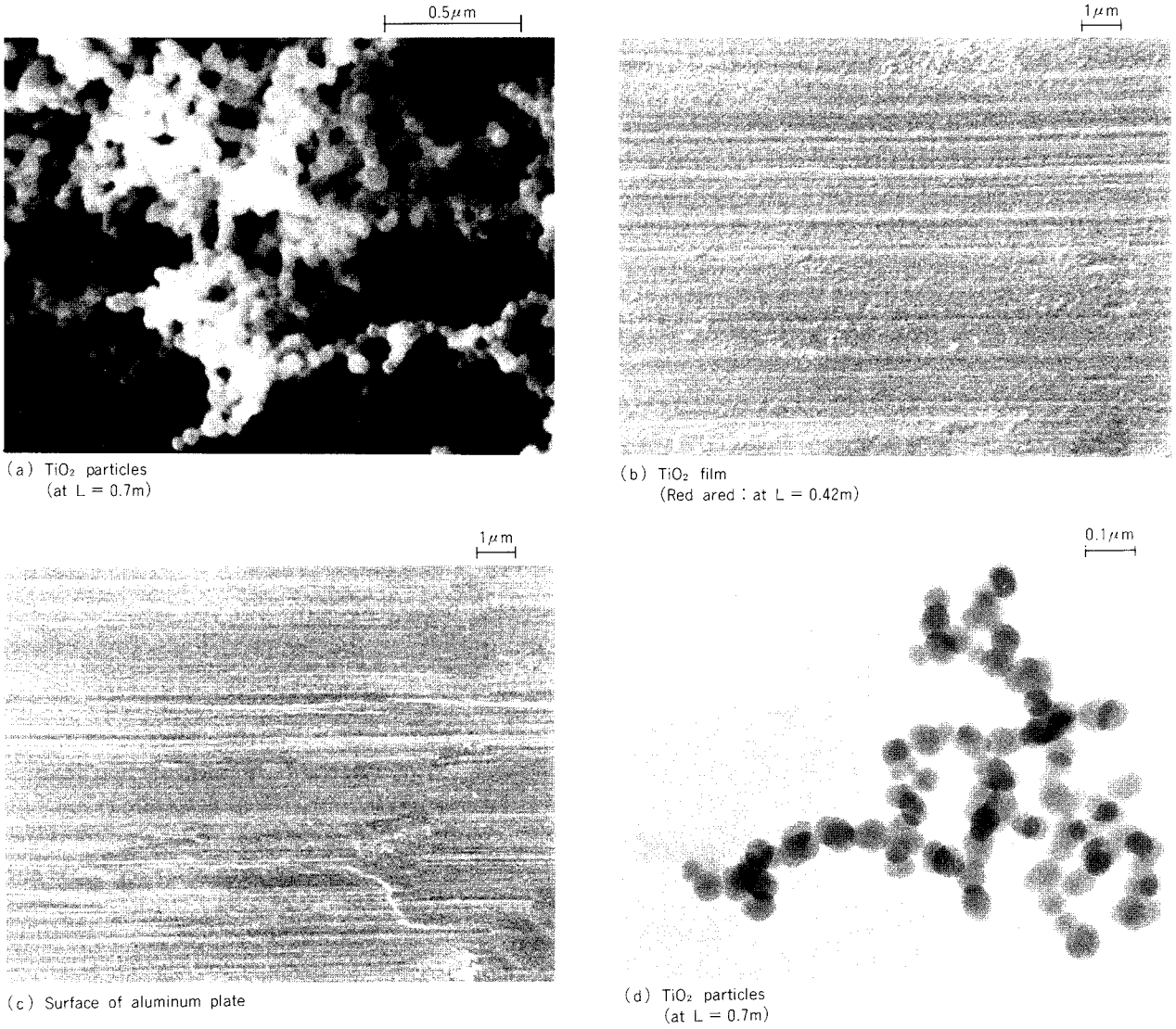

(a) TiO_2 particles (at L = 0.7m)

(b) TiO_2 film (Red ared : at L = 0.42m)

(c) Surface of aluminum plate

(d) TiO_2 particles (at L = 0.7m)

Fig. 4 EM photographs of TiO_2 particles and thin film on Aluminum plate by CVD [(a)~(c): SEM photographs, (d):TEM photograph]

Second, in the experiment under the reduced pressure 1.13×10^4Pa, a striped film emitting similar interference fringes to the above mentioned was formed from the point about 0.04m to 0.47m from the inlet as shown in **Fig.**3(b), while the white fine powder of TiO_2 was observed over the whole interval. **Figure 5** (a)shows a SEM photo. of film, the blue part, obtained in the experiment on the aluminum plate. According to this, the film surface is found having similar aspects to those of the experiments under atmospheric pressur(**Fig. 4** (b)). **Figure 5** (b)shows the white fine powder of TiO_2 deposited at the point 0.47m distance from the inlet in same condition. This powder consist of granular particles almost uniform in size, which is the similar results as the above-mentioned CVD experiment under atmospheric pressure.

The films and particles obtained in the above experiments were observed with a transmission electron microscope(TEM)and results are shown in **Figs. 4(d), 5(c)**. These figures indicate that mean diameter of the particles generated under atmospheric pressure and the reduced pressure of 1.13×10^4Pa is about 0.06μm and about 0.03μm, respectively.

Next, the experiment under the reduced pressure of 1.13×10^3Pa gave a striped film

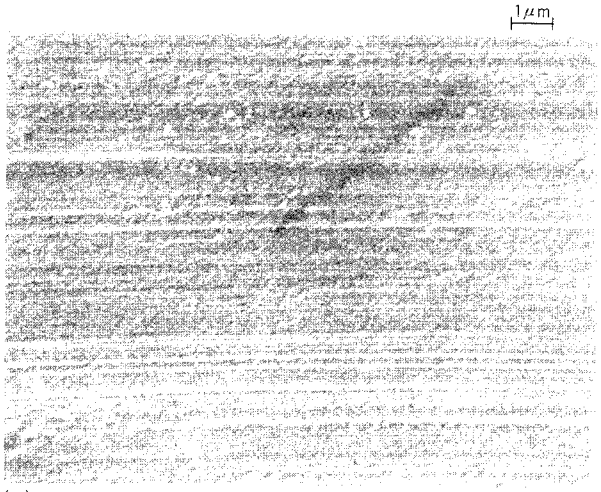

(a) TiO_2 film
(Blue ared : at L = 0.13m)

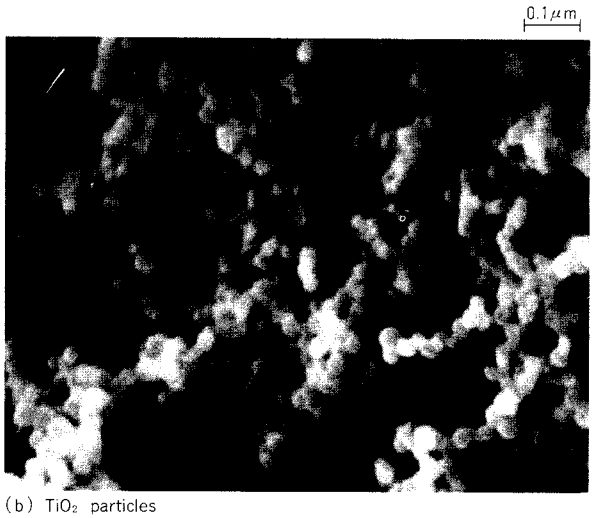

(b) TiO_2 particles
(at L = 0.47m)

(c) TiO_2 particles
(at L = 0.47m)

Fig. 5 EM photographs of TiO_2 film and particles on Aluminum plate by low-pressure CVD (at 1.3×10^4Pa) [(a), (b):SEM photographs, (c): TEM photograph]

emitting interference fringes changing from yellow to red over the interval from a point about 0.11m to the point 0.17m from the inlet. The interval of the stripes was found to be wider than of the above-mentioned 1.13×10^4 Pa case and the film emitting blue interference fringes was observed over the interval from a point about 0.17m to 0.51m from the inlet. The film emitting interference fringes changing from red to yellow over the interval from the

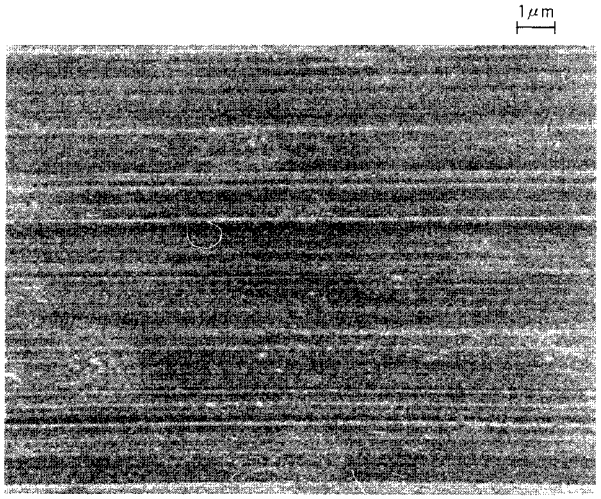

(a) TiO_2 film
(Blue area : at L = 0.35m)

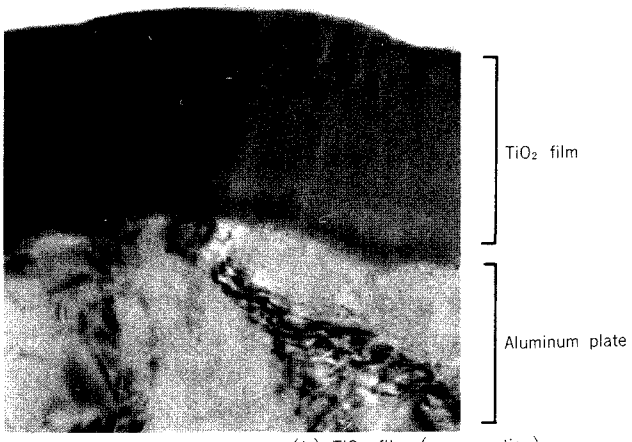

(b) TiO_2 film (cross section)
(Blue ared : at L = 0.35m)

Fig. 6 EM photographs of TiO_2 on film Aluminum plate by low-pressure CVD (at 1.13×10^3Pa) [(a):SEM photograph, (b):TEM photograph]

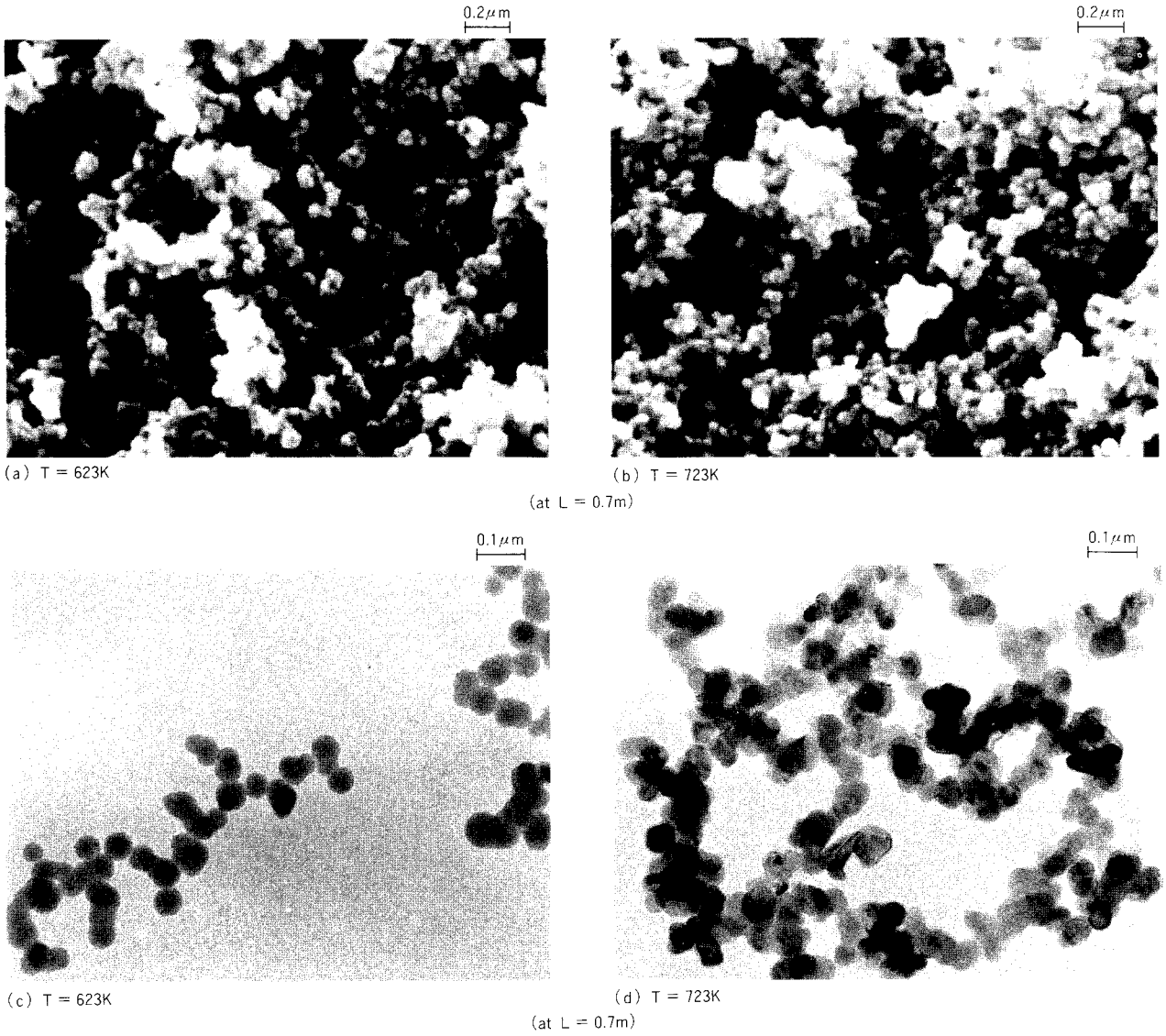

Fig. 7 EM photographs of TiO_2 particles on Aluminum plate by CVD [(a), (b):SEM photographs, (c), (d):TEM photographs]

successive point to a point 0.55m from the inlet. **Figure 6** (a)shows a SEM photo. of the film, the blue part, on an aluminum plate in the experiment under the above pressure condition. There are stripes like the above 2 experimental results, while the film surface evidently has no granular unevenness to be smoothed. **Figures 6** (b)shows a TEM photo. of the film cross section, the blue part and indicates in which thickness is about 300nm and that it is formed uniformly without space.

The aforementioned results clarify that by reducing the pressure in the reactor, the film formation becomes more favored that of particles. This is considered because diffusion phenomena of monomer and clusters including dimer, trimer, etc., become predominant due to the effect of reduced pressure.

(Ⅱ) Effect of Operating Temperature in the Reactor

Experimental results at a setting temperature of 623 and 723K under atmospheric pressure are schematically shown in **Figs.3** (d),(e), respectively. As is evident from each figure, film and particles have formed in reactor tube at each operating temperature. Furthermore, by a comparison of **Figs.3(a)**,

(d)and(e), as the temperature of the reactor tube is raised, the depositing end of the film and particles is shifted toward the inlet, the film area reduces and the interval of the stripes is narrowed, while the depositing part of particles is evidently extended. This is considered because raising the temperature in the reactor tube enhances the reaction rate of TTIP vapor, so that the generated monomer increases as the distance from the inlet decreases, resulting in an increases in the particles formed thereafter by immediate coagulation.

Figures 7 (a),(b) show SEM-observed results of white fine powder TiO_2 on aluminum plates obtained in the experiments. In each case, the particle size and deposition condition on the aluminum plates become quite clear. TEM-observed results of these particles are shown in **Figs.7**(c),(d). In both cases, the particle size is found to be about 0.06 μm through the TEM photos. Therefore, the operating temperature in the reactor could not greatly influence the size of the resulting particles.

Fig.3 (f) shows the experimental results at the setting temperature of 623K under reduced pressure of 1.13×10^{3}Pa. This indicates that

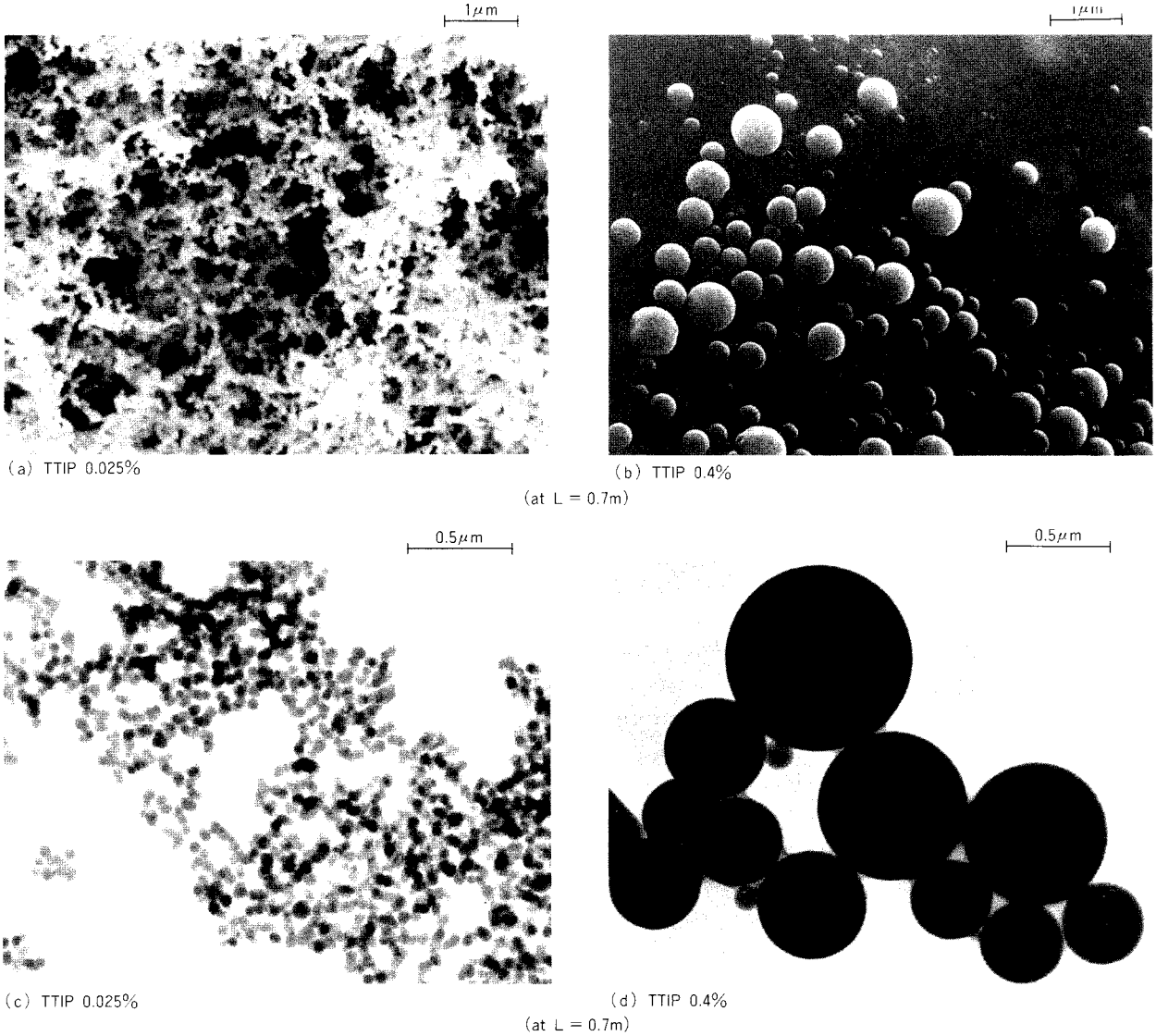

(a) TTIP 0.025%　(b) TTIP 0.4%
(at L = 0.7m)

(c) TTIP 0.025%　(d) TTIP 0.4%
(at L = 0.7m)

Fig. 8 EM photographs of TiO_2 particles on Aluminum plate by CVD [(a), (b) :SEM photographs, (c), (d):TEM photographs)

only filme is formed and **Figs.3**(c),(f) clarify that the depositing place film is shifted toward the inlet as in case under atmospheric pressure as previously mentioned. This is because of the increase in conversion results from raised temperature in the reactor tube.

(Ⅲ) Effect of Reactant Vapor Concentration

Fig. 3 (g) and (h) show the experimental results for TTIP vapor conentration 0.025 and 0.4% respectively under atmospheric pressure. As is evident from each figure, film and particles have formed in the reactor tube in each case. Furthermore, by a comparison of **Fig.3** (a),(g)and(h), as the reactant vapor concentration in the reactor tube increases, the depositing end of particles is shifted toward the inlet with a reduction in the film area. This shows that the coagulation of the monomers and clusters become predominant as the vapor concentration increases, which tend to from particles. **Figures 8** (a),(b) show SEM-observed results of white fine powder TiO_2 on aluminum plates obtained under those conditions. In each case, particles size is found to be almost uniform. TEM-observed results of these particles are shown in **Fig.8(c),(d)**. In both cases, it is found that the particles are in spherical in form and the particle size is about 0.5μm for 0.4% concentration and about 0.04 μm for a 0.025% concentration. Therefore, the TTIP vapor feed concentration evidently has a great influence on the size of the resulting particles.

Figures 3(i)and(j)show the experimental results for TTIP vapor concentration 0.025% and 0.4% respectively under the reduced pressure of 1.13×10^3Pa. As is evident from each figure, only film has formed in each vapor concentration. By comparison of **Figs.3(c)(i)** and (j),the film area tends to extend with increasing the vapor concentration. This is because the higher vapor concentration enhances the generation of monomers, resulting in a increased deposit on the reactor tube wall.

1.3 Comparative Study of Experimental Results and Numerical Calculation on the Formation of Thin film and Particles

It is quite difficult to evaluate correctly the process of formation for TiO_2 thin film and fine particles in an aerosol reactor, so that we cannot help approaching it by using an appropriate model at present. Okuyama *et al.*[3] have elucidated the process of formation for clusters and fine particles through the reaction of gas flowing laminarly in a tube by solving numerically the aerosol dynamic equation which is derived from the diffusion equation for evaluating the deposition of clusters and fine particles by incorporarting a simplified reaction and coagulation model. Comparative study of experimental results and numerical calulation results obtained by the same method were made in this paper. In this theoretical analysis, the monomer formation through thermal decomposition, Brown coagulation of monomers, clusters and fine particles and transport by laminar flow are taken into consideration with the following assumptions.

(1) At the tube inlet, gas flows with a well-developed laminar-flow velocity distribution which is not influenced by any temperature change.
(2) Particles are in spherical form and electrically neutral, ignoring their thermal migration.
(3) Particles coagulate to from a new spherical particle which has weight equal to the sum of each particle weight.
(4) All of the particles which collided with the reactor tube's wall are deposited on the wall surface.
(5) The molecules of TTIP vapor do not be deposited on the tube wall surface.
(6) The axial diffusion of monomers,clusters and fine particles in a tube are negligible compared with their convection.
(7) The heat of reaction for TTIP vapor and the heat of condensation for TiO_2 particles are negligible.

For numerical calculation, we treated a

substance composed of 5 molecules or under as a cluster and one composed of 6 molecules or more as a particle, since numerical calculations become more difficult with a raise in the reaction temperature or with an increase with TTIP vapor concentration. Furthermore, to determine the number of axial and radial steps, the calculation was repeated by changing the number of axial partitions from 70000 to 700000 and by changing the number of radial partitions from 30 to 100. By comparing the obtained results, 350000 for the number of axial partitions and 50 for the number of radisl partitions was found to give sufficient accuracy. Hence, most of calculations were made with 350000 axial partitions and with 50 radial partitions throgh the solution by the Crank-Nicolson method.

Among the above assumptions, assumption (1)seems to be hardrly realized in the reactor

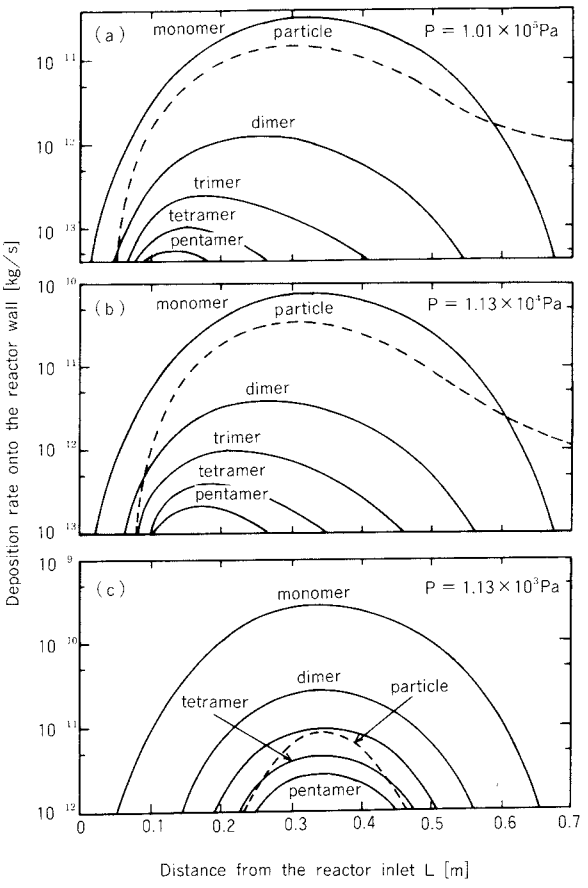

Fig. 9 Distributions of deposition rate onto the reactor wall when the operating pressure is changed

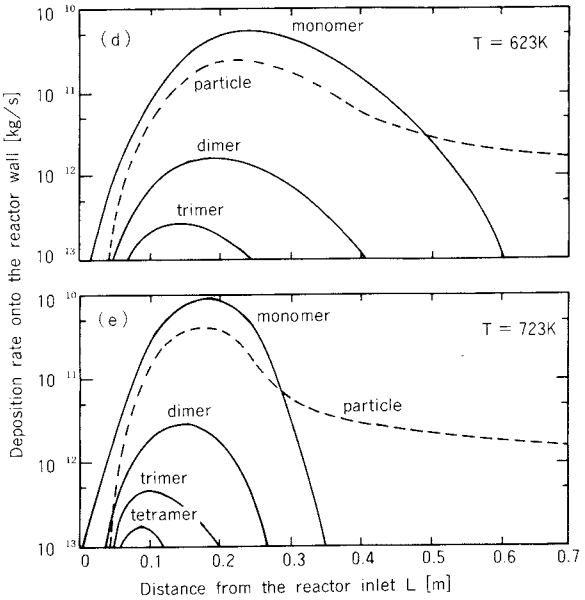

Fig. 10 Distributions of deposition rate onto the reactor wall when the temperature of reactor is changed

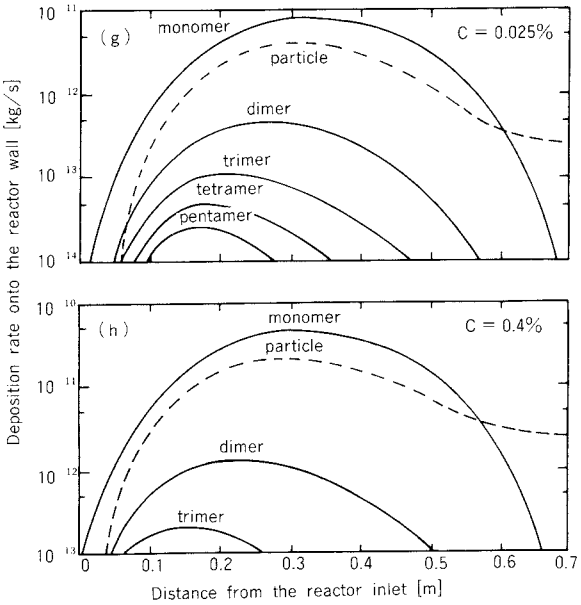

Fig. 11 Distributions of deposition rate onto the reactor wall when the supplied concentration of TTIP is changed

shown in **Fig.1** due to the influence of the inlet part, existence of temperature distribution in the reactor, etc., so that the following numerical calculation results can be compared with the experimental results qualitatively.

The results of the numerical calculation based the experimental condition mentioned previously(see **Table 1**)are shown in **Figures 9-12**.

Figures 9-11 show the distribution of

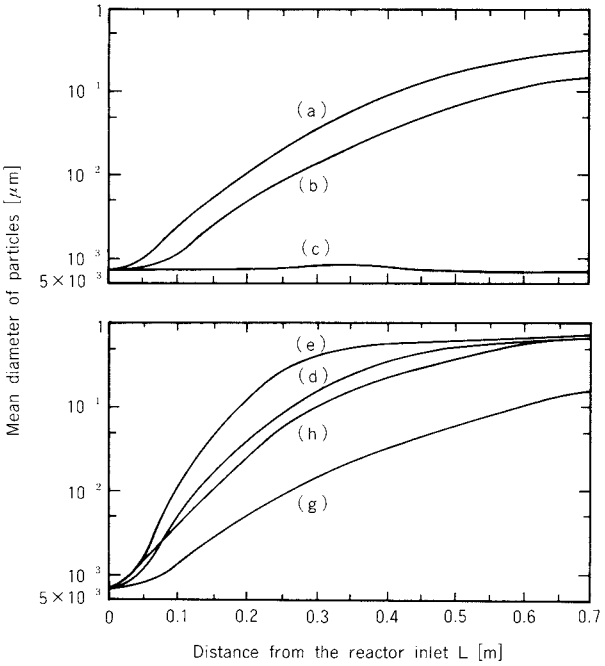

Fig. 12 Distributions of particle diameter in the reactor [The curves of (a)~(e), (g)and (h) correspond to those in Figs. 9~11)

deposition rate onto the reactor wall for the TiO_2 monomer, cluster and particle, where the axis of the abscissas expresses the distance from the reacor inlet and the axis of the ordinate expresses the deposition rate onto the reactor wall. **Figure 12** shows the change in the volume mean diameter of deposited particles, where the curve of(a)-(e),(g)and(h) express the calculation results corresponding to those in **Figs.9-11**. Comparative studies of the experimental results and numerical results and numerical calculation results on the formation of thin film and fine particles are mentioned below.

(I) Effect of Operating Pressure inside the Reactor

Fig.9(a)-(c) show the numerical calculation results for operating pressure in the reactor 1.01×10^5Pa, 1.13×10^4Pa and 1.13×10^3Pa, respectively. In each figure, the distribution of the deposition rates for the TiO_2 monomer, cluster and particle are of a convex from, which is known to be very much related to the temperature distribution in the reactor(see **Fig.2**).

In the reaction under atmospheric pressure, as is evident from **Fig.9(a)**, monomers are deposited in a small quantity at the inlet and outlet of the tube and in a large quantity at around the middle part of the tube. Since the particles are formed through the coagulation of the clusters including monomers, dimers, trimers, etc., their deposition quantities are increasing gradually toward the middle of tube from the inlet similar to the case of the monomers. Furthermore, it was found that they are deposited in a large quantity even around the outlet. Accordingly, judging from the deposition distribution, the film formation in the experiments under atmospheric pressure may be attributed to the deposition of clusters including monomers, dimers, trimers, etc., so that, in particular, the deposition of monomer has a significant influence on the film formation. On the other hand, particles are estimated to be deposited in a large quantity from the middle part of the tube to the outlet, which evidently agrees with the above experimental results as a tendency. From **Fig.12(a)** the particle diameter at the outlet of tube was found to be about 0.3μm for a calculated value which is considerably greater than the experimental value, about 0.06μm given by the TEM photo. The reason for this may be that a coagulum is formed from particles without fusion and collision between particles does not cause adhesion in all cases since the melting point rises or approaches that of the bulk material with increasing particle diameter.

Next, in case of 1.13×10^3Pa as shown in **Fig.9(c)**, an increase in the diffusion rate of the monomers and clusters due to a reduction in the pressure causes more and wider deposition than in case under atmospheric pressure. In addition, in this case, particles are deposited in small quantities. This is because the particles formation is difficult to occur due to the rapid deposition of the monomers and clusters onto the tube wall before they are coagulated to form a particle.

Therefore, in the experiment under reduced pressure 1.13×10^3Pa, it is expected that the film is chiefly formed while spreading axially in a tube, which is considered to agree with

the experimental results as a tendency. As for particle diameter, it is about $8\times10^{-4}\mu$m as a calculated value through the whole inside of tube as seen from **Fig.12(c)**,and is of the order of a cluster. This agrees with none of the observations of particles in the experiments. Furthermone, in case of 1.13×10^{4}Pa as shown in **Fig.9(b)**, evidently deposition of the monomer and cluster amounts to the quantities between the cases of atmospheric pressure and 1.13×10^{3}pa, while deposition of the particle is larger than in the case in **Fig.9(a)**, which explains well the tendency of the experimental results. As for the particle diameter, it is found about 0.15μm as a claculated value at the tube outlet as seen from **Fig.12(b)**and is quite different from the experimental results, about 0,04μm from the TEM photo. which is by similar reasoning as mentioned previously.

(II) Effect of Operating Temperature in the Reactor

Figure 10(d),(e)show the numerical calculation results for set temperature in the reactor 623 and 723K, respectively. In **Fig.9**(a)and **Figs.10**(d),(e), as the set temperature is raised, the deposition distributions of monomer, cluster and particle are shifted toward the inlet, which evidently agrees with the experimental as a tendency. As for the particle diameter, there is not so large a difference between the calculation and experimental results, while the coagulation effect becomes predominant as the operating temperature is raised, so that the particles grow.

(III) Effect of Reactant Vapor Concentration

Figure 11(g)and(h) show the numerical calculation results for TTIP vapor concentration 0.025 and 0.4% respectively under atmospheric pressure. **Fig.9** (a), and **Fig.11** (g)and(h) indicate that the deposition of particles and also the monomer and cluster increase as the TTIP vapor concentration increases, which evidently agrees with the experimental results. As for the particle diameter, **Figs.12(g)**,**(h)**indicate that it grows as the TTIP vapor concentration increases due to the predominant coagulation effect.

2. Conclusion

The following was clarified after investigating the formation of thin film and fine particles through the experiments by using a laminar flow aerosol reactor.

(1) The CVD experiments under atmospheric and reduced pressure elucidated that with reducing pressure the formation of film become more favored than that of particles and the interval of their stripes increases in the axial direction of the tube. Regarding the particles, spheres almost uniform in size are formed, while as for film, the interference fringe due to the diffraction of visible light is observed. Since its color varies with stripes, there appeared a distribution of film thickness.

(2) Since the conversion inside the reactor increases as the operating temperature of the reactor tube is raised, the rate of monomer formation increases in the inlet part, so that film and particles are apt to be formed on the side of the reactor inlet.

(3) Since the monomer formation increases as the concentration of the vapor supplied to the reactor is increased, in case of atmospheric pressure large particles are formed throgu coagulation and in case of reduced pressure the area of film extends.

(4) The above experimental results agree well qualitatively with the numerical solution of the diffusion equation including the terms for particles formation based on a simplified reaction and coagulation model, so that it became possible to estimate the influence of changes in the reactor condition including the pressure and temperature and in the concentration of vapor supplied to the reactor on the formation of film

and particles to some extent.

Nomenclature

C = supplied concentration of TTIP vapor into the reactor [%]
K_A = reaction rate constant [s^{-1}]
L = distance from the reactor inlet [m]
P = pressure gauge in the reactor [Pa]
Q = flow rate of carrier gas with TTIP vapor [m^3/s]
T = setting value of temperature in the reactor [K]

References

1) Kanai, T.,H.Komiyama and H. Inoue: *Kagaku Kogaku Ronbunshu,* **11**, 317(1985)
2) Okuyama, K.:*J.* Soc. Powder Technol, Japan, **26** ,3(1989)
3) Okuyama, K., R. Ushio, Y.Kousaka, J.H.Seinfeld and R.C.Flagan: *Kagaku Kogaku Ronbunshu* **16,** 526(1990)
4) Okuyama, K.,Y.Kousaka, N.Tohge, S,Yamamoto, J.J.Wu, R.C.Flagan and J.H.Seinfeld: *AIChEJ.,* **32**, 2010(1986)
5) Okuyama, K., J.J.Jeung, Y.Kousaka, H.V.Nguyen, J.J.Wu and R.C.Flagan: *Chem. Eng. Sci.,* **44**, 1369(1989)

Preparation of Ultrafine Particles by Nanopowder Process †
— Factors for Milling Rate and Contamination —

Masamitsu Nishida, Hamae Ando and Koichi Kugimiya
Central Research Laboratory, Matsushita Electric Industrial *

Abstract

Factors of milling rates and contamination due to abrasion of balls were investigated in order to obtain ultrafine powder of pure piezoelectric ceramics.

Higher milling rates and lower contamination from balls were obtained for smaller balls. Calcined piezoelectric powders of 1 μm in mean particle diameter were milled into the fine powders of 0.2 μm for about 7 min. It was estimated that milling rates of this case (0.4mm PSZ balls) was about 10^5 times as that of ball mill (ball size 10 mm). Even smaller ultrafine particles of 19 nm in mean particle diameter were obtained by milling for 90 min.

1. Introduction

As a method for obtaining uniform and high density ceramics, it is noticable that the method for synthesizing the powder of uniform fine particles with such a liquid phase method as co-precipitation method and for firing the ceramics using the said powder. The liquid phase method has such features that the composition of powder can be made uniform with ease and that the particle diameters can be equalized without much difficulty, but a comparatively higher cost is required for obtaining the raw materials. On the other hand, the conventional solid phase method involves such a demerit that it is difficult to obtain uniform ceramics because the particle diameter of powder is large, and moreover, uniform mixing is difficult, but has such merits the raw materials can be easily obtained in large volume at a comparatively lower price, that the said method can respond even to a complex composition and that mass-production can be achieved easily. To obtain uniform ceramics through solid phase method, enhancing the dispersing property of the raw material powder and obtaining the fine particles become the important factors. A ball mill is frequently used for pulverization in the solid phase method. In the past, it was difficult to mill powder to the size smaller than 1 μm, but it is reported lately that the small ball diameter in a mm unit can be milled into a particle diameter of sub-micron levrl by use of a ball mill[1)-5)].Also, in milling for 32 hrs by use of a vibration ball mill, ultrafine particles of 0.026 μm in an BET diameter can be obtained[6)].The powder can be milled into fine particles by the milling for many hours even with the use of the said ball mill, but recently a media agitating mill is attracting a great deal of attention as a fine grinding mill with a high milling rate. Stanley et al.[7)], grinding the barium ferrite with a variety of grinding

* 3-15, Yagumo-NaKa-machi, Moriguchi, Osaka, 570, Japan
TEL 06-906-4828

† This report was originally printed in. *J. of Japan Society of Powder & Powder Metallurgy*, **37** ,828-831 (1990) in Japanese, before being translated into English with the permission of the editorial committee of Japan Soc. of Powder & Powder Metallurgy.

machines and comparing the milling rates, obtained a fine 0.1 μm powder with a BET diameter by milling for 2 hrs by use of an attrition mill. The mixed quantity of impurities due to the abrasion of the balls in this case is conspicuously high at about 4%.

For obtaining uniform piezoelectric ceramics, the authors have studied the uniformity enhancement of powder and the obtaining of fine particles(nanopowder process) and the factors having an influence thereon, which are, to be reported hereafter. The nanopowder process being referred to here is the ultrafine milling process for milling the particle diameter of powder into the nanometer order within a very short time and also such a handling technique as the dispersion of the said powder.

The composition ratio[8] of the piezoelectric ceramics used is shown in the below formula.
$Pb_{.95}Sr_{.05}(Zn_{1/3}Nb_{2/3})_{.09}(Sn_{1/3}Nb_{2/3})_{.09}Ti_{.415}Zr_{.405}O_3 + 0.25$ wt% MnO_2

The used raw materials are the commercially available Pb_3O_4, $SrCO_3$, ZnO, SnO_2, Nb_2O_5, TiO_2, ZrO_2, and MnO_2. These materials have the mean particle diameter of 2.2 μm.

2. Evaluation Method of Powder

2.1 Particle diameter of powder

The particle diameter distribution of a specimen powder was measured by the sedimentation method, and its 50 wt% particle diameter was taken as the mean particle diameter. Regarding a part of the powder, the mean particle diameter was measured using an optical correlation method and the specific surface area was measured by the BET method.

2.2. Evaluation of dispersing property

The slurry which has been wet-mixed or milled by a pot mill was put into a test tube, and the powder was sedimentated by use of a centrifugal machine for measuring bulk powder. The ratio of this bulk with the true volume of power was taken as the sedimentation volume (cc/cc). For your information, the size of this sedimentation volume is a guidance of the dispersing powder property, wherein a small sedimentation volume means a good dispersing property of powder while, to the contrary, a large sedimentation volume means a bad dispersing powder property or shows that the particles aggregate and form secondary particles[9].

2.3. Evaluation of abrasion degree, etc.of balls

The volume mixed into the powder by the abrasion of balls was obtained from the change in the weight of the balls before and after their use, and was indicated in the value against the weight of powder.

3. Dispersing Property of Ceramic Powder

In the wet-mixing and milling of fine powder, the dispersing property of powder needs to be enhanced for raising the fluidity of the slurry. For that purpose, the effects of dispersing agent and volume of dispersion medium (total of pure water and dispersing agent)on the dispersing property of mixed powder were investigated. The experiment method was such that 2/3 mol of compounded raw materials (about 220g, or 32cc in the true volume of powder)and the pure water together the dispersing agent (the agent named Seramo D134 manufactured by Dai-ichi Kogyo Seiyaku Co., Ltd., a polycarboxylic acid ammonium system)were put into a 600 cc pot made of polyethylene (440g of agate balls of about 10-mm diameter, rotation at 155 rpm) and mixed for 20hrs, and then the sedimentation volume and the particle diameter were measured.As shown in **Fig.1,** when the compounded materials were mixed using a small dispersing agent value (0.6 wt% [solid matter]of powder), the sedimentation volume became conspicuously smaller compared with the case of using no dispersing agent. In the volume of dispersion medium without any dispersing agent, a volume of about 700 vol% of the true volume of powder was required for mixing, and in the case of a lesser volume than the above, the fluidity of the slurry became worse and the mixing was difficult. With the addition of a dispersing agent, the sedimentation volume dropped lower and the dispersing property increased more as the volume of dispersion medium

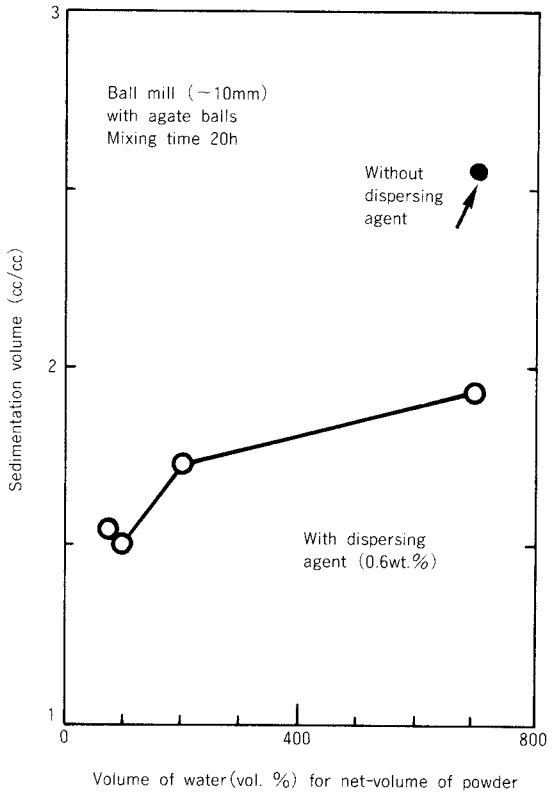

Fig. 1 Effects of dispersing agent and water content on sedimentation volume for raw mateirals.

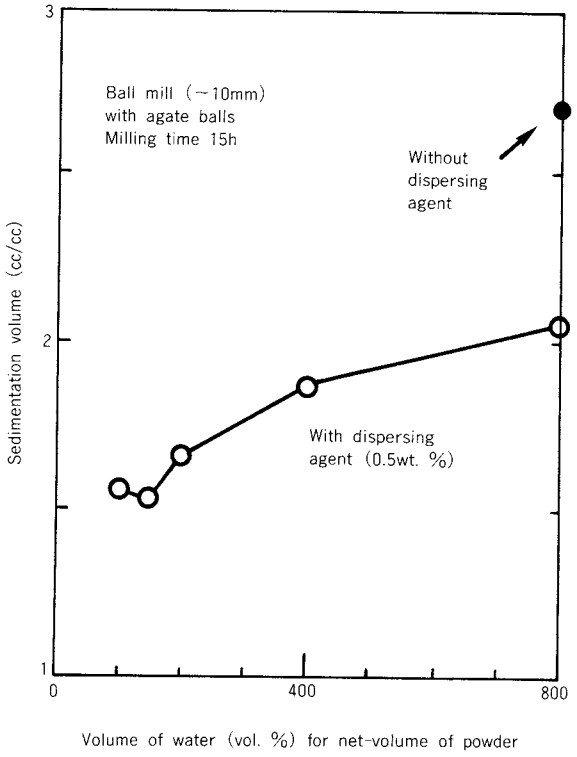

Fig. 2 Effects of dispersing agent and water content on sedimentation volume for calcined powder.

became smaller.For all the cases, the particle diameter of the power was in the order of 1.7 μm which was hardly milled.

Using the powder(with particle diameter being about 1 m)that was preparatorily ground for 30 min by use of an automated mortar after drying the said mixed slurry and calcining it at 850 °C for 2 hrs, the dispersing property of calcined powder was measured. The experiment method was almost similar to the case of mixing, but the volume of charged powder was 190g(about 24cc in true volume)with milling time for 15 hrs. The dispersing property indicated the same trend as case of mixing as shown in **Fig.2** .

4. Fine Milling by Use of Ball Mills

4.1 Fine milling of mixed powder(Milling/ mixing of raw materials)

For conducting uniform mixing and obtaining the fine particles simultaneously, and moreover, within a short time, the mixing method under conditions better in dispersing

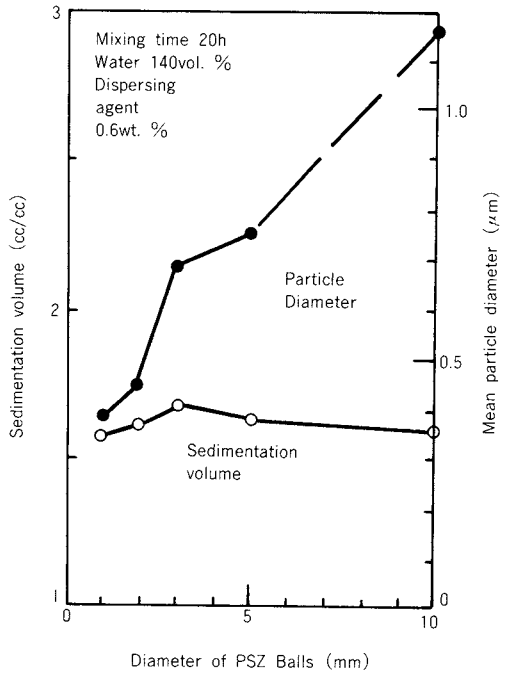

Fig. 3 Effects of diameters of balls on sedimentation volume and particle diameter for raw materials.

property in the preceding item, and moreover, using smaller balls was studied. The mixing method is identical to the preceding item except for using yttrium portion stabilized ziyconia balls(hereafter to be abbreviated as PSZ)of 1-to 10-mm diameter as the balls. As could be seen in **Fig.3**, finer particles could be obtained as the balls were smaller. The particles could be milled to about 0.4 μm in the mixing for 20 hrs and to about 0.2 μm in the mixing for 90 hrs. Moreover no difference was found in the sedimentation volume.

4.2 Fine milling of calcined powder

The previously mentioned calcined powder that had been preparatorily ground was also milled by the same method as that described above. As a result, the powder could be milled into finer particles as the balls were smaller as shown in **Fig.4**. The power could be milled to about 0.4 μm during milling for 15 hrs and to 0.2 μm during milling for 45 hrs. Furthermore, no difference was found in the sedimentation volume. As described above, the fine powder excellent in dispersing property could be obtained by the effects of a lesser water volume, dispersing agent and fine balls.

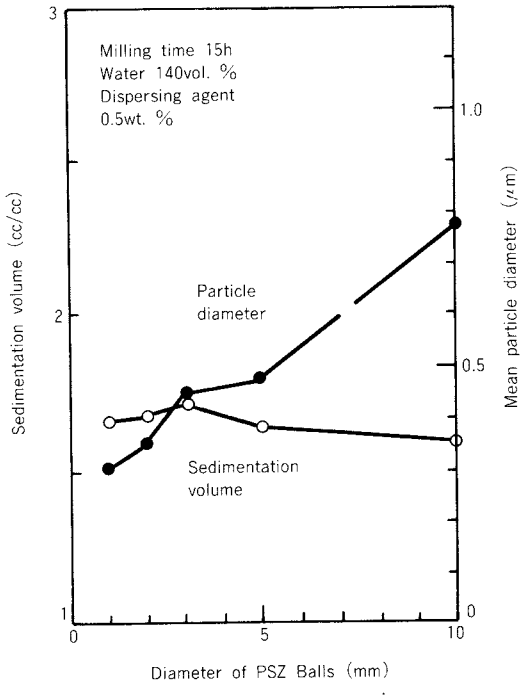

Fig. 4 Effects of diameters of balls on sedimentation volume and particle diameter for calcined powder.

5. Preparation of Ultrafine Particles by Nanopowder Process

The fine powder of 0.2 μm (sedimentation method) could be obtained with the mixing of a raw material powder and the milling of calcined powder for several tens of hours even by use of the ball mill, but the milling method by use of a media agitating mill was studied for obtaining fine particles within a short time. Various types of media agitating mills are available, which are for violently agitating the balls (PSZ) and the milled materials (raw material powder) that are charged into a milling vessel and for generating the shearing stress to mill them by turning at a high speed the agitator inserted into the milling vessel. The mill used are a horizontal continuous type DYNO-MILL Model KDL-PILOT (content volume: 1, 290 cc ; peripheral speed: agitator up to 14 m/s) manufactured by Willy A bachofen Corporation, and a Motormill Model M-50(content volume:40 cc; peripheral speed:10m/s)manufactured by Eiger Engineering Co., Ltd. A ball mill was also used(content volume: 600 cc ; rotation: 155rpm)for comparison's sake. The ball material was PSZ. The wet system milling was used, and the slurry consisted of 200cc of pure water and 1 wt%[solid matter]of dispersing agent against 100cc of the true powder volume.

5.1 Factors of milling rate and abrasion of balls

The milling rate became greater as shown in **Fig.5** when diameter of balls was made smaller, and the powder could be milled to the same particle diameter in about 1/5 time when the ball diameter was changed to 0.4mm from 1 mm. The abrasion volume of balls decreased remarkably when the size of balls was made smaller. The abrasion volume decreased to about 1/3 when the size was changed to 0.4 mm from 1 mm. In the case of a ball mill, the abrasion volume of balls is said to be in

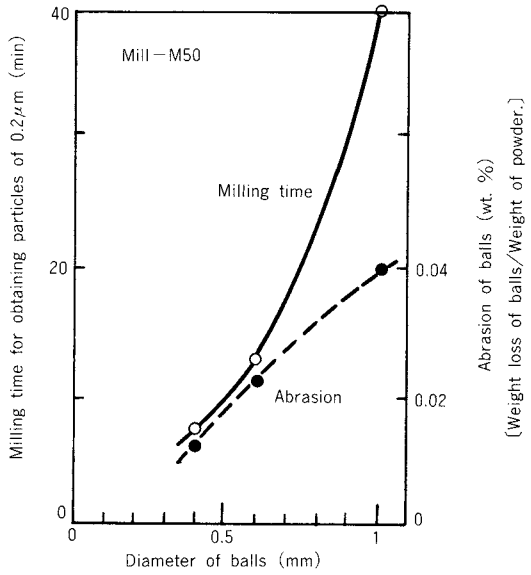

Fig. 5 Effects of ball size on milling rates and abrasion of balls for milling of calcined powder.

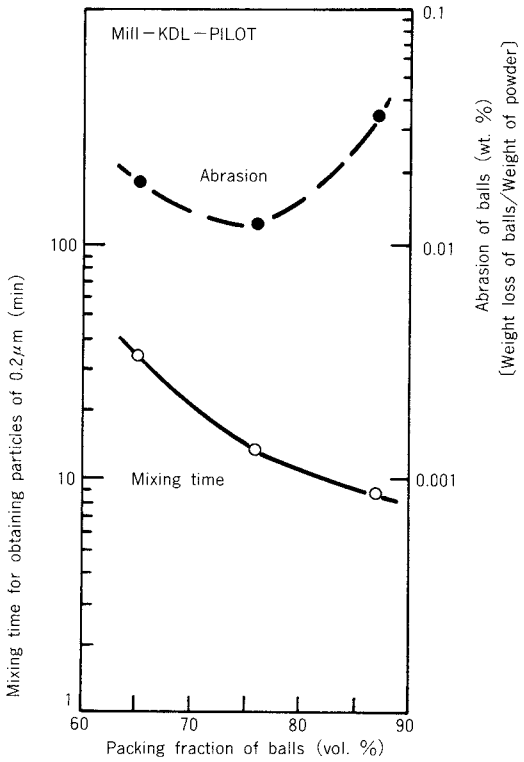

Fig. 6 Effects of packing fraction (balls) for wet-mixing of raw materials (balls－0.4mmPSZ, speed of agitator－14m/s).

a low rotation and does not to depend on the diameter of balls at a high rotation[10]. However, in this experiment, the abrasion volume was proportionate to the diameter of balls, and the abrasion volume decreased more as the size of ball became smaller. For information, the time required for milling the powder into the particle diameter of 0.2μm was obtained by measuring the change in the mean particle diameter of powder due to the milling time.

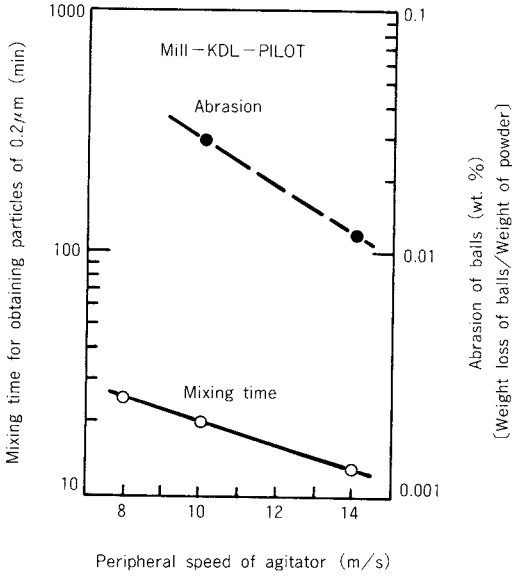

Fig. 7 Effects of peripheral speed of agitator for wet-mixing of raw materials (Balls－0.4mmPSZ, Packing fraction of balls－76vol%)

Figures 6 and **7** show the effect of packing fraction ball and the effect of agitator peripheral speed. More the packing fraction the milling rate increased higher. There was the optimum value of the packing faction in the abrasion volume. The greater the peripheral speed of the agitator, the milling rate increased higher and the abrasion volume of balls decreased, while the higher the peripheral speed, the abrasion volume of balls became less in the case of milling into the powder to the same particle diameter. Furthermore, the abrasion volume of the agitator proved to be in the order of 1/10 the abrasion volume of the balls in the event that the material was made of PSZ. In the ball mill, the milling effect is reported to be greater as the specific weight of balls is larger[3]. However, in the media agitating mill, the particle diameter of powder hardly changed depending on the specific weight of balls as shown

Table 1 Effects of materials (balls) on particle diameter and abration of balls for wet-mixing of raw materials.

Balls			Mean particle diameter μm	Abrasion of balls wt%
Materials	Specific gravity	Diameter mm		
Alumina	3.3	0.75	0.24	0.717
Zircon	3.7	0.65	0.19	0.064
Titania	3.9	0.6	0.20	0.062
PSZ	6.0	0.6	0.22	0.020

mixing time by M50−20min. Powder content−82.3wt%

Table 2 Effects of materials (balls) on particle diameter and abration of balls for wet-milling of calcined powder

Balls			Mean particle diameter μm	Abrasion of balls wt%
Materials	Specific gravity	Diameter mm		
Titania	3.9	0.6	0.24	0.022
PSZ	6.0	0.6	0.24	0.006

Milling time by M50−10min. Powder content−82.1wt%

in **Table 1** and **2**. This is supposed to be attributable to the lesser influence of the specific weight because the balls are forcibly agitated at a given speed by the agitator in the media agitating mill. In addition, the abrasion volume of balls is less in the case that the materials of balls are PSZ, titania and zircon, and the abrasion of PSZ is much less. The alumina abraded to a conspicuous extent.

The ultrafine particles of about 0.1μm(52 nm in BET diameter)could be obtained in the mixing for 40 min of raw maferials by use of the media agitating mill (Model KDL), and the ultrafine particles of about 0.1 μm(60 nm in BET diameter)could be obtained in the milling for 30 min of calcined powder. In the milling by use of the media agitating mill, the ultrafine particles of mean particle diameter being 19 nm (optical correlation method) could be obtained in the milling for 90 min as shown in **Fig.8**. The abrasion volume of particles in this case proved to be 0.033 wt% against the weight of powder(0.043 wt% against the weight of the balls). The mean particle diameter and milling time of powder are approximately in a straight line relationship even after milling for 90 min for both the logarithmic graphs, which indicate that the particle diameter has not yet reached the milling limit.

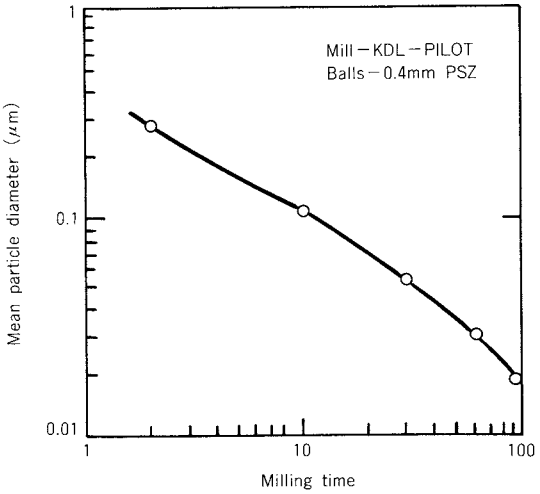

Fig. 8 Effect of milling time on particle diameter of calcined powder. (Mill−KDL-PILOT, Ball−0.4mmPSZ, Powder content−72.7wt%)

5.2 Comparison of milling rate with ball mills

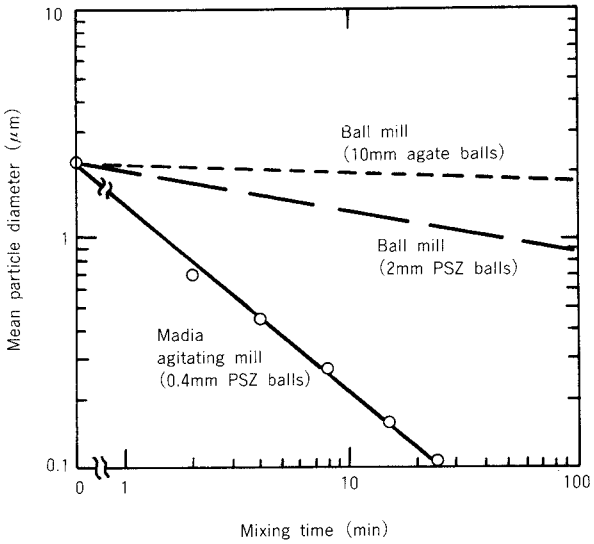

Fig. 9 Mixing of raw materials by media agitating mill (KDL-PILOT) and ball mills.

Fig.9 shows a comparison of milling rates with a media agitating mill and ball mills, and **Table 3** shows the milling rate equations. The milling rate of media agitating mill (PSZ balls of 0.4 mm), when obtaining the calcined powder of 0.2 μm, can be calculated from Table 3, which proved to be about 100, 000 times compared with that of conventional ball mills (agate balls of about 10-mm diameter) or about 500 times as compared with the ball mill for PSZ balls of 2-mm diameter.

Table 3 Comminution kinetics for media agitating mill and ball mills.

Mills	Experimental Equations
Ball mill (600ml) Agate balls (10mm)	$SS=0.42t^{0.22}+0.07$
Ball mill (600ml) PSZ balls (2mm)	$SS=0.68t^{0.36}+0.27$
Media agitating mill PSZ balls (0.4mm) (DYNO MILL)	$SS=13.4t^{0.60}-1.3$

SS—Specific surface (m^2/g)
t —Milling time (h)

6. Conclusion

The aforementioned study results in a nanopowder process which can be summarized as follows. (1)The dispersing property of powder could be conspicuously enhanced by adding a small volume of a dispersing agent and by mixing the raw material powder or milling the calcined powder with volume of dispersion medium being about one fifth as compared with the conventional volume (in the order of 150 vol%). (2)The sub-micron powder nice in dispersing property could be obtained by mixing the raw material powder or milling the calcined powder using small balls (about 2-mm diameter), and moreover, under the conditios stated in said Item(1).(3) Smaller the balls, the milling rate became higher, and at the same time, the abrasion volume of balls decreased for the milling of the media agitationg mill. In the case of using the PSZ balls of 0.4 mm, the ultrafine particles of several tens of nm (BET diameter) could be obtained in the mixing or milling for several tens of minutes.

References

1)K. Tanaka, K.Minai, K.Wakino and I.Uei: *J. of the Society of Material Science, Japan* **35,** 54(1986)

2)Sasaki, Tsuji, Tashiro, Igarashi and Okazaki.: Meeting for practical uses of $T_iB_aO_3$, XXX V-191-1175(1986)

3)K. Tanaka, K.Minai, K.Wakino and I.Uei: *J. of the Society of Meterial Science, Science, Japan* **36,** 29(1987)

4) Nishida Andow, Mihara: Shingaku Gihou, US 87-12, 35(1987)

5)Tashiro, Tsuji, Igarashi: *Ceramics Ronbunshu,* **96,** 579 (1988)

6)Tanaka, Inada, Wakino, Uei: *Yougyo Kyokai-shi,* **95,** 579(1987)

7)D.A.Stanley, L.Y.Sadler III, D.R.Brooks and M.A.Schwarth: *Ceramic Bulletin* **53,** 813(1974)

8)Nishida, Kawashima, Ueda and Ouichi: National Tech. Rept., **28,** 1115(1982)

9) "Powders-theory and application" *Maruzen* (Publisher) p.346 (1976)

10)K.Hashimoto: "Wear and Abrasion owing Powder", *(Sangyo-Gijutsu Center) p.254*

Review

Preparation of Micro Controlled Particles Using Aerosol Process Technology †

Kikuo Okuyama
Department of Chemical Engineering, Hiroshima University *

Kentaro Ohshima and Keiichi Tsuto
*Institute for Fundamental Research, Kao Corporation***

1. Introduction

The preparation of fine particles in the gas phase is now established as an important technique for producing carbon black, pigments, ceramics and magnetic materials. Especially,for the ultrafine particles with diameters less than 0.1μm and with low sintering temperatures, this method is expected to be useful in future industrial applications. The characteristics required to fine particles are a small agglomeration number, spherical shape, narrow particle size distribution and a controlled chemical composition as well as a controlled crystal structure. The development of a process to prepare fine particles with a well defined crystal structure and chemical composition has now become an important topic.

Fine particles are generally prepared by techniques involving solid, liquid or gas phase reactions. To prepare a homogeneous material, the solid phase method requires repeated calcination and crushing procedures. This leads to problems of impurity contamination, difficulties in graining, and it also tends to give irregular, non-spherical particles. Especially when preparing fine particles of superconducting oxides, extreme care must be taken with respect to impurity contamination. It is therefore difficult at present to prepare fine superconducting particles having a crystalline phase using a sol-gel method such as the liquid phase method directly.

* Higashi-Hiroshima 724, Japan
TEL.0824-22-7111

** Minato Wakayama 640, Japan
TEL.0734-26-8631

† Received July 20,1991

In most studies, the properties of fine particles prepared in the gas have been investigated experimentally as functions of the reaction temperature, flow rate and the reactive gas concentration.

But these are only preliminary studies carried out under limited conditions. Only a few studies have been reported involving the positive control of particle characteristics, such as size distribution, crystalline structure, shape etc.

In this paper we first review the preparation of fine particles by a gas phase method, i.e., the aerosol process. The characteristics and the particle generation processes are described in terms of gas-to-particle and droplet-to-particle conversion. Then methods to control the particle shape, surface state, crystal structure and size are detailed. Finally, examples of fine particles produced by controlling the preparation conditions are presented.

2. Generation of Fine Particles using Aerosol Processes

Fine particles are generated in the gas phase by various processes. Two typical processes are:

1. The bulk solid is crushed or a liquid is sprayed.
2. Molecular material collides in the gas phase and assembles into an aggregate.

Process 1 is known as the crushing and grinding process or the breaking-down process. Process 2 is the particle formation by

the condensation of vapor molecules and is called the building-up process. Particle generation processes can be classified as shown in **Table 1**. Among these particle generation processes, the process in which the particles dispersed in the gas phase are of submicrometer size is called the aerosol process and is shown in **Figure 1**. The main aerosol processes are the gas-to-particle conversion and droplet-to-particle conversion.

Table. 1 Classification of particle generation processes

Breaking-down process	Ⅰ. Atomization of liquids Nebulizer, Ultrasonic spray method etc. Ⅱ. Grinding of coarse particles Ball mill, Vibration mill etc. Ⅲ. Dispersion of aggregate(powder) Fluidized-bed, Ejector etc.
Building-up process	Ⅳ. Homogeneous nucleation Ⅳ-1 PVD : Physical Vapor Deposition Adiabatic expansion (Willson cloud chamber), Mixing with cooled air (generation of cloud /fog), Conduction cooling, radiation cooling etc. Ⅳ-2 CVD : Chemical Vapor Deposition Single/Multi component gas etc. Ⅴ. Heterogeneous nucleation Vapor condensation on particle's surface, Chemical reaction of gas on particle's surface etc.

2.1 Gas-to-Particle Conversion Process

The gas-to-particle conversion process may be subdivided further into processes which depend on condensation due to physical cooling of a high temperature vapor(Physical Vapor Deposition ; PVD) and processes involving chemical reaction in the gas phase(Chemical Vapor Deposition ; CVD).

In most conventional preparation methods of fine particles by CVD, the chemical reaction of a gas at high temperatures is the most important concern. The main processes, classified by heat, are

Ⅰ. Chemical Flame Process
Ⅱ. Plasma Process
Ⅲ. Laser Process
Ⅳ. Thermal Process using an Electric Furnace

The characteristics of these particle preparation processes are given in **Table 2**[1].

Table 3[2] summarizes the particle preparation methods reported over the last ten or so years. Many reports deal with particle preparation by plasma and thermal processes

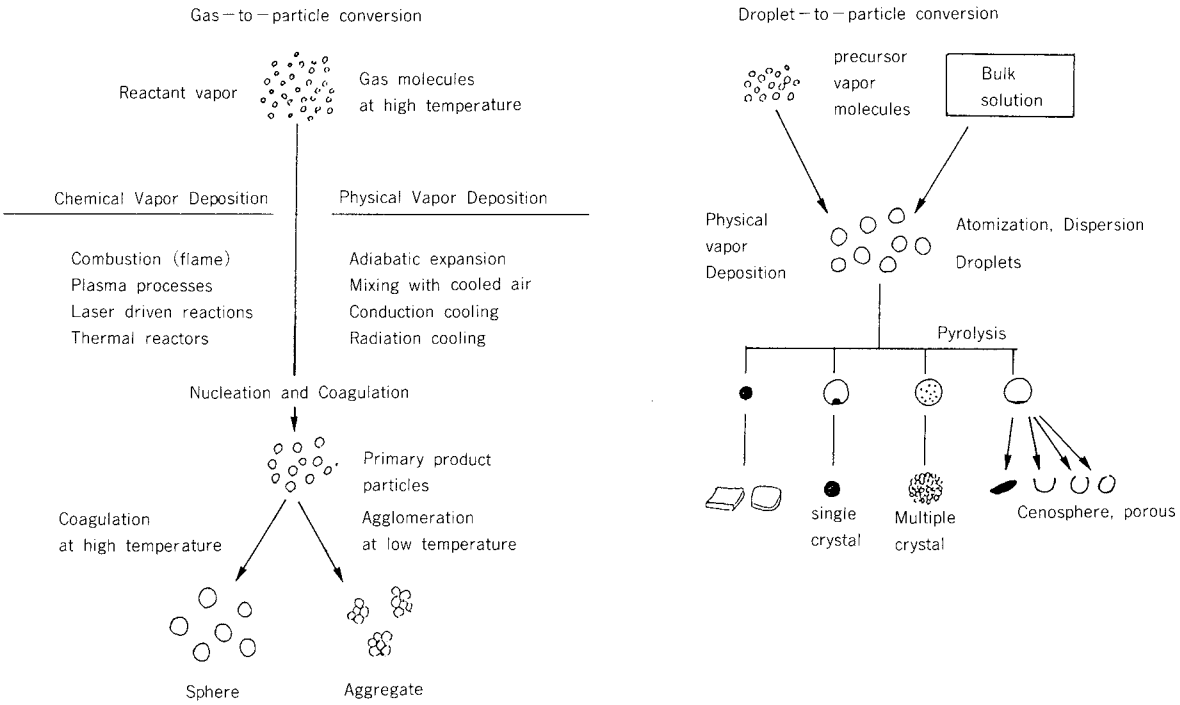

Fig. 1 Aerosol processes contributing to particle formation.

using an electric furnace. The type of reaction used in the experiments for particle generation varies and the reaction processes used to prepare metallic particles, for examples, are

Table 2 Aerosol based particle synthesis processes

Combustion (flame)	: Carbon blacks, Fume silica, Titanium dioxide, Optical waveguide preforms : 20-300nm elemental particle size : Significant agglomeration : 1200K<T<3000K : Reaction time, 1 ms-10ms Residence time, 10ms-1sec
Plasma processes	: Silicon carbide, Silicon nitride, Titanium diboride, Ceramic coatings : 3-200nm elemental particle size : Some agglomeration : T>5000K : Reaction time, 1μs-100μs : Residence time, 1ms-100ms
Laser driven reactions	: Silicon, Silicon carbide, Silicon nitride : 2-200nm elemental particle size : Extent of agglomeration nuclear : 1400K<T<1800K : Reaction time, 10μs-1ms : Residence time, 1ms-100ms
Thermal reactors	: Thermal carbon blacks, Metal oxides, Induced carbides, Nitrides, Metals, etc. : 2nm to 100 micron elemental particle size : Controllable agglomeration : Reaction time, 1ms-1sec : Residence time, 10ms-10sec

classified in **Table 4**[2].

Process A in Table 4 is a PVD process in which condensation occurs because of the physical cooling of a high temperature vapor. The Gas Evaporation Technique (GET) method is a typical example of such a process and here the particles are prepared by evaporation and condensation of metals in an inert gas under low pressure. Processes B-G show particle generation by CVD.

To initiate the gas-to-particle conversion process, the material to be condensed as fine particles is put into a super-saturated state by either chemical reaction or physical cooling. When the degree of super-saturation is high, enough particles are formed by homogeneous nucleation. As illustrated in **Fig.1,** spherical particles are generated when the temperature of the atmosphere is higher than the melting point of particle, while aggregated particles are generated at lower temperatures.

Particle generation by homogeneous nucleation is possible not only by PVD or CVD but by other methods as well. During particle formation the monomer generation rate, and therefore the generation rate of the super-saturation, may differ significantly from the particle generation rate. When the monomer formation rate is relatively slow, the saturation vapor pressure of condensing material is high, and the particle to be generated is liquid-like, the degree of super-saturation decreases and the evaporation of monomer from the clusters can not be neglected. In this case, the "classical droplet formation model" is valid for evaluating particle generation. On the other hand, when monomer generation is very rapid and the saturation vapor pressure of the material to be condensed is low, the degree of super-saturation becomes very high and the particle generation process can be evaluated using an aggregation model.

When the process is simplified by assuming that the chemical reaction is completed instantaneously and that the monomer generated immidiately aggregates by thermal motion to form fine particles, the number concentration N and the mean diameter of the fine particles formed after t sec are given by[3].

$$N = 0.1624\alpha^{-6/5}(KT)^{-3.5}(Mn_0 t/\rho_p{}^4 N_{av})^{1.5} \quad (1)$$

$$d_v = 2.274\alpha^{2.5}(KT/\rho_p{}^3)^{1.5}(Mn_0 t/N_{av})^{2.5} \quad (2)$$

where α is the sticking probability upon collision of two particles, K is the Boltzmann constant, N_{av} is Avogadro's number, M is the molecular weight, ρ_p is the particle density, n_0 is the initial number concentration of vapor molecules, and T is the absolute temperature. From Eq.(2), d_v is proportional to the 0.4 power of n_0.

When the reaction does not finish instantaneouly, various species ranging from the Å-sized monomer particles a few μm in size may exist simultaneously. To evaluate the generation of fine particles, it is necessary to relate the kinetics of molecular order to the behavior of the fine particles to be generated

Table 3 Preparation method of ultrafine particles using aerosol reactor

	Name of method	Content of method	Produced powder and its characteristic
Combustion process	Flame reaction method	• Thermal decomposition of anhydrous chlorides in diffusion flame of a hydrogen-oxygen reactor	Metallic oxide TiO_2, Fe_2O_3, SiO_2 10nm～200nm
		• Thermal destruction of hydrocarbons in a high-temperature of 1000°C	Carbon black ～30nm
Plasma technology	Electric arc method	• High voltage discharge is applied to a metal held between carbon electrodes	Oxide, carbide metal 10nm～100nm
	Plasma jet flame	• Heating of material hy plasma jet flame in inert gas	Fe-Co-Ni alloy
	Plasma gas phase reaction	• Vapor phase reaction between gas species in plasma jet	TiC, SiC 10nm～150nm
	Hybrid plasma method	• Metal vapor-carrier gas mixture is supplied to arc jet produced by high-frequency plasma jet	Si_3N_4, β-SiC, AlN 10nm～30nm
	RF(Radio Frequency) plasma evaporation method	• Two kinds of metallic vapors in a plasma flame are quenched	$NbAl_3$, Nb_5Si_3
		• CVD method using RF plasma	SiC, Si_3N_4 10nm～20nm
	Arc plasma sputtering method	• Atoms or molecules of high melting point materials or compound materials are supplied into gas phase	Fe, Ni, Ag, Si, SiC
	Nitrogen plasma method	• Particles are produced by an arc melting of metal in nitrogen gas	TiN, AlN, Si 20nm～300nm
	Activated hydrogen molten metal reaction method	• Particles are generated from the melted metal by arc discharge in the atmosphere of H_2 gas	Most of metal and metallic compounds
Laser driven process	Laser driven gas phase reaction	• Gas species are heated by laser (CO_2) to produce gas phase reaction	TiO_2, TiN, Al_2O_3, Si_3N_4, SiC, Si ～50nm
Thermal reactor using electric furnace	Thermal decomposition	• Metal carbonyl compounds, tetramethyl-disilane are thermally decomposed	Fe, Ni, SiC, Si
	Vapor phase oxidation method	• Metal chrolide, metal acelylacetonate, metal alkoxide vapors are oxidized to produce particles	Metal oxide Metal carbide
	Hydrogen reduction method	• Vapor of metal chloride is reacted with hydrogen gas	Ni, Fe-Co ～25nm
	High-temperature reaction in NH_3 gas	• Vapor of metal chloride is reacted with NH_3 gas in the temperature of 1200～1400°C	WC, Mo_2C, NbC, Si_3N_4, TiN 50nm～300nm
Gas evaporation technique (GET method)	Electron beam heating, laser heating, arc heating, induction heating, resistance heating	• Metals or high melting point materials are evaporated in an inert gas	Metallic refractory oxide

Table 4 Classification of chemical reaction involving homogeneous nucleation M, M' : Metallic elements, X, Y : Non-metallic elements or functional groups, g : Gas, s : Solid, f_p : Fine particles

A : Condensation	$M(g) \longrightarrow M(s, fp)$	PVD
B : Decomposition	$MX(g) \longrightarrow M(s, fp) + X(g)$	CVD
C : Partial decomposition	$MXY(g) \longrightarrow MX(s, fp) + Y(g)$	CVD
D : Oxidation	$M(g) + X(g) \longrightarrow MX(s, fp)$	CVD
E : Reduction	$MX(g) + Y(g) \longrightarrow M(s, fp) + XY(g)$	CVD
F : Displacement	$MX(g) + Y(g) \longrightarrow MY(s, fp) + X(g)$	CVD
G : Exchange	$MX(g) + M'Y(g) \rightarrow MY(s, fp) + M'X(g)$	CVD

Example B : Thermal decomposition of metal carbonyl compounds
C : Thermal decomposition of metal alkoxide
D : Production of zinc oxide
E : Reduction of metal chloride by H_2 gas
F : Reaction of metal chloride with oxygen
G : Reaction of metal chloride with water vapor

which is a very difficult task[4]. Furthermore in the particle generation equipment, there are distributions in the gas flow rate,temperature, and the concentration of the reacting vapor and the particles generated tend to aggregate or deposit to the wall of the reaction vessel. Modeling the entire particle generation process becomes very complex and still remains an important problem to be investigated[2,5].

On the other hand, experiments of particle generation by CVD provide the following results:

(1) The mean diameter of the primary particles is generally proportion to the 0.4 - 0.6 power of the partial pressure of the starting material.

(2) The mean diameter of the primary particles is inversely proportional to the reaction temperature and independent of the residence time. On the other hand, the mean diameter of aggregated particles, i.e., secondary particles, becomes larger with an increase in the reaction temperature and the residence time.

(3) The particle size distributions of many preparation methods are close to log-normal distributions and the geometric standard deviation is generally in the range of 1.4 -1.6.

2.2 Droplet-to-Particle Conversion Process

The droplet-to-particle conversion process is a method in which droplets in the micrometer size range are first produced by physical condensation of a high temperature vapor(IV-1 of **Table 1**), spraying or by one of the other methods shown in Table 1. The desired fine particles are produced by reaction of the droplets with the surrounding gas, drying or by thermal decomposition. Although this droplet-to-particle conversion process is classified in most cases as a liquid process, the particle generation occurs in the gas phase and is regarded here as an aerosol process. Since the droplet-to-particle conversion process employs a solution as the starting material, the droplets generated have a homogeneous concentration and therefore the chemical composition of the fine particles is homogeneous.

The reaction time is as short as a few seconds and the fine particles are produced continuously. Therefore, this process has numerous industrial applications.

In this process, the parameters influencing the shape and the surface state of the generated particles include the thermal decomposition

temperature and rate of solvent evaporation. As shown in **Fig. 1**, the particles produced may be hollow, porous, dense or broken. If the particles are classified by crystal structure, there are both single crystal aggregates and multi-crystal particles. The heating rate is a very important factor controlling both the shape and the crystal structure. When the temperature is very high, rapid vaporization near the surface occurs and concentration of the solution increases rapidly to produced super-saturated state. Nuclei are generated by homogeneous nucleation and multi-crystalline particles are formed. The center of the particle remains in a liquid state, and the particle is either broken apart or made porous by the gas formed inside the particle by continued reaction. On the other hand, when the heating rate is low, multi-crystals larger in size or single crystal particles are obtained. When the temperature is higher than the melting point of the particle, highly dense spherical particle with solid centers are obtained. When the crystal growth has some direction during the cooling process, squarish or flat particles are formed.

The diameter d_p of the fine particle prepared by this method is calculated from the droplet diameter D_p and solution concentration C_s using the following equation, and assuming that one particle (density ρ_p) is formed from each droplet(density ρ_s)

$$d_p = D_p(\rho_s C_s/\rho_p)^{1/3} \quad (3)$$

When the droplets have a size distribution rather than a single diameter, the distribution of the polydisperse-particles is obtained by applying this relation to each droplet size.

When the diameter of the droplet, Dp, or the solution concentration, C_s, is decreased the diameter of the fine particles is reduced. This equation is applicable only when the particle is formed at low evaporation rates and nucleus formation at the droplet surface, with subsequent growth or breakage due to evaporation does not occur.

3. Classification of the Preparation Methods of Fine-Particles by the Aerosol Process

Micro-controlled, multi-component particles with complex structure may be formed by the aerosol processes shown in **Fig. 1.** These may be classified into five different types shown in **Figure 2 :**

Type I: In this gas-to-particle conversion process, multi-component gases are introduced into the reactor. By either chemical reaction or physical cooling, a super-saturated vapor(B and D)is formed. When the degree of super-saturation is sufficiently high, fine particles are generated by homogeneous nucleation. These particles grow by coagulation and condensation of both B and D to form particles of varying composition. There may be particles containing a mixture of B and D, particles containing only B, particles containing only D, B particles coated with D, D particles coated with B as well as other combinations.

Type II *:* Particle C is formed in a particle generation process according to a Type I gas-to-particle conversion process and is introduced into the reactor to act as a seed, onto which both monomers and clusters of B are condensed forming a coating on the intial fine particles. This process is one of the methods used to improve the surface of fine particles by CVD.

Type III *:* This droplet-to-particle conversion process is exemplified by the formation of particles by spray-drying and vaporization thermal decomposition. Droplets containing precursors of a two component system(C and D) are formed by some spray dispersion process such as a nebulizer, ultrasonic spray or PVD of high temperature vapor, and are introduced into a high temperature reactor. Solvent (S) in he droplet vaporizes and the precursor in each droplet are converted to form multi-component fine particles(E and F) by a reaction with the surrounding gas or by thermal decomposition reactions.

Type IV *:* Fine particles (C)are suspended in a spray solution and the droplets formed each contain a particle as the seed. By reactions

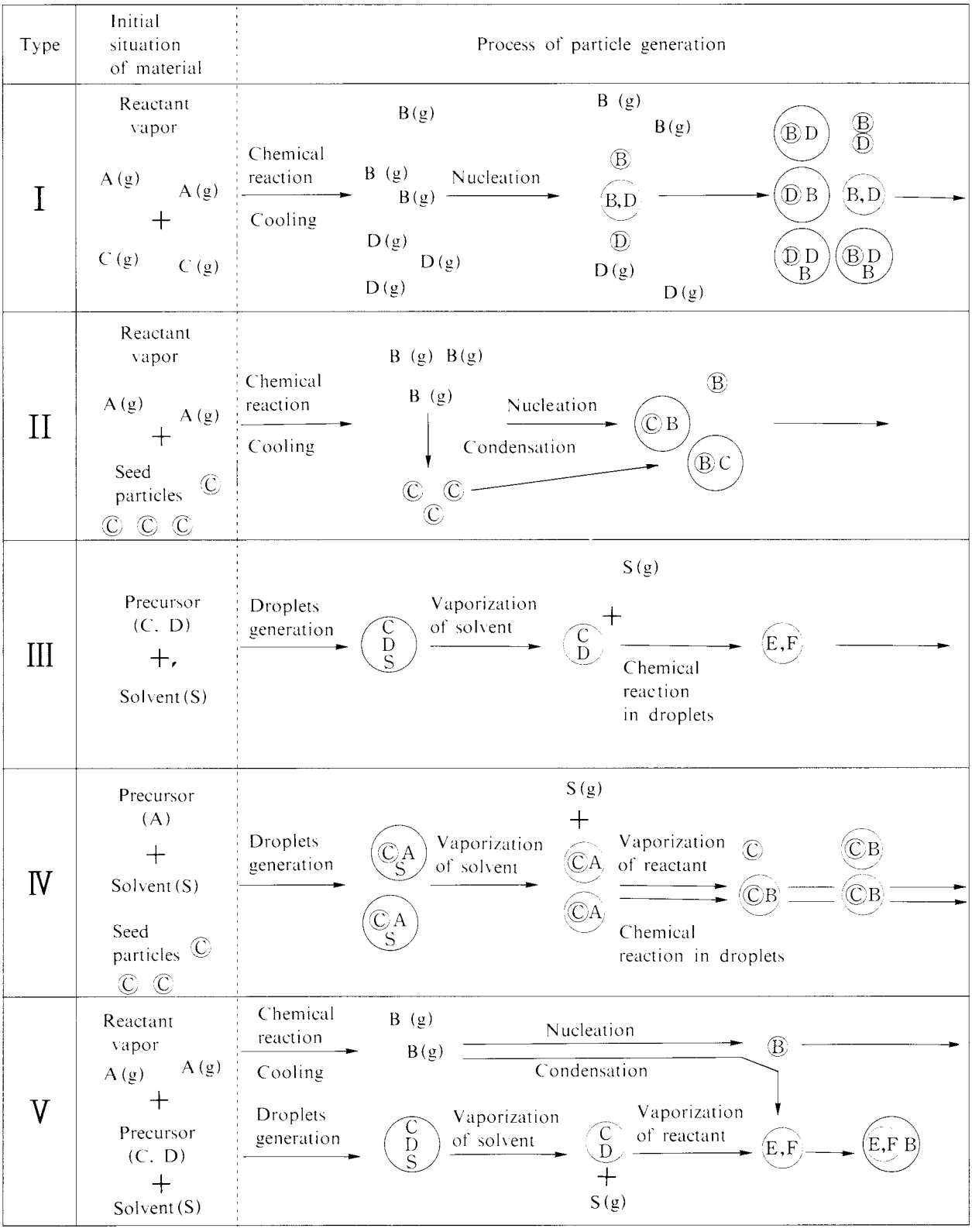

Fig. 2 Particle generation processes

within the droplet, composite particles with B and particles of C coated with B are formed.

Type V: This droplet-to-particle conversion process represents a process containing elements of both the type I gas-to-particle conversion and the type III droplet-to-particle conversion processes. Droplets containing multi-component precursors (C and D) are generated and introduced into a reactor with reactant vapor A. Solvent (S) is vaporized by heating or some other method and the precursors remaining (C and D) are converted to particles (E and F) by reactions within the droplet. Vapor A is converted to B and particles are formed by homogeneous nucleation and condensed onto particles containing E and F at the same time. This gives rise to the formation of pure B and composite particles (E and F) coated with B. In some cases, solvent (S) covers the fine particle to improve the particle's surface.

4. Characteristics of Fine Particles Generated by Aerosol Process

As described above, the use of the aerosol process produces complex particles improved by the presence of a surface coating and makes it possible to produce microcontrolled particles. In some caese, both monomer and particles form a deposit on the wall surface decreasing the particle generation yield, but at the same time the formation of a thin film has occurred. **Table 5** shows examples of metal oxides composites produced using the aerosol process[6].

The aerosol process easily produces particles having the following characteristics[6]:

- The particles contain fewer impurities thereby insuring high purity.
- Single or multi-crystal may be formed and the crystallinity and crystal structure can be controlled.
- The particles may contain multiple components.
- Coating the particles with mutiple layers is possible and particles with homogeneous chemical composition are also obtainable.
- The particles may be porous or dense.
- Particle size may range from small nanometer sized clusters to a few micrometers.
- Non-aggregated or aggregated particles with different void percentages are obtainable.

To control the characteristics of fine particles produced by the aerosol process, the phenomena which occur in each process in **Fig. 2** must be properly evaluated[6]. These include:

- The chemical reactions in the gas phase.
- The reaction of a single particle both at the surface and in the interior.
- The generation and growth process of a single particle including nucleation,

Table 5 Examples of metal oxide composite produced using aerosol process

Superconductive ceramic $M_wM_XM_YM_ZM_u$	at M = Cu, Tl, Ba, Sr, Pb, Sb, Y etc.
ex. Bi−Pb−Sr−Cu−O Ti−Pb−Ba−Cu−O	Electric conductive magnet Electric device
Ferroelectrcity ceramic $(M_wM_XM_YM_Z)O_3$	at = M = K, Zn, Pb, Nb, Fe, W, Ba, Ni
ex. $(Sr_{1-x}Ca_x)\{(Li_{1/4}Nb_{3/4})\}_{1-y}TiyO_3$— $K(Ta_xNb_{1-x})O_3$	Electric resonator Optical oscillator
Ferromagnetism ceramic $M_XM_YFe_{3-x-y}O_4$	at M = Mg, Zn, Mn, Ni etc.
ex. $Mg_{1-x}Zn_xFe_2O_4$	Elements composing circuit
Sialon ceramic $M_x(Si, Al)_{12}(O, N)_{16}$	at M = Li, Mg, Ca, Y or rare earth elements

evaporation and condensation.

- The physical process such as aggregation involving more than one particle.
- Deposition phenomena due to diffusion and thermal migration of both the gas and fine particles.
- The heterogeneous reaction rate of gas and the transport of heat and momentum in the temperature field.

5. Experiments on Fine Particle Generation by the Aerosol Process

In particle generation using the aerosol process, there are only a few examples reported in which the particle characteristics are controlled over a wide range. Here we report typical experimental examples of the control of fine particles produced on a laboratory scale.

5.1 Preparation of Oxide Particles by Hydrolysis and Thermal Decomposition of Metal Alkoxide Vapor[7,8](Gas-to-Particle Conversion Process)

Processes to generate fine oxide particles by hydrolysis or thermal decomposition of alkoxide vapor of Ti, Al, and Si are frequently employed. This method is a typical example of the gas-to-particle conversion process and is explained as follows.

Figure 3 illustrates an experimental apparatus[7] used to coat the surface of ultrafine particles of titanium dioxide (TiO_2) by alcoxysilane (AlcSi) which is an example of surface modification of fine particles shown as Type II in **Fig. 2**. By using nitrogen as a carrier gas, titanium tetraisopropoxide (TTIP) and a large excess of water are vaporized, mixed and introduced into a reaction furnace to prepare ultrafine amorphous particles of TiO_2. Then, propyltriethoxysilane ($PrSi(OEt)_3$) or tripropylmetoxysilane is introduced to coat the surface of the TiO_2 particles. **Figure 4** shows a TEM picture of the TiO_2 particles obtained by this method. This figure shows that the diameter of the primary particles can be controlled in the range of 10-100 nm by the proper choice of preparation conditions. The TiO_2 fine particles obtained

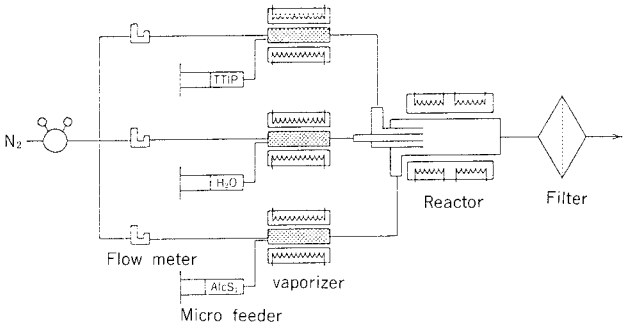

Fig. 3 Experimental apparatus for reforming TiO_2 particles. (Presented by Idemitsu Kosan Corp.)

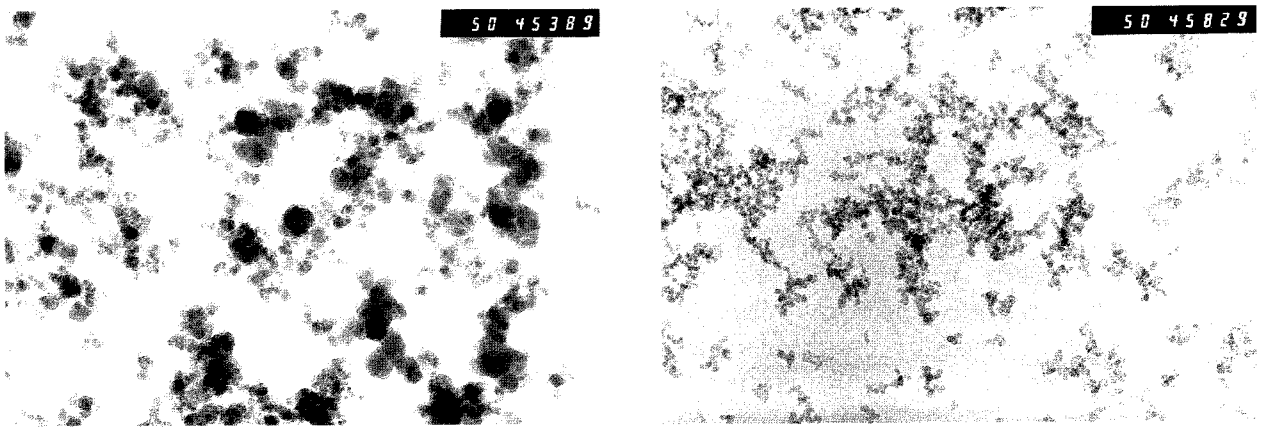

(a) $PrSi(OEt)_3$
TTIP Conc. 0.07mol%
$H_2O/TTIP = 50$
$AlcSi/TTIP = 0.1$

(b) $PrSi(OEt)_3$
TTIP Conc. 0.01mol%
$H_2O/TTIP = 300$
$AlcSi/TTIP = 0.7$

Fig. 4 TEM photographs of reformed TiO_2 particles. (Presented by Idemitsu Kosan Corp.)

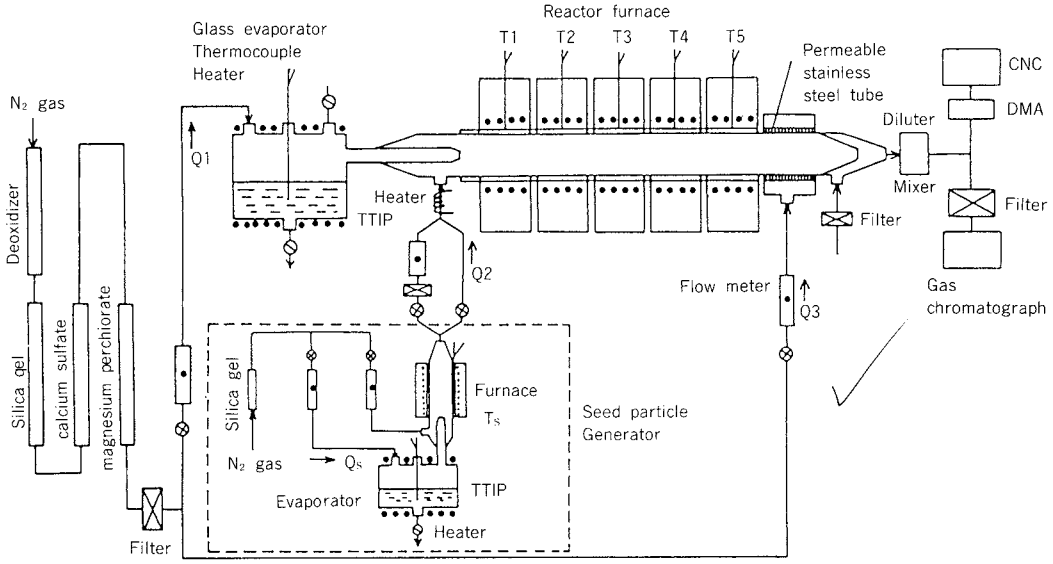

Fig. 5 Experimental apparatus for generating Ultrafine TiO_2 particles.

by this method can be easily dispersed in organic solvents and the diameter of the dispersed particles is small enough to allow good transparency in the visible light region. The characteristics to shield W light in the region near 300 nm(UV-B)are still maintained and it is found to be useful as a transparent W shielding agent.

Figure 5 shows the apparatus[8] used to prepare TiO_2 particles by thermal decomposition of TTIP vapor with the use of seed particles shown as Type II in **Fig. 2.** First, N_2 gas is introduced into an evaporator maintained at 40 °C to generate TTIP vapor. This is then mixed with N_2 gas containing seed particles at the entrace of the reactor and sent into the furnace. This furnace is composed of 5 stages to allow independent temperature settings. **Figure 6** shows the change in the number concentration of the particles at the exit of the pipe for 3 different seed particle sizes. The abscissa is the dimensionless number concentration of seed particles, N_s, divided by the number concentration of the particle generated by CVD in the absence of seed particles, N_{Jo}. The ordinate is the dimensionless value of the number concentration of particles generated, N_f divided by N_{Jo}. This figure shows that the effect of the seed particles is small at a low number concentration of seed particles while at a higher number concentration new particles are not generated due to a restriction of nucleation by the seed particles. This means that the seed particle is coated. At the same number concentration of seed particles, the seed particle with a larger size has a larger effect. The broken line in the figure shows the results of a numerical model and coincides qualitatively with the experimental results.

5. 2 Preparation of Silicon Particle by Thermal Decomposition of Silane Gas[9,10] (Gas-to-Particle Conversion Process)

Figure 7 shows the apparatus used to prepare silicon particles by the thermal decomposition of silane gas(SiH_4)with the use of seed particles shown as Type II in **Fig. 2.** First, silicon particles are generated by the reaction of silane gas at a concentration of **1**% in a reaction furnace at 900 K. These particles may have some distributions in size or may be aggregated. These particles, now acting as seeds, are mixed again with silane gas and introduced into the second reaction furnace. This reaction furnace has five stages with temperature gradients and allows for growth of the seed particle only without generating

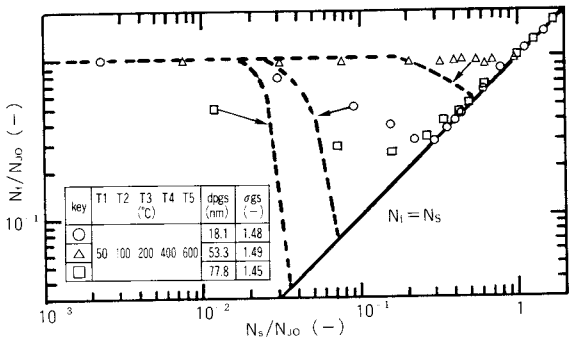

Fig. 6 Measured total number concentration, N_t, produced in the aerosol reactor as a function of seed particle number concentration, N_s, for different seed particle sizes.

new particles due to thermal decomposition. The temperature distribution of the second furnace should be set by considering the reaction mechanisms involved.

Figure 8 shows the effect of the concentration of silane gas added to the seed

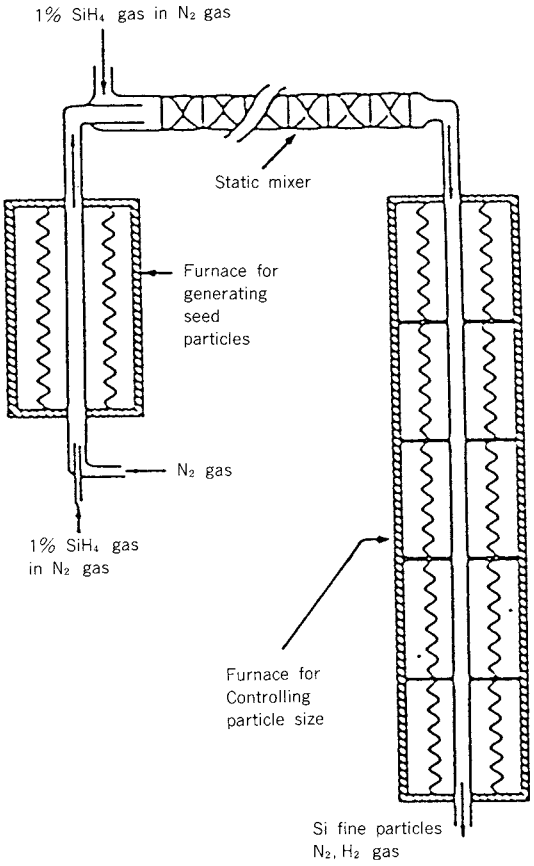

Fig. 7 Generation for Si fine particles by pyrolysis SiH_4 gas.

particles(mean diameter of 0.7μm and the number concentration of particles 10^5/cc) on the number concentration of the particles generated. When the silane gas concentration is lower than 3%, seed particles grow by condensation. However, at concentrations higher than 3%, new particles are suddenly generated by homogeneous nucleation. Thus

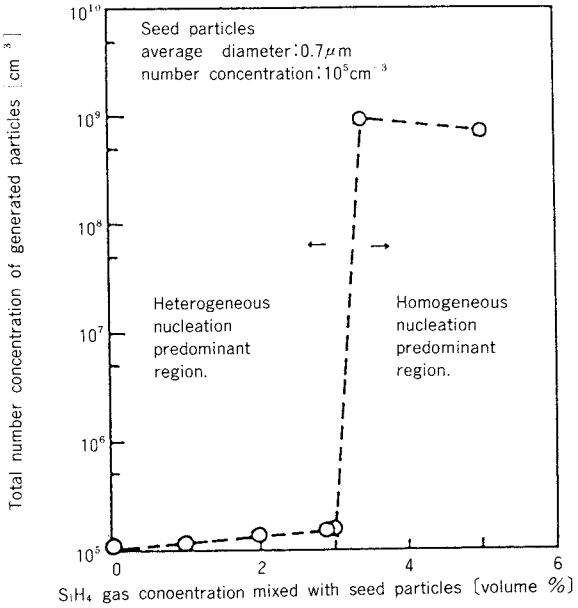

Fig. 8 Measured total number concentration as a function of SiH_4 gas concentration.

the gas concentration is an important factor.

Figure 9 shows the change in the size distribution of silicon particles when 1% silane gas was added. The broken line shows the size distribution of the seed particles themselves and the solid line represents that of the silicon particles after growth. The particle size distribution after growth is sharper than the initial distribution.

5.3 Preparation of Oxide Superconductor Particles by the Thermal Decomposition Reaction of Organometallic Vapor[11] (Gas-to-Particle Conversion Process)

The CVD method is now frequently used for the preparation of thin films of oxide superconductors. But there are only a few reports on the preparation of fine particles. Using the Type I method outlined **Fig. 2,** the

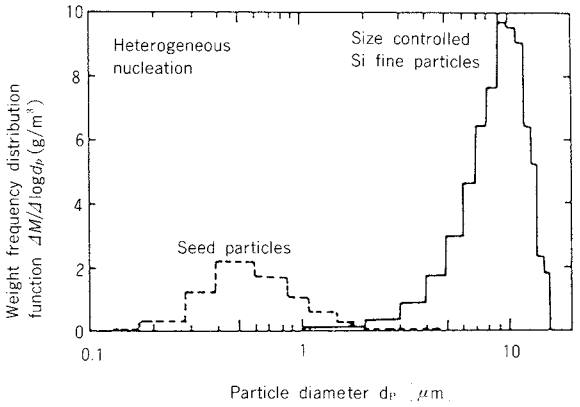

Fig. 9 Size distribution of seed particles and size controlled Si particles.

production of fine particles of bismuth oxide superconductor system has been attempted by using β-diketonate complexes of Ca, Cu and Sr and organometallic compound of Bi as the starting materials.

Figure 10 shows the experimental system. The horizontal five stage furnace consists of a vaporization stage followed by a reaction chamber. Powders of the starting materials, $Bi(Ph)_3$, $Cu(DPM)_2$, $Ca(DPM)_2$, $Sr(DPM)_2$ were put into evaporating dishes and heated in the vaporization section. The vaporization temperatures were adjusted so that the ratio of Bi:Ca:Sr:Cu was 2:1:2:2. These temperatures were 150 - 200 °C for $Cu(DPM)_2$ and $Bi(ph)_3$ and 200 - 250 °C for $Ca(DPM)_2$ and $Sr(DPM)_2$ and all temperatures were controlled independently. The vaporized starting materials were introduced into the reaction chamber by using Ar as a carrier gas. O_2 acted as an oxidizing agent and was introduced to the reaction chamber at the same time through a different path. Fine particles were prepared with carrier gas flow rates in the range of 300 - 900 ml/min keeping an Ar and O_2 gas ratio of 2:1, and with the temperature in the reaction chamber in the range of 750 - 900 °C.

Figure 11 shows X-ray diffraction pattern of the particles obtained at various reaction temperatures with a carrier gas flow of 750 ml/min and with a residence time in the reaction furnace of 14 sec. This figure shows that at a reaction temperature of 820 °C a peak of for the 10 K superconducting phase, indicated by an x appears. When the reaction temprature is raised to 825 -850 °C, peaks for both the 10 K and the 80 K(o)phases appear. In other words, the fine particles formed in this range of reaction temperature have a mixed phase of 10 K and 80 K. When the reaction temperature is raised further to 860 °C, only the 10 K phase is present. These results indicate that the reaction temperature appropriate for the growth of the 80 K phase is located near 825 °C, but that the particles are formed without a sufficient growth of 80 K phase due to a rapid flow rate and a short residence time.

The particle size distributions were measured at flow rates of the carrier gas of 300 and 600 ml/min. Ultrafine particles having a

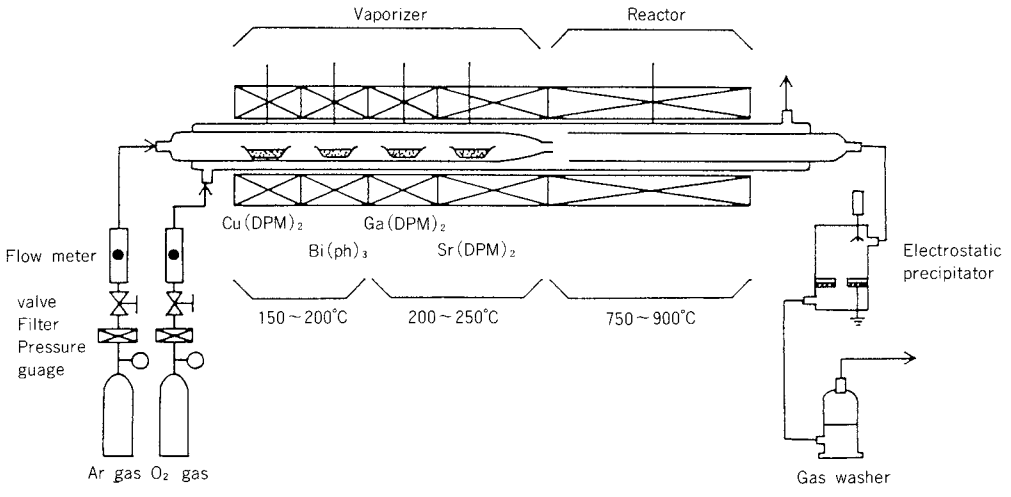

Fig. 10 Experimental system for producing ultrafine particles by CVD.

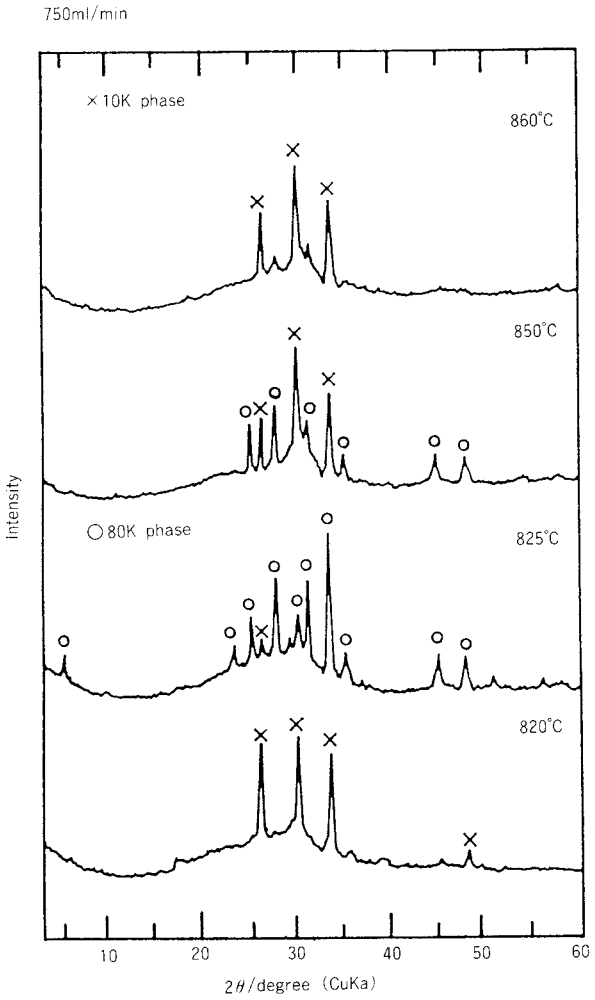

Fig. 11 X-ray diffraction patterns of $Bi_2CaSr_2Cu_2O_x$ particles at different temperatures.

relatively uniform size of about 60 nm at 300 ml/min and about 50 nm at 600 ml/min were obtained. At higher flow rates the particles are smaller. The shape of the particles was close to spherical.

One problem in the preparation of fine particles by this CVD method occurs when the reactor wall at the exit is cooled generating a temperature gradient and particles deposit by thermal migration. To prevent this lepositional loss is necessary to keep the reactor wall hot.

5. 4 Preparation of Fine Particles of Oxide Superconductor by Spray Pyrolysis Method[12](Droplet-to-Particle Conversion Process)

As an example of the preparation of fine particles by spray pyrolysis fine particles of the superconducting oxide with the composition $Bi_2Ca_1Sr_2Cu_2O_x$ were generated using a five stage furnace and the effect of the temperature gradient of the furnace and the flow rate of the carrier gas on the crystalline phase and shape was examined.

Figure 12 shows a schematic of the experimental apparatus used for the preparation of the fine particles[12]. The spray solution containing dissolved metal nitrates at the desired compositions was sprayed using an ultrasonic nebulizer and introduced into the reaction furnace with a carrier gas. Fine particles were generated in the reaction furnace and are collected by an electrostatic precipitator with a diffusion charger.

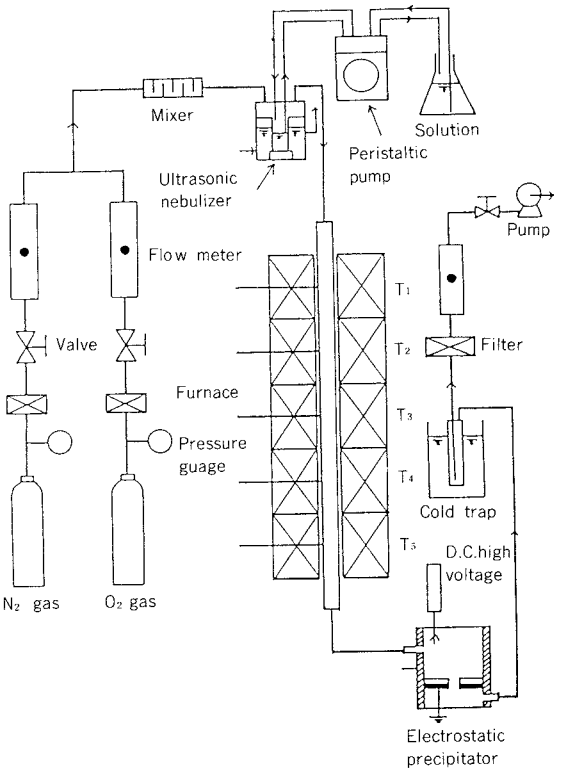

Fig. 12 Apparatus for generating superconductive metal oxide particles.

The reaction furnace has five stages capable of independent temperature control. The SEM picture of the fine particles obtained at a carrier gas flow rate of 2 l/min and with T_1~T_5=800 °C is shown in **Fig.13.** The temperature rises rapidly at the entrance of the

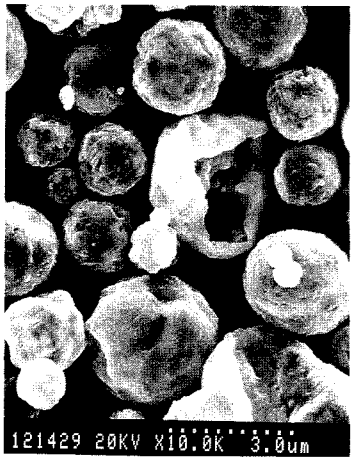

Fig. 13 SEM photograph of superconductive particles. (at $T_1 \sim T_5 = 800°C$, carrier gas flow rate = 2 l/min)

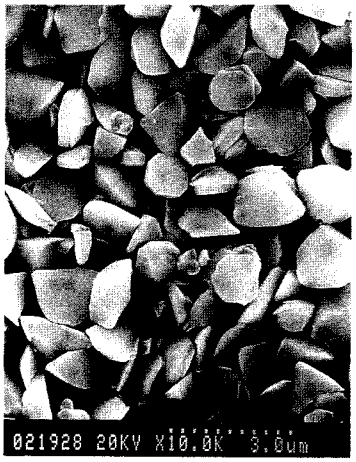

Fig. 14 SEM photograph of superconductive particles. (at $T_1 = 950°C$, $T_2 \sim T_5 = 800°C$, carrier gas flow rate = 0.2 l/min)

reaction furnace. The flow rate of the carrier gas was so rapid that nucleation occurred easily in the par ticle generation process and particles lacking a part of the core were observed.

Figure 14 shows a SEM picture of the particle obtained at $T_1 = 950\ °C$, $T_2 = T_3 = T_4 = T_5 = 800\ °C$ with a carrier gas flow rate of 0.2 l/min. At $T_1 = 950\ °C$, the particles are in a melted state and reactions take place in a liquid phase. Then, at $T_2 \sim T_5 = 800\ °C$, the particles become squarish and dense probably because the carrier gas flow rate was low and the temperature of 800 °C was appropriate for the growth of crystals.

5.5 Preparation of Oxide Particle by Vaporization and Condensation of Metal Alkoxide Vapor[13,14](Mixing Process)

Figure15 shows an outline of the apparatus. This is an example of particle preparation by the method labelled Type V in **Fig. 2.** First, silver chloride is heated at 645℃ and cooled to generate ultrafine particles on the order of nanometers. To this, metal alkoxide vapor(vaporization temperature of 96.5 °C)is mixed and cooled to generate a super-saturated atmosphere and to condense the vapor into droplets with a silver oxide particle as a nucleus(seed particle). When this is heated again and cooled, alkoxide droplets having uniform particle size are gener ated. When water vapor added, titanium oxide particles are generated by the reaction between the water and the alkoxide.

Figure 16 shows the size distribution of alkoxide droplets generated by the evaporation-condensation method and of the titanium oxide particles formed after mixing with water vapor. Although not completely

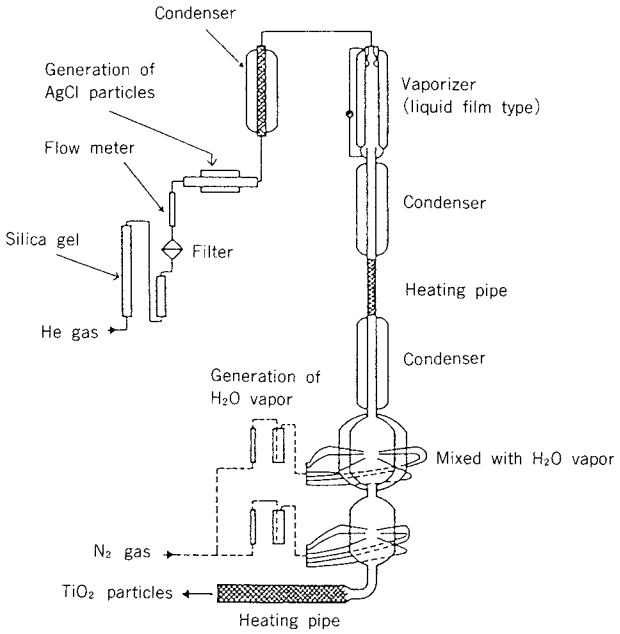

Fig. 15 Apparatus for generating TiO_2 particles by hydrolysis of alkoxide droplets.

homogeneous, particles of relatively similar size are obtained. By using this technique, the preparation of Al_2O_3, two component particles of TiO_2 and Al_2O_3, and TiO_2 particles with a polymer coating are reported. This technique allows us to prepare particles with mean particle diameters of about 0.06 - 1μm.

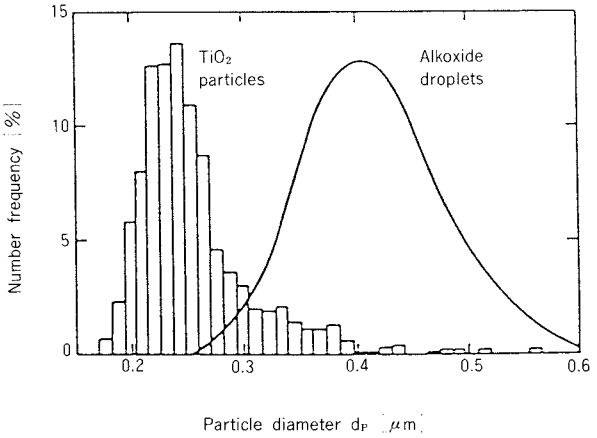

Fig. 16 Size distribution of alkoxide droplets and TiO_2 particles.

6. Concluding Remarks

The preparation of finely controlled particles by aerosol processes are becoming more important. Polydisperse particles having geomereical standard deviations in the range of 1.4~1.6 can be prepared easily by gas-to-particle as well as droplet-to-particle conversion processes. Finer control may be possible by changing the concentration of the reaction gas, the reaction temperature and other conditions. To obtain particles with narrower size distributions, further elaborations on the technique are required. Possibilities may include combination of droplet-to-particle conversion and seed-particle methods. In order to evaluate and improve the particle preparation processes demonstrated empirically, an improved approach based on aerosol science and technology is inevitable.

References

1) Flagan, R.C.,private communication, (1987)
2) Okuyama,K. and Yoshizawa A., Aerosol Kenkyu,**3**,6(1988)
3) Ulrich, G.D.,Combustion Sci. and Techn., **4**, 47(1971)
4) Okuyama, K., et al., AIChE Journal, 36, 409(1990)
5) Okuyama,K., Funtai-Kougakukaishi, **26**, 3, 195(1989)
6) Toivo, T. Kodas, Adv. Mater., **6**, 180(1989)
7) Okanishi, S., etal., preprints for 55th Meeting of Soc. of Chem. Engrs., Japan, H115, 323(1990)
8) Okuyama, K., et al., AIChE Journal, **32**, 2010(1986)
9) Alam, M.K. and Flagan, R.C., Aerosol Sci. Tech., **5**,237(1986)
10) Wu,J.J.Nguyen and Flagan, R.C., J. Appl. Phys., **61**, 82(1987)
11) Okuyama K. etal., preprints for 26th Autumn Meeting of Soc. of Chem. Engrs., Japan, SA116,17(1990)
12) Tohge, N., etal., J.American Ceramic Soc., in press(1991)
13) Visca, M. and Matijevic, E.,Colloid Interface Sci., **68**, 308(1979)
14) Partch, R.E., et al., Colloid Interface Sci., **105**,560 (1985)

Review

Application of Fuzzy Control to Processes handling Granular Materials and Powders †

Kenzo Wada
*Department of Mechanical Engineering, Faculty of Engineering, Yamaguchi University**

1. Introduction

The theory of "fuzzy sets" was proposed[1] by L.A.Zadeh who was a professor of Berkeley University of California. A linguistic expression essentially involves some vagueness in itself, and it can be considered that the fuzzy sets theory is suitable for the treatment of the vagueness. A vague statement is defined by using the concept of fuzzy sets. The vagueness can be treated quantitatively by a membership function, therefore the fuzzy sets theory is used in various fields.

In 1974,E.H.Mamdani[2], who was a professor of London University, applied a fuzzy reasoning to a control of steam engine and he showed the validity of the theory for the control. In the field of industry, Ostergaard and Holmblad have succeeded in the application of fuzzy control to a cement kiln at F. L.Smidth corporation of Denmark[3], thereafter the control system has been in operation. This was the first application of fuzzy control in industry. After this time, the fuzzy control has been applied to many systems such as an automatic train control system[4], the water purification system[5] and so on, the fuzzy control has received rapidly practical attention. It is not too much to say that the fuzzy control establishes one field of control. Recently, the fuzzy control is used in household elecctric products. It seems to be popularized.

In the fuzzy control, the control rules are composed of an aggregate of the linguistic statements such as "IF ~ Then ~ ". The control rule is made up on the basis of experience and heuristic knowledge which a skilled operator has cultivated for long years. Therefore, the fuzzy control demonstrates its power for the process which cannot be controlled by using conventional control methods. For instances, it can be considered that the fuzzy control exercises its power for the following processes.

- Process that it is difficult to know enough its dynamic charateristics
- Process with a strong non-linearity
- Process with a large dead time
- Process with time-variant parameters
- Process with an interaction between state variabls
- Process which cannot be controlled successfully by using conventional control methods

For the processes mentioned above, it can be considered that fuzzy control becomes much better control scheme.

On the other hand, in the field of the processes handling granules and powders, it is difficult to operate well the processes because powders and granules reveal complicated physical properties in their handling, and a peculiar behavior of the process may occur. Therefore, in the field of the processes handling granules, there has been a delay in the automation up to the present, when compared to other fields.

There are many kinds of troubles in the processes handling granules and powder[6]. For examples

- Troubles due to the physical properties
- Troubles owing to an unpredictable change in the motion of granules
- Troubles owing to an unpredictable

* Ube, Yamaguchi 755, Japan
TEL. 0836-31-5100 ext 276
† Received. Sep. 1, 1991

change in the state of surfaces of particles
- Troubles due to incomplete measuring techniques.

It is difficult to control the processes with the troubles mentioned above by using conventional control methods. The fuzzy control may be more available for such processes. It can be considered that the processes handling granules belong to a class of the fields where the fuzzy control can be fully utilized.

Until now, in almost all processes, conventional control systems have performed main roles for steady-state control. As for the control methods, PID and advanced control modes are applied to the processes. However, the control scheme described by a numerical formula is not suited for the control of the processes in non-steady states. The states, i.e., a steady state and a non-steady state have been treated separately from each other in control until today. Recently, a continuous operation from a non-steady state to a steady state has been required. However, the conventional control method is not suitable entirely for the such operations, and a manual operation by skillful operators and a human judgment are usually incorporated. In this case, the control rule is constructed on the basis of operator's experiences and heuristic knowledge. In this review, an outline of fuzzy control systems and their application to the processes handling granules are described. These processes consist of the following unit operations:

- Size reduction
- Dust collection
- Granulation
- Agitation and mixing
- Classification
- Transportation and feeding

Among these unit operations, the dynamic characteristics of transportation and feeding process are rather easily assessed when compared to the other unit operations, and the mathematical models are constructed to effect a conventional advanced control. For the other unit operations such as size reduction and dust collection, however their mathematical model cannot be easily obtained and a fuzzy control is expected to be effective for their control systems.

2. Outline of fuzzy control

2.1 Theory of fuzzy sets

In the fuzzy sets, the degree of belonging to the sets is given by a membership function. A fuzzy subset of a universe of discourse X is characterized by a membership function μ_A: $X \rightarrow [0,1]$ which associates with each element x of X, a number $\mu(x)$ in the interval $[0,1]$ which represents the grade of membership of x in A. Many of the basic identities which hold for ordinary sets(crisp sets)can be applied to the fuzzy sets. For instance

①	empty	$A=\phi$	$\mu_A(x)=0$
②	containment	$A \subseteq B$	$\mu_A(x) \leqq \mu_B(x)$
③	Union	$A \cup B$	$\mu_{A \cup B}=\mu_A(x) \vee \mu_B(x)$
④	Intersection	$A \cap B$	$\mu_{A \cap B}=\mu_A(x) \wedge \mu_B(x)$
⑤	Complement	$\bar{A}$	$\mu_{\bar{A}}(x)=1-\mu_A(x)$

The fuzzy reasoning is the method which derives one conclusion from some propositions as follows.

proposition : If the car is running fast then the car is dangerous
fact : the car is running very fast
conclusion : the car is very dangerous

rewriting in general expression

proposition : If x is A then y is B
fact : x is A
conclusion : y is B

where A and B and fuzzy subset. In the fuzzy reasoning, even if the fact differs slightly from the premise condition, it is possible to derive the conclusion corresponding to the premise condition. The conclusion can be obtained as follows. Let A be a fuzzy subset of a universe of discourse X, and let B be a fuzzy subset of a possibly different universe of discourse Y. A fuzzy relation $A \rightarrow B$ from a set A to a set B is defined by

$$R: \mu_{A \cdot B}(x,y)=\mu_A(x) \wedge \mu_B(y) \quad (1)$$

B is given by the composition of A and R: that is,

$$B = A \circ R \quad (2)$$

and B is characterized by the membership funcction

$$\mu_B(y)=\vee \{\mu_A(x) \wedge \mu_A(x) \wedge \mu_B(y) \quad (3)$$

Many compositional rules of inference such

as max-min composition, max-product composition and so on are proposed. Usually max-min composition is used as the method of fuzzy inference. A defuzzification of the fuzzy reasoning is performed by taking the center of mass of membership function B' (y):

$$y = \frac{\int y\mu_B(y)dy}{\int x\mu_B(y)dy} \quad (4)$$

2.2 The construction of a fuzzy control system

Fuzzy control rule is expresssed by a fuzzy implication of the form "IF～Then～". The execution of a set of fuzzy control rule is numerically performed by the method of fuzzy reasoning where the aggregation of the outputs inferred from various control rules is also nicely performed.

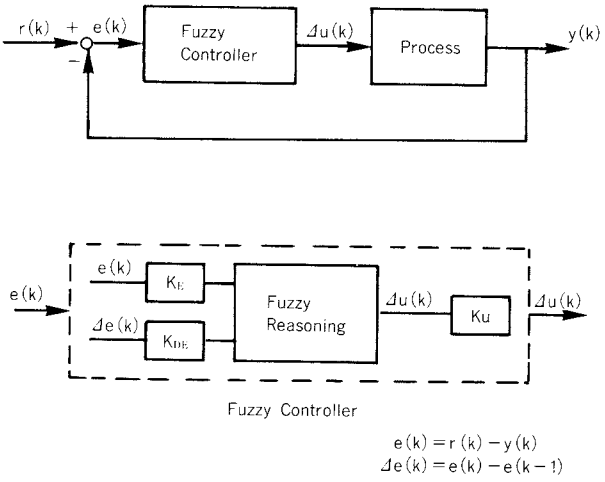

Fig. 1 Fuzzy control system

A fuzzy controller with two inputs and one output variables is considered in this section. The block diagram of the control system is shown in **Fig.1**. A process error E (= e(k)) and the change $\Delta E(=\Delta e(k))$in the error are taken as the input and the change $\Delta U(=\Delta u(k))$ in a manipulated variable is taken as the output of the fuzzy controller, where ΔU is inferred on the basis of E and ΔE. K_E, K_{DE} and K_U are gain constant for E, ΔE and ΔU, respectively. It is necessary to determine the

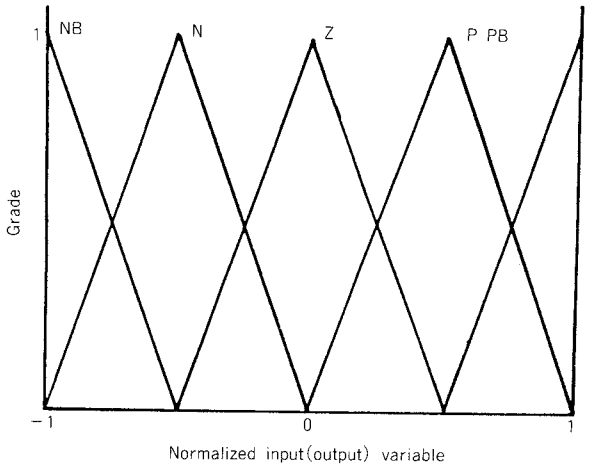

Fig. 2 Membership function

universe of discourse to give the semantics of a fuzzy variable, i.e., its membership function. The universe of discourse in fuzzy control is normalized into the interval [-1,1] . As the membership function, the triangle type membership functions as shown in **Fig.2** are usually used. The fuzzy control rule is expressed by a fuzzy implication of the form "IF～THEN～". For examples

R1: If E is N and ΔE is Z then ΔU is P
R2: If E is Z and ΔE is N then ΔU is P
R3: If E is Z and ΔE is Z then ΔU is Z
R4: If E is Z and ΔE is P then ΔU is N
R5: If E is P and ΔE is Z then ΔU is N

And the fuzzy control rules are summarized

Table 1

		ΔE		
		N	Z	P
E	N		P	
	Z	P	Z	N
	P		N	

in **Table 1**. A example of the reasoning process by max-min composition is illustrated in **Fig.3.** When $E=E'(0<E'<0.5)$and $\Delta E=\Delta E'(-0.5<\Delta E'<0)$, the reasoning is performed on the basis of rule 2, rule 3 and rule 5. the reasoning result $\Delta U'$ in the first rule(rule 2)is expressed as the dashed area, the area is regarded as the contribution of the first rule to

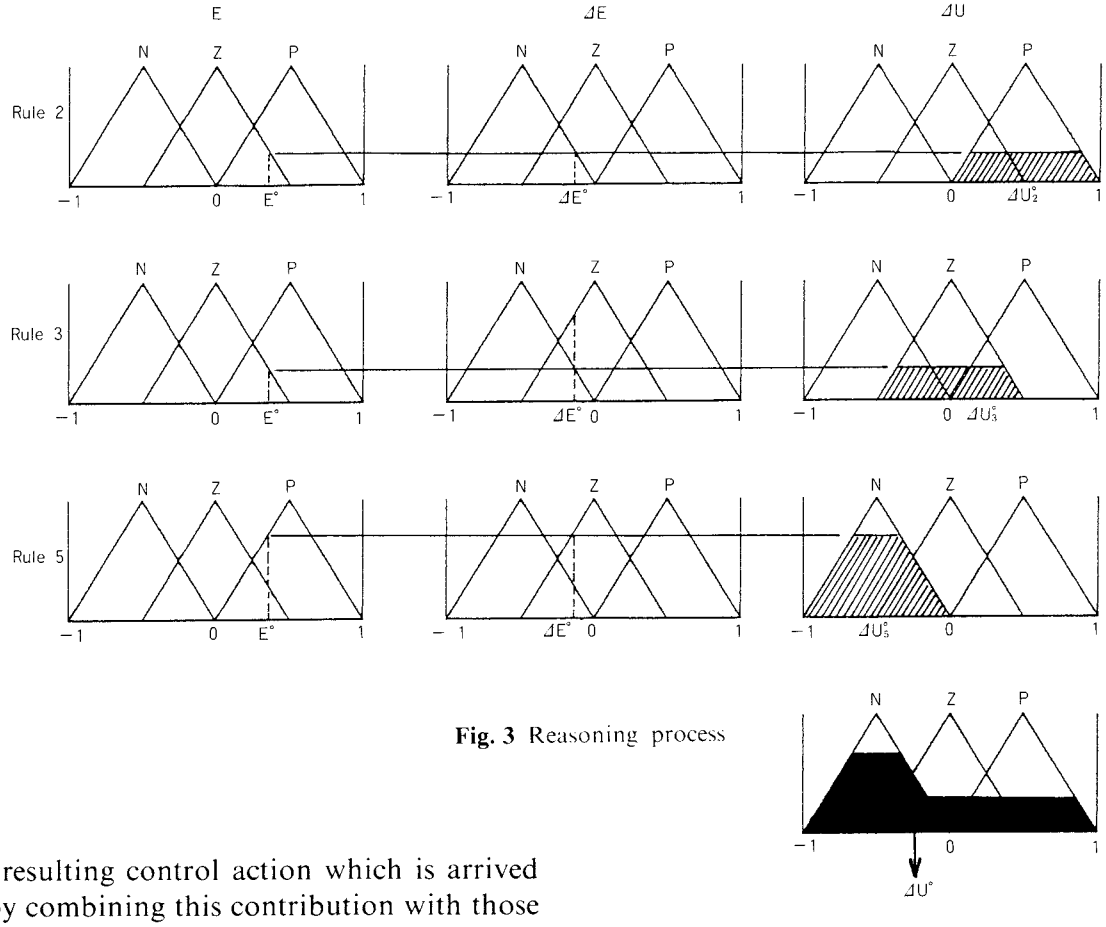

Fig. 3 Reasoning process

the resulting control action which is arrived at by combining this contribution with those of the subsequent rules. $\Delta U'$ expresses the composition result of the reasoning results derived from all rules. By taking the center of mass of the shaded area the defuzzification of the fuzzy reasoning is performed. As the result, the definite manipulated variable ΔU is obtained as the value at the position indicated by the arrow in the suport set. Since the value of $\Delta U'$ is normalized, the practical manipulated variable ΔU can be calculated by multiply the gain K_U to the $\Delta U'$:

$$\Delta U = K_U \times \Delta U'$$

In the fuzzy control, the control system as if the skilled operator is operating can be reallized. The features of fuzzy control are as follows.

1) It is possible to perform the actions comparatively similar to a human judgment and a human operation, and a smooth and more stable control can be expected.
2) Since causal relations can be expressed by simple numerical formula, a complicated process can be controlled successfully.
3) Control rules are constructed from many "IF~THEN~" rules and they are treated in parallel, it is possible consequently to control the state of process by taking the many factors synthetically into consideration.

The fuzzy control is implemented in accordance with the following procedure:

1) Investigate the characteristics of the process and find out the operation manual of the skilled operator
2) Decide the input variables and the output variables of fuzzy rules on the basis of given information
3) Decide the control rules and membership functions
4) Decide the normalized variables(gain)
5) Determine the manipulated variable using fuzzy reasoning
6) Apply the fuzzy control to a practical process and tune the membership functions according to the specifications for control.

3. Application of the fuzzy control to the processes handling granules and powders

3.1 Control of a grinding system

A size reduction process is one of the processes into which the fuzzy control is incorporated actively. In this section, examples of application of fuzzy control for a closed circuit grinding system[7] in a cement product process will be described. **Figure 4** shows the schematic diagram of a closed circuit grinding system. A grinding machine is a tube ball mill with two compartments. A raw material is ground by the motion of balls caused by the rotation of mill. The ground materials are transported to an air separator by a bucket elevator, and separated into large particles and fine particles. Only the fine particles become products. and the large particles are returned to the mill in order to grind them again.

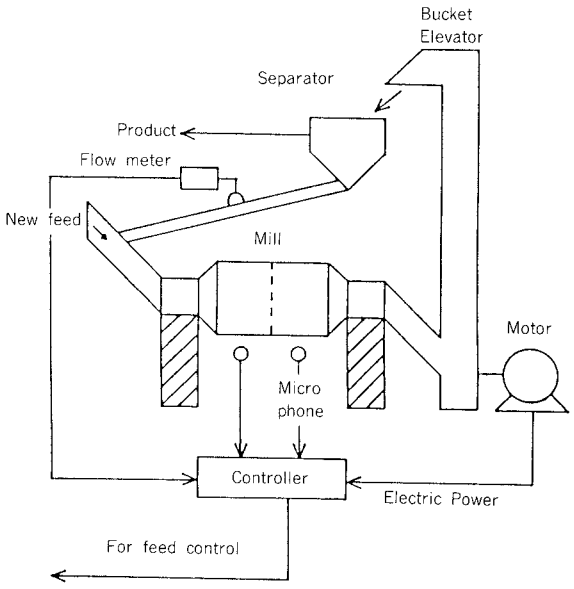

Fig. 4 Schematic diagram of the closed-circuit grinding system

In the grinding system, it is required to keep the size of particle constant and to increase the production as many as possible without choking the mill. It is known that there is an optimum circulating load at which the efficiency of comminution is maximum. Therefore, the mill is controlled so as to keep the optimum circulating load without choking the mill by manipulating the new feed quantity. The new feed and the tails from the air separator differ from each other in their residence time through the mill. It takes ten and a few minutes for the new feed and a few minutes for the tails to pass through the mill. The response of the production ratio to the new feed quantity is shown in **Fig.5.** From the figure, it is found that there is an optimal circulating load in the closed type mill, where the production ratio becomes maximum. Consequently, in the control system it is required to keep the circulating quantity to the optimum value by manipulating the new feed quantity. The circulating load for the change of the new feed quantity reveals such response as a integral element at right side of the optimum point, and at the left side it reveals such response as a lag element. Namely, it is difficult to control the grinding system by using conventional control methods because the response characteristics changes depending on the position of a running point.

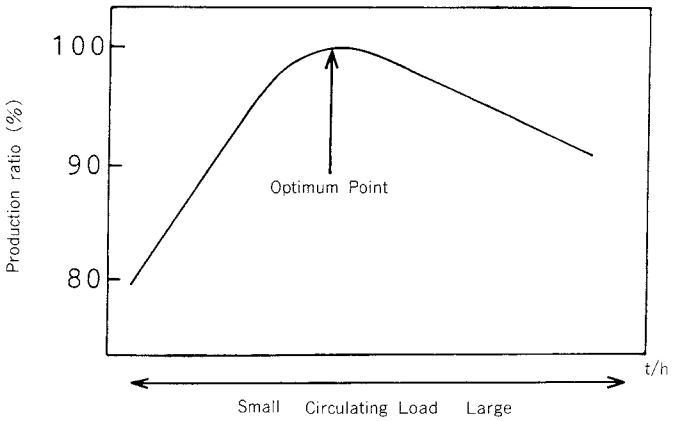

Fig. 5 Relation between the ratio of production for the new feed quantity and the circulating load

The state variables of the mill include the resident quantities of powders in the first and the second compartments, the quantity of tails (circulating load), the inflow quantity to the separator and the new feed quantity to the mill. The resident quantities in the mill can be detected by measuring the acoustic levels in the first and the second compartments of the

mill, or it may be detected by the intensity of vibration of the mill. The quantity of tails from the separator can be detected by an impact-type flowmeter. The quantity of materials entered into the air separator is detected by an electric current intensity or an electric power input to the bucket elevator. Usually, some of the state variables are used to control the process. The scheme of control depends on which state variables are detected.

H.Yanagihara *et al.* introduced the fuzzy control using ORPX system[8]. They constructed a state space by connecting each state with "AND", chose the representative point in each subspace by dividing the space of state into some subspaces and infer the manipulated variable on the basis of the point.
The rule consists of three groups. One is a rule at the start up and the others are rules for the operation at a steady state and an abnormal state. These groups are divided by "IF" sentences described by the crisp sets at the first stage of each rule, therefore a tuning of rules can be done easily without interference from each other.

The bucket elevator(BE)is equipped with an electric power control. The new feed quantity is determined on the basis of the error e_{BE} in the BE current(actual current-set current), the change in e_{BE} and the change dP in the electric power to BE, at every sampling instant.

M.Misumi *et al.* state in their paper as follows[9]. In the control using BE electric power, the fluctuation in each state variable has been restrained. However, the control performance for the change in grindability, the change in new feed quantity and the quantity of tails has not been improved. Furthermore, when the mill starts to be choked, the choking is enhanced further. In the control using the quantity of tails, although it is possible to detect the change in grindability, the response of process to the new feed quantity is slower. In the control using an acoustic emission, the process a good response with no lag time to the change in grindability and to the new feed and the quantity of tails. However, it is necessary to consider a proper countermeasure and compensation for the dust deposited around a sensor(microphone) and an acoustic emission from the adjacent another mills. Then, the fuzzy control is implemented by using the vibration of mill and BE electric power input. The inner state of mill can be detected quickly by using the vibration sensor and the vibration itself is not influenced by the adjacent another mills, and the load of mill can be measured by BE electric power input. The fuzzy controller consists of a stabilization system and an optimal control system. The stabilization system stabilizes the mill and the quality of product, and as the result, the productivity is improved and the amount of electric power consumed per an hour is decreased by the optimal control system.

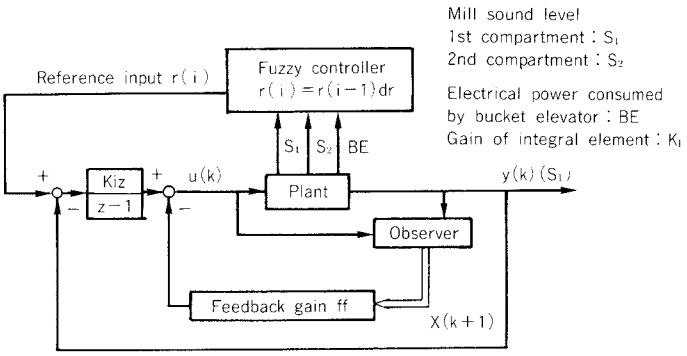

Fig.6 Block diagram of the closed-circuit grinding system

On the other hand, K.Wada *et al.* discuss the control method utilizing the acoustic level of the mill and the BE electric power input[10]. The block diagram of the system is shown in **Fig.6.** They construct the cascade type control system, namely, the fuzzy control is used as the higher hierarchy and an optimal control is put on the lower level. the BE electric power input is used instead of the optimum circulating load. In **Fig.6,** u(k)is the control input, and y(k)is the acoustic level of the first compartment of mill which is the output of the process. The acoustic levels $S_{1,2}$ in the first and the second compartment of the mill, and BE electric power input are used as the available information in order to control the process. The reference r(i)of the acoustic level S_1 is

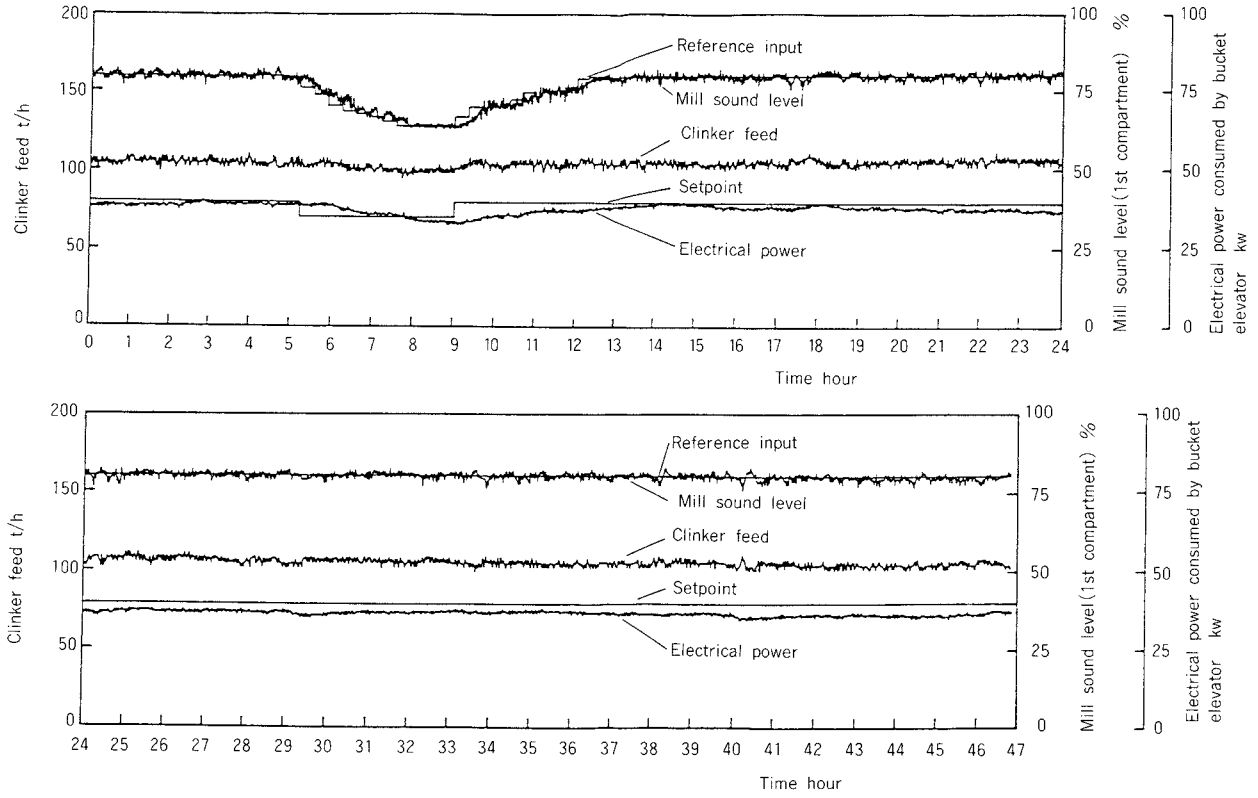

Fig. 7 Experimental results of the continuous operation

calculated by using a fuzzy reasoning so as to keep the optimal BE electric power input(the optimum circulating load). The optimal control method is used to get the desired value of the mill load. As the results, good responses are obtained when compared with PID control method. **Figure 7** illustrates the experimental results of the continuous operation. The experiments are performed under the following condition: at first, the optimal reference value of BE power input is set to 30% and after about five hours and twenty minute from the start of the operation, the reference value of BE power input is changed to 35% suddenly and after about nine hours the reference of BE power input is returned to 35% again. It is found that the reference of the acoustic level in the first compartment of mill is changed by the fuzzy reasoning so as to keep the optimal BE electric power input. As the results, good responses are obtained when compared with PID control method.

M.Nakagawa *et al.* performed the fuzzy control for an optimal operation of a vertical type roller mill used to crush raw materials[11]. The optimal operation of the vertical type roller mill is attained by improving the efficiency of comminution and by setting a quantity of supply so as to maximize the power of mill within the permitted limit. The fuzzy control is performed by using a fuzzy controller with two proposition of input, five propositions of output and thirty two rules. The control rules consist of the following three control loops:

Control loop of a quantity of sprinkle water in the mill

Control loop of an oil pressure of the mill roller

Control loop of the rotational speed of the belt feeder

The reference values of the quantity of sprinkle water, the oil pressure and the rotational speed are determined respectively by fuzzy reasoning, then the values are sent to the PID controller connected in cascade. By controlling these three states, the process can be controlled at the neighborhood of an optimal

point to increase the quantity of feed and to decrease the amount of electric power consumed per an hour.

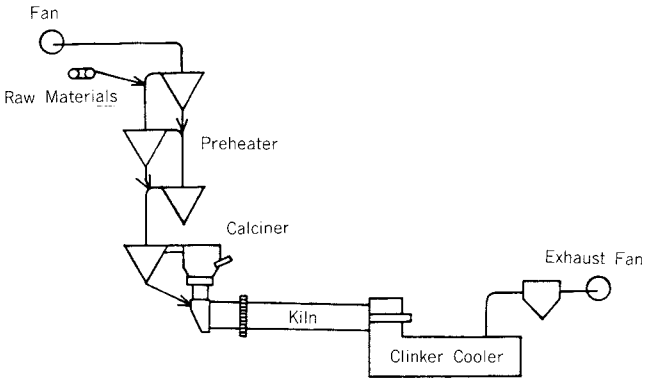

Fig. 8 Schematic diagram of the cement kiln

3.2 Control of a cement kiln

A cement kiln is the equipment that heats the materials crushed by a mill up to the temperature of about 1400 c and burns them to massive clinkers. The cement burning process consists of a temporary furnace, a kiln and a clinker cooler. The raw materials are fed into the higher end of the temporary furnace and the materials are burned with coal, and then enter into the kiln. A schematic diagram of the cement kiln is shown in **Fig.8.** The raw materials entered into the kiln are burned and moved downward with the rotation of the kiln, the burning temperature at the outlet of kiln becomes about 1450 c. Then the material is fed into the clinker cooler for cooling by air. The air heated there is sent to the temporary furnace and the heatcontent of the clinker is recovered as the air for combustion of the cokes. In the operation of kiln, the quantity of fuel, the rotational speed of kiln and the feed rates of raw materials are controlled in order to keep the combustion condition constant for the changes in the ingredient of raw materials and the inner state of the furnace. Since the phenomena taking place in the kiln is very complicated and the kiln operation is very difficult, the operation has been mainly dependent on the experiences and the insight of the skilled operators until now. Furthermore the process has a large lag time and there are many interactions among the pertinent state variables, and it has been difficult to control the kiln operation by using a conventional PID control method. An application of an optimal control to the process was also tried in the past, however satisfactory results could not be obtained because it was difficult to construct the process model of the kiln system. In 1980, F.L.Smidth company incorporated the fuzzy control into the control of the cement kiln, and very satisfactory results were obtained. Thereafter, the utilization of the fuzzy control has been accelerated and many examples of computer control of kiln are reported. Even the fuzzy controllers are available in the market.

Y.Chiba *et al.* reported the control procedure of the cement kiln as follows[12]. First, they divide the cement kiln system into four sub-process, i.e. warming up, steady state and shut down process. They apply the fuzzy control to the control of a non-steady state and a semi-steady state such as the feeding up and shut down processes. In the range where the characteristics of the processes can be expressed by AR(Auto Regressive)mode at the steady state, LQ(linear quadratic)control scheme is applied to the process. If the process gets out of that range, the control method turns to the fuzzy control from LQ control automatically. The set of the control rules is constituted from one hundred rules in the non-steady and semi-steady states, respectively. They reported that the kiln system, which has so far been considered difficult to control well, could be controlled well by using the fuzzy control.

S.Nakano built up an unique control system by incorporating automatic instruments for measuring the volume and the weight of clinker[13]. The kiln automatic control system is constructed from three subsystems, i.e. one is a data processing system, the second system consists of a judgment system of the burning state of the kiln and a malfunction detection system, and the third system is the decision-making system for the manipulated variables. The index indicating the state of combustion and the temperature of the materials burned

are calculated by the fuzzy reasoning. The manipulated variables are determined depending on the value of the index and the malfunction state of the process. The operations at the steady and non-steady states are expressed by a set of rules and twenty loops for the non-steady state are provided. The malfunction state is informed to operators by an alarm signal and the operation of the fuzzy control system is stopped.

K.Watanabe *et al.* are pursuing the CIM in order to improve a productivity[14]. They introduce a digital control system and try to expand the range of which the process can be controlled automatically. They propose a new control scheme by combining the fuzzy control and the optimal control. The control of kiln consists of a stability control which restrains the cgange of process within steady states and a recovery control which recovers the process from a non-steady state to a steady state. When a component of raw materials changes suddenly and the responses of the electric power input to the kiln and the burning temperature become different from the responses estimated by the model on which the optimal control system has been based design, the standard value of the manipulated variable is changed by the fuzzy reasoning. In the recovery control, when the sudden change of the torque of kiln is sensed, the controller recognizes it to be the falling of a liner installed inside of the kiln, namely, recognizes that the state is in non-steady, and the fuzzy control starts to operate.

3.3 Level control of a hopper using an image processing[15]

When a physical quantity in a process cannot be measured directly, if the change of state in a process can be sensed visually by using an image processing unit, then it is possible to control the process.

Two methods to visually sense the state of the process can be considered. One is the method by which the change of the state is sensed determinately. The other is the method by which the change of state may be recognized with some vagueness. It can be said that the latter is more similar to the human sensing. There are also two types of control method. One type consists of the conventional standard control method such as PID control and a modern control. The other type is a fuzzy control method that is similar to the scheme of control by a human operator. In the experiment, the change of controlled variable is sensed with some vagueness, and then the level is recognized by the fuzzy reasoning. The level is controlled by using the fuzzy control algorithm. An experimental apparatus is shown in **Fig.9.** The picture taken by the video camera is stored in the image processing unit at a speed of 1/30s per picture. The picture consists of 512×480 elements with the brightness level of 16 steps(0～15). Three masks are set in the frame of picture as shown in **Fig.10.** The length of a mask is 80 elements and the width is 20 elements. The brightness level in the mask where granules exist is higher and in the case of no granules the level is lower. Therefore, the level of granules in the hopper can be estimated by taking the average value of the brightness level in the masks. The level of granules is recognized on the basis of the brightness level by the following rules.

R1: If R_b is P then H is P
R2: If R_b is Z then H is Z
R3: If R_b is N then H is N

where R_b denotes the brightness level and H denotes a bed height in a hopper. **Fig.11** shows the recognized level. The solid line in the figure shows the recognized level and the dashed line shows the real level of granules in the hopper. The level is controlled using the following rules depending on the recognized level.

R1: If E is NB and ΔE is Z then U is PB
R2: If E is N and ΔE is Z then U is P
R3: If E is Z and ΔE is NB then U is PB
R4: If E is Z and ΔE is N then U is P
R5: If E is Z and ΔE is Z then U is Z
R6: If E is Z and ΔE is P then U is N
R7: If E is Z and ΔE is PB then U is NB
R8: IF E is P and ΔE is Z then U is N
R9: IF E is PB and ΔE is NB then U is NB

where, E, ΔE and U denote e(k), Δe(k) and u(k) respectively. and e (k)=R−Y(k) (R

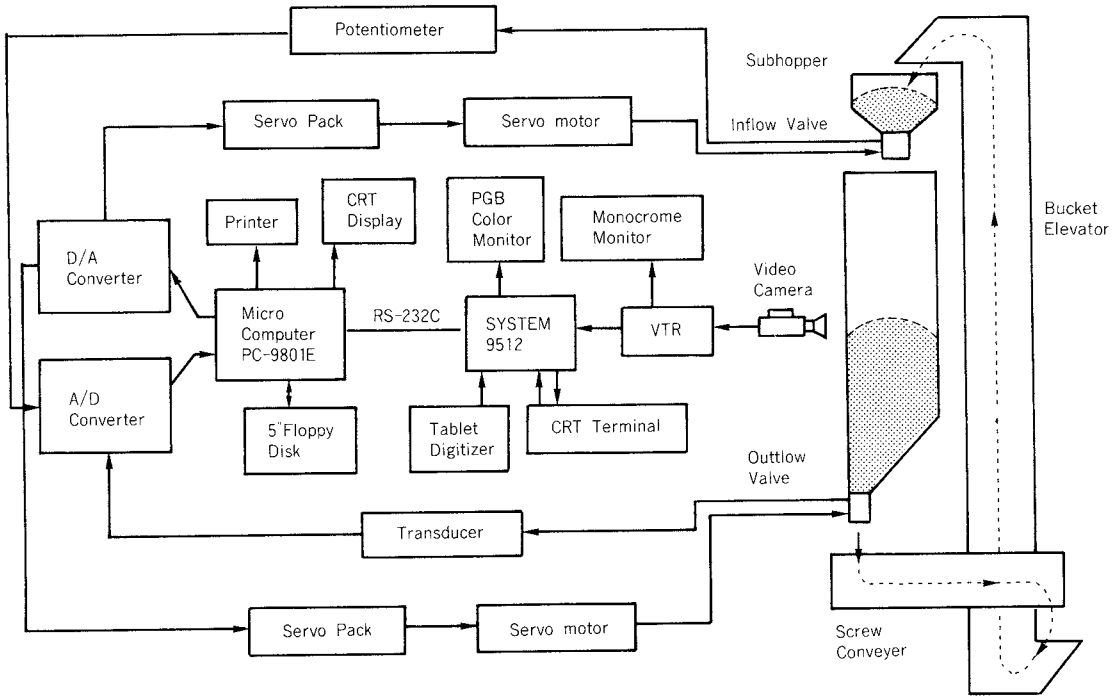

Fig. 9 Experimental apparatus of a level control

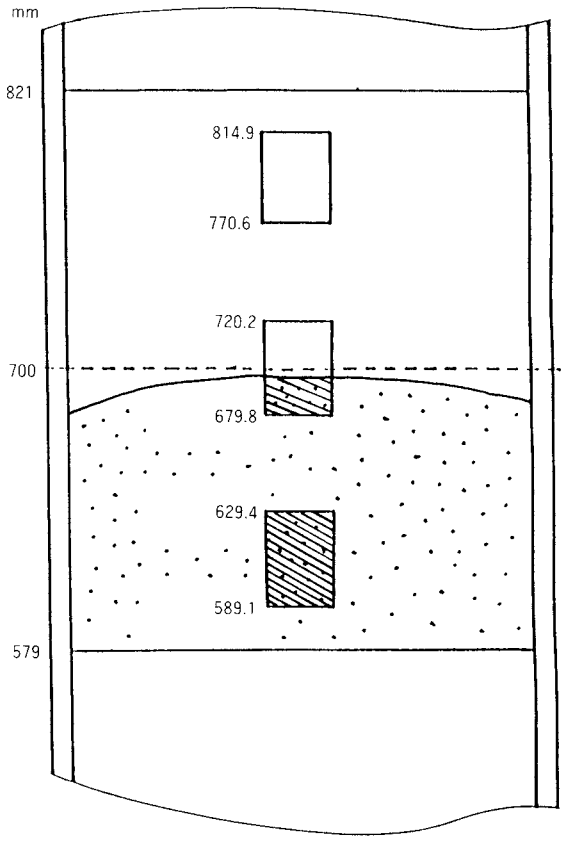

Fig. 10 Arrangement diagram of masks

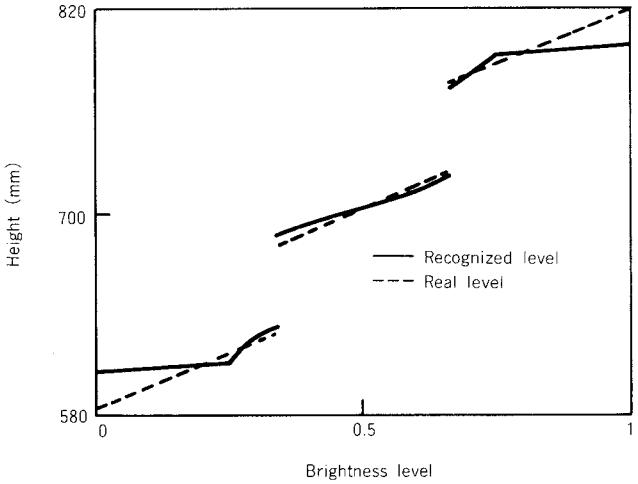

Fig. 11 Recognized bed level

denotes a reference value of the level and Y(k)is the value of the level of granules in the hopper at the sampling instant k), $\Delta e(k) = e(k) - e(k-1)$and u(k) is the manipulated variable. The shape of membership functions used in the fuzzy reasoning is shown in **Fig.12.** Experimental results are shown in **Fig.13.** The initial bed level is 620mm, the reference bed level is 700mm and the values of K_E, K_{DE} are 0.01 and 0.11 respectively. It is found that the level is controlled well.

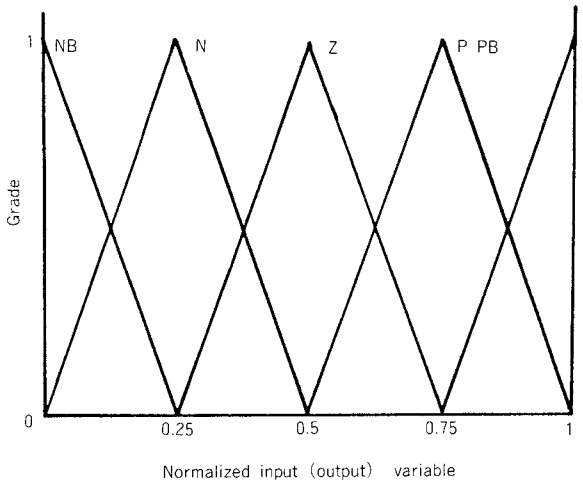

Fig. 12 Membership function used in the level control

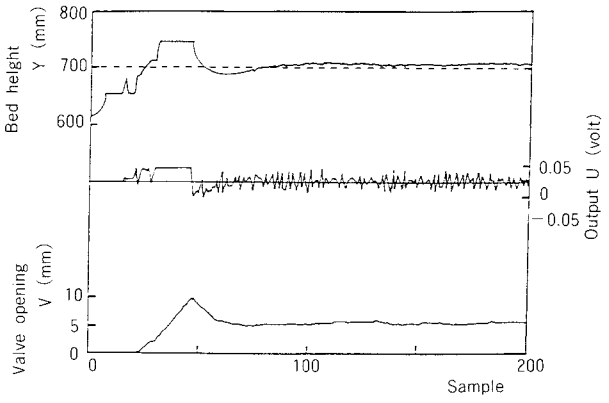

Fig. 13 Response of the process to the step reference input

4. Control of a fluidized bed[16]

The characteristics of a fluidized bed is influenced by various factors such as a gas velocity, a bed height, a size of particle and avoid fraction. The control system to maintain the bubbling fluidization condition against the change in the reference condition and a disturbance input has been investigated. It is difficult to construct a numerical model of the fluidized bed because of the complicated behaviors such as a generation of bubble, a combination of bubbles and a burst of bubbles in the bed. Consequently, the fuzzy control method is applied to the control of a fluidized bed. The fluidized condition is judged on the basis of results of analysis of the fluctuation of pressure drop through the bed by a FFT analyzer. Since the state of fluidized bed is dependent on the gas velocity through the bed, the gas velocity is controlled by adjusting the valve opening. As one of the factors representing the state of the fluidized bed, the average value G_{av} of the power spectrum of the pressure fluctuation over 0～10Hz is adopted. The relation between the valve opening and the average value G_{av} of the power spectrum is examined. The relation is shown in **Fig.14.** From **Fig.14,** it is found that

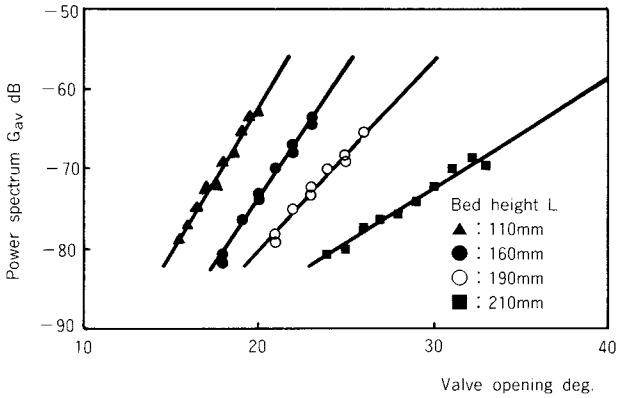

Fig. 14 Relation between the valve opening and the power spectrum G_{av}

they have a good linearity with each other for each bed height L. The value of G_{av} is used as control variable. The manipulated variable is determined by the following fuzzy rules using the value of G_{av}. Fuzzy rules are very simple used in this experiment and consists of the following three rules:

R1: If E_G is P then ΔU_{OP} is N
R2: If E_G is Z then ΔU_{OP} is Z
R3: If E_G is N then ΔU_{OP} is P.

Where, $E_G = R_G - G_{av}(k)$ (R_G is a reference value of G_{av})and ΔU_{OP} is the change in the manipulated variable. Control results by the fuzzy control are shown in **Figure 15. Fig.15.** shows the response wave when the reference condition is transferred from the minimum fluidization to the bubbling fluidization. The figures indicate the behavior of the valve opening U_{OP}, the average value G_{av} of the power spectrum and the pressure drop of the bed P_f with time in order from upper part respectively. **Figure 16** illustrates the response wave to

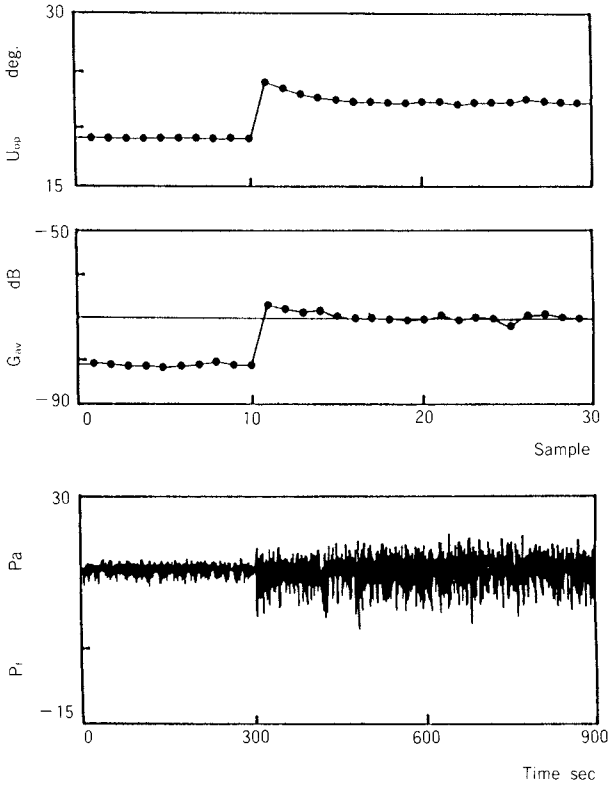

Fig. 15 Response of the fluidized bed (minimum fluidization → bubbling fluidization)

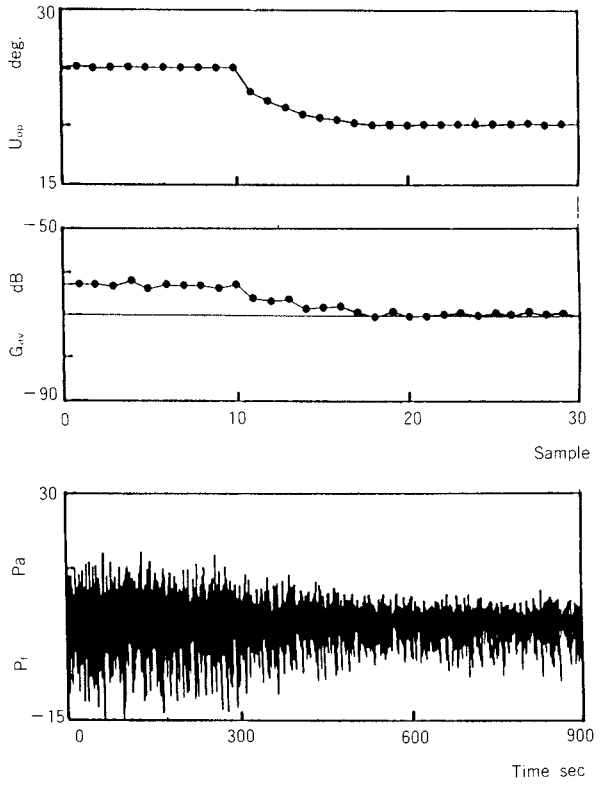

Fig. 16 Response of the fluidized bed (turbulent fluidization → bubbling fluidization)

the change from the turbulent fluidization to the bubbling fluidization. The response to the disturbance input is shown in **Fig.17.** As the disturbance input, a constant quantity of granular material is added to the top of the bed. The bed height is changed suddenly from L = 120 to L = 160. It is seen that the bed remains in the bubbling state in spite of the disturbance input. Although the state of bed once becomes in the state of fix bed instantaneously at the time when the disturbance enters into the bed, the bed recovers to the former state immediately. Thus, the fluidized bed could be controlled successfully by the fuzzy control method.

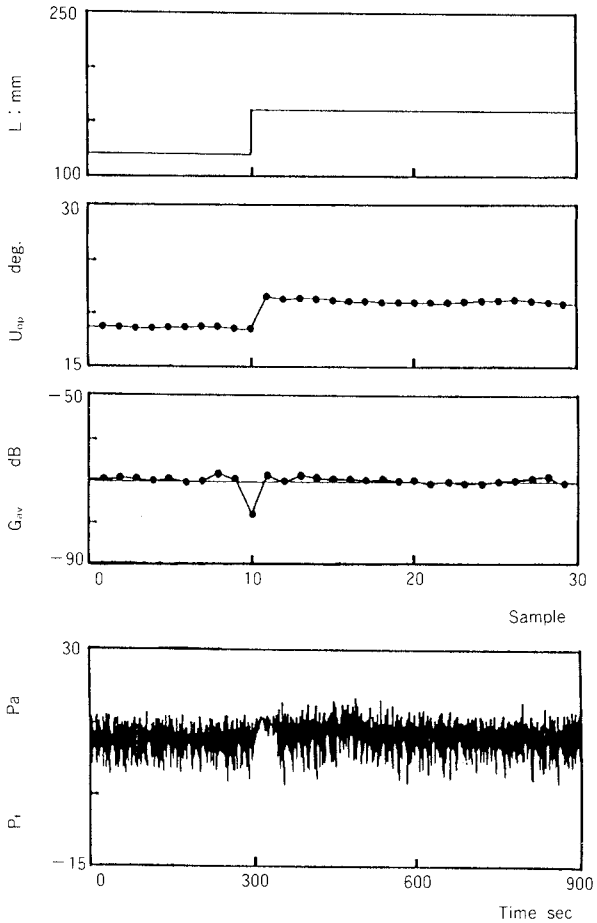

Fig. 17 Response of the fluidized bed for a disturbance input

5. Summary

The applications of fuzzy control to the process handling granular materials and powders are summarized by centering on the ex-

amples of fuzzy control in industries and the experiments at author's laboratory. Many examples of application have not been reported yet because it is only a short time elapsed since the start of application of the fuzzy control. However the fuzzy control is the very effective control method for the process that cannot be controlled enough by using the conventional control method in the past. it is considered that the fuzzy control comes to be incorporated actively into the process control in near future.

References

1) L.A.Zadeh: information and Control, **8**, 338/353 (1965)
2) E.H.Mamdani: Proc. IEE, 121-12, 1585/1588 (1974)
3) J.J.Ostergaard and L.P.Holmblad : Fuzzy information and Decision Processes. 389/399(1982)
4) S.Yasunobu, S.Miyamoto and K.Ihara : Trans. SICE(in Japanese), **19**, 873/880(1983)
5) O.Yanagishita, O.Ito and M.Sugeno : Systems and Control(in Japanese), 28-10, 597/604(1984)
6) S.Sakashita : KEISO(in Japanese), 29-10, 15/25 (1986)
7) S.Yashima: HUNSAI TO HUNTAIBUSSEI(in Japanese), 158/166, BAIHUUKAN(1986)
8) H.Yanagihara: KEISO(in Japanese), 32-8, 38/41 (1989)
9) M.Misumi, H.Kishi, M.Maruyama and H.Kojima: Proceedings of 46th cement manufacturing Technique Symposium(in Japanese), 48/55(1989)
10) K.Wada, A.Miwa, N.Hayano, M.Honda and H. Nakamura: Proceedings of Autumn Meeting of the Society of Powder Technology Japan(in Japanese), 66/70(1990)
11) M.Nakagawa and H.Ogata: Proceedings of 45th cement manufacturing Technique Symposium (in Japanese), 37/43(1988)
12) Y.Chiba and T.Serizawa: KEISO (in Japanese), 31-5, 35/39(1988)
13) S.Nakano, J.Nakai and Y.Kawamura: Proceedings of 46th cement manufacturing Tecnique Symposium (in Japanese), 40/47(1989)
14) K.Watanabe: KAGAKU KOUGYOU (in Japanese), **7**, 108/115(1990)
15) K.Wada, Y.Nojiri and N.Hayano:Proceedings of Autumn Meeting of the Society of Powder Technology Japan(in Japanese), 14/18(1990)
16) E.Morimoto, H.Nishibori, K.Wada and N.Hayano: 26th Technical meeting(Society of Powder Technology Japan)(in Japanese), 102/106(1991)

Dry Powder Particle Size Analyses for Dry Powder Processes (Restriction or Recommendation)†

Janez Stražišar
Mining Department, University of Ljubljana *

Abstract

It is generally known that the results of particle size analyses done in liquid suspension are more reliable than those in a dry system. This stems from the fact that most principles are based on sedimentation or electric conductivity changes in liquids. With the development of laser diffraction instruments for particle size distribution, the dry powder measurement became quite significant. Although we know the difficulties of dispersion of very fine particles in gases, we have to take into account the great importance of sample preparation procedures for the wet technique. This involves the influence of suitable liquid, the proper dispersant and the time of dispersion, The topic of this work is comparsion of the results obtained by dry and wet techniques on laser deffraction instruments evaluated by mass balance for air classification processes with a cut size under 10 micrometers. The comparison was carried out with different materials. Wet analyses were made with well-known instruments. The results are supplemented also by other principles of measurement. The accordance of analyses and mass balance for fractions of coarse and fine products with input material is greatly influenced by instrument quality. The differences in the results obtained with the same instrument by wet and dry techniques are relatively small even in the range of the low limit of the instrument. So it wouldn't always be necessary to make use of the wet technique, rather, more attention shoud be given to the quality and performance of the instruments.

1. Introduction

Particle size analyses are very important in process control and the determination of material properties. In the last decade, we could choose between several analyzers which function on the basis of laser diffraction. One of the main advantages of this instrument is the possibility of using the dry powder feeding system. The question arises at which lowest limit can a dry analysis be a good substitute for a wet one.

Data from the dry powder analyses are quite unfavorable, and some manufacturers do not have a dry system in their commercial programs although dry powder analyses are of great interest especially for on-line measurements. The report by K. Leschonski, S. Roethele, and U. Menzel (lit. 1) seems promising and points in this direction. The main problem lies in good preparation of gas suspension without agglomerates in the sample.

In the range of about one micrometer, there are different principles for laser diffraction scattering (Fraunhofer, Mie). Of greatest interest for the dry power technique are analyzers using low angle laser light scattering, or Fraunhofer's law. The particle size analyzer can be tested on the basis of two different performances, accuracy and reproducibility. Reproducibibity was determined in accordance with mass balance from size interval to size interval for the input material and for

* 61000 LJUBLJANA, AŠKERČEVA 20, SLOVENIA, YU
† Received April 29th, 1991

both classification products, the fine and coarse fraction. For each test, all of the three samples have to be analyzed. The description relevant to the evaluation of results is given in the next section. In the second part of this work, the same evaluation procedure was used for the comparison of dry/wet particle size analyses using our equipment.

2. Evaluation procedure

It is quite difficult to achieve the mass balance for a classification process if the reproducibility of the analyzer used is low. Common practice for determination of the reproducibility is a degree of agreement between measurements repeated several times as described in lit.(2). In our case, a good reproducibility means that we have a high agreement between the calculated and measured mass balance data for each particle size interval of input, fine and coarse product of classification. As an example for size interval i :

$m_{Ii} = m_{Fi} + m_{Ci}$

m_{Ii} mass fraction in input material

m_{Ci} mass fraction in coarse product

m_{Fi} mass fraction in fine product

or by analysis results :

$100.\triangle D_{Ii} = X_F.\triangle D_{Fi} + X_C.\triangle D_{Ci}$

X_F per cent of fine product

X_C per cent of coarse product

$\triangle D_{Ii}, \triangle D_{Fi}, \triangle D_{Ci}$ per cent in interval by analysis

Standard deviation is defined as :

STD.DEV. =

$$\left[\sum_{i=1}^{n} ((X_F.\triangle D_{Fi} + X_C.\triangle D_{Ci} - 100.\triangle D_{Ii}) / \triangle D_{Ii})^2\right]^{1/2}/n$$

n : number of particle size intervals in which the sample is divided

An example of such an evaluation for reproducibility or detection is given in Table 1. However, the determination of accuracy with standard powders is not included in this work, because it is reported on in the report by Allen and Davis (lit.2).On the other hand, the differences in analysis between the wet and dry technique do not correlate with the algorithm for the calculation of particle size distribution which is the main particularity of each laser diffraction instrument. At this point, it can be mentioned that the results of our tests are comparable in terms of reproducibility with the statements in lit. 2.

3. Results of the analyses

The main purpose of our work was to test some particle size analyzers with samples obtained by air classification. We also wanted to verify the agreement that can be expected between the wet and dry techniques using the same samples. The classification process was performed with a laboratory Alpine centrifugal classifier.

3.1. First example

The first sample of classification was calcite (A) in the range from 0 to 100 micrometers and with a cut size of about 10 micrometers. The amount of fines (B) is 40 %, and the amount of coarse product (C) is 60 %. The samples A, B and C were delivered to the manufactures of laser diffraction instruments. Recommendations for sample preparation procedures were enclosed. The recommendations prescribed water as a medium, Na-pyrophosphate as a dispersant, and they suggested 5 minutes as the time of dispersion in the ultrasonic bath. Particle size analyses are shown in **Fig.1** to **Fig.3**, The curves in the diagrams are not specified by types of instruments or manufacturers, because not all of our requests for permission to publish the results, had been received yet. Besides curves from laser diffraction analyzers, there are also data from other principles, such as sedimentation and the electrial sensing zone method. Results obtained by using the well-known Sedigraph 5100 are represented by large black marks. The results obtained by dry powder analysis on Microtrac SRA are marked with triangular symbols. Analyses by Sedigraph and Microtrac were conducted at our institute. Differences among the curves by the wet technique are relatively great, which is understandable and expected. However, the position of the analysis obtained by the dry

Table 1 Particle size analyses-Evaluation of results

size range micrometer	INPUT (A) ΔR	INPUT (A) ΣΔR	FINE (B) ΔR	FINE (B) ΣΔR	COARSE (C) ΔR	COARSE (C) ΣΔR
+64.9	4.00	4.00	0.00	0.00	7.50	7.50
+52.7 −64.9	3.10	7.10	0.00	0.00	5.09	12.60
+42.8 −52.7	3.10	10.20	0.09	0.09	4.50	17.10
+34.7 −42.8	3.90	14.10	0.09	0.19	6.00	23.10
+28.1 −34.7	4.90	19.00	0.10	0.30	8.00	31.10
+22.8 −28.1	6.40	25.40	0.39	0.69	11.00	42.10
+18.5 −22.8	8.19	33.60	1.00	1.69	14.10	56.20
+15 −18.5	9.60	43.20	2.60	4.30	15.60	71.80
+12.2 −15	10.00	53.20	6.00	10.30	12.20	84.00
+ 9.91−12.2	9.30	62.50	10.80	21.10	7.10	91.10
+ 8.04− 9.91	7.80	70.30	14.30	35.40	3.10	94.20
+ 6.52− 8.04	6.50	76.80	14.60	50.00	1.40	95.60
+ 5.29− 6.52	5.09	81.90	11.70	61.70	0.59	96.20
+ 4.3 − 5.29	4.00	85.90	9.40	71.10	0.40	96.60
+ 2.83− 4.3	5.60	91.50	12.90	84.00	0.40	97.00
+ 1.86− 2.83	3.30	94.80	7.50	91.50	0.30	97.30
+ 1 − 1.86	2.79	97.60	6.00	97.50	0.79	98.10
+ 0 − 1	2.40	100.00	2.50	100.00	1.90	100.00

Mass Balance ……Diff=A (From Analysis) − A (Calculated From B+C))

Percentage of Fine (B) =40percentage of Coarse(C) =60

size range micrometer	A	B	C	B+C	DIFF	VAR
+64.9	4.00	0.00	4.50	4.50	−0.12	0.01
+52.7 −64.9	3.10	0.00	3.06	3.06	0.01	0.00
+42.8 −52.7	3.10	0.03	2.70	2.74	0.11	0.01
+34.7 −42.8	3.90	0.03	3.60	3.64	0.06	0.00
+28.1 −34.7	4.90	0.04	4.80	4.84	0.01	0.00
+22.8 −28.1	6.40	0.15	6.60	6.76	−0.05	0.00
+18.5 −22.8	8.19	0.40	8.46	8.86	−0.08	0.00
+15 −18.5	9.60	1.04	9.36	10.40	−0.08	0.00
+12.2 −15	10.00	2.40	7.32	9.72	0.02	0.00
+ 9.91−12.2	9.30	4.31	4.26	8.58	0.07	0.00
+ 8.04−9.91	7.80	5.72	1.86	7.58	0.02	0.00
+ 6.52−8.04	6.50	5.84	0.84	6.68	−0.02	0.00
+ 5.29−6.52	5.09	4.68	0.35	5.04	0.01	0.00
+ 4.3 −5.29	4.00	3.76	0.24	4.00	0.00	0.00
+ 2.83−4.3	5.60	5.16	0.24	5.40	0.03	0.00
+ 1.86−2.83	3.30	3.00	0.18	3.18	0.03	0.00
+ 1 −1.86	2.79	2.40	0.47	2.87	−0.02	0.00
+ 0 −1	2.40	1.00	1.14	2.14	0.10	0.01

TOT. VAR. = .0740874416

STD. DEV. = 1.51216713 (% Per Interval) Intervals = 18

ΔR =weight % in range

ΣΔR = cumulative % oversize

Method-Instrument : Malvern Mastersizer (Cinkarna-Celje)

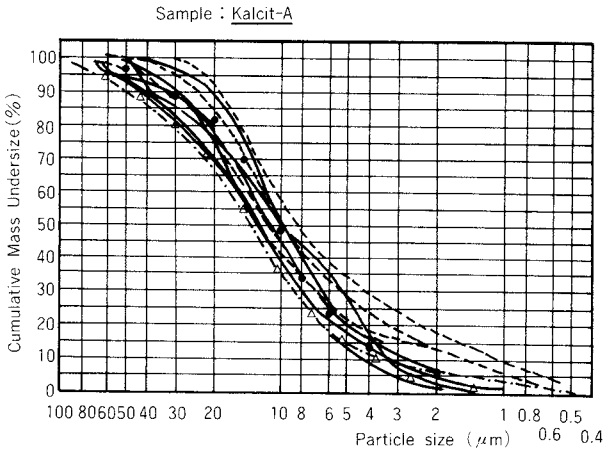

Fig. 1 Particle size analyses : calcite, sample A

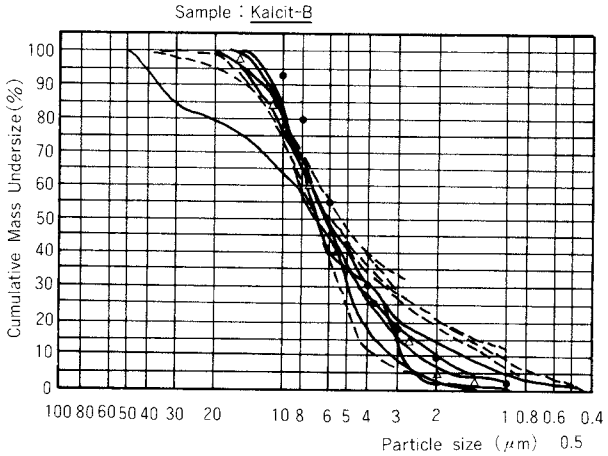

Fig. 3 Particle size analyses : calcite, sample B

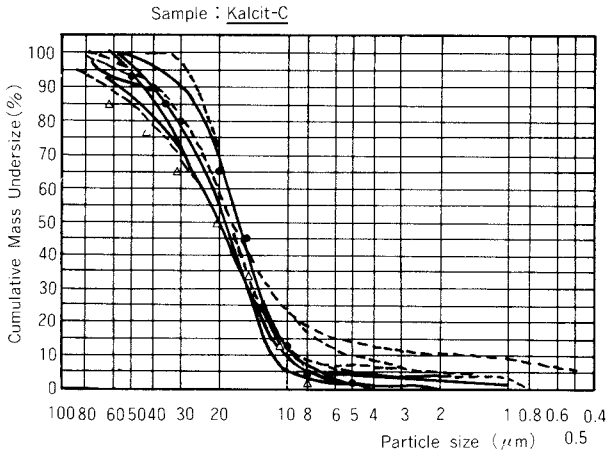

Fig. 2 Particle size analyses : calcite, sample C

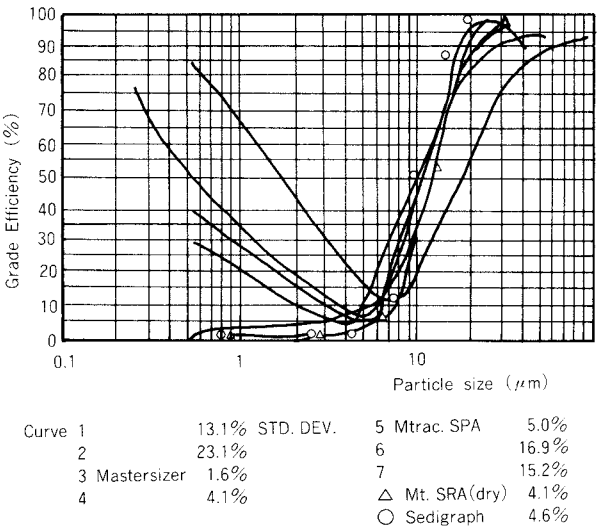

Fig. 4 Partition curves for the first example of classification

technique on Microtrac SRA. for the finest sample (B) was surprising. Discrepancies among the results of using the wet technique increase when partition curves for interpretation of the classification process are used, as can be seen in **Fig.4.** In this diagram, it is quite evident how great the differences can be in the description of the same process of classification. It is true that the differences arise from both types of instrument properties: accuracy and reproducibility, but it must be borne in mind that the same (laser diffraction) and wet techniques were used. Below the diagram, the values of the standard deviation in relationship to repuroducibility are given. Items obtained by Sedigraph 5100 and by dry powder feeding on Microtrac SRA are shown in **Fig.4**. The same diagram also shown in clearly indicates that the accuracy and reproducibility of the process description are not related.

3.2. Second example

The second example of classification process evaluation was also made with calcite,

but with finer particle size distribution and at a lower cut size, about 5 micrometers. Analyses were performed in our laboratory on Microtrac SPA and SRA with wet and dry techniques. As a part of **Fig.5** which shows partition curves, the values for the standard deviation with respect to reproducibility are also given. **Fig.6** shows curves of cumulative undersize, and **Fig.7** shows the differential curves of those analyses.

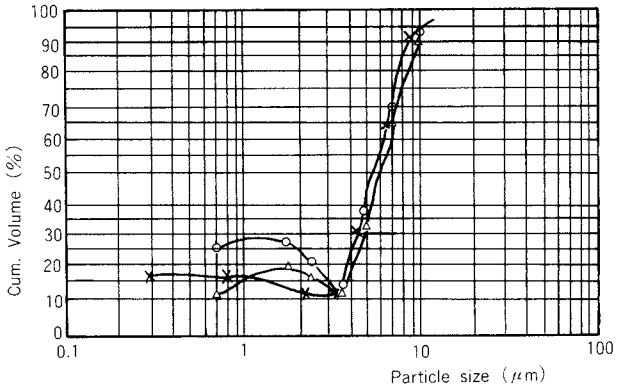

Fig. 5 Partition curves for the second example of classification

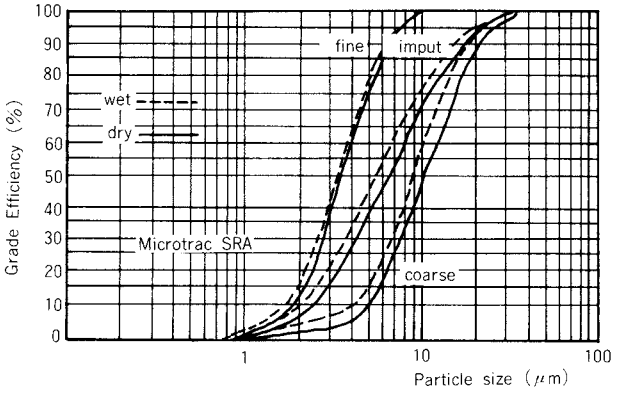

Fig. 6 Particle size analyses for the second example of classification

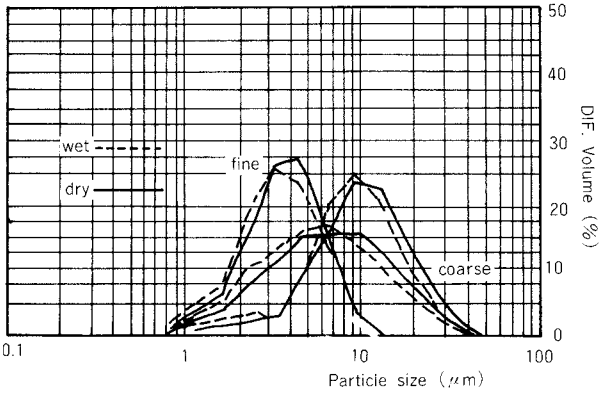

Fig. 7 Particle size analyses for the second example of classification

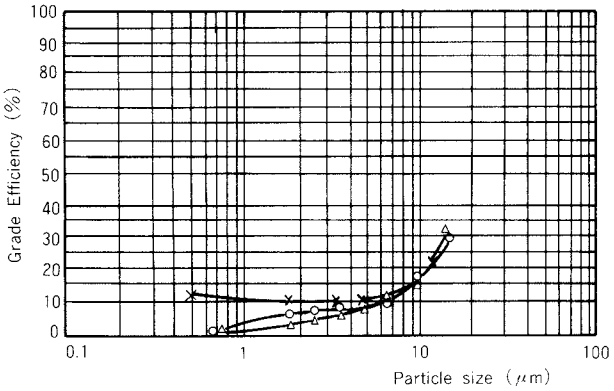

Fig. 8 Partition curves for the third example of classification

3.3. Third example

The third example of classification was executed with Aluminium hydroxide powder. The effect of classification was poor, which is significant for materials which are prone to form agglomerates. Regardless of this, the differences between the partition curves (**Fig.8**) obtained by wet and dry techniques are not so great. This example is also interesting as a case in which the finest distributions for samples were attained by the dry technique (**Fig.9** and **Fig.10**), although wet analyses were made in water and in the recommended organic medium.

4. Conclusions

The objective of this research project was to determine the possibility of adequately substituting the wet analysis with a dry one.

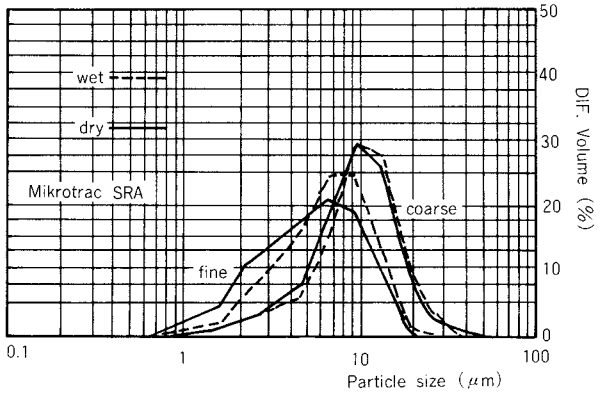

Fig. 9 Particle size analyses for the third example of classification

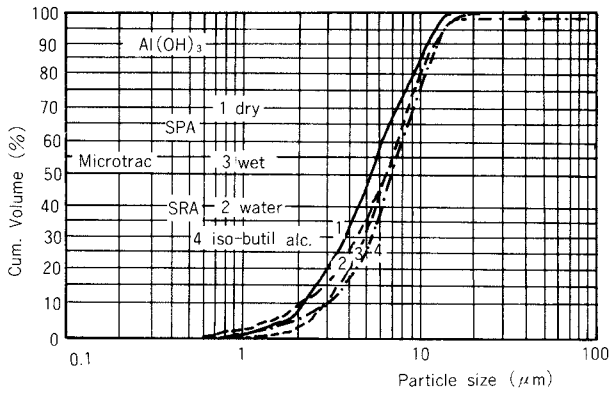

Fig. 10 Particle size analyses for the third example of classification

The wet analyses were carried out on different analyzers, and the dry ones are done on Microtrac SRA with some changes on the dry measurement cell. The results indicate that we can obtain the same information about the process with the dry as well as with the wet technique, even at the low limit range of the instrument. The differences between the partition curves under 5 micrometers are much greater in the analyses on instruments from various manufactures or in various models from the same producer. The reason lies in different algorithms for the determination of particle size distribution. In our case, the solid phase was dispersed in air flow with a velocity of about 30 meters per sec. This is a relatively undemanding condition, yet it is still sufficient for small discrepancies in the results obtained by the dry/wet technique.

The reproducibilities of the results obtained with dry analyses are the same as those obtained with wet analyses, but in comparison with other instruments and the wet technique, they are even better. We can expect to obtain equally small discrepancies in results with the dry/wet technique using other analyzers too, if the same conditions for gas suspension preparation are used. Comparisons were made only with a few samples, but we believe that similar results can be obtained for powders with similar distributions and properties. Extremely fine powders with a size distribution of under 2 or 3 micrometers are not the subject of this report. For such fine powders, good results can also be expected but only with careful and correct gas suspension preparation.

References

1) K.Leschonski, S.Rothele, U.Menzel:A Special Feeder for Diffraction Pattern Analysis of Dry Powders, PACHEW 1(4)161-166(1984)

2) T.Allen, R.Davies:Evaluation of Instruments of Particle Size Analysis, 4. European Symposium of Particle Characterization, Nuremberg 1989

3) R.Polke, M.Schafer, N.Scholz:Dispergieren feinster Feststoffpartikel, 4. European Symposium of Particle Characterization, Nuremberg 1989

An Electromechanical Valve for Solids †

Mojtaba Ghadiri and Catherine M. Martin
Department of Chemical and Process Engineering, University of Surrey *

Abstract

The operation and performance of a novel device, the Electromechanical Valve for Solids (EVS), for control of flow of granular materials are described.

The EVS applies a DC electric field to the granular material in a dense-phase state. This induces electrical interparticle forces which retard and can ultimately halt the flow, hence providing an actuating mechanism. The EVS has a very fast response time which makes it very useful for fast flow control. The response characteristics of the EVS and the results of flow control using a simple PID control action are reported.

1. Introduction

In many processes dealing with granular materials, the transfer of materials between various units of operation has often to take place at a prescribed rate. In such circumstances, the regulation and control of the flow is an important stage in processing and handling of granular materials. At present, this is accomplished by mechanical means such as a screw conveyor or a rotary star feeder, in which the material is translated forward at a rate depending on the angular speed of the screw or star. Although commonly used in industry for controlling the flow of granular materials, these devices have serious drawbacks which stem from the inherent features of their design and operation. For example, rotation of the screw against the stationary barrel causes attrition when handling delicate granules and erosion or seizure when hardling hard and abrasive materials. Also, the seal on the screw shaft, separating the system from the surrounding environment, is a fine component and may be easily damaged when handling dusty materials, especially at elevated pressures. Furthermore, these devices are slow in response, and have short term fluctuating characteristics and long term drift which make good flow control of processes with fast transients difficult.

The challenge faced in Particle Technology today is the development of new techniques for fast, reliable and accurate measurement and control of flow of particulate solids, as it has long been established for fluids. Recently some interesting 'non-mechanical' concepts have emerged, such as L, J and V valves based on aeration principles [1,2], and the Magnetic Valve for Solids [3]. In the latter, the presence of a magnetizable powder under the influence of a magnetic field generates interparticle force. These forces lead to the formation of particle chains which bridge the gap between the electrodes, and hence impede the flow of solids.

It is well known that similar effects can be produced by the use of electric fields without any need for addition of special materials [4-8]. Consequently, in a recent development inspired by the above work, we have pursued the use of electric fields for controlling the flow of granular materials. It has been shown that the flow of dry granular materials in a dense phase form can be controlled by the

* Guildford GB-Surrey GU2 5XH, England

† Received May 21st, 1991

application of a DC field, provided a suitably designed set of electrodes is used [9] . This discovery has led to the development of the Electromechanical Valve for Solids(EVS)for both on/off operation and flow control of granular materials [10] . As in other non-mechanical valves, the EVS has no moving parts and is mounted in situ with no external mechanical connections so that it does not suffer from the problems associated with the mechanical devices as discussed above. It provides good flow control with a wide turndown ratio and very fast response time. It may also be used under adverse conditions such as elevated pressures and temperatures. The design of the electrodes forms an important feature for satisfactory operation of the valve. In this paper, various aspects of the design, principles of operation and performance of the EVS are described.

2. Description of the device

The EVS comprises essentially of a set of two electrodes which is installed within the duct in the path of the flowing material. The electrodes are connected externally to a high voltage supply(EHT)unit for establishing an electric field. Typical electrode configurations are shown in **Fig.1** for cylindrical and rectangular ducts. The upstream electrode may be in the form of a number of wires stretched across the duct or may simply consist of pins protruding into the duct. The downstream electrode may conveniently be in the form of a wire mesh or parallel wires fixed across the duct.

For the EVS to operate at all, it is essential that the flow in the space between the electrodes is in dense phase form. The presence of the electrodes obviously obstructs the flow to some extent. Observations of particle motion in the space between the electrodes in a narrow rectangular column, providing essentially a two-dimensional flow, indicate that as soon as the flow is transformed into the lean phase in this region, the actuating mechanism is lost completely. Observations of particle motion in the region of the electrodes also indicate that halting of flow on application of the electric field is brought about by arching of particles over the mesh openings of the downstream electrode. Consequently, the key features in the design of the electrodes are that the geometry of the electrodes should be such that(a)the upstream electrode does not obstruct the dense phase flow of particles to an extent which could transform the flow into the lean phase form in the space between the electrodes, thus losing continuous interparticle and particle-electrode contacts:(b)the downstream electrode has sufficiently small openings so as to enable impeding and ultimately halting of the flow by the application of a suitably high electric field. To satisfy condition(b), there is usually some impeding of the flow by the downstream electrode even in the absence of an electric field, so that the flow past this electrode is always tranformed into the lean phase form. Consequently, the use of more than two electrodes is deleterious to the stability of the operation of the EVS.

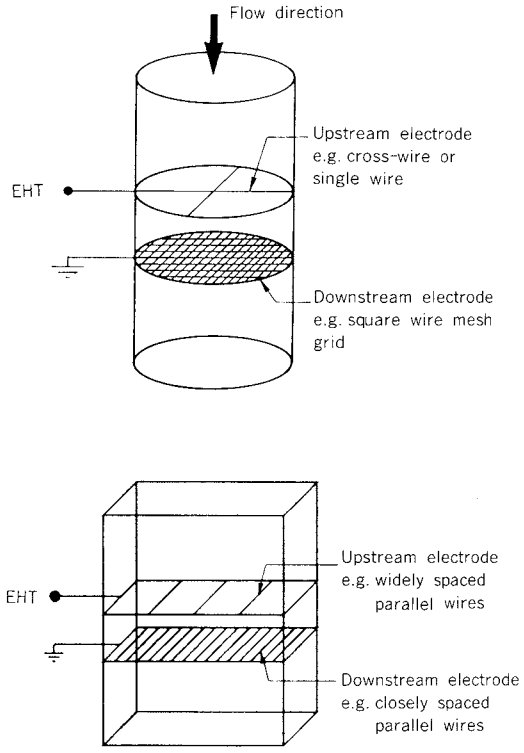

Fig.1 Typical electrode configurations of the EVS in cylindrical and rectangular ducts.

The feasibility of the concept of flow

control of granular materials by the application of an electric field has been demonstrated in two cylindrical columns of 64 and 115 mm I.D., and in a rectangular narrow slot of 200 mm × 12 mm. A large number of materials have been tested so far including sand, coal, salt, FCC catalyst powder, seeds, spray dried powders, and various chemicals and foodstuff. As the action of the EVS is to impede the flow of free flowing materials, for very cohesive materials discharge aids such as aeration or vibration may be needed. Once the material is made to flow, the EVS performs

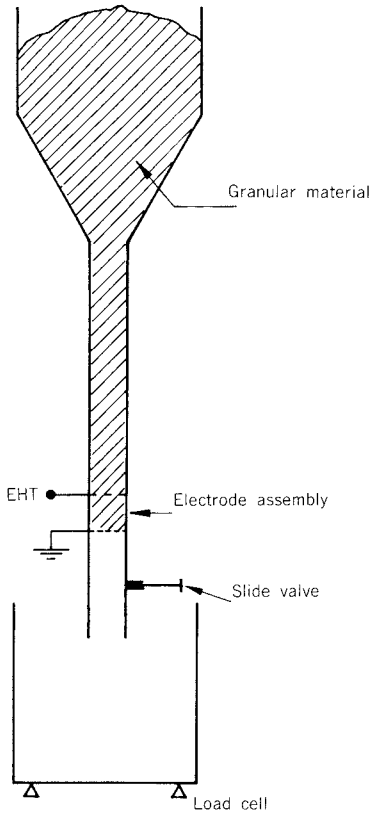

Fig.2 Schematic diagram of test rig for measuring flowrate through EVS.

just as for non-cohesive materials, as is described below.

Figure 2 shows a schematic diagram of the test rig incorporating the electrode assembly. A slide or a flap door is needed downstream of the electrodes. It is initially closed when filling the column and the storage bin, but is left open thereafter as the bed of material can be supported by the electric field.

If a continuous field is applied, a steady flowrate is obtained which is a function of the field magnitude. Alternatively, the electric field may be pulsed, where the frequency, pulse width and amplitude may all be varied to control the flow. The performance of

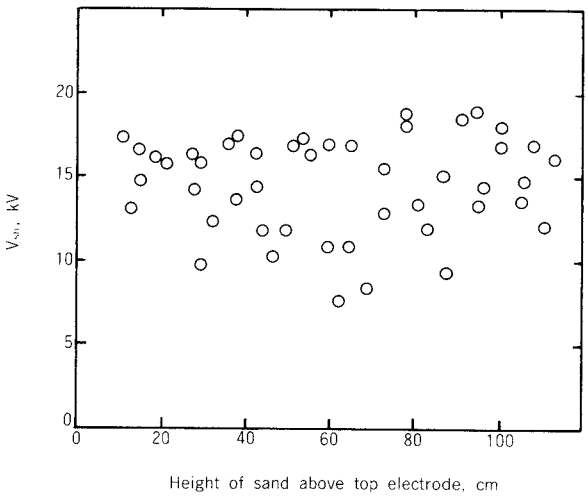

Fig.3 Effect of height of material on static holding voltage for 600-1200 μm sand in 115 mm column. Upper electrode: cross-wire; lower electrode mesh opening: 10 mm; inter-electrode gap (IEG): 36 mm.

these two modes of operation is discussed below.

2.1 Continuous DC Field

If an electric field is first set up to a suitably high level before opening the flap door, the particles between the electrodes will be frozen', thus supporting the material above the electrodes. No particles will flow when the door is opened except those in the space between the lower electrode and the flap door. If the voltage applied to the electrodes is then gradually reduced, a point is reached when the material begins to flow. This is referred to as the threshold of the static holding voltage, V_{sh}, which is found to be effectively independent of the height of material above the upstream electrode, but scattered within a range. A typical example is shown in **Fig.3** for sand. The scatter is observed for all materials and electrode configurations tested so far,

and is believed to be due to variations in the packing structure, which depend on the filling history, and possible switching between the active and passive states on the initiation of flow. The upper limit of V_{sh} is of interest here as it represents the maximum possible potential required to prevent the granular material flowing from a static state. Typical values of V_{sh} for several materials and electrode configurations are given in **Table 1.**

If the voltage is reduced to a value which allows the material to flow, a steady-state flowrate is attained which is a function of the applied voltage. The flowrates are obtained from the gradient of the weight versus time traces recorded by a load cell from which the collection vessel is suspended. The performances of the EVS for the cylindrical columns of diameter 64 and 115 mm are shown in **Fig.4** for sand in the size range 600-1200 μm. The electrode configuration shown in **Fig.1** was used here with 10 mm square openings in the downstream electrode and an inter-electrode gap (IEG) of 36 mm. The performance of the EVS for the rectangular column is shown in **Fig.5** for sand and glass ballotini both having a particle size range of 600-850 μm. In this case, the downstream electrode consisted of parallel wires extending across the duct as shown in **Fig.1,** with a spacing of 5mm between the wires, and the upstream electrode consisted of pins extending 1-2 mm into the bed at intervals of 10 mm along the front and back faces of the column. The curves shown in **Figs.4** and **5** were obtained by fitting the experimental data to a semi-empirical flow model, equation (3),

Table 1 Upper limits of V_{sh} for materials in varying electrode configurations.

Material	Column shape and size (mm)	Lower electrode openings (mm)	Inter-electrode gap (IEG) (mm)	Particle size (mm)	V_{sh} (kV)
Sand	Cyl. 64	Mesh. 5	36	0.3 −0.6	11
				0.6 −1.2	10
		Mesh. 10	36	0.6 −1.2	17
				1.2 −2.4	15
	Cyl. 115	Mesh. 5	36	0.3 −0.6	18
				0.6 −1.2	18
		Mesh. 10	36	0.6 −1.2	19
				1.2 −2.4	17
Coal	Cyl. 64	Mesh. 10	36	0.3 −1.4	4
	Cyl. 115	Mesh. 10	36	0.6 −1.2	11
Coal/Sand 50/50 wt%	Cyl. 115	Mesh. 10	36	0.6 −1.2	14
NaCl salt	Cyl. 64	Mesh. 5	20	0.35−0.6	10
	Rect	Slot. 5	20	0.35−0.6	12
Granulated sugar	Rect	Mesh. 3	20	0.18−1.7	5
Turnip seeds	Rect	Slot. 5	20	1.2 −1.7	3.5
Soap powder	Rect	Slot. 5	20	0.12−1.4	5
MgO powder	Rect	Mesh. 1.5	20	0.04−0.35	17
FCC powder	Rect	Mesh. 1	20	0.05−0.10	2

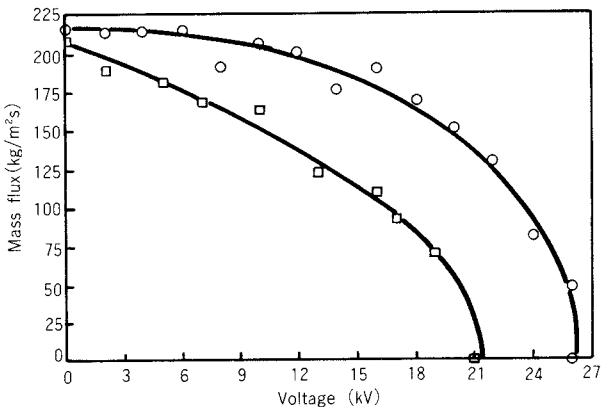

Fig.4 Effect of voltage on mass flux in cylindrical column for 600-1200 μm sand. Upper electrode: cross-wire; lower electrode mesh opening: 10 mm; IEG: 36 mm. Column diameter: ○, 115 mm; □, 64 mm. Best fit from flow model equation(3):——

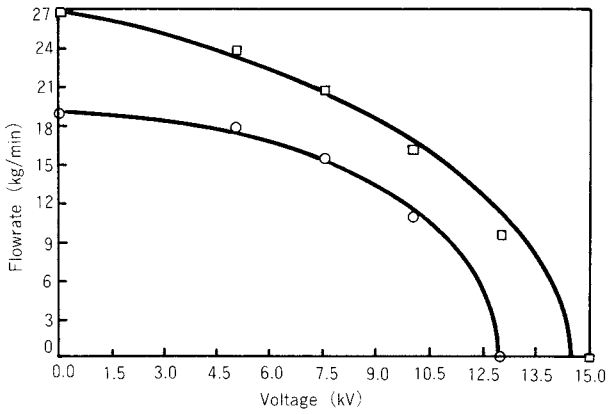

Fig.5 Effect of voltage on flowrate in rectangular column. Upper electrode: pins; lower electrode slot width: 5 mm; IEG: 20 mm. ○:sand(600-850 μm); □: glass ballotini(600-850 μm). Best fit from flow model equation(3):——

which is discussed below. **Figures 4** and **5** show that similar flow profiles are obtained in the cylindrical and rectangular columns. The results therefore show a common trend for the continuous DC field. The flowrate curves have a flat almost horizontal section at low voltages, followed by a nearly linear section at higher voltages. As the flowrate decreases to below about 50% of the full flow, the curves become quite steep and the flowrate drops off quickly to zero. Consequently, for good flow control using a continuous field, only that portion of the curve between full flow and about 50% of the full flow may be used. The low flowrate range is best handled by operating in the pulsating field mode, as is discussed below.

The current through the Valve presents an Ohmic relation with the applied voltage. For the results shown in **Fig.4** for sand, the current was about 25 μA at 25 kV, giving a remarkably low power consumption of 0.625 W.

2.2 Pulsating DC Field

In this mode, the pulse amplitude, frequency and width can all be varied in order to obtain a desired flow rate. The effects of varying the width and frequency of the pulse are shown in **Figs.6** and **7**, respectively, for different materials. In these tests, the pulse amplitude was set at a sufficiently high value

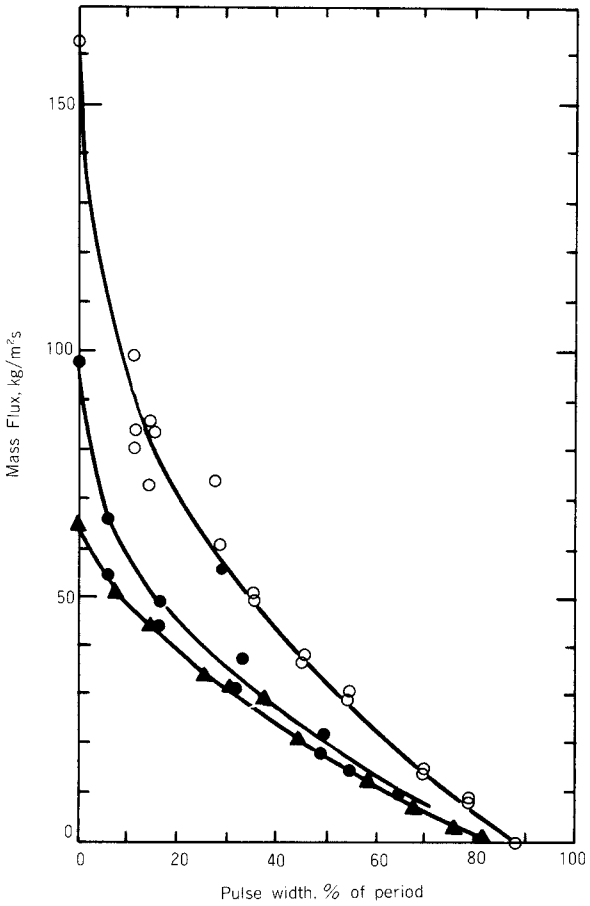

Fig.6 Effect of pulse width on mass flux for pulsating field operation. Pulse frequency = 1.5 Hz; pulse amplitude = 28 kV, particle diameter = 600-1200 μm; column diameter = 64 mm; upper electrode = cross-wire; lower electrode mesh opening = 10 mm square; IEG = 36 mm. ▲: coal; O: sand; ●: coal/sand(50/50 wt%).

in order to achieve fast and complete halting of the flow on application of a pulse. The data shown in **Fig.6** were obtained using the 64 mm diameter column with the electrode configuration shown in **Fig1.** The frequency response shown in **Fig.7** was obtained using the narrow rectangular duct, with the upstream electrode consisting of the pin arrangement as described above, and the downstream electrode consisting of parallel wires forming slots of 5 mm width.

The results in **Figs.6** and **7** show a trend opposite to that of the continuous field. For high flowrates, the curves are steep, providing poor control, whereas for small flowrates the curves

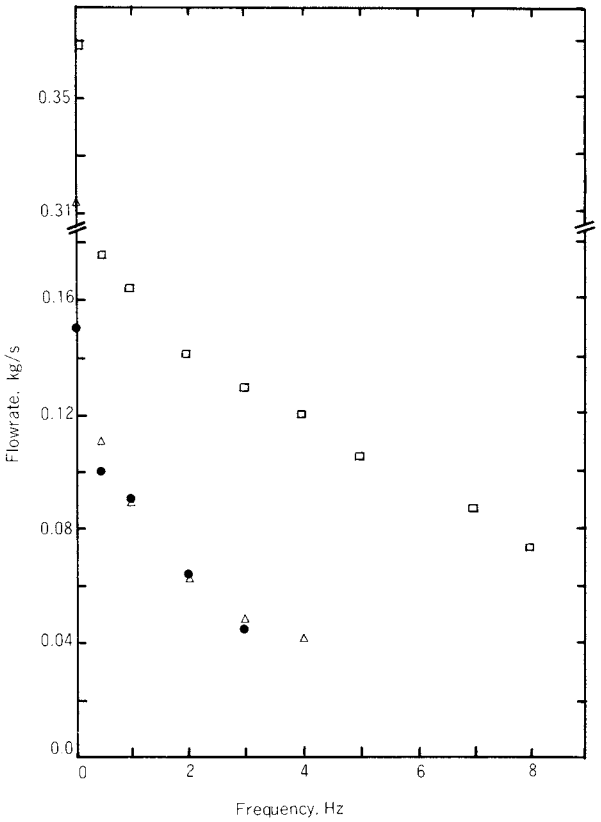

Fig.7 Effect of pulse frequency on flowrate for pulsating field operation in rectangular column. Pulse width = 50% of period. Upper electrode = 1-2 mm long pins spaced 10 mm apart; lower electrode = slots of 5 mm width; IEG = 20 mm. ●: turnip seeds(1.2-1.7 mm), pulse amplitude = 3.5 kV; △: sand (0.6-0.85 mm), pulse amplitude = 11 kV; □ :salt(0.35-0.6 mm), pulse amplitude = 12 kV.

become nearly linear with a small slope. Thus the two modes of operation complement each other to provide an overall wide turndown ratio for practical situations.

In **Fig.7,** the maximum frequency tested with each material was limited by the relatively long charging and discharging times of the overall circuit. This is because the field was pulsed by applying an inhibiting pulse to the low voltage input of the EHT unit, and therefore the EHT's capacitor had to be charged again each time the field was switched on and then discharged through the material when the field was switched off. The bulk resistivity of the material is therefore an important factor influencing the discharge time. The electrical properties of the materials tested here are given in **Table 2,** as measured in situ between the electrodes in the rectangular column using a Wayne Kerr electrical bridge. The NaCl salt had a much shorter discharge time than the sand or turnip seeds, due to its lower resistivity. It was therefore possible to pulse at higher frequencies with the salt.

The overall circuit response therefore represents the combined responses of the EHT unit, charging/discharging through the bed of material and particle movement in the region of the electrodes. The maximum frequency is at present limited mainly by discharging a large capacitor through the material. Much higher frequencies will be possible by switching the electric field at the high voltage output of the EHT unit, and shorting the electrodes, thus avoiding slow discharge of the EHT's capacitor through the material. The absolute upper limit of frequency depends on the charge relaxation time of the particles which is typically in the order of milliseconds. The development of such a high voltage switch is currently in hand.

Table 2 Electrical properties of materials as measured in situ across electrodes in rectangular column.

Material	Particle size (mm)	Resistance (MΩ)	Capacitance (pF)
Turnip seeds	1.27 −1.7	48	15
Sand	0.6 −0.85	43	12
NaCl salt (without anti-caking agent)	0.35−0.6	14	14

2.3 Closed loop flow control with the EVS

The potential of the EVS for setpoint flow control in a closed loop system has so far been investigated only for the continuous field mode of operation [11]. The test rig shown in **Fig.2** was used for disparsing NaCl salt (90-600) μm diameter from the 64 mm column with the electrode configuration shown in **Fig.1.** The gap between the electrodes was 20 mm and the downstream electrode

operation was carried out by a programme developed in-house using a Sinclair QL computer which was interfaced with the EHT for controlling the voltage, and with a tension load cell for monitoring the flowrate.

In order to exploit the fast response time of the EVS for fast control, it is necessary to use an equally fast sampling rate to monitor the instantaneous flowrate. In the system used here, the flowrate was calculated from the change in accumulated weight measured by the load cell over the sampling interval. Since the load cell had a continuous analog output which was digitised at the computer interface by a fast 16 bit A/D converter, it was possible, in principal, to use very fast sampling rates for monitoring the flowrate. However, it was found that the variability or 'noise' in the flowrate readings increased significantly with increasing sampling rate. This is illustrated in **Fig.8,** where the relative standard deviation calculated from twenty consecutive flowrate readings is shown for varying sampling intervals. **Figure 8** shows that it is necessary to use a sampling interval of about 1.0 s to reduce the relative standard deviation to 10 per cent. Therefore, although the load cell is capable of much faster output frequencies, precise and accurate measurements can only be obtained at frequencies less than about 1 Hz. This response results from the response of the load cell and the transportation time of the material from the electrodes to the weighing bin. For the experimental setup used here, where the height between the EVS and the bottom of the bin is about 1.0 m, the transportation time has a mimimum value of about 0.4 s, as estimated by the free fall of the particles.

Based on the results in **Fig.8,** a frequency of 1 Hz was used initially to monitor the flowrate through the EVS for the PID control operation. However, it became immediately evident that while 1 Hz was sufficiently slow to produce stable measurements for steady-state flow, an unacceptable amount of instability was produced in the case of transient flows produced by controlling to a setpoint. It was therefore necessary to base the

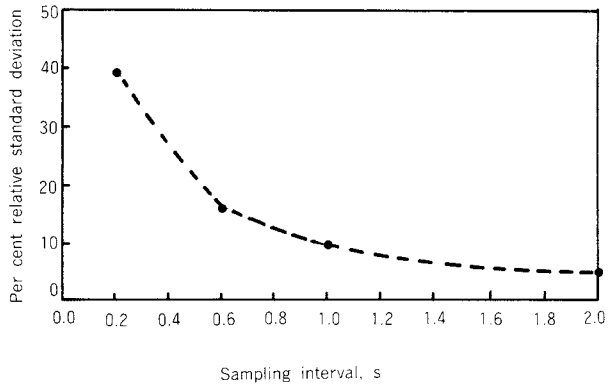

Fig.8 Effect of sampling interval on per cent relative standard deviation for flowrates measured using load cell interfaced with Sinclair QL computer.

PID control on a moving average flowrate calculated from five flowrate measurements at one second intervals. Using a moving average, to represent the instantaneous' flowrate, slowed down the system response significantly. However, using the moving average method at least allowed the response limitations of the load cell to be overcome in such a way that the control abilities of the EVS could be observed.

The response of the EVS to three changes in flowrate setpoint using a constant gain of 0.0678 kg s^{-1} kV^{-1} is shown in **Fig.9.** While the response is slow, the final setpoint error is negligible. For effective control, a PID

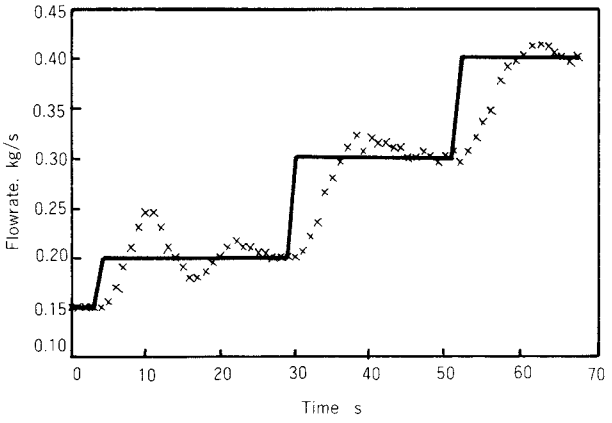

Fig.9 Response of EVS to PID control for changing setpoint with NaCl salt (90-600 μm)in 64 mm column with 5 mm mesh openings. Flowrate setpoint:——; measured moving average flowrate response: X.

method with constant gain is really only suited to linear processes. As shown by the performance curves in **Fig.4** and **5**, the response of the EVS is not linear over the full flowrate range. However, by taking a limited flowrate range over the full curve for control with constant again, the nonlinearity is small and acceptable control is obtained. The gain used for control in **Fig.9** was determined by trial and error tuning for a flowrate range of 0.15 to 0.45 kg s^{-1} where 0.45kg s^{-1} was the maximum flowrate when zero field was applied. The setpoint of 0.2 kg s^{-1} is at the low flowrate end of the full range, and therefore lies on the steep part of the valve performance curve, where the flowrate is very sensitive to any change in voltage. Therefore, the response of the EVS in **Fig.9** for the setpoint of 0.2 kg s^{-1} shows significant oscillation. The setpoints of 0.3 and 0.4 kg s^{-1} move progressively onto the flatter part of the valve performance curve, so that the oscillating response of the EVS to these setpoints become damped in **Fig.9.** Therefore, an obvious improvement to this control method would be the introduction of a self-tuning gain which is updated according to the flowrate response in the range of the the setpoint.

3. Analysis

The actuating mechanism which is considered to be responsible for the action of the EVS depends on the generation of electroclamping forces by a small electric current flowing over the particle surfaces in the region of the electrodes [12]. The electroclamping forces stem from the very nature of the material, i.e. being in particulate form. Individual particles are in point contact' with each other at rest or when they are moving in a dense phase form. When an electric field is set up across two electrodes inserted in a bed of particles, there will be some charge leakage through the bed via these contact points, provided that the particles are not too conductive so as to draw excessively high corrents, nor too resistive so as to draw such low current that there is negligible effect. Because the current path is constricted in the region of the contactpoint, the electric field in the gap surrounding the contact area is greatly enhanced. Depending on the size and shape of the contact area, this field is highly non-uniform and can be several orders of magnitude larger than the average field. This mechanism has been analysed by McLean [4], Dietz and Melcher [5]. and more recently and comprehensively by Moslehi and Self [6] to describe the adhesion of the precipitated dust layer in the electrostatic precipitators, and various effects in electro-fluidised and packed beds. The attractive forces between the particles resulting from this phenomenon are very high, and comparable in magnitude with other external forces such as those due to gravity, as in the case of the EVS, and those due to drag resulting from pressure drop in electrically enhanced fabric filters [13].

There are several theoretical models of the electroclamping force [4-6]. These models differ in details, depending on the mechanical properties of the contact points, and on the limit of electric field breakdown in the interparticle gap. However, they all relate the clamping force to the average applied electric field strength, E_a, for a single contact between two spheres, or between a sphere and a conductive plane, and can be represented by:

$$f_e = \alpha E_a^{\beta} \qquad (1)$$

where f_e is the interparticle electroclamping force, α is a function of the physical and electrical properties of the particles, and β is the power law index. The value of β depends on the characteristics of the contact point, i.e. its initial size and deformation under loading. For non-deforming contact points, β is analytically calculated and is equal to 2 [4]. However, there is usually some elastic deformation resulting from the electrical force alone, or from a combination of electrical and mechanical forces, and this leads to a less enhanced field in the gap surrounding the contact point, and hence to a lower power dependence. The models differ in the value of β, but they all fall within the range 1.2 to 1.5 [4,6]. In all these models, the elastic deformation due to the electric field is

described by the Hertz analysis. If the size of the contact point is very small, such as for very fine particles or for particles with sharp asperities, then the electric field could exceed the limit of breakdown; in this case β reduces to unity [5] . Recently it has been shown that the Hertz analysis may not adequately describe the pattern of contact deformation under an electric field [12] , so that the formulation of the models of the electroclamping force for a single contact may be in error. However, in the analysis of the macroscopic flow behaviour presented below, only a general analogy with equation(1) is made, without taking any prescribed value for the power index.

The geometry and configuration of the electrodes used here are such that the electroc lamping force can produce counteracting compressive stresses as well as a net upward force. The increased compressive stresses lead to higher shear stresses on the electrodes and on the walls, thus providing a means to support the weight of the bed. Indeed it is found that roughening the walls in the space between the electrodes results in a reduction in V_{sh}. The net upward force on the other hand can act to support the stable arches which form over the openings of the downstream electrode on halting of the flow. However, because of the complex geometry of the electrodes, a mathematical analysis of the mechanics of arching in the presence of these forces is somewhat involved. Consequently, a simpler geometry, i.e. that of a wedge on which planar electrodes have been installed, has so far been attempted. The results of this analysis are presented elsewhere [14] , where the arch span has been related to the electric field strengh.

To model the effect of the electric field on flow, an analogy has been made with the effect of interstitial gas pressure gradients on discharge of fine granular materials from hoppers and bins. Nedderman et al. [15] have shown that the Beverloo correlation could be modified to account for the effect of air drag on the flowrate such that

$$W \propto g^{1/2}\left[1+\frac{1}{\partial\rho}\frac{dP}{dr}\Big|_{r=r_o}\right]^{1/2} \qquad (2)$$

where P is the interstitial pressure, r is the radial coordinate in the conical hopper, and r_0 is the value of r at the orifice.

According to equation(2), the flow due to gravity is reduced by the gradient of the interstitial gas pressure at the orifice, which provides a net external force opposite to the gravitational force. In the case where an electric field is applied, the 'drag' force is considered to result from the electrical forces impeding the flow. Therefore as a first approximation, it is proposed that the drag effect caused by the field may take a similar functional form to that of equation(1), such that the following relationship describes the flowrate response to the applied field:

$$W = W_o\left[1-\lambda E_a^{\gamma}\right]^{1/2} \qquad (3)$$

where λ and γ are constants, and W_o is the flowrate without an applied field. For convenience in fitting parameters λ and γ to the experimental data, equation(3)has been rearranged such that

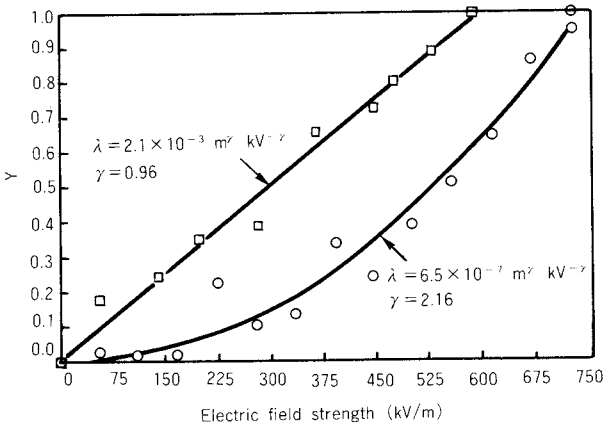

Fig.10 Fit of flow model, equation(4), to expermental data from **Fig.4** for cylindrical column. Experimentals: ○, 115mm; □, 64mm Best fit from model:——.

$$Y = \lambda E_a^{\gamma} \qquad (4)$$

Equation(4)has been fit to a large set of experimental data for W, W_0 and E_a, collected from both the cylindrical and rectangular

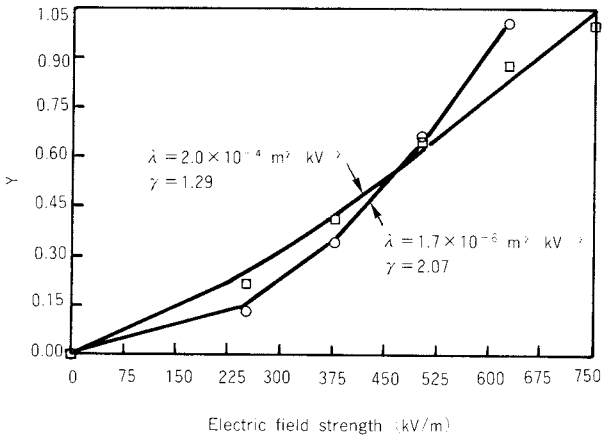

Fig.11 Fit of flow model, equation(4), to experimental date from **Fig.5** for rectangular column. Experimental:O, sand; □, grass ballotini. Best fit from model:——

columns, using a non-linear least squares routine to obtain values of λ and γ. In **Figs.10** and **11**, the experimental values of Y are compared to the best fit values from equation (4)for the same data shown in **Figs.4** and **5.** From **Figs.10** and **11**, it is clear that very good fits are obtained for individual data sets. However, when all the data sets are compared, the values of λ and γ cover wide ranges, with no apparent trends related to the experimental conditions. Therefore, while it seems that the flow model given by equation(4)is suitable for calibrating the EVS for practical operation, the formulation does not present a verifiable description of the process based on a fundamental mechanistic analysis, as is necessary for effective optimisation of the EVS and for application of the results to other processes where electric fields are applied to particulate solids. Therefore, in future, it is necessary to proceed with a more rigorous analysis, where the precisely defined electrical and mechanical stress distributions are incorporated into the macroscopic constitutive equations of motion. Indeed, the approach outlined above for modelling the steady-state flow in the EVS is a simplistic one, since the average value of the electric field is used in the analyses, without considering the effect of the highly non-uniform fields which are produced in the complex electrode configurations used here [10]. A model for the static holding voltage, V_{sh}, has been developed elsewhere using a well defined 2-dimensional field configuration, thus allowing a much more rigorous analysis[14]. This approach is obviously also necessary for successful modelling of the steady-state flow.

4. Conclusions

The EVS has considerable potential for use in a variety of bulk solids processes. In on/off operation, the EVS can be used for dosing and fast packaging. For controlling a continuously flowing material in a metering or feeding process, the EVS can achieve a wide turndown ratio by using a continuously applied voltage for large flowrates and a pulsating voltage for small flowrates. Using a simple PID control programme in a computerised closed loop system, the EVS produced good flowrate control with respect to final setpoint error, but the fast response of the EVS could not be exploited due to the limitations of the load cell for measuring the flowrate and due to the long transportation time.

For flow with a continuously applied field, a semi-empirical correlation is presented to describe the steady-state flowrate through the EVS as a function of the field strength. The correlation provides a good fit to the data for calibration purposes. However, the fitted parameters from the correlation do not appear to follow any trends. Therefore, a more rigorous mechanistic analysis of the interacting forces in the presence of non-uniform fields is necessary in order to develop a flow model which will be effective for design and optimization of the EVS.

Overall, the EVS offers many advantages over conventional mechanical valves for controlling the flow of granular materials. It has no moving parts and so wear of the material and the valve itself is reduced. In addition, the power consumption is remarkably low. Therefore, the EVS offers potential savings in both operating and capital costs. Most importantly, the EVS has a very fast response time which makes it very useful for fast flow control.

Acknowledgments

The development of the EVS was made possible by financial support from the Research Committee and the Technology Transfer Committee of the University of Surrey. Further research on the electromechanics of the valve is being continued with support from the Science and Engineering Research Council. The authors should express their gratitude to Prof. R. Clift and Dr. U. Tüzün for their interest in this work and their contributions to stimulating discussions.

Nomenclature

E_a = applied electric field, V m^{-1}
f_e = single contact electroclamping force, N
g = gravitational acceleration, m s^{-2}
P = interstitial gas pressure, Pa
r = radial position in conical hopper; = r_0 at orifice, m
V_{sh} = static holding voltage, V
W = mass flowrate, kg s^{-1}
W_o = mass flowrate through electrodes without electric field, kg s^{-1}
Y = parameter defined in flow model equation(4)
α = parameter in electroclamping force models, NV $^{\beta}m^{\beta}$
β = exponent in electroclamping force models
γ = parameter in electrically-modified flow model equation(4)
λ = parameter in electrically-modified flow model equation(4), $V^{-\gamma}$ m^{γ}
ρ = bulk material flowing density, kg m^{-3}

References

1) T.M. Knowlton, in "Gas Fluidization Technology", Ed. D.G. Geldart, Ch.12, p.341, John Wiley & Sons, Chichester, 1986.
2) L.S. Leung, Y.O. Chong and J. Lottes, *Powder Technol.*, **49** (1987)271.
3) E.Jaraiz-M., O. Levenspiel and T.J. Fitzgerald, *Chem.Eng.Sci.*, **38** (1983)107.
4) K.J. McLean, *J.A.P.C.A.* **27** (1977)1100.
5) P.W. Dietz and J.R.Melcher, *A.I.Ch.E.Symposium Series*, **74** No. 175(1978)166
6) G.B. Moslehi and S.A. Self, *IEEE Trans.Ind.Appl.,IA-20,* No.6(1984)1598.
7) H.A. Pohl, *Dielectrophoresis,* Cambridge University Press, Cambridge, 1978.
8) T.B. Jones, *Journal of Electrostatics,* **6** (1979), 69.
9) M. Ghadiri and R. Clift, European Patent Application No. 87308304. 2, 1987.
10) M. Ghadiri, C.M. Martin and J. E.P. Morgan, submitteditted to *Powder Technol.* (1991).
11) C.M. Martin and M. Ghadiri, BULK 2000: Bulk Materials Handling - Towards the Year 2000, London, UK, 29-31 October 1991.
12) C.M. Martin, M. Ghadiri, U. Tüzün and B. Formisani, 2nd Symposium: Advances in Particulate Technology, Guildford, UK, 15-17 April 1991.
13) M.Ghadiri, J.A.S. Cleaver and R. Seaton, 1st European Symposium on Separation of Particles from Gases, PARTEC, Nuremberg, 19-21 April 1989.
14) C.M. Martin, M. Ghadiri, and U. Tüzün, 2nd World Congress Particle Technology, Kyoto, Japan, 19-22 Septmember 1990.
15) R.M. Nedderman, U. Tüzün and R.B. Thorpe, *Powder Technol.,* **35** (1983)69.

Mineral Liberation-Influence of the curvature of the interfacial surface on the Locking Profile at different Comminution Size †

Ugo Preti
Institute of Applied Chemistry, University of Trieste *

Abstract

In the study of locked particles, the recent development of a theoretical understanding of the volume locking profile using textural transforms has been significant.

In all derivations, it was assumed that the interfacial surface area was flat. In this paper, the effect of a curved interfacial surface is explored. It was found that as the particle size approached the inclusion size, the volume locking profile became evermore asymmetric. Moreover, as this ratio approached one, there was a large movement of the Ferrara Point. Since the latter is a key parameter in defining the locking profile, its movement is significant.

1. Introduction

Locked particles are of significance in a variety of industries from the pharmaceutical to the mineral fields. Locked particles contain two or more solid constituents. For a clearer understanding of how these locked particles behave in different processes, it is important to understand and quantify the volume locking profile of particles. One problem not clearly defined in the locked particle field is the role of the curvature of the interfacial surface between the two or more constituents in the locked particle. In short, how does this interfacial curvature affect the volume locking profile curves ?

Given a mineral composed of two phases, α and β, a quantitative description of the liberation obtainable by comminution requires that the following parameters be known for each grain size class:

1- Values of the free particle fractions of phase α, of phase β and of the locked particle fraction, p_α, p_β and p_m respectively.
2- The distribution of locked particles as a function of their volume grade or of their density; this curve has been called locking-profiler (Meloy et al,1987).
3- Locked particles mean grade which can be quantifiable if the locking profile is known-point 2.

Assuming random fracture and that the particles are small compared to the inclusions (1)**, Meloy (1984) proposed an expression for the lockded fraction which is independent of texture and dependent on the specific interfacial surface area of the ore. Maintaining the same assumptions, Ferrara et al (1984) have proposed expressions for the free fraction s P_α, P_β—also independent of texture-as functions of the specific interfacial surface area and of the volume grade of phase β.

Meloy et al (1987), using a textural transform for the first time proposed an expression for the locking-profile, a symmetrical U-shaped curve, obtained assuming the interfacial surface to be flat. In a recent papaer, Ferrara et al. (1990) showed that, if the particles are small, the quantities P_α, P_β and P_m may be satisfactorily approximated by the above

* 1-34127 Trieste, Italy

† Received June 5th, 1991

** The term "particle" indicates a grain produced by comminution; the term "inclusion", the individual masses of phase β dispersed in phase α.

mentioned expressions, irrespective of the type of texture. However, the same parameters become dependent on texture when particles are large.

The symmetry of the locking-profile is a direct consequence of the assumption of the interfacial surface being flat. It is the aim of the present work to determine the effect of the texture, particularly of the curvature of the inclusions, on the locking-profile and to evaluate the error involved when assuming a flat interfacial surface, while in reality this surface exhibits significant curvature.

2. Curved Interfacial Surfaces

2.1 Assumptions and concepts

The method used to calculate the locking-profile resulting from textural transform models with a curved interfacial surface is similar to that employed for flat surface (Meloy et al 1987). It can be schematized asa follows:

1- Assume random fracture
2- Select a model of ore texture (textural trasform)
3- Assume particles resulting from comminution are spherieal.
4- By means of a variable z, penetration, define the position of a particle with respect to an inclusion; seek a correlation between z and the volume fraction, v, of phase β in the particle (see **Figure 1**):
5- Determine the probability that the particle is in the position defined by z. Then, determine the probability of a particle being characterized by a given volume fraction of phase β.

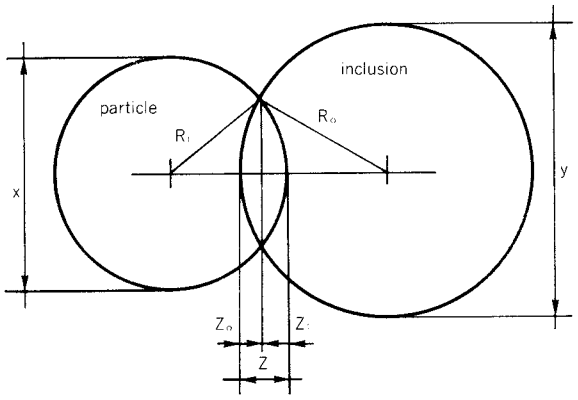

Fig.1 The smaller spherical particle contains part of the larger spherical inclusion.

The choice of the textural model for the textural transform, i.e.shape and distribution of the inclusions, should be made on a case by case basis by analyzing the ore under study. However, since the objective of this study is to determine how the curvature of the interfacial surface affects the shape of the locking-profile, the model to adopt has to imply a curved interfacial surface. Moreover, textural transform must permit simple mathematical treatment.

The inclusions (phase β) were assumed to be spheres of equal diameter randomly distributed in the gangue (phase α). The distance betwen spheres was assumed to be sufficient so that the probability of a particle simultaneously touching more than one inclusion was negligible. Finally, the particles were assumed to be smaller than the inclusions.

This type of texture, called granular texture, along with other types such as rod-like, band and boxes textures, has been utilized by Ferrara et al (1989), with only the aim of obtaining different expressions of the particle fractions P_α, P_β and P_m. Minerals with textures that can be approximated by such a model are frequent in nature (Preti et al. 1989); moreover this model allows one to use relatively simple algorithms. Although the model is simple, the determination of the locking-profile-as will be seen below-becomes complex (compared with models assuming flat interfacial surface).

2.2 Derivation of algorithms

In this section the algorithms are derived for the calculation of the following functions:

G(v) Cumulative distribution function of the locked particles as a function of the volume fraction of phase β:

g(v) Volume frequency distribution or locking-profile;

v_F Mean volume grade of the locked particles;

M(δ) Cumulative distribution function of the locked particles as a function of the

density δ.

$m(\delta)$ Frequency distribution function of density or locking profile.

2.3 Derivation of locking-profile

Define(see **Figure 1**)

z the penetration of the particle into the inclusion

x the particle diameter

R_o the inclusion curvature radius

R_1 the particle radius($x=2\cdot R_1$)

Φ_o and Φ_1, respectively the angles between the straight line joining the curvature centers and R_o and R_1.

z_o and z_1, respectively the segments indicated in the **Figure 1** ($z_o+z_1=z$).

The volume of the inclusion(radius R_o), embodied in the particle of radius R_1, may be expresed by the following Equation:

$$V=\pi/3\cdot[z_o^2\cdot(3\cdot R_o-z_o)+z_1^2\cdot(3\cdot R_1-z_1)] \quad (1)$$

Because the volume fraction is:$v=V/(4/3\cdot\pi\cdot R_1^3)$v is obtained ad:

$$v=\frac{z_0^2\cdot(3\cdot R_o\ z_o)+z1^2\cdot(3\cdot R_1 z_1)}{4\cdot R_1^3} \quad (2)^*$$

The values of z_1 and z_2 may be expressed as functions of z by solving the following system:

$$R_1\sin\Phi_1=R_o\sin\Phi_o$$
$$z_o=R_o(1-\cos\Phi_o)$$
$$z_1=R_1(1-\cos\Phi_1)$$
$$z=z_o+z_1 \quad (3)$$

Eliminating the variables Φ_o and Φ_1, one obtains:

$$z_1=(2\cdot R_o-z)\cdot z/[2\cdot(R_1+R_o-z)]$$
$$z_o=[(2\cdot R_1-z)\cdot z]/[2\cdot(R_1+R_o-z)] \quad (4)$$

Substituting Equations 4 in to Equations 2, one obtains the volume fraction as a function of z : $v=v(z)$.If $F(z)$is the cumulative distribution function of the particles having a penetration z in the inclusion, from the assumption of random fracture it follows (2) that:

$$F(z)=\frac{(R_o+R_1)^3-(R_o+R_1-z)^3}{(R_o+R_1)^3-(R_o-R_1)^3} \quad (5)$$

and defining $G[v(z)]$ as the cumulative distribution function of the particles having a volume fraction less than $v(z)$, one obtains:

$$G[v(z)]=F(z) \quad (6)$$

Deriving Equation 6 yields:

$$g(v)=f(z)\cdot dz/dv$$

from Equation 5 one obtains:

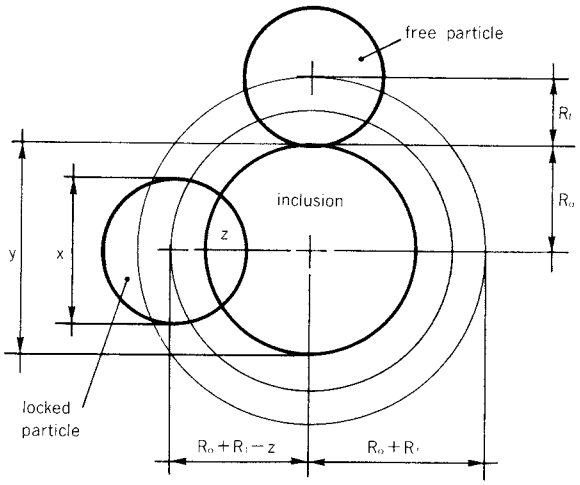

Fig.2 A free and a locked particle.

$$g(v)=\frac{3\cdot(R_o+R_1-z)^2}{(R_o+R_1)^3-(R_o-R_1)^3}\cdot\frac{dz}{dv} \quad (7)$$

Combining Equation 2 with Equation 4 yields a derivable expression of $v(z)$. This derivation leads to a final expression of dv/dz with z the only variable. Neither the derivation nor the expression of the derivatire are reported in the paper. Since $dz/dv = 1/(dv/dz)$, by substituting this into Equation 7 it is possible to obtain the $g(v)$ as a function of variable z.

*For particle to be locked its center must fall in the volume $V_1=4\cdot\pi\cdot\{(R_o+R_1)^3-(R_o+R_1)^3\}/3$ (see **Figure 2**)

2); to have a pentration $Z<z$, its center must lie within the volume: $V=4\cdot\pi\cdot\{(R_0+R_1)^3-(R_0+R_1-z)^3\}/3$.

The above Equations do not permit a direct determination of the values of the functions G(v) and g(v) for a given value of v. The auxiliary variable z must be introduced. That is, for a given value of z, it is possible to calculate v,(Equations 2 and 4) and the corresponding values of G(v) and g(v) (Equations 5,6 and 7). With this procedure it one can draw the locking-profile.

By using the same method of deriving the locking-profile, but with the assumption of a flat interfacial surface, Meloy et al. (1987) have been able to eliminate the variable z and have obtained distribution functions directly dependent on v. This is possible because the assumption of a flat surface allows one to obtain expressions that are easier to handle.

When the values of G(v) or g(v) must be calculated for a specific value of volume fraction(v=K), a numerical method may be used by seeking the value of z that equals the function v(z)-K to zero; then the value of z is determined and substituted into expressions of distribution functions. Since the derivative dv/dz is known, this numerical calculation may be done using Newton's tangent method.

2.4 Calculation of the Ferrara Point

In a previous paper by Meloy et al (1987), the Ferrara-Point was defined as that point the coordinates of which are the mean volume grade of the locked particles, $v_F = \int v \cdot g(v) \cdot dv$, and the related value of the density function $g(v_F)$. The Ferrara-Point is a characteristic point of the locking-profile. It has the property of being invariant on passing from the locking profile expressed in volume fractions vs. v to that expressed in weight fractions vs. the reduced density δ. When the interfacial surface is flat, then $v_F = 0.5$, that is, the volume grade of the locked particles is 50%, and the locking-profile is a symmetrical curve. When convex inclusions are considered, the V_F values are less than 50% and vary with the ratio of particle to inclusion curvature. Moreover, in these cases the locking-profile becomes an asymmetrical curve.

Since the function g(v) is not known in an explicit form, a direct calculation of the Ferrara-Point by means of the integral reported above is not possible. The desired values may be obtained using the following procedure.

Since

$$v \cdot g(v) \cdot dv = v(z) \cdot f(z) \cdot dz \qquad (8)$$

then:

$$v_F = \int_0^1 v \cdot g(v) \cdot dv = \int_0^X v(z) \cdot f(z) \cdot dz \qquad (9)$$

The integral of Equation 9 may be solved numerically. Once v_F is known, the corresponding value of z may be found from Equations 2 and 4. This calculation has been performed numerically.

2.5 Calculation of the locking-profile as a function of density

The locking-profile as a function of the volume grade may be calculated by means of models that consider only the geometry of the system. This method may be used when methods of image analysis are employed in the experimental analysis of the locked particles.

In the laboratory, float sink tests are used. Data are presented as mass frequency distribution (mass vs. density fraction) or as cumulative mass frequency distribution. In this case, for the model to be applicable, it is necessary to find relationships between the volume frequency distributions and the mass frequency distributions. This may be done by using the reduced densities(3)*.

If $m(\delta)$ is the mass frequency distribution, g(v) the volume frequency distribution, δ the reduced density and v the volume grade of the particle, it is possible to convert volume data to density data by means of the following

*If s is the density, and s_L and s_H are the densities of the light phase and the heavy phase, respectively, a reduced density may be defined, Meloy et al. (1987), such that: $\delta = s/(s_H - s_L)$

simple relataionships:

$$g(v) = \delta/\delta_o \cdot m(\delta) \quad \text{and} \quad v = \delta - \delta_L \quad (10)$$

where δ_o is the mean density of the locked particles. for $\delta = \delta_o$ corresponding to the Ferrara Point we have $g(v) = m(\delta)$

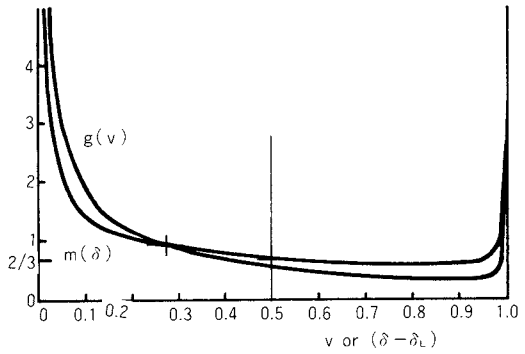

Fig.3 Mass and volume locking profiles for an inclusion-of-particle size ratio of 2.0. Ferrara Point:$v_F = 0.27$;g(v-)=0.91

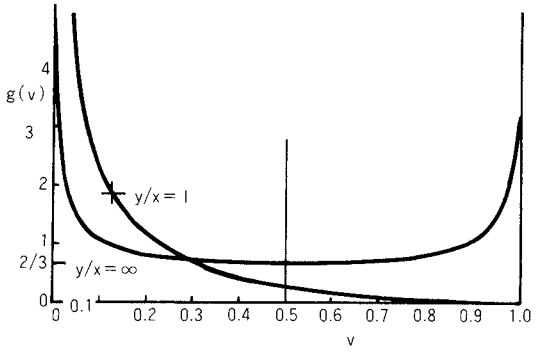

Fig.4 Volume frequency distribution, g(v), vs.volume fraction v, for two values of the inclusion-to-particle ratios. Ferrara Point:y/x=1, v_F = 0.13,g(v_F)=0.87;y/x=∞.v_F=0.50,g(v_F)=0.68

3. Results

In this section the effect of inclusion curvature and of the ratio of inclusion-to-particle diameter on locking profile, the Ferrara Point, the volume and density locking profiles and the movement of the Ferrara Point are examined. Four Figures are presented that summarize the data- **Figures 3** through **6** .

As the diameter of the particle approaches the diameter of the inclusion, the asymmertric nature of the locking profile becomes pronounced. This asymmetry of the locking profile is valid for both volume and mass locking profiles. **Figure 3** shows both the mass and the volume locking profiles for an inclusion-to-particle size ratio of 2.0. This same Figure shows that the Ferrara Point has moved from the 50% volume to the 27% volume point.

In **Figure 4**, two extreme inclusion-to-particle ratios are plotted. With a ratio of 1, the locking profile is highly asymmetric, while with a ratio of infinity, as would be expected, the volume locking profile becomes symmetrical. Note that the Ferrara Point position varies significantly with the change in the inclusion-to-particle size ratio.

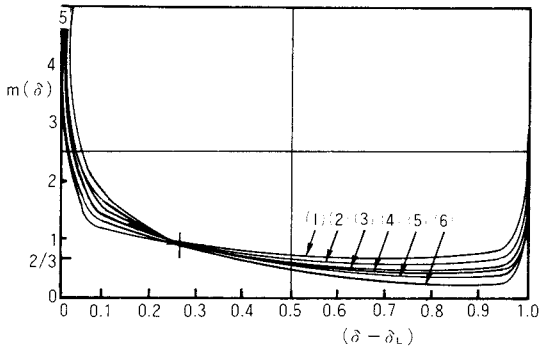

Fig.5 Variations of the locking profiles with reduced density δ_L. (1)δ_L=0.2,(2)δ_L=0.5,(3)δ_L=1,(4)δ_L=2,(5)δ_L=5,(6)δ_L=∞. Ferrara Point:v_F=0.27;g(v-)=0.91

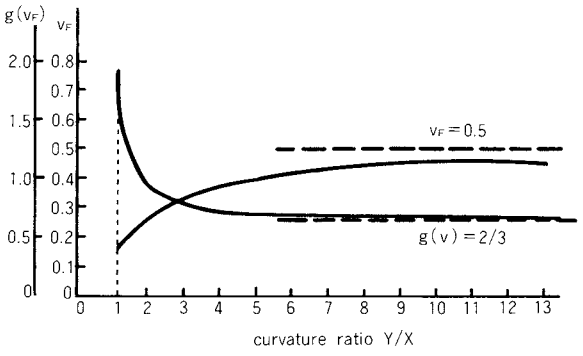

Fig.6 Positions of the Ferrara Point vs. inclusion-to-particle curvature ratios.

For flat interfacial surfaces, the volume locking profile is symmetrical but the mass locking profile is asymmetric. However, for curved interfacial surfaces the mass locking profile is, as expected, more asymmetric with the degree of asymmetry increasing as the reduced density δ_L increases. This variation may be seen in **Figure 5** . However, the Ferrara Point remains fixed for a given ratio of inclusion to particle size.

Since the Ferrara Point is the defining feature of the locking profile, its movement increases with a decrease in the inclusion-to-particle diameter ratio. **Figure 6** shows that with decreasing inclusion-to-particle diameter ratio, the Ferrara Point moves farther away from the 50% position on the locking profile curve. At the other extreme, when the diameter ratio approaches infinity, the volume locking profile becomes symmetrical.

4. Discussion

This discussion is divided into two parts: assumptions and results. While the assumptions and textural transforms were simple, they made the mathematics difficult. The results were not unexpected, however.

To derive the effect of inclusion curvature on the locking profiles, it was assumed that both the inclusions and the particles were spherical. Not only does this assumption avoid the problem of characterizing the shape of both the particle and the inclusion, but it also avoids the problem of defining the rotational orientation of the particle and inclusion in space. Because of complex geometries involved, closed solutions to the locking profiles were unobtainable, forcing one to use numerical methods.

However, after careful consideration, the authors have concluded that the assumption of spherical particles and inclusions is valid. Using oriented double pyramids and bicones yields, the same locking profile results. It is concluded that the results are valid for a wide range of particle and inclusional shapes.

This analysis is made possible by the use of textural transforms. These chaos-to-order geometric trasforms permit one to discard much of the textural data in a solid while retaining only those textural features relevant to the problem under study. Without textural trasforms developed by Meloy (1987) such analysis would not be possible.

Volume locking profile asymmetry becomes more pronounced the lower the inclusion- to-particle diameter ratio becomes. Thus, for the same size inclusions large particles have a different locking profile than the smaller particles. As particles become smaller, the locking profile asymmetry disappears and the profiles become the same as for flat interfacial surface.

Of all the findings the most unexpected was the wide movement of the Ferrara Point with variations in the inclusion to particle diameter ratio. Since the Ferrara Point is the defining parameter of the locking profile, its movement is significant in defining the shape of the curve and in characterizing the asymmetry of the volume or mass locking profile.

Since the Ferrara Point's position on the locking profile curve is sensitive to the amount of interfacial area curvature, the Ferrara Point's position may be used as a measure of the amount of interfacial area curvature present in an assemblage of particles. One could take the degree of deviation of the Ferrara Point from the 50% point as a measure of interfacial area curvature.

It would be desirable to develop an effective method of measuring the position of the Ferrara Point. Such a method is believed possible, and this possibility is under examination.

5. Conclusion

For large locked particles, curvature in the interfacial area affects the shape and asymmetry of their locking profile. The greater the interfacial curvature, the greater the deviation of from symmetry. As the asymmetry of the locking profile increases, so does the distance the Ferrara Point from its position on a symmertrical locking profile curve. Specifically, it was found that:

1. Curvature in the interfacial area between phases in a locked particle causes

an asymmetry in the locking profile curve.

2. For a fixed value of interfacial curvature, the larger locked particles have a more pronounced asymmetry in their locking profile curve.
3. As the particle size becomes small compared with the inclusion size, the volume locking profile curve becomes symmetrical, irrespective of the value of interfacial area curvature.
4. With increasing interfacial curvature the Ferrara Point moves increasingly from its 50% volume position on the symmetrical curve.
5. Because the Ferrara Point is sensitive to the interfacial area curvature, the Ferrara Point's position is a measure of the effect of interfacial area curvature.
6. A method is needed to measure the position of the Ferrara Poin.
7. Textural Transform is invaluable in solving Locked Particle Problems.

References

1) Ferrara, G.,Groppi, G.,Guarascio, M. and Preti, U., 1984. Sulla Liberazione dei Minerali mediante Comminuzione. Primo Seminario sulla Macinazione dei Minerali, Universita' di Trieste, Trieste, pp. 5-24.
2) Ferrara. G, Preti.U, and Meloy.T.P, 1989. Inclusion shape mineral texture and liberaion Int. Journal Mineral. Processing, Vol **27**,: 295-308.
3) Meloy, T.P.,1984, Liberation Theory-eight, modern, usable theorems. Int. J.Miner. Process., 13: 313-324.
4) Meloy, T.P., Preti, U.,Ferrara, G., 1987. Liberation-Volume and Mass Lockedness Profiles Derived-Theoretical and Practical Conclusions. Int. J. Miner. Process., **20**: 17-34.
5) Preti.U, Ferrara.G, Meloy.T.P, 1989 Characterization of the texture and liberation analysis of Minerals. 4th European Symposium Particle Characterization, N'u'rnberg, Vol.2, pp.579-598.

Air Classification : Computer Models and Experimental Results †

S.R de Silva *and* **D.C. Walsh**
POSTEC-Research *

S.T. Johansen *and* **T. Bergstrom,**
SINTEF. Div. of Metallurgy **

S. Bernotat
Inst. fur Mech. Verfahrenstechnik, T.U. Braunschweig * **

Abstract

Computer simulations of the flow fields in centrifugal air classifiers have been undertaken in order to improve both the performance and efficiency of the commercially available Acucut air classifier.

Although the simulations have led to a much greater understanding of the nature of the flow likely to prevail in such systems, accurate predictions have been found to be strongly dependent on the assumption of correct inlet flow conditions during the initiation of the simulations.

In spite of the fact that these simulations assumed axial symmetry (which is an oversimplification), they have enabled the identification of a number of engineering modifications which have contributed to reducing the cut size, and increasing the efficiency, of an Acucut Laboratory classifier.

1. Introduction and Program Objectives

The specifications for top sizes, especially for ceramics and fillers, have tended to become finer and finer - with a desire being expressed for top sizes around 1-3 μm and median sizes less than 0.5 μm. If produced by mechanical means, this type of top size requirement can only be achieved either by repeated grinding in wet mills or by allowing very long residence times in batch mills. Alternatively, however, such sizes can be produced by air classification-a method that is particularly attractive if a market also exists for the coarse fraction from the classification process. An air classifier capable of achieving these specifications is the the Acucut classifier, shown in **Figure 1.**

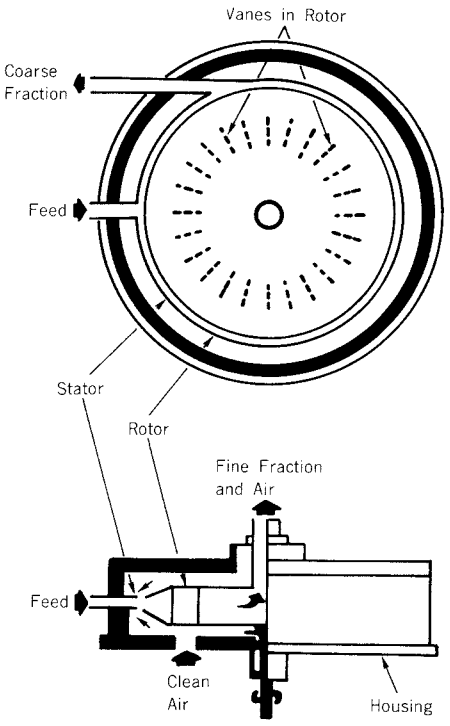

Fig. 1 The Acucut air classifier

* Porsgrunn, Norway
** Trondheim, Norway
* ** Braunschweig, Germany
† Received June 11th, 1991

It consists of a rotor, made of two dished plates separated by a blade cage, which produces a forced vortex flow field. The air flow through the rotor is produced by a Rootes type blower located downstream of the classifier. The classifying zone is restricted to within the rotor. The air flow enters the classifying zone through a very narrow gap between the rotor periphery and the stator. The original design required the air velocity in this gap to be maintained at between 60 and 110 m/s. This causes a highly turbulent dispersion zone through which the coarse particles and agglomerates must pass before reaching the coarse fraction exit. The air flow causes a high pressure loss in the gap, and the classifying zone is thus under negative pressure. This permits the feed to be sucked into the zone, via a converging/diverging nozzle, the throat of which is dimensioned to allow no more than 10%of the total air to enter the zone through this nozzle.

It is necessary that the entering feed material be accelerated to the rotational velocity of the air flow in order to prevent particles above a desired size from entering the blade cage. This is achieved in the expanding section of the rotor where the inward radial velocity is deliberately slowed down. The actual cut is intended to occur just outside the blade cage through which only those particles below the desired size are allowed to pass.

Three sizes of these units were originally developed. The rotor diameters were 300 mm(A12), 450 mm(B18) and 600 mm(C24). The two smaller units were capable of very fine cuts, but the efficiency of the units was highly susceptible to feed rates, as shown in **Figure 2.** Grade efficiency as used in this figure is given by,

$$T(x) = c * q_c(x)/q_F(x)$$

where c is the mass fraction of the feed reporting to the coarse fraction, $q_c(x)$, $q_F(x)$are the weight density distributions of the coarse fraction and feed, respectively.

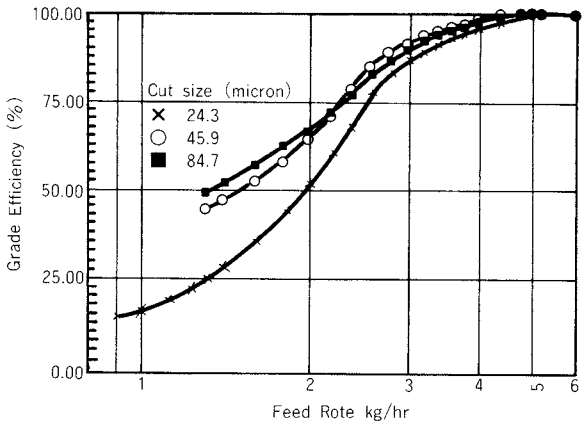

Fig. 2 Grade efficiency curves for an Acucut B18 with an increasing feed rate. Rotor speed 2000 rpm, airflow 340 Nm^3/h

Attempts were made to improve on this situation by both changing the method by which the feed was introduced [1] , and/or by increasing the air flow [2]. The first attempt involved introducing the feed via the top rotor plate, as shown in **Figure 3.**

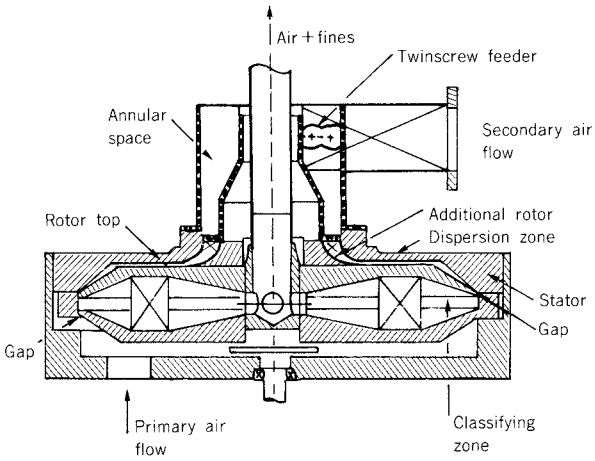

Fig. 3 Modified feed system for an Acucut B18 proposed by Leschonski and Boeck [1]

This modification was considered likely at the time to lead to unacceptably high rotor wear, although variations of it have been used in at least two new systems [4,5] . Furthermore, it nullified what was though to be one of the classifier's major innovations-the highly turbulent dispersion zone. The sharpness of cut results, however, were clearly better than

in the standard version, as seen in **Figure 4.** Y_F is the fines yield, and $K_{25\ 75}$ is the ratio of the sizes at which T(x)has the values 0.25 and 0.75.

De silva [2] demonstracted that it was also possible to maintain high sharpness of cut values at high loadings if the air flow was increaed, see **Figure 5**.

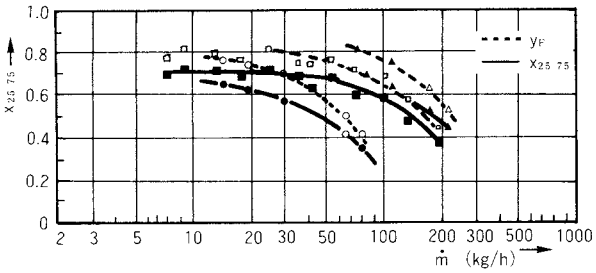

Fig. 4 Improved sharpness of cut obtained by Leschonski and Boeck using the modified feed entry shown in **Figure 3.** [1]

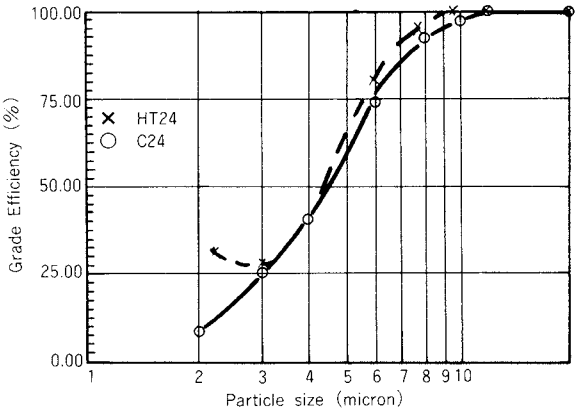

System	C24	HT24
Feed	Limestone	
Feed Rate.(kg/h)	375	1900
Rotor Speed(rpm)	1600	2100
Air Flow (m^3/h)	1275	2210
Production(kg/h)	140	570
Recovery (g)	70	50

Fig. 5 The effect of higher air flow on the grade efficiency. Acucut model C. (HT stands for high throughoput, and the machine is identical to a model C)
------ = 1900 kg/h, 2210 m^3/h, 2100 rpm
——— = 375 kg/h, 1275 m^3/h, 1600 rpm

It is, however, clear that fine fraction recovery is reduced at these loadings, although the rate of production was increased four-fold.

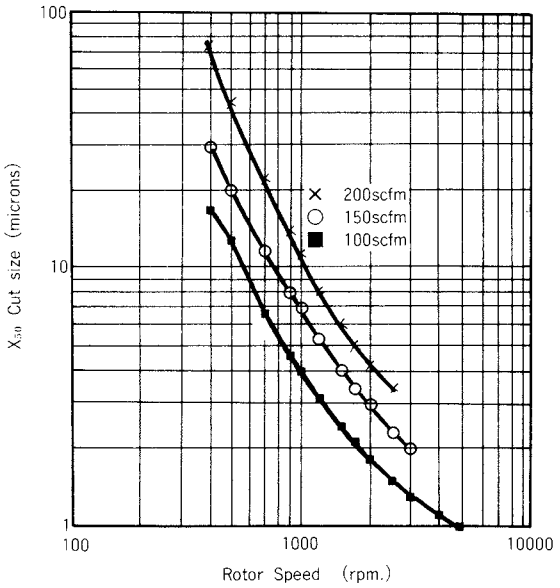

Fig. 6 Cut size as a function of rotor speed and air flow for an Acucut B18 air classifier

Increasing air flow also leads to very high pressure losses in the rotor stator gap-and simultaneously leads to coarser cuts as shown in **Figure 6.** Thus the rotor speed has to be increased to compensate-leading to still higher pressure losses.

This then was the point of departure for the development program. The aim was two-fold. First, to determine whether computer modelling could be applied to improving our understanding of the flow fields in the classifying zone, and secondly to determine whether engineeing modifications could be carried out to obtain improved efficiencies and lower cuts predicted by the model. It was always realized that simulations and experiments must be carried out sequentially, the results from the one to be used to improve those from the other on an on-going basis.

2. Preliminary Simulations

The preliminary simulations used the model geometry shown in **Figure 7,** and the turbulent modelling program Fluent (TM).

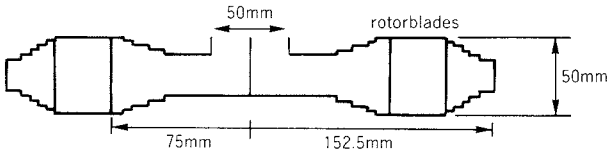

Fig. 7 Model geometry used in the computer simulations of the flowfields in an Acucut A12 classifier

The mathematical model used solves the Navier-Stokes equation using the well-known K-ε model.

The particulate phase is described by continuity equations for five simultaneous size classes where the particle velocities are calculated from the gas velocity and their settling velocity in the centrifugal field. The model entirely neglects interparticle collisions and agglomeration effects. Furthermore, one has to make an assumption regarding what happens to particles which reach the system boundaries (the rotor plates). Either one can assume that these particles leave the system as the coarse fraction, or we can assume that no deposition occurs. The reality is likely to be somewhere in-between with particles reaching the rotor plates gliding along them inside a wall boundary layer as a result of the strong centrifugal forces.

The existence of relatively large particle concentrations will alter the mean flow and dampen the turbulence in the classifier. These effects can only be allowed for by guess-work. Full details of the assumptions made in the modelling are found elsewhere [3] .

The grade efficiency curves are calculated by calculating the particle concentrations for a sufficiently large number of particle sizes. The grade efficiency for each size class is then calculated from the mass flow of particles reaching the fines exit.

The equations were solved using standard finite difference techniques, and the geometry of the classifier was represented by a polar coordinate system. This causes some inaccuracies at the walls where the grid lines are not parallel to the wall and yield irregularities where none, in fact, exist.

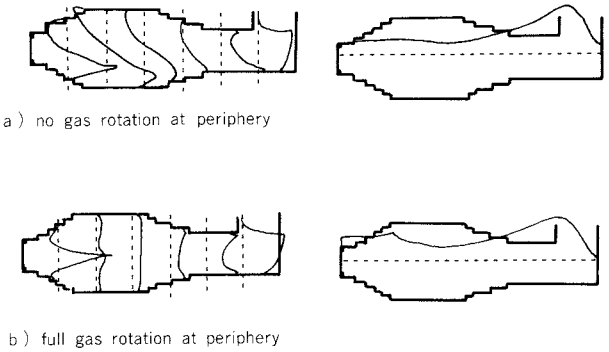

Fig. 8 Distribution of radial velocity contours (left)and tangential velocities(right) at 2000 rpm and 100 m^3/h. Main flow is from left to right.

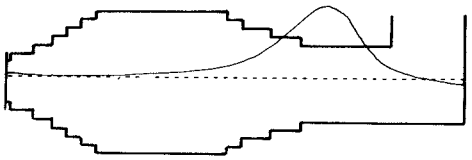

Fig. 9 Concentration of 4μm particles along a radius, predicted by the model. Rotor speed is 2000 rpm, air flow is 100 m^3/h.

The results are shown in **Figure 8** in the form of tangential velocity distributions and radial velocity contours. **Figure 8** a) shows the case when the simulations assumed no rotational velocity at the rotor periphery, while **Figure 8** b) shows the results when full rotational velocity was assumed. What was more interesting was the result shown in **Figure 9** for the concentrarion of 4μm particles along a radius.

If it is assumed that the cut occurs at the periphery of the blade cage, All 4 μm particles should pass through the blades. **Figure 9** shows that they do, but that they are unable to reach the outlet. The reason lies in the nature of the vortices in the rotor. These simulations indicate that a forced vortex(V_ϕ/r=const.)only exists within the rotor blade cage, whereas free vortices($V_\phi r^n$=const.) exist outside. Thus V- increases from the inside diameter of the blade cage to the exit thus increasing the centrifugal force (V_ϕ^2/r) acting on the particles and preventing them from

moving inwards.

3. Modified Rotor Design

The simulations led to certain modifications being carried out to the rotor. One of these was the extension of the blade cage all the way to the outlet. This was intended to ensure that no free vortex was set up inside the blades. Secondly, a set of studs were machined on to the outer periphery of the two rotor plates on the outside. These, it was hoped, would ensure that the flow fields of Figure 8b) rather than those of Figure 8a) would be obtained.

Third, the cross section of the rotor was reduced from the point where the original blades ended towards the centre. This would further help the rapid removal of fines by increasing the inward velocity of the air flow to a greater extent than in the previous rotor.

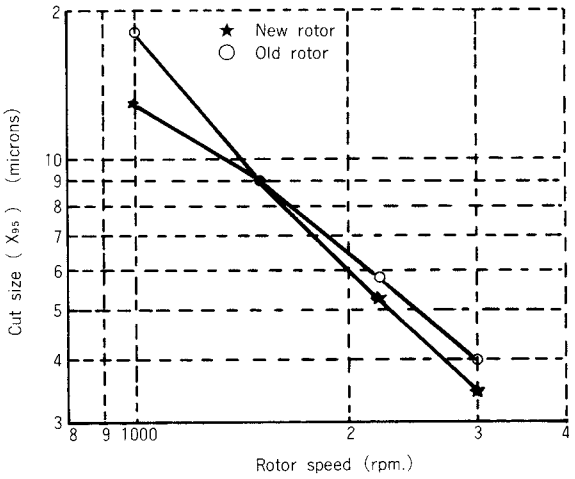

Fig. 10 x_{95} versus rotor speed for the old and new rotors

The results were mixed. The variation of the x_{95} values with the rotor speed for the old and new rotors is shown in **Figure 10,** while the fines recovery against speed is shown in **Figure 11.** The fines recovery is defined as

$$R(x)=f * q_f(x))/q_F(x)$$

where $q_F(x)$and $q_f(x)$are the weight density distributions in the feed and fines, respectively, and f is the fraction of the feed entering the fines. There is almost no noticeable improvement in performance.

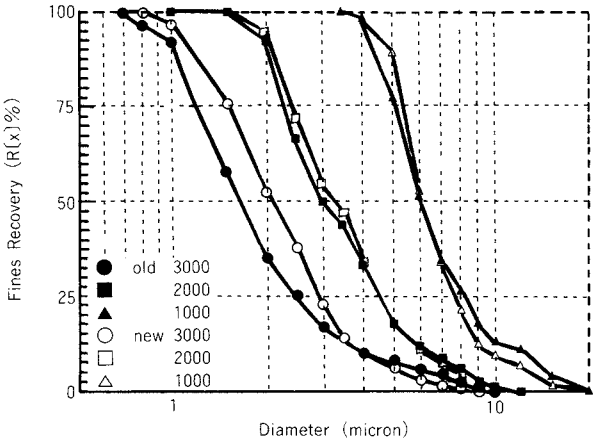

Fig. 11 Fine fraction recovery against rotor speed for the old and new rotors

These results indicated one of two things. Either the simulations were not really reflecting reality, or the conditions necessary to produce the desired flow fields were not achieved. Further simulations were therefore performed.

4. New Simulations/Results

The new simulations used the geometry of the modified rotor as shown in **Figure 12.**

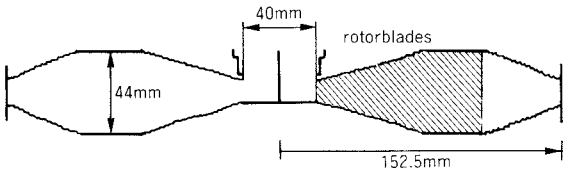

Fig. 12 Rotor geometry used in the new simulations

The critical points for which answers were sought were a) does the flow actually rotate at the rotor periphery, and b) is there really a build up of particles within the rotor blades when the blades do not extend to the centre. The simulations and experiments lasted nearly a whole year. Many conflicting results were obtained which led to a thorough inves-

tigation of the experimental procedures. Gradually, the experiments and simulations began to show increasingly good agreement. Some special modifications were carried out to ensure that the most promising boundary conditions were in fact also being obtained in practice.

Figure 13 and **14** show the decay of the rotation as the air flow passes through rotor/stator gaps of 200μm and 1000μm, respectively.

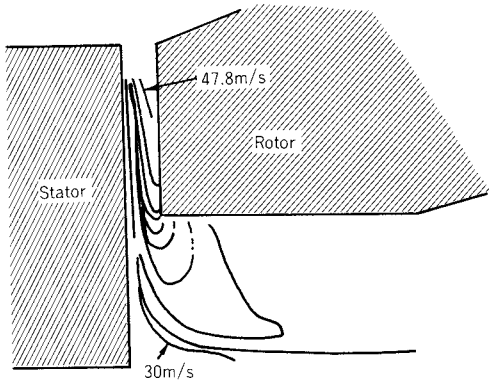

Fig. 13 The contours of tangential velocity as a rotational air flow passes through a 200μm rotor/stator gap. Rotor tip velocity is 47.8 m/s(3000 rpm)

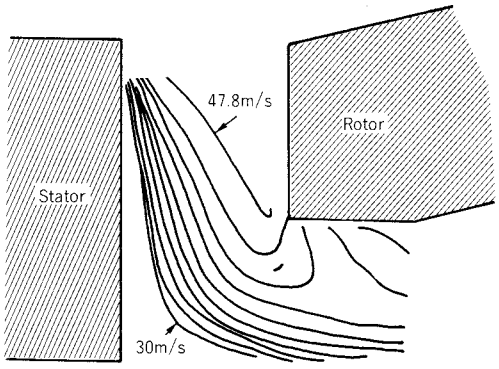

Fig. 14 Contours of tangential velocity as a rotational air flow passes through a 1000μm rotor/stator gap. Rotor tip velocity is 47.8 m/s(3000 rpm)

The figures demonstrate that the rotational velocity imparted to the air on the outside of the rotor is significantly reduced in the rotor/stator gap. On the Inside of the rotor the actual tip speed of 47.8 m/s decays to

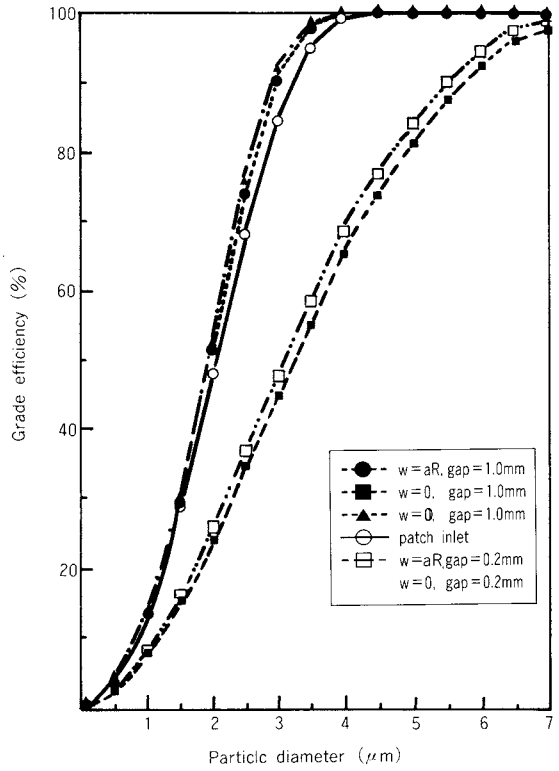

Fig. 15 The effect of the assumed tangential velocity at the rotor periohery on the grade efficiency curve

30 m/s within 1 mm of the inner rotor plates-regardless of the width of the gap. **Figure 15** confirms that the width of the gap does not play any significant role in determining the top size in the fines, while the actual tangential velocity at the periphery very certainly does.

These results demonstrate that, somehow, the peripheral velocity of the rotor must be transmitted to the air flow, well inside the rotor, in order to maintain top size control.

The next question was the effect of the rotor blades on the flow field. As mentioned earlier, it was found that if the inner diameter of the blade cage was 150 mm, then the forced vortex produced within the blades degenerates into a free vortex and prevents particles, which pass the blades, from leaving the classifier. Extending the blades to the centre outlet (inner diameter of the blade cage is 40 mm) was expensive in terms of rotor manufac-

turing and it did not appear to give any improvements in performance. **Figure 16** shows the concentration profiles of 2μm particles for inner blade cage diameters of 40, 60, 80 and 150 mm. The figures show no build up expect in the last of the above. This figure is not strictly comparable with **Figure 9** since in that case the simulated rotor speed was 2000 rpm(size penetrating 4μm), whereas in **Figure 16** the penetrating size is 2μm(rotor speed is 3000 rpm).

Thus, it appears that some leeway is available in designing the blade cage. It was also calculated that the pressure loss over the rotor increased from 5.7 kPa to 13.7 kPa when the inner diameter of the blades was increased from 40mm to 150mm. Experimental results confirm that there is a reduction in the pressure loss with the new rotor - but mainly at high rotor speeds. We have obtained reductions of more than 50% under otherwise identical condition (c.f. **Figure17**). These savings are quite significant when operating at very fine cut sizes.

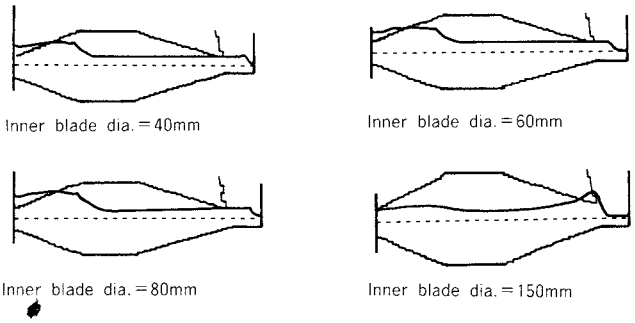

Fig. 16 Concentration of 2μm particles along a radius. Rotor speed is 3000 rpm, Air flow is 100m^3/h

The above simulations led to further rotor modifications which cannot yet be revealed but the results of which are presented in the next section.

5. Results after Second Rotor Modification

The results after second set of modifications are quite clearly better, as shown in **Figure 18.** It is clear that much better top size control has

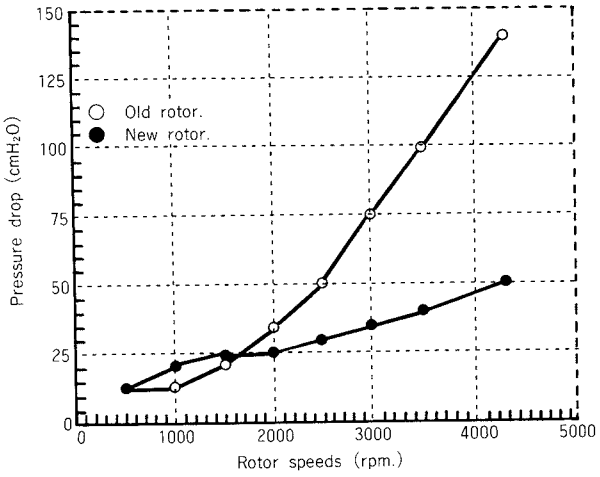

Fig. 17 The influence of rotor speed on pressure drop across the classifier for old and new rotors after modification

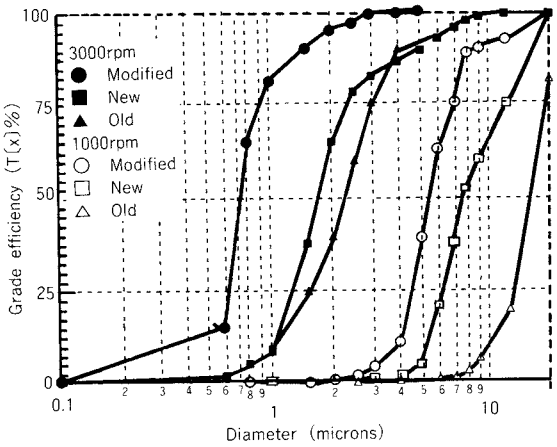

Fig. 18 Comparison of results from a)old rotor b)new rotor(after first modifications)and c)modified new rotor(after second set of modifications)

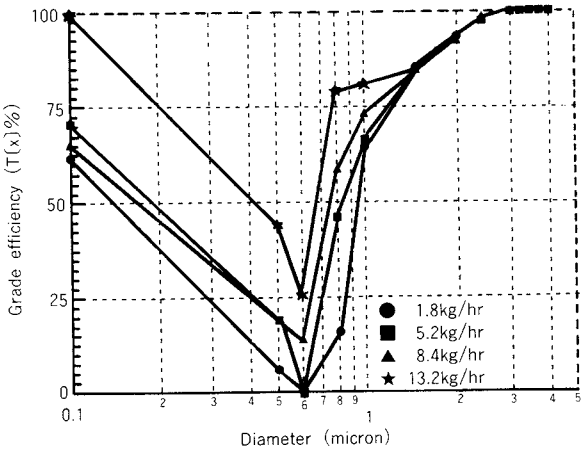

Fig. 19 The effect of loading on the grade efficiency curves at 3000 rpm and 110 -/h

been achieved, and top sizes of 2μm appear well within reach.
The problem of loading has, however, not yet been solved. The classifier still shows sensitivity to feed rate, and efficiencies deteriorate at loadings over about 0.05 kg/kg (**Figure 19**).
The reduction of the pressure loss over the classifier will, however, allow the use of higher air flows and higher rotor speeds. We are working on further modifications to improve the ability of the classifier to handle larger loads and will also try out external dispersion to effect further increases in performance. The predicted and experimental grade efficiency curves now show a reasonable agreement (**Figure 20**), and we expect complete agreement to be achieved when the simulations are extended to three dimensions, and the effect of particle loading on the flow is fully accounted for.

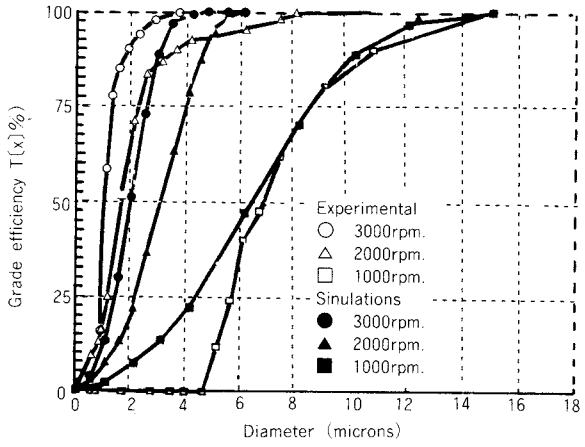

Fig. 20 Predicted and experimental grade efficiencies at 3000, 2000 and 1000 rpm. Air flow is 110 m^3/h

6.Conclusions and Future plans

Computer simulations are viable means of improving the performance of process equipment in which complex flow fields are encountered. It is, however, necessary to constantly compare model predictions with experimental results in order to ensure that the boundary conditions used in the model are achieved in practice, either by modifications to the model or to the piece of equipment. This requires a close cooperation between the experimenter and the modeller, with each being required to acquire an insight into the possibilities and limitations of the other.
of the other.
It is expected that still better agreement between models and experiments will be obtained when the simulations are extended to three dimensions. We are also working on a curved coordinate system which will fit the boundaries of the classifier better than the grid used in these simulations. Finally, we expect to incorporate an improved model for particle momentum which will allow for particle-particle and particle-wall collisions.

Acknowledgement

The authors wish to express their gratitude to the Nordisk Industrifond for providing a large part of the financing for this project, the NTNF for the award of a DEMINEX Fellowship to Dr. Bernotat to visit Norway for six months, and the many Nordic industries who have provided both financial and moral support during the slow progress we have made.

References

1) Leschonski, K Boeck, T: "Die Bedeutung des Dispergierens und Dosierens bei Feintrennung in Windsichtern" Europ. Sym. Particle Technology Amsterdam(1980), 746/761
2) de Silva, S.R.: "Neue Windsichter zur Herstellung Superfeiner" Fullstoffe Chemie Technik **8** (1979)5, 219
3) Johansen, S.T. Anderson, N.M. de Silva, S.R.: "A two Phase Model for Particle Local Equilibrium Applied to Air Classification of Powder" Powders Techn.(1990)
4) Yamada, Y.: "Effect of Circulating Mechanism on the Air Classifier." Powder & Bulk Solids Conference, Chicago(1989).
5) Tilger, J. Heidenreich, E.: "A new Classification Principle for the Particle Size range d $<5\mu$m." Part. Part. Syst. Charact. **8** (1991)8-11

New Wet Classitication Hydrocyclones for Fine Mineral Slurries †

Kari Heiskanen
Laboratory for Mineral and Particle Technology, Holsinki University of Technology *

Abstract

Wet clasification has been challenged by the needs of the industry to produce finer and finer powders in slurry form. Hydrocyclones have maintained their position as the most important classifiers in wet mineral processing. Due to the recent developments in hydrodynamic modelling, the understanding of the flow phenomena has become rather clear and has allowed the design of hydrocyclones suitable for special purposes. New cyclones have good separation efficiencies and low imperfection values.

1. Introduction

This paper will discuss the lastest developments in hydrocyclones for mineral slurries.

With specifications of mineral powder slurries becoming more stringent, the important of a well controlled product has become more important. The particle size distribution should be enginnered to suit the following process that utilizes the produced slurry. Comminution alone is seldom enough to ensure that the product conforms to a desired specification, and it is often very difficult to control with respect to maximum particle size and even more so with respect to size distribution form. Classsification offers a way of influencing both the size and the shape distribution.

Particle size distributions can be altered with classification by separating a small fraction of fines to overflow (desliming) or by classifying a small fraction of coarse away (degritting). For many products the particle size is such that wet classification is not suitable for desliming effectively as the particle sizes to be separated are beyond the possibilities of existing wet classifiers at any higher pulp density. Degritting, on the other hand, is a viable process for improving product quality and /or saving energy in production by combining a coarser grind with degritting.

The aim was to obtain a small hydrocyclone with a high separarion efficiency and a good "degritting" ability at fine sizes. ("Degritting" in this case is to separate particles over 10-15μm)(Heiskanen, Vesanto 1990).

Small diameter hydrocyclones have been developed for fine paricle separation from the 1950's, and since then, cyclone geometries have been studied in detail. The disadvantages of the cyclones still prevail. The separation efficiency decreases when the cut size become finer because of the high bypass flow of liquid to the underflow.

Hydrodynamic modelling with the program FLUENT was used extensively to find solutions to design details like orifice openings and gap geometry of the lower washing section.

* SF-01250 Espoo, Finland.

† Received July 8th 1991.

2. The TC-cyclone

Many attempts have been made to improve the efficiency of an ordinary hydrocyclone. Changes in the cyclone geometry have been tried and special design hydrocyclones introduced. One obvious way of improving cyclone performance and obtaining a clean underflow is to reduce the by-pass by replacing fines containing water in the underflow by clear water (Kelsall and Holmes 1960). These modifications
75-600 mm diameter hydrocyclones operating in grinding mill circuits. Most of such modifications disturbed the flow field in the lower parts of the cyclone thus producing as expected a clean underflow but as an unwanted effect a coarser d_{50} and coarse particles in the overflow. The original Twin Vortex (TC) cyclone was developed to avoid excess flow field disturbances and to operate mainly in coarse grinding circuits. The Twin Vortex cyclone is made of two parts. The primary part of the TC-cyclone consists of an upper part of an ordinary hydrocyclone with its feed and overflow orifices and the cylindrical body and the vortex finder. The conical part of an ordinary hydrocyclone is replaced with a cylindrical part having a larger diameter than the cyclone main body has. This is the washing section. This cylindrical washing section has a central adjustable cone and tangential water addition holes in it. Coarse material entering the washing section from the gap formed between the cone and the body leaves tangentially from the side of the washing section to enter the second part of the TC-cyclone, which is essentially a normal hydroyclone with a geometry such that it separates a fine dilute overflow.

Commercial TC-cyclones from 80 - 500 mm in diameter have been found to operate with a higher efficiency and with a lower pressure drop than normal hydrocyclones (Heiskanen et al. 1987).

3. Hydrodynamic modelling

The classic paper of Kelsall (1952) described what was probably the first experimental study of the flow pattern inside an hydrocyclone. The results have been quoted often since. During the last decade, more detailed and accurate information related to specific designs has started to become available in the literature. There have been two reasons to this newly increased interest in studing cyclone fundamentals. First, computer algorithms and computer calculation power have developed so that the complete Navier-Stokes equation together with equations of turbulence and particle-fluid interactions can be numerically solved for different boundary conditions and different geometrical forms. The other reason is the advancement of sophisticated measuring instruments. Laser-Doppler anemometry allows accurate measurement without interference of all of the flow components at the chosen points of a hydrocyclone. Experiments conducted by Rajamani and Hsieh(1988a, 1988b, 1988c) confirm the basic flow pattern already measured by Kelsall but give a far more detailed picture of the flows. The same by the independent measurements of Gu and Li (1987).

Rietema (1961) used a solution of the Navier-Stokes equation when developing equations describing cyclone pertormance. The first ones to use computers to simulate flow in Rietema (1961) used a solution of the Navier-Stokes equation when developing equations describing cyclone performance. The first hydrocyclones were Bloor and Ingham (1973). In simplifying the equations to be able to solve them numerically, they assumed inviscid flow and simplified the assumption on turbulentic eddies.

Later, there was an increasing number of attempts to simulate hydrocyclones by solving the complete Navier-Stokes equation numerically. Boysan (1984) describes the mathematical modelling of gas cyclone separation. He has validated the results with the laser Doppler velocimetry data reported by Escudier (1980). Pericleous and Rhodes (1986) have used a computer code called Phoenics to solve a two dimensional case. This code assumes the flow to be steady, two-dimensional and axially symmetric. Equations were solved for continuity, momentum and species concentration. The solid particles

in the hydrocyclone were represented using the equations for species concentration, each equation modelling a particular size range of the said particle. Source terms were included in these equations to simulate the particle's relative velocity from the centrifugal and drag forces. They took into account the fact that as particle concentration increases, the particle and the fluid equations become interdependent due to changes in the mixture density and effective viscosity. The first results were validated with Kelsalls data. The movement of particles was modelled by using an algebraic slip approach, and the turbulence was modelled with a simple mixing length model. A later report by Rhodes, Pericleous and Drake (1987) has also given results that are similar to those obtained experimentally by Kelsall. Another computer code which has been used successfully is a code named Fluent (Johansen 1990, Johansen et al. 1990a, 1990b). Both of these codes are based on a finite element approach and usually assume rotational symmetry at least for the main body of the cyclone. Johansen has used the Algebraic stress model for turbulence. He and his co-workers use five particle-size classes a the algebraic slip approach for particle liquid relative movement.

Rajamani and Hsieh (1988a, 1988b, 1988c) have also used a similar technique to obtain a numerical solution. The turbulent viscosity was modelled by the unidirectional Prandtl mixing length model. Their study is among the first comparing Lasser-Doppler velocimeter experiments with computational results in wet hydrocyclones. The experiments were done with a glass cyclone immersed in a water bath. The computational tangential velocities showed a rather good correlation with the measured values as did the axial velocity. The radial velocity component was correct in its form.

The solution depends greatly on the mathematical model chosen to simulate turbulence. The often used k-ε model is not suitable for hydrocylones due to the effects of high swirl(Pericleous et al. 1986, Johanssen et al. 1990). The results of Boysan(1984)show that the k-ε model for the turbulentic viscocity does not give good predictions especially for the tangential velocity component. Most researchers have used the mixing length theory, but Johansen has used the Algebraic stress model. Duggins and Frith(1987)have modified the k-ε model to incorporate two different turbulent viscosities both varying in magnitude across the flow field. The viscosities for axial and radial momentum equations are calculated from the basic k-ε model and the viscosity for the tangential momentum equation from a mixing length expression.

The main problem in the hydrodynamic modelling of mineral pulp hydrocyclones is the fact that particle/particle interactions are not well understood from the theoretical point of view. Another very important point affecting the results is the definition of the boundary conditions.

The results of different research show that hydrodynamic simulation can be used to estimate the form of the flow field rather well in the lower part of a hydrocyclone operating at low solids content. The exactness of the result depends very much on the boundary conditions and the solids concentration. From experience one can say that in its present state hydrodynamic modelling can be used to spot"points of interest". It can identify with reasonable accuracy areas with elevated turbulent energy, flows which decrease the efficiency of classification, etc. As an example **Fig.1** is given. It shows the flow velocity vectors of some small cyclone designs at the vortex finder. As can be seen from fig.1, Fluent program predicts an eddy flow at the cyclone roof from the inlet opening towards the vortex finder and then down the vortex finder wall. The same can be found in the experimental results of Hsieh and Rajamani (1988a). It must be noted that the cyclone diameter was only 10 mm so that the thickness of the vortex finder was a more important variable than in the larger hydrocyclones. The results also show that the form of the vortex finder tip may induce a turbulentic eddy close to the tip.

With the programs the computation of separation efficiency is quite tedious and time consuming, but they yield reasonable results

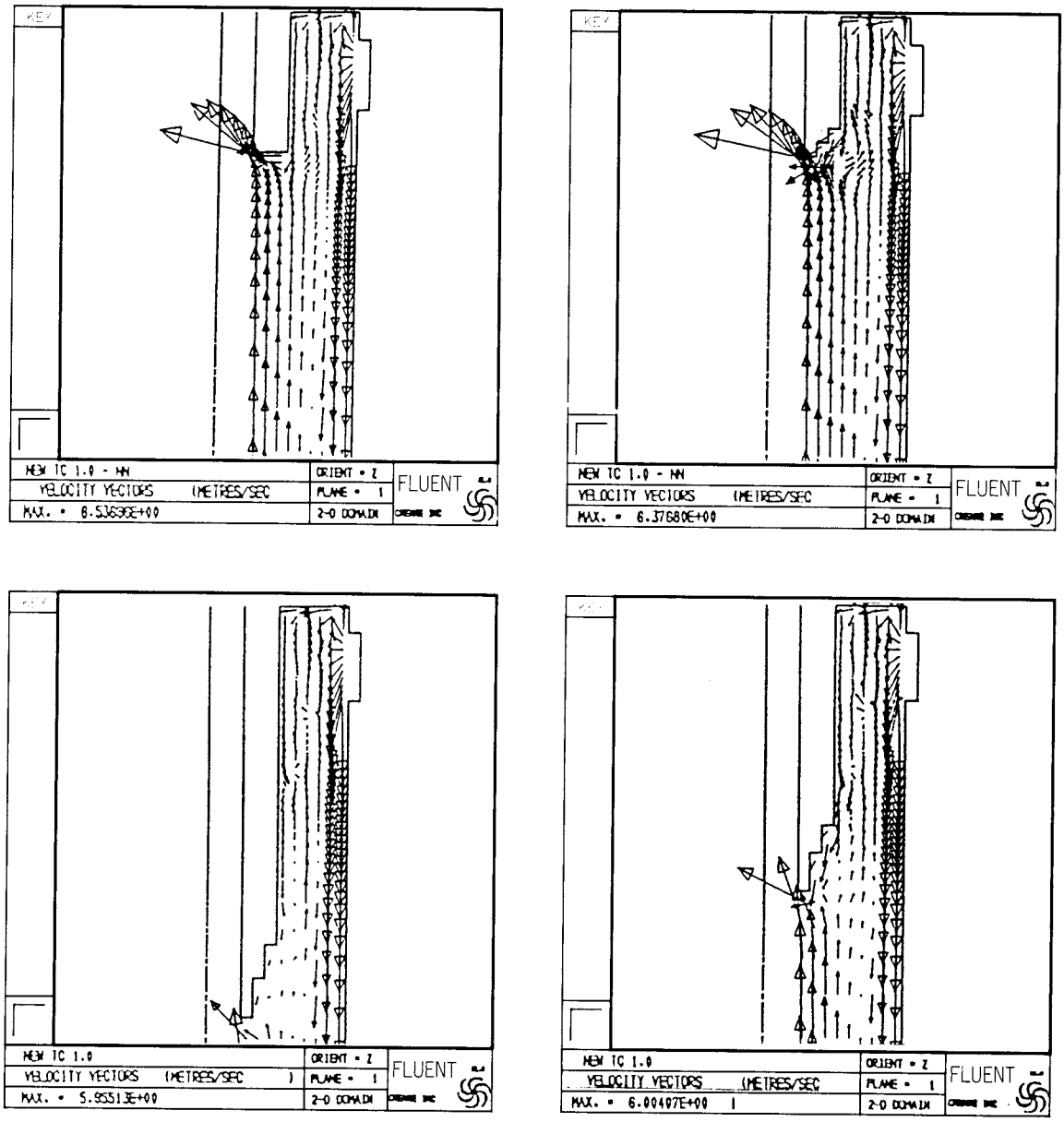

Fig. 1 Flow field predictions for the 10 mm TC-hy drocyclone.

at low pulp densities. It became clear during the simulations of this work that the predicted separation efficiency curve started to deviate from the experimentally obtained values when the feed solids fraction was above 5%v/v.

4. The miniature TC-cyclone

The computational assumptions made by Johansen using the commercial code Fluent has been used to develop a set of new small hydrocyclones 10, 25 and 50 mm in diameter. They were developed from an original design called the Twin Vortex hydrocyclone (TC) which was designed for coarser cuts and larger diameters (Heiskanen K.et al. 1987, Heiskanen K., Ovaskainen P., 1988).

In larger TC-cyclones the separation limit was determined almost entirely by the first stage. It was also clear from previous studies that the rate and the way of wash water injection played a crucial role in primary cyclone operation, both its cut size and its efficiency.

If a similar flow pattern and particle trajectories could be scaled to smaller sizes the small TC-cyclone could have a low by-pass, a small amount of fines in the coarse

stream. A somewhat coarser cut-size would result in a better imperfection than in an equivalent ordinary cyclone. In small scale cyclone, the effects of turbulence and the wall effects become more important than in a larger unit. Therefore, the points of interest in scaling down were the feed inlet and the upper cylindrical part above the vortex finder. Another point of interest where these wall the gap between the cyclone cylindrical body and the counter cone of the wash water feed arrangement.

The computational grid used was more dense at the feed and at the wash water section. (**Fig.1**) All the flows below the vortex finder were assumed to be rotationally symmetric. Different designs were evaluated by computing the separation efficiency curves. Grade efficiency curves were calculated by calculating the trajectories of 1000 particles in each size fraction. The best computational designs were manufactured and tested to obtain a cyclone design that fulfilled the requirements. **Figure 2** shows computed separation efficiency curves for different wash water designs.

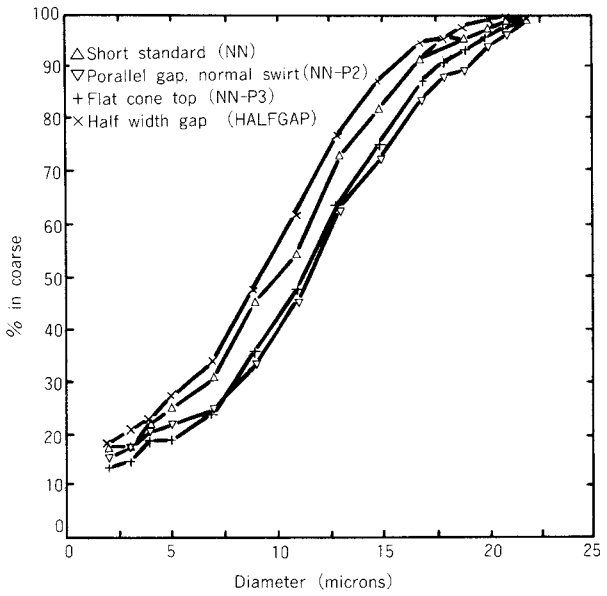

Fig.2 Computed separation efficiency curves of different wash water designs.

The geometry of the upper part with its feed and vortex orifices was computed first by classical methods to save expensive Fluent computations.

Many different scale-down (up) methods have been presented to determine the geometry of the hydrocyclones to operate in the different applications. The methods given by Plitt (1971,1976), Yoshioka and Hotta (1955) and also Lynch and Rao (1975) are often used for this purpose. The geometries derived from these mathods were not considered very suitable as the starting point to scale down was a high feed solids situation and the scale down factor from larger TC-cyclone was too large.

Matcshke and Dahlstrom have discussed a scale-up method for 10 mm to 50 mm hydrocyclone (1958,1959). Also the results of Haas et al. (1957) for 0.16 to 0.50-in hydrocyclones and the model published by Svarovsky (1987) were used for the scale-down method. Some designs obtained from these methods were simulated with Fluent. The chosen initial geometry of the upper part of the small diameter TC-cyclone was quite close to the geometry discussed by Rietema (1961). The lower part of the small TC's were extensively simulated using Fluent with emphasis on the wash water section.

Nomal commercial cyclones were used as secondary cyclone. The obtained cyclone design was mechanically designed to allow feed pressures up to 16000 kPa and slurry velocities up to 20 m/s in the feed orifice.

5. Test procedure and equipment

TC-cyclones of 10 mm, 25 mm and 50 mm diameter, which were dimensioned with the methods described above, were tested using different feed slurries. During the tests hydrocyclone of ordinary geometry were used for comparison. Cyclones were constructed of steel and polyurethane, and no transparent models were fabricated.

All tests were carried out in a hydrocyclone test rig which consists of a mixer, a slurry pump and connections for cyclones. Operational parameters, flows, by-pass, grade efficiency, cut and particles size were recorded

during the tests. The test materials used were limestone, talc and kaolin. These materials were selected due to their use and their particle form. The mean particle size of feed varied from 5 to 20 μm.

The grade efficiency curve was determined as the probability of the coarse particle in order to report to the final underflow combining both overflows in the calculation. The reduced report to the final underflow combining both overflows in the calculation. The reduced grade efficiency curves were also calculated but they did not differ significantly from the unreduced curves for the TC-cyclones. The cut size, d_{50}, of a TC-cyclone and of an ordinary hydrocyclone was defined as the particle size at 50 % on the grade efficiency curve.

The efficiency of the separation was determined as an inperfection value

$$I = (d_{75c} - d_{25c})/2 * d_{50c}$$

where d_{25c}, d_{75c} and d_{50c} are defined from the reduced grade efficiency curve.

Another method for determining separation efficiency was the sharpness index given by Eder(1961):

$$Et = d_{25c} / d_{75c}$$

The pressure drops were measured with water using different feed flow rates and using different feed, overflow and underflow orifices. The pressure and volume flow of wash water had to be taken into consideration when the volume capacities of TC-cyclones were compared to those of ordinary cyclones.

Size distribution measurement was problematic. A Coulter Counter Multisizer was used to measure the coarser end of the distributions, but even with a 15 μm orifice tube the method could not be extended to fine enough sizes due to electronic noise. X-ray sedimentation was used to record the main part of the distribution. The finest end of the distribution is not very accurate due to Brownian motion and convection. Other methods like far-field laser diffraction and photon correlation spectroscopy were not deemed suitable for these rather broad and fine distributions.

6. Results

6.1 Capacity

The need of wash water of a TC-cyclone was found to be from 10 to 30%of the feed flow. The pressure of washing water had to be from 0.8 to 1.1 times the feed pressure. These results were similar to the results larger TC-cyclones(Heiskanen et al 1987).

A small TC-cyclone had a slightly higher feed flow rate than an ordinary hydrocyclone of the same size. The difference was 10-20% depending on the wash water addition and geometry of the TC-cyclone. **Figure 3** shows the pressure drop versus volume capacity of different size TC-cyclone.

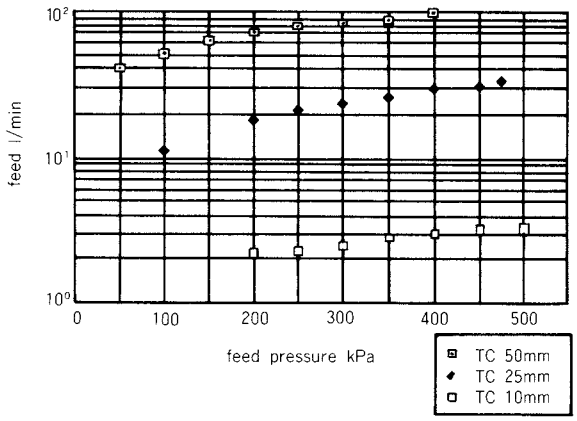

Fig.3 The volume capacities of small TC-cyclones.

6.2 The cut size and size distribution

It could be expected that the cut size would be coarser in a small TC-cyclone than in an ordinary cyclone due to the form of the locus of zero vertical velocity. In all tests the cut sizes were indeed coarser with the same pressure loss and capacity.

The d_{50c} values for a 50 mm TC-cyclone varied from 18 to 48 μm while those of an ordinary hydrocyclone were between 13 to 28 μm. With 25 mm cyclones, the variation was respectively from 16 to 24 μm and from 12 to 24 μm, and with 10 mm cyclones it was from 4.9 to 12.9 μm for a TC-cyclone and from 3.4 to 10.5 for an ordinary hydrocyclone.

The cut size depended not only on the geometry but also on the amount of wash water.

The effect of the wash water rate was so strong that the total cut size could be changed during operation by changing the wash water flow.

Figure 4 shows the change in the cut size of the first stage of a 10 mm TC-cyclone when the amount of wash water varied from 14 to 38 % of the feed flow.

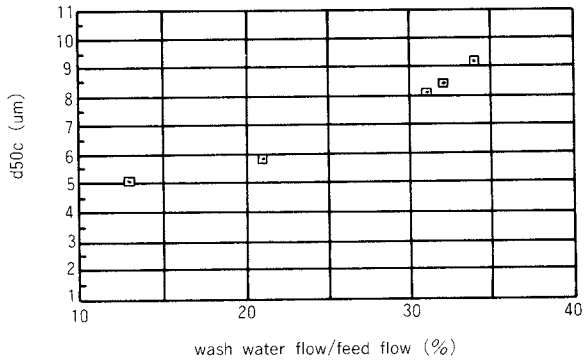

Fig.4 The effect of wash water on the cut size in the first stage of a 10 mm TC-cyclone.

The form of LZVV was expected to cause an overflow with a coarse tail ie. small amounts of particles in the range of 3-5 times d_{50c}, but no such phenomena was found. Typically, in an ordinary cyclone with a 5 μm cut size the amoun of larger than $3 * d_{50c}$ was 6-12% and larger than $5 * d_{50c}$ was 0.1-0.2%. The corresponding amounts were typically for $3 * d_{50c}$ 0.2-0.4% and for $5 * d_{50c}$ 0.0% for a TC-cyclone. When classifying the same material, this meant that both had the same amount of +10 μm particles or that the TC-cyclone had less of those even if the TC-cyclone had a coarse d_{50c}. **Fig. 5** shows a classification test made with a fine talc slurry. The overflow product of the TC-cyclone is slightly coarser than that of an ordinary cyclone. The underflow of the TC-cyclone is remarkably coaser containing much less fine particles.

6.3 The efficiency and pulp distribution

The separation efficiencies of the TC-cyclones were found to be better than those of the ordinary hydrocyclones in all cases and with all materials. Typical cut sizes and separation efficiency values of different size cyclones are shown in **Table 1.**

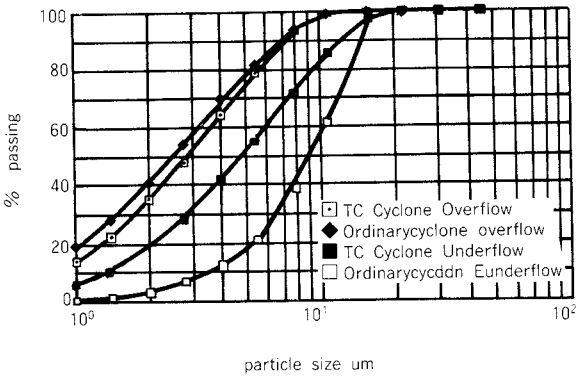

Fig.5. The products of talc slurry classification.

The washing action was also successful in these fine cyclones. The by-pass of fine material was always well below 5 % in TC-cyclones. Thus, the efficiency curve and the reduced efficiency curve were quite similar in contrast to those of ordinary cyclones.

Separation efficiencies of the separation shown in **Fig.5** are given in **Fig.6**. These demonstrated results show both a fine product that is of equal fineness with a coarser cut size and a superior separation efficiency for the TC-cyclone.

This means that the TC-cyclones will operate excellently in applications where a small amount of coarse particles have to be removed from a slurry which has a wide particle size distribution. When using a 10 mm TC-cyclone for classifying fine kaolin or talc slurry, the recovery of material below 2 μm was 90 - 95 % with a cut size of 4 to 12 μm. While using an ordinary cyclone the recovery of fines was only 60 - 70 % with a finer cut size.

In many previous studies of fine particle separation in small diameter hydrocyclones, it was verified that fine separation needs a dilute feed slurry. The density of the feed for 10 mm cyclones has to be less than 5 % of the volume if high separation efficiencies are to be expected, and even densities below 0.05 % v/v are recommended (Svarovsky 1984, Williamson et al 1984). During this study it was found that using a 10 mm TC-cyclone the feed density can be higher than that. During a series

Table 1 Cut sizes and efficiencies obtained in talc, kaolin and limestone tests for a 10 mm unit.

Cyclone type	slurry	d_{50c} (μm)	Et	I
50mm cyclones				
TC	talc	20.0	0.41	0.47
TC	talc	30.0	0.62	0.23
ordinary	talc	18.0	0.12	0.23
ordinary	talc	28.0	0.68	0.18
25mm cyclones				
TC	limestone	24.2	0.50	0.39
TC	limestone	38.0	0.55	0.24
ordinary	limestone	13.0	0.13	0.81
ordinary	limestone	24.0	0.27	0.60
10mm cyclones	kaolin			
TC	kaolin	12.6	0.22	0.78
TC	kaolin	7.2	0.53	0.33
ordinary	kaolin	4.1	0.11	1.10
ordinary	kaolin	4.2	0.32	0.64

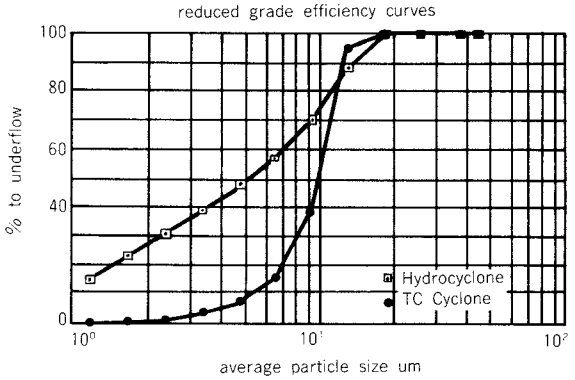

Fig.6 Separation efficiencies of a 10 mm cyclone classifying fine talc slurry.

of experiments made using a kaolin slurry having a d_{50c} of 10 μm the separation efficiency of the TC-cyclone remained high even when the feed density was 10.4 % v/v as shown in **table 2.** The reason for this is that the TC-cyclone has no conical section where the slurry density will increase and tangential velocity will dissipate. The second TC-cyclone stage is fed with a dilute slurry due to the addition wash water.

Table 2 The separation efficiencies with different feed densities for a 10 mm unit.

feed density % v/v.	d_{50c}	Et	I
5.8	7.2	0.53	0.33
9.3	10.1	0.68	0.16
10.4	10.1	0.66	0.18

7. Conclusions

New TC-cyclones with diameters of 10, 25 and 50 mm were tested for fine particle separation. The comparative tests were carried out using hydrocyclones of ordinary geometry and of the same size as the TC-cyclones.

TC-cyclones operate with higher separating efficiencies than ordinary hydrocyclones. A TC-cyclone has a coarser cut size than that of an ordinary hydrocyclone of the same size.

The feed capacity of a TC-cyclone was slightly higher than in an ordinary cyclone. A TC-cyclone also needs washing water the amount of which was found to be 10 to 30 % of the feed flow rate.

It was possible to vary the cut size of a TC-cyclone during operation so that the sep-

aration efficiency remained high by changing the amount of wash water.

The recovery of fine particles is much better with a TC-cyclone than with an ordinary hydrocyclone. One of the best applications of the TC-cyclone was found to be the removing of a small amount of coarse material from a lurry having a fine particle size distribution.

The feed slurry density can be higher with a TC-cyclone. When a 10 mm TC-cyclone was used, the feed density was up to 10.4 % - vol, and separation efficiency was still good.

References

Bloor M.I.G., Ingham D.B.,(1973):Theoretical investigations of the flow in a conical hydrocyclone. Trans. Inst. Chem. Eng., **51**, pp 36-41.

Boysan F.,(1984): Mathematical modelling of cyclone separation. Lecture motes, Selected Topics in Two Phase flow, Lecture series no 9. Trondheim. pp 137-165.

Duggins R.K., Frith P.C.W.,(1987):Turbulence effects in hydrocyclones. Proceedings, 3rd Int. Conf. on Hydrocyclones, BHRA, ed. Wood P., Elsevier, pp 75-81.

Eder Th.,(1961): Die Tromp'sche Kurve Als Mittel der Verfahrenstecshreibung. Aufbereitungs-Technik Nr. 4,.

Escudier M.P., Bronstein J., Zehnder N.,(1980): JFM **98**, 49.

Flintoff B.C., Plitt L.R., Turak A.A.,(1987): Cyclone modelling: A review of present technology. CIM bull, sept., pp 39-50.

Gu F. and Li W.,(1987): Measurement and study of velocity fields in various cyclones by use of laser doppler anemometry. Proc. 3rd Int. Conf. Hydrocyclones Oxford, BHRA, ed. P.Wood, Elsevier, 65-74.

Haas P.E. Nurmi E.O., Whatley M.E and Engel J.R.,(1957): Midget hydrocyclones remove micron particles. Chem. Eng. Progr., **53**, No 4, 203.

Heiskanen K., Vesanto A., Eronen H.,(1987): A high performance hydrocyclone design- The Twin vortex cyclone. Proceedings, 3rd Int. Conf. on Hydrocyclones, BHRA, ed. Wood P., Elsevier, pp 263-268.

Heiskanen K., Ovaskainen P.,(1988): New developments in multistage cycloning, ACHEMA 88, Int. meeting on Chem. Engng and biotechn, Frankfurt, Germany.

Heiskanen K., Vesanto A.,(1990): A new type of a hydrocyclone for fine particle separation. 7th Europ. Symp. Comm. Preprints, part 2, pp 703-711.

Horsley R.R., Allen D.W.,(1987): The effect of yield stress on hydrocyclone performance in the mining industry. Proceedings, 3rd Int. Conf. on Hydrocyclones, BHRA, ed. Wood P., Elsevier, pp 269-275.

Hsieh K.T, Rajamani K.,(1988a): Phenomenological model of the hydrocyclone: Model development and verification for single phase flow. Int. J. Min. Proc., **22** pp 223-237.

Hsieh K.T, Rajamani K.,(1988b): Phenomenological model of the hydrocyclone: Numerical solution and verification of particle movement, Procedings XVI IMPC, Stockholm, Sweden, ed. Forssberg E, Elsevier, pp 377-388.

Johansen S.T,(1990): On the modelling of disperse two-phase flows. Dr. dissertation, University of Trondheim, Norway.

Johansen S.T, De Silva S.P., Vesanto A.,(1990): Multiphase turbulence modelling as a tool in the optimization of classification equipment. Proc. Second World Congr. Particle Technology. Kyoto, Japan, pp 135-142.

Johansen S.T, Anderson N.M., de Silva S.R.,(1990):A two-phase model for particle local equilibrium applied to air classification of powders. Powder Technology.

Jull N.A.,(1972): Parameters for hydrocyclone selection. Proc. Can. Min. processors, Jap.

Kelsall D.F.,(1952): A study of the motion of solid particles in a hydraulic cyclone. Trans. Inst. Chem. Eng., **30**, pp 87-108.

Kelsall D.F.,(1953): A further study of the hydraulic cyclone. Chem. Eng., Sci, **2**, pp 254.

Kelsall D.F. and Holmes J.A.,(1960): Improvement of classification efficiency in hydraulic cyclones by water injection. Proc. V IMPC, London, IMM.

Lynch A.J., Rao T.C.,(1975): Modelling and scale-up of hydrocyclone classifiers. Preprints XI IMPC, Cagliari, Italy.

Matschke D.E. and Dahlstrom D.A.,(1959)Miniature hydrocyclones. Part 1- energy requirements. Chem. Engng Progr., **54**, No 12, 60-64.

Matschke D.E. and Dahlstrom D.A.,(1959)Miniature hydrocyclones. Part 2- Solid elimination efficiency. Chem. Engng Progr., **55**, No 1, 79-82.

Mular A.L., Jull N.A.,(1980): The selection of cyclone classifiers and pump boxes for grinding circuits. Chapter 17. Mineral processing Plant Design. AIME, New York. pp

Pericleous K.A., Rhodes N.,(1986): The hydrocyclone classifier- A numerical approach. Int. J. Min. Proc., **17**, pp 23-43.

Plitt L.R.,(1971): The Analysis of Solid-Solid separations in Classifier. CIM Bull. apr. pp 42-47.

Plitt L.R.,(1976): A mathematical model of the hydrocyclone classifier. CIM Bull. dec. pp 114-123.

Plitt L.R., Booth D.A.,(1989): Response surface characterization of hydrocyclone. Preprint SK 2, 2. Int. Fachtagung FIA, Freiberg, DDR. pp 203-210.

Plitt L.R., Flintoff B.C.,(1987): Roping in tydrocyclones. Proceedings, 3rd Int. Conf. on Hydrocyclones, BHRA, ed. Wood P., Elsevier, pp 21-34.

Rajama K., Hsieh K.T.,(1988c): Hydrocyclone model: A fluid mechanical approach. SME annual meeting, Phoenics, Arizona.

Rao T.C.,(1966): The characteristics of hydrocyclones and their application as control unit in comminution circuits. Ph.D.diss. University of Queensland,(Unpublished).

Rhodes N., Percleous K.A., Drake S.N.,(1987):The prediction of hydrocyclone performance with a mathematical model. Proceedings, 3rd Int. Conf. on Hydrocyclone, BHRA, ed. Wood P., Elsevier, pp 51-58.

Rietema K.,(1961): Performance and design of hydrocyclone - I, II, III, IV. Chem. Eng. Sci.,**15**, pp 298-325.

Svarovsky L.,(1987): Selection of hydrocyclone design and operation using dimensionless groups. Proc. 3rd Int. Conf. Hydrocyclones, Oxford, BHRA, ed. P.Wood, Elsevier, 1-5.

Williamson R.D. and Bott T.R.,(1984): Small particle separation in a hydrocyclone Proc. 2nd Int. Conf. Hydrocyclones, Bath, BHRA.

Yoshioka N. and hotta Y.,(1971): Liquid cyclone as a hydraulic classifier. Chemical Engineering Japan **19**, 632-640(translated).

Review

The Characteristics of Comminution with High Pressure Roller Mills †

Klaus Schönert
*Institute for Mineral Processing, University Clausthal**

Abstract

High pressure roller mills have been used successfully for grinding brittle materials since 1985. The advantages of this new technology are, less energy consumption, less wear and noise emission and a smaller mill size compared with ball mills. The HP-roller mill achieves comminution in a particle bed stressed by a high pressure. The performance of this mill differs from that of a ball mill with respect to the decoupling of throughput and comminution action. To operate a HP-roller mill, one has to understand the features of interparticle breakage, the interdependence of milling force and energy absorption, the capacity issue and the wear problem.

1. Introduction

High pressure roller mills are capable to comminute finely brittle materials with remarkably less energy and at a higher specific throughput than ball or roller-table mills. The first units were installed in 1985, and as of now about 200 mills are in operation, most of them for cement clinker and raw materials but also for slags, burnt lime, coal, limestone, diamond ore, silicium carbide and other brittle materials.

The principle design is shown in **fig.1**. Two rollers are mounted within a strong frame. The bearing beocks of one roller are fixed and those of the other roller are movable and pressed against the material bed within the gap by a hydraulic force system. The maximum pressure on the bed can be adjusted with respect to the material properties, the feed size and the wanted fineness, In most applications a pressure between 100 and 200 MPa is advantageous.

Most of the primary particles are broken, fragments are rebroken and the bed is compacted up to relative bulk density of 75 to 85 percent regardless to a possible agglomeration, which can be enhanced up to the formation of flakes. The agglomerates are disintegrated in a following hammer-, impact- or ball mill. Then the material is sent to a classifier, and the coarse portion is recirculated.

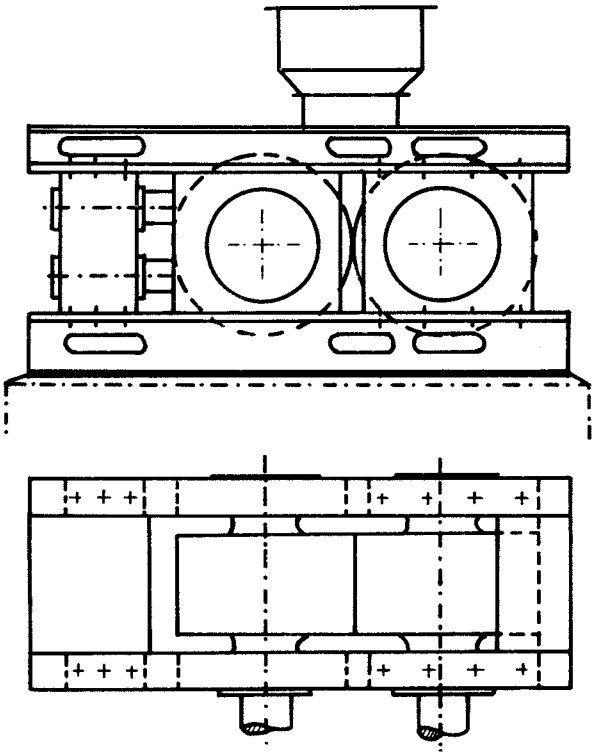

Fig.1 Sketch of a HP-roller mill

The high pressure roller mill and the procedure meet the three criteria for an effective grinding process: (1) the direct tran-

* D-3392 Clausthal-Zellerfeld, Germany

† Received August 2nd 1991

sport of the material into the active volume in which it is stressed, (2) the possibility to adjust the tressing intensityat an optimum value, and (3) the direct discharge of the fine material after being produced/1/.

2. Characteristics of interparticle breakage

The term "interparticle stessing" describes the situation in which particles are stressed by other ones as happens in a material bed between two plates, if all particles are smaller than the bed height. The result is called "interparticle breakage" . The stress field in a particle and its breakage depend on the number of neighbours, which varies with respect to the size distribution and the packing structure. As long as the average stressing intensity is the same every where, the situation is called "homogeneous interparticle stressing".

Actual interparticle stressing often differs from the homogeneous case by edge effectt and material motion as the bed is unconfined. The edge particles contact the compressing plates and are stressed, therefore, with a somewhat higher intensity. This effect becomes negligible as the bed height exceeds the maximum particle size by a factor of four and the bed diameter the height by a factor of three /2/. In an unconfined bed the outer particles will be pushed away sidewards. The energy absorption and also the portion of broken particles depend strongly on geometrical configuration /3/.

In practical applications HP-roller mills often are operated with a feed size distribution of up to twice the gap width. Then the rollers nip the coarse particles, stress and break them, and the bed consisting of the smaller particles and those fragments are formed below the nipping area; **fig.2** demonstrates this situation.

To understand the phenomena of interparticle stressing and breakage it is reasonble to study a confined bed under the condition mentioned above. The general features are as follows /4,5,6/:

(1) The compaction diagram can be approximated by the equation:

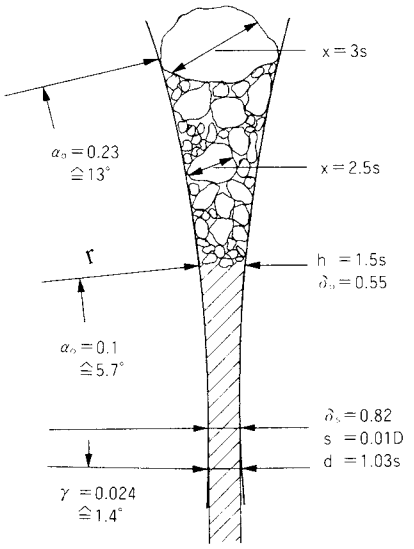

Fig.2 Material bed in the gap, sketch on scale

$$\theta = (\delta - \delta_0)/(1 - \delta_0) = 1 - \exp\{-(p/p_c)^n\} \quad (1)$$

δ_0, δ = the initial and final relative bulk density, p = the pressure, p_c = the characteristic pressure depending on the material and feed size distribution, characterizing the resistance of the bed against compaction, and n = the curve shape factor depending mainly on the material. The value of p_c and n have to be determined experimentally.

(2) Using the above equation the energy absorption E_M^* can be expressed by an equation such as,

$$E_M^* = P_c\, H(p/p_c,\ \delta_0,\ n) \quad (2)$$

as long as the energy regain due to the relaxation of the bed is negligible, which normally gives an overestimation of some percentage.

(3) It is not possible to break all particles by one stressing. The fraction of broken particles S can be approximated by the equation:

$$S/S_\infty = 1 - \exp\{-(E_M^*/E_{Mc}^*)\beta\} \quad (3)$$

E_M^* = energy absorption, E_{Mc}^* = the characteristic value of E_M^* characterizing the particle strength and depends on the material and particle size, S_∞ = the limiting value of S also depending on material and particle size, β = the curve shape factor; S_∞, E_{Mc}^* and β have to

be determined experimentally.

(4) The product size distribution becomes finer with increasing pressure and increasing energy absorption, respectively, but converges against a limiting distribution.

(5) The breakage function can be approximated with a truncated logarithmic normal distribution

$$B=\int_{-\infty}^{t} h(\tau)d\tau$$

$$h(\tau)=(2\pi)^{-1/2}\exp\{-\tau^2/2\}$$

$$t=(1/\sigma)(\ln\eta-\ln\eta_{50}) \qquad (4)$$

$$\eta=\zeta/(1-\zeta)$$

$$\sigma=(1/2)(\ln\eta_{84}-\ln\eta_{16})$$

$$\zeta=x/x'$$

The measures ζ_{50} and σ depends on the material and also on particle size and energy absorption. The breakage functions are not normalizable; an example is shown in **fig.3**. It is possible to express the influence of particle size and energy absorption by power functions:

$$(\zeta_{50}/\zeta^*_{50})=(x/x^*_a)^a(E_M/E^*_{M,b})^b$$
$$(\sigma/\sigma^*)=(x/x^*_c)^c(E_M/E^*_{M,d})^d \qquad (5)$$

So the breakage function of one material is given by ten parameters; for quartz, as an example, it was evaluated:

$\zeta_{50}=0.36$, $x^*_a=650\mu$ m, $E^*_b=10.5$ J/g,
$a=-0.27$, $b=-0.34$,

$\sigma^*=2.23$, $x^*_c=770\ \mu$m, $E^*_d=8.75$ J/g,
$c=0.05$, $d=0.12$

(6) The breakage is mainly determined by the absorbed energy, the stressing velocity and the moisture only show a minor influence with the following tendencies: the velocity effect decreases with increasing hardness (no effect with quartz); the moisture influences the breakage positively, but this effect decreases with decreasing hardness at slow velocities.

(7) The material hardness influences the breakage effects as expected; the fraction of broken particles and the breakage functions converge against their limiting values at lower energy levels as the hardness decreases, s. **fig.4.**

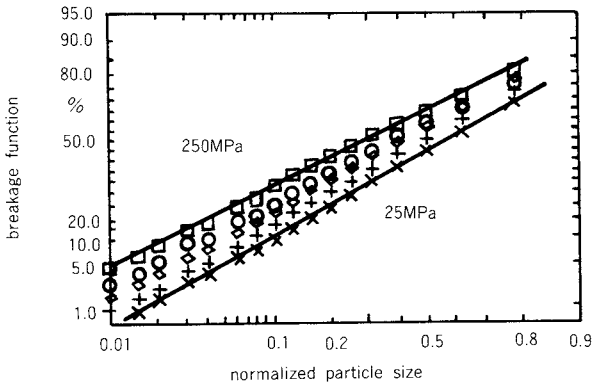

Fig.3 Breakage functions of the quartz fraction 1.6/2.0mm, plotted in a top cutted logarithmic normal distribution diagram

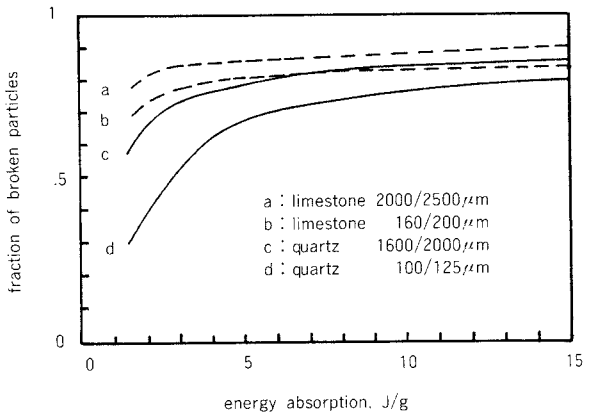

Fig.4 Fraction of broken particles of limestone and quartz fractions

3. Operation of HP-roller mills

Three major aspects have to be considered in operating a mill:power draft, capacity and wear. These three factors can be controlled generally by one or more operational parameters and are also related to each other, but it depends on the type of mill, which operational parameters influence them and to what. The size reduction in one passage through a mill is mainly determined by the specific

energy E^*_M, which is related to the power draft P and the mass flow through the mill $\dot{M}$:

$$E^*_M = P/\dot{M} \quad (6)$$

In a closed-circuit operation with a classifier, the throughput of the circuit $\dot{M}_c$ and the recirculating load $\dot{M}_r$ defines the circuit factor k:

$$k = (\dot{M}_c + \dot{M}_r) / \dot{M}_c = \dot{M} / \dot{M}_c \quad (7)$$

Eq. 6 can be rewritten as,

$$E^*_M = P / k \dot{M}_c \quad (8)$$

and the specific energy for comminution in a circuit is given by,

$$E_M = k E^*_M \quad (9)$$

The capacity of a ball mill can be varied within a fairly wide range without any change in the power draft. The power draft is adjustable by changing the ball filling ratio or the liner shape the speed normally cannot be adjusted. The capacity, therefore, determines the specific energy. The situation with HP-roller mills is quite different.

3.1 Energy absorption in a HP-roller mill

The energy absorption E^*_M of the material at one passage follows from the torque T, the number of revolutions n and the mass throughput $\dot{M}$:

$$E^*_M = 2 \pi n T / \dot{M} \quad (10)$$

The mass throughput also depends on n and is given by the following equation if the material does not slip at the exit of the compression zone,

$$\dot{M} = \delta_s \rho \sigma D L u = \pi \delta_s \rho \sigma n D^2 L \quad (11)$$

δ_s=the relative bulk density in the gap clearance, ζ=the material density, σ=(s/D)=the relative gap width, D and L the diameter and length of the roller.

After introducing eq. 7 into eq. 6, the speed can be cancelled, so it does not influence the energy absorption directly. The torque is caused by the milling force F; both are related to each other according to:

$$T = \beta F D \quad (12)$$

β=force acting angle. Now, eq. 6 can be rewritten as:

$$E^*_M = (2\beta / \delta_s \sigma) (F / \rho D^2) \quad (13)$$

Experiments have shown that β and also the term($\delta_s \sigma$)are almost independent of the force. Equation 9, therefore, indicates the proportionality between the energy absorption and the milling force, which always can be adjusted to achieve the energy absorption which is desired for the actual process.

3.2 Capacity of a HP-roller mill

The capacity is given by eq. 10. The proportionality to the speed cannot be valid up to infinity, so the relative gap width σ must depend on it.

Fig.5 shows some throughput characteristics of a lab-scale mill (D=200mm, L=100mm) /7/; this type of curves is always found. In general, the throughput of plane rollers decreases with increasing hardness of the material, but the material influences are reduced with corrugated rollers. Some val-

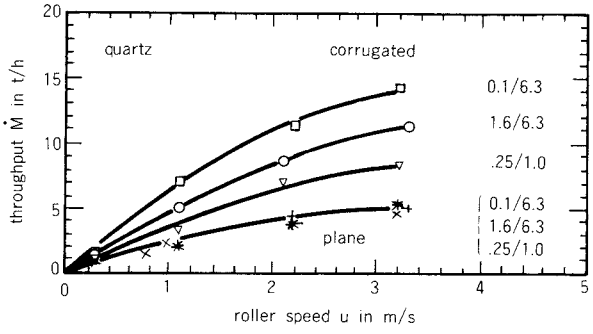

Fig.5 Throughput $\dot{M}$ over roller speed u of a lab-scale mill(D=200 mm, L=100 mm), plane and corrugated rollers(height 1 mm, width 2 mm, distance 6 mm), quartz feed 0.25/1.00, 1.6/6.3, 0.1/6.3 mm.

Table 1 Capacity index ν_0 in percent measured with the lab-scale mill. D=200mm, L=100mm

feed	plane rollers		corrugated rollers	
	quartz	limestone	quartz	limestone
0.25/1.00mm	1.20	1.65	1.70	2.40
0.8 /3.2 mm	——	——	2.10	2.70
1.6 /6.3 mm	1.10	2.00	2.90	2.85
0.4 /6.3 mm	——	——	3.05	2.90
0.1 /6.3 mm	1.40	2.20	3.55	3.10

ues of the capacity index v_0 (see eq. 15) are listed in **Table 1** to give a first impression on the influence of material, feed size and roller surface structure /7/.

The throughput is almost independent of the milling force, thus, the capacity, is controlled by mechanisms acting in the region above the compaction zone; this region should be called the "acceleration zone". Inside it, two processes are performed: first the narrowing of the material stream width, and second the acceleration of the particles. The energy for these processes is caused by the friction forces acting from the roller surface on the particles and is transmitted into the material stream by the particle-particle friction. As a result, the wall and the internal friction influences the throughput. The first one is the most important because it enables the energy to be created.

The normal force and the coefficient of friction determine the friction force. The normal force is given by the difference in the normal component of the gravity minus the centrifugal force arising as the particles move along the curved surface of the rollers. With velocity u_p and the size x of the particle, the centrifugal acceleration is given by:

$$a_c = 2\,u_p^2 / (D+x) = 2\,u_p^2 / D \leqq 2u^2/D \quad (14)$$

In the lab-scale mill with D=200 mm and at u=1 m/s the maximum centrifugal acceleration of 10 m/s^2=g occurs. The normal component of the gravity is less than g, so the centrifugal effect can be expected to influence the throughput. High speed films have shown some particles moving off the roller as the speed exceeds about 1m/s. **Fig.6** are sketches from two films taken at 1000 frames per second. One shows the situation with plane rollers at 3.3m/s. The particles (limestone 6.0/8.0mm)have much slip and a tangential velocity of only 0.6 m/s. The corrugated rollers run with 1.1 m/s, and the tangential particle velocity reaches 0.5 m/s. The time between the two frames is about 20 ms. The radial movement of the dotted particles can only be caused by the centrifugal force and is only possible if the bed around them is loosened. The centrifugal force also acts on the other particles, which are kept on the rollers by their neighbours, and reduces the friction force.

It seems to be reasonable to try an approximation of the throughput characteristic by the following expression,

$$\dot{M} = Au - Bu^2$$

$$\nu = \dot{M}/\rho DLu = \nu_0 - kz \quad (15)$$

$$z = u/u_c = u/\sqrt{gD/2}$$

The throughput index v_0 is the key value in the capacity issue. **Fig.7** shows a (v,z) -plot for quartz; the results can be expressed by eq. 15; more detailed informations are given in /7/. Production mills have rollers of 1 to 2 m diameter and are operated with a speed up to 2 m/s, so z ranges between about 0.6 and 1.0; the centrifugal effect may be less than in the lab mill. It seems to be reasonable to attend to the characteristic speed u_c in sizing the capacity of roller mills.

Beside the centrifugal effect, the throughput can be reduced by the fluidization effect since

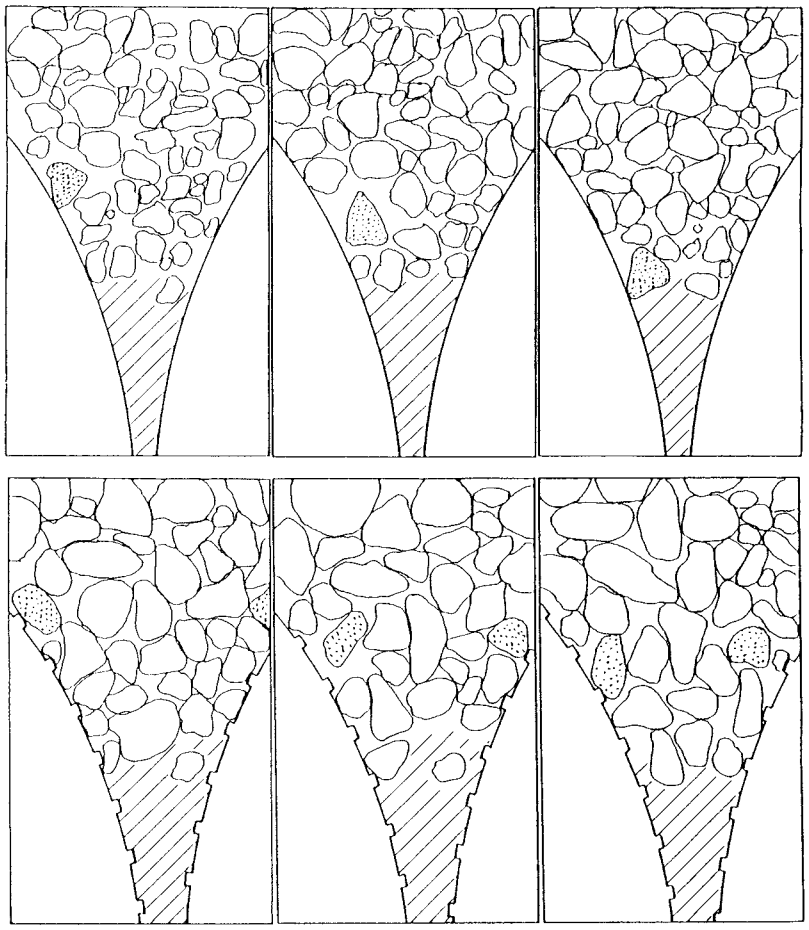

Fig.6 Movement of particles in the acceleration zone, sketches from two high speed films(1000 frames per second), time distance about 20 ms, for details see text

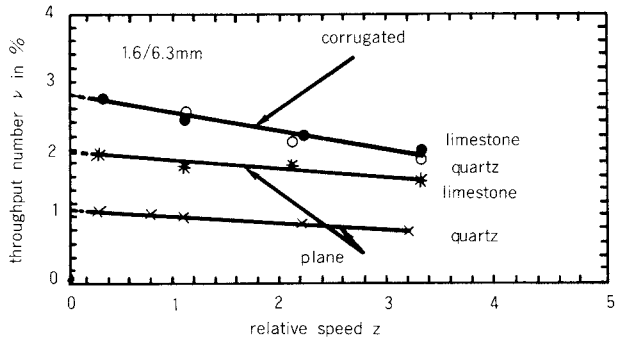

Fig.7 Throughput number ν over relative speed z for a lab-scale mill (D=200 mm, L=100 mm), feed 1.6/6.3 mm, plane rollers: quartz(x), limestone (∗)corrugated rollers: quartz(○), limestone(●).

the feed contains fine material. The compaction of the bed squeezes off the air, which mostly flows upwards into the acceleration zone. The volumetric flow $\dot{V}_L$ and the average air velocity v_o through the entry cross-section of the compression zone follows from the equations:

$$\dot{V}_L = \gamma(\dot{M}/\zeta)(\delta_s - \delta_o)/\delta_s\delta_o = \gamma\, h\, L\, w_o(\delta_s - \delta_o)/\delta_s \qquad (16)$$

$$v_o = \gamma\, w_o(\delta_s - \delta_o)/\delta_s \leqq \gamma\, u(\delta_s - \delta_o)/\delta_s \qquad (17)$$

γ=the portion of the upwards flow, δ_o=the relative bulk density at the entrance, w_o=the material velocity at the entrance, u=the roller speed. For an estimation it should be assumed that γ=0.5, δ_o=0.55, δ_s=0.8, resulting in v_o=0.16 u_o. The settling velocity c of a 100μm

quartz particle in air is about c=1m/s. The fluidization velocity of a particle bed is given by $v_o = c(1-\delta)^n$; with n=5 follows $v_o = 0.018$ c=0.02m/s. These figures show the possibility of partial fluidization, which also reduces the throughput if the feed contains fine particles.

For a better understanding of the throughput characteristic more fundamental research is needed.

3.3 Wear of rollers

The specific wear of a mill is expressed normally in terms of worn-off mass M_w related either to the ground mass M_c or to the consumed energy E.

$$w_M = M_w / M_c = \dot{M}_w / \dot{M}_c = k\ \dot{M}_w / \dot{M}$$

$$w_E = M_w / E = \dot{M}_w / P = \dot{M}_w / \dot{M}\ E^*_M \quad (18)$$

$$w_M / w_E = k\ E^*_M = E_M$$

Although these terms are useful for describing technical opreations, the average thickness d_w of the layer worn off one roller in one revolution represents a more reasonable figure for fundamental considerations and comparing different materials and mills. This is bacause the wear is caused on the roller surface and the throughput due to the gap width. Using the denotations already introduced, d_w can be calculated from w_M or w_E, the throughput number ν, the density of the ground material ρ and that of the wear material ρ_l as follows:

$$d_w/D = (\rho/\rho_l)(\nu/2k)\, w_M$$

$$d_w/D = (\rho/\rho_l)(\nu/2)(w_E E^*_M) \quad (19)$$

These equations show that the specific wear decreases with increasing roller diameter as long as d_w and the throughput number remain constant.

The operation time t_{op} is limited by the thickness d_l of the material layer, which can be worn off before rewelding.

$$t_{op} = \pi (d_l / d_w)(D/u) \quad (20)$$

Experiences with limestone and cement clinkers have shown that d_w is in the order of 10^{-9}m=$10^{-3}\mu$m /8 /. Assuming d_l=0.01 m, D=1.5m, (ρ_l/ρ)=2.6, u=1.5m/s, ν=0.015 and k=1 for pre-milling and k=4 for fine-milling, it follows that $w_M = (0.23\text{-}0.92).\ 10^{-6}$ and t_{op}= 8700 h. The specific wear is very low even with a value of d_w that is ten times higher. The operation time arises as the real problem because it is inversly proportional to d_w.

The wear mechanisms are not fully understood, although hard work is going on at this issue. Recently, a paper was published containing many data /9/. The particles in the acceleration zone slip greatly on the roller surface, but the normal forces are very low. The pressure on the surface increases steeply in the compression zone; **fig.8** shows an example for limestone 0.5/0.8mm measured with a 2mm pin inserted in the roller. The compaction also causes some tangential movement of the material at the surface. Both facts together, the high pressure and the small amount of slip, are probably the main reasons for the wear. Because high pressure is needed for the comminution and cannot be avoided, one has to try to reduce the slip inside the compression zone. One important fach is that the slip increases at high compaction above a relative bulk density of 85%.

4. Selection of mill size

The selection of the proper mill size has to consider the mass throughput, the maximum particle size in the feed and the investment costs. The throughput is given by eq. 11. Introducing the relative speed z, the characteristic speed u_c, the throughput number ν and the length-diameter ratio $\lambda = L/D$, mill size $\dot{M}$ reads:

$$\dot{M} = (\nu z \lambda / \sqrt{2})\ \sqrt{g}\ \rho D^{2.5} \quad (21)$$

At a fish approxination, the investment costs are proportional to the mill volume V_m, which can be characterized as:

$$V_m \sim D^2 L = \lambda D^3 \quad (22)$$

with eq. 21 one rewrites:

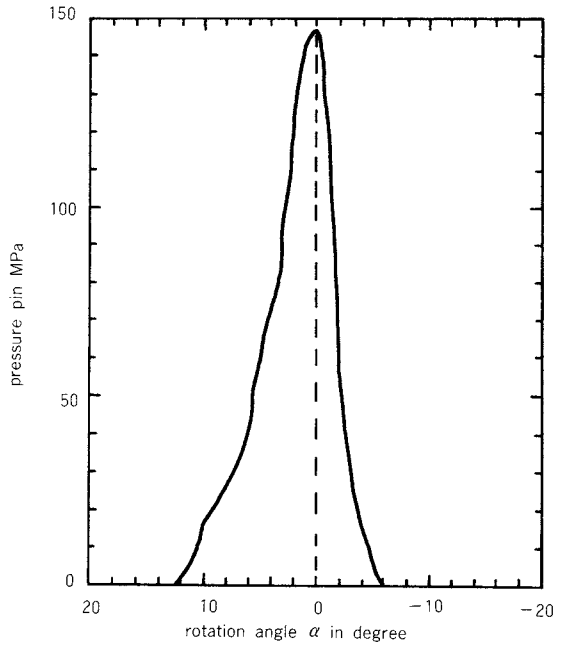

Fig.8 Pressure distribution in the compression zone, lab-scale mill (D = 200 mm, L = 100 mm), limestone feed 0.5/0.8 mm, roller speed 2.2 m/s

$$V_m \sim (1/\lambda)^{0.2} (\dot{M}/\nu z)^{1.2} \qquad (23)$$

As long as λ varies in the usual range of about 0.5 to 1.2 the length-diameter ratio has only a small influence on the mill volume, if $\dot{M}$ is given, z kept constant and ν does not change as λ is varied. A decrease of λ from 1.2 to 0.5 increases V_m by about 12%. so the value of λ can be chosen with respect to desing problems.

The mill size selection has to be focussed on the roller diameter D to satisfy the demand of the throughput, and again the question arises as to how the throughput number ν depends on the operating conditions, the surface structure and the roller diameter itself. The diameter should be chosen with respect to the maximum feed particle size x_{max} if it exceeds the gap width s. A large (x_{max}/s)-ratio can cause local pressure peaks, so it should be smaller than 2 to 3. With the relative gap width $\sigma = (s/D)$ it follows that:

$$(D/x_{max}) = \{\sigma (x_{max}/s)\}^{-1} \qquad (24)$$

σ itself depends on the (x_{max}/s) ratio, the material and the structure of the roller surface; it ranges for plane rollers between about 0.01 for hard and about 0.02 for soft materials. With corrugated rollers, σ increases up to 0.015 until 0.025 depending on the feed size distribution since the material shows a minor influence. Taking these figures, a fairly large range arises for the minimum (D/x_{max})—rafio: with $\sigma = 0.025$ and $(x_{wax}/s) = 2$ tesulh$_2$ $(D/x_{max}) = 20$ and with 5 = 0.01 and $(x_{max}/s) = 3$ follows-$(D/x_{wax}) = 33$.

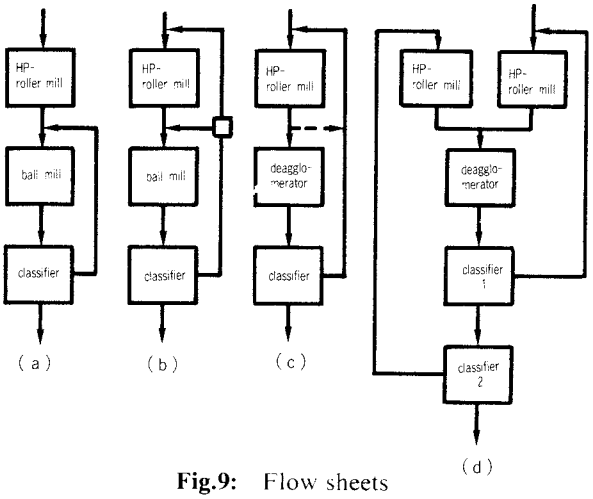

Fig.9: Flow sheets

5. Flow sheets

A HP-roller mill can be used in different modes, some possible flow sbeets are shown in **fig9.**

In the first applications the mill was installed ahead an already existing ball mill-classifier circuit, see **fig.9a.** This premilling mode had the advantage of minimizing the risk at the introduction of this new technology. The HP-roller mill increases the throughput by 15 to 30%, in some caese even more, and reduces the total specific energy consumption by 10 to 20 %. These results are achieved if the HP-roller mill produces at least-10% of fine material, and the ball charge is modified.

The potential of energy saving can be used better as the comminution action in the HP-roller mill is enhanced by partially re-circulating the classifier coarse to it; fig. 9b shows this hybrid-milling mode. Many instal-

lations for cement clinker grinding are working successfully according fig. 9a and 9b/10-13/. In the fine-milling mode, fig. 9c, all classifier coarse is sent back to the HP-roller mill, which then is followed by a hammer or impact mill to deagglomerate the flakes. New classifiers are developed which have integrated a deagylommeration system, so the circuit only consists of two parts. The energy saving increases up to 50% compared with a ball mill circuit. With decreasing classifier cut and sharpness, the mill feed contains more and more fine material, which may worsen the introduction into the compression zone. The quiet running of the mill is disturbed by shattering of the rollers; a recirculation of a portion of flakes reduces the shattering and improves the mill performance. This is indicated with the dashed line in fig. 9c. HP-roller mills in the fine milling mode are used successfully for cement raw material (-200μm), burnt lime (-100μm), cement clinker (-80μm), limestone (-20μm and even -10μm)and other brittle materials/10, 14-18/.

Fine and very fine milling should not be done in one step, a two step flow sheet seems to be more reasonable. One possibility is shown in **fig. 9d** consisting of two HP-roller mills, one deagglomerator and two classifiers. In this way the recirculating load to each mill is reduced, and furthermore, each mill can be adjusted better to the optimum condition.

6. Outlook

The quick introduction of HP-roller mills into technical operations during the last years proves the advantage of this new grinding technology for brittle materials. Some problems have appeared with respect to design details and wear, but this is normal in establishing a new system especially as it happens so fast. The behaviour of this mill differs from the well-known ball mill, so one has to learn and to get accustomed to it. The application will be broadened in the future, especially in the area of ores and fine materials/17, 18/.

Until now only a small amount of fundamental research and modelling has been done, and more is needed. Although this mill and its operation looks very simple, many questions are still unanswered. The most important issues are: (1) the capacity in general and especially with fine feed, (2) wear mechanisms and wear materials, (3) microcrack forming, (4) profiled roller surfaces, influences on capacity and wear, (5) reweldding techniques, (6) segmented roller liners, (7) modelling, and (8) influences on down-stream processes as flotation and leaching. One should compare the situation with the enormous research and development efforts in ball milling.

References

1) Schönert, K.
Energetische Aspekte des Zerkleinerns sproder Stoffe
Zement-Kalk-Gips, **32**(1979)1, 1/9

2) Aziz, J. A.; Schönert, K.
Einzelkornzerkleinerung und Gutbettbeanspruchung von
Zementklinker-Fraktionen
Zement-Kalk-Gips, **33**(1980)5, 213/218

3) Hanisch, H.; Schubert, H.; Clemens, P.
Energy consideration in particle bed comminution
6th European Symposium Comminution, Nurnberg, 1986, 223/232

4) Schwechten, D.
Trocken-und Naßmahlung sproder Materialien in der Gutbett-Walzenmuhle
Diss. TU Clausthsl, Germany, 1987

5) Müller, F.
Hochdruckzerkleinerung im Gutbett bei Variation von Feuchte und Beanspruchungsgeschwindigkeit
Diss. TU Clausthal, Germany, 1989

6) Schönert, K.; Müller, F.
Darstellung von Bruchanteil und Bruchfunktion der Gutbett-Beanspruchung
Aufbereitungs-Technik (1990)5, 248/256

7) Schönert, K.; Lubjuhn, U.
Throughput of high compression roller mills with plane and corrugated rollers
7th European Symposium Comminution, Ljubljana, 1990, preprints part 2, 747/763

8) Wüstner, H.
Druckzerkleinerung, neue Wege der Energieeinsparung beim

Mahlen von Zementkliner und Huttensand
Zement-Kalk-Gips, **38**(1985)725/727

9) Brüggemann, H.; Knobloch, O.; Müller, M.
A test method for prediction of wear rates in high pressure grinding rolls
s. ref 7, 837/851

10) von Seebach, M.; Patzelt, N.
Betrieb von Mahlanlage mit Gutbett-Walzenmuhlen fur
Rohmaterial und Zement
Zement-Kalk-Gips, **40**(1987)7, 337/344

11) Thurat, B.; Wolter, A.
Gutbett-Walzenmuhlen zur Feinmahlung von Zementrohmehl,
Kohle und Kalk
Zement-Kalk-Gips, **42**(1989)4, 179/183

12) Schwarz, S.; von Seebach M.
Optimization of grinding in high pressure grinding rolls and downstream ball mills
s. ref. 7, 777/780

13) Kellerwessel, H.
Praxis der Hochdruck-Gutbettzerkleinerung
ZKG International **43**(1990)2, 57/64

14) Plank, F.W.; Bauerochs, M.; Oberheuser, G.
Erkenntnisse mit der Gutbettdruckzerkleinerung von
Branntkalk und Kalkstein
Zement-Kalk-Gips, **40**(1987)1, 1/6

15) Hochdahl, O.; Rosemann, H., Patzke, J.
Erste Betriebsergebnisse der Combi-Mahlanlage im Zementwerk Lagerdorf
will be published in ZKG International

16) Oberheuser, G.; Strasser, S.
Roller press finish grinding of various products-possibility and application
s. ref. 7, 789/802

17) Schwechten, D.
Experience in dry grinding with high compression roller mill to fineness below 20 micron
s. ref. 7, 803/820

18) Weller, K.R. et.al.
The response of some Australian ores and industrial minerals to high pressure rolls grinding
s. ref. 7, 821/835

Review

State Diagrams of Gas/Solid Flows with Partial Phase Separation †

O. Molerus and K.-E. Wirth
Lehrstuhl fur Mechanische Verfahrenstechnik
*Universitat Erlangen-Nurnberlg**

Abstract

Preferable operational conditions of gas/solid flows are often situated in the transitional regime between two well defined modes, typical examples being pneumatic transport in a horizontal pipe and circulating fluidized beds. The energetic optimum of horizontal pneumatic transport is situated in the transitional regime between strand flow and fully developed flow in which regimes with different physical factors (wall friction of sliding material or single particle wall impact, respectively) prevail. The circulating fluidized bed may be regarded as the transition from a bubbling fluidized bed to pneumatic transport vertically upwards. Experimental results indicate particle slip velocities which are quite a bit higher than predicted by single particle fall velocity, hence indicating strong phase separation in terms of clusters.

In both situations, empirical correlations fail because they ignore the complicated structure of the system in question, i.e. being transitional. On the other hand, even very sophisticated modelling can fail, because it is mostly based on inherent a priori assumptions concerning the state of flow.

As an alternative, comparably simple models of two phase flows in horizontal pipes and for circulating fluidized beds are presented. The models originate from very obvious visual observations and from considerations of momentum exchange between the two phases. The evaluation of the respective resulting sets of algebraic equations can be represented in terms of state diagrams for gas/solid flows with partial phase separation.

1. Introduction

In process design, favorable conditions e.g. with respect to energy consumption are often located at the intersection of two different mechanisms each of which prevails far away from the optimum (**Fig. 1**).

In some cases, simple superposition of both mechanisms might result in a rough but sufficiently accurate description of the system's behaviour in the intermediate regime. In general, however, what is more likely to occur is that the interference of the two mechanisms defines the system's behaviour in

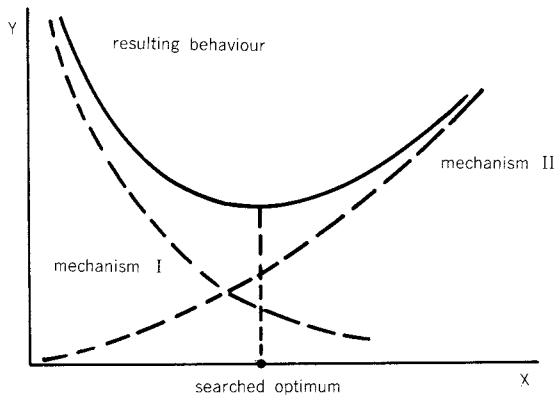

Fig.1 Optimum conditions at the intersection of two mechanisms.

* Cauerstr. 4, 8520 Erlagen, Germany

† Received July 26th 1991.

the optimum regime, i.e. a simple superposition must fail. In the present paper, it is shown that pneumatic conveying in horizontal pipes follows the latter mentioned scheme.

To introduce the second part of the paper the state diagram for pure, simple, compressive substances in terms of the well known T-v-diagram, i.e. as temperture versus specific volume (**Fig. 2**) is briefly recalled .

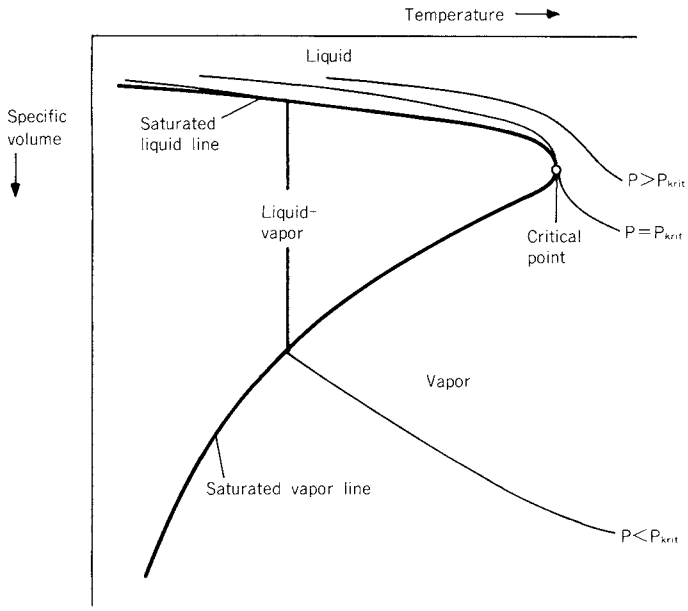

Fig.2 T-v-diagram for pure compressive substances.

The most striking feature of circulating beds can be seen in the evaluation of measurements as well as of momentum and mass balances, i.e. experimental as well as theoretical results in a state diagram which shows surprising analogy to the T-v-diagram for compressive substances. In anticipation of the later section of the paper, it is pointed out that the saturated liquid line of the T-v-diagram corresponds to the bubbling fluidized bed at the bottom end of a circulating fluidized bed, whereas the saturated vapour line corresponds to the steady-state entrainment of particles above the transport disengaging height (TDH).

2. Pneumatic Conveyance in Horizontal Pipes, Experimental Results

2.1 Experimental Results

The experimental results obtained with a horizontal glass conveyance duct of 0.04 m inner diameter are shown in **Fig. 3** . Measured pressure drops for polystyrene with a particle diameter of 2.3 mm are plotted versus superficial gas velocity. Exact dosage of particulate material allowed variation of superficial gas velocity at a constant solid mass flow rate.

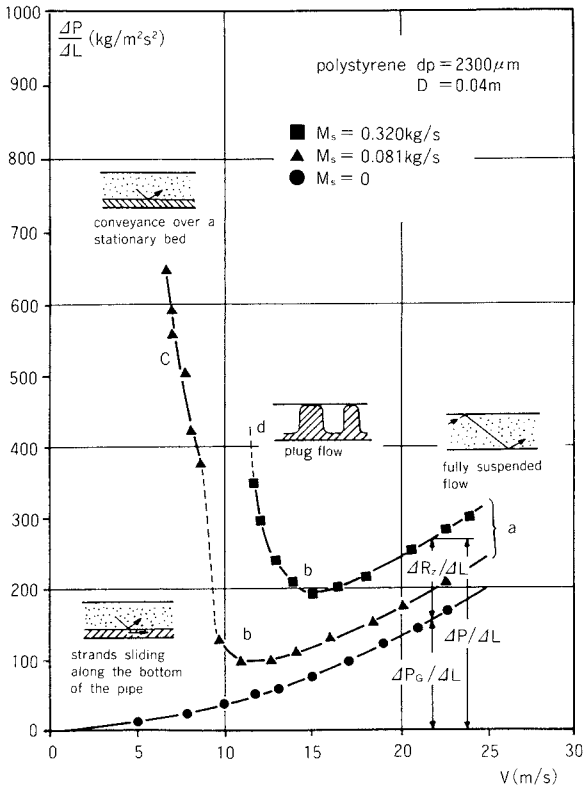

Fig.3 Measured pressure drops for the conveyance of polystyrene in a glass tube and the visually observed flow pattern.

At high air velocities the particles are uniformly distributed over the pipe cross-section. This state is referred to as fully suspended flow(a). At low air velocities a segregation of the suspended particles occurs and the state of strand type conveyance is achieved(b). In this conveyance state, under conditions of constant solid mass flow, the pressure drop increases with decreasing air velocity. There is no sharp transition from fully suspended flow to strand type conveyance. The transition is gradual. At low air velocities and low solid mass flow rates, the strand is stationary, and the pressure drop

increases suddenly(c). In this conveyance state the solids will be conveyed over the stationary bed essentially in the form of fully suspended flow. Between this conveyance state and strand type conveyance there is a small velocity range in which dunes are conveyed. No stable pressure drop occurs in conjunction with this type of conveying. Therefore, pressure drop is presented in the form of broken curves in **Fig. 3** . At high solid mass flow rates, no particles settle out on the bottom of the pipe. Here a direct transition from strand type conveyance to plug flow occurs for solids of large particle sizes, and blockage of the system develops in the case of fine-grained solids(d).

2.2 Requirements for Rational Modelling Resulting from the Experimental Observations

Pressure drop measurements together with visual observations result in the following requirements on a rational theory of pneumatic transport in horizontal pipes:

1. For a given mass flow rate of a solid material, the energetic optimum is situated in the lowermost part of the pressure drop curve, i.e. in the regime of strand flow, hence that regime must be modelled as accurately as possible.
2. For higher mass flow rates of solid material with decreasing superficial gas velocity, the regime of often unsafe plug flow is attained. Conservative design requires exact knowledge of that upper boundary of the stable strand flow regime.
3. For lower mass flow rates of solid material a jumplike increase in pressure drop to the regime of conveyance over a stationary bed is observed. Conservative design again requires exact knowledge of the left end of the stable strand flow regime.

2.3 Theoretical State Diagram of Stable Strand Flow

As **Fig. 3** suggests and as is usually done in the description of pneumatic conveyance, the pressure gradient $\triangle P/\triangle L$ is subdivided into $\triangle P/\triangle L = \triangle P_G/\triangle L + \triangle P_z/\triangle L$ whereby the term $\triangle P_G/\triangle L$ is calculated as for single phase gas flow and the term $\triangle P_z/\triangle L$ is attributed to particle transport.

The scope of the present paper is mainly with methodical aspects. Thus, only the basic assumptions are reported here; details of the calculation procedure may be read elsewhere [1] .The most significant assumption originates from visual observations:

Those particles, which are flying fully suspended in the strand-free part of the pipe cross-section, are transported above the strand at velocity v_G. Upon impact, an impinging particle is slowed down to the strand velocity w and further transported as part of the strand. At steady state, every particle-strand impact of an impinging particle results in another particle being expelled from the strand and accelerated by the air flow to velocity V_G. In other words, the moving strand is assumed to be driven by impinging particles and to be retarded by wall friction.

For the derivation of the additional pressure drop equation, a pipe element $\triangle L$ is subdivided into two balance regions over which force and mass balances are set up (**Fig. 4**).

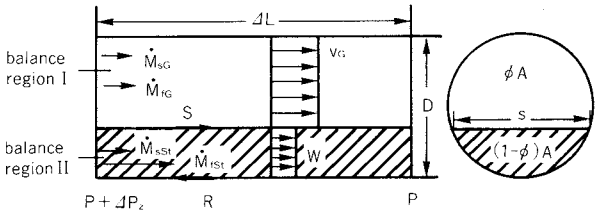

Fig.4 Balance regions in pipe element Δ L.

Balance region I consists of the flow above the strand. Equilibrium of forces exists when the shear force is equal to that of the pressure gradient.

$$\triangle P_z \Phi A = S.$$

Balance region II is set up around the strand. Force equilibrium occurs when the sum of the shear and pressure gradient force is equal to the force of friction,

$$\triangle P_z (1-\Phi) A + S = R.$$

The friction force R between the strand and the pipe wall is equal to the product of the strand's weight less the buoyancy and the coefficient of sliding friction f_r,

$$R=(\rho_s-\rho_f)(1-\epsilon)(1-\Phi)A\triangle Lgf_r.$$

The shear force S acting on the surface of the strand is equal to the product of the shear stress on the strand's surface and the strand's surface $s\triangle L$,

$$S=\tau s\triangle L.$$

The shear stress τ is, therefore, equal to the product of the change in momentum $\triangle J$ of a single particle on impact with the strand,

$$\triangle J=m(v_G-w)$$

and the number flow rate per unit surface area of particles impinging on the strand surface,

$$\dot{n}=k\frac{\dot{M}_{SG}}{m\phi A}$$

This results in the following equation for the shear stress at the surface of the strand:

$$\tau=\dot{n}\triangle J.$$

By introduction of the mass balances for gas and solid, these equations can be rearranged into three equations [1]. These three equations contain only one empirical factor which has to be determined from experiments. This constant defines the intensity of the momentum exchange between impinging particles and the moving strand. For particles that are not too fine, this factor can be assumed to be constant, as is e.g. the drag coefficient of coarse-grained particles.

Numerical solution of the mentioned three equations results in a state diagram for horizontal pneumatic conveyance (**Fig. 5**) which combines the following six non-dimensional groups:

$$\frac{v}{\sqrt{\frac{\rho_S}{\rho_f}(1-\frac{\rho_f}{\rho_S})(1-\varepsilon)Ggf_r}}\equiv \text{Fri friction number}$$

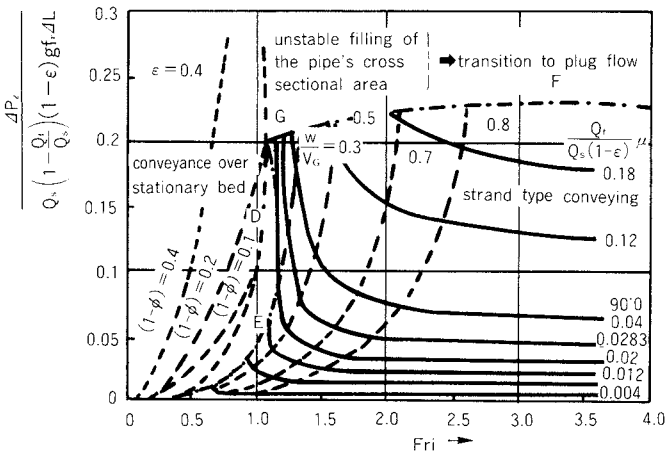

Fig.5 State diagram for stable strand type conveyance.

$\frac{\rho_f}{\rho_S(1-\varepsilon)}\mu$: ratio of volume flow rates solid and fluid

ε : void fraction of the strand

$\frac{\Delta Pz}{\rho_S(1-\frac{\rho_f}{\rho_S})(1-\varepsilon)gf_r\Delta L}$: non-dimensional additional pressure drop

$1-\Phi$: relative covering of the pipe's cross-section by the strand

$\frac{w}{v_G}$: ratio of the strand's velocity to the fluid velocity above the strand

The friction number Fri, the volume flow ratio and the void fraction are given quantities for a particular comveyance system. The non-dimensional additional pressure drop, the relative covering of the pipe's cross-section by the strand and the velocity ratio then are unknown variables of the conveyance system in question. To determine of these three unknown characteristics, data mass and momentum balances of gas and solid material provide three equations. Therefore, a representation of the non-dimensional pressure drop,

$$\frac{\Delta Pz}{\rho_S(1-\frac{\rho_f}{\rho_S})(1-\varepsilon)gf_r\Delta L}=F\left(Fri,\frac{\rho_f}{\rho_S(1-\varepsilon)}\mu,\varepsilon\right)$$

can be calculated. The calculated curves of the additional pressure drop are presented in **Fig. 5** .The non-dimensional additional pressure drop is plotted vs the Fri-number with the volume flow ratio as a parameter. The equations for the additional pressure drop with sliding strands hold for steady state conditions.The stability of these steady states against small disturbances, however, is not given by the mathematical derivation. The only working points that will be stable are those for which the reduction of the velocity ratio, caused by a disturbance, momentariy results in a greater stationary solid mass flow. Therefore, as is obvious from **Fig. 5** , stable pneumatic conveyance with sliding strands will prevail at all working points in which the slope of the curve for constant volume flow ratio is negative and for which the slope of the curve for constant velocity ratio is positive. These considerations yield the boundary OEGF of the steady state conveyance with stable strands. The left boundary is separeted from the regime of conveyance with a stable deposit of particles by a small regime of unsteady state(OEGDO)which is observed experimentally as a jump in pressure drop with reduction in gas velocity. The upper boundary separates the state of stable strands from unsteady conditions of conveyance which are observed experimentally as transition to plug flow. Obviously, the properties of the state diagram **Fig. 5** predicted from theory coincide with the experimental observations depicted in **Fig. 3** . Evaluation of the state diagram **Fig. 5** proceeds as follows: The friction number Fri can be calculated for given superficial gas velocity v. For a given solid/gas-mass flow ratio μ the non-dimensional grou $(\rho_f \mu)/[\sigma_s(1-\varepsilon)]$ can be calculated, too. Thereby, a point in the state diagram **Fig. 5** is determined. First, one can prove whether the calculated point is truly situated in the regime of stable conveyance with particle strands. Then, one can read from the ordinate the appropriate non-dimensional pressure drop. Within the regime of stable strands, the dotted lines $w/v_G = \text{const.}$ represent the ratio of strand velocity to the gas velocity v_G in the free space above the strand.

Within the regime of stable strands, the non-dimensional pressure drop represents at the same time that relative part of the cross-sectional area of the pipe which is occupied by the strand. In**Fig. 6** ,for example, own measurements are compared with predictions according to the state diagram, **Fig. 5** .

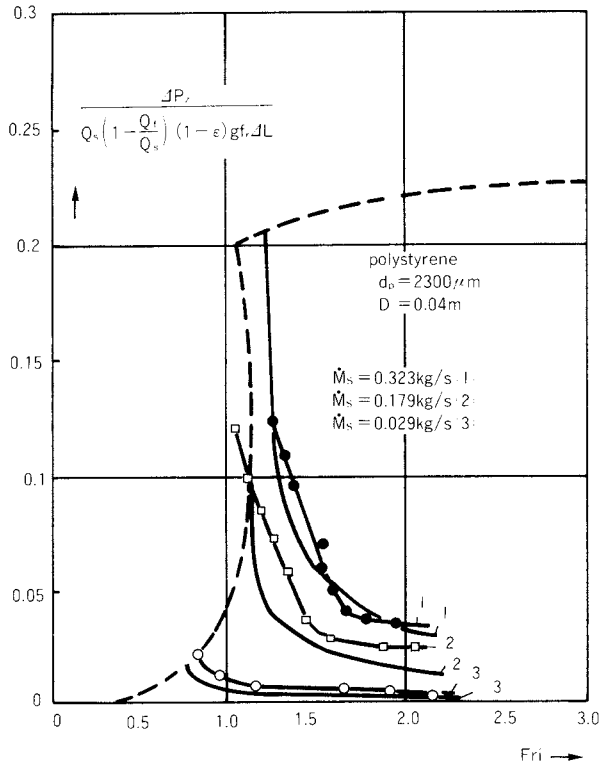

Fig.6: Pneumatic conveyance with sliding particle strands, comparison of prediction and measurements for polystyrene ($\varepsilon = 0.4$).

2.4 Conclusions with Respect to Pneumatic Conveyance in Horizontal Tubes

From the preceding consideration, the following conclusions with respect to pneumatic transport in horizontal tubes can be drawn:

1. Pneumatic conveyance in horizontal tubes follows the general scheme of **Fig. 1** , i.e. it shows a distinct minimum of pressure drop as a function of superficial

gas velocity (**Fig. 3**). This minimum can indeed be identified as being the result of two counter acting mechanisms, namely decreasing additional pressure drop due to sliding strands (compare **Fig. 5**) and increasing gas component P_G (compare **Fig. 3**).

2. Theoretical modelling does not start from first principles but from visual observation of a geometrically well defined object, i.e. the strand moving at the pipe's bottom. This visual observation is taken as being a priori; there is no detailed discussion on the how's and why's. This simplification leaves only the magnitude of one parameter to be determined by experiment.
3. The key word for the theoretical treatment is "partial"(with respect to phase separation). One part of the particles is conveyed fully suspended above the moving strand. These particles drive the strand against wall friction by impact. strand against wall friction by impact.
4. The physical significance of the described approach here is substantiated by the fact that it predicts quite accurately not only the pressure drop but- and more important- the operational regime in which stable strand flow transport takes place.
5. Steady state solutions can be completely misleading if not complimented by stability analysis.

3. Fast Fluidization and Circulating Fluidized Beds

With superficial upward gas velocity largely exceeding single particle fall velocity, the well known features of bubbling fluidized beds, i.e. distinct gas bubbles and visible upper bed surface gradually disappears. Instead, the bottom end dense bed change to the turbulent state, and severe solids carry over is observed. In that regime of so-called "fast fluidization" steady state conditions are only maintained by feeding new solid material at a sufficiently high rate (**Fig. 7** (a)). Steady state conditions can also be maintained by recirculating solid material carried over via an external cyclone and a stand-pipe (**Fig. 7(b)**).

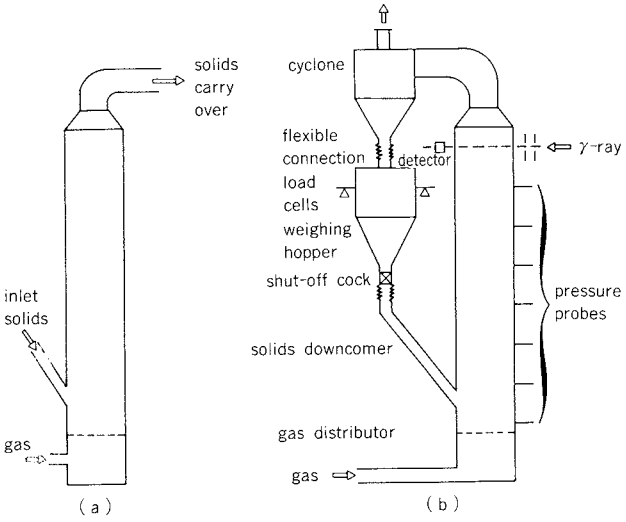

Fig.7 Fast fluidization(a) and circulating fluidized bed(b), experimental set-up.

Within the context of processes in the petrochemical industry, it is interesting to remember that the first commercial fluid catalytic cracking plant(Baton Rouge refinery of Standard Oil of New Jersey, 1942)operated in the fast bed mode [2] (**Fig.8**).

The operation of this type of plant, however, was not free of difficulty. Dust collection and control of solid hold-up posed problems. As a result, industry switched to the bubbling fluidized bed. Recent development efforts tackle once more the use of the fast bed mode in the petroleum fluid cracking process. This would bring the fluid cracking process back to the operation in that mode, which marked its first commercial prototype.

The real breakthrough in establishing the circulating fluidized bed process probably was Lurgi's calciner for aluminium hydroxide(1971).

During the last decade, the strongest impact on further development of circulating fluidized beds resulted from air pollution by coal fired power plants. Direct addition of crushed dolomite into the combustion chamber drastically reduces SO_2-emission, whereas a rather low combustion temperature (850 °C) together with staged air supply

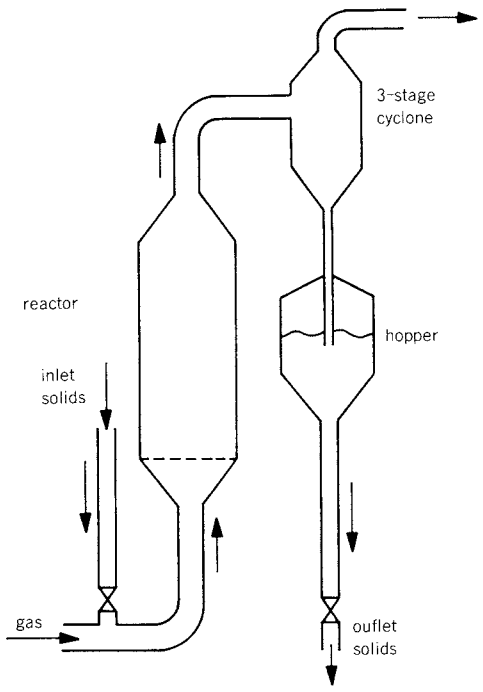

Fig.8 The upflow (fast bed) design used in the first cat-cracker [2].

suppresses NO_x formation.

Circulating fluidized bed boilers fulfilled expectations concerning the emission levels of SO_2 and NO_x quite reasonably. The pioneers of circulating fluidized bed technology, however, had an experience which was similar to that in the petroleum refinery industry forty years before: Due to the system's complex fluid mechanics, the behaviour of a given configuration was not predictable with sufficient accuracy.

This fact resulted rather often in later design modifications on the basis of observed malfunctions of the initial design. Any progress in the direction of a safer design, therefore, requires a modelling of the circulating fluidized bed's fluid dynamics, which must be detailed enough in order to be useful. This task was the main goal of the approach which is presented in the following.

3.1 Axial Pressure Profiles in the Upstream Part of a Circulating Fluidized Bed

With an experimental set-up as shown on the right hand side of **Fig. 7** the following rather simple measurements can be performed:
1. Superficial gas velocity in the upstream part.
2. Axial pressure profile in the upstream part.

Fig. 9 presents measured axial pressure profiles in a bed of glass beads with a particle diameter of 90μm, for different superficial gas velocities. The solids content in the circulating fluidized bed was constant in all the experiments shown in this diagram. The pressure gradient decreases with increasing height of the plant at all three gas velocities. The largest pressure gradient occurs immediately above the gas distributor where a turbulent fluidized bed exists.

When gas flows through this fluidized bed, solid particles are entrained by the gas flow and thus transported to the upper regions of the bed. As easily demonstrated, strands and

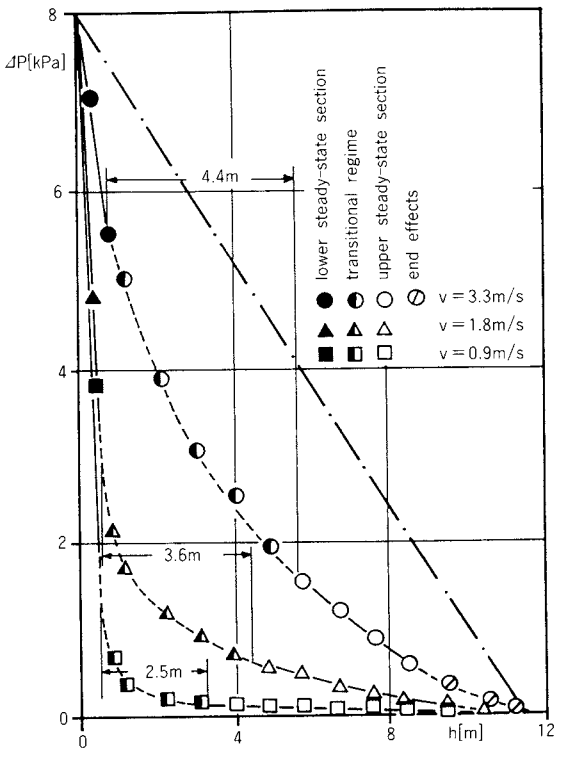

Fig.9 Axial pressure profiles at different superficial gas velocities ($d_P = 90\mu m$).

clusters of high solids concentrations are also ejected from the fluidized bed. Therefore, the solids mass outflow rate from the fluidized bed exceeds that which can be supported by the gas flow through the plant. This results in the excess solids mass flow falling back into the bed. Thus, solids concentration decreases with increasing height of the plant, and therefore the pressure profile flattens out with increasing height of the circulating fluidized bed. Above a certain height, the solids concentration is so small that it can be completely entrained. This means that, at this height, the solids concentration and therefore the pressure gradient become constant. The distance between the steady-state sections with constant pressure gradients is referred to as "Transport Disengaging Height"(TDH).

The outlet of the circulating fluidized bed does influence the pressure profile at the top of the plant. Particularly at higher gas velocities, it can be seen from **Fig. 9** that the pressure gradient between the upper steady-state section and the top end decreases. When the gas velocity is sufficiently high, the solids in the circulating fluidized bed are homogenously distributed throughout the plant. Neglecting the presssure drop necessary for the acceleration of solid particles in the vicinity of the gas distributor, the pressure gradient is constant throughout the entire upstream portion. In this case, the flow pattern in the circulating fluidized bed corresponds to that in vertical pneumatic conveyance where, beyond the acceleration zone, the pressure gradient also remains constant with increasing height of the conveyance pipe. The pressure profile for this case is shown as a broken line in **Fig. 9**.

3.2 Pressure Gradients in the Steady-State Sections

Column diameter of the upstream part and range of superficial gas velocities guarantee that wall effects are negligible. Thus, the pressure gradient is directly proportional to the solids concentration at that height.

Since the pressure gradients in the TDH section of a circulating fluidized bed lie

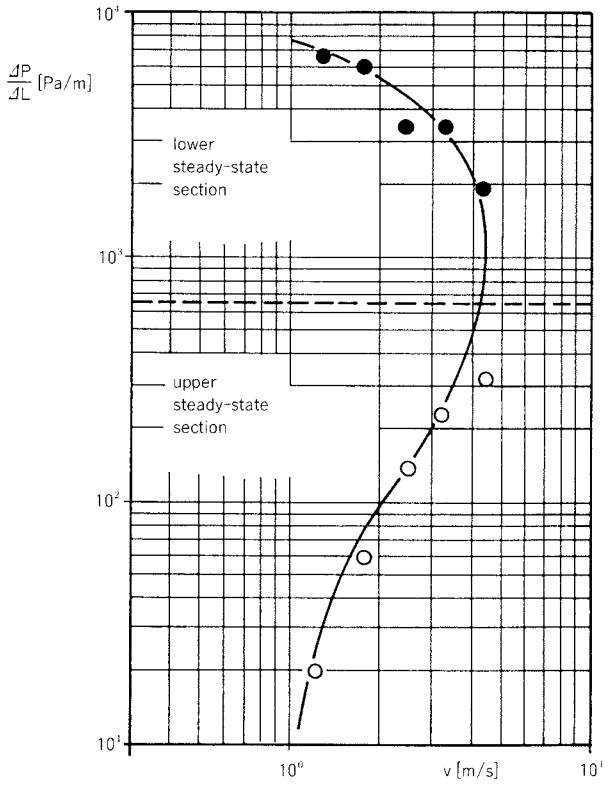

Fig.10 Pressure gradients in the steady-state sections versus superficial gas velocity (glass beads, $d_P = 90\mu m$).

between those of the lower and upper steady-state sections, the knowledge of these two pressure gradients is of particular importance. In **Fig. 10** ,the pressure gradients in the lower and upper steady-state sections are plotted against the superficial gas velocity. The pressure gradient which would have been established, if the solid particles were homogeneously distributed in the bed, is shown as a broken line in **Fig. 10** .The upper branch of the curve describes the pressure gradients in the lower steady-state section of the circulating fluidized bed where, immediately above the gas distributor, a bubbling or a turbulent fluidized bed does exist. The gradients in the upper steady-state section, is described by the lower branch of the curve in **Fig. 10** . While the pressure gradient in the lower section of the plant decreases with increasing gas velocity, that in the upper section of the plant increases. With increasing gas velocity, both curves approach the pressure gradient for a homogeneous distribution of solid particles.

Fig.11 shows a schematic representation of the pressure gradients for both steady-state sections in the circulating fluidized bed. In the range of gas velocities between the minimum fluidization velocity u_{mf} and the terminal settling velocity of a single particle w_f, a classical bubbling or turbulent fluidized bed exists immediately above the gas distributor. When the fluidized bed plant is sufficiently high, no entrainment of solid particles takes place. Therefore, the pressure gradient in the upper steady-state section of the plant is zero. The fluidized bed expands with increasing gas velocity.

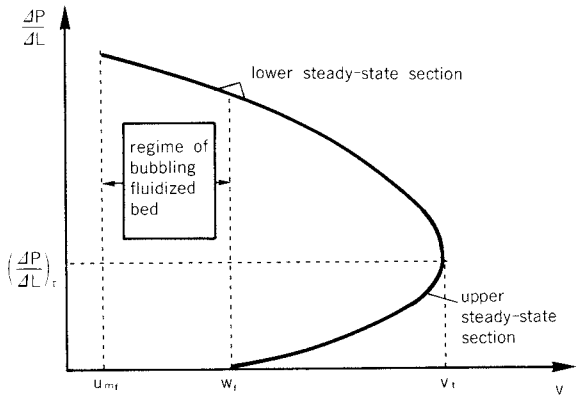

Fig.11 Schematic representation of pressure gradients in the steady-state sections of a circulating fluidized bed as a function of superficial gas velocity.

This results in a decrease of the pressure gradient in the bed. If the superficial gas velocity exceeds the terminal settling velocity of a single particle, some solid particles become entrained. These particles are transported by the gas flow to the upper steady-state section of the circulating fluidized bed. The higher the superficial gas velocity is the larger the solids concentration in the upper steady-state section which can be carried by the gas flow is. Therefore, the pressure gradient in the upper section also increases with increasing gas velocity. Consequently, the lower branch of the curve in **Fig. 11** characterizes the capacity of the gas flow to carry solids. Since the fluidized bed in the lower section of the plant expands further in this range of the superficial gas velocity, the pressure gradient in the fluidized bed decreases further.

At the superficial gas velocity v_T, the so-called transport velocity, the pressure gradient in the lower steady-state section of the plant is equal to that in the corresponding upper section. For gas velocities in excess of v_T, the pressure gradient in the upstream part is constant when the pressure drop for the acceleration of solid particles is neglected. Therefore, only in the range between the terminal settling velocity of a single particle and the transport velocity, an axial pressure profile with two steady-state sections is possible.

Apart from minimum fluidization velocity u_{mf} and terminal settling velocity of a single particle w_f, the transport velocity v_T is a further characteristic velocity of a vertical gas-solids flow. For a fine-grained catalyst for instance, the measured transport velocity amounts to $v_T = 1.8$ m/s. The terminal settling velocity of this catalyst is $w_f = 0.039$ m/s.

3.3 Partial Phase Separation, the Essential Feature of Circulating Fluidized Beds

From inspection of the schematic diagram, **Fig. 11** , it is quite obvious, that with high pressure gradients, i.e. high solids concentration in the lower steadystate section even at superficial gas velocities $v > w_f$, partial phase separation in terms of a bubbling or more likely a turbulent fluidized bed must take place, because otherwise two different steady -states could not be observed in the upstream portion of a circulating fluidized bed. However, also in the upper steady-state section, partial phase separation is observed. This statement can be verified experimentally as follows (compare right hand side of **Fig.7**):

The solids circulating mass flow rate can be measured by short time shut-off of downstream part below a weighing hopper. Solids concentration in the upper part of the column can be obtained from e.g. γ-ray absorption measurement. The mean solids rise velocity is

easily calculated from these two quantities. Evaluation of measurement data indicates mean slip velocities between gas and solid, which largely exceed single particle fall velocity. Thus, even rather global measurement techniques substantiate the essential role of partial phase separation for the phenomenon in question, i.e. the fluid dynamics of circulating fluidized beds.

3.4 Modelling of the Fluid Dynamics of Circulating Fluidized Beds

For the modelling of circulating fluidized beds, however, an additional difficulty has to be mastered: With strand flow type pneumatic conveyance or with bubbling fluidized beds for instance, modelling can start from clearly defined objects (sliding strands at the bottom end of the pipe's cross sectional area, and rising gas bubbles).

With turbulent fluidization in the lower steady-state section and with strands of clusters in the upper steady-state section of a circulating fluidized bed, no geometrical objects exist that can be more or less well defined. Therefore, modelling starts with an implied assumption, the usefulness of which can be justified only by a comparison with experimental results.

A dense phase is assumed which consists of a multitude of strands, clusters or the like. These clusters are surrounded by a lean phase which is rather poor in solid particles (**Fig.12**).

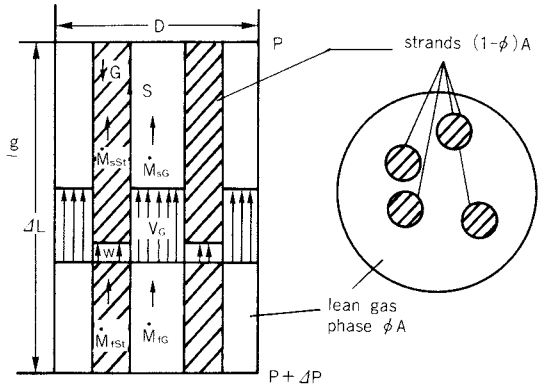

Fig.12: Strands in a pipe element.

The single strands are considered to be cylindrical aggregates of particles with an undefined cross-sectional shape. The porosity of the strands is assumed to be equal to that at minimum fluidization (ε_{mf}). The symetry axes of the strands are parallel to the direction of gravity. The fractional area occupied by the strands is (1-Φ). It is assumed that the strands have a piston-like velocity profile, and the solid particles in the strand do not undergo relative motion with respect to one another. All strands move at the same velocity w. The relative gas velocity in the strands is assumed to be proportional to u_{mf}/ε_{mf} and the pressure gradient.

A dilute gas-solids flow exists in the lean gas phase. The relative velocity between the gas and the solids particles is, thus, equal to the terminal settling velocity of a single particle, w_f. The velocity of the gas flow is v_G in the lean phase.

3.5 Momentum Transfer Between Lean Phase and Strands

From the previously described modelling of strand flow type pneumatic conveyance, one significant feature is adopted, namely that the strands are pushed mainly by impacting particles.

When the solid particles strike the surface of a strand at a velocity v_s, they are decelerated to the velocity of the strand w and then trasported within them (**Fig.13**). At steady-state conditions, for every particle striking the strand, another particle is ejected from the

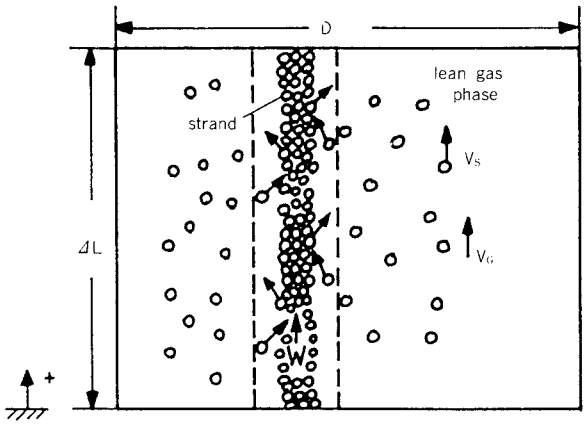

Fig.13: Momentum transfer close to the surface of strands.

strand. The pushing force exerted on a strand's surface is therefore proportional to the loss of momentum of the striking particles, i.e. it is proportinal to the velocity difference (v_s - w). Detailed analysis of the momentum transfer [3,4] results in the relationship for the pushing force exerted on the strands' surfaces over the vertical distance $\triangle L$,

$$S \alpha \rho_f v_G (v_s - w) C_{st} \triangle L.$$

The reasoning for that relationship is as follows: Under circulating fluidized bed condition, the type of gas flow is turbulent. Thus, in the lean phase axial as well, lateral turbulent fluctuations of the gas flow are observed. Fluctuation intensities are assumed to be proportional to the mean gas velocity in the lean phase. Particles in the lean phase are displaced in a lateral direction by the lateral fluctuations of the gas flow. Hence, the mass flow rate of hitting particles per unit of strand surface is assumed to be proportional to $\rho_f v_G$. The total force exerted is proportional to the strands' surface, i.e. to the product of circumference C_{st} of all strands and length $\triangle L$. The lack of an easily identifiable geometrical object is reflected by the fact that the strands' circumference C_{st} is unknown. At this point, only plausible arguments will bring forth results.

With wall effects being insignficant, only three geometrical parameters are involved, namely circumference C_{st} of all strands, particle diameter d_p and the column's cross sectional area A. It is assumed that the non-dimensional group,

$$\frac{C_{St}\, d_p}{A} \approx \text{const.} \ll 1$$

is a characteristic parameter of the fluid dynamics in circulating fluidized beds. This statement is substantiated by the following intuitive argument: Due to the large difference in the mean axial velocity of the particles in the lean phase v_s and the strand velocity w, particles coming from the lean phase hit the strands along trajectories with rather small angles. The depth of the zone of momentum transfer between the strands and hitting particles thus is of the order $C_{st} d_p$. The previously derived relationship, thus implies constancy of the ratio of the zone of momentum transfer to the column's cross sectional area. Combination of the two last relationship gives,

$$S = \lambda\ \rho_f\ v_G (v_s - w)(A/d_p) \triangle L$$

with a factor λ which defines the intensity of the momentum transfer between strands and lean phase. This factor has been determined from experimental results as $\lambda = 0.0053$. This very small numerical value coincides with the intuitive consideration that the momentum transfer zone is rather small in comparison with the column's cross sectional area.

3.6 State Diagrams for Segregated Vertical Upwards Gas-Solid Flow

Mass and momentum balances for gas and solids in the strands and in the lean phase result in six algebraic equations. Details of the procedure can be read elsewhere [3,4]. These equations can be rearranged so that they combine the following six dimensionless groups:

Dimensionless pressure drop: $\dfrac{\Delta P}{(\rho_s - \rho_f)(1-\varepsilon_{mf}) g \Delta L}$

Volumetric flow ratio: $\dfrac{\rho_f \mu}{\rho_s (1-\varepsilon_{mf})}$

Particle Froude number: $Fr_p \equiv \dfrac{v}{\sqrt{\left(\dfrac{\rho_s}{\rho_f} - 1\right) d_p g}}$

Archimedes number: $Ar \equiv \dfrac{d_p^{\,3}\, g(\rho_s - \rho_f)\rho_f}{\eta^2}$

Void fraction of the strands: ε_{mf} .

Thus numerical solution of the six equations gives,

$$\frac{\Delta P}{(\rho_s - \rho_f)(1-\varepsilon_{mf}) g \Delta L} = f\left(Fr_p; \frac{\rho_f \mu}{\rho_s (1-\varepsilon_{mf})}; Ar; \varepsilon_{mf}\right).$$

The numerical solution can be represented in the form of state diagrams as follows: A given combination of gas and sollid is represented in terms of the dimensionless groups as Ar=const. The strand porosity is assumed to be constant, e.g. $\varepsilon_{mf}=0.4$. Variation of the numerical value of ε_{mf} showed that the state diagrams are not very sensitive to variation in ε_{mf} within plausible limits. For any given Ar = const, ε_{mf} = const, the dimensionless pressure drop $\triangle P/[(\rho_s-\rho_f](1-\varepsilon_{mf})g\triangle L]$ can be plotted against the Particle Froude number with the volumetric flow ratio as a parameter. This result means that for any particular combination of gas and solid material, i.e. for a given Archimedes number, one corresponding state diagram must be calculated. In **Fig. 14** , the resulting state

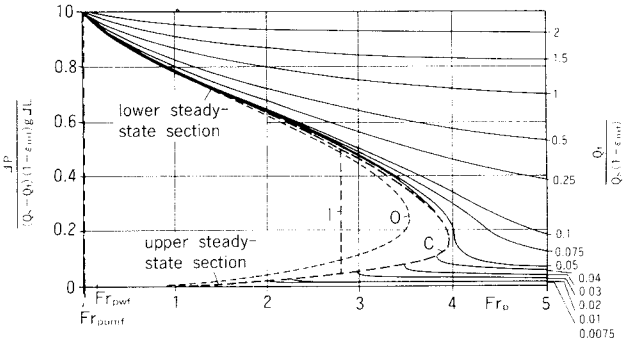

Fig.14 State and pressure drop diagram of segregated vertical gas-solids flow (Ar=10, $\varepsilon_{mf}=0.4$).

diagram is shown for Ar = 10 and ε_{mf} = 0.4. The field of operational points of the circulating fluidized bed is bounded by a theoretical curve for no net transport of solid particles (curve 0). The blank regime inside that curve corresponds to particles continuously falling down. This theoretical result conforms to the well known fact that a circulating fluidized bed with two steady-states, i.e. with lower and upper steady-state sections, exists only when one prevents the particles from leaving the system downwards, i.e. with bottom closure by a gas distributor or a cone.

The state diagram is based on momentum balances. Thus, the curve 0 meets the abscissa, i.e. the vanishing pressure drop for the last particle already leaving the system, i.e. for $Fr_p = Fr_{pwf}$. On the other hand, dimensionless pressure drop,

$$\frac{\Delta P}{(\rho_s-\rho_f)(1-\varepsilon_{mf})g\,\Delta L}=1$$

corresponds to minimum fluidization. Thus, the curve 0 reaches that limit for $Fr_p = Fr_{pmf}$. The diagram, **Fig. 15** ,is based on calculated steady-state solutions. Stable steady-states, however, must be stable against perturblations. Stability analysis of the operational points in **Fig. 15** shows that stable operational

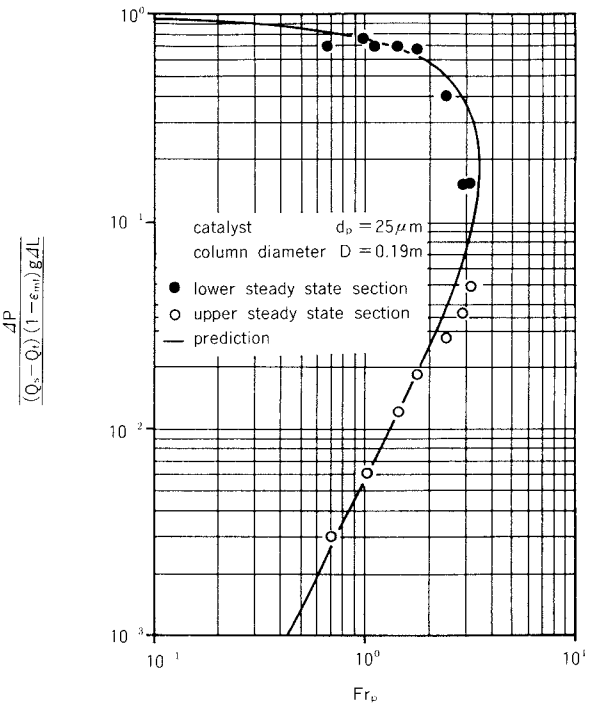

Fig.15 State diagram for circulating fluidized beds, a comparison of prediction and measurements (catalyst, $d_p=25\mu m$)

points end at curve C. With this result in mind, it is interesting to inspect these lines for the non-dimensional volumetric flow ratio,

$$\frac{\rho_f\,\mu}{\rho_s(1-\varepsilon_{mf})}=\text{ const.}$$

which end at the lower part of curve C. This lower part of curve C represents the upper steady-state section of a circulating fluidized bed. At steady state operation with inert solid material, there is no net feed of solid particles, i.e. a given solids content is circulated. Thus, for a varied superficial gas velocity, i.e. varied

Particle Froude number pressure drop and circulating mass flow, i.e. in the state diagram dimensionless pressure drop and volumetric flow ratio, will adjust along the lower branch of curve C. In the lower steady-state section, i.e. at the upper branch of curve C, rather high volumetric flow ratios are closely situated to the limiting curve C. Thus, the operational points are close to that curve. This theoretical result, which contains only one empirical factor, namely the momentum transfer factor λ, indeed shows striking analogy to the schematic diagram, **Fig. 11** , which has been deduced from pressure drop measurements. The two operational points of the lower and upper steady-state section are linked by a vertical straight line, e.g. line I in **Fig. 14** . In **Fig. 15** , experiment and prediction are compared for a catalyst ($d_p = 25\ \mu m$). Due to the log-log representation, curve C is deformed in comparison with the linear representation of **Fig. 14** . For superficial gas velocities exceeding v_T, i.e. in the state diagram for $Fr_p > Fr_{pT}$, only one steady-state operational point exists for a given Fr_p and given volumetric flow ratio result $(\rho_f \mu) / [\rho_s (1 - \varepsilon_{smf})]$.

This result means that for $Fr_p > Fr_{pT}$, the solid material is evenly distributed over the column's height. In that regime, the circulating solid mass flow rate, i.e. in the state diagram, the volumetric flow ratio depends only on the mass of the solid material which is present in the plant. For a given superficial gas velocity, the constant pressure gradient over the column's height as well as the mass flow rate of circulating solids are functions of superficial gas velocity and solid mass in the plant. These general features can be demonstrated quite convincingly by pneumatic transport vertically upwards at the constant feed rate of the solid material.

Fig. 16 presents the measured pressure gradient in upward vertical pneumatic conveyance of a catalyst plotted against the superficial gas velocity. The parameter is the mass flow rate per unit area of the conveyed solids. In addition, the regression curve of measured pressure gradients in the steady-state

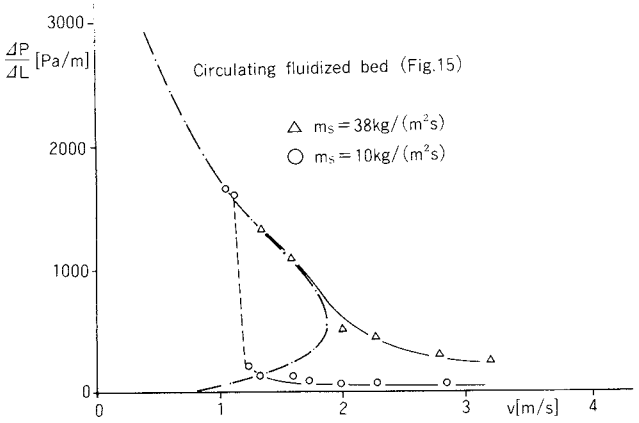

Fig.16: Comparison of measured pressure gradients in pneumatic conveyance and in steady-state sections of a circulating fluidized bed(catalyst $d_p = 25\ \mu m$).

sections of a circulating fluidized bed is also shown (dash-dot line). In pneumatic conveyance, at a constant mass flow rate of solids, the pressure drop due to the transportation of solids increases with decreasing superficial gas velocity. When a low solids mass flow rate e.g. 10 kg/(m² s)is conveyed, on decreasing the gas velocity to below a critical value, the pressure drop increases sharply. At low pressure drops, the solid is conveyed in the form of strands and clusters, whereas at high pressure drops, the solid is transported as a migrating fluidized bed, i.e. in the regime of so-called "fluidized bed conveyance". A sudden increase in pressure drop produces an equally sudden change in the flow pattern.

If a higher solids mass flow rate is pneumatically conveyed, e.g. 38 kg/(m² s), there is no sudden rise in the pressure drop when gas velocity is decreased. At these mass flow rates of solids, the pressure drop increases continuously with decreasing gas velocity. This means that the flow pattern also changes continuously. However, at high gas velocities, the solids are conveyed in the form of strands and clusters; on decreasing the gas velocity, a gradual change of the flow pattern towards fluidized bed conveyance takes place. The pressure drop profile in the range of the fluidized bed conveyance is practically identi-

cal to that in the lower steady-state section of a circulating fluidized bed. The superficial gas velocity, at which in pneumatic conveyance at low solids mass flow rate the pressure drop suddenly increases, is the same as that at which an identical solids mass flow rate is entrained in a circulating fluidized bed. Hence, the flow patterns in the upper steady-state section of a circulating fluidized bed and in pneumatic conveying at critical velocity are identical.

3.7 Predictive Power and Physical Significance of the Model

The experimental results depicted in **Figs. 15** and **16** prove the consistency of the approach proposed here.

State diagrams as shown in **Fig. 14** for Ar = 10 represent the relevant data of the operational points of circulating fluidized beds. Therefore, one can read off different properties, namely pressure gradient which is equivalent to the concentration of solids, as well as the mass flow rate of the circulating solids. This operating parameter is necessary for the design of the cyclone. For three different gas-solids systems, i.e. three different Archimedes numbers, the carried over measured solids mass flow rates are plotted in dimensionless form against the dimensionless superficial gas velocity in **Fig. 17**. The measurements were carried out in an experimental plant with an overall height of 12 m and a square cross-section with a side lenght of 0.17 m. A detailed description of the experimental set-up is given elsewhere [4] . The plant was operated in such a way that two steady-state sections occurred. Thus, the operating points were located on the limiting curve C where the physical properties of the gas-solids flow are responsible for the circulating solids mass flow rate and not the solids content of the bed. To compare the measurements with the proposed model when two steady-state sections are present, the calculated circulating solids mass flow rates are additionally plotted in **Fig. 17**. From the comparison between the predicted and experimental results, the following conclusions can be drawn:

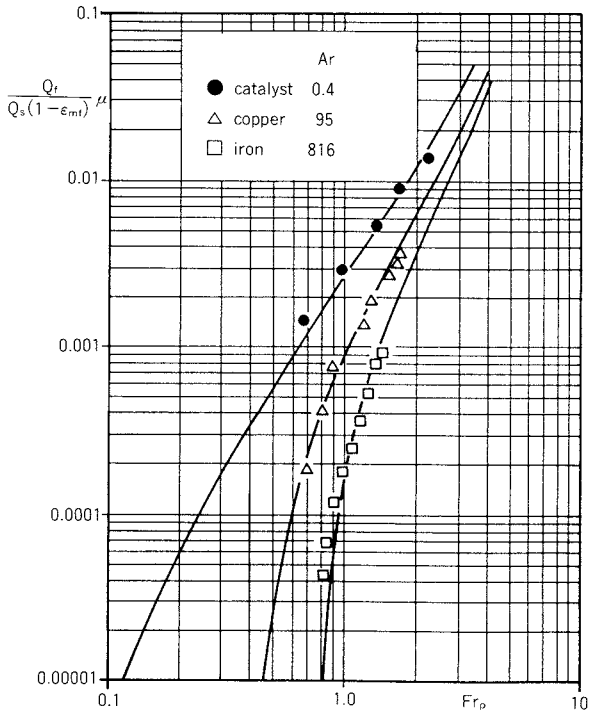

Fig.17: Comparison of measured and calculated circulating mass flow rates of solids when two steady-state sections exist in the circulating fluidized bed.

1. The predicted and experimental results agree very well. This fact confirms that the model proposed here of the fluid dynamics of circulating fluidized beds not only reflects the general features of the fluid dynamics quite well but can also be used for quantitative predictions.
2. The experimental results have been obtained for a wide variation of the Archimedes number($0.4 < Ar < 816$)and, thus, indicate that the assumption of a constant momentum transfer factor λ is accurate enough even for a wide range in variation of solid material physical data.

4. Symbols used

A	[m^2]	cross-sectional area
C_{st}	[-]	circumference of strands
D	[m]	pipe diameter
d_p	[m]	particle diameter

f_r	[-]	coefficient of sl iding friction
g	[m s^{-2}]	gravitational acceleration
h	[m]	height of circulating fluidized bed
$\triangle J$	[kg m s^{-1}]	change of momentum
k	[-]	constant
L	[m]	length of pipe element
m	[kg]	mass of particle
$\dot{M}$	[kg s^{-1}]	mass flow rate
$\dot{m}$	[kgm^{-2} s^{-1}]	mass flow rate per unit area
$\dot{n}$	[s^{-1} m^{-2}]	number flux of particles
$\triangle P$	[kgm^{-1} s^{-2}]	pressure drop
$\triangle P_G$	[kg m^{-1} s^{-2}]	pressure drop due to air flow
$\triangle P_z$	[kg m^{-1} s^{-2}]	pressure drop required for horizontal transport of solid material
R	[kg m s^{-2}]	force of friction
s	[m]	width of particle strand
S	[kg m s^{-2}]	pushing force on strand
u_{mf}	[m s^{-1}]	minimum fluidization velocity
v	[m s^{-1}]	superficial gas velocity
v_G	[m s^{-1}]	gas velocity in lean gas phase respectively over the strand
v_s	[m s^{-1}]	solids velocity with vertical solids transport
w	[m s^{-1}]	velocity of strands
w_f	[m s^{-1}]	terminal settling velocity of single particle

Greek Symbols

ε	[-]	porosity of the horizontal strand
ε_{mf}	[-]	minimum fluidization porosity
λ	[-]	mometum transfer coefficient
τ	[kg m^{-1} s^{-2}]	shear stress
Φ	[-]	fractional free cross-sectional area of pipe
η	[kg m^{-1} s^{-1}]	viscosity
μ	[-]	mass flow ratio

Subscripts

f	gas
G	lean gas phase
max	maximum
s	solid
St	strand
T	transport

Dimensionless groups

$$Ar \equiv \frac{d_p^3 g(\rho_s-\rho_f)\rho_f}{\eta^2}$$ Archimedes number

$$Fr_p = \frac{v}{\sqrt{\left(\frac{\rho_s}{\rho_f}-1\right)d_p\ g}}$$ Particle Froude number

$$Fr_{pw_f} = \frac{W_f}{\sqrt{\left(\frac{\rho_s-\rho_f}{\rho_f}\right)d_p\ g}}$$ Particle Froude number built with terminal settling velocity of single particle

$$F_{pumf} = \frac{u_{mf}}{\sqrt{\left(\frac{\rho_s-\rho_f}{\rho_f}\right)d_p\ g}}$$ Particle Froude number built with minimum fluidization velocity

$$Fri = \frac{v}{\sqrt{\left(\frac{\rho_s}{\rho_f}(1-\frac{\rho_f}{\rho_s})(1-\varepsilon)D\ g\ f_r\right.}}$$ Friction number

$$\mu = \frac{\dot{M}_s}{\dot{M}_s}$$ mass flow ratio

$$\frac{\rho_f}{\rho_s(1-\varepsilon_{mf})}\mu$$ volumetric flow ratio with vertical solids transport

$$\frac{\rho_f}{\rho_s(1-\varepsilon)}\mu$$ volumetric flow ratio with horizontal solids transport

5. References

1) Wirth, K.-E. and Molerus: O. Prediction of Pressure Drop in Horizontal Segregated Pneumatic Conveying with Particle Strands Sliding along the Bottom of the Pipe. Ger. Chem. Eng. 4(1981), 278-284.

2) Murphree, E.V.; Brown, C.L.; Gohr, E.J.; Jahnig, C.E.; Martin, H.Z. and Tyson, C.W.: Improved fluid process for catalytic cracking. Pap., Am. Inst. Chem. Eng. Meet. 19(1944)

3) Wirth, K.-E.: Fluid Mechanics of Circulating Fluidized Beds. Chem. Eng. Technol. 14(1991), 29-38.

4) Wirth, K.-E.: Zirkulierende Wirbelschichten-Strömungsmechanische Grundlagen, Anwendung in der Feuerungstechnik. Springer Verlag, Berlin, 1990.

Review

Electrically Charged Air Filters†

R. C. Brown
*Health and Safety Executive**

Introduction

The value of electrostatic filters can be most easily understood from a comparison with purely mechanical filters. Filters act by means of a number of processes, the most basic being interception(1). In this process, illustrated in **Fig.1**, particles are carried by the streamlines of the air passing through a filter, and whether or not they are captured will depend on whether or not the particles are brought into contact with a fiber as they pass through. The detailed theory of this process is given elsewhere(2)but features are that the capture efficiency tends to be small, and that it has a quadratic dependence on the particle diameter.

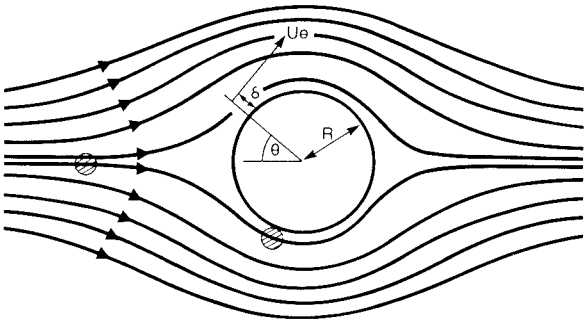

Fig.1 Particle capture by interception. A particle is illustrated at two different times, on a single streamline, which brings it into contact with a fiber, where it is captured.

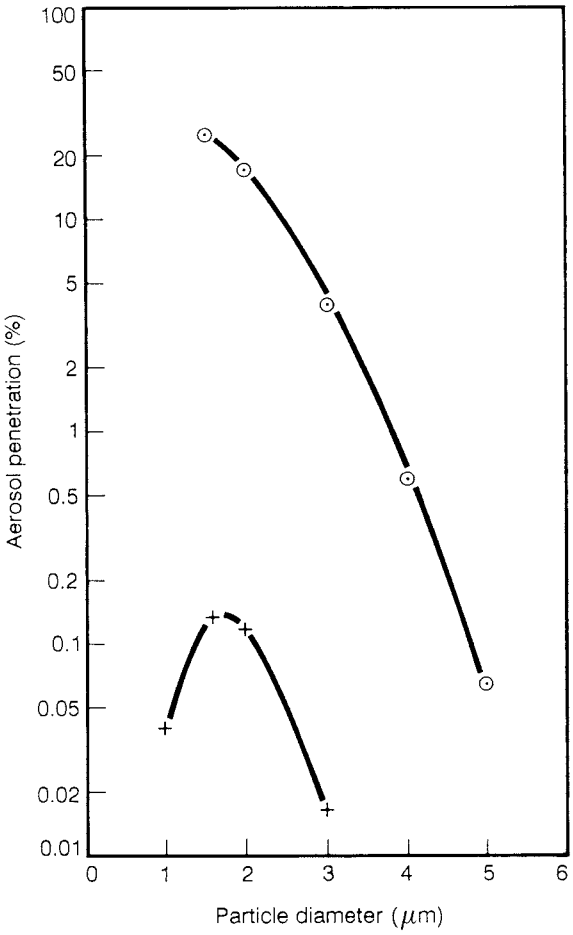

Fig. 2 Penetration of monodisperse aerosol particles of a range of sizes through filter material. ⊙-Electrically neutral material. + − electrically charged material.

The simplest type of respirator filter, a preformed cup of material forming a mask for use against dusts of low toxicity which pose a nuisance rather than a hazard, gives performance results (3) that can be well approximated by the assumption that this process acts alone; and specimen results are given in **Fig.2**

It is clear that a filter of this sort has a fundamentally low efficiency in capturing particles of the size 1-2 μm; and such particles constitute a serious respiratory hazard (4). The filter in question is made from normal textile fibers, with a diameter of about 20μm. Natural fibers tend to be of this size, and synthetic fibers capable of being processed on normal textile equipment are comparable, and so it is clear that such simple mechanical filters

* Broad Lane Groad Sheffield S3 7HQ, United Kingdom

† Received July 1991

can give only limited protection.

Filtration efficiency can be increased if the filtration velocity is raised, since this will bring inertial effects into play; but this will also increase the pressure drop across the filter and the energy expended in filtration. If the velocity is reduced, diffusional capture will occur, without any energy penalty, but filtration velocity low enough to make this process effective in such filters seriously limits the quantity of air that can be filtered.

A considerable improvement can be achieved by the use of ultrafine fibers, but such fibers tend to be fragile, and they may become detached from the filter during use, becoming a respiratory hazard of their own(5). For this reason, the use of fibers with a permanent electric charge on them is an attractive proposition. As an example of their general effectiveness, a simple mask made of material carrying an electric charge gives the performance curve illustrated in **Fig.1**.

1. Type of electrically charged material available.

Electrically charged filter material has a history of several decades; in fact such a material was used for a period of years before its mechanism of action was well-understood. A number of materials carrying permanent electric charge are used at present. Electrically charged filter materials may be classified in a number of ways, such as the means whereby the material becomes electrically charged: triboelectric charging, corona charging or charging by induction.

1.1 Triboelectrically charged material.

The exchange of electric charge between two contacting materials is well known, if incompletely understood. The first recognised electrostatic filter (6) obtained its charge by triboelectric exchange. Particles of resin, when mixed with fibers of wool, develop a negative charge, the wool fibers charging positively (7,8). Resin is a good insulator, and its low conductivity is sufficient for the charge on the filter material to be stable. Wool can be considered to be a conductor, and so it will develop whatever charge is necessary to reduce the electrostatic energy of the system to a minimum; and the configuration that achieves this takes the form of charges that are the electrical images of the electrostatic charges of the resin. An electron micrograph of the material itself is shown in **Fig.3a**. The presence of a conductor means that on a macroscopic level, the charge on the material is low. It contains positive and negative electric charge almost in balance.

A second type of material that develops its charge by triboelectric means is material made from a binary mixture of polymer fibers (9,10). If two yarns of dissimilar polymers are rubbed together, they will exchange charge in a consistent way so that one species will develop a positive charge and the other a negative. Experiments of this sort can be used to produce a triboelectric series, defined so that fibers of a type high in the series develop a positive charge when rubbed against those below them. Different observers do not quite agree on the series, probably because generic names are used to describe classes of polymers, the members of which are not chemically identical, but in general wool is the most electropositive fiber, nylons are slightly less electropositive followed by cellulose-based polymers and polyolefins in that order, with aromatic and halogenated fibers at the negative end of the series. The mixed-fiber filter that is made in this way, like the resin wool, has high charge on a microscopic level and much lower charge on a macroscopic level. An electron micrograph is shown in **Fig.3b**.

1.2 Corona charged material.

A common means of applying an electric charge to a polymer is by way of a corona discharge. A point electrode at a high potential emits ions of its own sign, and these will drift under the influence of the electric field to a collecting surface of lower potential. If the surface is that of an insulator, a charge will develop. If the insulator is a thin sheet of polymer, resting on a conductor, a compensating charge of the opposite sign will develop as the polymer is stripped away from its

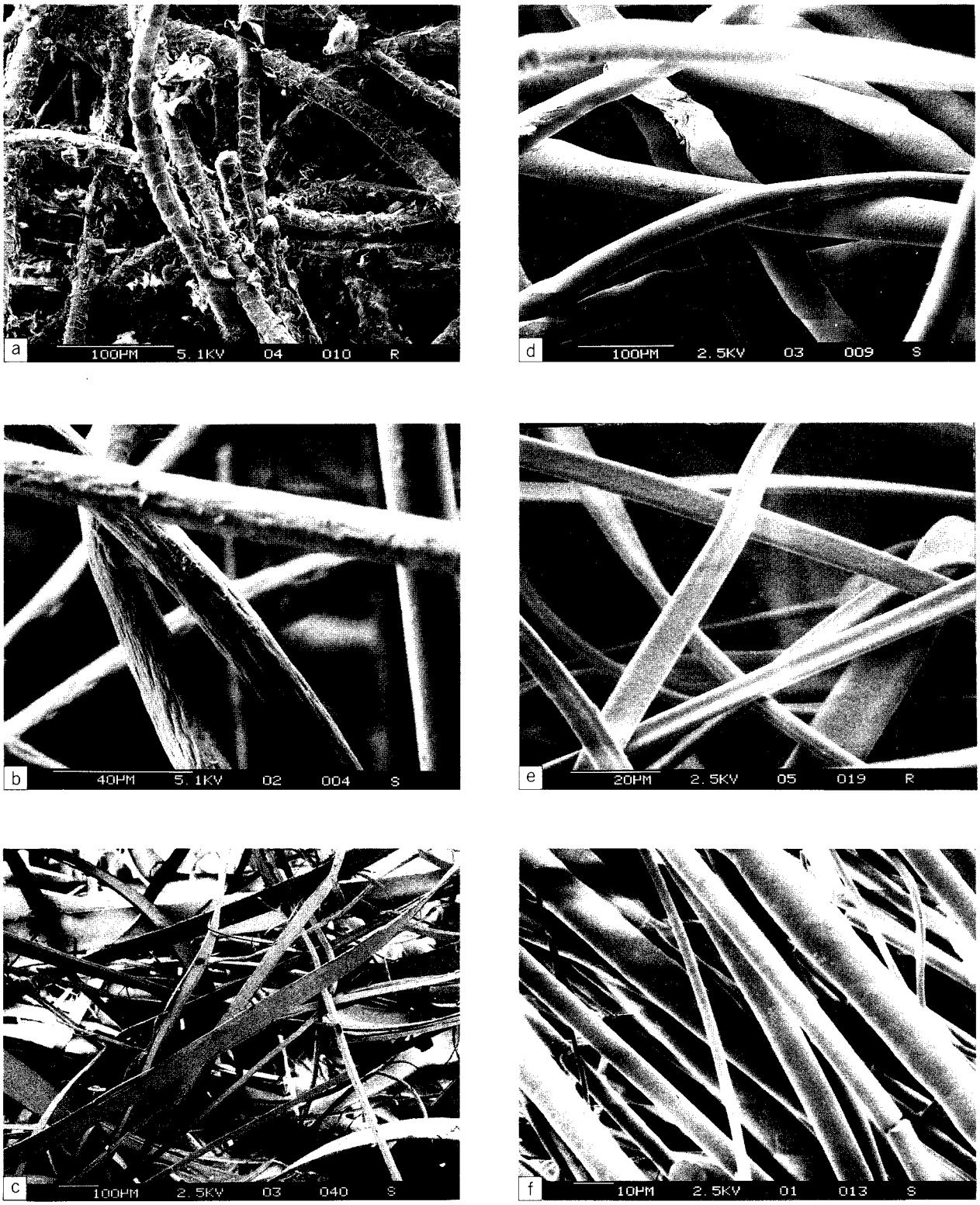

Fig.3 Electron micrographs of electrically charged filter material.

a) Resin wool material
b) Mixed-fiber material
c) Electret material charged in sheet form and fibrillated
d) Electret material charged by other means
e) Polycarbonate material produced by extrusion from a solution
f) Polypropylene material produced by extrusion from a melt

backing, giving charge in a sheet dipole configuration, which is more stable than unipolar charge. Alternatively the sheet dipole may be produced by means of two coronas, opposite is sign, applied one to each face of the material.

In the sheet dipole configuration the material is often termed an electret. Strictly speaking electrets are polymers with a frozen-in electric polarisation(12), their form being analogous with that of a magnet, just as the word 'electret' is analogous with the word 'magnet'. However the word is now so widely applied to material with real charge that it can be considered to be an acceptable term.

Polypropylene forms a good electret, and it has a further interesting property. If a sheet of the polymer is stretched it suffers considerable molecular realignment, becoming strong along the direction of stretching and weak in the direction perpendicular to it. This allows the sheet to be split into fibers by a process termed fibrillation, and these fibers, with their now line-dipole configuration of charge, can be carded and made into a filter, again with a high microscopic level of charge and low macroscopic level(13,14,15,16). An electron micrograph of the material, in **Fig 3c,** shows the rectangular shape of the fiber cross-section.

Another type of electret material is described in the literature (17) and a micrograph of this material is shown in **Fig 3d**. The method of manufacture must be different from that of the material above, because the fibers are circular in cross-section, and it might be produced by polarisation of the material after felting (18). If this is so the material will be a true electret and, unlike the material described above, in which any fibers that retain a line dipole configuration during carding will be randomly orientated, it will consist of aligned dipoles.

1.3 Material charged by induction

Induction of charge is the third form of electric charging mechanism exploited in the production of electrically charged filter material, the process being similar to that used in the production of electrically charged sprays (19,20). A conductor placed in an electric field will develop a surface charge that will reduce its own internal field to zero. If the conductor is isolated the charge developed will be dipolar in form but if it is attached to another body and subsequently detached, a unipolar charge may be imparted to the conductor. This charged body can then move under the influnce of the electric field that induced the charge in the beginning, as do the small droplets produced by electrostatic spraying.

Electrostatic spraying involves the extrusion of a filament of charged liquid which breaks up into droplets under the influence of surface tension. If, however, this liquid is replaced by a polymer solution or melt, the high viscosity of the liquid will delay its breaking up into droplets, and under appropriate conditions the liquid filament may solidify into a fiber before this can occur. When such a fiber eventually detaches it may deposit onto the collecting electrode and produce a structure rather like an airlayed felt.

Fig 3e shows fibers produced in this way from a solution of polycarbonate(21), and Fig 3f fibers produced from a melt of polypropylene (22). The latter fibers have a circular cross section, and an occasinal large sphere of material is present, such inclusions being known as 'shot'. The solvent spun fibers have a characteristic bilobar cross section, probably caused by the outer layer solidifying first, resulting in a higher surface area/volume ratio than would exist for a cylindrical fiber.

One effect of this process is the production of highly attenuated fibers. As mentioned above, conventional spinning rarely pruduces fibers with diameters much below 20μm, whereas electrostatically extruded fibers can have diameters as low as 1 or 2μm. A problem is that the fibers cannot be carded or produced by normal textile equipment, and so there will be limited control on the filter structure. An advantage is that the mechanical capture efficiency will be greater, complemented by the electrostatic action, which is

rather weaker than that which can be achieved by triboelectrification or corona charging.

1.4 Miscellaneous electrically charged material.

Spurious electric charge may occur on materials
This is not, however, an unmixed blessing because although electric charge invariably improves the performance of a filter, it has problems associated with it, as will be described later in the article, and its unexpected presence can lead to misplaced confidence about filter performance which a greater understanding of filtration would have prevented.

With the induction-charged material described above, the electrostatic process was originally designed to produce fine fibers; the electric charge was a bonus. Fine fibered thermoplastics may also be produced by attenuating spun fibers with the aid of an air jet(23)and this process can result in the development of a fairly large amount of spurious charge, which may develop from contact and exchange between the melt and the spinneret, or as a result of manipulation of the filter medium shortly after it is formed.

2. Non-fibrous electrostatic filter

An electrostatic filter can be made from an electret sheet and a sheet of conductor, both aligned parallel to the airflow(24,25). The electret sheet is planar and the conductor is corrugated, the two being wound together to form a system of pores in which the electric field is everywhere perpendicular to the flow direction. This means that, in principle, the entirety of an aerosol can be precipitated(26), whereas in a fibrous filter acting by a normal depth-filtration process, the penetration decreases exponentially but remains always finite. Its existence illustrates that a conductor can form an essential part of an electrostatic filter with a stable charge. Unfortunately, the filter's capture efficiency for neutral particles is relatively weak, since the electric field within it, the form of which can be obtained by means of a self-consistent charge calculation (25) is rather more uniform than would be ideal. Nevertheless, the usefulness of the material has been demostrated by its ability to capture bacteria(27).

3. Magnitude and configuration of electric charge.

The most obvious way of measuring the electric charge on a filter is to place a sample in a Faraday ice-pail connected to an electrometer. If this procedure is followed for any of the materials described above, the result is a very low level of charge(28). This behaviour could be anticipated as a result of a simple examination of the materials, because they show no obvious sign of being electrically charged. In textile vocabulary they would be described as 'dead'. It is clear then that any charge that they do contain consists of positive and negative charge almost completely in balance.

Measurement of the level of bipolar charge can be carried out in a number of ways. The charge can be destroyed, in a controlled manner, by a known dose of ionising radiation, whilst the filter performance is being measured(7,28). A quantity of charge of each sign will be removed by the X-ray beam, according to its strength, which is defined in terms of the degree of ionisation that it produces(29). If incremental doses of radiation are given to the filter, and the penetration of a test aerosol though it is measured as a function of integrated dose, results similar to those plotted in **Fig.4** are obtained. As the integrated dose increases the penetration increases to a level beyond which further irradiation causes no change. The end point is difficult to identify with absolute precision, but the number of ions required to bring about the neutralisation can be related to the charge that the filter originally held, which can then be related to the charge per unit area of fiber.

Experimental results show that in some cases the electric field caused by the charge would exceed the normal breakdown field of the air, which, for uniform fields over large

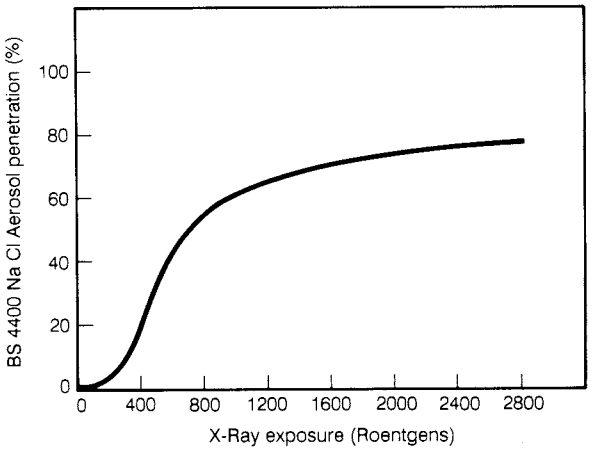

Fig.4 Penetration of a standard aerosol through irradiated filter material as a function of cumulative radiation dose.

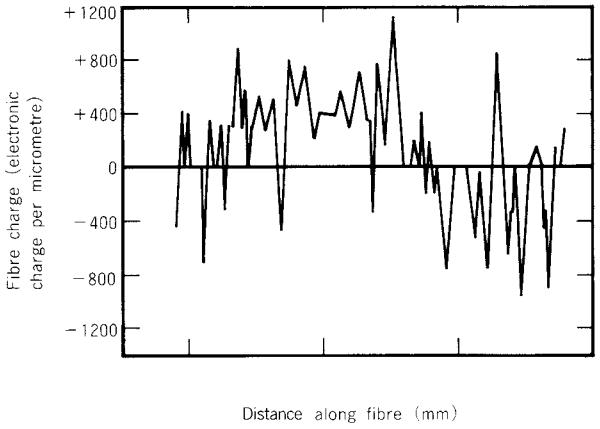

Fig.5 Scan of the electric field close to a fiber of electrostatically extruded material. Taken from Baumgartner et al(1986)I.E.E.E. Transaction E1-21 477-486 © I.E.E.E. 1986.

distance, is about 3×10^6 volts per metre. Short range fields, like that caused by a uniformly charged cylinder can exceed this value (30), but some of the measured charge levels are even higher, and this implies that the charge on a fiber varies over fairly short distances; since general solutions of Laplace's equation, which describes electrostatic potential, indicate that the range of an electric field varies over distances comparable with the spatial variation of electric charge.

An alternative method of charge analysis involves a microcopic study of the filter charge. A fiber is suspended vertically, and held in tension by means of a small weight attached to its end, and a pair of electrodes producing a high field is moved down its length. Charge on a segment of fiber will cause it to be attracted to the appropriate electrode as it passes, and the deflection can be related to the charge on the fiber (17). An example of such measurements is shown in **Fig 5**.

This method gives a microscopic picture of the fiber charge, and it reveals that the configuration of charge is highly complicated, as the X-ray method Suggests. A drawback is that the charge on the fibers may be significantly altered by contact with other fibers as the fiber under study is withdrawn from the material.

A final method, applicable only to the electret material, is to measure the strength of the dipolar charge on the sheet of fiber-generating polymer before fibrillation has been carried out(31). This method is the least satisfactory, since although it is undoubtedly capable of giving an accurate measure of the charge on the polymer at this stage in the manufacture process, it is very likely that the charge is altered as the material is subjected to the same sort of processing that results in other types of material developing all of the charge that they have.

4. Particle Capture by Electric Forces

Electrically charged fibers attract both charged and neutral particles. The capture, by a fiber, of oppositely charged particles by coulomb forces is self-evident. The capture of neutral particles comes about by the action of polarisation force. The electric field of the fiber induces a dipole in the neutral particle, the strength of which depends upon the volume of the particle and the dielectric constant of its constituent material. The component of the induced dipole that is nearer to the fiber is subjected to an attractive force slightly larger than the repulsive force acting on its counterpart, since the electric field diminishes with distance from the fiber, and it is this slight imbalance that causes the particle to be attracted whatever the sign of charge on the fiber.

The motion of particles in the vicinity of a charged fiber will consist of two components, the drift velocity under the influence of the electrostatic forces, as indicated in Fig 6, tending to effect particle capture, and the convective velocity of the air, tending to take the particle past. The likelihood of capture can be related to the quotient of these two velocities, which will be a dimensionless parameter(32).

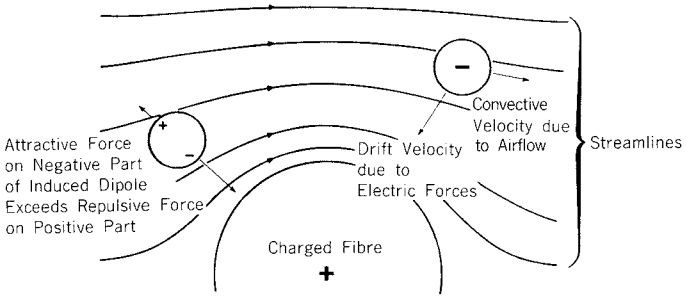

Fig.6 Capture of charged and neutral particles by a uniformly charged filter fiber.

If a fiber is uniformly charged, with a charge density of Q per unit length, the electric field, E, outside will be independent of the coordinate angle, θ, and will depend only on radial distance r, being given in magnitude by

$$E=\frac{Q}{2\pi\varepsilon o\hat{}} \tag{1}$$

where $\varepsilon 0$ is the permittivity of free space. If the fiber carries a line dipole charge so that the charge varies as the cosine of the angular coordinate of the fiber surface, the electric field will be given by

$$E\check{}=\frac{ada^{3}\cos Q}{(1+s)450\hat{}2} \tag{2}$$

$$E_{Q}=\frac{ada^{3}\sin Q}{(1+D)4\varepsilon o^{\hat{}2}} \tag{3}$$

where $\sigma \cos \theta$ is the surface charge density, df is the fiber diameter and D is the dielectric constant of the material of the fiber. D does not appear in the expression for the field outside a uniformly charged fiber because there is no internal field to feel the influence of the dielectric properties of the fiber.

Multipole configurations can be analysed in a similar way to the dipole, and more complicated charge configurations can be built up by adding the simpler forms together or by considering three-dimensional charge arrangements, but a basic understanding of behaviour patterns does not require this level of detail.

The drift velocity of a particle is simply the product of the force acting and the mobility, μ, which is given by

$$\mu=\frac{1}{3\pi\zeta dp} \tag{4}$$

where eta is the coefficient of viscosity of the air and dp is the particle diameter. Equation 4 means that, neglecting constants, the dimensionless parameters describing the capture of particles are

$$N^{Qq}=\frac{Q^{2}}{\zeta\zeta oUodpda} \tag{5}$$

$$N_{Qo}=\frac{Q^{2}dp^{2}}{\zeta\epsilon oUoda^{3}} \tag{6}$$

where Q is a measure of the charge per unit length of fiber, q is the charge on the particle, $\varepsilon 0$ and 3 eta are constants.

Expressions relating single fiber efficiency to these dimensionless parameters can be obtained(33,34,35,36), though these rely on assumptions being made to some extent about the configuration of charge on the fiber. However, an appvoximate summary of what is found is that the single fiber efficiency increases monotonically with the appropriate dimensionless parameter, the relationship being linear in the case of the longest range of force, which is r-1, occurring when a uniformly charged fiber acts on a charged particle. The relationship become weaker as the range of force become shorter(37). A weak

dependence of capture efficiency on the dimensionless parameter has been observed experimentally(31,38)

Important generalisations can be made, even on the basic of this cursory treatment. The advantage of fine fibers is apparent, as is the generally beneficial effect of carrying out filtration at low velocity; the contract between the two being that whereas fine-fibers bring a penalty of increased airflow resistance, low velocity has a concomitant advantage of reduced resistance. The particle size dependence varies with the capture process. Coulomb forces are more effective for smaller particles, provided that charge is constant, and polarisation force are more effective for larger particles. The most difficult particles to remove by electrostatic filters will be small neutral particles.

5. Experimental measurement of filter performance

Experiments with monodisperse aerosols enable some of the variations to be eliminated, especially if the aerosols can be produced in a well-defined charged state. The charge on the filter cannot be described exactly, but a comparison between its behaviour in the electrically charged and the electrically neutral condition is useful.

The experimental production of monodisperse aerosols often results in their charge level being high, and it is common pratice to pass the aerosols through the region of ionised air produced by an ionising radioactive neutraliser, to reduce the level of charge. Protracted exposure will reduce the charge on the aerosols to a level close to that given by thermodynamic equilibrium (39), though in practice aerosols treated in this way tend to have a charge level rather higher than the equilibrium level. It is difficult to produce uniformly charged or neutral particles with a diameter greater than about 0.5μm.

A number of experiments have been carried out with particles of submicrometer size in the charged and the neutral conditions (38,40,41,42,43,44,45). The work of the various authors shows basic agreement, and the results from (45) are plotted in Fig 7. A most penetrating particle size is consistenly observed for neutral particles, caused by the competition of diffusion effects and polarisation forces, unlike the most penetrating particle size through mechanical filters (1) which involves interception rather than polarisation; and the assumption of an equilibrium charge distribution on an aerosol leads to a prediction of two minima in efficiency, with a local maximum between (46). The effect of a single charge on a very small particle is critical, whereas a much large charge must be placed on large particles if coulomb forces are to exceed polarisation forces.

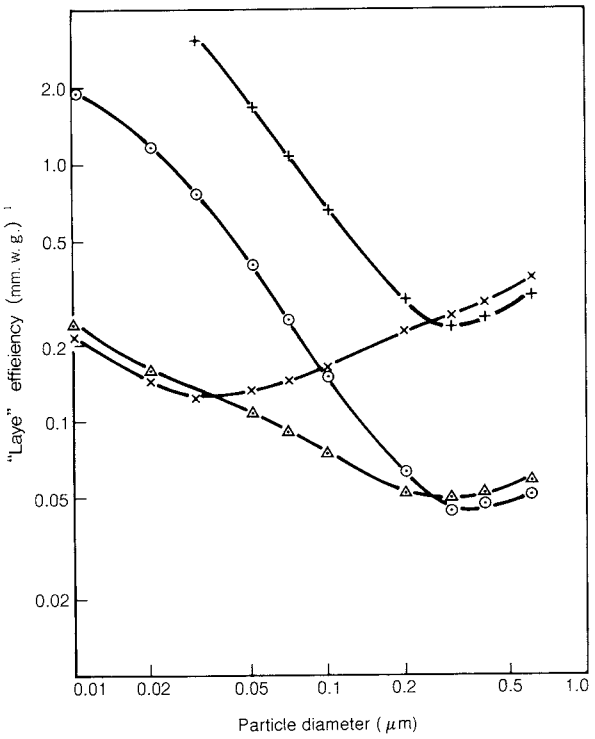

Fig.7 Layer efficiencies of fibrous filters tested with submicrometre aerosols: + charged filter/charged particles; x charged filter/neutral particles: ⊙ neutral filter/charged particles; neutral filter/neutral particles.

6. Charge stability during storage

The electrically charged state is one of high energy and is, therefore, potentially unstable. If a filter is heated to any constant temperature, it suffers a loss of efficiency in a

relatively short period of time, after which its behaviour stabilises. If its temperature is raised further, the pattern of behaviour is repeated and the filter again stabilises, but at a higher level of aerosol penetration than before. The stable level is temperature dependent, as shown in Fig 8 (47). The explanation of this is that the charge on the filter is held in bound states with a range of binding energies. At any temperature charge that is held in relatively shallow levels is lost and that bound more tightly is retained, but the cut off point is altered with the temperature. In fact this behaviour occurs after filter material is made (private communication with several manufacturers); the initial level of performance suffers some deterioration immediately after manufacture but then becomes stable.

Humidity can also affect charge stability (48,49) and it seems that it has more effect on materials with a high affinity for moisture. When materials are humidity sensitive, the effect of elevated temperature and humidity together is much more serious than the effect of either separately.

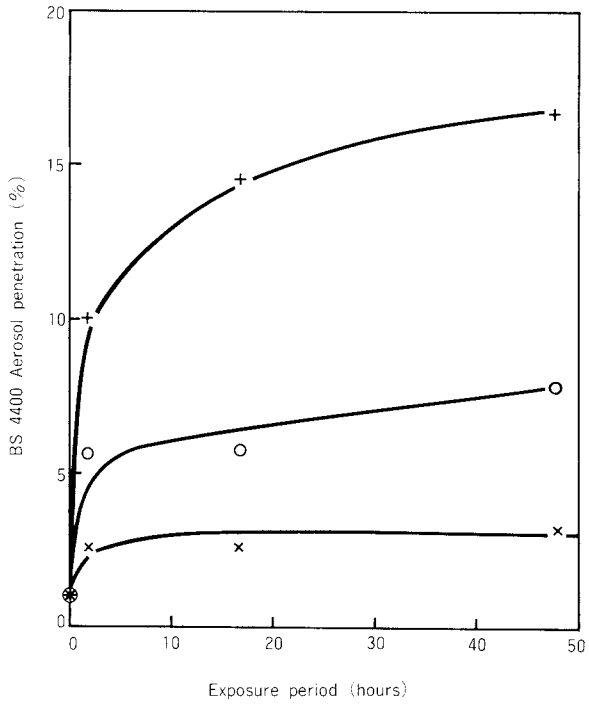

Fig.8 Time dependence of performance of electrically charged resin wool filter at elevated temeratures: x 90℃ ; + 110℃

7. The effect of dust loading on the performance of electrically charged filters.

Loading mechanical filters with dust tends to increase both efficiency and pressure drop because the captured dust tends to form tree-like structures, dendrites, which act like additional fibers. Loading electrically charged filters may cause the efficiency to increase by this process or it may reduce it by destroying the effect of the charge. The two processes can occur at different stages during, loading which means that behaviour is often hard to predict, and not always repeatable. Frequently the results of loading experiments are difficult to interpret, but in the situation where exposure is at a relatively low rate, charge loss is the dominant process, and not dendrite formation.

In this situation, the penetration of an aerosol through a loaded filter can be shown(51)to be a simple function of the mass of aerosol per unit area of filter with which the filter is loaded, ML.

$$\ln\left(\frac{P_T(M_L)}{P_T(o)}\right) = \beta TL\ ML \qquad (7)$$

Where PT is the penetration of a test aerosol through the filter (the test aerosol and the loading aerosol may be different), and β is an index that quantifies the extent to which a particular aerosol causes performance loss of a particular filter material. Where experiments can be carried out accurately, the exponential increase of penetration with M_L, predicted by equation 7, is observed to an aproximation, as shown in Fig 9(51). β-values for a number of different aerosols acting on resin wool and electret material are plotted in Fig 10 (51), from which it is clear that the variation in β amongst different materials exposed to the same aerosol is relatively small, whereas the variation amongst samples of the same material exposed to different aerosols is considerable. This simple relationship can be explained if it is assumed that the aerosol acts by screening the fiber charge. The screening charge developed would be expected to be approximately proportional to the charge

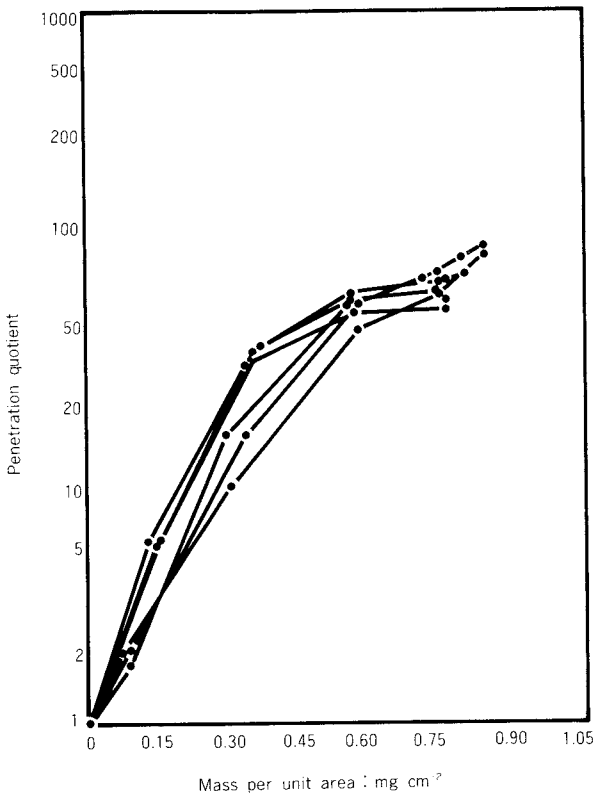

Fig.9 Log-quotient plot of penetration of standard aerosol through electret filters loaded with foundry fume produced by arc/air burning process

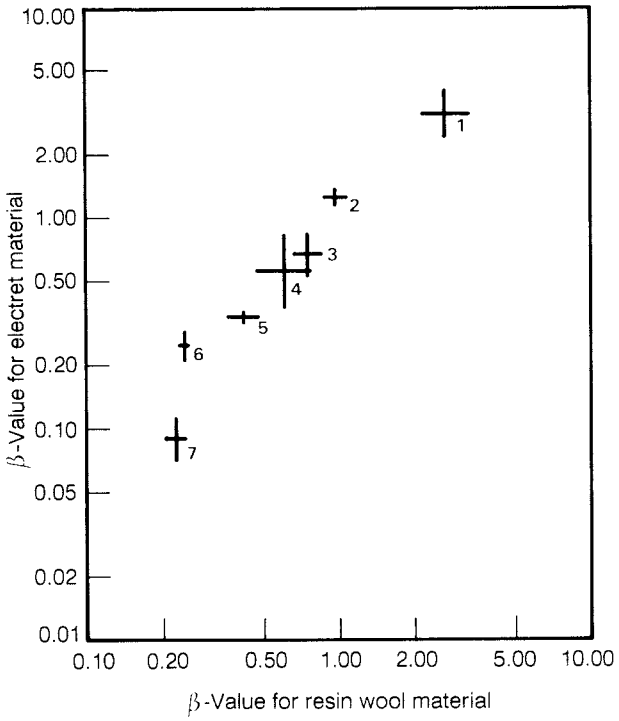

Fig.10 Comparison between β-values for electret and resin-wool materials:

1 foundry fettling fume
2 foundry burning fume
3 lead smelting fume
4 lead battery dust
5 coke-oven fume
6 silica dust
7 refractory brick dust

being screened, and so the fractional reduction in single fiber efficiency would be more or less independent of the charge. If, on the other hand, the process were one of charge neutralisation, the effect would be more marked in the case of filter materials that held a lower level of charge, and this is not observed. Moreover, measurements of the level of charge on industrial aerosols (52) show that there is simply not sufficient charge available to neutralise electrostatic filters.

A further comparison, between the β-values for resin wool material and polycarbonate material (a fine-fibered solvent-spun material), is shown in Fig 11 (51). Most of the points lie on a straight line similar to the data of Fig 10, but the two corresponding with lead smelting fume and coke oven fume do not. Since the behaviour of the resin wool material is similar to that of the electret and consistent with theory, it is assumed that it is the values of β for the polycarbonate that are erratic. That for lead- smelting fume is lower than the general pattern would indicate, and that for coke oven fume is higher. The smelting fume is very likely to be highly agglomerated, and, therefore clogging, and an increase in the pressure drop of the polycarbonate material confirms this, accounting for the γ-values. The coke oven fume is high in solvent content, and laboratory experiments have shown that soluble polymers are particularly sensitive to this type of fume; indicating that solvent interaction is the cause of high β-values.

Laboratory experiments shed light on the fundamentals, and experiments have been carried out (53) in which electret and polycarbonate materials were loaded with monodisperse aerosols of various sizes, generated

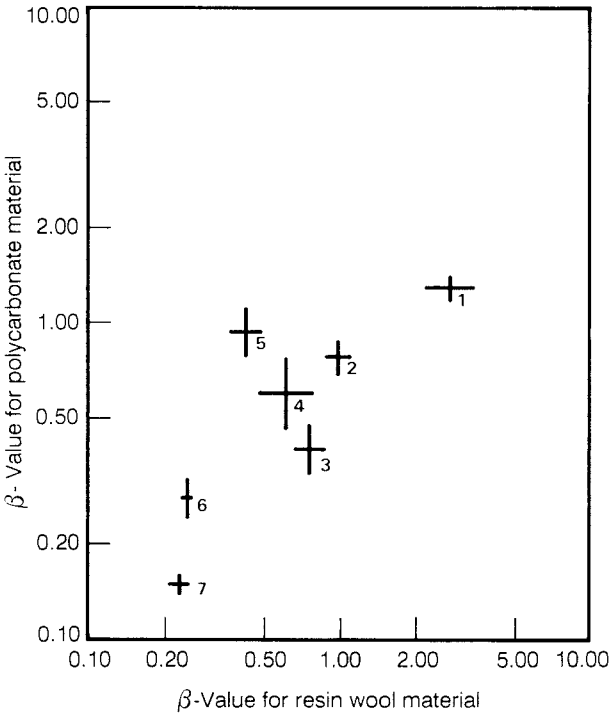

Fig.11 Comparison between β-values for polycarbonate and resin-wool materials:
1 foundry fettling fume
2 foundry burning fume
3 lead smelting fume
4 lead battery dust
5 coke-oven fume
6 silica dust
7 refractory brick dust

from an oily material, Di-ethyl-hexyl sebacate (DOS), and a solid, sodium chloride. The authors plotted both pressure drop and penetration as a function of mass load per unit area. The pressure drop across the fine-fibered material was recorded in detail, and it was observed that the larger solid particles, 0.1μm in diameter, were more clogging than the smaller, 0.06μm. The liquid aerosols were much less clogging but the results showed a similar size-dependence. The difference between solid and liquid aerosols can be explained by the tendency of oil to spread over the fiber surface, since the fibers are made from oleophilic materials, whilst the solids will form structured deposits. The spreading of the oil over a surface can be described in terms of interfacial tensions but exact predictions are difficult without measured values of these parameters.

Similar materials were loaded with aerosols in different charged states(54), a neutral aerosol being found considerable more clogging to both filter materials than a partly charged aerosol. The latter aerosol caused a practically monotonic decrease in filtration efficiency, whereas the penetration of the neutral aerosol reached a maximum, after which it decreased on further loading. The authors related the experimental results to a theoretical model based on particle trajectory calculation and fitting of adjustable parameters to empirical values.

Summary

The advances in practical developments of electrically charged filter materials during the past few years have been matched by an increase in fundamental understanding of their behaviour. The materials have a very useful place in situations where high filtration efficiency is required, along with a low resistance to airflow. Their widest use at present is in respirators, but they are also used in vacuum cleaners and in air cleaning on a larger scale.

They are more efficient in the capture of charged aerosols, but high efficiencies can also be achieved in the capture of neutral particles. The description of both capture processes is considerably simplified by the use of dimensionless parameters.

The thermal stability of charge is very good under normal conditions of storage and use. However, filtration efficiency tends to diminish with aerosol load, and so it is important that they are not used for periods extending beyond that in which their performance is good.

© British Crown Copyright, 1991

References

1) Davies C N(1973)'Air Filtratio', Academic, London
2) Brown R C and Wake D(1991)'Air filtration by interception-theory and experiment' J Aer Sc **22** 181-186

3) Wake D and Brown R C(1988)'Measurement of the filtration efficiency of nuisance dust respirators against respirable and non-resprirable aerosols' Ann Occ Hyg **32** 2 295-315
4) Orenstein A J (1960)'Proceedings of pneumoconiosis conference, Johannesburg 1959' Churchill, London
5) Howie R M, Addison J, Cherrie J, Robertson A and Dodgson J(1986) 'Fiber release from filtering facepiece respirators' Ann Occ Hyg **30** 131-133
6) Hansen N L(1931) 'Method for the manufacture of smoke filters or collector filters' British Patent BP 384052
7) Walton W H(1942)'The electrical characteristics of resin-impregnated filters' CDE Porton report no 236
8) Feltham J(1979) 'The hansen filter' Filtration and Separation, **16** 370-372
9) Smith P A, East G C, Brown R C and Wake D(1988) 'Generation of triboelectric charge in textile fiber mixtures and their use as air filters' (J Electrostatics **21** 81-98
10) Brown R C, Wake D, Blackford D B, East G C and Smith P A(1988) 'The use of electrically charged polymers in air filters' 1st international conference on the electrical optical and acoustic properties of polymers, Canterbury 5-7 September 1988
11) Schick M J(1975) 'Surface characteristics of fibers and textiles' Sekker, NY
12) Sessler G M(1980) 'Electrets', Springer Verlag, Berlin
13) Turnhout J van, Albers J H M, Hoeneveld W J, Adamse J W C, and Rossen L M van (1979) 'Non-woven electret fiber: a new filtering medium of high efficiency' Int Phy Conf Ser **48** 337-349
14) Turnhout J van and Albers J H M(1979) 'Electret filters for high-efficiency air cleaning' Proceedings of 2nd World Filtration Congress, London, Filtration Society, London
15) Turnhout J van, Hoeneveld W J, Adamse J W C and Rossen L M(1979) 'Electret filters for high efficiency and high flow air cleaning' 14th Annual meeting of the IEEE Industry applications society, Cleveland.
16) Turnhout J van, Adamse J W C and Hoeneveld W J(1980) 'Electret filters for high efficiency air cleaning' J electrostatics 8 369-379
17) Baumgartner H, Loeffler F and Umhauer H(1985) 'Deep-bed electret filters-The determination of single fiber charge state and collection efficiency' IEEE Transactions E-21 No 3 477-480
18) Shimokobe I, Izumi K and Inoue M(1985) 'Electrostatic polarizing of nonwoven polypropylene sheets' Proceedings of the Annual meeting of the Institute of Electrostatics, Japan, Oct 19-20, 1985, (in Japanese)
19) Taylor G T (1969) 'Electrically driven jets Proc. Roy Soc **A313** 453
20) Hayati I, Bailey A I and Tadros T F(1986)Nature **319** 41-43
21) Schmidt K(1980) 'Manufacture and use of felt pads made from extremely fine fibers for filtering purposes' Melliand Textilberichte **61** 495-497'
22) Trouilhet Y (1981) Advances in web forming, EDANA, Brussels
23) Wente V A(1956) 'Superfine thermoplastic fibers' Ind Eng Chem **48** 1342-1346
24) Brown R C and Blackford D B (1983) 'Air filtration by charged elements aligned to the airflow' Filtration and Separation **20** 349-351
25) Blackford D B and Brown R C(1986) 'An air filter made from an electret and a conductor' IEEE Transactions on Electrical Insulation **E1-21** 471-476
26) Brown R C(1982) 'The behaviour of electrostatic filters made of fibers or sheets arranged parallel to the airflow' J Aer Sc **13** 249-253
27) Linsheg S, Baoji C and Yude W (1988) 'Electret filters used for getting rid of bacteria' Electrets; 6h Int. Symp. IEEE
28) Brown R C(1979) 'Electrical effects in dust filters' Proceedings of the 2nd world filtration congress, Filtration society, London
29) Attix FH and Roesch W C (1968) 'Radiation dosimetry' Academic, NY
30) Harper W R(1967) 'Contact and frictional electrification' OUP, Oxford
31) Fjeld R A and Owens T M(1988) 'The effect of particle charge on penetration in an electret filter' IEEE Transactions on Industry Applications **24** 725-731
32) Emi H(1990) 'Fundamentals of aerosol filtration' J Aer Res Japan(in Japanese)4 246-255; English translation in KONA Powder and Particle(1990) **8** 83-91
33) Duchin S S and Deryaguin B V (1958) 'Towards a method of calculating the precipitation of disperse particles from a flow interrupted by obstacles' Kolloid Zh **20** 326-328,(in Russian); HSE Translation 7221(1978)
34) Natanson G L (1957) 'Deposition of aerosol particles by electrostatic attraction upon a cylinder around which they are flowing' Dokl Akad Nauk USSR **112** 696-699, (in Russian); HSE Translation 7222 (1977)

35) Pich J (1977) 'Analytical method for the calculation of deposition of particles from flowing and central force fields in aerosol filters' Environmental Science and Technology **11** 606-612

36) Pich J Emi H and Kanaoka C (1987) 'Coulombic deposition mechanism in electret filters' J Aer Sc **18** 29-35

37) Thorpe A and Brown R C(1991) 'Studies of electrically charged filters using neutral monodisperse aerosols' 5th Aerosol society conference

38) Lathrache R and Fissan H (1989) 'Grundlenge Untersuchungen zum Abscheideverhalten der Elektret-Filter Teil 2: Bewertung der Filtrationseigenschaften' Staub-Reinhaltung der Luft **49** 365-370

39) Keefe O Nolan P.J. and Rich T.A Proc. R. Irish Acad. 6OA 27-45

40) Lathrache R, Fissan H and Neumann S (1986) 'Deposition of submicron particles on electrically charged fibers' J Aer Sc **17** 446-449

41) Lathrache R and Fissan H(1989) 'Grundlenge Untersuchungen zum Abscheideverhalten der Elektret-Filter Teil 1: Bestimmung der Abscheidegrade' Staub-Reinhaltung der Luft **49** 309-314

42) Baumgartner H, Loeffler F and Umhauer H(1985) 'The collection performance of deep-bed electret filters' Proc Int Symp. Electrets, Heidelberg 772-777

43) Baumgartner H and Loeffler F(1986) 'A basic theoretical and experimental study of particle collection in electret fiber filters' 5th World filtration Congress, Ostende, 2.11-2.22, Filtration Society, London

44) Baumgartner H and Loeffler F(1986) 'The collection performance of electret filters in the particle size range 10nm-10μm' J Aer So **17** 438-445

45) Trottier R A and Brown R C(1990) 'The effect of aerosol charge and filter charge on the filtration efficiency of submicrometre aerosols' 1990 European Aerosol conference, Zurich

46) Lathrache R and Fissan H (1986) Enhancement of particle deposition in filters due to electrosatic effects' 5th World Filtration Congress, Proceedings, Ostende, 7.55-7.63, Filtration society, London

47) Brown R C(1989) 'Review: Modern concepts of air filtration applied to dust respirators' Ann Occ Hyg **33** 615-644

48) Ackley M W(1982) 'Degradation of electrostatic filters at elevated temperature and humidity' World Filtration Congress III 169-176, Filtration society, London

49) Ono M, Tonoya Y and Takenaka A(1985) 'Filtration quality of electret surgical masks after storing in moist air' Proceedings of the Annual meeting of the Institute of Electrostatics, Japan, Oct 19-20, 1985,(in Japanese)

50) Ando K Takahashi K Togashi R and Okumura Y (1990) 'Properties of electret filter with low pressure drop and high filtration efficiency', Proceedings of 5th International Aerosols Conference, Kyoto, Pergamon

51) Brown R C, Wake D, Gray R, Blackford D B and Bostock G J (1988)' The effect of industrial aerosols on the performance of electrically charged filter material' Ann Occ Hyg **32** 271-294

52) Vincent J H, Johnston A M, Jones A D and McLachlin C Q (1983)IOM report No TM/83/15

53) Lathrache R, Fissan H and Neumann S (1986) 'Dynamic behaviour of electrostatically charged fibrous filters' Aerosols: Formation and Reactivity, 2nd Int Aerosol Conf, Berlin, 712-715, Pergamon

54) Baumgartner H and Loeffler F (1986) 'Experimental and theoretical investigation of the time-dependent collection efficiency of electret filters' Aerosols: Formation and Reactivity, 2nd Int Aerosol Conf, Berlin, 708-711, Pergamon

Review

Powders for Thermal Spray Technology †

Herbert Herman
Thermal Spray Laboratory
State University of New York at Stony Brook *

1. Introduction

The thermal spray industry is most dependent on that which it understands least. For many years, since the 1950's when thermal spray began as a clearly definable industry, less concern was paid to the materials to be sprayed than the means through which they were to be sprayed equipment. Clearly, equipment has always been important to the industry, and, in fact, the cutting edge of the technology is now highly focussed on equipment developments. However, it is clear that these developments will add little to the evolution of the thermal spray industry in the absence of proper feedstock material.

Thermal spraying is a technique which, in general, uses a device(the gun)to melt and propel a material onto a substrate where it rapidly solidifies(at a rate of 10^6 °C/sec), forming a well-adhered coating. Of special interest here are four methods of thermal spraying:

- Plasma Spray
- Combustion Flame Spray(powder and wire)
- Hypervelocity Oxygen-Fuel (HVOF) spray
- Two-Wire Electric Arc Spray

These methods, and variations of them, have wide use in industry, being employed to form protective coatings of a variety of materials for numerous and diverse applications.

In this article will be reviewed powders which are employed in the first three techniques of thermal spray. Wires will not be discussed. Brief descriptions of plasma, combustion and HVOF spray techniques will first be given, followed by an overview of feedstock materials for these processes.

1.1 Plasma spraying is a well established means for depositing dense coatings of powdered materials ranging from plastics to bronze to refractory ceramics(1,2). The plasma gun, **Fig. 1,** enables high through-put processing at temperatures in excess of 10,000 °C. Therefore, virtually any powder can be plasma sprayed. The normal particle size is from 10 to 100 micrometers.

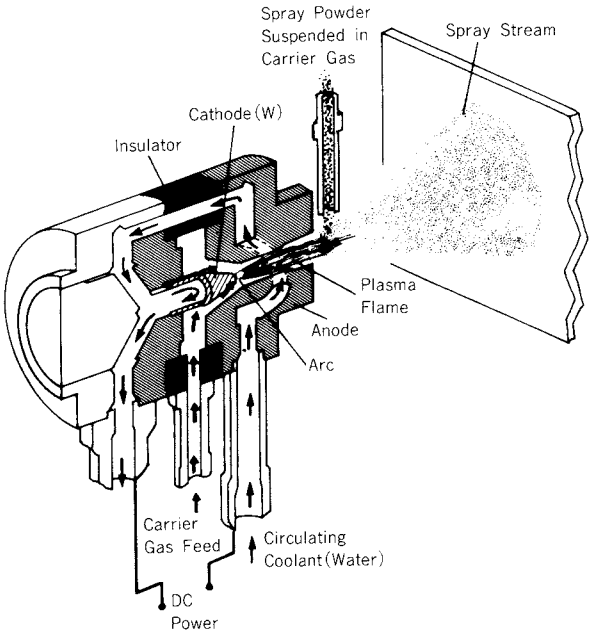

Fig.1 Typical direct current, non-transferred arc plasma spray gun with external powder injection. An arc is struck between the tungsten cathode and the water-cooled copper anode, creating a plasma flame which exits through the annular anode at near sonic velocities. Most plasma guns use argon (mixed with diatomic gases such as hydrogen)as the plasma gas and operate at power levels between 35 and 80 kW.

* Stony Brook, NY 11794-2275,USA

† Received July, 1991

Of special interest is the plasma spray deposition of hard facings such as WC/Co, ferrous alloys, and bronze for repair of shafts and valve parts, monel and chrome oxiele for repair of ship's propellers, ceramic refractory oxides, such as alumina and alumina-magnesia spinel for electrical insulation, zivconiabasecl oxides for thermal and five oarriers, and aluminatitania for wear applications. Plasma spraying is used extensively for applying nickel-based alloys for corrosion control(e.g, Hastelloy). and for high temperoture hot goserosion-oxidation protection in morine, stationary, and oircvaff gos turbines (e.g., NiCoCrAIY). For some high performance applications, in order to obtain true bulk density and extremely high adhesion strength, plasma spraying is carried out in a reduced-pressure environment (i.e., "Vacuum Plasma Spraying"-VPS)or through the use of a shrouded flame, where, for example, argon gas excludes oxygen from the vicinity of the flame and workpiece. The benefits of VPS and the shrouded plasma will increase in importance in years to come. Automation of the plasma gun and the workpiece is becoming very common in industry. This will have important influences on the specifications of feedstock powder.

1.2 Combustion flame spraying generally employs an oxyacetylene flame to melt and spray either powder or wires at temperatures significantly below that of plasma. However, flame spraying is simpler in principle and in operation than is the plasma and is generally less expensive to run. It can be argued that flame spraying can be more operator-forgiving than plasma and, therefore, can be used by less well trained personnel. However, flame spraying, due to its lower flame temperature and lower particle velocity, yields a less dense coating, having lower adhesion strength than does the plasma flame.

1.3 HVOF -The hypervelocity oxy-fuel gun represents a major evolution of thermal spray technology. HVOFe based on rocket flame science, is able to deposit an extremely dense, well-adhered coating of hard facing WC/Co alloy to hardness levels equivalent to, and, in some cases, exceeding such coatings deposited using the Union Carbide Detonation Gun (D-Gun). HVOF-formed hardfacings have properties superior to such materials plasma sprayed in air. Industrial laboratories currently using HVOF are making numerous claims as to dramatic results obtained with a wide variety of coating materials(e.g., Hastelloy, Stellite, alumina). However, as of this writing, the claims that HVOF can form dense, well-bonded refractory ceramics remain unsubstantiated.

1.4 Particle-Plasma Interactions

In the most modern plasma spray torches, the powder is carried by a gas, argon or nitrogen, and enters the plasma flame just outside the nozzle from which the flame exits. As shown in **Fig.2,** the particle size distribution plays a key role on how the coating is formed. For example, the fine particles(# 1)(for example, <10 micrometers) will melt closest to the

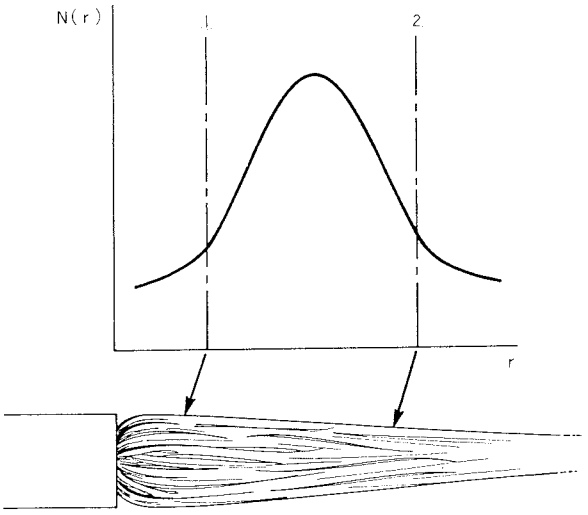

Fig.2 Gaussian particle size distribution, the number of particles, N(r), plotted versus the particle size. Particles such as those of # 1 having a small diameter(e.g., <5 micrometers)melt near the torch exit, whereas larger particles, such as # 2,(e.g., $>$ 200 micrometers)take longer to melt and do not become molten for some axial distance from the nozzle face. Typical distributions for refractory ceramic are $+20/-70$ micrometers.

nozzle or will bounce-off of the flame-these "fines" may not arrive at the substrate, but may be lost through vaporization. The larger particles(#2)(say,<70 micrometers)may actually be lost through plummeting through the flame due to their large mass and momentum or they may not receive enough enthalpy to melt prior to impact, in which case they will either bounce-off of the part or be imbedded within it as an "unmelted" particle.

Ideally, the mean particle size will depend on the particle melting point and its shape, but for most applications the particle size distribution should be fairly narrow (for example, +20/−70 micrometers for most refractory oxides).

2. Feedstock Powders-Background

Metal alloys and ceramics, generally, differ in the manner in which they are fed into thermal spray guns. But overall, metals are produced in the form of powders, and wires and ceramic materials are produced in the form of powders and sintered rods. Combustion flame spray uses powder or wire of metals and powder of ceramics. The HVOF process employs a fine powder. Plasma uses powder for feedstock. The plasma process requires very careful control of particle chemistry and geometry.

There have been a number of controversies surrounding the role of powder characteristics on thermal spray behavior and coating properties. In general, it can be said that spherical, monosized and chemically homogeneous powders are preferable to powders with facetted shape, with wide size distributions, having a non-uniform distribution of components. It is commonly accepted within the thermal spray industry that one does not use a better powder than is required to accomplish a task. It has just been in recent years that innovative powder producers have been able to deliver desirable product for reasonable(i.e., competitive) prices. These producers have contributed to a new, badly needed attitude within the thermal spray industry that quality in feedstock powder is indeed possible and will yield discernibly superior results.

In the following will be reviewed the processing and testing of feedstock powders.

2.1 Processing/Production of Feedstock Powders

In general, metal and ceramic powders differ in their mechanical properties and sensitivity to environmental factors. Thus, for ease of description, they will be treated separately. It should be noted, however, that there are a wide range of intermetallic compounds, exemplified by the aluminides, which have features of both metal alloys and of ceramics. They are generally treated as reactive metals due to their sensitivity to oxygen.

a. Metal Powders

Powders of metals and their alloys are formed in a variety of ways. It is especially important to note that unlike ceramics, metals are generally non-brittle and it is therefore impractical to employ solid impaction or comminution ball mills to reduce size. The higher performance metal powders are water or gas atomized and, in fact, atomization is becoming so commonly utilized that it is employed for the production of even the low value powders, such as ferrous alloys.

It is also possible to form composites and alloys powders through diffusion sintering processes. In the former, two or more elemental constituents interdiffuse at high temperature, forming an enhanced, chemical uniformity. Sometimes the interdiffusion gives rise to a sintering process in which the particles become strongly bonded to one another. In such a situation it is required(when possible)to mechanically reduce particle size.

Another means of forming an alloy from multiple constituents is through mechanical alloying. In this method, ductile metals are mechanically deformed by mutual impact, yielding a physical intermixing with attendant interdiffusion and thus alloying. The mechanical mixing system is commonly referred to as an "attritor". Not only are alloys formed using this method, but intermetallic com-

pounds are formed, as well as dispersoids. Depending on the constituent elements employed, mechanical alloying is carried out in the presence of agents such as stearic acid and methanol to control the balance between fracturing, welding and alloying.

A rather more recent technique of using mechanical energy to process powders is mechanofusion(3). In this process, there is rotary action between a cylindrical vessel and a curved hammer which crushes powder, the layers of which are scraped off of the cylinder wall. The process can take place in a controlled atmosphere, so that reactive materials (e.g., titanium, intermetallic compounds) can be processed. The possibility of employing mechanofusion to form composites between diverse constituents (e.g., ceramic-metal, ceramic-polymer, metal-polymer) is just starting to be recognized. The process, while very promising for forming unique plasma spray feedstock powders, is rather complex, and is in need of further study.

Atomizing is carried out in a variety of ways. Water and gas atomizations are commonly employed to produce powders for the thermal spray industry. In the case of water atomization, the molten stream is impacted by high pressure water. Processed powders involving water atomization are limited to metals which will not undergo severe oxidation. Water atomized particles are irregular in shape and thus do not flow as well as gas atomized particles, which are spherical.

Gas atomization is simple in principle. A continous stream of melt is atomized by gas at high pressure. The gas can be inert and the chamber can be vacuum tight, enabling the formation of oxygen-free powders, for example of reactive metals. There is a great deal of flexibility in gas atomization.

Another atomization method is the rotating electrode process in which material in the form of a rod electrode is rotated around its axis at some 250 RPS while being melted by an electric arc, a plasma arc, or an electron beam. Both gas atomization and rotating electrode atomization yield spherical particles. The latter process is discussed in some detail in Refs. 4-6.

Centrifugal atomization is a process related to the rotating electrode process. In the centrifugal atomization process, a crucible rotates, ripping out discrete particles which strike a cold surrounding wall, resulting in RSP powder(7).

Atomization processes are reviewed in Refs. 8-9.

More recent developments in metal powder production involve ultrasonic gas atomization, a method of atomization where the melt stream is subjected to intense shock waves. This technique yields powders in the <50 micrometer range and results in high quench rates. For example, yields of 80-90 $\%<44$ micrometer sizes for stainless powder have been obtained using ultrasonic atomization (10).

Table 1 is a listing of various production methods.

Table 1

Chemical Processes
Solid State Phase Decomposition
Thermal Decomposition
Liquid Phase Precipitation
Gas Phase Precipitation
Electrolytic Processes
Mechanical Comminution
Machining
Milling
Impact Attrition
Mechanical Alloying
Mechanofusion
Water Atomization
Gas Atomization
Vacuum Atomization
Ultrasonic Atomization
Microatomization (Impact)
Plasma Melting
Centrifugal Methods
Rotating Electrode
Centrifugal Atomization
Spark Discharge Atomization

b. Ceramic Powders

Ceramic powders for thermal spraying are

processed through a variety of techniques. The means of production of the powders will determine the particles shape and size distribution, which will be of great importance in flow to the gun and in melting within the flame. In the case of mixed oxides, powder processing will also influence the chemical uniformity of the powder particles and this too will be important in melting and, therefore ultimately in deposition efficiency. Of central importance, thus, will be the relationship between the means of powder production and the physical properties and extreme service performance of thermally sprayed coatings.

Oxide powders for thermal spraying are generally prepared in one stage or in a combination of stages of sintering, fusing or spray drying. Sintering involves mechanically combining the constituent oxides in the required proportions and heating at high temperature to effect alloying through solid state diffusion. In some cases, sintering is interrupted and the mass is crushed(e.g., in a ball mill)to enhance mechanical intermixing, followed by further heating, crushing, sintering, etc. Obviously, the greater the number of sintering-crushing cycles, the greater will be the production cost; therefore, a point of diminishing returns is quickly reached. The sintered-crushed powder, generally referred to as "reacted", has a significant volume fraction of chemical inhomogeneities. As will be discussed later, these inhomogeneous regions can represent deficiencies in spray efficiency.

Fused oxide powders are formed through melting and solidification of the constituent oxides. Inhomogeneities will result only through non-equilibrium solidification phenomena(e.g., coring)and these, in general, will be small in extent.

Spray drying is a technique in which small constituent particles are adhered by a binder, generally organic, which burns off in the flame during thermal spraying. Spray drying is carried out for a variety of reasons, a major motivation being the production of composite powders for thermal spray application. Spray drying is also used to agglomerate fine particles to sizes required for the thermal spray process.

In addition, there are several techniques of agglomeration, including combining the powders with the binder in a vat and heating and mixing to drive off the binder's solvent.

The above processes, either singly or in combination, lead essentially to particles which have a lesser or greater extent of chemical uniformity or to composite powders.

More recently, new non-conventional means have been employed to process ceramic powders. For example, in a process akin to gas atomization of metals, some preliminary experiments have been performed on gas atomirration of refractory oxides. This writer has, in fact, carried out a comprehensive evaluation of gas atomized yttria partially-stabilized zirconia, over a range of compositions and particle sizes, and has found the product to be as good as, and in some cases, superior to fused and mechanically reduced product(11).

Another means of spray atomization involves actually plasma spraying of spray dried powders and collecting the melted and solidified powders. This is actually a commercial means for processing spherical metal and ceramic powder for plasma spray feedstock. In **Fig. 3** is shown the sequence of processing of powders of hexagonal barium oxide ferrites (12). This complex powder is very difficult to process and, in fact, due to phase equilibria limitations cannot be prepared by the fusing route. Pictured in **Fig. 3a** is the spray dried ferrite and **Fig. 3b** shows the ferrite at a higher magnification, where a poorly bonded particle is noted. If the powder shown in **Fig. 3b** is sintered at about 1000℃ for several hours, some densification occurs, but the powder is not significantly improved; **Fig. 4a.** If, on the other hand, the powder particles are passed through a plasma gun, where they are melted, solidified in-flight, and collected, the resulting powder, **Fig. 4b,** is found to have significantly increased densification, together with a largely spherical shape. Note the decreased particle diameter in the plasma treated powder. It should be noted that the powder represented by **Fig. 3a** could not be effectively plasma sprayed to form a coating, where as the spheroidized particles of **Fig. 4b** formed an

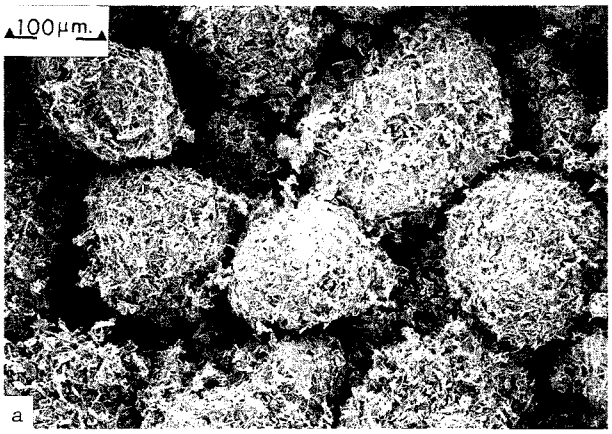

Fig.3.a,b. Hexagonal barium oxide ferrite as-sprayed dried. Different magnifications, SEM.

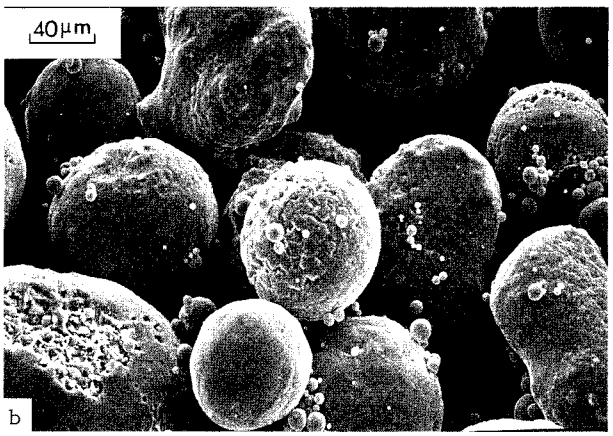

Fig.4a. Material of **Fig. 3b** as-sintered in air at 1000℃ for several hours. SEM.

Fig.4b. Particles depicted in **Fig. 3a** after passing through a plasma gun. SEM.

As a result of the rapid expansion of research and development within the ceramics powder industry, new powder processing techniques have evolvcd which can yield a relatively pure product at reasonable cost. These so-called "chemical preparation" methods include solution methods, vapor phase methods, and salt decomposition. Of these chemical methods two have particularly interesting features: sol gel and co-precipitation. Both methods involve dissolution of soluble salts in say, water, or dissulution of metals in acid solution. Using these meyhods, it is possible to form very complex compositions and to still maintain chemical homogeneity. For the co-precipitation route, the solvent is evaporated. Various sub-routes for ceramic powder processing employ different methods for solvent evaporation(e.g., spray draying, emulsion drying).

In the case of sol gel processing, suspensions

excellent coating.

The above physical-mechanical methods of ceramic powder preparation, both the traditional and melt spray methods, result in levels of impurities which for most applications are tolerable. In fact, it was not so many years ago(1970-80)when this was the case. More recently, it has become evident that purity will be more important, as thermal sprayed coatings are used for high performance applications(e.g., electronics, magnetics). Even in thermal barrier applications, the presence of excessive amounts of iron or silicate can have a definite deleterious effect on high temperature performance.

of colloids are formed by precipitation from aqueous solution. The gel is formed by one of various evaporation techniques and following evaporation and drying stages, a dry, spherical particle results, which is chemically uniform. If the spherical particles have a very fine size

distribution, they can be sintered or spray dried and sintered to achieve increases in size and to enhance particle density.

Chemical techniques of ceramic powder processing can be found in Refs, 13-14.

Table 2 given below, represents a chart of processing methods for ceramic powder. It is a modification of a chart published by Johnson (15).

3. Testing and Evaluation of Feedstock Powders

It has only been in relatively recent years that thermal spray suppliers and users started to pay some attention to feedstock powder specifications. In years past, until perhaps the late 1970's, the user community took for granted the statements of producers and distributors that a given powder was appropriate for a given application.

It was the aircraft industry that finally outlined stringent requirements and stipulated that powder feedstock must meet certain standards. These requirements opened the door to

Table 2 Categorization of Ceramic Powder Preparation Techniques

Powder preparation technique				Advantages	Disadvantages
Conventional comminution				Inexpensive Unaggregated powders Wide applicability	Limited purity Limited homogeneity Large particulates
Chemical preparation	Solution methods	Solvent vaporization	Simple evaporation Spray drying Spray roasting or EDS Fluid bed drying Emulsion drying Sol-gel or glass Freeze drying	High purity Small particles Compositional control Chemical homogeneity	Expensive Aggregation of particles Poor for nonoxides
		Precipitation or coprecipitation			
	Vapor-phase methods	Vaporization-condensation Vapor decomposition Vapor-vapor reaction		High purity Very small particles Low aggregation Good for nonoxides	Expensive Difficult multi-component materials
	Salt decomposition			Used for solution techniques Simple apparatus	Aggregation of particles
Fusing	Mechanical Reduction			Chemical uniformity	Particles not spherical. Can have impurities Equipment costs high
Atomization	Gas atomization Microatomization			Chemical uniformity Uniformity Spherical particles	Equipment costs high
Flame treating (Hosp-Metco)	Passing through a flame/plasma gun			Spherical particles	Needs small sized feedstock.

enhanced market competition, and new organizations entered the community of suppliers.

During the 1970's and 1980's, while materials users and suppliers began to redefine the dynamics of the market, certain facts began to emerge. Applications and end-users started to make both cost and technical demands on suppliers, creating some serious, rather more "scientific" thinking on the part of producers and distributors. For example, for many years it was thought that the means through which powders were made had little to do with coating performance. That this is not the case is now clear.

An example of the importance of feedstock processing methods is in the field of ceramic coatings. In particular, Al_2O_3-based TiO_2 is commonly used as a wear coating. The Al_2O_3 endows the coating with hardness whereas the TiO_2 leads to a decrease in friction coefficient. The net effect is that Al_2O_3-TiO_2 (with 13 and 40% of TiO_2)is a highly effective wear resistance coating.

A study carried out at Stony Brook examined the differences in slurry wear behavior between a fused(cast and crushed) versus a composite product(16). There is little question that the fused product(for 13 and 40% of TiO_2)is far superior in wear behavior than is the composite coating. The most significant difference noted between the coatings obtained from these two processes is that the fused ("prealloyed") powders resulted in a greater range of acceptable spray parameters than do coatings formed from the composite powders. The fused powders, having a more uniform chemistry within the particles, melt at essentially the same melting point-or at least a narrower melting point range-than would obtain for a product produced by compositing.

A key message here is that chemistry, and the distribution of constituents within the particles, is of great importance in meltability of the particles within the flame, whether it be combustion or plasma. But, other aspects of feedstock material are also important, and, in some circumstances, vital for the efficient operation of thermal spray system.

3.1 Powder Characterization and Testing

The list of characteristics of feedstock powder is extensive. Only those issues important for thermal spray considerations will be listed and addressed here:

Chemical composition and purity.
Size, shape and surface roughness.
Surface area.
Density of particles(i.e., porosity of particles).
Surface films and absorbed impurties.
Flow and related features.
State of agglomeration.

a. Chemical composition and purity.

Particle chemistry and purity can be determined by a variety of chemical analysis techniques, including surface chemical spectroscopy. Wet chemical analysis is widely employed to determine average chemistry, but the matter of chemical uniformity is not so simple. For example, by appropriate mounting and sectioning, it is possible to take a microprobe trace across a powder cross-section. If the power is a solid solution, it may be possible to learn something of solute distribution within particles by noting the width of the diffraction peaks, assuming that the particles are so fine that then themselves do not contribute signficantly to peak broadening

In the case of chemical analysis of various metal powers, there are numerous chemical analysis techniques specified by ASTM for the specific metal system. These are conveniently listed in Ref. 17.

b. Particle Size Distribution and Particle Shape.

Size considerations for thermal spray, especially advanced spray methods such as plasma and HVOF, are of the greatest importance if a quality deposit is to be achieved. Of central importance in these considerations is the particle-flame interaction. Modelling research, together with attendant laser diagnosticmeasurements, in general, require sharp partsicle size distributions, a condition which is impractical to attain in practice. This

difficulty is due principally to economic matters and not technical limitations. There are means at hand for achieving separation of relatively sharp distributions. But the exercise of discarding fines and large practice (even though these discards will be recycled)to achieve the desired distribution must increase costs, due to extra handling, time, labor, and materials loss. Therefore, current producer proctice is to quote bulk powder prices for, e.g., −325(defined as able to pass through a screen having 325 openings per square inch or having sieve openings of 0.0017 inches on a side). For high performance requirements, when the size distribution is more stringent, one frequently requests +10 micrometer-325, which states that particle size falls between 10 and 45 micrometers.

Particle size distributions are important due to the way the particles interact with the flame. That is, for a given flame, as discussed for **Fig. 2,** the interaction is required to be optimum in the sense that "too small" particles may vaporize or be totally rejected by the high velocity flame and particles that are "too large" may be injected totally through the flame(and thus be lost)or may not melt totally and act as imbedded unmelted particles.

The proper particle size distribution will be related to the physical characteristics of the feedstock material, the particle shape, particle surface characteristic, etc.

Typically, particle size distributions are determined by the following methods:

i. Sieving in conjunction with mechanical or ultrasonic agitation, enabling the measurements of sizes between 5 to 800 micrometers. Sieves are specified according to ASTM 11. Sieves are usually certifiecl using glass spheres from U.S. National Institute of Technology and Standards. Standards are also issued by the Metal Powder Industries Federation (mPIF Standard 05)and the International Standards Organization(ISO Standard 4497). These standards specify the time of sieving through certified sieves. They, however, cannot correct the problems associated with sieving, such as overloaded, blanked, or damaged sieves. Furthermore, irregularly shaped particles and agglomeration of particles can clog sievers with resulting distorted size fractions.

There are a number of variations on the theme of mechanical sieving. While this technique may appear the most straight-forword, nonetheless there frequently are mismatches with other normally used techniques, as will be described subsequently.

ii. Light scattering (Microtrac), with an effective particle size measurement range of 2 to 100 micrometers. This technique is both reproducible and convenient and can readily be interfaced to a computer to give valuable size distribution information. Generally, a He-Ne laser is used in conjunction with Fraunhofer diffraction to yield cones of scattered light, having angles which are inversely proportional to particle size.

Perhaps one limitation(which is not really serious)is that the particles must be suspended in a fluid which is carried by a tube across the light beam. In general, water is used, but clearly, there are circumstances where the water must be substituted with alcohol or light oil. Of particular importance is that only a very small amount of sample is required and measurements take only several minutes.

iii. Light Obscuration methods involve simply using the opacity of particles in a fluid to note the absorption of light passing through the particle-fluid containing cell. There is a sensor availoble for ranges of particle sizes of interest. The technique can measure particles from 1 to 9000 micrometers. Of course, the overall particle size distribution determined using the light obscuration method will depend on the fraction of particles(of all sizes)contained within the measureing volume. Micro-processor control and appropriate computer programs will be required to solve for the sought after size distribution.

iv. Sedimentation analysis using Sedigraph (0.1-100 micrometers) or the Micromerograph (2-300 micrometers) all meaure the rate of settling of or particles within a fluid. This technique is dependent on Stoke's law, which states that the frictional force on a spherical body moving through a fluid is proportional to the product of the particle

velocity, fluid viscosity and the sphere's radius. There are a number of variations on this theme, the key concern in all of these techniques being to avoid convection currents within the fluid. There are ASTM standards associated with sedimentation methods: with particular reference to light and x-ray turbidimetry, ASTM B430 is applicable. In these methods, a beam of either optical or x-ray radiation is passed through the fluid, and the transmitted intensity is monitored as a function of time. The Stoke's law equation is then used to determine size and number.

v. Microscopy ; optical microscopy(0.5-100 micrometer, can be used in conjunction with selected statistical methods to determine particle size distribution. Of course, shapes can also readily be determined. Microscopy is particularly useful if the particles are irregularly shaped. There are a number of programs for image analysis for optical microscopy. And there are various well established methods for properly mounting the particles for optical and SEM analysis.

Particle shape cannot be separated from particle size analysis. As size measuring instruments become more sophisticated and become more dependent on the various algorithms required to extract meaningful distributions from the data, shape starts to emerge as a more influential factor. This investigator, for one, welcomes the introduction of spherical powders onto the market. A particle size distribution obtained from spherical particles, is simply more accurate than one from irregularly shaped particles. For example, consider a diffraction or scattering based on the measuring instrument. It is not likely than a universal shape correction factor will be introduced into the analysis scheme. There is no real need for pessimism, however, since it possible to characterize some statistically meaningful particle sizes for non-spherical powders. However, when the particles are discs or fiber, problems will arise that will have to be dealt with. These questions are discussed at length in Ref. 18.

vi. Comparison of the Various Methods of Particle Size Distribution

It is now well appreciated that particle size distributions measured by different techniques yield different distributions and sometimes these differences are significant. For example, it is well known that laser scattering and light obscuration methods yield different distributions of identical samples, and, not surprisingly, both are different from the mechanical sieve and sedimentation methods. Diffevences arise from particle shape influences and agglomeration of particles, among other things.

A careful examination of the particle size analysis techniques used today in powder-technology would lead to the conclusion that measurements of the same powder sample using different techniques would not be expected to lead to the same results. For example, optical size measuring devices are widely used, but their measurement is based on the theory that the particles are all spherical.

It is essential that we recognize that different types of instruments will yield different particle size distributions, especially if we are dealing with non-spherical powders. If, in fact, we must use different techniques or instrumentation to measure the same powders, we should seek to have spherical powders and the size distribution should have been obtained accurately using, for example, microscopic image analysis. In fact, various "round robin" testing programs have been carried out, but a formal well-organized test program is called for. The protocol for such a testing program should be constructed with great care, since it has been shown that in using the same technique principle, but with instruments of different manufacture, it is possible to obtain variations which by some measures are significant (19).

The trends of particle analysis are interesting and need to be followed closely by the thermal spray industry. For example, there have been proposals and some promising results using a universal approach to size and shape analysis, perhaps with significant implications for on-line analysis. Beyvel et al combined Fraunhofer diffraction, Mie scattering and light extinction in a single optical instrument covering four orders of magnitude of particle size(20).

With specific reference to automation of

particle size analysis, perhaps to the extent that such measurements can be incroporated on-line in the thermal spray process, much work has to be done. In general, dynamic light scattering offers the most convenient, accurate and certainly the fastest means of analysis. With the appropriate premise, as mentioned above, light scattering methodology(Microtrac)and light obscuration techniques(HIAC) provide adequate speed and statistical accuracy. There are emerging a wide range of automation systems based on the methodologies and principles discussed above(21).

c. Surface of Particles

Surface analysis of fine particles, both metals and ceramics, is a complex task and, in general, not considered in the characterzation of thermal spray feedstock. The two features of the surface which might be of some importance for thermal spraying are surface chemistry(for example, absorbed films and oxides on metals)and surface porosity, which under certain circumstances could play a role in meltability and, for ceramics, could lead to porosity within the coating.

For the most part, powder surface analysis will not be important for the vast majority of the thermal spray community. There will be cause, however, such as in the vacuum plasma spraying of reactive metals(e.g., zirconium. titanium)where adsorbed oxides will be of the greatest importance.

In the following will be described methods of chemical and physical analysis of particle surfaces.

i. Surface chemical analysis of powders is an extension of the vast array of surface science methodologies which have evolved in last decade. The techniques that are currently important and which can be applicable to powders are:

Auger Electron Spectroscopy (AES)
X-Ray Photoelectron Spectroscopy(XPS)
Electron Spectroscopy for Chemical Analysis (ESCA)
Secondary Ion Mass Spectroscopy (SIMS).

One problem with the use of these surface spectoroscopic techniques is the need to operate the specimen chamber at a relatively high vacuum. This vacuum could represent a problem for powdered materials, due to the long-term outgassing of the specimen. Adsorbed and absorbed gases are trapped into both the bulk of the powder mass and also in the fine porosity of the surfaces. Therefore, special mounting and outgassing steps are needed to perform the analysis.

The depth of penetration of the spectroscopic methods is ten's of Angstroms or less. It is, therefore, frequently required to ion-etch away atomic layer-after-layer of the powder surface to examine the outer periphery of the powder particles.

Appropriate references for the use of these surface analysis methods as applied to powders are Refs. 22-24.

ii. Surface area, density and porosity of powders have been studied extensively. Two interesting sources of information are Refs. 25 and 26.

Surface area is generally determined by gas adsorption methods(BET), where-in the surface area is based on noting the amount of gas which is adsorbed as a monomolecular layer on the powder surface. Nitrogen is commonly used as the adsorbed gas. This technique can also be used to find surface pore volume and size for pores ranging in size from 14 to 600 Angstroms.

Permeametry measures the resistance to fluid flow through a compacted powder. Using permeation techniques, it is possible to determine specific surface area(meters^2 per meters^3)and average particle size.

Pychometry, which is based on the principle of displacement, is commonly used to find density using helium or mercury as the displaced fluid. This technique gives no information as to pore size.

Mercury porosimetry is a well established technique for giving substantial information on pore size and distribution, from 30 to 10^6 Angstroms. Mercury is forced into the surface pores by applying pressure, the amount of pressure required depending on the pore size distribution. Of ourse, mercury intrusion porosimetry cannot be used if the powder foems an amalgam with the mercury, for example,

with aluminum alloys.

d. Flow and Related Features/Agglomeration

The flow of powder feedstock particles into the injector is related to a number of important physical properties of the powder. It is important to note that poor powder flow (e.g., clumping, inconsistent flow rate) can significantly influence the properties of the thermal spray deposit. It is, therefore, necessary to be able to characterize flow properties. In this regard, although metal and ceramic powders behave somewhat differently, vis-a-vis flow properties, the means of flow measurement do not really depend on the type of powder.

Agglomeration can represent a serious problem relative to flow of powders. Little study has been directed at agglomeration, although the chemical and powder metallurgical industries have directed efforts at controlling it. On the other hand, as discussed above, spray drying and associated processes are used to form mixed powders through the purposeful use of agglomeration techniques.

The standard means of measuring flow is through the use of a Hall Flowmeter, which is nothing more than a calibrated funnel. There are variation on the theme, but the essential principle involves the rate at which powder flows out through the funnel. The method of calibration and operation is specified in the following standards: ASTM B213, MPIF 3, ISO 4490, JIS 7-2503-1966, DIN 82-69.

The key variables affecting flow rate include : interpaticle friction; particle shape and size ; type of material ; environmental factors(humidity) ; weight of the bulk. Relative to thermal spray oxide particles, there are problems, for example, associated with electrostatic charge which can lead to serious clumping, and; therefore, poor feeding. This can be avoidcd through techniques such as proper grounding of the feeder and the feed-tube and by applying a low-intensity vibration to the feeder.

Relative to powder feeders, there are a number of different types available. However, there are no "universal" feeders and it is important to have available the types of feeders for specific categories of powders; for example, a fluidized bed feeder is not appropriate for spraying a powder containing a mechanical mix of two or more different materials or for spraying a powder having a very wide size distribution-since, in both cases, particle separation from top to bottom could occur with time.

Useful discussions of powder flow characteristics are contained in Ref. 17, and in various publications of the MPIF and the American Ceramics Society.

4. Conclusions

Powders for plasma spraying and attendant technologies are in need of thorough characterization and analysis. This reality has been recognized only in recent years and, in fact, there remains some confusion about which characteristics a given powder should have to achieve an excellent coating. Particle size, shape, surface features, chemistry are all important considerations, but these powder features, like spray parameters, must be optimized to realize an accepted economy of operation.

Nevertheless, new concepts of powder processing, together with intelligent characterization considerations, are leading to novel deposits having high performance capabilities across a number of technologies. The future holds exciting prospects for the powder technologist to serve the thermal spray industry.

References

1) Herman, H: *Scientific American,* **256,** 113(1988).
2) Herman, H: *MRS Bull.,* **13,** 60(1988)
3) Tanno, K: *KONA,* **8,** 74(1990)
4) Champagne, B. and R. Angers: *Powder Met. & Powder Tech.,* **16,** 359(1980).
5) Chanpagne, B. and r. Angers; *Modern Dev. in Powder Met.,* **12,** 83 (1981), MPIF, Princeton, NJ.
6) Hodkin, D.J., P.W. Sutcliffe, P.G. Mardon and L.E. Russell: *Powder Met.,* **16,** 227(1973)
7) Dougherty, T.S.: *Powder Met.,* **11,** 342(1968).

8) Lenel, F.V.: *Power Metallurgy-Principle & Practices,* (1980)MPIF, Princeton, NJ.
9) German, R.M.: *Powder Metallurgy Science,* (1980), MPLF, Princeton, NJ.
10) Grant, NJ: J. Metals, **35,** 20(1983).
11) Herman, H: Unpublished research.
12) Saha, B., R.K. MacCrone and H. Herman: Unpublished research.
13) Johnson, D.W. and P.K. Gallapher: *Ceramic Processing Before Firing,* (1978), Wiley, NY.
14) Johnson, D.W.: *J. Amer. Cer. Soc.,* **60,** 221(1981).
15) Johnson, D.W.: *Adv. in Powder Tech.,* p. 23,(1981), ASM Intern., Metals Park, OH.
16) Zatorski, R.A. and H. Herman: *High Performance Ceramic Films and Coatings,* pp. 591-601, Elsevier(1991).
17) *Power Metallurgy,* Vol. **7** of *Metals Handbook,* 9th Ed.,(1984), ASM Inter., Metals Park. OH.
18) Meloy, T.P. and N.N. Clark: *Shape Characterization of Angular Particle Related to their Behavior,* 1st World Congress of Particle Technology, Part 1, Particle Characterization, Nurnberg, FRG(1986), pp 93-103.
19) Leschonski and K. Legenhausen: *Comparison of Different Particle Size Analysis Instruments and Influences of the Errors in Measurement on the Characterization of Classification Processes,* pp. 235-254, *ibid.*
20) Beyvel, L.P., M. Symons and R. Wood: *Optical Instrument for Monitoring the Particle Size Distribution in the Range 0.1-1000 Micrometers,* pp. 155-164, *ibid.*
21) Sheppard, L.M: *Cer. Bull.,* **67,** 87(1988).
22) Bonini, J.J. and K.K. Sankaran: *Evaluation of Blended Elemental Powders for Titanium Missile Structural Applications, Prog., in Powder Metall,* **38,** MPIF, 1982, Princeton, NJ.
23) Ferris, D.P: *J. Powder Metall. and Powder Tech.,* **19, 11(1983).**
24) Cross, Y.M. and J. Dewing: *Surf. Interface Anal.,* **1,** 26(1979).
25) Lowell, S. and J.E. Shields: *Powder Surface Area and Porosity, 2nd Ed.,* (1984)Chapman and Hull, NY.
26) op cit., ref 15, pp. 202-261.

Review

Field-Flow Fractionation: A Versatile Technology for Particle Characterization in the Size Range 10^{-3} to 10^{2} Micrometers †

J. Calvin Giddings, S. Kim Ratanathanawongs and Myeong Hee Moon
*Field-Flow Fractionation Research Center Department of Chemistry University**

Abstract

This article provides an overview on the use of field-flow fractionation (FFF)for particle size analysis and for the characterization of other particle properties such as density, porosity, and the thickness of adsorbed layers. While FFF is a relatively new technology for particle characterization, it is one of the most versatile and powerful techniques now avaiable for characterizing particle populations. The unique features contributing to the effectiveness of FFF include high resolution, relatively high speed, adaptability to different types and sizes of particles, and the ability to collect narrow fractions for further characterization by microscopy and other techniques.

For background, the mechanism of FFF is described in two parts, one applicable to particles over 1 μm diameter and the other relevant to submicron size particles ranging down to 1 nm size. It is shown how particle size distributions are obtained for a variety of particulate materials in both size ranges. The strategies needed for measuring particle properties other than size and size distribution are discussed.

1. Introduction

Field-flow fractionation (FFF) is a family of techniques that affords a unique capability for characterizing populations of particles[1~11]. The methodology works by separating particle samples into narrow fractions for which various properties can be immediately deduced. The fractions can be readily collected and further characterized by a host of supplementary techniques including optical and electron microscopy, photon correlation spectroscopy, inductively coupled plasma-mass spectroscopy, and other chemical and physical techniques. The properties that can be obtained for the individual fractions by FFF measurements alone include, depending upon the experimental circumstances, particle mass, size, density, charge, porosity, shell thickness (for hollow and layered particles), and the thickness of adsorbed films. When the propaties measured for the fractions are assembled for the entire particle population, the distributions and averages of the above properties are obtained. Among these distributions is the size distribution curve, which can be acquired at higher resolution levels than generally offered by other techniques, thus revealing finer details of the distribution.

FFF is a small-scale elution technique in which a narrow plug (generally 10-100 μL) of suspended sample is injected into a flow stream of carrier liquid (which can be aqueous or nonaqueous) that sweeps the sample into a special FFF channel within which separation takes place. The separated fractions emerge at different times from the outlet end of the channel and pass through a detector (usually a turbidimetric sensor)

* Salt Lake City, Utah, 84112, USA

† Received July 20th, 1991.

which is used to measure the relative concentrations of the separated fractions. Since the retention (passage) time in the channel can be correlated with particle properties (see Section 3), the detector signal at any given time indicates the relative amount of particulate material having a specific value of the relevant property, which may be size, mass, or some other particle characteristic as described above. A plot of detector signal versus time—called the fractogram-then provides the information necessary to generate the corresponding distribution curve. The final step involves the use of computer software that converts the experimental fractogram into the desired distribution curve.

If the information provided by the fractogram is not sufficient to fully characterize the particle population, or if any doubt exisis abour the meaning of the data output, then particle fractions can be readily isolated by a fraction collector as they emerge from the detector. These fractions can then be subjected to virtually any other characterization technique(such as microscopy)capable of examining small samples of particles. None of the conventional particle sizing techniques allows such simple interfacing with other techniques to clarify, refine, and expand the information available pertaining to particulate samples.

Because FFF works with small injected samples, its uses are more analytical than preparative. The reduction in sample amount (to enable, for example, the characterization of microgram or nanogram quantities) is limited only by the detector sensitivity, while the increase in sample amount (for preparative purposes) is limited by various overloading phenomena to somewhere in the milligram range. For preparative operation in the gram and kilogram range, a high resolution technique related to FFF known as continuous SPLITT fractionation (CSF) has been developed[12~14].

We note that the FFF process can be readily automated by using an autoinjector to introduce successive samples into the system. Repetitive operation is then controlled and data analysis performed by computer[15].

The high resolution and high speed of one FFF subtechnique (termed sedimentation/steric FFF) applied to micron-size particles is illustrated in **Fig. 1.** Here the fractogram is shown for a mixture of seven monodisperse latex microsphere standards ranging from 4-29 μm diameter. The complete resolution of these particles is achieved in a time of less than 3 minutes. Each specific particle diameter produces a separate peak as can be quickly verified by microscopy.

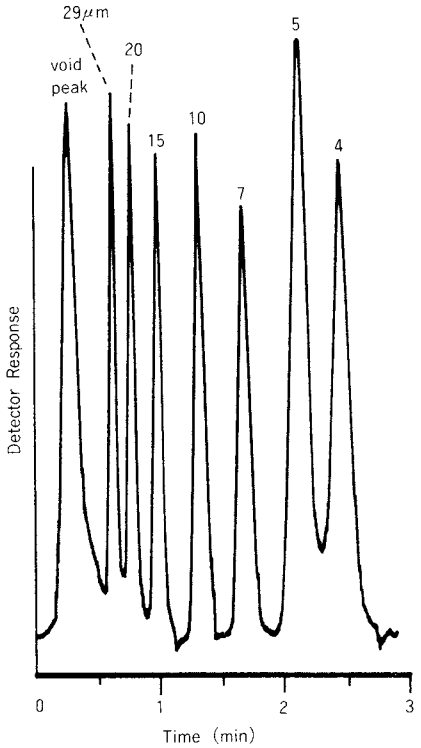

Fig.1. High resolution and high speed separation of seven polystyrene latex standards in the 4-29 μm diameter range by sedimentation/steric FFF. This run was obtained using the sedimentation FFF system described in Section 4 spun at 1327 rpm with a flowrate V= 6.01 mL/min.

Most particulate materials do not consist of a few discrete sizes as observed for latex standards; rather they are continuous distributions that produce broad continous fractograms. However, the running of latex standards is invaluable in assessing the resolution of any particle sizing instrumentation. Any technique that cannot resolve latex standards because of inadequate resolution will almost inevitably broaden and

distort the true size distribution curve of the sample of interest. Such low resolution techniques care at risk of missing extra modes and other features of the distribution curve that are important in governing product quality.

For FFF, vesolution can also be evaluated by examining the micrographs of collected fractions(see later). However, since no such separation and collection capability is found for most techniques, their resolution is difficult to determine except by using artificially narrow particle standards such as the latex standards.

2. Mechanism of FFF

Once particles enter the FFF channel they travel at different velocities along the channel axis and thus emerge at different times. For particle characterization it is important to understand(a)the mechanism of separation and(b)the relationship between particle properties and particle retention time, a relationship needed to obtain size distribution and other information.

The FFF channel is a thin ribbonlike channel as illustrated in **Fig. 2a.** The particle pulse enters the channel and is carried along its length by the flowstream. However, the velocity of any given particle depends upon the velocity of the flow lamina that it occupies. By applying an external field across the face of the channel such that the field extends over the channel's thin dimension, particles having different characteristics can be driven into different laminae where they assume unequal velocities and are thus separated[1~3,6,7].

The detailed mechanism of one form of FFF is illustrated in **Fig.2b,** which shows a blown-up view of the channel interior and the two major confining walls. The parabolic flow profile set up between the walls is also illustrated. Different flow laminae have different velocities (as indicated by the arrows) depending upon their position along the parabolic curve. For example, any particle located near the center of the channel will be carried rapidly by the high velocity flow at the apex of the parabolic profile. A particle close

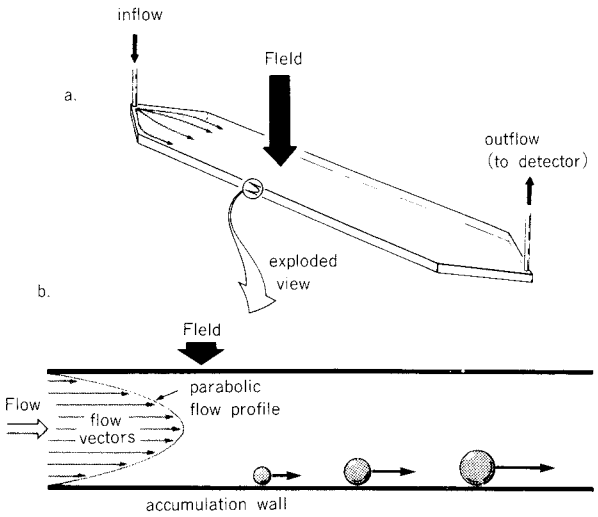

Fig.2 a. Schematic diagram of ribbonlike FFF flow channel.

b. Blown-up view of flow profile and particle positions as they are distributed across the thin dimension (typically 100 to a few hundred μm) of the channel for steric mode FFF operation.

to the wall will be carried much more slowly because the fluid velocity diminishes as the wall is approached. The applied field serves the purpose of driving particles with different characteristics into different laminar positions where they suffer different displacement velocities.

Figure 2b shows how this process works for the subtechnique of sedimentation/steric FFF (Sd/StFFF), which was used to produce the fractogram of **Fig.1**. Here micron-size particles are driven by the field (in the case of **Fig.1** a sedimentation field) toward the accumulation wall of the channel. Although the particles are driven toward the wall, they do not quite touch its surface because shear-induced hydrodynamic lift forces oppose the driving force of the field and keep the particles elevated somewhat above the wall. Because of their smaller sizes, the centers of the smaller particles approach the wall more closely than do those of the larger particles. The smaller particles, because they are caught up in the slower laminae near the wall, are thus displaced along the channel axis at a slower velocity than are the larger particles. The different velocities(illustrated by the arrows of

different lengths in **Fig. 2b**) give rise to the separation.

The above mechanism, applicable generally in the size range 1-100 μm(and sometimes beyond), is termed the *steric* mechanism of FFF[16,17]. As the lift forces increase relative to the driving forces and the particles become more highly elevated, the steric mode of operation gives way to the hyperlayer mode[18]. However, the distinction between steric FFF and hyperlayer FFF is not important for present purposes and will not be further discussed.

Submicron size particles, subject to more severe Brownian motion, form a diffuse cloud(see **Fig. 3**) near the accumulation wall rather than a single unique position like the larger particles[1~3,6~8]. The diffuse cloud, having an exponential concentration distribution, corresponds to the normal mode of FFF operation, which is applicable to particle diameters extending from 1 or 2μm down to 10^{-3} μm, or 1 nanometer. The elution order in the normal mode is inverted relative to that in the steric mode with the smallest particles eluting ahead of their larger counterparts.

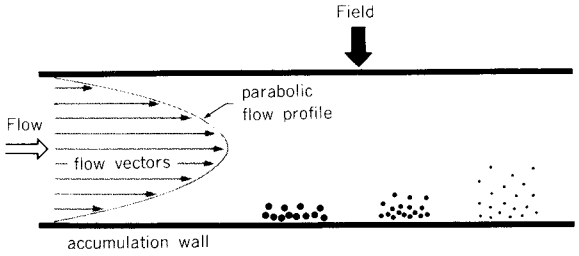

Fig.3 Illustration of mechanism of normal mode FFF applicable to submicron size particles. Because of strong Brownian motion acting against the field, each of the three particle sizes shown is distributed as a thin cloud near the accumulation wall of the channel.

In principle, the fields that are used to generate separation in FFF can be any influence or gradient that extends across the thin dimension of the channel and is capable of driving particles into different laminar positions[6,11]. The fields that have been employed in the order of their frequency of use are sedimentation, thermal (consisting of a temperature gradient), crossflow, electrical, and magnetic. Other fields are possible. Each field or gradient generates a driving force based on a different property of the sample particles and thus yields a different kind of information about the particle population. In addition, each field generally requires its own instrumentation that must be customized specifically for use with that field.

For sedimentation FFF, the thin ribbonlike channel is coiled around the inside circumference of a centrifuge basket (see Section 4). The field strength is governed by the rotation rate of the basket-channel system.

In flow FFF, the channel is sandwiched between two highly polished copper bars, one heated and one cooled. The temperature gradient creates the desired driving force through the phenomenon of thermal diffusion.

In thermal FFF, the channel is sandwiched be permeable to the carrier fluid so that the carrier can percolate into the channel from one wall, cause the displacement of particles to the opposite (accumulation) wall, then egress through the permeable accumulation wall. The transverse flow or crossflow so generated is superimoposed on the normal channel flow that continues to sweep particles along the channel axis. Wall permeability is gained by constructing the channel walls of frit elements; for the accumulation wall, the frit is covered by an appropriate membrane(see Section 4).

Sedimentation FFF has been the most widely used technique for particle analysis, particularly in the submicron size range[11,19]. Flow FFF, a newer technique, is rapidly gaining ground in particle size analysis [20]. Thermal FFF has been used mainly for polymer analysis but recently it has shown a capability for separating particles both in aqueous and nonaqueous suspensions[21].

We note that the field used in FFF is oriented perpendicular to the direction of flow and thus to the axis of separation. This unique perpendicular orientation of the field relative to the separation axis distinguishes FFF from

more widely used methods such as sedimentation, elutriation, and electrophoresis[22]. The perpendicular arrangement of these two displacement axes allows the field and the flow to be varied independently. This independent control provides great flexibility in achieving high speed and high resolution goals.

3. Relationship of Particle Properties to Retention Time

Particle properties are deduced from their retention time *tr*, which equals the time required to displace the particle through the channel. Thus it is essential to establish a relationship between *tr* and particle properties such as size, mass and density. Because of the complicated role of hydrodynamic lift force in influencing the lamina occupied by a given subpopulation of particles, the *tr*-property relationship in steric and hyperlayer FFF (applicable generally to diameter $d \geqq 1\mu$ m)is established empirically. For the normal mode of operation (used primarily for $d \geqq 1$ μm), the *tr*-property relationship is established by theory.

While the capability of FFF for submicron size analysis is perhaps most unique and has been by far the most common application to date, FFF is also a powerful and versatile technology in the supramicron($d \geqq 1\mu$m)size range. We will address steric FFF first, which is mainly applicable to $d \geqq 1\mu$m.

When crossflow is the driving force (giving the subtechniques of flow/steric FFF or flow/hyperlayer FFF), *tr* is related to particle diameter *d* by the empirical logarithmic relationship[23]

$$\log\ t_{r_1} = S_{df}\ \log + \log\ t_{r_1}(\text{flow FFF}) \qquad (1)$$

where t_{r_1} is the retention time of a particle of unit diameter and S_{df} is the diameter-based selectivity for flow FFF(the subscript *f* designates flow), a term that describes the sensitivity of *tr* to changes in *d* according to the definition

$$S_{df} = \left| \frac{\mathrm{d}\log tr}{\mathrm{d}\ log\ d} \right| \qquad (2)$$

Particle retention in sedimentation/steric FFF is best described by a slightly more extended relationship[24]

$$\log t_r = -S_{ds}\log d + S_{\Delta\rho}\log G\Delta\rho + \log t_0 \qquad (\text{sed. FFF}) \qquad (3)$$

where t_0 is again a calibration constant and S_{ds} is the diameter-based selectivity defined as in Eq.(2), but in this case applicable to the sedimentation field. (Typically, $S_{ds} \cong 0.75$ and $S_{df} \cong 1.25$.) The parameter $S_{\Delta\rho}$ is the density-based selectivity and G is the field strength expressed as acceleration.

Particle retention under the influence of a sedimentation field depends not only on particle diameter but also upon particle density, which is accounted for by the second term on the right of Eq.(3)in which $\Delta\rho$ is

$$\Delta\rho = |\rho_p - \rho| \qquad (4)$$

where ρ_p is the particle density and ρ is the (buoyant) density of the liquid carrier.

Equations (1) and (3) show that the crossflow (Eq.(1)) and the sedimentation (Eq.(3)) driving forces are complementary to one another, relating t_r to different properties or combinations of properties. For flow FFF, Eq. (1) shows that *tr* depends solely upon *d*, which is a kind of hydrodynamic diameter. For sedimentation FFF, t_r depends upon both *d* and particle density ρ_p. Thus the choice of techniques depends upon the information sought. For particles of uniform composition such that $\Delta\rho$ is fixed, either technique will yield a size distribution. If the composition and $\Delta\rho$ vary, flow FFF still yields a size distribution but sedimentation FFF yields a mixture of size and density data. While this may be a disadvantage for the sedimentation field, we have developed some strategies for obtaining density information from sedimentation FFF, which can make the latter technique advantageous if the acquisition of

such density information is important[25].

The calibration constants in Eqs. (1) and (3), S_{df}, S_{ds}, $S_{\Delta\rho}$, t_{r1} and t_O, are fixed empirically. These calibration parameters and the corresponding calibration plots of Eqs. (1) and (3) can be most easily established by using latex particle standards. For example, the fractogram of **Fig. 1** provides a series of t_r versus d values for sedimentation/ steric FFF. A calibration plot of log t_r versus log d based on the data of **Fig. 1** is shown in **Fig. 4.** The plot provides a value (specifically 0.694) of S_{ds}, which is the negative slope. Measurements must be made at other values of field strengh G to eatablish $S_{\Delta\rho}$; if neither G nor $\Delta\rho$ vary, then the center term on the right side of Eq. (3) can be absorbed into the final constant t_O. If a sample being characterized has a different density (and thus a different $\Delta\rho$) from that of the latex calibrant,an adjustment of the rpm to make the product $G\Delta\rho$ equal for sample and calibrant will make possible the direct use of the latex calibration curve[24].

As mentioned above, the t_r- property relationship for submicron size particles (using the normal operating mode of FFF) is governed by theoretical equations. Specifically, no matter what the field type, t_r is related to the force F exerted on a particle by the field in accordacnce with expression[1~3,6~8]

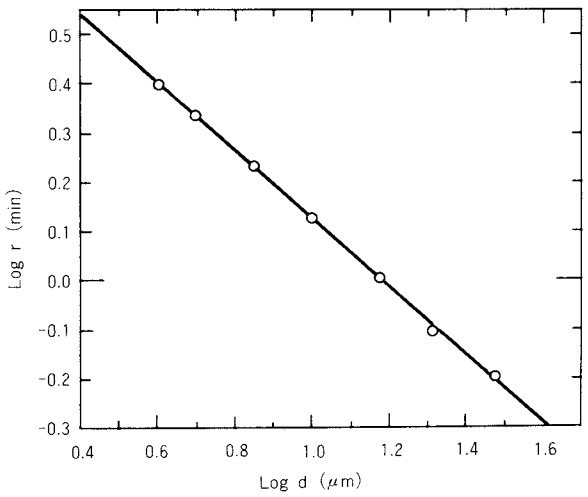

Fig.4 A linear calibration plot obtained using measured retention time(t_r)values from **Fig. 1** for latex spheres of different diameter(d).

$$t_r = \frac{t^0}{\frac{6kT}{Fw}\left(\coth\frac{Fw}{2kT} - \frac{2kT}{Fw}\right)} \cong \frac{Fwt^0}{6kT} \qquad (5)$$

where w is the channel thickness, K is Boltzmann's constant, T is temperature, and t^o is the void time, equal to the time necessary to displace carrier fluid through the channel. The approximation on the right, valid when $Fw >> 6kT$, shows that tr is roughly proportional to the force F exerted on the particle.

Equation(5) shows that t_r is sensitive to, and will provide a measure of , any particle property upon which F depends. For example, in sedimentation FFF, F depends both upon particle mass m and density according to

$$F = mG(1 - \rho/\rho_P) \qquad (6)$$

Thus particle mass and density parameters can be obtained from the appropriate sedimentation FFF experiments[26]. Alternatively, F can be expressed in terms of particle diameter d (where d is now the effective spherical diameter) and ρ_P instead of m and ρ_P

$$F = \frac{\pi}{6} d^3 G(\rho_P - \rho) = \frac{\pi}{6} d^3 G\Delta\rho \qquad (7)$$

As is the case for steric FFF, if p_ρ is a known constant, then a measured t_r value leads to a calculated F value through Eq.(5)and a m or d value through Eq.(6)or(7). In this way the mass or size of a particle or the distribution for a particle population can be obtained. For flow FFF force F depends solely upon the particle diameter amd shows no variation with particle density. Specifically F is given by Stokes law

$$F = 3\pi\eta dU \qquad (8)$$

In this case d is the Stokes diameter of the particle, η is the carrier viscosity, and U is the velocity of crossflow. Generally U is expressed in terms of the volumetric flowrate V_c of the crossflow stream by the expression $U = V_c/bL$,

where b and L are the channel breadth and length, respectively.

4. FFF Instrumentation

FFF instrumentation for particle and polymer analysis has been under development in the University of Utah laboratories since the 1960s when the concept of FFF was first described[27]. This instrumentation was improved continuously in the 1970s and 1980s[28]. The first commercial apparatus was a DuPont (Wilmington, DE,USA) sedimentation FFF system first released in 1986. This system is no longer being actively marketed.

Commercial instrumentation patterned more directly after our laboratory systems includes a thermal FFF apparatus first made available by FFFractionation, Inc.(Salt Lake City, UT, USA), in 1987. This was followed by a sedimentation FFF instrument, first marketed by FFFractionation in 1988, and a flow FFF system, first available in 1991. A photograph of the FFFractionation sedimentation FFF instrument (Model S101) is shown in **Fig.5**.

Although the intent of the present article is to provide an overview of particle characterization by FFF, the experimental results presented below (with two exceptions) are new. It is therefore appropriate, both for perspective and for specificity, to further describe the instrumentation used to produce these results. Since both sedimentation FFF and flow FFF systems were used to acquire experimental data, these two systems (and their variations) will be described sepatately below.

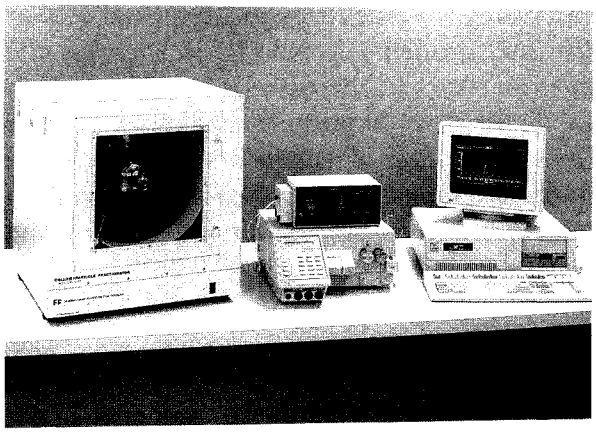

Fig.5 Photograph of Model S101 sedimentation FFF instrument from FFFractionation.(Courtesy of FFFractionation, Inc., Salt Lake City, UT, USA.)

Our laboratory sedimentation FFF systems (as well as the commercial version produced by FFFractionation) is based on achieving particle separation in a thin ribbonlike channel like that shown schematically in **Fig.2a.** However, the channel, rather than being straight, is curved to fit around the inside of a centrifuge basket where it is clamped between rigid concentric rings. The rotation rate is controlled by computer. The carrier liquid enters and exits the channel by means of special rotary seals[28]. The sample (usually 10-50 μL in volume) can be injected either by an injection valve or by a syringe. Following separation in the channel, the fractions are eluted into a derector, usually consisting of a commercial HPLC UV detector serving as a turbidity sensor. The data are then collected and analyzed by a computer.

The radius of rotation of the channel is 15.1 cm for both the laboratory and the commercial systems. However, the channel dimensions (particularly the thickness) are varied somewhat (see below) to best suit the sample under investigation. For most of the results presented in this paper, the tip-to-tip channel length is $L=90$cm, the channel breadth $b=1.0$ cm, and the channel thickness $w = 127$ μm. The flowrate V through the channel was varied depending upon resolution and speed requirements.

Flow FFF also makes use of a ribbonlike channel, but in this case the channel is linear in form as represeated in **Fig. 2a.** Two flowstreams, oriented perpendicular to one another, pass through the channel. One flowstream (channel flow) transports the separated sample down the length of the channel while the other (crossflow) provides the field. The cross and channel flowrates are regulated by adjusting a variable pressure restrictor that is connected to either the detector outlet or the

crossflow outlet. Sample injection and detection are accomplished in the same manner as that used in sedimentation FFF[20].

In flow FFF the channel is clamped between two rectangular blocks (usually made of Plexiglass). Inset into each block is a flat panel of ceramic frit. The panel in the top block ensures that a homogeneous flow enters and moves across the channel thickness while the panel in the bottom block provides a rigid permeable support for the semipermeable membrane that serves as the accumulation wall. The primary function of the membrane is to retain the sample particles within the channel. The choice of membrane is determined by physical characteristics, compatibility with the carrier, needs based on sample characteristics (e.g., particle diameter and surface chemistry), and pressure-drop considerations. Ultrafiltration membranes have often been used in flow FFF systems. These membranes may be considered as universal membranes because of their general suitability for all of the particle sizes commonly encountered as well as for large macromolecules. Microfiltration membranes possessing different pore sizes have also been employed. Membrane composition is important for the reduction of particle-membrane interactions (and thus particle adsorption).

Several flow FFF channels were used in this work. The dimensions of the channels and the membranes employed are reported in **Table 1.**

The dimensions of the different FFF channel systems reported above are seen to vary considerably. The channel length and breadth are primarily determined in each case by considerations that relate to the integrated operation of the entire instrumental system; these considerations will not be described here. The most fundamental and operationally significant dimension of the channel is its thickness w. In recent work we have tended more and more toward thinner channels. For example, in sedimentation FFF, where a 254 μm (0.01 inch) channel has long been considered standard, we have recently been doing much of our work with 127 μm thick channels[25].
(In FFF we have thermal reduced w in one case to 50 μm[29].) The thinner channels are more difficult to fabricate at the high uniformity levels required. In addition, they must have smaller volumes in the associated connecting tubing and detector cells and they must not be used for particles that are so large that the channel can become clogged. The operable size range is also somewhat reduced by thinner channels; the thinner channels cannot separate particles at the small and large size extremes that can be fractionated by thicker channels, all other factors (including field strength) being equal.

Offsetting the disadvantages of thin channels are several advantages. At the same field strength and retention times, particles emerging from a 127 μm channel are four times more concentrated in the effluent stream (whose flowrate is reduced fourfold) than those exiting a 254 μm channel. This higher concentration improves detectability. In addition, the relaxation time--the time required for particles to approach their equilibrium distributions upon entering the channel--is reduced in proportion to the decrease in w. There is also some reduction in possible perturbations caused by secondary flow. Finally, for the steric mode of FFF, small particles (down to and below 1 μm) can be eluted rapidly from the thinner channels without requiring extraordinary flowrates.

5. Size Distribution for Supramicron Size ($d > 1\,\mu$m) Particles

The size distribution of particles exceeding 1 μm diameter can be measured by both sedimentation FFF and flow FFF. Measurements made by sedimentation FFF will be described first. For particles in this larger size range, the steric mode of operation (see **Fig.2b**) is used. The means of calibration, described briefly above, are provided in more detail in a recent publication[24].

Fig.6 shows a fractogram obtained for a polydisperse Geon 213 PVC sample, a low porosity blending resin produced by BF Goodrich Company. This fractogram was obtained at 530 rpm with a flowrate V of 6.01 mL/min. The broadness of the Geon peak, in

contrast to the sharpness of the peaks in **Fig.1** , confirms that the sample is polydisperse. However, nearly any instrument will yield a broad featureless response function like that in **Fig.6** for a polydisperse sample. Unfortunately, for most techniques the authenticity of the response curve is difficult to confirm and the resolving power (generally unrelated to the number of channels specified for a method) cannot be readily ascertained for the sample, although it can estimated (as discussed previously) using monodisperse latex standards. However for FFF, as noted earlier, fractions can be collected and subjected to further examination to verify resolution and accuracy. For the Geon run shown in **Fig.6** , a series of fractions were collected and subjected to microscopy. The position of collection of four such fractions (9, 12, 15, and 19) are shown on the fractogram of **Fig.6** . The accompanying panels in **Fig.6** show the micrographs of these four fractions plus the micrograph of the original (unfractionated) sample. The micrographs make it clear that fractionation has been achieved as predicted. These fractions show that very little aggregation has occurred over the bulk of the particle size range. However, the examination of a fraction collected from the void peak (not shown) confirms the presence of afew large aggregated clusters.

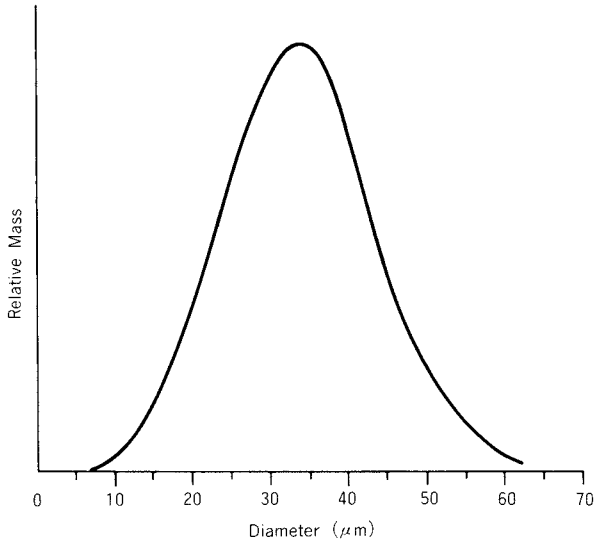

Fig.6. Curve showing detector reponse *versus* time(i.e., the fractogram)obtained for a Geon 213 low porosity PVC sample. The position at which seveal fractions(identified as fractions 9, 12, 15, and 19)were collected are shown. The micrographs of the collected particle fractions demonstrate a clean division of the particle population into narrow size groups by the FFF process. This run was carried out at an rpm of 530 and a flowrate $V = 6.01$ mL/min.

In order to obtain a size distribution curve for the Geon sample, a proper calibration curve must be established. As shown in the last section, the product $G\Delta\rho$ must be the same for the sample and the calibrant. Since the density of the porous Geon sample is greater than that of polystyrene (1.33 *versus* 1.050 g/mL), the calibration run for polystyrene must be carried out at 1327 rpm rather than the 530 rpm used for Geon. Since the polystyrene calibration run of **Fig.1** and its plot shown in **Fig.4** were originally obtained at 1327 rpm for the purpose of characterizing Geon, the calibration plot of **Fig.4** is already perfectly matched to the Geon run.

When the parameters of the calibration plot are combined with the digitized response data of the fractogram shown in **Fig.6** , a size distribution curve is produced. This curve is shown in **Fig.7** .

Particles of irregular shape can be characterized by sedimentation/steric FFF as well. As an example of this, **Fig.8** shows a fractogram obtained for an alumina powder. The micrographs obtained for fractions 5,9, and 16 verify the fractionation of the alumina into distinct size classes. Since the alumina run was made at 284 rpm and $V = 14.45$ mL/min, the polystyrene latex calibration run (not shown) was carried out at 2200 rpm (based on an assumed alumina density of 3.97 g/mL) using the same flowrate. The latex calibration plot combined with the fractogram yielded the size distribution curve also shown in **Fig.8** . A cumulative size distribution curve for the alumina is shown as well. We note that in exploratory work we have been able to fractionate needlelike particles by FFF. However, the necessary calibration procedures have not been worked out.

Similar results in fractionating and

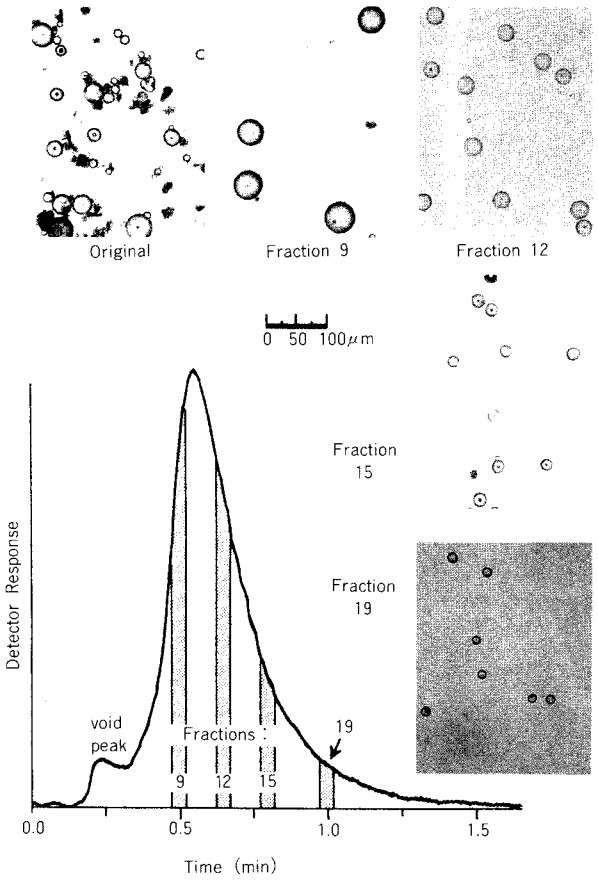

Fig.7 Particle size distribution curve obtained for the Geon PVC sample using the FFF run of **Fig. 6.**

characterizing particles can be obtained using flow FFF. For diameter $d > 1$ μm, flow FFF is usually operated in the hyperlayer (which resembles the steric) mode, Flow/hyperlayer FFF has a somewhat higher selectivity than Sd/StFFF, but without programming the range of particle diameters that can be achieved in a single run is rather limited, being only about tenfold. However, when field strength and flowrate conditions are changed, the range can be shifted up or down. Most of our Fl/HyFFF runs have been used for particles in the overall size interval from 0.5 μm up to 50 μm. Applications in this range include latex particles, pollen grains, biological cells, and silica particles [20,30].

As suggested earlier, the breadth of the size window that can be semected for any given run within the overall size range of 0.5-50 μm can be increased by using progamming. Programming, a technique in which the field strength and/or flowrate is changed during the run, is used frequently to expand the sizerange available for submicron size particles using FFF in the normal mode [31,32]. The extension of programming technology to flow/hyperlayer FFF to similarly expand the available particle size window has only recently

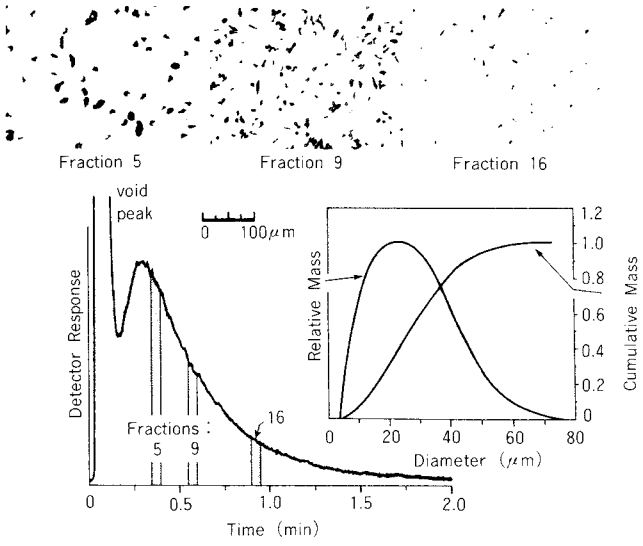

Fig.8 Fractogram of an alumina sample obtained using sedimentation/steric FFF. The micrographs of three fractions(5,9, and 16)collected from the FFF run are shown. The size distribution curves deduced from the fractogram are also given.

been achieved [23]. In **Fig.9** we illustrate the power of programmed flow/hyperlayer FFF in the fractionation in a single run of polystyrene latex particles in the size range from 1 to 48 μm.

Size calibration curves for flow/hyperlayer FFF are most readily obtained using polstyrene latex standards as described above for sedimentation/steric FFF. However, for the flow FFF method, retention is independent of density (compare Eqs. (1) and (3)) so that no density compensation procedure need be used. Thus both the sample run and the calibration run are carried out at the same field

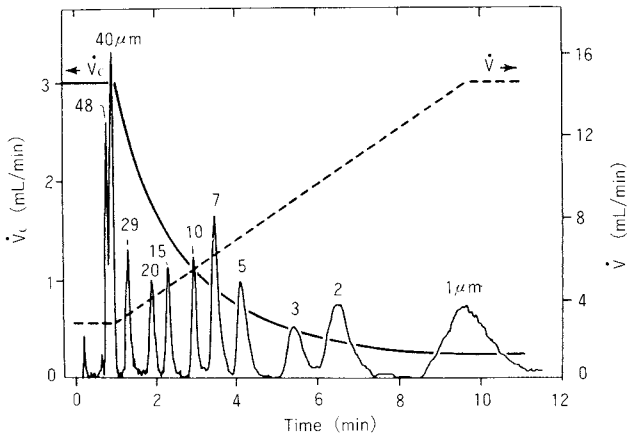

Fig.9. Separation of eleven polystyrene latex beads in the 1-48 μm size range using dual programmed flow FFF. The results were obtained using channel system I(see **Table 1**). The channel flow-rate V and the cross flow are Vc were varied during the run as shown by the plotted lines.(Reprinted with permission from Ratanathanawongs, S. K. and Giddings, J. C. *Anal, Chem.* (submitted). Copyright American Chemical Society.)

strength.

Flow/hyperlayer FFF has been used for the rapid characterization of HPLC silica [33] . **Fig.10** shows the fractogram obtained for a nominal 5 μm diameter porous chromatographic silica using nonprogrammed flow/hyperlayer FFF. The diameter scale that has been superimposed on the fractogram was obtained from a polystyrene latex calibration run. The results show that this particular material is anomalously broad and likely not suitable for high resolution chromatography.

As before, fractions of the sample were collected and subjected to microscopy. micrographs of various fractions are shown in the panels of **Fig.10** . The size distribution curve deduced for this silica based on the fractogram of **Fig.10** and the calibration run is shown in **Fig.11** .

We note that reliable size distrbution curves for porous particles in the size range of HPLC silica are difficult to obtain. Light scattering methods generally lack the necessary resolution for these often narrow distributions. Electrozone methods are subject to error

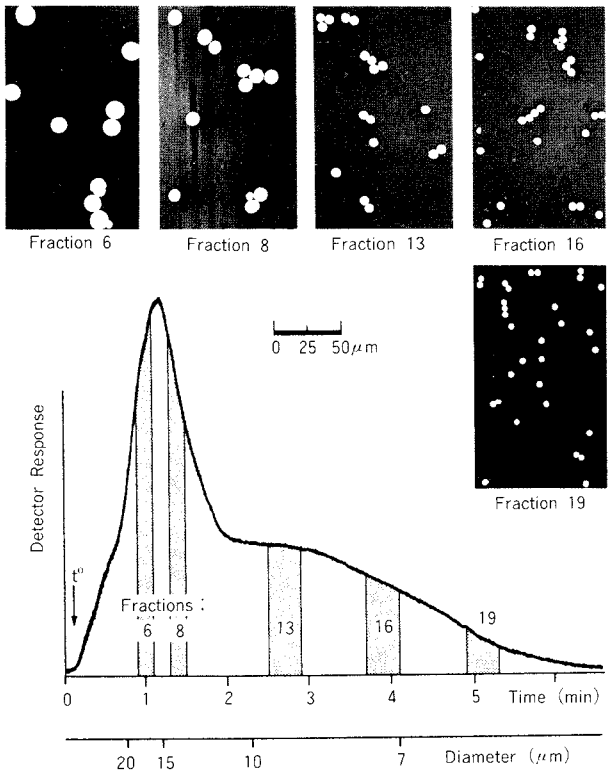

Fig.10. Fractogram of silica particles used to sock chromatographic columns obtained by flow/hyperlayer FFF. The positions of collected fractions are indicated and the micrographs of these fractions are shown. These results were obtained using channel system II with $\dot{V} = 6.00$ and $Vc = 1.56$ mL/min.

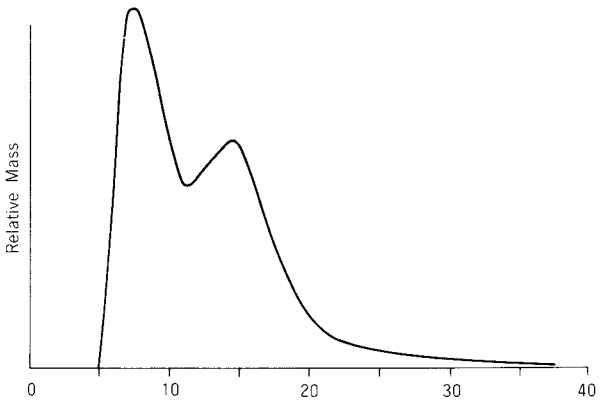

Fig.11 Size distribution curve for chromatographic silica deduced from the FFF fractogram of **Fig. 10.**

because of conductivity through the pores [34]. While a correction can be attempted to compensate for this effect, there is no simple way to account for changes in pore conduct-

ivity from one particle population to another or even from one particle to another. The pore condictivity, in general, will be a complex function of both pore volume and of pore connectivity in the particle, both of which may vary considerably for different samples.

6. Size Distribution for Submicron Size ($d < 1\mu m$) Particles

Particle populations with $d < 1$-$2\mu m$ can be characterized both by sedimentation FFF and flow FFF systems operating in the normal mode. The relationship between retention time t_r and particle diameter d, rather than being obtained from empirical calibration plots as above, is acquired from the theoretical expressions of Eqs. (5)-(8). For particles in the approximate size range 0.5-2 μm, these equations must be corrected for steric effects [35]. Particle populations that span both the normal and steric FFF size range (e.g., those having a range 0.2-5 μm) are difficult to characterize.

In work at the Field-Flow Fractionation Research Center we have applied sedimentation FFF to the size analysis of many submicron size materials including numerous latexes and emulsions, clays, viruses, subcellular particles, metal particles, silver halides, pigments, silicas, and colloidal particles found in natural waters. Other research groups have developed a large number of additional applications.

The fractogram of a sample of colloidal zirconia is shown in **Fig.12 a**. (This fractogram, obtained using a 254 μm thick channel, was previously reported in the literature [36].) This fractogram is typical for single mode submicron particle populations. Multimodal populations show multiple peaks (see later).

The fractogram of **Fig.12a** can be converted by computer software into the size distribution curve of the submicron zirconia. This distribution is shown in **Fig.12b**. If any question should arise about any aspect of this distribution (e.g., what fraction of particles in a certain size range are simply aggregates of the smaller particles), fractions can be collected and electron microscopy applied to more fully characterize the material.

The minimum particle size that can be characterized by FFF depends upon doth the type of field used and its strength. Particles that are

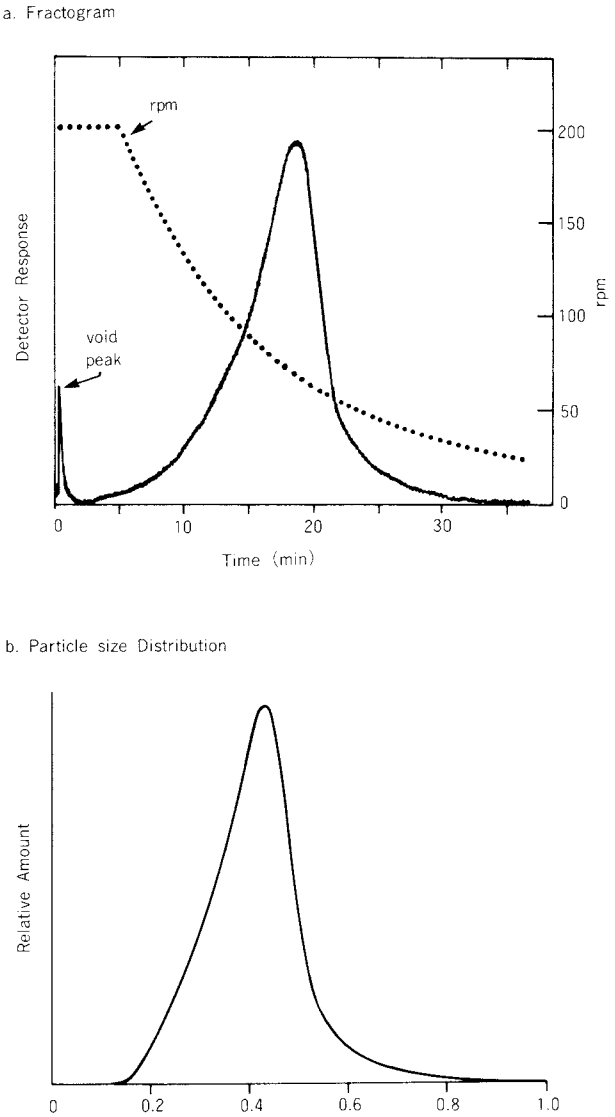

Fig.12. a. This fractogram of colloidal zirconia is typical of that for monomodal particle distribution. For this run the field strength(rpm)is programmed as shown.

b. Particle size distribution curve obtained from the fractogram in a.(Reprinted with permission from Giddings, J. C., Myers, M. N., Moon, M. H., and Barman, B. N. In *Particle Size Distribution II*, Provder, T., Ed., ACS Symposium Series No.472; American Chemical Society : Washington DC1991; Chapte 13. Copy right 1991 American Chemical Society)

below the effective range of operation are poorly resolved from one another although they can be well resolved from larger paricles that fall within the working size range. Although there is no sharp cutoff for the minimum resolvable size, in general the resolution is seriously hampered when the driving force F falls below the level

$$F < \frac{6kT}{w} \tag{9}$$

For sedimentation FFF a combination of Eqs. (7) and (9) shows that the minimum resolvable particle diameter d_{min} is approximated by

$$d_{min} = \left(\frac{36kT}{\pi w G \Delta\rho} \right)^{1/3} \tag{10}$$

Plots of d_{min} versus $G\Delta\rho$ are shown in **Fig.13** for two channel thicknesses (w= 127 and 254 μm) that are found to be highly practical for sedimentation FFF operation. The calculations underlying these plots are based on T= 298 K. The plots show that for a field strength $G = 10^3$ gravities (approximately the upper limit of our laboratory equipment and the FFF ractionation instrument) d_{min} values are about 0.03 μm for $\Delta\rho$ = 1 g/mL. Lower and higher values of d_{min} ar found for particles of higher and lower densities, respectively. To analyze much smaller particles, it is necessary to go to higher G values or to utilize flow FFF.

Flow FFF operates similarly to sedimentation FFF but its capabilities are somewhat different. Flow FFF, as noted earlier, gives density-independent particle size results, unlike sedimentation FFF. The resolution achievable by flow FFF is not quite as high as that of sedimentation FFF but it is generally much better than that of non-FFF systems, and thus adequate for most practical purposes (see **Fig.14**). Most importantly, flow FFF can be applied to particles of considerably smaller diameter than sedimentation FFF[20].

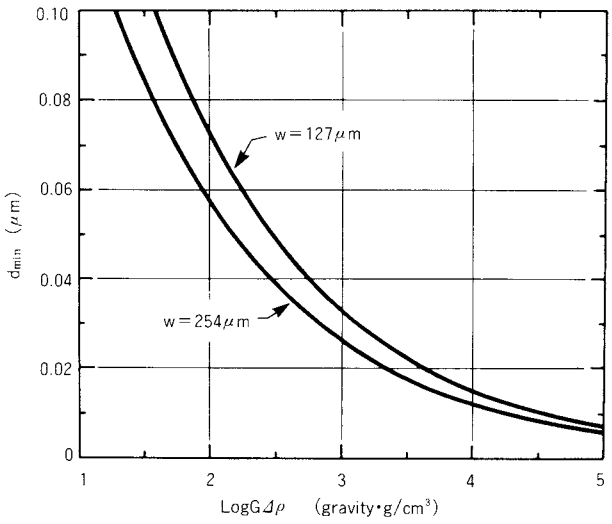

Fig.13. Plots of the minimum particle diameter (d_{min}) that can be resolved using the normal mode of sedimentation FFF operated at different levels of field strength G (in gravities)and different density difference $\Delta\rho$(expressed in g/cm^3). The two plots correspond to two different channel thicknesses(as shown)that have been found effective for sedimentation FFF operation.

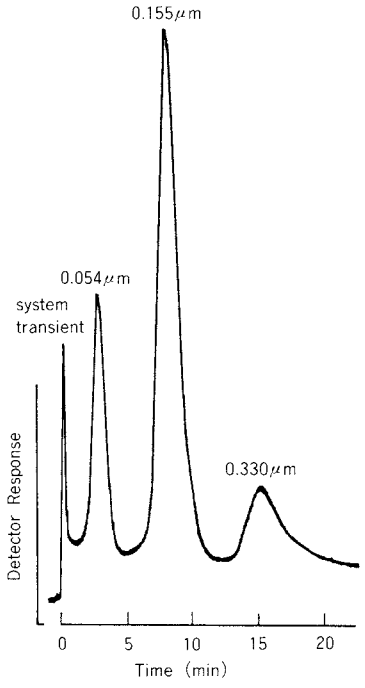

Fig.14. The resolution of submicron polystyrene latex beads by floe FFF(shown here)is somewhat inferior to that of sedimentation FFF but is higher than that of other techniques in this size range. The fractogram shown here was obtained from flow channel III at a channel flowrate $\dot{V}$ = 4.20 and a cross flowrate $\dot{V}c$ = 2.74 mL/min.

By combining Eqs. (8) and (9) we find that the minimum diameter resolvable by flow FFF is given approximately by the equation

$$d_{min} = \frac{2kT}{\pi w \eta U} \qquad (11)$$

This equation shows that for a modest crossflow velocity $U = 10^{-3}$ cm/s in a channel of thickness $w = 254$ μm, the minimum resolvable diameter is 10^{-7} cm or 1 nm. Thus flow FFF is not only a practical technique for the separation of particles in the common 0.1-0.5 μm size range, but it extends to diameters as much as 100 times smaller and has thus been found applicable in our laboratories to the separation of fine grained materials such as proteins, lipoproteins, humic acids, viruses, seed latex, carbon black, and small colloidal silica particles.

In **Fig.15** we show the flow FFF fractogram obtained for small polystyrene latexes in experimental flow channel Ⅳ (see **Table 1**) with $V = 4.06$ and $V_c = 3.27$ mL/min. These particles were sent to us by a major supplier of latex standards who was unable to characterize (even by electron microscopy) these smaller latexes. Although the fractograms could be converted into size distribution curves by the procedures noted above, we have elected instead in **Fig.15** to simply superimpose on the diagram a diameter scale calculated from the theoretical expressions, namely Eqs.(5) and(8). The positions of the peaks relative to the diameters scale show that the mean diameters range from ~9-18 nm.

We noted before that a multimodal particle distribution will generally produce a multimodal fractogram. This is illustrated in **Fig.16** for an industrial styrene-butadiene latex. When the bimodal fractogram is converted into a size distribution curve (**Fig.16b**), it produces a bimodal distribution. Note that by using flow FFF instead of sedimentation FFF on this material it is not necessary to know the latex density. On the

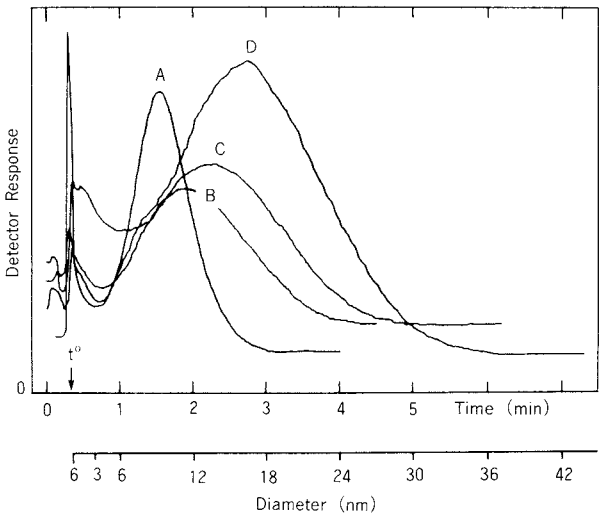

Fig.15. Fractogram and calculated diameter scale for four small diameter polystyrence latexes that are difficult to characterize by other means. There results were obtained using flow channel IV along with $\dot{V} = 4.06$ and $\dot{V}c = 3.27$ mL/min.

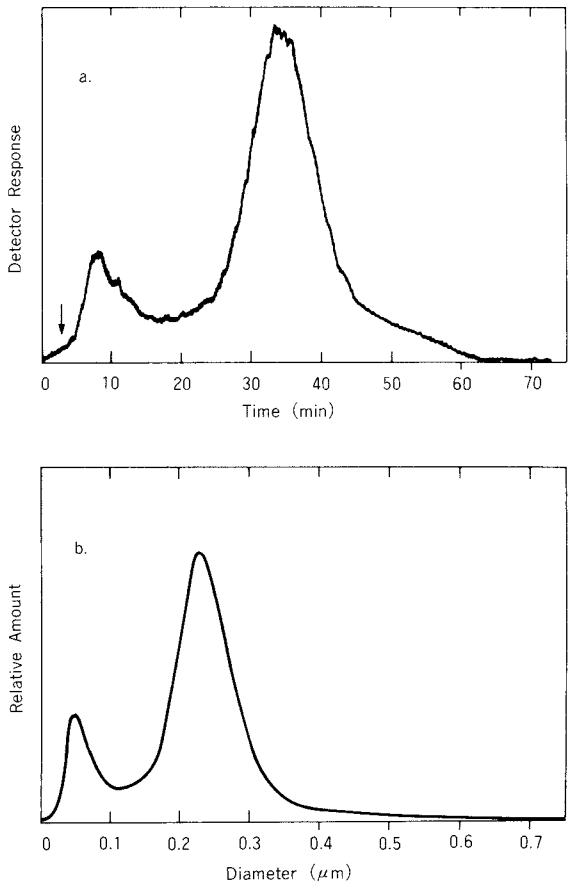

Fig.16. Flow FFF of styrene-butadiene latex using channel V. **a** Fractogram. **b.** calculated size distribution curve. The flowrates were $\dot{V}$ 1.88 and $\dot{V}c = 1.00$ mL/min.

other hand, density values cannot be measured by flow FFF whereas numerous mass and density related parameters can be measured using a sedimentation driving force. This capabulity wull be explained in the following section.

7. Other Particle Characteristics Measured by FFF

As noted earlier, in addition to measuring particle size distributions by FFF, we have employed FFF techniques for the measurement of a variety of particle properties, including particle density, porosity, aggregation kinetics, thickness of adsorbed layers, diffusion coefficients, thermal diffusivities, and polydispersities of narrow distributions. In addition, prospects exist for measuring shape factors and their distribution by FFF. It should be possible to extend our size and density measurements to a capability for simultaneously measuring the size and density distributions of complex particle populations such as those commonly found in environmental and biological samples.

The capability of FFF for providiug a broaderbase of information than conventional techniques on particle populations is a consequence of several features of FFF operation. Among these enabling features are:(a) FFF is basically a high resolution separation methodology;(b) narrow fractions can be readily collected and further characterized by other techniques including other FFF methods;(c) either fundamental theory or empirical calibration can be used to relate particle properties to observed retention times; and(d) a number of different FFF techniques based on different fields are sensitive to different particle properties and can be used to deduce those properties.

Several examples of the measurement of properties other than size are described briefly below. Most of these measurements apply to submicron size particles but we will also describe a technique used for measuring the density(and thus porosity) of larger particles as well.

To begin with, we note that the retention time in sedimentation FFF (operating in the nomal mode) is a function of both particle mass m and particle density ρ_p (along with the carrier density ρ). The nature of this dependency is shown by Eqs.(5) and(6). If all densities are known, then the particle mass can be directly related to retention time[37]. This observation constitutes the basis for obtaining size and size distribution data as described above (see Eq.(7) and Section 6). However, the tr- particle mass relationship can be utilized for a variety of particle characterization problems, a few examples of which are noted below.

If the carrier medium in which the particles are suspended also contains chemical substances that tend to adsorb on the particle surface, the particle will gradually accumulate an adsorbed film of the substance. This film adds to the particle mass and will thus cause a shift in the retention time[38]. The amount of added mass can be calculated precisely using Eq.(5) and a modification of Eq.(6) that accounts for the film mass. By measuring the mass adsorbed at different concentrations of the dissolved substance, an adsorption isotherm can be obtained. The sensitivity of this method is enhanced if the density of the adsorbed surface film is greater than that of the particle. An example is the adsorption of protein on latex particles, a subject of considerable interest in the clinical industry. We have shown in a recent study that adsorbed layers of proteins and other substances having an average thickness as low as 1 Å is measureable by sedimentation FFF[38]. A parallel study on the adsorption of water soluble polymers was carried out by Caldwell et al[39].

In the above study[38] it was found that the exposure of polystyrene latex microspheres to human γ-globulin led not only to the adsorption of thin films (with average thickness 5-20 Å) of γ-globulin (from which adsorption isotherms could be determined), it also caused the low order aggregation of the latex beads. Aggregation, of course, causes a stepwise increase in particle mass and is thus readily measured by sedimentation FFF. Thus the low order aggregation of mono-

disperse particle populations will generate a series of peaks in the fractogram, one for the single unaggregated particles (the singlets), another for clusters of two (the doublets), and other separable peaks for the higher order clusters[40]. The area of each peak will represent the relative population of the corresponding particle cluster. Thus the above latex after 106 hours exposure to γ-globulin yielded substantial doublet and triplet populations as deduced immediately from the multimodal shape of the fractogram.

The ability to isolate and detect different sized clusters in aggregated materials has made it possible to follow the detailed kinetics of cluster formation and disruption using polymethylmethacrylate (PMMA) latex as a model colloid[40,41]. For more complex colloids, a combination of sedimentation FFF and electron microscopy would be needed for a detailed analysis of the distribution of aggregated clusters.

Not only can FFF isolate clusters of different aggregation number n (n = number of elementary particles in the cluster), its sensitivity is such that it can distinguish small differences between clusters of equal n that reflect unusual features of the particle population and, in some cases, of its origin. Thus in a recent study of 0.586μm PMMA latex by sedimentation FFF, two doublet peaks were observed[41]. One was retained about 10% longer than the other, showing(see Eqs.(5) and(6)) that the particles in that peak had a mass approximately 10% greater than that of the particles in the earlier doublet peak. Electron microscopy of the collected fractions showed that the particles appearing in the earlier peak were more tightly fused together than the doublets eluting later. An annealing mechanism was ruled out because the FFF results clearly demonstrated that the doublets differed 10% in mass, whereas no mass change would accompany annealing. The results were consistent with a two stage latex formation process. The fused doublets apparently first formed by aggregation after the first stage of growth and subsequently continued to grow through the second stage, finally yielding the tightly fused doublets. These doublets have a smaller mass than those initially formed after the second stage of growth because the new growth was excluded around the contact point between the two spheres. The mass difference of 10% could be used to calculate the diameter of the first stage latex, which was 0.3 μm. This result was consistent with the measurement of the dimensions of the two doublets based on EM.

We note that the unusual features of this latex could probably be deduced from meticulous EM studies. However, a routine EM examination would suggest nothing unusual about this latex whereas the appearance of a second doublet peak in the fractogram of a sedimentation FFF run draws immediate attention to the unusual features described above.(EM remains invaluable as a complementary tool to FFF for working out geometrical details.) Thus FFF, because of its high resolution, provides not only detailed information about particle populations but transparent information whose major and minor features stand out. Such detailed features are becoming more important as the manufacturing, processing, and utilization of particulate materials is subject to increasingly demanding requirements.

Differences is particle mass can be discerned, measured, and interpreted as described in the above examples providing particle densities are known. If particle densities are unknown, then a single retention measurement cannot distinguish between mass and density effects since they jointly govern retention (see Eqs.(5) and(6)). However, if several runs are made with carriers of different density ρ, the particle mass(or diameter) and density can both be determined. A special plotting procedure has been devised for this purpose[26]. In recent work it has been shown that latex particle densities can be determined with extraordinary accuracy(to about 0.002 g/mL) using this sedimentation FFF procedure[42]. The procedure works best when applied to particles that are close to the density of the carrier[43] (usually water) but approximate densities have been obtained for particles as diverse as quartz[44] and viruses[45].

Similar procedures for determining the density of large particles($>1\mu$m) by steric FFF are under development. However, a procedure has already been devised in which the density of supramicron size particles can be determined by a combination of the measurement of FFF retention and the determination of the mean particle diameter of the FFF fraction by microscopy[25]. This procedure has been used to determine the density (and thus the porosity) of chromatographic support materials. It was used to determine that the density of the Geon 213 sample described in **Fig.6** and **7** has a value of 1.33 g/mL.

Since retention in flow FFF lacks a dependence on particle density, no density information can be obtained using this method. However, retention in the normal mode of flow FFF depends directly upon the diffusion coefficient D, thus making it possible to obtain D values (and the associated Stokes diameters) from flow FFF retention measurements.

One of the most profound challenges in particle characterization is that of characterizing particle populations that exhibit significant variations in two independent particle properties such as size and density. These complex populations are common in most foodstuffs, soils, and environmental materials, as well as in many industrial products (e.g., cement). A particle size distribution does not fully characterize these materials. They would be far better characterized by a two-dimensional distribution in which size and density (the latter reflecting chemical composition) are the independent coordinates. Since size and density parameters can both be obtained from sedimentation FFF, it appears feasible to construct two-dimensional size-density "maps" of particle populations based on sedimentation FFF data. However, it is our belief that a more productive route involves a coupling of sedimentation FFF with flow FFF. We are currently working out the methodology for combining these two FFF techniques with the goal of providing a far more detailed means than presently exists for examining the detailed microfeatures of complex colloids.

The above strategy involves the separation and elution of fractions from one system and the shunting of these fractions into a second system to further break the subpopulation down according to the different properties governing fractionation in the second system. Since sedimentation and flow FFF have different dependencies on size and density, the experimental results can in principle be converted into the above mentioned two-dimensional distribution.

The capabilities and potential capabilities cited above constitute only limited examples of the scope of FFF in particle characterization. Since FFF is still a relatively youthful technology, its inherent strengths and versatility have not yet been widely adopted and exploited. Once these intrinsic capabilities are more broadly recognized, FFF can be expected to find a place as a major new technology for the increasingly demanding task of better characterizing the ubiquitous particulate materials of industry and of our everyday surroundings.

Acknowledgment

The work was supported by Grant CHE-9102321 from the National Science Foundation.

Nomenclature

d : particle diameter
d_{min} : minimum resolvable particle diameter
F : force exerted on a particle by the field
G : field strength expressed as acceleration
K : Boltzmann constant
m : particle mass
S_{df} : diameter-based selectivity for flow FFF
S_{ds} : diameter-based selectivity for sedimentation FFF
$S\Delta\rho$: diameter-based selectivity
t_r : retention time
t_o : calibration constant
t_{r1} : retention time of particle of unit diameter
t^o : channel void time
T : temperature
$\dot{V}$: channel flowrate
$\dot{V}c$: cross flowrate
w : channel thickness
η : carrier viscosity
ρ : density of liquid carrier
ρ_p : particle density

References

1) Giddings, J.C.: *J. Chromatogr.*, **125,** 3(1976).
2) Giddings, J.C., M.N. Myers and J.F. Moellmer: *J. Chromatogr.*, **149,** 501(1978).
3) Giddings, J. C.: *Anal. Chem.*, **53,** 1170A(1981).
4) Kirkland, J.J. and W.W. Yau: *Science,* **218,** 121(1982).
5) Giddings, J.C., G. Karaiskais, K.D. Caldwell and M.N. Myers: *J. Colloid Interface Sci.*, **92,** 66(1983).
6) Giddings, J.C.: *Sep. Sci. Technol.*, **19,** 831(1984).
7) Giddings, J.C. and K.D. Caldwell: "Field-Flow Fractionation", *Physical Methods of Chemistry,* Vol. 3B, eds. B.W. Rossiter and J.F. Hamilton, Wiley, NewYork, 1989, pp. 867-938.
8) Caldwell, K.D.: *Anal. Chem.*, **60,** 959A(1988).
9) Janca, J.: "Field-Flow Fractionation: Analysis of Macromolecules and Particles", Marcel Dekker, New York, 1988.
10) Oppenheimer, L.E. and G.A. Smith: *Langmuir,* **4,** 144(1988).
11) Giddings, J.C.: *Chem. Eng. News,* **66** (Oct.10), 34(1988).
12) Giddings, J.C.: *Sep. Sci. Technol.*, **20,** 749(1985).
13) Springston, S.R., M.N. Myers and J.C. Giddings: *Anal. Chem.*, **59,** 344(1987).
14) Giddings, J.C.: *Sep. Sci. Technol.*, **23,** 119(1988).
15) Perkins, G.: Second International Symposium on Field-Flow Fractionation, Salt Lake City, Utah, Feb. 4-6, 1991.
16) Giddings, J.C. and M.N. Myers: *Sep. Sci. Technol.*, **13,** 637(1978).
17) Koch, T. and J.C. Giddings: *Anal. Chem.*, **58,** 994(1986).
18) Giddings, J.C., X. Chen, K.-G. Wahlund and M.N. Myers: *Anal. Chem.*, **59,** 1957(1987).
19) Caldwell, K.D.: "Field-Flow Fractionation of Particles", Chapter 7 in *Modern Methods of Particle Size Analysis,* ed. H.G. Barth, John Wiley, New York, 1984.
20) Ratanathanawongs, S.K. and J.C. Giddings: "Separation and Characterization of 0.01-50 μm Particles Using Flow Field-Flow Fractionation." Chapter 15 in *Particle Size Distribution II,* ed. T. Provder, ACS Symp. Series No.472, American Chemical Society, Washington, D.C., in press.
21) Liu, G. and J.C. Giddings: *Anal. Chem.*, **63,** 296(1991).
22) Giddings, J.C.: *Unified Separation Science,* John Wiley, New York, 1991.
23) Ratanathanawongs, S.K. and J.C. Giddings: *Anal. Chem.*, submitted.
24) Giddings, J.C., M.H. Moon, P. S. Williams and M.N. Myer: *Anal. Chem.*, **63,** 1366(1991).
25) Giddings, J.C. and M.H. Moon: *Anal. Chem.*, submitted.
26) Giddings, J.C., G. Karaiskakis and K.D. Caldwell: *Sep. Sci. Technol.*, **16,** 607(1981).
27) Giddings, J.C.: *Sep. Sci.*, **1,** 123(1966).
28) Giddings, J.C., M.N. Myers,K.D.Caldwell and S.R. Fisher: "Analysis of Biological Macromolecules and Particles by Field-Flow Fractionation", pp. 79-136, in *Methods of Biochemical Analysis,* Vol. 26., ed. D. Glick, John Wiley, New York, 1980.
29) Giddings, J.C., M. Martin and M.N. Myers: *J. Chromatogr;* **158,** 419(1978).
30) Giddings, J.C. B. N. Barman and M.-K. Liu: "Separation of Cells by Field-Flow Fractionation and Related Methods", Chapter 9 in *Cell Separation Science and Pechnology,* ed. D. Kompala and P. Todd, ACS Symp. Series No.464, American Chemical Society, Washington, DC.
31) Giddings, J. C. and K. D. Caldwell: *Anal. Chem.*, **56,** 2093(1984).
32) Williams, P. S., L. Kellner, R.Beckett and J. C. Giddings: *Analyst(London),* **113,** 1253(1988).
33) Ratanathanawongs, S.K. and J.C. Giddings : *J. Chromatogr.*, **467,** 341(1989).
34) Ohmacht, R. and Halasz, I: *Chromatographia,* **14,** 155(1981).
35) Giddings, J. C. *Sep. Sci. Technol.*, **13,** 231(1978).
36) Giddings, J. C., M. N. Myers, M. H. Moon and B. N. Barman: "Particle Separation and Size Characterization by Sedimentation Field-Flow Fractionation", Chapter 13 in *Particle Size Distribution II,* ed. T. Provder, ACS Symp. Series No.472, American Chemical Society, Washington, DC, in press.
37) Giddings, J. C., G. Karaiskakis and K.D. Caldwell and M. N. Myers: *J. Colloid Interface Sci.*, **92,** 66(1983).
38) Beckett, R., J. Ho, Y. Jiang and J. C. Giddings: *Langmuir,* in press.
39) Li, J.-T. and K. D. Caldwell: *Langmuir,* in press.
40) Giddings, J. C., B. Barman and H. Li: *J. Colloid Interface Sci.*, **132,** 554(1989).
41) Barman, B. N. and J. C. Giddings: *Langmuir,* submitted.
42) Ho, J. and J. C. Giddings: *J. Colloid Interface Sci.*, submitted.
43) Nagy, D. J.: *Anal. Chem.*, **61,** 1934(1989).
44) Yonker, C. R., H. K. Jones and D. M. Robertson: *Anal. Chem.*, **59,** 2573(1987).
45) Caldwell, K. D., G. Karaiskakis and J. C. Giddings: *J. Chromatogr.*, **215,** 323(1981).

Review

Describing Filtration Dynamics from the Perspective of Fractal Geometry †

Brian H. Kaye
Professor of Physics, Laurentian University *

1. Introduction

Filtration, the removal of fineparticles from streams of fluid passing through a filter, is a complex process which has been studied intensively for many years, (1,2,3). Progress in understanding some of the fundamental elements of filtration dynamics has been partially inhibited because of the complexity and multiplicity of factors contributing to the filtration process. Recently the development of fractal geometry has offered the filtration scientist some new descriptive parameters for describing the structure of filters and the dynamics of filtration (4). Recent research has also suggested possible techniques for deducing important information on the forces operative during the progress of a filtration operation and physical significance of the structure of fineparticles being filtered. It is the purpose of this communication to review the basic concepts of fractal geometry being employed in the study of the filtration process, describe recent applications of fractal geometry in the study of filtration systems and to indicate where fractal geometry may be of interest and utility to the practising technologist. Although many of the concepts presented in this communication can be extended to study filtrationof liquids, this communication will forcus primarily on the filtration of aerosols.

2. Basic Concepts of Fractal Geometry

Fractal geometry was created, and set out in the seminal publication Fractals, Form, Chance and Dimension by B. Mandelbrot (5 and 6).

One of the basic concepts of fractal geometry is that the space filling ability of rugged boundaries and/or lines can be described by means of a fractal addendum to the topological dimension of a system as illustrated in **Figure 1**. All of the lines of **Figure 1,** if made of rubber, could be stretched out to make a straight line and hence they all have the topological dimension 1. The fractional addendum to the topological dimension given in **Figure 1** obviously can be linked intvitively to the rugged appearance of the line. Fractal characterization of systems can be applied in any dimensional space, but in this communication we will focus on the use of fractal geometry to describe systems embedded in two dimensional space. To deduce the fractal dimension of convoluted lines such as that of **Figure 1(d)** one makes a series of estimates of the lengh of the line at various levels of inspection. One then deduces the fractal dimen-

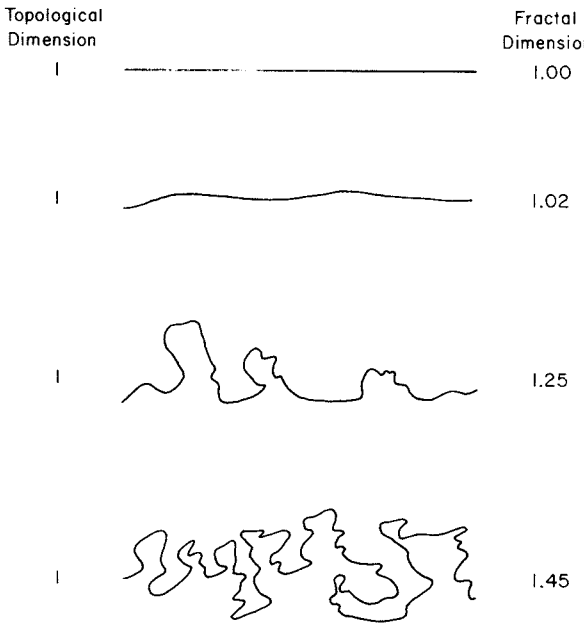

Fig.1 The fractal dimension of a rugged line is a measure of the structure and space filling ability of the curve.

* Sudbury, Ontario, P3E 2C6 .CANADA

† Received January, 1991

sion from the increase in the length estimate as the inspection resolution is decreased. For example consider the series of sketches presented in **Figure 2.** The length of the line is

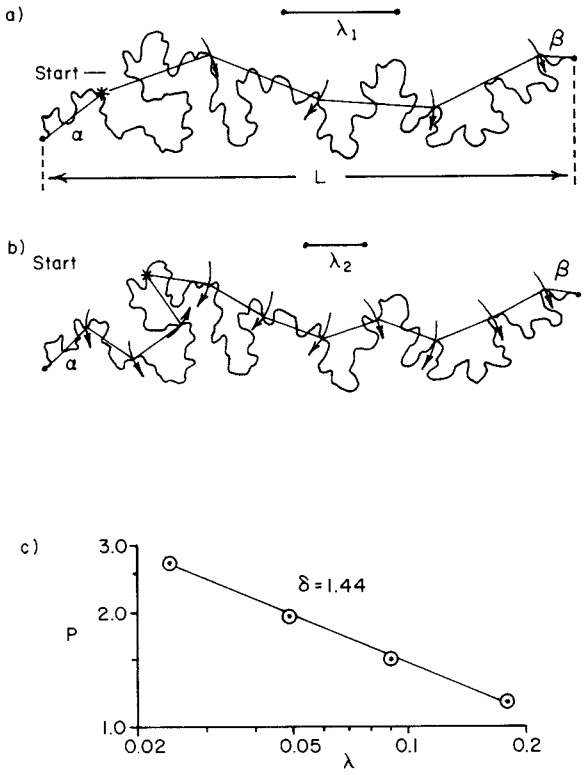

Fig.2 One method of measuring the fractal dimension of a rugged line is to make a series of estimates of the length of the line using a pair of compasses set to various stride lengths.

- α : Short chord from the start of the line to the start of the walk.
- β : Short chord from the end of the walk to the end of the line.
- L : Projected length of the line.
- λ : Normalized Stride length used to estimate the length of the line.
- P : Normalized Length estimate of the line.
- δ : Fractal dimension of the line.

explored with a pair of compasses in the following manner. First of all the separation of the compass points is set at the distance λ. One then places the pivot point of the compasses at an arbitrary point near the begining of the line such as α in the sketch. One then swings the compass until it cuts the line as illustrated in the sketch. A straight line chord is drawn between the starting point and the intersection point. The pivot point of the compasses is now moved to this intersection point and a second intersection with the line by the swinging of the compass is located. A second chord is drawn. In this way the whole line is replaced with a set of chords which become the estimate of the lenght of the line at the resolution inspection parameter λ. It is convenient to normalize the data for the length estimate and the stride magnitude using the distance between the two ends of the rugged line. The perimeter estimate at the stride length λ obviously depends upon the starting point for the estimation of the length of the line. Therefore it is good experimental practice when carrying out an experiment of this kind to make estimates of the length of the line at several starting points. In **Figure 2(c)** the perimeter estimates are plotted against the resolution parameter. It can be seen that the data points can be linked by a straight line relationship. Mandelbrot has shown that the slope of such a data line relationship is the magnitude of the fractal addendum to the topological dimension required to create the fractal dimension of the system. Thus for the line of **Figure 2** the fractal dimension is given by the relationship.

$$\delta = 1 + | m |$$

Later in this communication we will show how there may be some advantages to be gained in constructing filters from crimped fibers. The crimp of the fiber can be described by the fractal dimension evaluated in a way similar to that shown in **Figure 2**.

A mathematical curve which can be used to describe a structure of a fibrous filter is the Sierpinski carpet (6). One of many different Sierpinski carpets which can be constructed is shown in **Figure 3**. This particular carpet can be shown to have what is known as a Sierpinski fractal dimension of 1.89. The first three stages its construction are illustrated in the **Figure 3(a)**. One first divides the available area into 9 equal squares and the middle square is removed. The process is now repeated with each of the remaining squares to

produce the system with 9 holes as shown in the second part of **Figure 3(a).** This construction algorithm is then repeated to create the next stage of the carpet. If one continues this construction algorithm indefinitely, one generates a figure which in theory has no area and an infinite number of infinitely thin threads. The fractal dimension of such a system is deduced by plotting the rate at which a carpet disappears as smaller and smaller holes are resolved in the inspection process. Thus in **Figure 3(b)** the remaining normalized area of the carpet β is plotted against the size of the hole just resolved in normalized units α. The normalizing factor is the total area of the carpet.

At first sight the ideal Sierpinski carpet appears to bear little resemblance to real

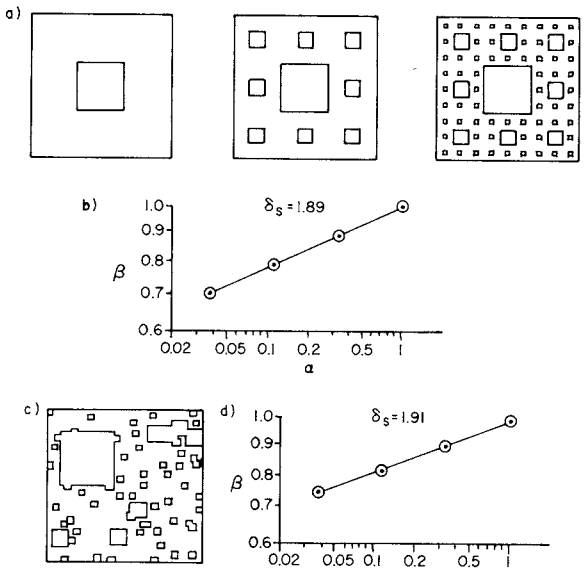

Fig.3 The Sierpinski Carpet can serve as a model for the structure of a filter.

(a) Three stages in the construction of a specific Sierpinski carpet.

(b) The Sierpinski fractal is deduced from rate of disappearance of the carpet as the resolution of inspection is increased.

(c) A statistically self-similar version of the carpet disappears more slowly than the ideal carpet.

α : Normalized Size of hole resolved.

β : Normalized Background area of carpet remaining.

δ_s : Sierpinski fractal dimension of the system.

filters; however, if one randomizes the locations of the holes of part three of **Figure 3(a)** one generates the system shown in **Figure 3(c).** This self similar version of the Sierpinski carpet now bears a resemblance to real filter systems especially if one now alters the shape of the holes in a random manner while keeping the area constant. The appearance of a Sierpinski carpet with randomized holes for an advanced stage of construction is shown in **Figure 3(d).** The randomized version of the Sierpinski carpet is described as a statistically self similar version of the ideal carpet.

The randomization of the location of the holes in the carpet permit holes to fall on holes. Therefore the statistically self similar version of the carpet disappears more slowly than the ideal carpet. This is demonstrated by the experimental data of the second part of **Figure 3(c).** The Sierpinski fractal dimension is deduced by subtracting the slope of the dataline on this Richardson plot from 2. The slope used in such calculations is the slope the graph would have on log-log scales of the same magnitude. Thus, one does not use the visual slope of **Figure 3** to calculate the Sierpinski fractal of the filter system, but the mathematically calculated slope.

In **Figure 4** an electron micrograph of a fibrous filter studied by Clarenburg and Piekkar is shown (9). When the data for this real filter system is plotted on the log-log scales there appear to be two different data lines as shown in **Figure 4(b).** In many studies of filter systems carried out at Laurentian University this dual slope system is a very common phenomenon which is apparently due to two different mechanisims. The first cause of the dual slope for the structure of many filters appears to be the use of two different sized fibers to construct the filter. Many filters are made by adding fine fibers to a coarser support matrix of other fibers. A visual inspection of **Figure 4** would suggest that this particular filter had been made by the use of finer fibers on a coarser matrix of thicker fibers. The other factor which seems to contribute to the creation of two data lines on the Richardson plot used to investigate the magnitude of the Sierpinski fractal, is the persistence of large

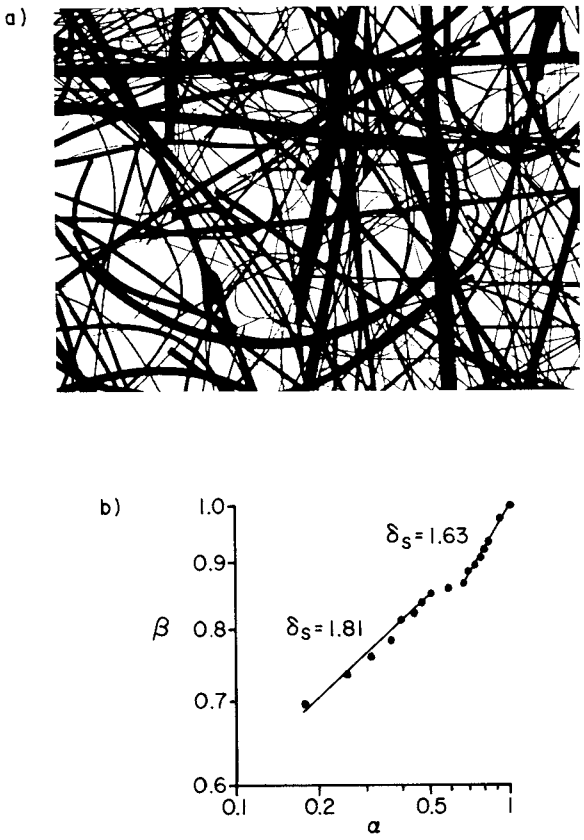

Fig.4 A fibrous glass filter studied by Clarenburg and Piekaar exhabits two distinct regions on a Richardson plot.
(a) Electron micrograph of the filter structure.
(b) Richardson plot of the data for calculation of the Sierpinski fractal dimension of the filter.
α : Normalized Size of hole resolved.
β : Normalized Background area of carpet remaining.
δs : Sierpinski fractal dimension of the system.

holes as the filter felt is created. This aspect of filter structure will be discussed in a later section of this communication (4).

Two of the first scientists to draw the attention of filration workers to the potential usefulness of fractal geometry techology in describing filtration systems were Ensor and Mullins (7). They studied the capture of monosized latex aerosol fineparticles onto the fibers of a filters. In **Figure 5** one of the photographs from their publication on the subject is shown. It can be seen that the unit spheres of the aerosol system form dendritic structures on the fibers which are known as capture trees. The growth of such capture trees can be modelled using digital computers. The first studies of this kind were carried out to study the formation of agglomerates formed when unit spheres were deposited at random on a nucleating center; a process which simulates the growth of soot fineparticles and is known technically as diffusion limited aggregation or DLA. The first simulated DLA studies were carried out by Whitten and Sander (8). The way in which they simulated the growth of a DLA agglomerate is illustrated in **Figure 6.** A pixel of the digitized space, representing a unit sphere, joins in a random manner the growing agglomerate at the center of the digitized space by means of a randomwalk. (If during the randomwalk the pixel leaves the digitized area it is considered to be lost and a new pixel is introduced at random around the periphery of the available digitized space). In **Figure 6(b)** three stages in the growth of such a simulated agglomerate are shown. In **Figure 6(b)** three extensive Whitten and Sander DLA agglomerates are shown. They are statistically self similar systems. In the original Whitten and Sander program it was assumed that if a meandering pizel met the growing agglomerate orthogonally it was captured with a one hundred percent probability. One can modify the construction algorithm to allow for a reduced probability of capture on encounter.

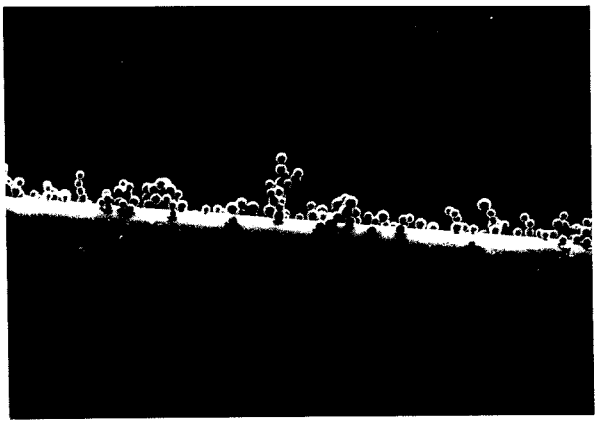

Fig.5 Ensor and Mullins demonstrated that capture trees on fibers have fractal structure.

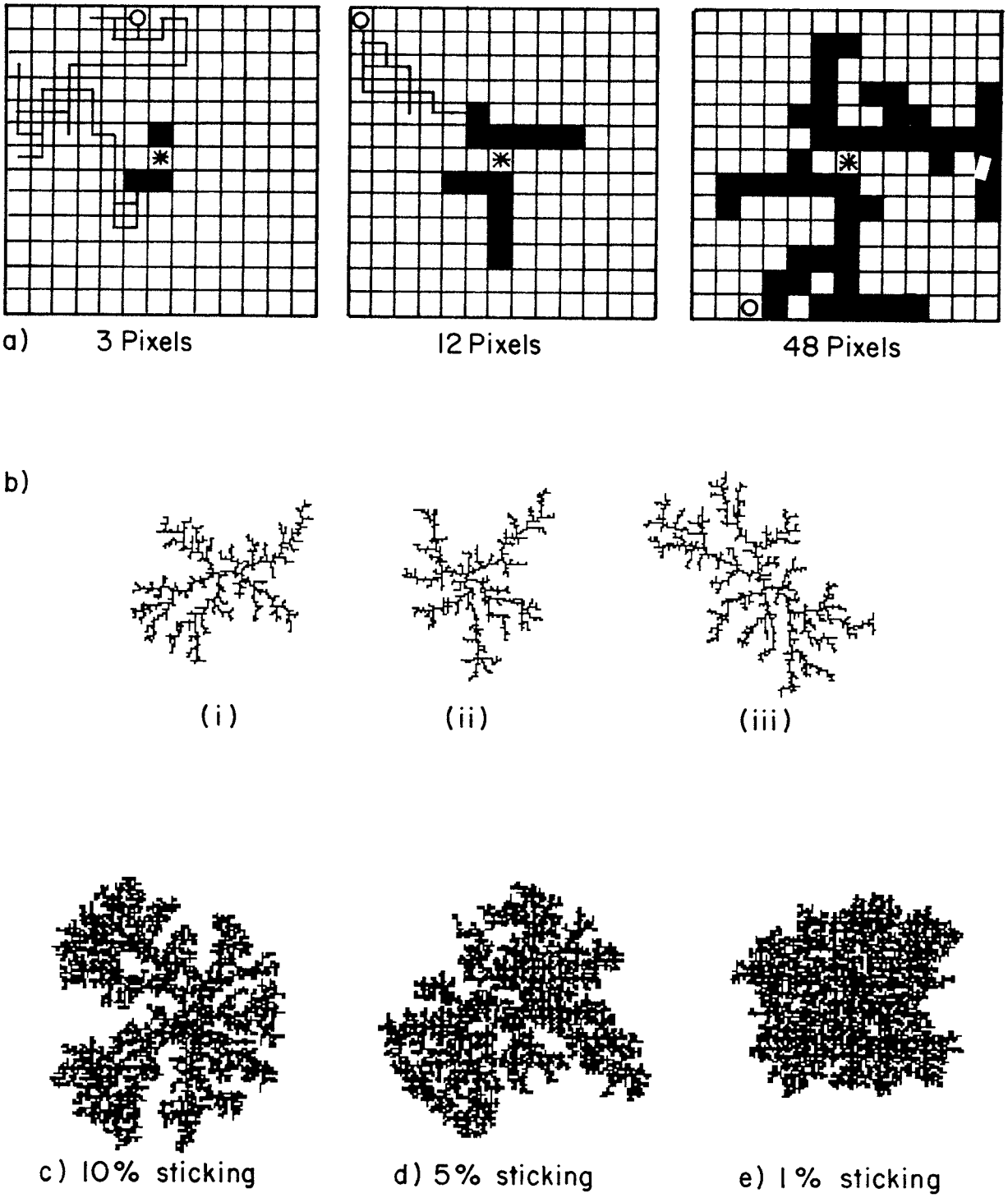

Fig.6 Whitten and Sander simulated the growth of fractal agglomeration using Monte Carlo routines.

(a) Three stages in the growth of an agglomerate showing the arrival of the third, twelfth, and forty eighth pixels.(* denotes the nucleating centre and the small circle the start of the walk.)

(b) Three stasistically self-similar Whitten-Sander agglomerates.

(c) An agglomerate grown with a 10%sticking probability.

(d) An agglomerate grown with a 5%sticking probability.

(e) An agglomerate grown with a 1%sticking probability.

Thus in **Figure 6(c)(d)(e)** three different agglomerates, grown with 10%, 5% and 1% probability of sticking are shown. It can be seen that as the probability of capture decrease the resultant agglomerate becomes denser and more compact. In the early literature on the use of descriptive parameters derived from the concepts of fractal geometry there was insufficient awareness of the fact that there are many different fractal dimensions that can be used to describe the system such as those shown in the various parts of **Figure 6.** In particular there is some confusion between what is now known as the density fractal dimension and the boundary fractal dimension. The density fractal dimension is sometimes called mass fractal dimesion but in this communication we will use the term density fractal. The density fractal dimension is a measure of how densely the substance of the agglomerate occupies the space in which it grows. The density fractal dimension has been studied by several workers, thus Schaefer, Hurd and co workers have characterized the fractal dimension of silica agglomerates (10, 11, 12, 13). A discussion of such techniques is beyond the scope of this review communication and we will restrict our considerations to a simple graphical technique for determining the desity fractal as illustrated in **Figure 7.** In this technique a set of search circles are placed on the center of the agglomerate and the number of intersections made by the agglomerate with the rings is recorded (14). It can be shown that if the intersections per ring are plotted on log-log scale that the slope of the line generated by the data is the fractal addendum to be added to the topological dimension of the system, ie. the density fractal dimension equals 1.66 for the data of **Figure 7(b).** If one accumulates the number of intersections per total perimeter of the search circle as one moves outwards from the center of the agglomerate then the slope of the new data line is actually the fractal dimension itself. Thus for the data of **Figure. 7(b)** accumulated intersection data gives the value of 1.67.

It has been shown that many fumed fineparticles such as diesel soot, carbonblack

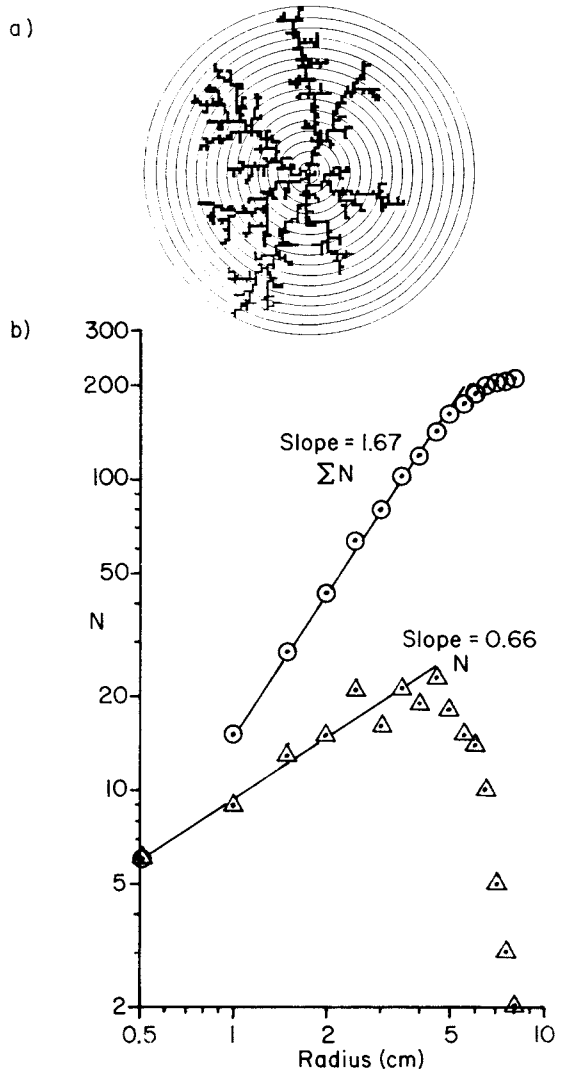

Fig.7 The density fractal of an agglomerate can be deduced from intersection frequencies with a set of standard search circles.
(a) Search circles imposed on an agglomerate.
(b) Cumulative and differential intersection data for the agglomerate.
N: number of intersections of a particular circle with the agglomerate.
$\int$ N: Cumulative intersections for all circles smaller than or equal to the current radius.

pigment and fumed silica used as a flow agent have fractal type structures (6, 15). If one is looking at a system such as diesel soot the density fractal describes the internal porosity and is a measure of the available surface for adsorption of dangerous chemicals. This fractal dimension will also govern reaction rates when the fineparticles are exposed to active

chemicals. The toxic burden and reactivity of a respirable dust fineparticle are important properties of material to be filtered by a respirator; and moreover, the density fractal dimension will be a useful quantity when considering the dynamics of the fluffy type fineparticle, such as deisel soot, since it will be a factor in the Stokes equation used to interpret the dynamics of the body (16). However when considering the dynamics of the soot fineparticle an important factor will be the viscous drag experienced by the fluid moving around the profile. Depiction of the flow pattern and structure of agglomerates in three dimensional space is difficult. For the purposes of this discussion we can illustrate the role played by the fractal structure of the agglomerate in determining its falling speed in a viscous fluid by considering two dimensional systems.

If we consider a fractally structured agglomerate in three dimensional space, its surface area is very high and tends towards infinity (perhaps a better term when discussing the concepts of the surface area of the fractally structured agglomerate is to state that the mass of the agglomerate is fixed but that the surface area is indeterminate). However one must distinguish very carefully between the internal and available surface of the agglomerate and its effective surface area when falling through a fluid. In two dimensional space the perimeter of the agglomerate represents the indeterminate surface area of the system. The effective perimeter is extremely high if one is considering chemical reaction. If, however, one looks at the way in which the system behaves in a viscous fluid, one can impose an envelope boundary on the system which will

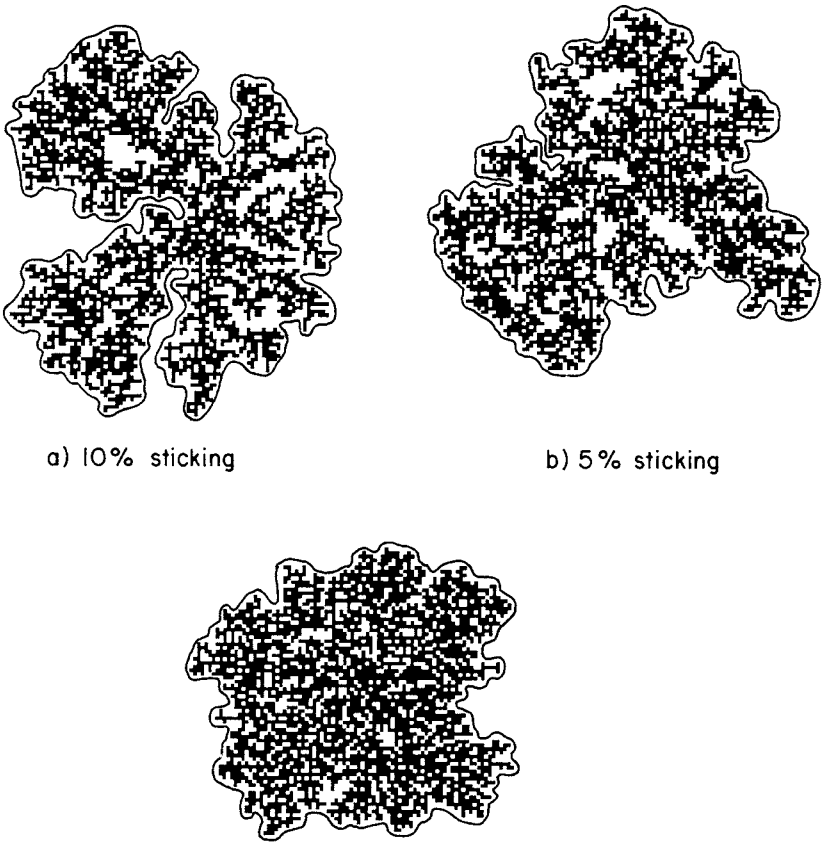

Fig.8 The boundary fractal of the Whitten and Sander type agglomerate of figure 6(c),(d), and(e)are an important parameter governing the falling speed of the agglomerate in a viscous fluid.

probably determine its functional behaviour with respect to settling dynamics and capture probabilities when moving through a filter. Thus in **Figure 8(a)** boundary fractals have been drawn around the agglomerates of **Figure 6(c)(d)(e).** These envelope boundary lines have a fractal structure. In the study of aerosol systems and other fineparticles these types of boundaries are described by means of a boundary fractal dimension. Richter and colleagues have studied three dimensional models of clusters in space but most of the experimental work on the structure of agglomerates in aerosols has been carried out by making measurements on projected images of the agglomerate (17, 6). In **Figure 9(a)** a widely used method for characterizing the boundary fractal of agglomerates, originally developed by Schwarz and Exner, is illustrated (18). The original electron micrograph of this agglomerate was presented in the technical literature by Medalia (19). In this method, called the equipaced method, the profile is first digitized and then estimates of the perimeter are made by constructing a polygon in the following manner. Starting at a point chosen at random one marks out a number of steps and then a chord is drawn from the starting point to the finishing point. Thus the polygons constructed for a step of five paces, ten paces and fifteen paces are shown in **Figure 9(a).** The perimeter of the polygons constructed in this way are unbiased estimates of the perimeter at the resolution represented by the number of steps taken between the beginning and the end of the chords. A whole series of perimeter estimates against resolution parameter in normalized format are summarized in the Richardson plot of **Figure 9(b).** it can be seen that two data lines are present in the Richardson plot. The straight line relationship for the coarser resolution inspection of the agglomerate structure represents the gross morphology of the profile. It is described as the structural boundary fractal of the agglomerate. The higher resolution data represents an exploration of the texture of the profile, and the fractal dimension is called the textural boundary fractal. When reporting a fractal dimension of a boundary one should always quote the range of inspection over which the fractal dimension data relationship is manifest on the Richardson plot.

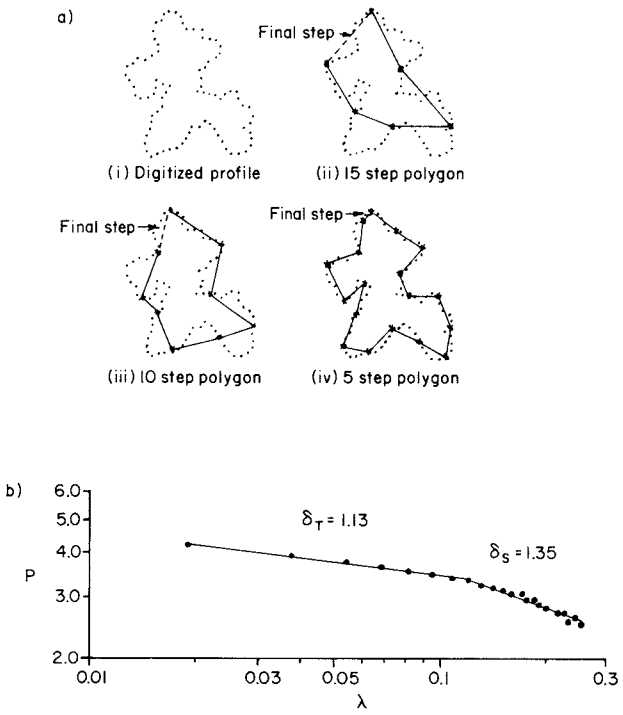

Fig.9 The equipaced method for determining the boundary fractal dimension of an agglomerate generates highly resolved data.

- λ : Normalized Resolution of inspection of the profile.
- P : Normalized Resolution estimate of the profile for resolution λ.
- δ_S : Structural fractal dimension of the profile.
- δ_T : Textural fractal dimension of the profile.

3. Exploring the Possible Usefulness of the Sierpinski Fractal as a Descriptive Parameter of Filter Structure.

The use of the Sierpinski fractal dimension to describe filter structure is a relatively new technique and studies reported to date have been of a theoretical nature. However it shuold be noted that Ensor has expressed the opinion that many of the empirical equations reported in the technical literature for describing the flow of fluids through a filter system will turn out to be functions of the fractal structure of the filter (20). The possi-

ble importance of the Sierpinski fractal as a filter structure descriptive parameter can be appreciated from the simulation studies carried out by Kaye and co-workers (4). Their basic technique for simulating the structure of a fibrous filter is illustrated in **Figure 10.** Most

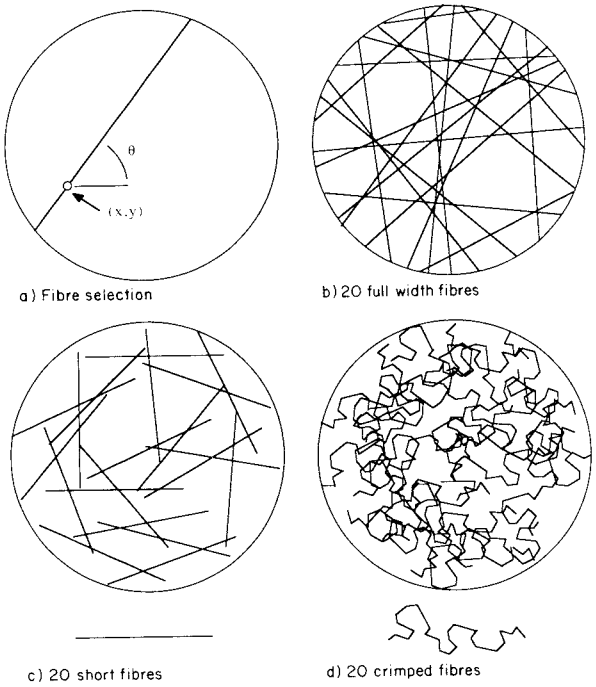

Fig.10 Fibrous filters can be simulated using computer graphics as shown.

of the fibrous filters in common use are created by allowing a felt of fibers to build up on a support system. In a felt-making process the fibers, usually in liquid suspension, arrive at random on a support grid. The fibers are superimposed on each other until the felt achieves a consistency which can exist without the support grid. The definition of what constitutes a randomly arriving fiber is quite complex, but it can be shown that in the definition of the felt-making process there is an implicit assumption: randomness means that the center of any fiber has the equal probability of occupying any x, y coordinate pair within the area of the felt and that the direction of the fibre with regard to a fixed direction defined by the angle θ is such that all linearly distributed values of θ are equally probable. The structure of the felt that one constructs in this way depends upon whether one uses long fibers or short fibers. Thus in **Figure 10(b)** a simulated embryonic felt created by the accumulation of 20 long fibers is shown. If one constructs a simulated filter using short fibers one has to consider whether one lets the fibers cross the perimeter of the simulation area or whether one assumes that the flow system carrying the fibers to the felt making support constrain the fiber movements so that they can only touch the edge of the growing area. This latter assumption was made for the case of the embryonic felt made from 20 short fibers shown in the **Figure 10(c).** This appears to create an edge effect which has to be taken into account in any simulation studies. Also because of the end effects of the short fibers, it is difficult to determine exactly what constitutes an operative aperture in the structure of the filter. This problem is currently under active investigation at Laurentian University. It appears that the size of the operative apertures within a filter can be considerably reduced if one uses crimped fibers in the construction of the filter. Thus in **Figure 10(d)** the straight fibers of part (c) have been replaced with the crimped fiber, shown in the diagram, being placed along each of the straight fibers of the array of part (c). We are currently investigating the effect on the size distribution of the apertures in the fibrous filter when fibers of various crimp (fractal dimension)are used to construct the felt.

In **Figure 11** the main features of an extensive study of simulated filter structure are shown.(4) In this simulation study, short fibers of various lengths were allowed to overlap the boundary of the simulated filter area. The fibers were permitted to have lengths between 25 and 75 pixels. All lengths within this range were equally probable. On the left hand side of the figure the appearance of the felt for various numbers of fibers is shown. On the right hand side the Richardson plots used to calculate the Sierpinski fractals of the felt systems are summarized. A visual inspection of the felt shows that as the fibers accumulate a few large holes, such as the one outlined in the bottom felt, seem to persist. Manufactures of filters knew of this problem 60 years ago and used to pre-treat filters intended for use

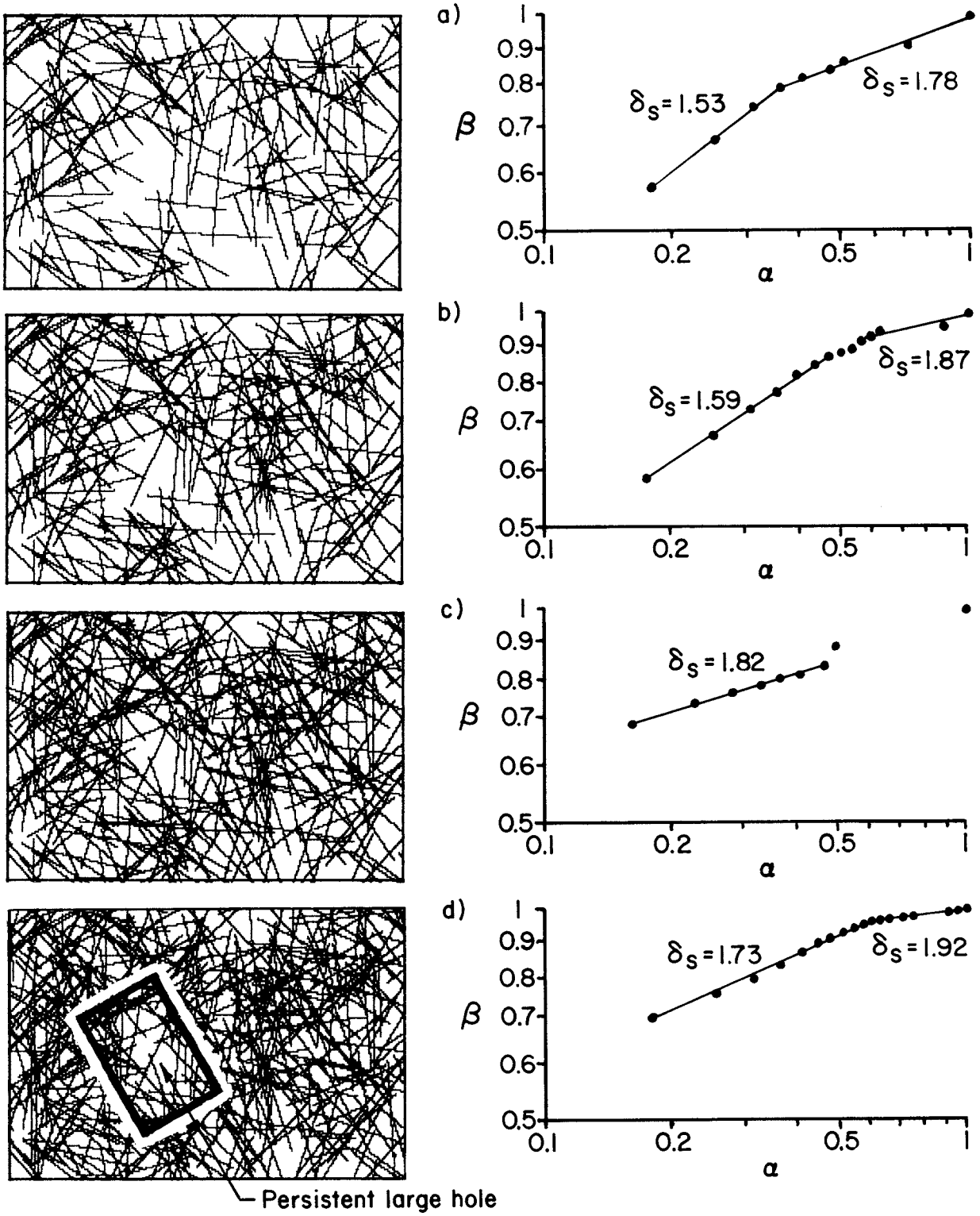

Fig.11 The Sierpinski fractals of felted fibre systems are efficient descriptors of the structure of the felt.

(a) A felt of 200 fibres. (c) A felt of 400 fibres.

(b) A felt of 300 fibres. (d) A felt of 500 fibres.

α : Normalized Size of hole resolved.

β : Normalized Background area of carpet remaining.

δ_s : Sierpinski fractal dimension of the system.

in respirators with a coarse smoke. The main flow of air through a filter with a few large holes is through these large holes, because if one looks at the hole as being the equivalent of a pipe, the radius of the pipe appears to the fourth power in Poiseulles formula describing flow of fluid through the pipe. When a respirator filter was treated with the smoke the flow of air through the filter would guide the larger smoke fine particles to the holes, thus blocking them. Smoked filters in respirators were known to be far more efficient than untreated filters.

A possible explanation of the peristence of a few large holes as the filter builds up is related to the probability of fibers arriving at the surface intercepting a large whole. Thus if one looks at a sub area delineated by the solid line in ll(d)the area of the large hole is a small fraction of the field of view. Thus the chance of a fiber hitting this major hole to alter its structure is quite low. The probability is proportional to the area of the big hole divided by the area of the entire filter. In the wet filter making process the fibers arriving at the surface are guided by the relatively low rate of liquid drainage through the assembled mass. There is thus no basic flow towards the large holes in the felt assembly process. It would seem that a good way to create an efficient filter would be to make a felt by a paper making process and then switch to a dry process in which additional fibers were directed onto the support matrix by air flow. The air flow would be much more likely to concentrate into a few large holes, sealing them with the incoming fibers.

The making of filters is an area where commercial secrecy is practiced so it is not known if this type of modified process has been tried by manufactures of filters. Current work is proceeding into how quickly the hole distribution of the felt changes when one deliberately increases the probability of deposition according to the hole size present in the simulated filter. It should be noticed that from an information point of view no information embedded in the Sierpinski fractal system is available in the size distribution of holes. However the Sierpinski fractal is a convenient summary of a great deal of data which has a reasonable expectation of being related to operational parameters of the filter. Thus the data of **Figure 11** suggests that far more effort should be placed on removing the upper region of the Sierpinski fractal graph, i.e,. eliminating large holes rather than concentrating on testing or characterizing filters. Furthermore it is likely that a combination of Sierpinski fractal plus average hole size will have a direct relationship to the operational performance of the filter. The first publications on the fractal structure of filters only appeared in 1989 and the field is obviously developing rapidly.

Another major type of filter used in filtration technology is the depth filter. As yet no studies of the Sierpinski fractal of a depth filter have appeared; however, the potential for such studies is illustrated by the data summarized in **Figure 12.** The data of **Figure 12** show that the holes in a slice of bread can be described by means of Sierpinski fractal. The Sierpinski fractal for the large holes describes

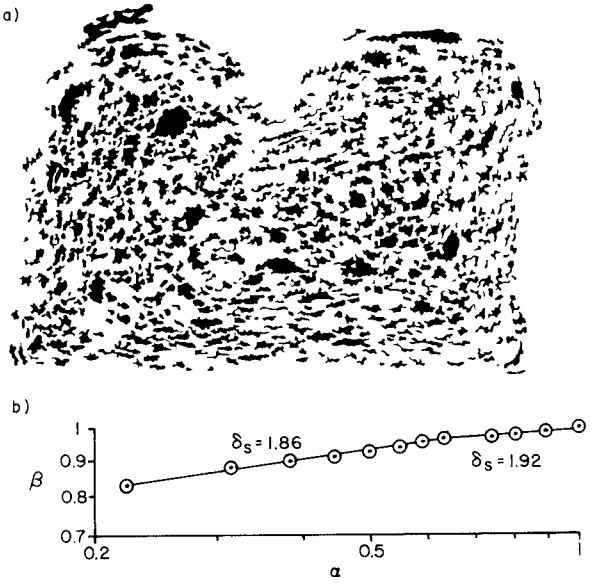

Fig.12 The structure of porous bodies such as a slice of bread can be described by means of the Sierpinski fractal dimension.
(a) A stylized appearance of a typical slice of whole wheat bread.
(b) Richardson plot for the Sierpinski tractal calculation.
α : Normalized Size of the resolved.
β : Normalized Background area of carpet remaining.
δ_S : Sierpinski fractal dimension of the system.

the visual structure of the bread and the Sierpinski fractal of the high resolution data can be related to the "bite response" experienced when the bread is eaten. These are both important parameters which have to be controlled in the mass production of bread(21). The use of the slice of bread as a model for a depth filter is not as remote as it may seem to be since it is recorded that sailors on long voyages were aware of the fact that they could create efficient carbon filters by over toasting a piece of bread. For a depth filter it is likely that the Sierpinski fractal at coarse resolution governs the flow characteristics of a liquid through the depth filter.

4. Fractal Structure and Capture Dynamics of Fineparticles in a Filter.

The filtration capture of respirable dust is an important area of occupational health and hygiene studies. Specialists who have studied the dangers of respirable dust have used the aerodynamic diameter of a fineparticle as a useful descriptive parameter for characterizing dust which pose a respirable hazard to workers in dusty environments. The aerodynamic diameter is the size of the sphere of unit density material which would have the same falling speed in air as the dust fineparticle (3). The aerodynamic diameter is useful when considering the movement of the fineparticles moving in o and out of the lung or into a filter; but, once inside the filter or the lung the physical size of the fineparticle becomes an important parameter when considering both the capture dynamics and the actual hazard posed by the dust to the lung. In **Figure 13** some sets of isoaerodynamic fineparticles prepared by Kotrappa, using the spiral centrifuge developed by Stober and co-workers, are shown (22). The structural fractal dimension of these profiles as measured by Kaye is given under the profiles (6). It can be seen that within any isoaerodynamic group there is a wide range of shape and structure variation. In general it can be seen that the larger the structural fractal dimension, the larger the profile with respect to the smallest member within the group. For example the uranium dioxide profile with a fractal dimension of 1.15 is at least three times bigger than the simple compact profile having a fractal dimension of 1.04. If the occupational hygienist converts the aerodynamic diameter to the Stokes diameter using the known density of uranium dioxide it can be seen that the estimated amount of uranium dioxide represented by the total capture of all of the profiles shown in the diagram would probably be too small by at least one order of magnitude. Thus a failure to take into account the rugged structure of the profile probably grossly underestimates the amount of material deposited in the lung when a given number of fineparticles are deposited, if the only measurement made on the dust is the aerodynamic diameter. If one is interested in the rate at which the inhaled dust reacts with the fluids of the lung one would again grossly underestimate the chemical reactivity if one assumed that all of the uranium dioxide fineparticles were simple dust grains such as the one with a profile fractal dimension of 1.04 as compared to the grain with the fractal dimension of 1.15.

When one starts to consider the danger from adsorbed toxic chemicals on the surface of the dust, again a simple knowledge of the aerodynamic diameter of the fineparticle would lead to gross underestimation of the burden of the material deposited in the lung when the dust is absorbed. The dusts of **Figure 13** are all relatively dense and compact fineparticles compared to the ones that can occur if one is looking at material which is produced by a fuming process. (The uranium dioxide and thorium dioxide of **Figure 7, 8** were produced by precipitation with the uranium dioxide being subjected to subsequent ball milling). The underestimation of material in the lung from aerodynamic size data for fumed particles can be appreciated by considering the large diesel soot agglomerate shown in **Figure 14** (23). In **Figure 14** this profile is shown as a uniformly dense structure since this is the form of the profile used in the fractal characterization process. However the original agglomerate as viewed under the electron microscope has an open structure and is

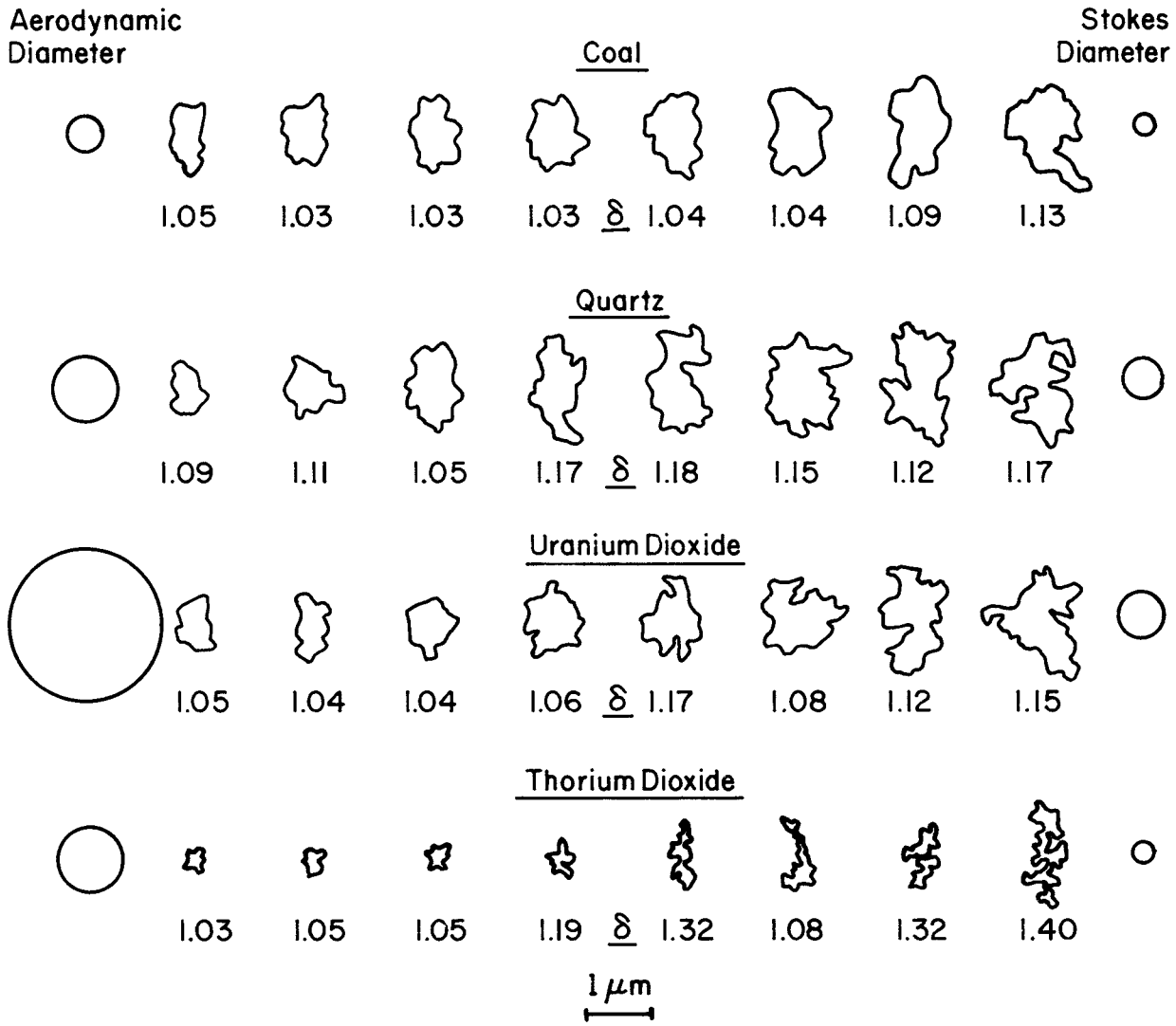

Fig.13 Fractal description of the structure of hazardous aerosol fineparticles could be an important consideration when studying the dynamics of the fineparticles inside a filter.

composed of spheres two orders of magnitude smaller than the agglomerate, which has a physical size of approximately 8 microns (24). A physical size of 8 microns would fail to meet the occupational health and safety definition of a respirable hazard dust; however, if such a dust had its falling speed measured by means of many of the aerodynamic instruments, such as the various cascade impactors, its size would be reported as being much smaller than one micron because of its open fluffy type structure (3). Its internal surface area is enormous, and if such a particle were to enter the lung or the digestive tract it would carry larger quantities of adsorbed toxic chemicals generated by the burning of the diesel fumes than would be calculated from its aerodynamic size. Because of a focus on the aerodynamic properties of such dust, scientists were somewhat surprised to find they could filter them relatively easily, and there is some evidence that in fact the major hazard from diesel exhaust soot is not lung damage, but cancer of the digestive system and/or bladder, since the very light fluffy fineparticles are captured and moved into the digestive tract, not the depth of the lung (25). A measurement of the fractal dimension of such an agglomerate may be a means of characterizing both the filterability and hazard from adsorbed chemicals of such dusts.

The Richardson plot for an exploration of

the structure of this diesel soot agglomerate is shown in **Figure 14 (b).** It can be seen that the fractal dimension of the soot profile is 1.43. Erosion-dilation studies of the structure of this agglomerate indicate that it has probably been formed by the collision of at least 11 agglomerates (15). This example shows that when considering the problems of filtering the dust and fumes created by a fuming and/or combustion process, one should not rely on the aerodynamic data alone to predict the filterability of the product. It may well be that smoke such as diesel exhaust fumes can be filtered with a much coarser filter than anticipated from the measured aerodynamic diameters of the smoke fineparticles. Prior to the initiation of a filtration process for a given smoke or fume, the structure of the fineparticles should be examined by means of an electron microscope, and a basic knowledge of its physical length, aspect ratio (length to breadth of the profile as viewed under a microscope) fractal dimension and aerodynamic diameter should be studied before choosing a filter for the dust or fume.

An important problem in the design of filters for a given process is choosing th right type of fiber in the filter for the specific dust to be contained. The force of attraction, which varies for various dust-fiber combinations between the fiber and the passing dust fineparticle, can probably be deduced from the fractal structure of the capture tree growing on the fiber. Studies of such a possibiluty are however at an early stage because of the lack of analytical procedures for characterizing the capture trees which grow in three dimensions. Kanaoka and colleagues have published pictures of deposits on single fibers which have obvious fractal structure (26). Studies are underway both by Professor Kanaoka and at Laurentian University to characterize the fractal structure of such deposits. The type of information that can be collected in two dimensional space by projecting the rugged structure of the deposited fineparticles into a two dimensional plane can be appreciated by the work reported by Trottier and colleagues (27).

In **Figure 15** the profile of a deposit on a glass fiber filter traced from an electron micrograph reported by Trottier et al. is shown. It can be seen that the ruggedness of this boundary has a fractal dimension 1.37. It is interesting to note that this is virtually the same as the ruggedness reported by Ensor and Mullins for the projected boundary of the deposits shown in **Figure 5.** They reported a coarse resolution boundary fractal dimension of 1.38. This value is typical of the value reported for the projected profiles of fumed fineparticles formed by the interraction of

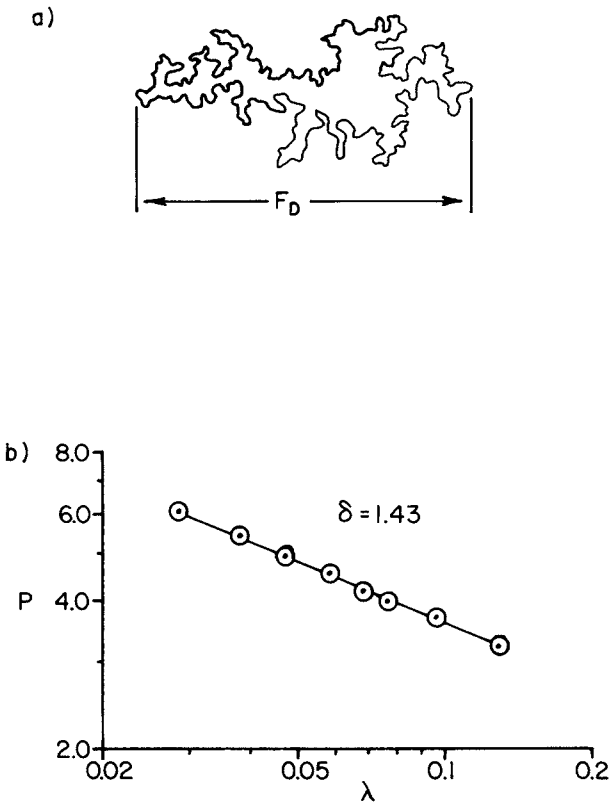

Fig.14 To be able to predict the filterability of fine3 particles such as diesel fuel soot one needs to know the aspect ratio, the physical length and the fractal dimension of the profile as well as the aerodynamic diameter.
(a) Profile of diesel soot fineparticle
(b) Richardson plot of data collected for the inspection of the diesel soot profile.
λ : Normalized Resolution of inspection of the profile.
P : Normalized Perimeter estimate of the profile for resolution λ.
δ : Fractal dimension of the profile.

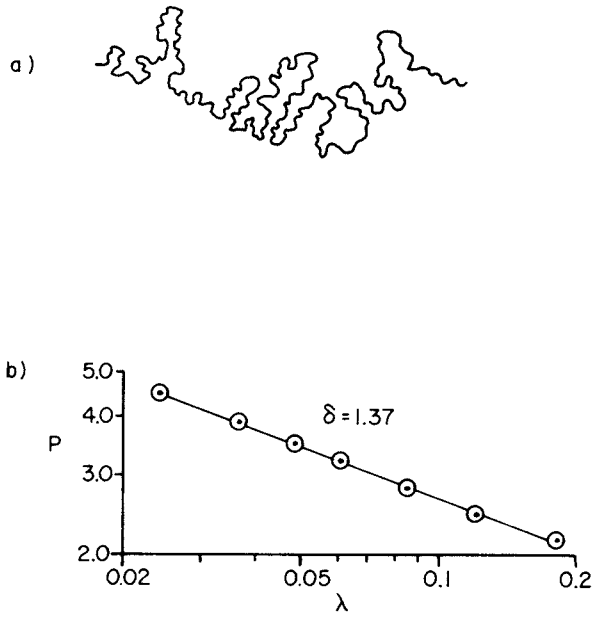

Fig.15 The fractal dimension of the projected boundary of the deposited fineparticle captured by a fibre contains information on capture dynamics.

μ : Normalized Resolution of inspection of the profile.

P : Normalized Perimeter estimate of the profile for resolution λ.

δ : Fractal dimension of the profile.

agglomerates in a turbulent formation zone. (Note agglomerate profiles as high as 1.65 have been reported: but 1.38 to 1.43 is a more widely reported empirical structure fractal dimension for a projected boundary). This ruggedness is also similar to the 1.43 reported for the diesel exhaust of **Figure 14.**

Specialists in filtration technology differentiate between three major capture mechanisms for aerosols passing through a fibrous filter (3). These are termed interception, impaction and diffusion. Interception is the mechanism by which the large fineparticles are captured by a fiber when the fiber is small compared to the size of the fineparticles. Impaction occurs when the fineparticles have sufficient energy to be unable to move away from the fiber with the flow of the medium carrying the fineparticles. Diffusion loading of fibers occurs when Brownian motion of the fineparticles is significant with respect to the velocity of the flow through the filter. In

Figure 16 some simulated capture trees created by Trottier et. al. in a simulation study of diffusion loading fibers are shown. The type of deposit created by diffusion loading is shown and the projected boundaries of such loadings have a fractal dimension of 1.36. For the aerosol of 0.05 micron aerodynamic sodium chloride used to generate the data of **Figure 15,** diffusion loading would be the major capture mechanism. It is very interesting that the two boundary fractal dimensions, from experiment and theoretical simulation, agree to within 1%. In **Figure 17** the type of boundary generated by the deposition of 0.4 micron sodium chloride aerosol on a glass

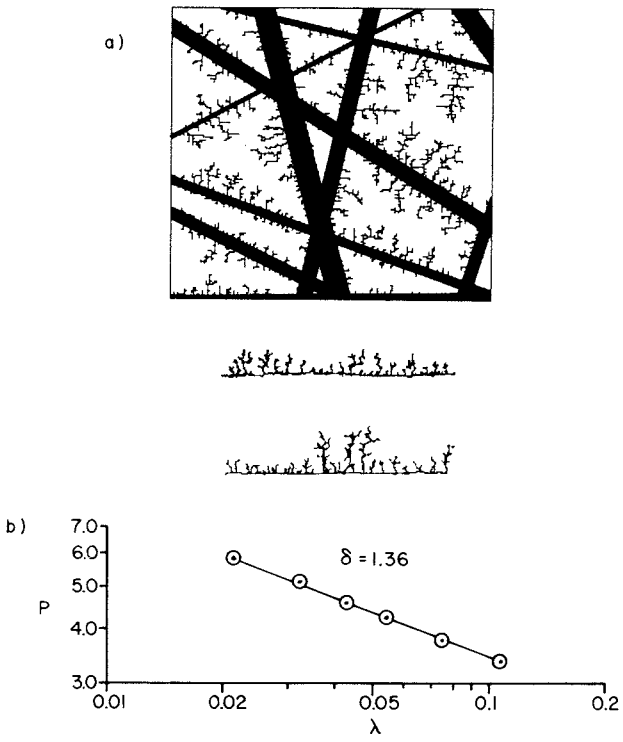

Fig.16 Computer simulation of the diffusion loading of the fibers of a filter manifest deposit boundaries of fractal dimension 1.36.

(a) Simulated loaded filter for diffusion capture, and typical filter deposit projected boundaries.

(b) Richardson plot for one boundary in(a).

λ : Normalized Resolution of inspection of the profile.

P : Normalized Perimeter estimate of the profile for resolution λ.

δ : Fractal dimension of the profile.

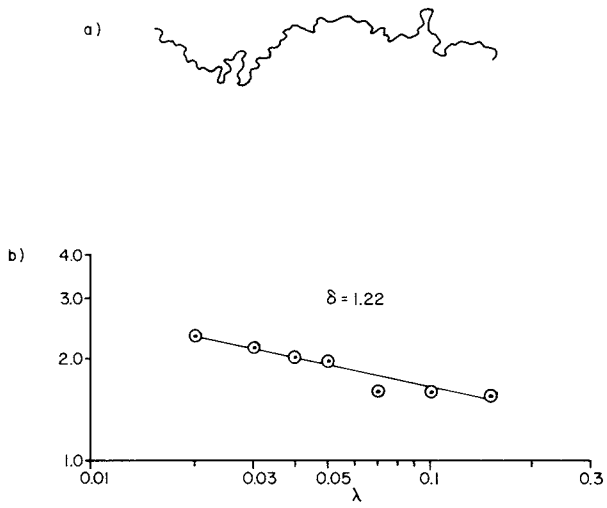

Fig.17 The fractal dimension of the project boundary of a glass fiber loaded with 0.4 μm aerosol of sodium chloride is 1.22.

λ : Normalized Resolution of inspection of the profile.

P : Normalized Perimeter estimate of the profile for resolution λ.

δ : Fractal dimension of the profile.

fiber is shown. Trottier reports that for this type of profile the fractal dimension is 1.22. The 0.4 micron aerodynamic is just about the magnitude between the turnover from diffusion loading to impaction loading of the fibers. It is also interesting to note that 1.20 is typical of the values reported for the boundary fractal of agglomerated fineparticles when the agglomeration process has been quenched in the early stages of agglomeration. In **Figure 18** the fractal dimension of a simple agglomerate and a complex agglomerate are shown (these are synthetic agglomerates in two dimensional space (8)). In **Figure 19** the appearance of a filter which is being loaded with aerosol fineparticles when only impaction is contributing to the loading of the filter is shown. It can be seen that the fractal dimension of such agglomerates is of the same order as that for the simple agglomerates of **Figure 18,** and not too different from the boundary reported with a real aerosol in **Figure 17.**

In occupational health and safety there is a growing concern that any respirator to be used in a given work environment must be tested with the actual dust to which the worker is exposed. Testing repirators with test dust such as lead welding fumes for nickel sulfate dust is an extremely difficult and complex subject and it may well be that preliminary studies with single fiber loading may give good guidance as to what type of filter will be effective in the work area. Studies such as those carried out by Kanaoka using single fibers will be very informative. An alternative strategy will be to use the type of whisker particle collector studied by Schafer and Pfeifer (28). Thus , in **Figure 20** an array of alumina dust fineparticles captured on what the authors describe as a whisker collector is shown. In part (b) a highly magnified photograph of one of the profiles is shown. It can be shown that such dust fineparticles have fractal dimensions and we can expect many studies of this type of capture and characterization of fineparticle profile (11).

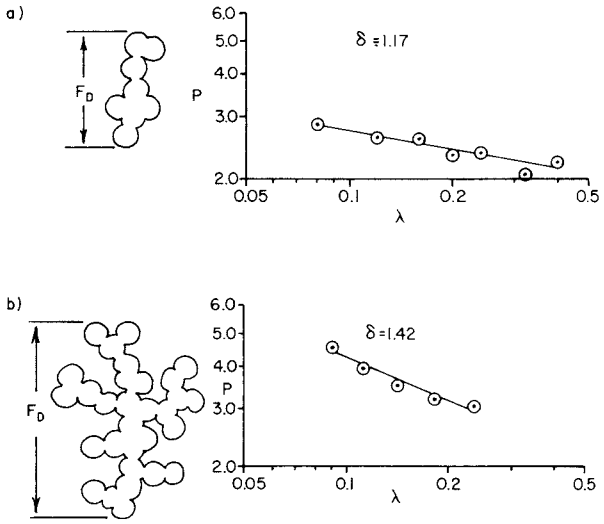

Fig.18 Relatively simple structured agglomerates have lower fractal dimensions than those which appear to have formed by the collision of primary agglomerates.

λ : Normalized Resolution of inspection of the profile.

P : Normalized Perimeter estimate of the profile for resolution λ.

F_D : Projected length of the profile(Feret Diameter).

δ : Fractal dimension of the profile.

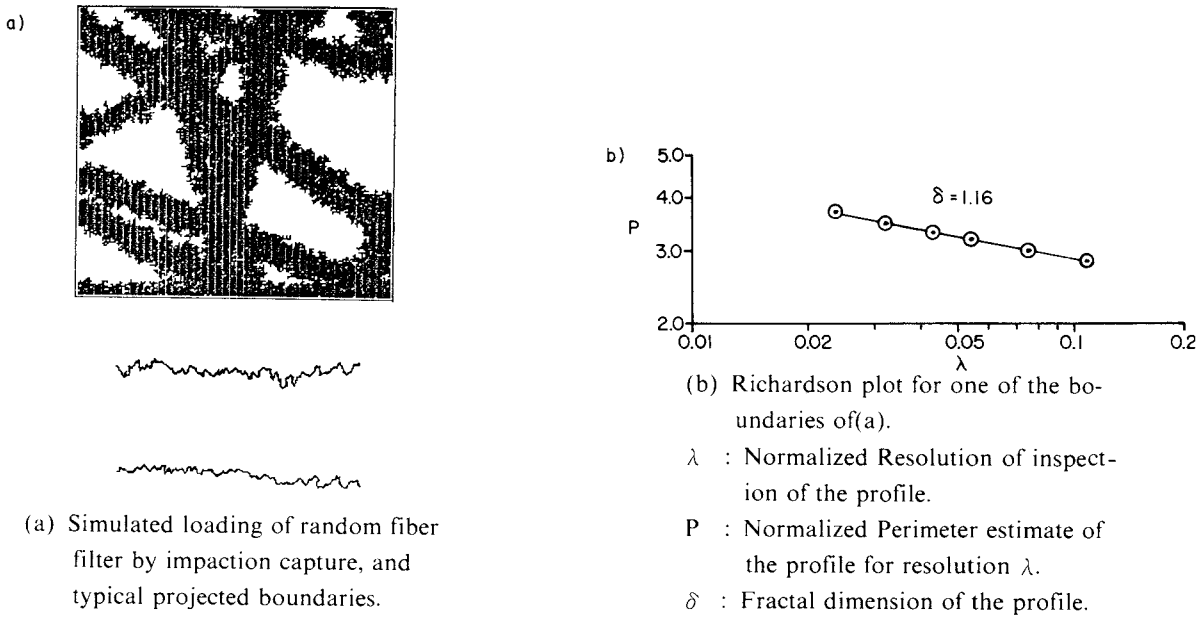

(a) Simulated loading of random fiber filter by impaction capture, and typical projected boundaries.

(b) Richardson plot for one of the boundaries of(a).

λ : Normalized Resolution of inspection of the profile.

P : Normalized Perimeter estimate of the profile for resolution λ.

δ : Fractal dimension of the profile.

Fig.19 A simulation of impaction loading of fibres by Trottier et al generating a projected boundary of fractal dimension of 1.16.

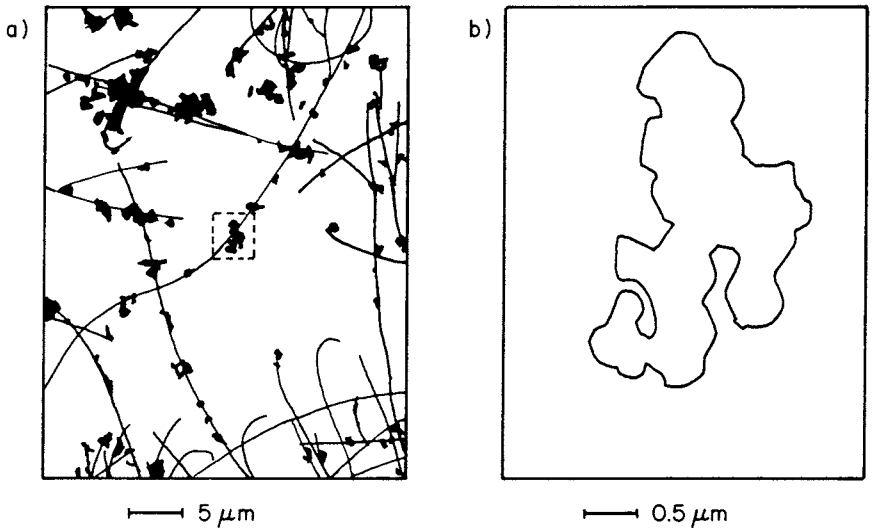

Fig.20 The whisker particle collector used by Schaefer and Pfeifer can be used to study fineparticle capture by fiber in a direct manner.

(a) General view of fibers of the whisker particle collector.

(b) Enlarged view of a single profile.

Conclusion

Fractal geometry appears to offer many new descriptive parameters to be used by the filtration specialist. There is, however, a great need to develop analytical procedures for studying the fractal structure of filters and the capture trees which manifest themselves as the filtration process proceeds.

Acknowledgements

Some of the work reported in this communication was supported by the Ontario Ministry of Labour. The author wishes to thank G. G. Clark for preparing the diagrams and R. A. Trottier for providing the material for **Figure 15, 16, 17** and **19.**

References

1) Fayed, M.E., and L. Otten: Handbook of Powder Science and Technology, Van Nostrand, Reinhold, New York, (1984).
2) Davies, C.N.: Air Filtration, Academic Press, (1973).
3) Shaw, D.T.: Fundamentals of Aerosol Science, John Wiley & Sons, (1978).
4) Kaye, B.H.: "Describing Filter and Filtration Processes Using the Concepts of Fractal Geometry", Proceedings of the 2nd Symposium on Particles Detection, Adhesion and Removal held as part of the Fine Particle Societies Annual Meeting, Boston, August 22-26, (1990). Proceedings Ed., K. Mittal, (In press).
5) Dr. Mandelbrot's first book *Fractals, Form, Chance and Dimension* was published in 1978 by W.H. Freeman of Los Angles. In 1983 Dr. Mandelbrot considerably revises and extended the original book which was published under the title *The Fractal Geometry of Nature*, Freeman, San Francisco, (1983). Dr. Mandelbrot has indicated that he prefers people to quote this book as the foundation book for fractal geometry and not the earlier edition. (Personal Communication from Dr. Mandelbrot).
6) An introductory text on the basic concepts of fractal geometry as applied to filtration is to be found in the book B.H. Kaye, *A Randomwark Through Fractal Dimensions*, VCH Publishers, Suite 909, 22 East 23rd Street, New York, N.Y., 10010-4606 U.S.A.
7) Ensor, D.S. and M.E. Mullins: "The Fractal Nature of Dendrites formed by the Collection of Particle on Fibers", Part. Character 2 (1985) 77-78.
8) Whitten, T.A. and L.M. Sander: "Diffusion Limited Aggregation: a Kinetic Critical Phenomenon" Phys. Rev. Lett., **24** (1981), 1400 -1403
9) Piekaar, H.W. and L.A. Clarenburg: "Aerosol Filters - Pore Size Distributions in Fibous Filters," Chem. Eng. Sci., **22** (1967), 1399-1408.
10) Schaeffer, D.W.: "Fractal Models and the Structure of Materials", in the Materials Research Society Bulletin, Volume 13, Number 2, (February 1988), 22-27.
11) Schaeffer, D.W.: "Polymers, Fractal and Ceramic Materials", Science, Volume 243, (24th of February 1989), 1023-1027.
12) Hurd, A.J.: The Electrostatic Interraction Between Interfacial Colloidal Particles", J. Phys. A., **18**, L1055-L1060.
13) Hurd, A.J.: Two Dimensional Diffusion Limited Aggregation of Interracting Particles in Extended Abstracts of Fractal Aspects of Materials, 1985, Fall Meeting of the Materials Research Society, December 2-4 (1985), Boston. Book of Abstracts available from the Materials Research Society, Suite 327, 9800 McKnight Road, Pittsburgh, PA.
14) Kaye, B.H.: Section 2.1 pages 55-65 in The Fractal Approach to Heter geneous Chemistry, Ed. D. Avnir, John Wiley and Sons, 1989.
15) Kaye, B.H.: "Characterizing the Structure of Fumed Pigments Using the Concepts of Fractal Geometry," Part. Syst. Charact... B(1991)63-71
16) Kaye, B.H.: "Exploring the Physical Significance of the Fractal Structure of Hazardous Dust Produced by Fuming and/or Precipitation Processes" (in press).
17) Richter, R., L.M. Sander and Z. Cheng: "Computer Simulations of Soot Aggregation". Journal of Colloid and Interface Science, Volume 100, Number 1, July(1984), 203-209.
18) Schwarz, H. and H.E. Exner: "The Implementation of the Concept of Fractal Dimensions on a Semi-Automatic Image Analyzer," Powder Technology, **27**(1980), 207-213.
19) Mewdalia, A.I.: "Dynamic Shape Factors of Particles." Powder Technology, **4**(1970-71), 117-138.
20) Ensor, D., Research Triangle Institute, North Carolina, personal communication.
21) The data for the fractal structure is taken from the forthcoming book "Discovering the Surprising Patterns of Chaos and Complexity" by B.H.Kaye.
22) Kotrappa, P.: "Shape Factors for Aerosols of Coal Uranium Dioxide in the Respirable Size Range", in T. Mercer, E. Morrow and W. Stober(Ed.) "Assessment of Airborne Particles", Charles C. Thomas, Springield, Illinois,(1973), ch. 16.
23) This diesel oil soot profile was photographed by R.G. Pinnick, Department of Army, White Sands Missile Range, New Mexico, 88002-5501.
24) An electron micrograph of the original dust profile is to be found on page 109 of reference 6.

25) See newstory "Cancer Genes for Pastry Cooks ?", New Scientist, 19th July,(1986). p. 28.
26) Kanaoka, C., H. Emi, S. Hiragi and T. Myojo: In "Aerosols: Formation and Reactivity." Second International Aerosol Conference, Berlin, Pergamon, Great Britain,(1986).
27) Trottier, R., G. Clark and A. Hoffman: "Fractal Characterization of Experimental and Simulated Dendritic Capture Tree Growths in Filter Systems", Paper presented at the 8th annual meeting of the American Association for Aerosol Research, Reno, Nevada, October(1989).
28) Schaefer, H.J., and J. Pfeifer: "Sizing of Submicron Aerosol Particles by the Whisker Particle Collector Method." Part., Part. Syst. Charact. 5(1988)174-178.

Symposium on Powder Technology

The 2nd Hosokawa Symposium on Powder Thchnology and the 25th Symposium on Powder Thchnology were held under the auspices of the Party of Powder Thchnology (Japan) at the Osaka Chamber of Commerce and Industry on August 27 and 28, 1991.

The 2nd Hosokawa Symposium on Powder Thchnology, attended by approximately 80 participants, focused mainly on discussions about powder technology under the theme Synthesizing Composite Fine Particles: Method and Application. Eight papers, each highlighting a specific aspect of the technology, and a key lecture were given. All participants engaged in lively discussions.

The 25th Symposium on Powder Technology was attended by more than 380 participants. Its main theme was "Processes for Attaining High Performance in Fine Grinding." Five lectures were given, followed by active discussions. The Chamber's conference room could barely contain the enthusiasm of the participants.

The 2nd Hosokawa Symposium on Powder Thchnology
Synthesizing Composite Fine Particles: Method and Application

Lectures and Discussions

Chairmanship: Yasuo Kousaka (University of Osaka Prefecture)

•Characterization of Composite Fine Particles	Mamoru Senna (Keio University)
•Mechanofusion Technology and Its Boundaries under vacuum atmosphere.	Kiyoshi Nogi (Osaka University)
•Evaluation of Composite Particles by Mechanofusion Treatment	Toshiki Tanaka (Hosokawa Micron Corp.)

Chairmanship: Tohei Yokoyama (Hosokawa Micron Corp.)

Key Lecture •Synthesizing and Solidifying Composite Powder through Mechanical Alloying	Ryuzo Watanabe (Tohoku University)

Chairmanship: Toshio Oshima (Himeji Institute of Technology)

•How to Evaluate Fine Particle Dispersion in the Compositing Process	Keijiro Terashita (University of Osaka Prefecture)
•Solid Lubricant using the Mechanofusion Process	Akihiro Murata (Matsumura Oil Research Corp.)
•Compositing Processes of Cu/Al_3O_3 and Al_3O_3/Cu using Mechanofusion Procees under Vacuum Atmosphere.	Hisashi Kaga (Hokkaido Industrial Technology Center)

Chairmanship: Yoshinobu Morikawa (Osaka Sangyo University)

•Flame Spraying Materials using Mechanofusion Process	Hiroshi Ito (Kurume College of Technology)
•Synthesizing TiB_2 film through Plasma Spraying of Ti and B Composite Powder	Shuichiro Katoh (Nippon Aluminum Co.,Ltd.)
•General Discussion	Chairmanship: Masafumi Arakawa (former professor, Kyoto Institute of Technology)

The 25th Symposium on Powder Technology

Session 1 Grinding Efficiency from the Viewpoint of Energy Consumption

Chairmanship: Kei Miyanami (University of Osaka Prefecture)

- Consideration of Enengy Consumption in Grinding — Genji Jimbo (Nagoya University)
- Grinding Performance of High Compression Roller Mill-ECOPLEX — Katsuji Toyotate (Hosokawa Micron Corp.)

Session 2 Characteristics and Efficiency in Grinding

Chairmanship: Tatsuo Tanaka (Professor emeritus, Hokkaido University)

- A Study of the Limmitations of Grinding — Yoshitaka Kuwabara (Goverment Industrial Research Institute, Nagoya)
- Some Phenomena Related to the Process of Wet Grinding — Toyokazu Yokoyama (Nagoya University)
- Ultra-fine Grinding in Nano-Powder Process — Kouichi Kugimiya (Matsushita Electric Industrial Co., Ltd.)

Academic publication concerning powder technology in Japan (1990)

Journal of the Society of Powder Technology, Japan Vol. 27(1990)

Title	Author(s)	Page
〈**Original Report**〉		
● The Effect of Particle Size on the Flowability of Cohesive Powders	H.Tsunakawa	4-10
● Discharge of Aerated Granular Materials from a Standpipe with an Orifice	T.Takeshita, K.Atsumi, and G.Jimbo	18-22
● Spontaneous Ignition of a Dust Deposit —The Effects of Time-Periodically Varying Ambient Temperature—	H.Liang and T.Tanaka	23-29
● Particle Growth in a Continuous Tumbling Fluidized Bed Coater	E.Abe and H.Hirosue	72-78
● Application of Fuzzy Control Method for Level Control of Hopper	K.Wada, N.Hayano and H.Oka	79-84
● An Effect of the Dispersion State of Fillers on the Electric Conductivity of Composite Conductive Plastics	P.Lyoo, K.Terashita and K.Miyanami	140-145
● Dispersion and Conthnuum Models of Powder Elasticity	H.Okamoto	146-152
● The Production of Metal/Ceramics Composite Particles by a Mechanofusion Process	K.Tanno, T.Yokoyama and K.Urayama	152-158
● Relationship between Adhesive Force and Dispersibility of Sub-micron Particles	H.Yamamoto and S.Shioji	159-164
● The Effect of Surfactant on Ultra-fine Grinding done Simultaneously with the Surface Treatment of Magnetite Particles	K.Uchida, N.Asoo, H.Komizu, A.Goto, F.Ikazaki, K.Kamiya, M.Kawamura, S.Shimizu, and A.Tasaki	165-168
● Computer Simulation on Aggregated Structure of Fine Particles in Slurry	T.Kimura, M.Arakawa, K.Hirota and H.Murata	218-224
● Classification Mechanism of an Air Classifier Using Centrifugal Force (Part 3) —Effects of Air Folw Rate and Blade Attitude Angle on Cut Size—	Y.Sato, T.Nagamine and Y.Yamada	225-230
● Elutriation and Circulation in a Concave-Shaped Gas-Solid Fluidzed Bed	L.Wen and G.Huali	294-300
● The Measurement of the Size Distribution of Irregular Particles by Liguid-solid Fluidization in a High Reynolds Number	E.Obata, H.Takahashi M.Akiyoshi and K.Ando	301-307
● Flow Characteristics of Vibrating Powder Bed	M.Satoh, T.Shigemura F.Hamano, A.Fujimoto and K.Miyanami	308-314
● A Study on Size Measurement of Ultrafine Particles	H.Yamamoto and S.Shioji	372-376
● The Measurement of Extinction Coefficients of Mono-dispersed Spherical Particles by Monochromatic Light	M.Mizuno, J.Tsubaki and G.Jimbo	377-382
● Determination of Mean Particles Size by Diffuse Reflectance Fourier Transform Spectrometry	A.Tsuge, Y.Uwamino, T.Ishizuka and K.Suzuki	383-387
● Particle Size Analysis by Capillary Hydrodynamic Chromatography(C-HDC)	H.Yamamoto and T.Nomura	388-393
● Particle Size Analysis for Micro-Particles by Capillary Hydrodynamic Chromatography	N.Shiragami	394-398

Title	Author(s)	Page
● The Influence of Molecular Flow on the Specific Surface of a Fine Powder Measured by the Air-Permeability Method —Significance and Necessity of Modification—	A.Inagami, A.Suganuma and T.Hamada	399-403
● Effects of Reynolds Number and Aspect Ratio on the Deposition of Airborne Particles on a Quadrilateral Prism	K.Ushiki, S.Yuu and S.Hanatani	450-456
● Improvement of the Flowability of Particles by Dry Coating Method and Its Evaluation	K.Terashita, K.Umeda and K.Miyanami	457-462
● An Evaluation Model for Anisokinetic Sampling of Particle Concentration Measurement with Dusts Emitted from Stacks	M.Samata	463-469
● Alkoxylation of Surfaces under Ordinary Contact with Alcohols	S.Shioji and H.Yamamoto	470-475
● Flow Characteristics in a Horizontal Pneumatic Conveyance at Low Fluid Velocities(Part III) —Additional Pressure Drop and the Friction Factor—	M.Ochi	510-514
● Effect of the Powder Feed Rate and the Rotational Speed of the Impeller on the Performance of a Mixer-type Disperser	H.Masuda, S.Kawaguchi and K.Gotoh	515-519
● Flow Behavior of a Wet Particle Fluidized Bed	M.Nakajima, Y.Ota, R.Yamazaki and G.Jimbo	520-533
● Comparing Applicability of the Models to the Powder Reactoin Rate Controlled by a One-way Diffusion Process	A.Shimizu, Y.Hao and J.Saitou	526-589
● The Continuous Forming of Fine Powder into Small Granules by a Single Rotating Conical Vessel with Grinding —The Effect of Operating Conditions on Granule Size—	M.Sugimoto, N.Yokota, and M.Sugihara	590-596
● Time Dependence of Rheological Properties and Particle Aggregation Structure of Fine Particles in a Slurry	T.Kimura, and M.Nakamura	597-602
● Solution Chemistry and Interfacial Phenomena in an Aqueous, System Containing Plural Salt-type Minerals —Coexistence of Fluorite and Calcite—	M.Tsunekawa, E.Ogata, N.Habata, T.Takamori and T.Hirajima	603-608
● Discrimination of the State of the Surface of Modified Particles in a Liquid Medium by the Use of AC-Impedance	Y.Fujigara, Y.Yoshimura, H.Honda and M.Koishi	609-663
● Surface-treatment of the Ceramic Powders through Pulverization in a Reactive Atmosphere by Means of Ball Mill(2) —Pulverization of Al_2O_3 in a Reactive Atmosphere by Means of Ball Mill—	H.Utsugi, A.Endo, N.Suzuki, Y.Go and N.Baba	664-672
● Free Setting of a Cylindrical Particle in Stagnant Water	F.Saito, K.Arai and M.Kamiwano	673-679
● Analysis of Friction Properties of Non-Cohesive Mono-sized Granular Materials in Relationship to the Void Fraction	S.Nomura, F.Itoh and T.Tanaka	680-685
● On the Particle Cut Size of Cyclone Dust Collector(Part 1) —Imaginary Cone Model for Particle Cut Size and the Chracterisitics of the Spiral Flow through Cyclones of a Tangential Entry Type—	K.Ikemori	686-692
● Performance of a Three Dimensional Cen-	Z.Tanaka and K.Ito	739-742

Title	Author(s)	Page
trifugal Particle Size Classifier	and T.Takahashi	
● On the Particle Cut Size of Cylone Dust Collector(Part 2)	K.Ikemori	743-749
● Estimation of the Mean Particle Strength of a Single Particle by a Powder Compression Test	N.Yamada, E.Abe and H.Hirosue	792-796
● Solitonic Dynamics Applied to Information Processing in a Granular Medium	H.Okamoto	797-803
● Separation of Asbestos Flbers by Length —Procedure for Obtaining Different-length Samples for Biological Experiments—	T.Myojo and N.Kohyama	804-810
● The Effect of Additives on Size Reduction and Modification by Impact comminution(III) —In-situ Surface Modification of Fine Powdered Polypropylene—	E.Yamanaka, T.Tanaka K.Hamada and M.Senna	811-816

Funsai (The Micromeritics) No.35(1991)

Title	Author(s)	Page
● Preparation of Semiconductive SnO_2-Sb_2O_3 Fine Powder by Mechano-Chemical Reaction	F.Shiomi, M.Nakamura and T.Kimura	4-10
● Amethod for Detecting Small Vibration of Particle by LDV —Aiming at particle size and its electrostatic charge measurement—	Y.Nakajima, T.Sato and F.Saitow	11-20
● Dry Grinding of Calcite by a Impeller Rotating at High Speed in a Flat-bottom-baffled Vessel —Effects of impeller shapes and grinding aids—	M.Kamiwano	21-31
● Particle Size Classification by a Centrifugal Air Classifier under Reduced Pressure	I.Aoki and T.Matsuyama	32-44

Kagaku Kogaku Ronbunshu Vol. 16 (1990)

Title	Author(s)	Page
● Mixing Characteristics and Optimum Condition of a Horizontal Gas-Solid Agitated Vessel with Paddle-Blades on Double Parallel Axes	T.Tenda, M.Takao, S.Komori and Y.Murakami	64-68
● Analysis of Gas Flow in a Solid-Gas Cross Flow Moving Bed by the Finite Element Method	H.Takahashi, O.Ohno and T.Takeuchi	116-244
● Behavior of Particle Flow Dynamics in Model Apparatus of Pilot Scale Swirling Entrained Bed	A.Morihara, S.Koyama and S.Nogita	245-251
● Morphology of Particle Agglomerate on a Fiber in Air Filter	S.Hiragi, C.Kanaoka and K.Yamada	251-258
● Mechanism of Low-Temperature Synthesis of Carbon Films by Photo Enhanced Chemical Vapor Deposition	T.Yasuda and H.Komiyama	259-497
● Production of Polycrystalline Silicon from Monosilane in a Fluidized Bed —Clogging, particle growth and fines formation in SiH_4/Ar system—	T.Kojima, H.Hiroha, K.Iwata and T.Furusawa	498-506
● Preparation of AIN Fine Particles by Gas-Phase Reaction	S.Chiba, S.Honma,	507-511

Title	Author(s)	Page
in an Ultrasonic Field	Y.Oyama and K.Shinohara	
● Formation of Carbon Whiskers by Pyrolysis of Benzene under Gas Phase	M.Matsumoto, T.Hashimoto, K.Murata and S.Goto	512-518
● Vapor-Phase Formation of Ultrafine Particles of Si and Ge Oxides	K.Ueyama, K.Ohta, N.Kohno, A.Jino, H.Kawazoe, Y.Matsuda, and S.Furusaki	519-525
● Evaluation of Fine Particle Formation by CVD in Laminar-Flow Aerosol Reactor	K.Okuyama, R.Ushio, Y.Kousaka, J.H.Seinfeld and R.C.Flagan	526-534
● Experimental Control of Preparation of Thin Film and Fine Particles by CVD	K.Ohshima, Y.Torimoto, K.Tsuto, K.Okuyama, R.Ushio and Y.Kousaka	535-542
● Preparation of Composite Ceramic Particles by Gas-Phase Reactions in Fluidized Bed	A.Kobata, T.Okubo, K.Kusakabe and S.Morooka	543-550
● Particle Size Control of TiO_2 Ultrafine Particles by CVD Method	K.Kashima and H.Sugiyama	551-556
● Numerical Analysis of Particle Growth Zone in Diffusion Mixing CVD Reactor	K.Sunouchi and H.Komiyama	557-563
● Particle Formation from Polymer Emulsion under Slow Coagulation Condition	T.Iwasaki, K.Momose and H.Sakabe	627-685
● Production of Polycrystalline Silicon from Monosilane in a Fluidized Bed – Effects of diluent properties on gas conversion and properties of produced silicon –	T.Kojima and O.Morisawa	686-693
● Continuous Kneading of EMI Shield Material and Its Evaluation	K.Terashita, Y.Mizuno, P.J.Lyoo and K.Miyanami	715-722
● Minimum Spouting Velocity and Peak Pressure Drop in Spouted Beds	F.Ogino, L.Zhang and Y.Maehashi	788-795
● Optimal Allocation of Sensors for Identification of Faulty Sensors	J.Chen and H.Matsuyama	796-804
● Vibration Milling Using Rod Media	M.Hasegawa, T.Honma and Y.Kanda	805-811
● Design of Photochemical Converter of Solar Energy with Semiconductor Electrodes	R.Ito, Y.Inoue and M.Hayamizu	812-819
● Numerical Analysis of the Mixing Process for High Viscosity Pseudoplastic Liquids in Mixers with Various Plate Types of Impeller	M.Kaminoyama, F.Saito and M.Kamiwano	820-829
● Instantaneous Measurement of Particle Size and Flow Rate by the Parameters of Impact Sound between Particles and a Circular Plate	J.Hidaka, A.Shimosaka, H.Ito and S.Miwa	1067-1073
● Effect of Size Distribution on Compressive Property of Fine Powders	M.Suzuki, Y.Nakatsuji, M.Hirota and T.Oshima	1074-1079
● Electrical Conductivity of Suspensions of Binary Particle Mixtures	M.Furuuchi, T.Fukagawa, Y.Suzuki and K.Gotoh	1080-1086

Hosokawa Micron Corporation presents two new products.

□ ECOPLEX Fine Grinding System —High Compression Roller Mills—

ECOPLEX is the latest high compression roller mills, and was developed by ALPINE AG (Germany), a member of Hosokawa Micron Group. ECOPLEX gives the new, highly economical size reduction technology.

For brittle materials, regardless of whether hard or soft, the technology of size reduction is undergoing a major change.

"Fine size reduction under high presure" with high compression roller mills is grainding increasingly in importance.

Especially with brittle, hard materials, and when ultrafine powders are demanded the systems provide impressive increases in throughput, savings in energy, and drastic reductions in wear costs. ECOPLEX Fine Grinding systems have already found many applications in Eupore.

Features

- Increases in throughput up to 50% and energy savings up to 30%.
- Low wear size reduction even with hard materials.
- Low noise emission due to quiet running.
- Compact construction permits the integration into existing systems, even when space is at a premium.

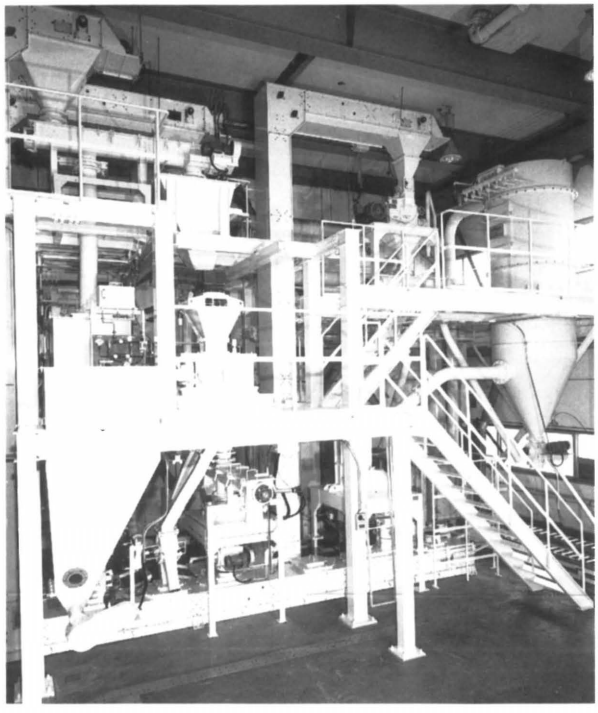

□ New Model Powder Characteristics Tester PT-N

The Powder Characteristics Tester PT-N has been developed to improve handing, efficiency and accuracy in testing the bulk properties of powders.

Measuring such properties has great importance in the design of powder processing equipment.

Analyzing such characteristics is also a daily routine for quality control of powdered products.

The Powder Characteristics Tester provides seven measurements with a single unit.

Mechanical Measurements
① Angle of repose
② Compressibility
③ Angle of spatula
④ Cohesiveness
⑤ Angle of fall
⑥ Dispersibility
⑦ Angle of difference

Supporting Measurements
① Aerated bulk density
② Packed bulk density
③ Uniformity

Features of the PT-N

- Provides seven mechanical measurements and three supporting measurements with a single unit.
- A newly introduced dialog display (LCD) panel assures easy operation.
- Prints measurements and calculated data.
- A clear plastic enclosure covers the front of the unit, and a built-in vaccuum cleaner keeps the work enviroment dust free.
- RS232C port can connect the unit to personal computers for data communication.

HOSOKAWA MICRON

LEADERS OF POWDER PROCESSING TECHNOLOGY, ENVIRONMENTAL SYSTEMS, FILTER MEDIA AND PLASTIC PROCESSING SYSTEMS.

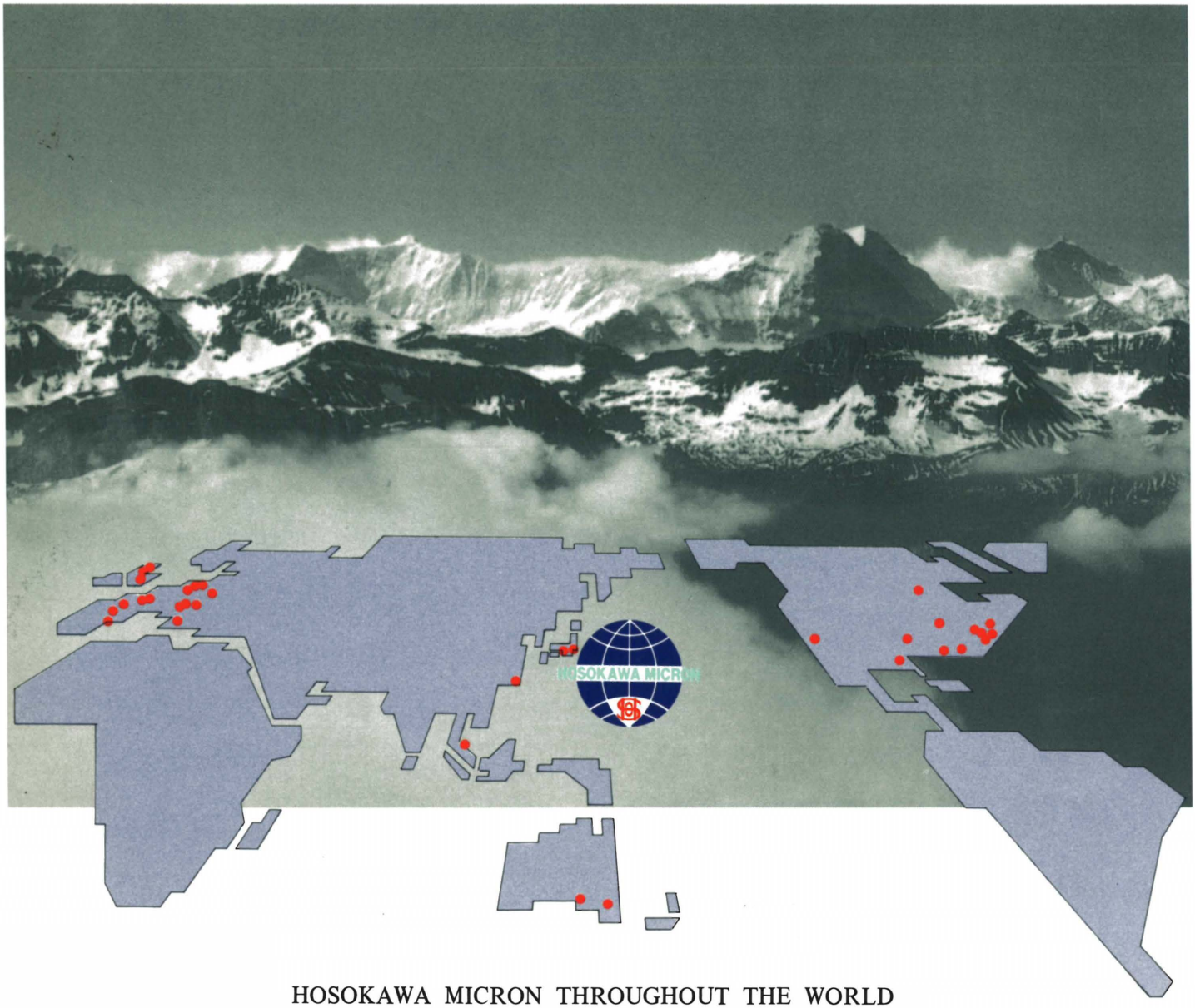

HOSOKAWA MICRON THROUGHOUT THE WORLD

Asia/Australian Block
Hosokawa Micron Corporation
5-7, 3-chome, Hommachi, Chuo-ku, Osaka 541, Japan
Telephone: 06-263-2555 Fax: 06-263-2552

Americas Block
Hosokawa Micron International Inc.
780 Third Avenue, New York, NY10017, U.S.A.
Telephone: 212-826-3830 Fax: 212-826-6612

European Block
Hosokawa Micron International BV.
World Trade Center, Strawinskylaan 249,
1077XX Amsterdam, Holland
Telephone: 020-673-5571 Fax: 020-676-2061